UNIVERSITY *of* TASMANIA

School of Physical Sciences

H I Absorption in the Fourth Galactic Quadrant

Courtney Brown

June 2015

Supervisors:
Prof. John Dickey
Dr. Joanne Dawson

Submitted in fulfilment of the requirements for the Degree of
Doctor of Philosophy

Declaration of Originality

This thesis contains no material which has been accepted for a degree or diploma by the University or any other institution, except by way of background information and duly acknowledged in the thesis, and to the best of my knowledge and belief no material previously published or written by another person except where due acknowledgement is made in the text of the thesis, nor does the thesis contain any material that infringes copyright.

Signed:

Date: 17/06/15

Authority of Access

The publishers of the papers comprising Chapters 3, 4 and 5 hold the copyright for that content, and access to the material should be sought from the respective journals. The remaining non published content of the thesis may be made available for loan and limited copying and communication in accordance with the Copyright Act 1968.

Signed: _____

Date: 17/06/15

Statement of Co-Authorship

The following people contributed to the publication of work undertaken as part of this thesis:

Candidate	Brown (nee Jones), C.	University of Tasmania, CSIRO Astronomy & Space Science
Co-Author 1	Dickey, J.M.	University of Tasmania
Co-Author 2	Dawson, J.R.	University of Tasmania, CSIRO Astronomy & Space Science, Macquarie University
Co-Author 3	McClure-Griffiths, N.M.	CSIRO Astronomy & Space Science
Co-Author 4	Anderson, L.D.	West Virginia University
Co-Author 5	Bania, T.M.	Boston University

Chapter 3: *Kinematic Distance Assignments with* H I *Absorption*
Candidate (85%), Co-Author 1 (15%)
Candidate was the primary author and with Co-Author 1 contributed to the idea, its formalisation, development and refinement. Writing was done primarily by the Candidate, with some paragraphs and feedback provided by Co-Author 1.

Chapter 4: H I *Absorption toward* H II *Regions at Small Galactic Longitudes*
Candidate (80%), Co-Author 1 (10%), Co-Author 2 (5%), remaining Co-Authors (5%)
Candidate was the primary author and with Co-Authors 1 and 2 contributed to the idea, its formalisation, development and refinement. Writing was done primarily by the Candidate, with some paragraphs provided by Co-Authors 1 and 2. Feedback and editing for the purposes of publication was provided by the remaining authors.

Chapter 5: *A Complete Atlas of* H I *Absorption toward* H II *Regions in the Southern Galactic Plane Survey (SGPS I)*
Candidate (85%), Co-Authors 1, 2 and 3 (15%)
Candidate was the primary author and with Co-Authors 1 and 2 contributed to the idea, its formalisation, development and refinement. Writing was done primarily by the Candidate. Feedback and editing for the purposes of publication was provided by the Co-Authors 1, 2 and 3.

Signed _____ _____

Date:_____ _____

Prof. John Dickey, Primary Supervisor
School of Physical Sciences, University of Tasmania

Abstract

The position of the Sun, within the Milky Way, prohibits us from observing our Galactic system as a whole. Our knowledge of the structure of our Galaxy has increased dramatically; however, there is still no consensus on many seemingly simple questions. Primarily, How many spiral arms does the Milky Way have?, Where are they? And, What's on the far side of the Galactic center?

Galactic H II regions are the formation sites of massive OB stars. Because the main sequence lifetimes of OB stars are short - only ∼tens of millions of years - they thus reveal the locations of current star formation sites. They are therefore found only in locations of active star formation, primarily the spiral arms; H II regions are therefore the archetypal tracers of Galactic spiral structure.

The systemic velocity of each H II region, from an observed radio recombination line (RRL), can be applied to a Galactic rotation model in order to calculate the kinematic distance to the region. In the inner Galaxy, line of sight distances are bi-valued such that a single systemic velocity corresponds to two line of sight distances equidistant to the sub-central (tangent) point. Kinematic Distance Ambiguity Resolutions (KDARs) can be made via an analysis of neutral hydrogen (H I) absorption towards each region.

We determine a modification of the terminal-velocity KDAR method which investigates H I absorption in velocity channel intervals, rather than in single channels. In addition, we use H I absorption associated with known Galactic structures (in longitude-velocity space) to provide lower-limits on line of sight distances. In this manner we are able to constrain the line of sight distance to over 200 H II regions; including regions located in the extreme inner Galaxy.

We also compile a complete census of HII regions with known RRL velocities, taken from the literature - and the H I emission/absorption spectrum pairs toward them – within the bounds of the Southern Galactic Plane Survey; a total of 252 regions.

As the result of this work, the list of known fourth quadrant H II regions for which a KDAR analysis has either been prepared for, or attempted, is now exhausted – comparable to the northern hemisphere at the conclusion of Anderson & Bania (2009). This exhaustion of candidates in the northern hemisphere was overcome through the undertaking of large-scale HII region discovery surveys. The results of which more than doubled the number of known HII regions within the surveyed longitude range – reinvigorating HII region kinematic distance studies in the northern hemisphere.

Following the candidate selection strategies of the northern surveys, we perform a pilot HII region discovery survey in the southern hemisphere. Using the Australia Telescope Compact Array we confirm 28 H II region candidates as genuine regions for the first time.

As a result of these analyses, we have made the largest study of H I absorption towards H II regions in the fourth Galactic quadrant ever performed – as well as providing datasets for future works.

Acknowledgements

I was extremely lucky to be able to complete this particular PhD project. Firstly, because I was able to continue the topic of my Honours research; and secondly (as well as most importantly), a suite of data products and international surveys would be completed (seemingly) just in time to inform, and direct, the next stage of my work. As a result, I was able to 'launch' myself into research that reflected works completed for the Northern Hemisphere, but were positioned in the (relatively) unstudied Southern skies.

In addition to the succession of world class data I've been able to work with; my supervisory team has also provided a strong foundation of support, scientific rigour, and confidence in my ability. John, a stalwart of ISM astronomy, is ever eager to view a new plot or soundboard a data analysis idea. Without his guidance and support, this thesis would not exist. Simon Ellingsen, while no longer a formal member of my supervisory team, has always provided assistance and has an ever-open door. More recently, Jo has provided an exceptional role model of an early-career researcher. Her dedication to astronomy, and attention to detail is unfailing. Thank you also to Karen—for everything.

My office mates have also left their mark on this thesis. Paul, Vassant and Dave have made the whole PhD (well, whole tertiary) journey much more joyous. I love being part of such a dynamic department—where astronomers, fluid dynamicists and particle physicists can share a workspace. Combined with the guys next door (Anita, Jay and Chris), we've shared too many laughs, beers, songs and memories to recount.

Milly and the Pub Day Crew (who bet me I'd never mention them in my PhD thesis) have also made the last seven years of university much more fun, and caffeinated. Thanks also to the Bandies who continue to provide the opportunity to blast some Shostakovich or Maslanka after a long day of data reduction.

I am also indebted to my family, and new In-Laws, who have remained committed to my work (even when I wasn't sure what to do next). My Mother, Carol, never faltered when her fourteen year old daughter came home from school and announced that she wanted to be an astrophysicist. Eleven years later, her support remains resolute. Greg and Sue, who together have committed decades to education in Tasmania, have also fostered two concurrent PhDs 'in the household'—a task which completely boggles my mind.

Finally, it is Dan that gets the greatest share of my thanks. No one has had more first hand experience of dealing with a tired and grumpy observer after an overnight LBA run or fortnight at Parkes (let alone on a normal day!). Above all, Dan has encouraged my studies, even when it meant living 1677km—approximately one Lunar radius—apart. I look forward to the next chapters of our lives, proud in the knowledge that we can achieve anything we put our minds to.

Contents

List of Figures

List of Tables

List of Equations

Chapter 1

Introduction

The structure of our own Galaxy remains an active area of research—impeded by our location *within* the system. The Sun's position, about two-thirds of the way from the centre, allows for a quasi-complete 'edge–on' view of our Galaxy; however a 'face–on" view is, as yet, incomplete.

It is now sixty years since the first observations of the 21cm neutral hydrogen spin-flip transition—and ninety years since the realisation that the Milky Way is a separate galactic system. Our knowledge of the structure of our Galaxy has increased dramatically; however, there is still no consensus on many seemingly simple questions. Primarily, *How many spiral arms does the Milky Way have?*, *Where are they?* and *How did they come to be?*

1.1 The Discovery of the Milky Way: 1734–1924

Astronomy has been practised, in one form or another, since before recorded history. Knowledge of celestial phenomena and patterns was used for the creation of calendars, determination of the seasons, and navigation. However, the idea of galaxies is relatively modern.

In the early eighteenth century, Thomas Wright speculated that many visible nebulae were systems separate to our Galaxy (see Figure 1.1):

> *That this in all Probability may be the real Case, is in some Degree made evident by the many cloudy Spots, just perceivable by us, as far without our starry Regions, in which tho' visibly luminous Spaces, no one Star or particular constituent Body can possibly be distinguished; those in all likelihood may be external Creation, bordering upon the known one, too remote for even our Telescopes to reach. (Wright & Hoskin 1734)*

This multi-galaxy ideal, dubbed the 'island-universe' theory, was further developed by Immanuel Kant in 1775; although the term itself may have first been coined by von Humboldt in *Kosmos* (1850), which itself was presented for the first time in an English translation as "world islands". The theory of 'island universes' continued to be speculated upon by philosophers, but astronomers themselves did not participate largely in these discussions (Hubble 1936).

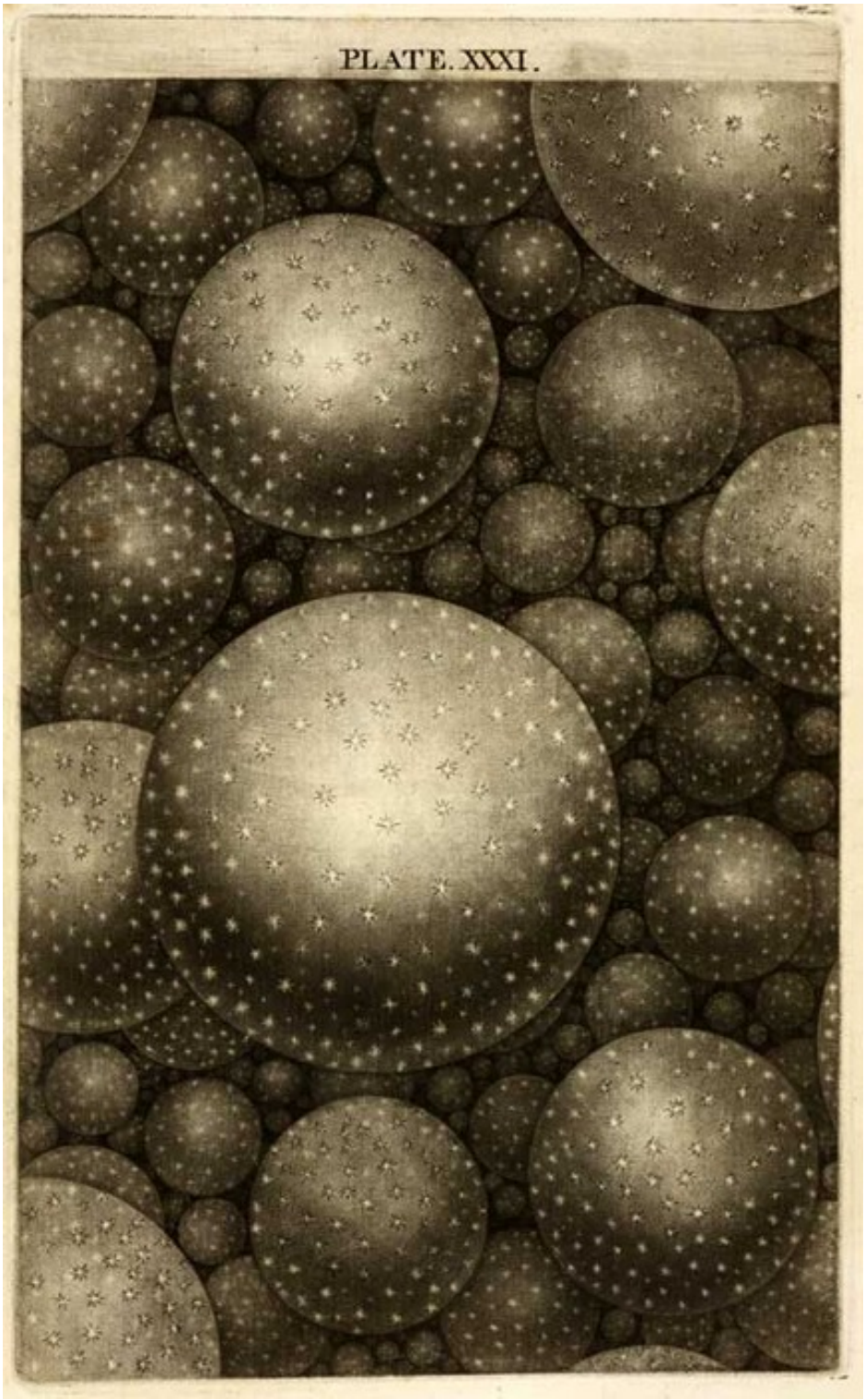

Figure 1.1: From Wright & Hoskin (1734) Plate XXXI. *Which you may if you please, call a partial view of immensity, or without much impropriety perhaps, a finite view of infinity, and all these together, probably diversified*

1.1.1 Early Maps of the Milky Way

Figure 1.2: Figure 4 from Herschel (1785): *From this figure however, which I hope is not a very inaccurate one, we may fee that our nebula, as we obferved before, is of the third form; that is: A very extenfive, branching, compound Congeries of many millions of ftars.*

William Herschel—who discovered Uranus; moons of Uranus and Saturn; infrared radiation from sunlight as well as composing twenty-four symphonies and other musical works—was an original proponent of the single-galaxy theory. Along with his sister, Caroline, Herschel documented nebulae and star clusters, publishing the first edition of the *Catalogue of One Thousand New Nebulae and Clusters of Stars* (Herschel 1786)*.

In an effort to characterise "the construction of the heavens", William Herschel embarked on a campaign of 'star gauging' observations—counting the number of stars in over 600 directions on the sky. Three assumptions were critical to this endeavour: firstly, that all stars had a similar intrinsic luminosity†, secondly, that the distribution of stars was uniform throughout the system, and finally, that the telescopes could see through the entire siderial system (Hoskin 1989). Therefore, if there were many stars along a line of sight, the edge must be very distant—conversely, a small number of stars visible to any direction on the sky must infer that the edge of the system was closer.

Figure 1.2 became the first attempt to describe the shape of the Milky Way. The Sun (depicted in Figure 1.2 as the darker star) was placed *"perhaps not in the very centre of its thickness……in one of the great strata of the fixed stars, and very probably not far from the place where some smaller stratum branches out from it."*(Herschel 1784).

Despite Herschel, himself, reconsidering the uniform distribution of stars in the Milky Way—and recognising that it was likely that his telescope could not see to the edge of the stellar system (further discussed in Proctor 1880; Paul 1993)—Figure 1.2 remained the standard representation of the Milky Way over sixty years after it was first published (Belkora 2003). Friedrich Georg Wilhelm von Struve, who along with Friedrich Bessel had begun

*Further iterations of the catalogue were continued by Herschel's son, John, and the catalogue was the principal precursor to John Dreyer's *A New General Catalogue of Nebulæ and Clusters of Stars, being the Catalogue of the late Sir John F. W. Herschel, Bart, revised, corrected, and enlarged* (Dreyer 1888), now known as the New General Catalog.

†Despite the fact that his own research into binary star systems suggested that brightness did not directly represent distance (Paul 1993)

stellar parallax measurements, returned to the question of Galactic structure in his *Etudes* (Struve 1847); combining subsequent generations of Herschel star counts with parallax measurements to refine and reform Figure 1.2.

Profoundly, Struve suggested an absorbing medium must exist within the stellar system; noting that Herschels' star counts should have discovered many more faint (distant) stars. Still bounded by the assumption that all stars shared a single luminosity, Struve provided a mathematical function to describe the density of stars within parallel planes of the Milky Way. The *Etudes*, written in French, were highly regarded by John Herschel and George Airy. However, Johann Encke, director of the Berlin Observatory was extremely critical of Struve's statistical approach, commenting *"It appears to me of great importance for astronomy that the assumptions and parallaxes of the* Etudes *do not get into our astronomical and popular writings"* (Encke 1848, cited in Belkora 2003).

John Herschel eventually rejected the method of star gauging, believing nebulae (rather than individual stars) to be the most important cosmological 'observational unit'. Using a twenty-foot reflecting telescope with eighteen inch mirrors, John Herschel described the morphology of M51; a bright central region, surrounded by a ring of stars (see top of Figure 1.3). He suggested the Milky Way may have a similar ring-like structure (Paul 2006).

In 1845 the Birr Castle six foot aperture reflecting telescope, named the "Leviathan of Parsonstown", was also used to observe M51 (see bottom of Figure 1.3). The unprecedented resolving power of this *gigantic telescope*[*] (as described by Airy 1848) provided the first evidence of spiral structure in a distant nebula.

The main goal of these observations was not to investigate structure; but instead to establish whether individual stars could be resolved within distant nebulae; which would then imply separate stellar systems. In a review of these early observations, Bailey et al. (2005) comment, *"It is conceivable that none of the [astronomers] would have found the spiral arrangement worthy of note."* Through the popularisation of observations of distant nebulae, combined with the advent of photography, it became evident that spiral structure was more common than first supposed. These observations of separate spiral nebulae provided evidence for 'separate Milky Ways' and furthered the island universe (multi-galaxy) theory.

A ring morphology, prompted by John Herschel's observations of M51, could be supported by single and multi-galaxy proponents alike; and was therefore further developed by astronomers around the world. Richard Proctor, for example, argued that the resolution of stars within distant nebulae provided unrefutable evidence that they were located within our galactic system; as even the most powerful telescopes could not hope to penetrate the entire extent of the galactic zone.

Proctor's ring model (top of Figure 1.4) was influenced by naked-eye observations of the band of the Milky Way across the night sky. The Sun was in the centre of the system, in a region which was particularly void of stars; whereas the band of the Milky Way, composed

[*]The telescope remained the world's largest aperture telescope from its erection in 1845 until 1917 (Belkora 2003)

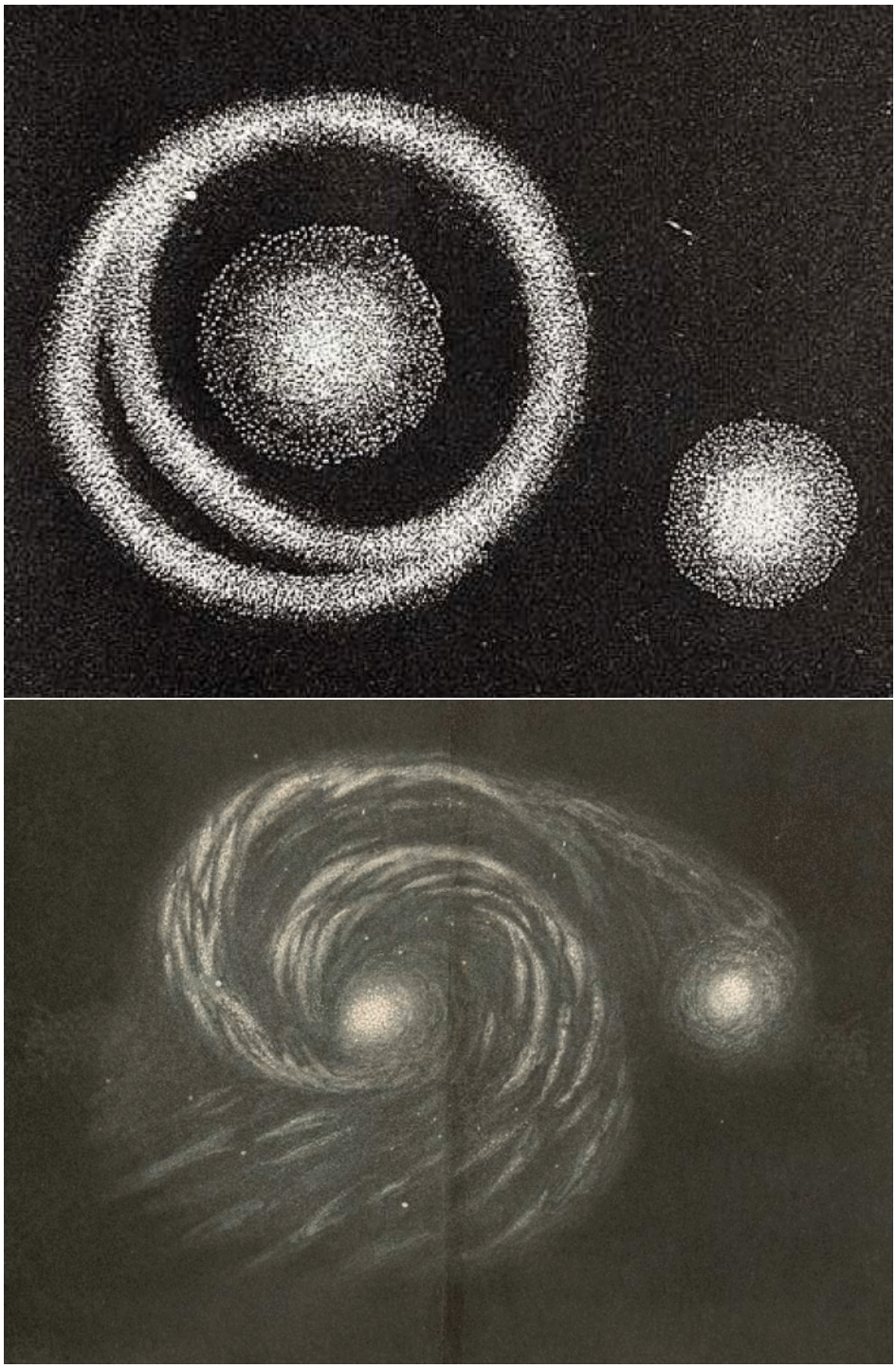

Figure 1.3: Observations of M51 as stetched by John Herschel, using 18 inch mirrors in 1828 (top); and Lord Rosse, using the six foot aperture telescope in 1845 (bottom). Both images are published as plates in Nichol (1846).

of stars and star clusters constituted *"a belt or zone of stars, separated from us by a comparatively starless interval"* (Bickerton 1879). This model required the existence of variation in luminosities across the stellar distribution, in contrast to the assumptions made by the Herschels. This in itself was not a new idea, vast differences in size and *splendour* had already been measured in binary, and other multiple, star systems (Proctor 1902).

Stephen Alexander, an astronomer at Princeton, proposed a modification to Proctor's ring model; that *"the Milky Way and the stars within it constitute a spiral with several (it may be four) branches and a central (probably spheroidal) cluster"* (Alexander 1852). Placing the Sun at the centre of the system, Alexander based his model on the grouping of known clusters and nebulae—which was not as uniform as a ring—and was in keeping with the growing number of observed spiral nebulae. Proctor also presented a spiral-like morphology for the Milky Way, but doubted that any single spiral with branch structure (bottom of Figure 1.4) would best describe the entire Galactic system as had so far been observed. Cornelius Easton, recognising the ever increasing number of observed spiral nebulae, also presented a spiral structure for the Milky Way. However, he, like Proctor, noted that it was not reckoned to be approximately correct (Easton 1900).

Further investigations and descriptions of the Galactic system were offered by various authors, perhaps the largest contribution being that of Jacobus Kapteyn. Over 120 years after Herschel's map (Figure 1.2), Kapteyn initiated a major study of the Galactic distribution of stars (Figure 1.6). The project involved forty observatories and resulted in the *First Attempt at a Theory of the Arrangement and Motion of the Sidereal System* (Kapteyn 1922), which described the Milky Way as a flattened ellipsoid, about 10 kiloparsecs in size, with the Sun located approximately 650 parsecs from the centre of the Galaxy.

These early maps of our Galaxy all suffer from a lack of understanding of interstellar absorption, at optical wavelengths, due to dust. For example, Kepteyn couldn't observe stars that were more than about 10 kpc away due to the fact that their light was completely extinguished by absorption in the intervening medium. Others, observing clusters of stars or distant nebulae (with total luminosities much greater than a single star), could observe to greater distances; but did not account for the absorption of light—resulting in overestimates of the dimensions of our Galaxy.

1.1.2 The Great Debate

In 1872 Richard Proctor remarked, *"the Copernicus of the sidereal system is not to be expected for many generations"* (Proctor 1872). At the beginning of the twentieth century, nearly a century after William Herschel's death, two conflicting ideas on the shape of the Universe persisted. The theories can be succinctly condensed into two camps of thought; those belonging to the prominent astronomers Harlow Shapley and Herber Curtis.

The most progressive step in understanding Galactic structure would take place at a debate at the Smithsonian Museum of Natural History on 26 April, 1920; in what is now termed the Shapley-Curtis, or Great Debate.

The importance of this event is summarised in the introductory text *The Physical Universe: An Introduction to Astronomy*:

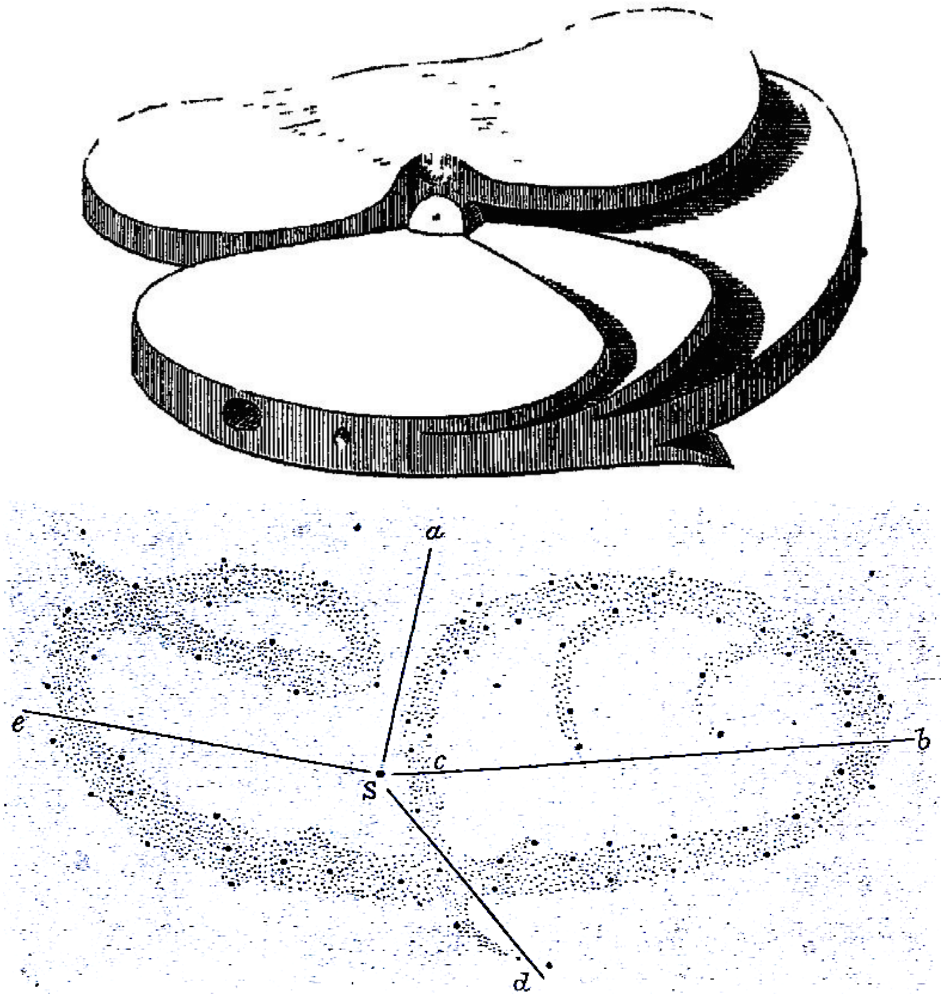

Figure 1.4: Figures 4 and 5 (colours inverted) from Proctor (1902). Top: Galactic flat ring, modified to account for observed peculiarities in the Milky Way - the structure preferred by Proctor. Bottom: one of several spiral curves which could account for the observed stellar system.

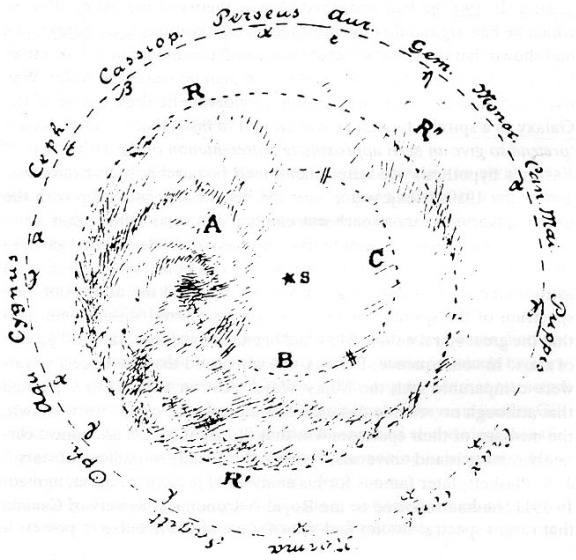

Figure 1.5: Figure 6 from Easton (1900): *I wish to insist upon the fact that Fig. 6* does not pretend to give an even approximate representation of the Milky Way*, seen from a point in space situated on its axis. It only indicates in a general way how the stellar accumulations of the Milky Way might be distributed so as to produce the galactic phenomenon, in its general structure and its principal details, as we observe it.*

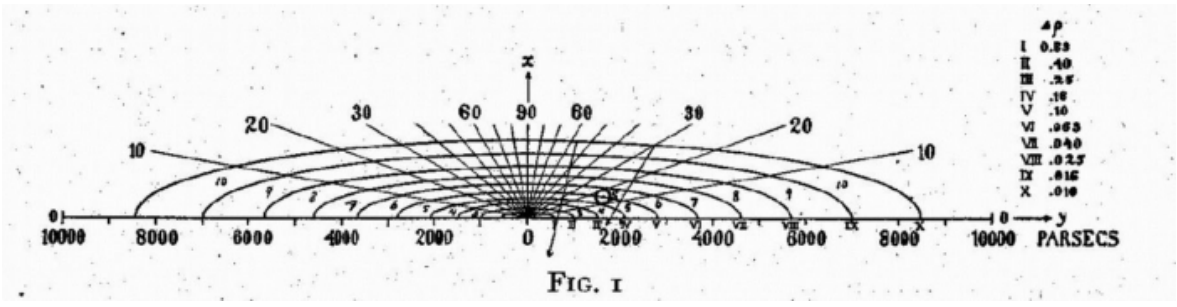

FIG. 1

Figure 1.6: Figure 1 from Kapteyn (1922): *A section of equidensity-ellipsoids through the sun (which has been assumed to be the center of the system) at right angles to the plane of the Milky Way.*

> *The Shapley–Curtis debate makes interesting reading even today. It is important, not only as a historical document, but also as a glimpse into the reasoning process of eminent scientists engaged in a great controversy for which the evidence on both sides is fragmentary and partly faulty. This debate illustrates forcefully how tricky it is to pick one's way successfully through the treacherous ground that characterizes research at all the frontiers of science. (Shu 1982)*

The Debate nearly did not take place, due to a number of political and personal factors (reviewed by Smith 1985). These included Shapley's cautiousness at confronting Curtis, an experienced public speaker, while presenting for the then vacant position of Director of the Harvard College Observatory; and as other topics, including vivisection, or a discussion of oceanography by the Prince of Monaco, had also been suggested for the meeting. Smith (1985) add that it was only during friendly post-Debate correspondence that each side fully comprehended the other's arguments. Indeed, Shapley later commented, *As for the actual 'debate', I must point out that I had forgotten about the whole thing long ago, and no one had mentioned it to me for many years. Then about eight or ten years ago, it was talked about again. To have it suddenly come up as an issue, and as something historic, was a surprise, for at the time I had just taken it for granted. Curtis was right partly, and I was right partly."* (Shapley 1968).

1.1.2.1 Shapley's Model

Shapley argued that the dimensions of the Milky Way were immense, so large in fact that all known nebula must be contained within, such that the universe contained only one Galaxy. The dimensions of Shapley's Milky Way—a disk of approximately 300,000 light years (∼92 kpc) in diameter[*]—were based on observations of globular clusters; which he believed were tens to hundreds of thousands light years distant (Shapley 1918). Despite other astronomers finding evidence of reddening towards distant stars, Shapley measured the distance to the Hercules Globular Cluster (M13) as 100,000 light years[†] in 1915 and found no evidence of reddening. He recommended, and Kapteyn agreed, that any extinction or reddening effects could be ignored for stars within the Galaxy (Smith 1985).

Further evidence for the huge dimensions of the Shapley model included erroneous interpretations and measurements of Andromeda. First, two supernovae (SN 1885 A and SN 1895 B) were observed in Andromeda and NGC 5253 respectively. If Andromeda was indeed another galactic system, the supernovae must possess the unprecedented and unimaginable luminosity of a billion suns[‡]. It was much more reasonable, therefore, to deduce that the nebulae were contained within the Milky Way system, and that the (at that time unknown) supernova were standard nova explosions well known to astronomy.

The 1885 supernova reinvigorated studies of Andromeda. In 1887 Isaac Roberts interpreted photographs of the spiral as a "solar system in the process of condensation from a nebula" with the (super)nova described as planets. Finally, and perhaps the most incorrect,

[*] approximately two to three times as large as the current estimate

[†] too far by a factor of five; he also over-estimated the cluster's linear diameter by a factor of 20 (Sandage et al. 2004)

[‡] We now understand that supernovae have luminosities on the order of $10^{10} L_{\odot}$.

Karl Bohlin, presented the parallax distance measurement for Andromeda as just 19 light years* (Bohlin 1907).

Similar erroneous measurements, by the well respected Adriaan van Maanen, included photographic "evidence" of rotation in the Pinwheel Galaxy (M101) at a rate of 0.02 seconds of arc per year (Clark 2004). After scaling to a position outside the Milky Way, these rotation velocities would exceed the speed of light—hence, M101 and other such nebula must be located within the Galactic system (Croswell 1999).

Along with the differences in the overall size of the Galaxy, the other major defining factor of Shapley's model was the position of the Sun; about half way from the centre of the system. Shapley correctly assumed that the centre of the galactic system was located towards Sagittarius, due to crowding of globular clusters in that direction.

Shapley's Milky Way addressed many of the incumbent problems of galactic astronomy. The model was received with eagerness from some, and outright hostility from others. Walter Baade remarked that he admired the way *"Shapley finished the whole problem in a very short time, ending up with a picture of the Galaxy that just about smashed up all the old school's ideas about galactic dimensions. It was a very exciting time, for these distances seemed to be fantastically large, and the old boys did not take them sitting down"* (Baade & Gaposchkin 1963).

1.1.2.2 Curtis' Model

Curtis' model placed the Sun at the centre of the Milky Way; which in turn was one in a multitude of galaxies. Curtis also argued that distant 'spiral nebulae' were in fact spiral galaxies, just like our own. During the Debate, while Shapley focused on the size of the galactic system, Curtis concentrated on the question of island universes (Crowe 1994).

Unlike Shapley, Curtis argued that the existence of *occulting matter* could not be ignored; indeed there were many examples of edge-on spiral nebulae exhibiting a *"dark lane down centre"* (Hoskin 1976). Furthermore, Curtis argued, that dust in the Milky Way's disk could account for the high galactic latitutde bias for spiral nebulae (Croswell 1999).

As Alexander, Proctor and Easton had done; Curtis combined the existing, limited, evidence for ring, or spiral, structure within the Milky Way with observations of distant spiral nebulae. He argued that several spiral nebulae produced spectra typical of star clusters, practically indistinguishable from the plane of the Milky Way—and therefore, they must constitute systems of stars, even if the stars could not be resolved with current telescopes (Curtis 1920).

While Shapley had argued that the 1885 and 1895 supernovae were examples of ordinary nova, Curtis suggested that they represented a different phenomenon. All other observed novae were much fainter, and generally, were proposed as a distance indicator to other spiral nebulae (Hoskin 1976).

He calculated that the dimming of nova seen in photographic plates of spiral nebulae suggested distances on the order of 20 million light years† (Hoskin 1976). Furthermore, if

*current estimates are on the order of 2.5 million light years (Karachentsev et al. 2004)

†This estimate is the average distance calculated from about 26 novae; including novae in NGC 4321, NGC 6946 and NGC 4527 which have modern day distance estimates on the order of 20-50 million light years

the Milky Way was located at these great distances, it would appear about 10 arcminutes in diameter; the same size that many spiral nebulae appeared on the sky (Curtis 1917).

In 1921 Curtis summarised his model of general structure of the galaxy (Shapley & Curtis 1921, a *Bulletin of the National Research Council* in which both Shapley and Curtis presented papers):

1. The stars are not infinite in number, nor uniform in distribution.
    - Our galaxy contains (possibly) a billion suns.
    - A large proportion of these stars are probably within the ring structure suggested by the appearance of the Milky Way, or are arranged in large and irregular regions of greater star density.
2. The galaxy is shaped much like a lens, the thickness being less than one-sixth of the diameter.
3. Our Sun is located close to the centre of our galactic system.
4. A spiral structure has been suggested for our galaxy, but the evidence for such a structure is not very strong (except by the analogy of spiral nebulae). However, a spiral structure is neither impossible nor improbable.

1.1.2.3 Hubble's Reliable Distance Measure

The Great Debate highlights the lack of consensus in early 1920 on the size, composition or structure of our Galaxy. Nor was their any agreement as to the best method for resolving these problems. Shapley and Curtis had exchanged cordial correspondence both before, and after the Great Debate. But it was only after the event, that both sides "got to grips with each other's arguments"(Smith 1985).

Edwin Hubble is famously credited for resolving the Great Debate, albeit some four years later, through the discovery of a cephid variable star in Andromeda. This discovery allowed for a reliable distance to the nebula to be calculated ($\sim$ 1 million light years*, Hoskin 1976); and the existence of external galaxies therefore proved. These results were first published in the New York *Times*, and then in Hubble (1925). This work led to the Hubble 'tuning fork' sequence of galaxy classification (Hubble 1926) and within a few months, the first investigations into relativistic cosmology had taken place.

I present this historical overview, not to provide a detailed review of nineteenth century astronomy— Trimble (1995); Paul (1993) and Oort (1972) provide excellent reviews of the nature of the Galactic system leading up to, and including, the Great Debate—but to emphasise two important factors:

*much closer to present day estimates than the Bohlin estimate

- the importance of distance data; both in the reliability of any distance measurements, and in the number of tracers with reliable distance calculations or constraints:

  This thesis is primarily a collection of distance measures, to Galactic structure tracers, of various reliabilities. While we have extended our knowledge well beyond the catalogues of stars and nebulae collected by the Herschels, and now understand at least some of the parameters and properties of the optical wavelength absorbing interstellar medium (ISM); *"the challenge [remains] to refine distances to spiral arm tracers and to minimise their uncertainties (Foster & Brunt 2014)."*

- to remind the reader that our understanding of the Milky Way as a separate galactic system has pervaded for only ninety years.

1.2 Large Scale Structure of the Galaxy

1.2.1 The Interstellar Medium

While the existence of interstellar matter within the Milky Way was beyond doubt by the 1920s (Sandage et al. 2004); the relative *importance* of this diffuse, absorbing, medium within the Milky Way, was one of the major differentiations between the Shapley and Curtis galactic models (see Section 1.1.2).

Hubble's resolution of the Great Debate (Section 1.1.2) provided unequivocal evidence that the Milky Way was a separate galactic system. Furthermore, the limitations of optical astronomy—especially in observations through the dense Galactic disk—were highlighted. New tools that could pierce through to the extremities of our own Galactic system, or study the intervening interstellar matter, were required to move beyond the barriers of Galactic optical stellar astronomy.

One of the first quantitative analyses of interstellar matter was performed by Robert Trumpler in 1930. Trumpler measured the absolute magnitudes of stars in 100 open clusters, from spectral properties, then calculated their distances from the stars' apparent magnitudes. He reported a photographic extinction rate of 0.67 mag kpc^{-1} and further commented that the absorption mainly takes place along the galactic plane (Trumpler 1930). Applying the Cephid Luminosity-Period relationship to 156 δ Cephei stars, Joy (1939) calculated an extinction of 0.85 mag kpc^{-1}*. By 1940 several astronomers had used photoelectric photometric techniques to prove the distribution of this absorbing gas was not uniform—although the 'global' average extinction rate was $\sim$ 1 mag kpc^{-1}—it is necessary to evaluate the extinction along each line of sight (Longair 2006).

We now understand this interstellar medium (ISM) to be a inhomogeneous, dynamic, tenuous medium; comprised of atoms, ions, molecules and solid particles (dust) in various states of motion, density, and temperature (see Figure 1.7 and Table 1.1). The ISM is concentrated

*In the same paper, Joy computed the distance to the Galactic center to be 10 kpc and the circular orbital velocity of the Sun to be 296 km s^{-1}—comparable to the modern IAU values of 8.5 kpc and 220 km s^{-1} respectively.

near the Galactic plane and along the spiral arms, and accounts for about $10 - 15\%$ of the total baryonic mass of the Milky Way (Ferrière 2001). The ISM is also directly connected to stellar evolution, in that the stars and ISM coexist and evolve together (Burbidge et al. 1957).

Gas constitutes $\sim 99\%$ of the ISM (with the remainder accounted for by dust); and of this gas, 90% by number (or 75% by mass) is atomic hydrogen. The gas primarily appears in two forms: clouds of atomic or molecular hydrogen and ionised hydrogen near hot young stars (i.e. H II regions). Despite the complexity of environments within the ISM (see Table 1.1), the medium is often modelled using just three phases (McKee & Ostriker 1977). These three phases—the hot ionised medium (HIM), warm neutral medium (WNM) and cold neutral medium (CNM)— can each be investigated through observations of interstellar hydrogen.

This thesis uses H II regions (Section 1.3), and neutral atomic hydrogen (as a tracer of the intervening ISM) along sightlines toward them (Section 1.4), to investigate the large scale structure of the Galaxy. The neutral hydrogen transition directly traces the WNM in emission and the CNM in absorption, while radio free–free emission from H II regions traces the ionised gas.

1.2.2 Galactic Coordinates

The first Galactic coordinate system was defined from optical observations in 1932, but was later modified by radio observations (and then adopted by the IAU, see Sullivan 2005). Figure 1.8 depicts the definition of Galactic coordinates, which use the Sun and Galactic centre as reference positions. Galactic Longitude (l) is the angle measured eastward along the Galactic equator from the Galactic center. Galactic latitude (b) measures the angular distance of an object to the Galactic Equator, with positive latitudes denoting a north direction (for example the North Galactic pole has a latitude of $b = +90^o$).

Galactic longitude further defines four Galactic quadrants; usually denoted with Roman numerals. The Sun is retained as the origin with the direction of the Galactic centre dividing the first and fourth quadrants—such that Quadrant I encompasses longitudes $0^o < l < 90^o$, whereas Quadrant IV includes longitudes $270^o < l < 360^o$. Due to the orientation of the Earth, with respect to the rest of the Galaxy, Quadrant I is primarily visible only from the Northern hemisphere while Quadrant IV is mostly only visible from the Southern Hemisphere*.

1.2.3 Galactic Dynamics

Bertil Lindblad (1927) was the first to propose an axis-symmetric dynamical model of the Milky Way, consisting of two dynamical subsystems. The central subsystem was comprised of a non-rotating, spherical halo of globular clusters, where random motions were balanced by gravity. The second subsystem was composed of stars in the Galactic disk.

Intrigued by this model, Jan Oort used the motion of stars in the Solar neighbourhood to present the first observational evidence for differential rotation within the Galaxy. Oort (1927) suggested that observed velocities could then be used, alongside a model of Galactic

*For example, the Green Bank Telescope can observe to a lower limit of $l \gtrsim 350^\circ$

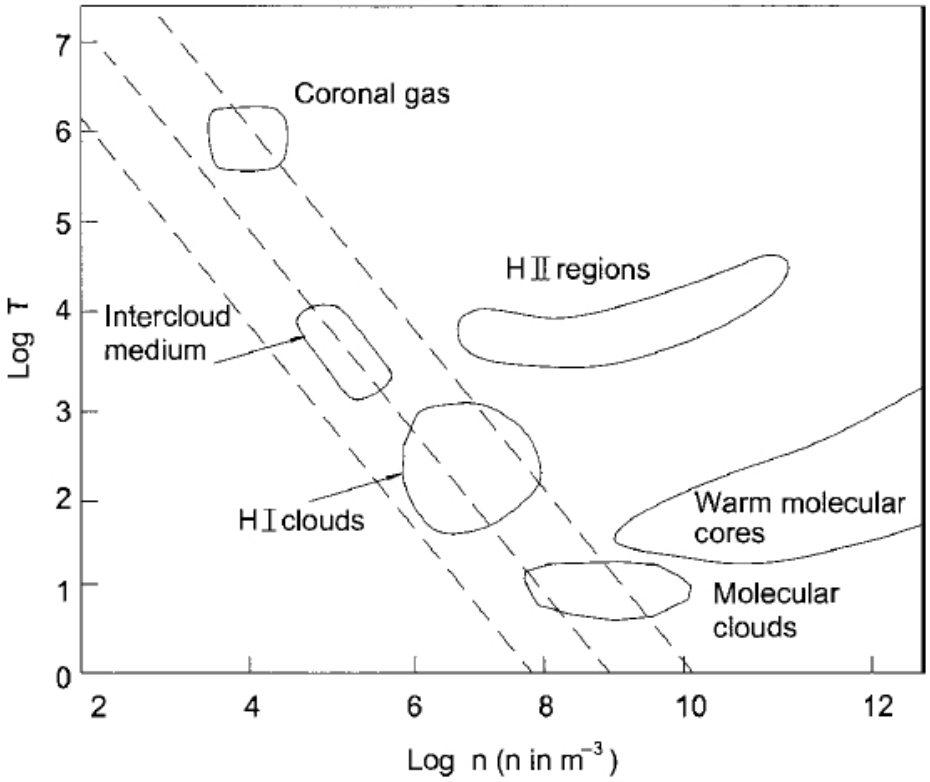

Figure 1.7: Figure 6.15 of Choudhuri (2010). Phases of the ISM in density–temperature phase space. The dashed lines represent lines of constant pressure.

Phase	Temperature (K)	$N_{\rm H}$ (cm $^{-3}$)	f_V%
HIM	$\geq 10^{5.5}$	0.004	50
WIM	~ 8000	$0.1 - 0.3$	$10 - 25$
H II regions	10^4	$1 - 10^5$	–
WNM	$5000 - 8000$	$0.5 - 0.6$	$30 - 40$
CNM	100	30	1
Diffuse H_2	10	100	0.1
Dense H_2	$10 - 50$	$10^3 - 10^6$	0.01
Stellar Outflows	$50 - 10^3$	$1 - 10^6$	–

Table 1.1: The temperature (K), column density (cm $^{-3}$) and percentage filling factor (by volume), f_V, for various phases of the ISM. All values are approximate, especially for the percentage volume filling factor (which remains very uncertain Tielens 2005). Data supplied by Dickey et al. (2003) and Tielens (2005).

rotation, to determine distances—a method independent of *"possible absorption from interstellar space"*.

The following Sections detail the derivation of rotation models for the Galaxy.

If all matter in the Galaxy travelled in purely circular orbits around the Galactic centre; the circular velocity, Θ, can be expressed in terms of angular velocity, Ω, and Galactocentric radius, R; $\Theta = \Omega R$.

For a disk in circular, cylindrical rotation, any particular Galactocentric radius corresponds to a single rotational velocity. The observed radial velocity (V), of a point at $G(l, b)$ is given by:

$$V = R_0[\Omega(R) - \Omega_0]\sin(l)\cos(b) \tag{1.1}$$

A schematic of these parameters, and those used in the derivations of Section 1.2.4 appears as Figure 1.9.

1.2.3.1 Galactic Rotation Models

The Milky Way, and other spiral galaxies, do not adhere to strict cylindrical rotation; although non-circular and random motions exist, the motion of objects in the Galaxy is well modeled by circular orbital motions described by a 'rotation curve' which can be empirically derived from observations. Rotational velocities through the entire disk of the Galaxy are measured using Doppler shifts; the rotation curve is then provided by a function of rotational velocity with respect to Galactocentric radius.

Rotation curves are the major tool for determining the distribution of mass[*], dynamics, evolution and formation of spiral galaxies. Most Sb galaxies (possibly including the Milky Way) have rotation curves with a steep rise within the central 100pc, a maximum orbital velocity at a few hundred parsecs followed by a decline to a minimum at 1-2 kpc, a gradual rise due to the main disk out to approximately 6kpc and a nearly flat outer-rotation curve (Sofue & Rubin 2001).

Figure 1.10 depicts three axis-symmetric rotation curves, for the Milky Way, from Clemens (1985); Brand & Blitz (1993) and McClure-Griffiths & Dickey (2007); all are scaled using the IAU's Galactic constants ($\Theta_0 = 220$km s^{-1}, $R_0 = 8.5$ kpc)[†].

Throughout this thesis, the rotation model of McClure-Griffiths & Dickey (2007) is used for the inner Galaxy ($R < R_0$):

$$\Theta(R) = \Theta_0 \left(K_1 + K_2 \frac{R}{R_0} \right) \tag{1.2}$$

[*]Rotation curves provided the first evidence for the existence of dark matter

[†]The original values of Oort (1927) were $\Theta_0 = 272$km s^{-1}, $R_0 = 5.1$ kpc

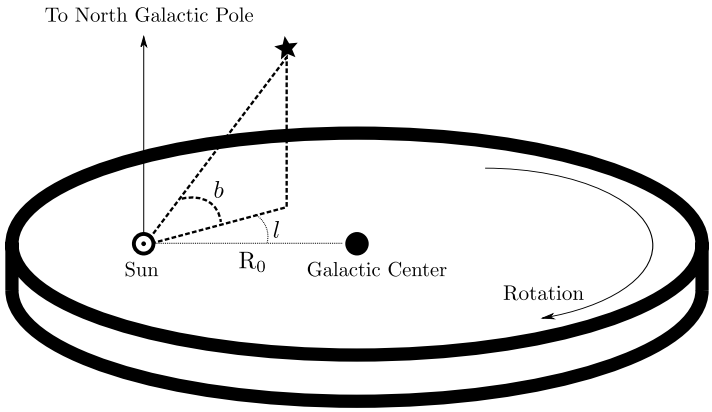

Figure 1.8: Schematic of Galactic co-ordinates

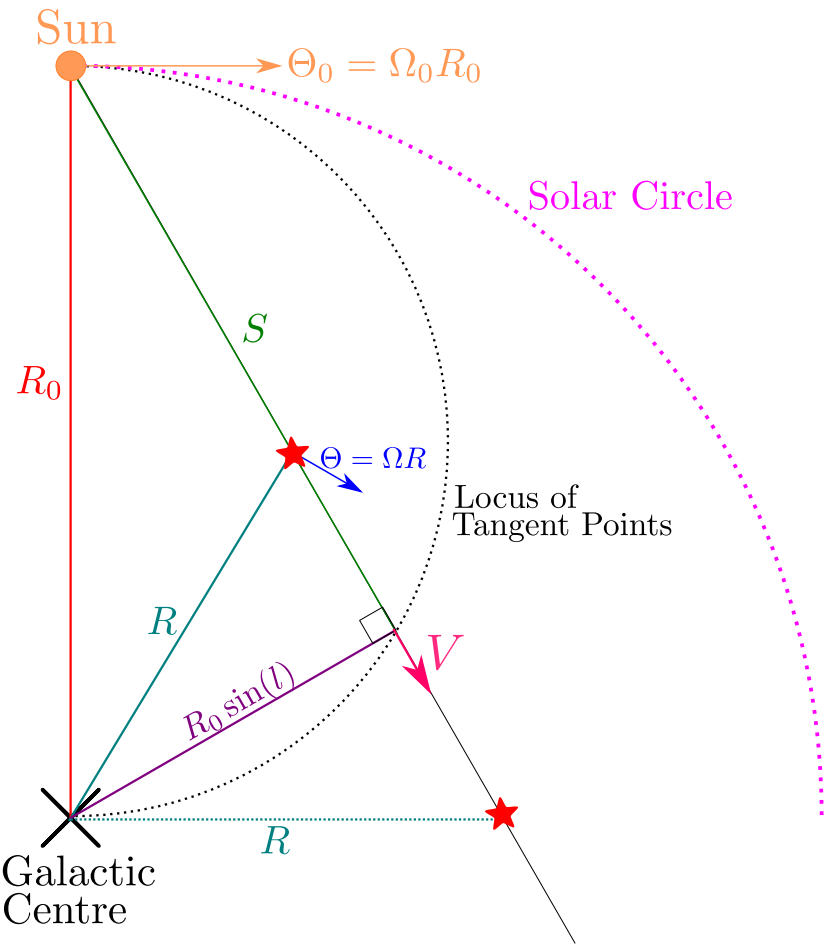

Figure 1.9: The parameters used in the derivations of line of sight distances in Section 1.2.3. The near and far kinematic distances are marked by red stars; note they have the same Galactocentric radius (which is unique for each radial velocity, see Equation 1.4) and are equidistant from the tangent-point location.

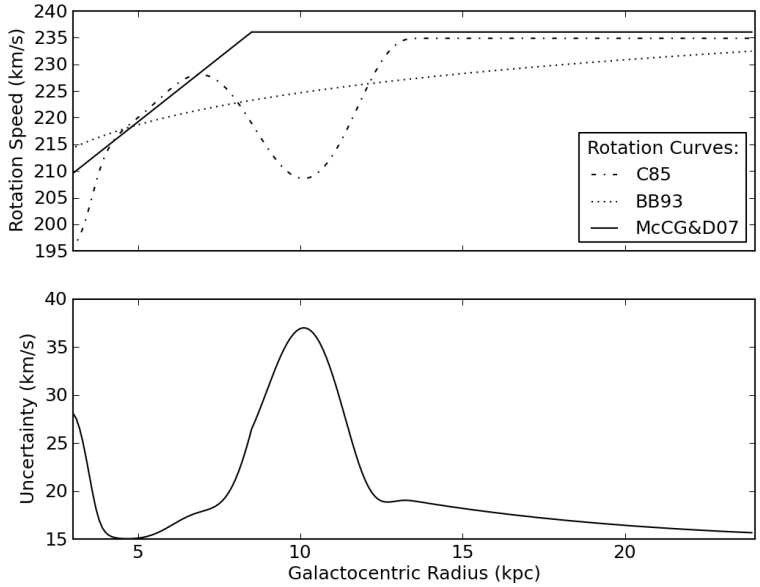

Figure 1.10: Top: Three axis-symmetric rotation curves: Clemens (1985); Brand & Blitz (1993) and McClure-Griffiths & Dickey (2007) for Galactocentric radii from 3-24 kpc. Bottom: The difference between models from the top panel, added in quadrature to a constant non-circular streaming motion velocity (of15km s^{-1}). Note that the McClure-Griffiths & Dickey (2007) model is extended in the outer Galaxy with a flat rotation model $\Theta(R_{Gal}) = \Theta_0$—this composite is the rotation model used throughout this thesis.

where $K_1 = 0.887 \pm 1\%$ and $K_2 = 0.186 \pm 4\%$. This rotation curve is valid for $0.35 < R/R_0 < 0.95$, and is the most densely sampled rotation curve available for the Milky Way between 3kpc$\leq R \leq$ 8kpc. The model is extended with a flat rotation model $\Theta(R) = \Theta_0$ in the outer Galaxy ($R > R_0$, see solid line in top panel of Figure 1.10).

1.2.4 Line of Sight Distances and the Kinematic Distance Ambiguity

Extending the derivation of Section 1.2.3, and making use of the McClure-Griffiths & Dickey (2007) rotation curve (i.e. Equations 1.1 and 1.2), allows for calculations of kinematic, line of sight distances (S, green line in Figure 1.9).

1.2.4.1 The Inner Galaxy

For the inner Galaxy use the rotation curve of McClure-Griffiths & Dickey (2007), see Figure 1.10.

Substituting Equation 1.2 into Equation 1.1, we can obtain:

$$
\begin{aligned}
V &= R_0 \left[\frac{\Theta}{R} - \frac{\Theta_0}{R_0}\right] \sin(l)\cos(b) \\
&= R_0 \sin(l)\cos(b) \left[\frac{\Theta_0 \left(K_1 + K_2 \frac{R}{R_0}\right)}{R} - \frac{\Theta_0}{R_0}\right] \\
&= R_0 \Theta_0 \sin(l)\cos(b) \left[\frac{K_1}{R} + \frac{K_2 - 1}{R_0}\right]
\end{aligned} \tag{1.3}
$$

Solving for R gives:

$$
R = \frac{R_0 K_1}{\frac{V}{\Theta_0 \sin(l)\cos(b)} - K_2 + 1} \tag{1.4}
$$

In reference to Figure 1.9; for a triangle formed by connecting R_0, R and S, the Law of Cosines gives S:

$$
S = R_0 \cos(l) \pm \sqrt{R^2 - R_0^2 \sin^2(l)} \tag{1.5}
$$

Substituting Equation 1.4 into Equation 1.5, we can solve for $S(V, l)$:

$$
\begin{aligned}
S &= R_0 \cos(l) \pm \sqrt{\left(\frac{R_0 K_1}{\frac{V}{\Theta_0 \sin(l)\cos(b)} - K_2 + 1}\right)^2 - R_0^2 \sin^2(l)} \\
&= R_0 \left(\cos(l) \pm \sqrt{\left(\frac{K_1}{\frac{V}{\Theta_0 \sin(l)\cos(b)} - K_2 + 1}\right)^2 - \sin^2(l)}\right)
\end{aligned} \tag{1.6}
$$

Equation 1.6 is double-valued; each radial velocity corresponds to two distances along the line of sight, equidistant from the tangent (subcentral) point. The tangent point ($R = R_0 \sin l$) corresponds to a single line of sight distance (see Equation 1.5)—and therefore the tangent point location is the only unambiguous distance within the inner Galaxy.

This inner Galaxy Kinematic Distance Ambiguity (KDA) is a direct result of axisymmetric rotation curves, and remains a significant obstacle to the determination of reliable line of sight distances (e.g., Kolpak et al. 2003).

1.2.4.2 In the Outer Galaxy

The same principals of derivation apply to the outer Galaxy ($R > R_0$). However, the rotation models have larger uncertainties in the Galactic rotation speeds beyond the solar circle. For example, Brand & Blitz (1993) determined that the outer Galaxy velocity field is slightly rising with departures up to 17 km s^{-1}; Honma et al. (2007) prefer a flat rotation curve;

whereas Hachisuka et al. (2009) discuss the possibility of a rotation curve that falls by 20 km s^{-1} beyond the Solar circle.

Throughout this thesis, we assume $\Theta(R) = \Theta_0$ for the outer Galaxy (see Figure 1.10). As for the inner Galaxy, we substitute our chosen rotation curve into Equation 1.1:

$$\begin{aligned} V &= R_0 \left[\frac{\Theta_0}{R} - \frac{\Theta_0}{R_0} \right] \sin(l) \cos(b) \\ &= \Theta_0 \sin(l) \cos(b) \left[\frac{R_0}{R} - 1 \right] \end{aligned} \tag{1.7}$$

Solving for R gives:

$$R = R_0 \left[\frac{V}{\Theta_0 \sin(l) \cos(b)} + 1 \right]^{-1} \tag{1.8}$$

We return to the triangle formed by connecting R_0, R and S (Equation 1.5); but note that in the outer Galaxy, $R > R_0$, and also $R > R_0 \sin(l)$, such that the ambiguity in S is removed:

$$\begin{aligned} S &= R_0 \cos(l) + \sqrt{R^2 - R_0^2 \sin^2(l)} \\ &= R_0 \cos(l) + \sqrt{R_0^2 \left[\frac{V}{\Theta_0 \sin(l) \cos(b)} + 1 \right]^{-2} - R_0^2 \sin^2(l)} \\ &= R_0 \left[\cos(l) + \sin(l) \sqrt{\frac{\Theta_0^2 \cos^2(b)}{[V + \Theta_0 \sin(l) \cos(b)]^2} - 1} \quad \right] \end{aligned} \tag{1.9}$$

We now have $V(R, l)$, $R(V, l)$ and $S(V, l)$ for the inner and outer Galaxy.

1.3 H II Regions

Only O and B class stars ($T_{\rm eff} > 25000$ K, M$\gtrsim 10 M_\odot$) emit a significant flux of photons above the Lyman limit (13.6 eV; the energy required to ionise hydrogen from the ground–state). These ultraviolet photons photodissociate nearby H_2 molecules into atomic hydrogen; then photoionise this atomic gas to create an H II region. They are therefore signposts of massive-star formation in the Milky Way.

H II regions display a wide range of physical conditions. Observationally derived classes have been proposed based on density and size; these are summarised in Table 1.2. The balance between photoionisation and radiative recombination (of thermal electrons and protons to form neutral hydrogen atoms*) processes determine the overall degree of ionisation, and size, of the region (Strömgren 1939). Upon ionisation, any remaining energy over the

*Thermal electrons can also excite trace species within the region.

Class	Size (pc)	Density (cm^{-3})	Ionised Mass ($M_\odot$)	No. Ionising Stars
Hypercompact (HC)	$\lesssim 0.03$	$\geq 10^6$	$\sim 10^{-3}$	$\simeq 1$
Ultracompact (UC)	$\lesssim 0.1$	$\geq 10^4$	$\sim 10^{-2}$	~ 1
Compact	$\lesssim 0.5$	$\geq 5 \times 10^3$	~ 1	~ 1
Classical	~ 10	~ 100	$\sim 10^5$	few
Giant	$\sim 50 - 100$	~ 30	$10^3 - 10^6$	$\sim 10^2$
Supergiant	> 100	~ 10	$10^6 - 10^8$	–

Table 1.2: Typical characteristics of classes of H II regions. Summary of tables from Tielens (2005) and Kurtz (2005).

ionisation potential is carried away by photo-electron kinetic energy collisions with other electrons—leading to an overall Maxwellian velocity distribution within the region (Tielens 2005).

The first H II region to be discovered, also the most observed, is the Orion Nebula (see Figure 1.11)—which is ionised by the four O and B class Trapezium stars. Despite being visible to the naked eye, Galileo made no mention of the nebula when he was investigating the star cluster λ Orionis. Rather, the discovery is credited to Nicholas Peirsec in 1610 (Harrison 1984). Over the centuries since, thousands of H II regions have been discovered*.

H II regions provide a wealth of information for Galactic and extragalactic studies. Most pointedly for this thesis is the link between the velocity distribution of H II regions and the kinematics of the Galactic disk (see Sections 1.3.2.3 and 1.3.1).

1.3.1 H II Regions as a Tracer of Galactic Structure

Walter Baade (1944) presented the first evidence that different spectral classes of stars formed different populations within (spiral) galaxies. In observations of M32, NGC 205 and Andromeda, Baade noticed that open star clusters, O and B type stars were exclusively located in spiral arm regions—he collectively classed these as Population I objects†. For external galaxies, it is relatively easy to observe luminous young stars, and H II regions, delineating narrow, sharply defined spiral arms. Baade & Gaposchkin (1963) described H II regions as *"strung out like pearls along the arms"* (see Figure 1.12).

These stars, and their associated H II regions, live less than ~ 10 million years. Compared to orbital periods of typical spiral galaxies (~ 100 million years), and they are therefore 'zero age' objects compared with their host galaxies (Binney & Tremaine 2011). The physical parameters of H II regions span orders of magnitude in scale; the classes most closely linked to star formation (and therefore are the best spiral arm tracers) are the smallest, densest (and presumably youngest) stages—compact, ultracompact and hypercompact H II regions (Kurtz 2005).

*On November 13, 2013, SIMBAD Astronomical Database included 27,264 entries of type 'H II [region]'
†Population II objects included short-period Cephids and globular clusters.

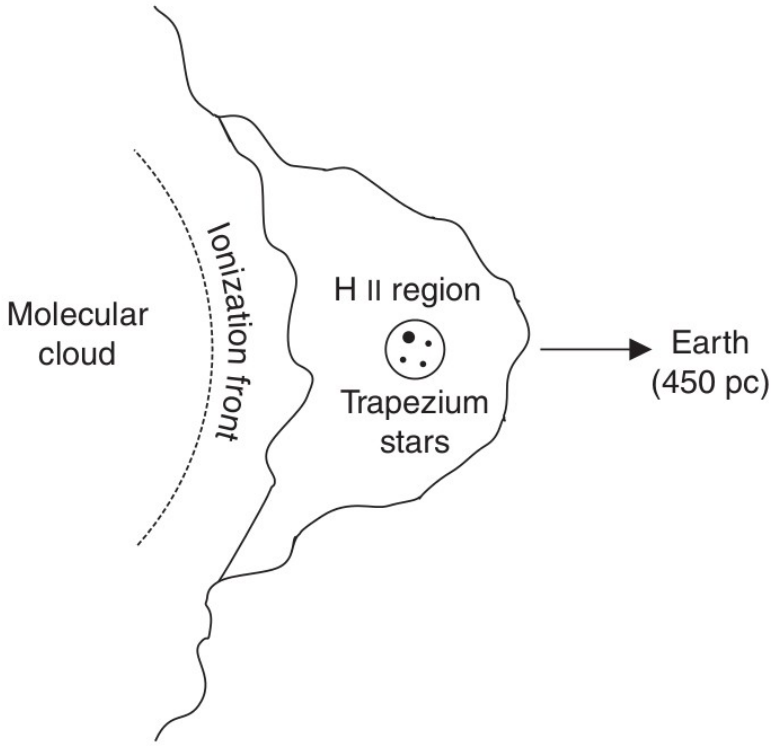

Figure 1.11: Top: HST Image of the Orion Nebula: The optical B, V and H-alpha filters are shown in blue, green and yellow respectively. The infrared filters I and Z are both shown in red. Image Credit: heic0601a; NASA, ESA, M. Robberto (Space Telescope Science Institute/ESA) and the Hubble Space Telescope Orion Treasury Project Team. Bottom: Schematic diagram of the Orion Nebula from Pradhan & Nahar (2011). The Trapezium stars ionise the giant molecular cloud (to the left), while forming a blister-type nebula (as viewed from Earth).

Figure 1.12: M51, the Whirlpool Galaxy (see Figure 1.3), as imaged by the Hubble Space Telescope. H II regions (pink clumps) are "strung out like pearls along the arms". Image Credit: NASA, ESA, S. Beckwith (STScI), and The Hubble Heritage Team STScI/AURA

1.3.2 Emission Characteristics

The optical spectra of H II regions is dominated by line emission from H, He and trace ions (e.g., O II, O III, N II). In addition, H II regions are strong sources of thermal free-free radio emission from ionised gas and also infrared emission from warm dust (Tielens 2005).

1.3.2.1 Optical

The brightest optical spectral line from H II regions is the Hα Balmer series line at 656.3 nm (the $n = 3 \rightarrow n = 2$ transition)—although many other forbidden emission lines from carbon, nitrogen and oxygen are also present, see Figure 1.13. As the energy required to excite the electron to the $n = 3$ state is similar to the ionisation potential for hydrogen, H II regions consist of a mix of electrons and ionised hydrogen that are constantly recombining into atomic hydrogen.

Unfortunately for optical studies, the distance limit for parallax or photometry, due to extinction, is about $\sim$ 6 kpc (Hou & Han 2014). Therefore longer wavelength studies are required to investigate more distant H II regions through the Galactic plane.

1.3.2.2 Infrared

The presence of dust in H II regions is inferred from scattered light measurements and infrared continuum emission—caused by grains heated by ultraviolet stellar radiation and Lyman–α

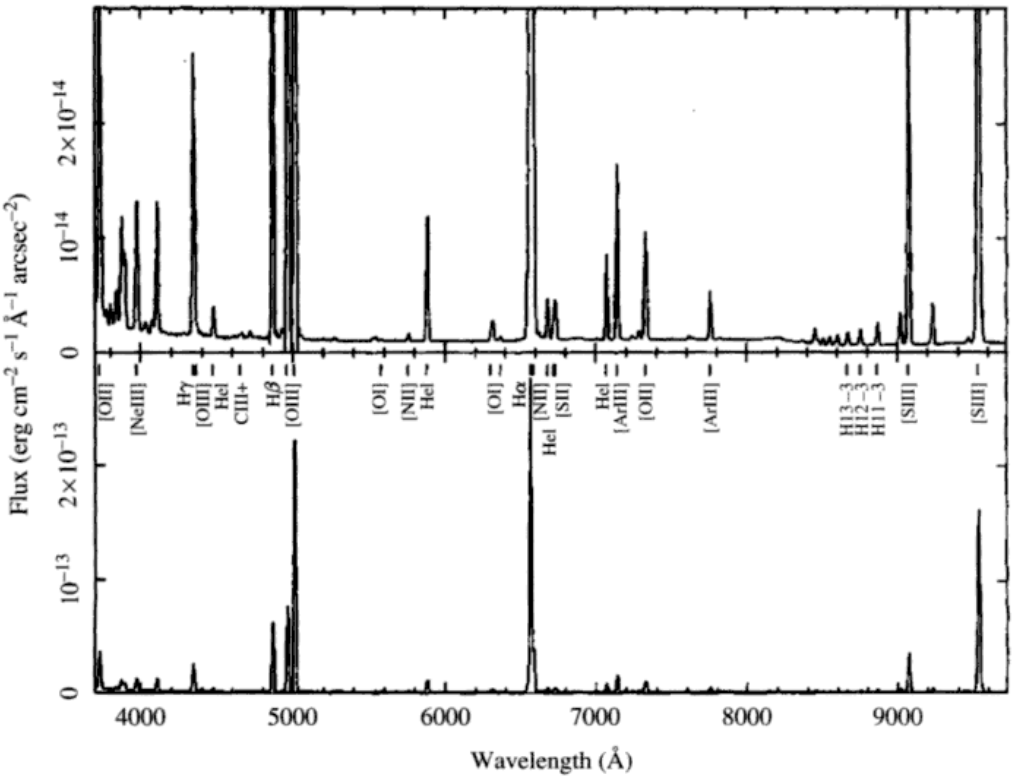

Figure 1.13: Optical-Ultraviolet spectrum of an H II region; Figure 1 of Baldwin et al. (1991).

photons.

Hydrogen emission lines from H II regions also exist in the infrared regime, and these were first observed in the Orion Nebula in 1970 (Wynn-Williams 1984). The most readily observable infrared hydrogen lines are the Brackett-α and Brackett-γ ($n_{\rm low} = 4$; 4.050 μm and 2.165 μm respectively). The strong Paschen-α transition ($n_{\rm low} = 3$, 1.875 μm) coincides with atmospheric H_2O, making it hard to observe except for redshifted, extra-galactic, objects (e.g. observations by Neugebauer et al. 1980).

H II regions also have diagnostic infrared morphology. Bubble, ring, or partial–bubble structures are common at mid-infrared wavelengths; where the emission is assumed to arise from polycyclic aromatic hydrocarbons excited by ultraviolet radiation (Churchwell et al. 2006). This near-infrared emission bubble or ring usually encloses any mid-infrared ($22 - 24$ μm) emission from the region (Pavlyuchenkov et al. 2013).

1.3.2.3 Radio

H II regions are also visible in the radio regime via continuum emission from Bremsstrahlung radiation and recombination emission lines. The total luminosity of the continuum emission is typically a factor of hundreds larger than that of the radio recombination lines* (e.g., Brown 1987). Radio recombination lines are discussed in detail in regards to tracing H II regions in Section 1.3.3.

Comparing the radio continuum and recombination line emission provides an insight into

*This is the opposite to the optical scenario, where line radiation overwhelms the continuum.

several physical properties of the H II region. For example, the line to continuum ratio provides an estimate of the region's electron temperature.

1.3.3 Radio Recombination Lines

Recombination lines occur when electrons and ions recombine to form highly excited atoms. These newly bound electrons cascade downwards from high principal quantum numbers (n), eventually resulting in a ground state atom. When these emission lines occur at radio wavelengths, they are termed Radio Recombination Lines (RRLs). RRLs are intrinsically weaker than their optical counterparts—optical recombination lines (ORLs, including the Balmer series 656 nm Hα transition, see Section 1.3.2.1)—but both RRLs and ORLs are affected by radiative and collisional effects in the same ways (Balser 2006). However, RRLs are simpler to interpret, compared to ORLs or infrared recombination lines, in that they require no dust extinction corrections before analysis (Tielens 2005) and that higher velocity resolutions are easily achieved.

In the first Annual Review of RRLs, Dupree & Goldberg (1970) suggested that RRL velocity detections from H II regions could be applied to a rotation model, to ascertain their spatial distribution—and therefore the structure of the Milky Way. This method employs the RRL velocity as the H II region's systemic velocity in, for example, Equation 1.9, to determine the line of sight distance. The first such work was performed by Georgelin & Georgelin (1976); however, they were unable to perform KDARs and as such, were only able to calculate distances to outer Galaxy H II regions (see left panel of Figure 1.14). Investigations of spiral structure, using H II regions as tracers, continue to this day; indeed using H II regions to infer Galactic structure is the subject of this thesis!

RRLs, by definition, trace ionised gas throughout the interstellar medium; this covers a wide variety of processes and environments. For example hydrogen RRLs can be used to trace H II regions as well as planetary nebulae (Sorochenko 1990). RRL observations are most useful when combined with infrared data. If the region has been sufficiently studied in the infrared (for example between $2 - 300$ μm), the derived total infrared luminosity can then be used to infer the luminosity of the nebula's exciting star (or stars)—hence providing the nature of the excitation source; discriminating between planetary nebulae* and H II regions (Brown 1987).

An historical overview of the discovery and development of RRL transitions can be found in Appendix A.2.

1.3.3.1 RRLs from H II Regions

If RRL emission is detected from an H II region candidate (basically a radio continuum source with infrared colours suggestive of one or more O or B-stars), then the source is confirmed to be an H II region. Furthermore, the line intensity and shape of a detected RRL carry vital

*Planetary nebulae are regions of ionised hydrogen surrounding the hot cores of white dwarfs (typical values are $T > 10^5$ K, $1 \lesssim \mathrm{M/M_\odot} \lesssim 8$).

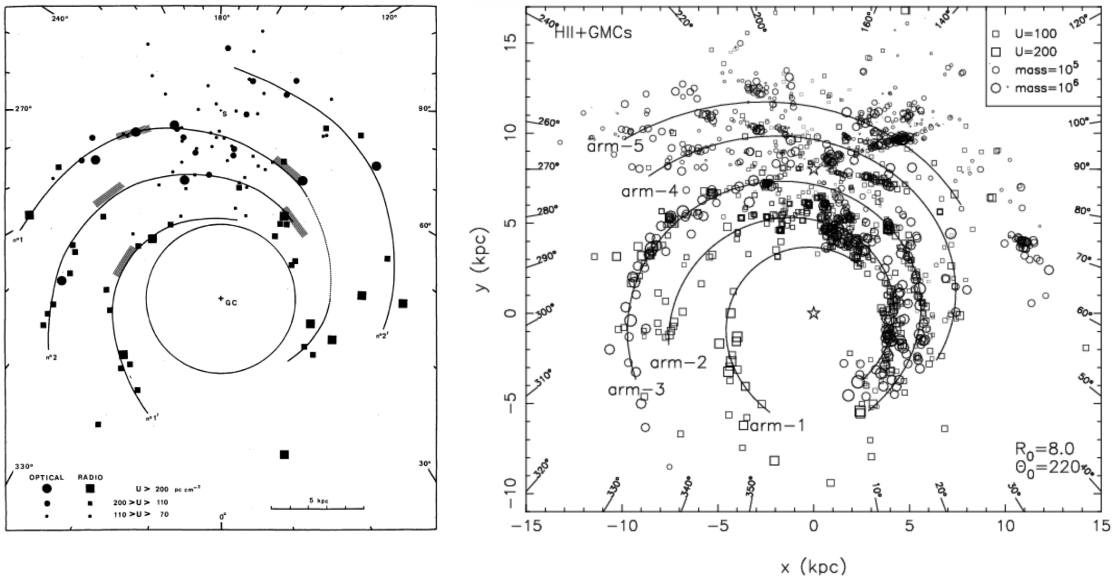

Figure 1.14: Thirty years of Galactic H II region mapping. Left Panel: Figure 11 from Georgelin & Georgelin (1976): *Spiral model of our Galaxy obtained from high-excitation-parameter* H II *regions.* Right Panel: adapted from Figure 9 of Hou et al. (2009) *The distribution of* H II *regions and Giant Molecular Clouds, overlaid with the best fitting polynomial logarithmic-arm model.*

information about the dynamics and thermodynamics of the nebula (Lockman 1990a). RRLs are one of the only ways to directly obtain velocity information from the ionised environments of the Galaxy.

The velocity information carried by the detected RRL transition is vital for determining the distance to the region, and association with other objects. With hydrogen RRLs available across the entire radio spectrum (see Figure 1.16), and as the velocity of an H II region can be measured from any transition, the choice of observing frequency is typically limited by the available observing instruments (Lockman 1990a).

If multiple, distinct, RRL velocities are detected along a particular line of sight, then it is probable that several H II regions are within the antenna beam. Lockman (1980) suggested that muti-RRL lines of sight would become more common in future (more sensitive) surveys; and that this would provide evidence that most lines of sight in the inner Galaxy pass through the envelope of at least one H II region. The sample of the most recent large scale RRL survey, the Green Bank Telescope H II Region Discovery Survey (GBTHRDS, Bania et al. 2010), found multiple RRL components from nearly a third of their target sources.

This thesis focuses on RRLs from hydrogen. However, some H II regions also show RRLs from elements heavier, but with lower ionisation potentials, than hydrogen—most notably carbon (see Figure 1.15). This emission primarily comes from the photodissociation region surrounding the H II region where the gas is denser and cooler (Hollenbach & Tielens 1999).

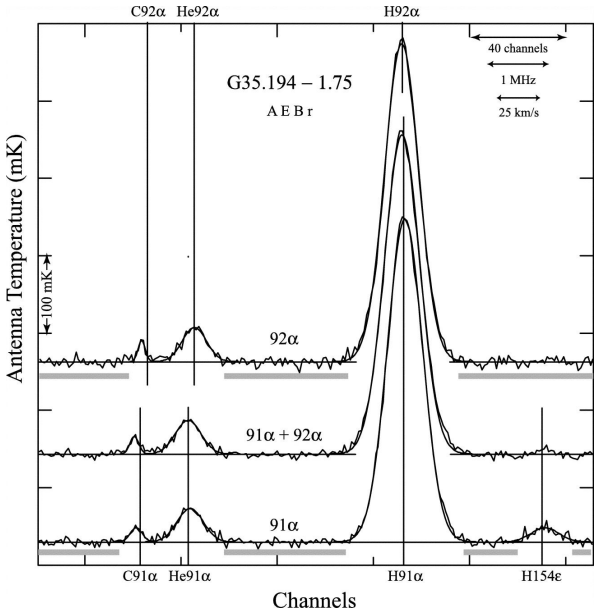

Figure 1.15: Observed recombination-line spectra from the 91α and 92α transitions of hydrogen, helium, and carbon observed in the HII region G35.194-1.75 by Quireza et al. (2006).

1.3.3.2 Theory

The following theoretical overview is based on Gordon & Sorochenko (2002) supplemented with further references where appropriate.

The frequencies of hydrogen RRLs can be calculated from the energy difference between electrons moving from the $(n + \Delta n)$ to n^{th} orbital levels:

$$\begin{aligned} \Delta E = h\nu &= \frac{m_e e^4}{2\hbar^2}\left[\frac{1}{n^2} - \frac{1}{(n+\Delta n)^2}\right] \\ \therefore \nu &= \left(\frac{2\pi^2 m_e e^4}{h^3 c}\right) c\left[\frac{1}{n^2} - \frac{1}{(n+\Delta n)^2}\right] \end{aligned} \tag{1.10}$$

The factor in large parentheses is termed the Rydberg constant, R_∞. This constant can be corrected to allow for a finite nuclear mass, M, and when the analysis of Equation 1.10 is repeated in the atomic centre-of-mass frame, R_M replaces R_∞:

$$\begin{aligned} R_\infty &\equiv \left(\frac{2\pi^2 m_e e^4}{h^3 c}\right), \text{ see Equation 1.10} \\ R_M &\equiv R_\infty \left(1 + \frac{m_e}{M}\right)^{-1} \end{aligned} \tag{1.11}$$

such that the most accurate RRL frequencies are given by:

$$\nu = R_M c\left[\frac{1}{n^2} - \frac{1}{(n+\Delta n)^2}\right] \tag{1.12}$$

Uncertainities in the frequencies of RRL transitions are therefore influenced by the precision to which the components of R_M (i.e., m_e, e, h and M), as well as c, are known*. The Rydberg constant is now known to a precision better than seven parts in one trillion (Mohr et al. 2008).

Complete tables of RRL frequencies can be found in either Lilley & Palmer (1968) or in the Appendices of Gordon & Sorochenko (2002). Figure 1.16 displays the approximate distribution of Hnα frequencies between 2 and 10 GHz.

The observed full width at half intensity for most RRLs is on the order of $\sim 20 - 25$ km s^{-1}. However, the Einstein A coefficient, and therefore the natural line width, of RRLs is small:

$$A_{\rm RRL} \approx 2.4 \times 10^{10} \left(\frac{\ln n}{n^5} \right) \qquad n > 20$$
$$\frac{\Delta\nu}{\nu_0} \approx \frac{1.2 \times 10^{-6} \ln n}{n^2} \tag{1.13}$$

Using H109α (a readily observed RRL near 5 GHz) as an example, the natural line width is 1.3×10^{-4} km s^{-1} (using Equation 1.13 then transforming into velocity units), i.e., 10^5 times smaller than the observed line width. Observed line widths are therefore dominated by collisions, and can be modelled by a combination of a broadening processes (dominated by Doppler Broadening).

Figure 1.16: Approximate distribution of Hnα RRL frequencies from $2 - 10$ GHz ($148 < n < 87$).

1.4 Neutral Hydrogen

This thesis uses ground state, neutral hydrogen (H I) to investigate the structure of the Galaxy, as well as to resolve the KDA for H II regions. The following sections provide an overview of the role of hydrogen in the interstellar medium (§1.2.1) before describing the use of H I as a tracer of spiral structure (§1.4.1) and line theory (§1.4.2) of the transition. A history of the H I transition is presented in (Appendix A.1).

*For the case of hydrogen, the nucleus is a single proton; therefore $M(\mathrm{H}) = m_p \approx 1836.1 m_e$

H I is detectable in most spiral galaxies and in some elliptical galaxies. In the Milky Way, H I clouds occupy 5% of the volume of the ISM, but contribute nearly 40% of the mass. Compared to the stellar distribution, the distribution of H I is clumpy and diffuse—usually appearing as clouds up to 100pc in size (Bertin 2000). H I is distributed throughout the entire disk, in a 'gas disk' typically three times the extent of the stellar distribution in scale height above the plane (Kalberla & Kerp 2009). In spiral arms, the density of the H I gas can become high enough to form molecules, and in turn, the Giant Molecular Clouds from which stars are born.

1.4.1 H I As a Tracer of Galactic Structure

The prediction, and subsequent detection, of the 21-cm H I line provided astronomers with a tool to trace hydrogen in its neutral form (see Section A.1 for a historical overview of the transition). Within months of the discovery of the 21 cm transition the nature of Galactic rotation and the thickness of the disk were discussed in the literature (reviewed by Lockman 2002); within a year, the spiral structure of the Galaxy was being uncovered (van de Hulst et al. 1954). The understanding of the distribution of neutral hydrogen, especially in the Galactic plane, evolved quickly. Continued international cooperation resulted in maps of the entire Galactic plane (see left panel of Figure 1.17); which reported several H I spiral arms (Sagittarius, Orion and Perseus arms). Increased sensitivity, from ever increasing single-dish dimensions, resulted in ever more detailed maps (right panel of Figure 1.17). Lockman (2002) states that *"knowledge of the large scale structure of the Galaxy has been the single most important achievement of Galactic 21-cm* H I *studies"*.

In February 1970 a "Spiral Workshop" was held at the University of Maryland to discuss the various contemporary models of Galactic structure. The spiral arms, as traced by H I emission was hearalded as the only *"way to study the whole Galaxy"* but it was also acknowledged that *"there is so much 21-cm emission that we're confused by it"* (Lockman 2002). The disagreement between optical and radio studies, as well as differing rotation models for the first and fourth Galactic quadrants were also discussed.

The Galactic disk seen in H I emission is transparent; however the emission features are often difficult to separate (see Figure 1.21) and this crowding (in velocity space) can be misinterpreted as enhancements of density. While the H I arms in the outer Galaxy are distinct, in the inner Galaxy H I emission profiles are too confused to glean clear spiral arms. Indeed, H I surface density distribution maps (for example Figure 1.17) are insufficient to infer distinct spiral arms (Kalberla & Kerp 2009)*.

Spiral arms in the inner Galaxy are better delineated in tracers with a higher arm–interarm contrast, or tracers which are simply less ubiqutous than H I emission (Tielens 2005). Today, models of the large-scale morphology of the Galaxy are more often tested against the H I emission data, than derived from it (Burton 1976, Englmaier & Gerhard 1999 in Lockman

*The same argument can be applied to observations of CO, especially the ^{13}CO rotational transition—in that spiral structure derived from diffuse CO emission is far from clear (Nakanishi & Sofue 2003, 2006), but denser, giant molecular clouds serve as an excellent tracer of spiral structre (Hou & Han 2014).

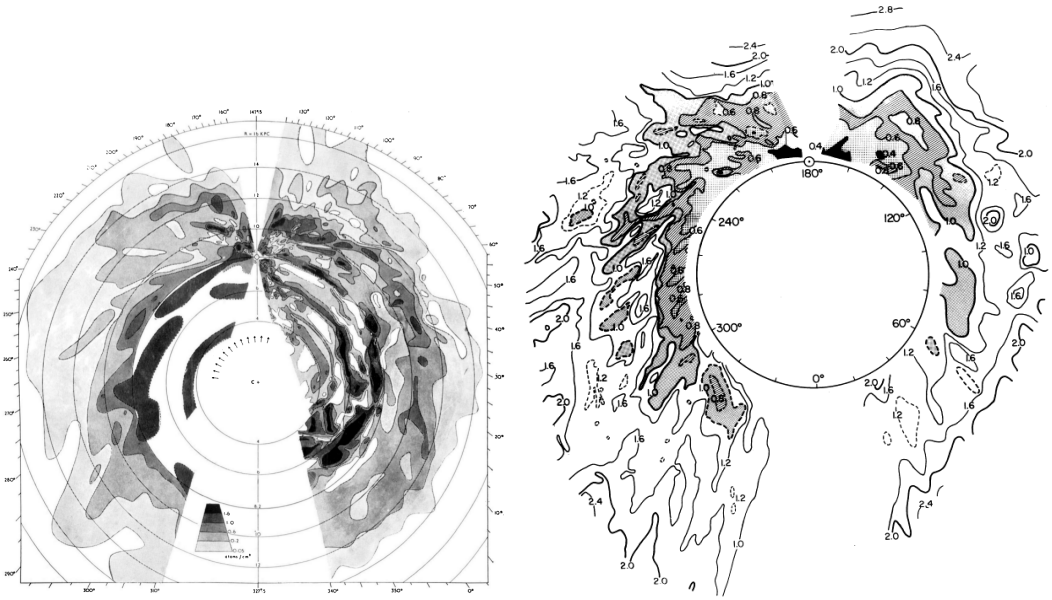

Figure 1.17: Left: Figure 4 from Oort et al. (1958): *Distribution of neutral hydrogen in the Galactic System. The maximum densities in the z-direction are projected on the galactic plane, and contours are drawn through the points.* Right: Figure 3 from Henderson et al. (1982): *Contour map of $z_{1/2}(R, \phi)$, the half-thickness of the neutral hydrogen layer. Contours are labelled in kpc.*

2002).

The H I line does provide an opportunity to investigate denser phases of the ISM (i.e. the CNM), but through *absorption* rather than in emission; absorption traces colder (denser) gas that should be confined to the spiral arms.

1.4.1.1 H I in Absorption

In the Milky Way, about 40% of H I, by mass, is in the CNM. The first observation of H I absorption in the Galaxy occurred only a few years after the line was detected in emission (Hagen et al. 1955).

The H I transition can be seen in absorption against bright continuum sources*. If extragalactic continuum sources are used, H I absorption can be traced through the total extent of the Galactic disk, analogous to H I emission measurements. However, Galactic scale H I absorption studies are hampered by insufficient numbers of bright continuum sources (Normandeau 1999) and are further limited by relatively stringent instumental requirements, compared to emission observations (Dickey et al. 2003).

Despite these setbacks, most of our knowledge of the CNM comes from H I absorption studies (Gibson 2010). Cold H I clouds, traced by H I absorption, seem to be concentrated at certain Galactocentric radii, linking the clouds to the global spiral structure (Ford et al. 2008). Theory suggests that lower pressures in the outer Galaxy may imply that at the edges of the Milky Way, all the H I is in the Warm Neutral Medium (WNM) phase. Nevertheless, the distribution of cold H I has been mapped in the outer Galaxy, such that the most distant

*H I absorption can also be detected in self-absorption against background H I emission, termed H I Self-Absorption (HISA).

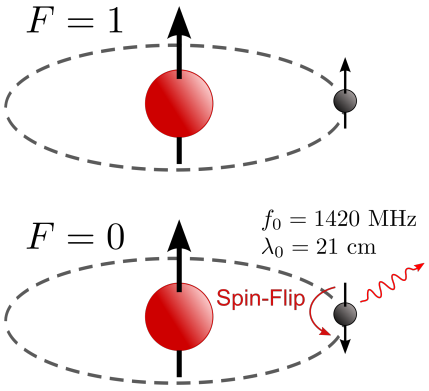

Figure 1.18: Schematic of atomic hydrogen spin states. The 21-cm, H I line is a hyper-fine transition, created when the electron changes (flips) spin state.

spiral arms can be traced with H I absorption (Strasser et al. 2007).

1.4.2 Theory & Spectrum Extraction

The energy levels of the ground state hydrogen atom differ slightly as a result of the relative orientation of the spin of the proton and electron. The transition between these spin states ($1^2S_{1/2}$, $F = 0$ and $F = 1$) has a probability (given by the inverse of the Einstein A coefficient) of ∼once every eleven million years, and produces a narrow emission line (of natural width $\Delta\nu \approx 10^{-11}$ Hz) at a wavelength of ~ 21 cm.

The excitation temperature, termed the spin temperature (in the case of H I), T_S, is given by the ratio of electrons and their statistical weights ($g_1 = 3$ and $g_0 = 1$) in the upper and lower spin states:

$$\frac{n_1}{n_0} \equiv \frac{g_1}{g_0} \exp\left(-\frac{h\nu_o}{kT_S}\right) \tag{1.14}$$

For lines of sight through the Galactic plane, $T_S \approx 10^2$ K, and therefore the H I line sits within the Rayleigh–Jeans regime ($h\nu/kT << 1$),

hence the radiative transfer equation can be written in terms of brightness temperature, T_b:

$$\frac{dT_b(\nu)}{d\tau(\nu)} = T_S - T_b(\nu) \tag{1.15}$$

where optical depth is given by $\tau(V)$ and T_b is a function of intensity, I_ν ($T_b = I_\nu c^2/2k\nu^2$).

Assuming a single, isothermal, gas cloud along a line of sight; Equation 1.15 can be rewritten, in terms of velocity (V), as:

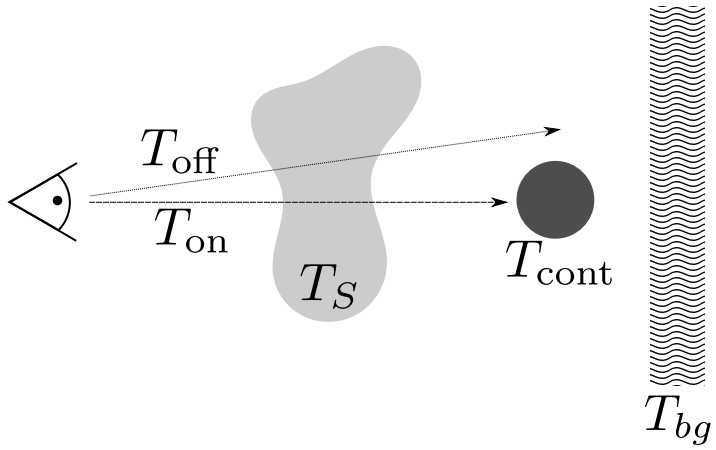

Figure 1.19: Lines of sight through an absorbing cloud both 'on' and 'off' the continuum emission source. Parameters of Equations 1.17 and 1.18 are labeled.

$$T_b = T_{\rm S}\left[1 - e^{-\tau(V)}\right] + T_{BG}e^{-\tau(V)} \tag{1.16}$$

where T_{BG} is the brightness temperature of any background radiation incident on the cloud.

The Emission/Absorption (E/A) method observes H I spectra coincident with, and adjacent to, discrete continuum sources. In order to calculate an absorption value, $e^{-\tau}(V)$, the brightness temperature as a function of velocity, V, both on ($T_{\rm on}$) and off the source (i.e. the emission spectrum, $T_{\rm off}$) are compared (see Figure 1.19).

Working from Equation 1.16; for a velocity, V, the simplest radiative transfer assumption for gas at a single physical temperature ($T_{\rm S}$), along lines of sight toward the source, and slightly 'off' the continuum emission source provide:

$$T_{\rm on}(V) = T_{\rm S}(V)(1 - e^{-\tau(V)}) + (T_{\rm bg} + T_{\rm cont})e^{-\tau(V)} \tag{1.17}$$
$$T_{\rm off}(V) = T_{\rm S}(V)(1 - e^{-\tau(V)}) + T_{\rm bg}e^{-\tau(V)} \tag{1.18}$$

where the only difference is the contributions to the total background radiation incident on the cloud (i.e, there is no appreciable difference between $T_{\rm S}$ and $\tau(V)$ from the 'on' and 'off positions). Here $T_{\rm cont}$ is the continuum source brightness temperature, $T_{\rm S}$ is the spin temperature of the foreground cloud(s) and $T_{\rm bg}$ represents the brightness temperature of any other background contribution (i.e., not from the target continuum emission source, see Figure 1.19). Figure 1.20 displays an example on and off source spectrum pair, with the components of Equations 1.17 and 1.18 labelled.

1.4.2.1 Methodological Details

Large scale H I emission fluctuations, are present on all angular scales (Green 1993; Dickey et al. 2001), such that uncertainties in $T_{\rm cont}$ and $T_{\rm on}$ are negligible with respect to those of $T_{\rm off}$.

In order to mitigate the effect of of these fluctuations, three 'off' source positions were selected for each continuum target; averaged to provide an overall average emission spectrum. The fluctuation between off source positions (i.e. $3\sigma_{T_{\rm off}}$, where $\sigma_{T_{\rm off}}$ is the standard deviation between brightness temperatures of three emission spectra per velocity channel) can be seen as the grey envelope in Figure 1.20. The three 'off' source pixels were chosen with attention to the restrictions discussed by Anderson & Bania (2009)—i.e., the on and off source spectra should be located as close as possible to each other so that the same background is sampled in both; the off source positions should be located off the target continuum source and away from other continuum sources.

The single 'on' source spectrum was extracted from the H I datacube pixel which corresponded to the highest continuum temperature (generally the centre of a compact source)—therefore there is no fluctuation envelope on the $T_{\rm on}$ spectrum in Figure 1.20. Continuum maps were inspected with the KARMA package (Gooch 1996) to ascertain the pixel positions for the 'on' and 'off' spectra to be extracted from the H I cubes.

Assuming that the 'on' and 'off' spectra both sample the same gas, subtraction of one from the other removes the common $T_{\rm bg}$ and $T_{\rm s}(V)$ terms, allowing the absorption depth to be calculated directly:

$$e^{-\tau} = \frac{T_{\rm on} - T_{\rm off}}{T_{\rm cont}} \tag{1.19}$$

Figure 1.21 displays an example absorption spectrum (towards the same continuum source as Figure 1.20).

Uncertainty in Absorption Spectra As for most H I emission/absorption studies, the noise level in the absorption spectrum is not dominated by radiometer noise, but rather the precision with which the absorption can be subtracted from background emission (see Equation 1.19 or Dickey et al. 2003).

The on and off source spectra (see Figure 1.20) are made up of one and three constitutent spectra respectively. The one sigma error in the overall $e^{-\tau}$ spectrum, denoted the absorption uncertainty envelope ($\Delta_{\rm abs}$, see Figure 1.21), is dominated by differences between the three emission, off source, spectra:

$$\Delta_{\rm abs}(V) = \left| e^{-\tau(V)} - \left(\frac{T_{\rm on}(V) - (T_{\rm off}(V) + 3\sigma_{T_{\rm off}})}{T_{\rm cont}} \right) \right| \tag{1.20}$$

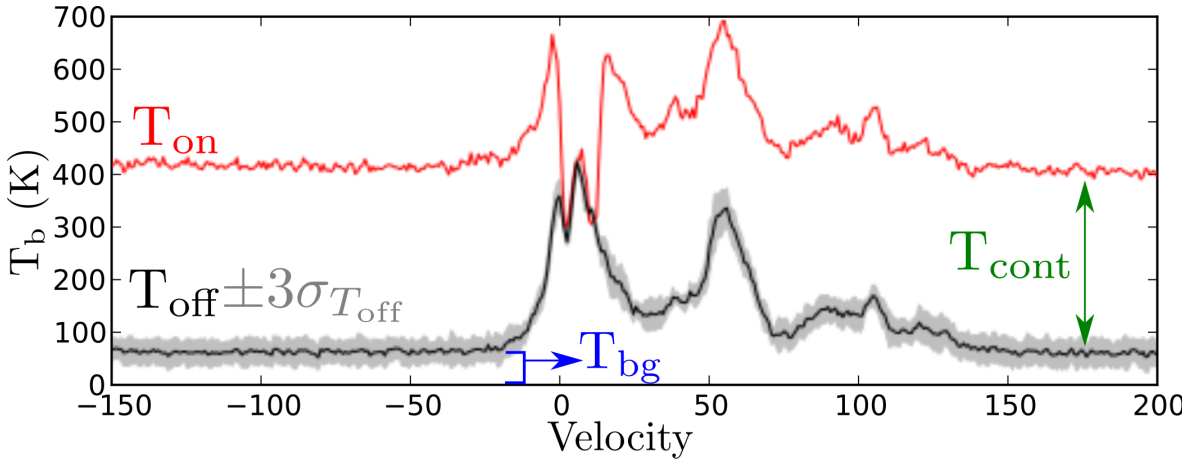

Figure 1.20: Brightness temperature of sample $T_{\rm on}$ (peak brightness, shown in red) and average off source (black) spectra for G269.133-1.137. The grey envelope around the average off source spectrum represents a 3σ variation between the three off source positions. Components of Equations 1.17 and 1.18 are labelled.

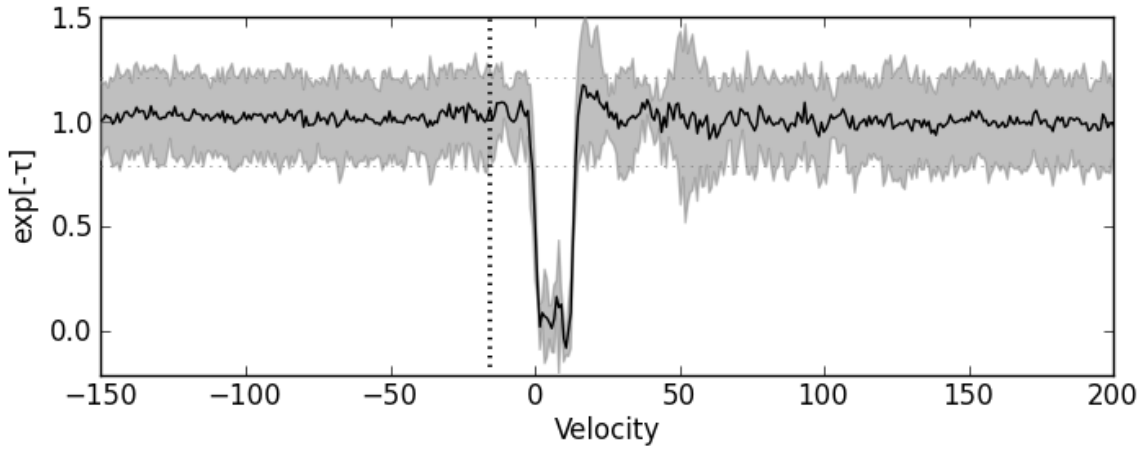

Figure 1.21: H I absorption spectrum for G269.133-1.137 (i.e the same source as Figure 1.20). The grey envelope is the absorption uncertainity envelope, $\Delta_{\rm abs}(V)$, see Equation 1.20. The vertical dotted line is the terminal velocity as computed from the McClure-Griffiths & Dickey (2007) rotation model.

1.5 Terminal Velocity KDAR Method

In the inner Galaxy, each velocity can be mapped to two line of sight distances (this is the KDA discussed in Section 1.2.4, see Figure 1.22)—except the terminal velocity, which maps unambiguously to the tangent, or sub–central point. However, if there is an interstellar cloud between a radio continuum emission source and the observer (see Figure 1.19), the Doppler shift of its absorption lines indicates its kinematic location—via a model for Galactic rotation (see Section 1.2.3).

Therefore if the continuum target source (with a velocity different to the tangent point velocity) is on the near side of the tangent point, there can only be absorption from clouds with velocities less than, in absolute value, the radial velocity of the target. However, if absorption is found at velocities up to the maximum possible absolute radial velocity due to Galactic rotation (i.e. the terminal velocity), then the source must be on the far side of the tangent point. The terminal velocity KDAR method is described in detail by Kolpak et al. (2003) and is represented in Figure 1.23 (from the same work).

This method forms the basis of all KDAR attempts within this thesis. Chapters 3 and 4 present slightly altered methodologies, however they retain the use of H I associated with known velocity features to constrain the lower–limit for line of sight distances towards H II regions.

Note that this method does not necessarily give the line of sight distance to the absorbing cloud itself, but instead to the background continuum source. The distances to absorbing clouds remains ambiguous, *unless* they are located in the outer Galaxy; associated with a known Galactic structure feature (see Chapter 4); or are located in front of a near–side continuum source. The location of the absorbing clouds can still be investigated in Longitude-Velocity space without KDARs.

The terminal velocity method is quite simple to execute *if* the H I absorption spectrum is of sufficient quality. However, there are regions of the Galaxy which are unsuitable for the H I terminal velocity analysis. Large non-circular motions render regions of high-latitude (Swaters et al. 1997) and lines of sight through the Galactic centre region ($|l| < 10^\circ$) unsuitable for the H I terminal velocity method. For wedges of longitude $75^\circ < l < 90^\circ$ and $270^\circ < l < 290^\circ$, where $|dV/dS|$ is small, the KDAR method is weakened; a small uncertainty in velocity corresponds to a large uncertainty in line of sight distance.

For the annulus defined by Galactocentric radii 4 kpc $< R <$ 7 kpc, the H I terminal velocity method is valid. However, molecular clouds (especially CO) have a smaller intrinsic velocity dispersion and may be more suitable for determining KDARs.

The value of the terminal velocity depends on the assumed Galactic rotation curve, see Figure 1.22. Roman-Duval et al. (2009) determine that the choice of rotation curve does not alter line of sight distances, to most molecular clouds, by more than 10%—unless the cloud was located near the tangent point, where the difference increased to 30%. Kolpak

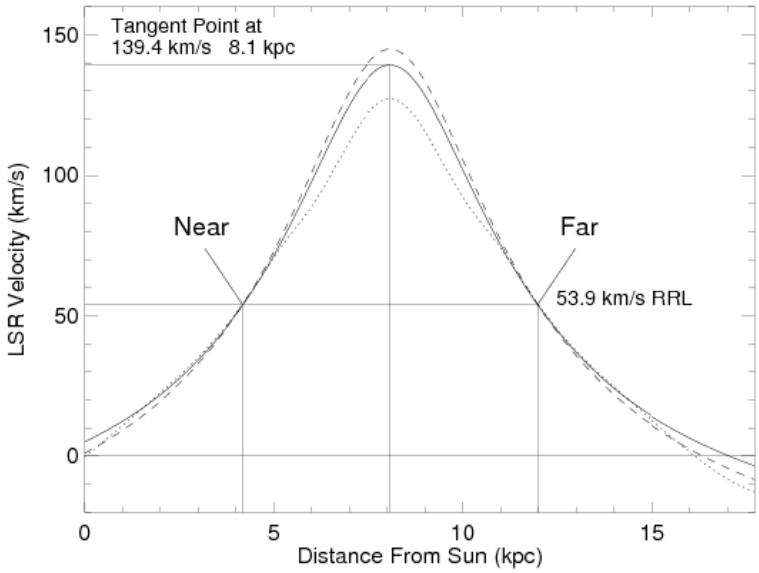

Figure 1.22: Figure 1 of Anderson et al. (2009). Line of sight LSR velocity vs line of sight distance for the H II region at G18.15-0.28 (note that for lines of sight in the fourth quadrant, the sign of velocity would be reversed. The H II region has a measured RRL velocity of 53.9 km s^{-1} which indicates the H II region is located *either* 4 or 11 kpc from the Sun (i.e. the inner Galaxy KDA). Three Galactic rotation models are shown; that of Clemens (1985, dotted), Brand (1986, dashed), and McClure-Griffiths & Dickey (2007, solid, used throughout this thesis)—the differences between the models is most obvious at the tangent point.

et al. (2003) concur with the findings of Roman-Duval et al. (2009), finding small differences between kinematic distances provided by various rotation curves (typically 5-10%).

It should be noted that while the numerical values for the kinematic distances depend on the choice of Galactic rotation curve, the 'near' or 'far' KDAR remains an important *and valid* scientific investigation.

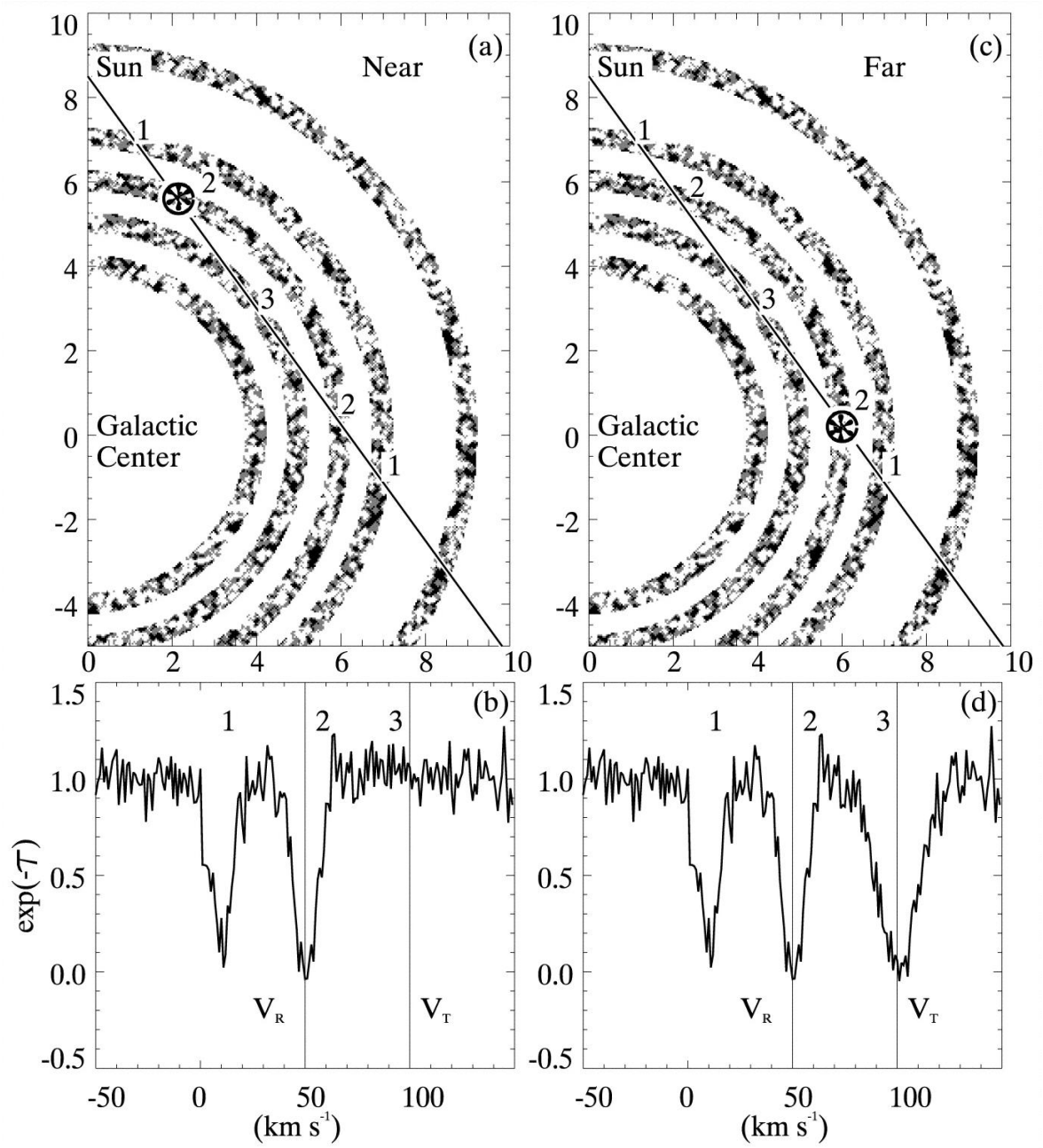

Figure 1.23: Figure 1 from Kolpak et al. (2003). *Face-on schematic diagrams of the Galaxy for (a) near and (c) far kinematic distance. The numbered ticks mark distances in kiloparsecs from the Galactic center. Panels b and d show the schematic spectra corresponding to the sight lines indicated in panels a and c, respectively.*

1.6 Thesis Motivation

As noted in previous Sections, H I absorption needs to be measured against a background continuum source. In the fourth quadrant, the sample of known extragalactic sources has been extensively studied by Strasser (2006), Strasser et al. (2007) and Dickey et al. (2009). Consequently, this thesis uses a previously uninvestigated sample Galactic H II regions. This technique is described by Wendker & Wrigge (1996), who suggested that as many H I sight lines, towards as many H II regions as possible, should be investigated.

One of the drawbacks of using Galactic continuum sources is ambiguous line of sight distances as a result of the inner Galaxy KDA. Throughout this thesis, we don't focus on the mapping of ISM parameters as suggested by Wendker & Wrigge (1996), but instead the Galactic distribution of the H II regions themselves. The number of H II regions known in the fourth quadrant, compared to the first quadrant, is low—no large scale H II region discovery surveys have been made since the work of Caswell & Haynes (1987). Furthermore, the number of southern H II regions with known line of sight distances is also low.

The aim of this thesis is to use H I, and the terminal velocity KDAR method (see Section 1.5) to determine the line of sight locations of fourth quadrant H II regions. H I absorption has been used to provide KDARs for over forty years (see, for example Figure 1.14). These investigations can then lead to further analysis of the structure of our own Galaxy.

1.6.1 Thesis Overview

This introductory Chapter first explored the early phase of investigations into the structure of our own Galaxy. This thesis builds on the subsequent discoveries of the twentieth century (see Table 1.3), to continue efforts to map our own Galaxy.

Chapter 2 describes the various datasets used throughout this thesis; these include H I line, radio continuum, infrared data and H II region RRL catalogs.

Decade	Milestone
1920s	The Milky Way is a separate Galactic system
	Differential model for Galactic rotation
1930s	First quantitative analyses of interstellar matter
1940s	Observations: H II regions deliniate spiral arms in external galaxies
	Prediction of H I and hydrogen RRL transitions
1950s	Discovery of H I line (in emission and absorption)
	Evidence of spiral structure of Milky Way from H I
1960s	Discovery of RRL transitions
1970s	Three phase model of ISM
	Galactic struture sought via distribution of H II regions
1980s	Large–scale H II region discovery surveys

Table 1.3: Overview of Chapter 1 (and Appendix A), reporting milestones of the discovery and development of the tracers and methods used within this thesis.

Chapter 3, published as Jones & Dickey (2012), proposes a modification of the H I terminal velocity KDAR method of Kolpak et al. (2003). Rather than using the maximum velocity of H I absorption to discriminate between the kinematic near and far distances, the integrated absorption over particular velocity ranges is investigated. This modified method was first tested against first quadrant H II regions with KDARs from Anderson & Bania (2009), and then applied to regions without known distances in the fourth quadrant.

The premise of the H I terminal velocity KDAR method is to identify sites of absorption with known (unambiguous) velocities—in this case the sub–central point— *in front of* the continuum emitting H II region. In Chapter 4, published as Jones et al. (2013), this logic is extended to associate known structures in the Extreme Inner Galaxy (EIG, $R_{\rm Gal} < 4$ kpc) with H I absorption in longitude–velocity space. As a result, we constrain the line of sight distances to H II regions within $|l| < 10^{\circ}$—an area of the Galaxy unsuited to the terminal-velocity KDAR analysis.

Chapter 5, published as Brown et al. (2014), presents H I emission and absorption spectrum pairs towards *every known* H II region visible to the Southern Galactic Plane Survey (McClure-Griffiths et al. 2005, discussed in Chapter 2). This catalog allows for the H I absorption to be investigated in longitude–velocity space.

As the result of Chapter 5, the sample of known fourth quadant H II regions which has been prepared for, or had an attempted, KDAR analysis is now exhausted—comparable to the first quadrant sample at the conclusion of Anderson & Bania (2009). In order to rejuvenate the H II region sample, Chapter 6 searches the data of the H_2O southern Galactic Plane Survey (HOPS, Walsh et al. 2011, an existing unbiased RRL survey) for unknown H II regions; which can be confirmed without undertaking any new observations.

In the northern hemisphere, the exhaustion of KDAR candidates was overcome through new targeted H II region discovery surveys—most notably the Green Bank Telescope H II Region Discovery Survey (see Chapter 2). Chapter 6 reviews the criteria for identification of H II region candidates, and considerations required for H II region discovery observations with the Australia Telescope Compact Array (ATCA). Following these preprations, Chapter 7 details two short programs of ATCA H II region discovery observations.

Finally, Chapter 8 offers an overview of the results of this thesis—and promotes the undertaking of a large–scale Southern H II Region Discovery Survey.

Chapter 2

Common Data Sets

In order to avoid unnecessary duplication, the archival datasets from Chapters 3, 4 and 5 are described here.

2.0.2 Neutral Hydrogen H I Datasets

The physics and theoretical nature of the H I transition was described in Section 1.4.2. Here, we describe the H I datasets that provide H I emission and absorption spectra along lines of sight toward H II regions.

2.0.3 International Galactic Plane Survey

The majority of this thesis is derived from analysis of 21-cm, International Galactic Plane Survey (IGPS) H I data. The IGPS is the result of a global collaboration and includes four centimetre-wavelength surveys; the Southern Galactic Plane Survey (SGPS, McClure-Griffiths et al. 2005), the VLA Galactic Plane Survey (VGPS, Stil et al. 2006), the Canadian Galactic Plane Survey (CGPS, Taylor et al. 2003) and the Effelsberg Medium-Latitude Polarization Survey. Combining interferometric and single-dish observations, the component surveys of the IGPS form a uniform dataset, with a resolution of about $1'$, that covers 90% of the Galactic disk (Stil et al. 2006).

Within the Milky Way, there are extended H I structures on the order of ∼tens of arcminutes; likely to correspond largely to the extended WNM, but also to some parts of the CNM. The interferometric component surveys of the IGPS are only sensitive to spatial frequencies larger than those probed by the shortest baseline of the telescope array—as a result, large-scale structure is not probed by the interferometers and is hence unobservable ("resolved out"). The missing (extended structure) information can be 'filled in' by a single dish telescope (with a diameter at least 1.5 times the shortest interferometer baseline). The process of combining single-dish data with interferometer observations, in order to recover large-scale structure, is known as 'short-spacing correction' or 'zero-spacing correction' (Kalberla & Kerp 2009). Each component survey of the IGPS has been short-spacing corrected, resulting in unprecedented data quality (Stil et al. 2006; Kalberla & Kerp 2009).

The component surveys of the IGPS used in this thesis are further described below.

Survey Name	Longitude Range	Latitude Range	Resolutions Spatial ($''$)	Velocity (km s^{-1})
H I *and 21-cm Continuum*				
Southern Galactic Plane Survey I (SGPS I)	$253^\circ < l < 358^\circ$	$\|b\| < 1.5^\circ$	130	0.82
VLA Galactic Plane Survey (VGPS)	$18^\circ < l < 65^\circ$	$\|b\| < 1^\circ$	60	1.56
H I *Line Only*				
Southern Galactic Plane Survey II (SGPS II)	$5^\circ < l < 20^\circ$	$\|b\| < 1.5^\circ$	120	1.0
ATCA H I Galactic Center Survey (ATCA HIGCS)	$-5^\circ < l < 5^\circ$	$\|b\| < 5^\circ$	120	1.0
Radio Continuum Only				
NRAO VLA Sky Survey (NVSS)	(entire sky north of $-40^\circ\delta$)		45	-

Table 2.1: The sky coverage and other survey parameters of the H I line and radio continuum datasets used in this thesis.

2.0.3.1 Southern Galactic Plane Survey, SGPS

The Southern Galactic Plane Survey covers 325 square degrees of the Galactic plane over the fourth and first Galactic quadrants (SGPS I and SGPS II respectively). The SGPS was designed for absorption studies, which require knowledge of both continuum and H I flux in order to accurately measure optical depth. To this end, the SGPS provides both H I line data, and continuum maps (Haverkorn et al. 2006), which are used for source detection and identification within this thesis.

Throughout this thesis we use the continuum *included* combined Parkes-ATCA data. These cubes were specifically produced for H I absorption studies, and they provide accurately calibrated data at the highest angular resolution of the SGPS. All SGPS continuum and line cube data are available online via the Australia Telescope National Facility (ATNF) H I Surveys archive*.

SGPS data has been used extensively in a large number of fields, including studies of H I self-absorption (e.g. Gibson et al. 2005; Kavars et al. 2005), the cold neutral interstellar medium in the outer Galaxy (e.g. Strasser et al. 2007), Galactic structure (e.g. McClure-Griffiths et al. 2004) as well as investigations of particular individual sources (e.g. Kothes & Dougherty 2007).

Continuum Calibration of the SGPS The SGPS line data is recorded in units Jy beam^{-1}. The following unit transformation (to K) is used to convert the brightness temperature of the emission spectrum, and continuum temperature, in order to report and compare parameters for each source (e.g. continuum temperatures in Tables 3.1 and 5.2 or the top panels of figures in Appendix C) . Note that the calculation of an absorption spectrum (Equation 1.19) does *not require* this conversion.

Firstly, we assume a two-dimensional Gaussian beam solid angle, Ω (Equation 2.1), then we solve for the flux density, S, for an unresolved source (Equation 2.2) in terms of antenna

*http://www.atnf.csiro.au/research/HI/common

temperature, T_A:

$$\Omega = \frac{\pi}{4\ln(2)} \left(\mathrm{FWHM}_\phi \mathrm{FWHM}_\psi\right) \tag{2.1}$$

$$S = \frac{2k}{\lambda^2} \Omega\, T_A \tag{2.2}$$

Theoretically, the antenna temperature is the convolution of the beam response with the sky brightness temperature distribution, integrated over the entire sky. Substituting $\lambda = 21.1$ cm, creating dimensionless variables, and using the SGPS synthesized beam solid angles given in Table 4 of McClure-Griffiths et al. (2005) results in:

$$T_b\,(\mathrm{K}) \approx 606 \left(\frac{S}{\mathrm{FWHM}_\phi \times \mathrm{FWHM}_\psi}\right) \left(\frac{\mathrm{Jy\ beam}^{-1}}{\mathrm{arcseconds}^2}\right) \tag{2.3}$$

The continuum temperature is estimated from the difference in on and off spectra across a range of velocity channels in which there is no H I signal. For most spectra we used the velocity channel range 100 km s^{-1} $< V <$ 175 km s^{-1} as this avoids both expected Galactic circular rotation velocities, as well as the ends of the spectrum band (see Figure 1.20).

2.0.3.2 VLA Galactic Plane Survey, VGPS

The VLA Galactic Plane Survey is the northern counterpart to the SGPS - providing both 20 cm H I line data and continuum emission from the Galactic plane*. The VGPS was carried out by the Very Large Array and zero-spacing corrected with Green Bank Telescope and Effelsberg Telescope observations.

The VGPS was completed after the CGPS and SGPS and provided the first overlap areas such that the component surveys of the IGPS could be compared. Despite differences in instrumentation and image-processing, the differences between the VGPS and SGPS are small (Stil et al. 2006).

2.0.4 The ATCA H I Survey of the Galactic Center

The Australia Telescope Compact Array H I Galactic Center Survey (ATCA HIGCS, McClure-Griffiths et al. 2012) covers the area $|l| < 5°$, $|b| < 5°$, over the velocity range $-309 \leq V_{\mathrm{LSR}} \leq$ 349 km s^{-1} with a velocity resolution of 1 km s^{-1}. This Survey complements, and connects, the two components of the SGPS; resulting in continuous coverage of the inner Galactic plane. Unlike the IGPS, no continuum images were released with the H I dataset.

In keeping with the methodology of the SGPS, the ATCA HIGCS was supplemented with short-spacing data from the Parkes Radio Telescope. All ATCA HIGCS data are publicly available†.

*VGPS data are available via ftp from www.ras.ucalgary.ca/VGPS/VGPS_data.html

†http://www.atnf.csiro.au/research/HI/sgps/GalacticCenter/Home.html

2.1 Radio Continuum

Analysis of H I absorption requires the presence of a background radio continuum emission source. Many of the H I datasets include complementary continuum data (see below); here we describe stand-alone continuum surveys used in this thesis.

The NRAO VLA Sky Survey

The National Radio Astronomy Observatory Very Large Array Sky Survey (NVSS, Condon et al. 1998) covers 82% of the sky (north of $\delta = -40^\circ$) at 1.4 GHz, and consists of 2326 $4^\circ \times 4^\circ$ continuum maps for each Stokes parameter and a catalogue of continuum emission sources*.

Only the Stokes I maps were used for this thesis. It should be noted that the NVSS maps are completely interferometric and therefore are not sensitive to the largest spatial frequencies; as a result many larger, diffuse, emission regions, particularly those in the Lockman et al. (1996) catalogue, are not detectable.

2.2 H II Region Catalogs

Catalogues of RRLs provide systemic velocities for, and confirm the presence of, H II regions. Large-scale surveys of RRLs from H II regions were performed in both the northern and southern hemispheres during the 1960s to 1980s.

The catalogues are summarised in Table 2.2.

Wilson et al. (1970)

Wilson et al. (1970) detected the H109α RRL toward 130 H II regions in the southern sky ($189^\circ < l < 50^\circ$) using the Parkes Radio Telescope (with a beam HPBW of $4'$). The aims of this survey were to extend existing northern surveys into the southern sky, to obtain source velocities to aid in tracing the overall spiral structure of the Galaxy, and to investigate if the asymmetry in the northern/southern H I rotation curves was reflected in the motion of H II regions. The Wilson et al. (1970) survey is a component of the NRAO-CSIRO-MIT H109α-line survey; which is virtually complete for all sources with a peak flux at 5000 MHz greater than $\gtrsim 1.5$ Jy.

Downes et al. (1980)

The Downes et al. (1980) survey is complete for sources with peak flux densities > 1 Jy for $0^\circ < l < 60^\circ$ and $|b| < 1^\circ$, and > 2 Jy for $357^\circ < l < 0^\circ$, from the Altenhoff et al. (1979) continuum source catalogue. In addition to the discovery of H II regions, the Downes et al. (1980) study investigated the electron temperature gradient across galactocentric radii and the galactocentric source distribution. As with many of the RRL surveys discussed here, Downes et al. (1980) concurrently observed H_2CO towards their target sources, and used absorption signatures to obtain KDARs (in a similar manner to which we use H I throughout

*The full NVSS survey is available via anonymous ftp from http://www.cv.nrao.edu/nvss/

Survey	No.	RRL	Sky Coverage	HPBW	Telescope
Wilson et al. (1970)	130	H109α	$189^\circ < l < 50^\circ$	$\sim 4'$	Parkes
Downes et al. (1980)	262	H110α	$0^\circ < l < 60^\circ$	$2.6'$	Effelsburg
Wink et al. (1982)	85	H76α/H90α	$359^\circ < l < 214^\circ$	$2.6'/1'$	Effelsburg
Caswell & Haynes (1987)	316	H109α–H110α	$210^\circ < l < 360^\circ$	$\sim 4'$	Parkes
Lockman (1989)	462	H85α, H87α–H88α H100α–H101α H110α H125α/H127α	$350^\circ < l < 253^\circ$	$\sim 3'$ $\sim 5'$ $\sim 6'$ $\sim 9'$	NRAO 140 ft at Green Bank
Lockman et al. (1996)	130	H109α/H111α H126α/H127α	$358^\circ < l < 231^\circ$	$\sim 6'$ $\sim 9'$	NRAO 140 ft
Sewilo et al. (2004)	72	H110α	$10^\circ < l < 65^\circ$	$\sim 3'$	GBT
GBTHRDS Bania et al. (2010)	448	H87α–H93α	$344^\circ < l < 67^\circ$	$\sim 1.3'$	GBT

Table 2.2: Overview of RRL surveys detailed in Section 2.2. The reference, number of H II regions detected with RRL emission, RRL transitions observed, longitude range of survey (H II discovery surveys are confined to the Galactic Plane, usually $|b| \lesssim 1.5^\circ$), Half Power Beam Width (HPBW) and survey telescope are listed for each study. Many studies observed RRL transitions over a range of frequencies, in these instances the beam size for each frequency range is listed.

this thesis)—noting their distribution of H II regions is consistent with the spiral pattern of Georgelin & Georgelin (1976).

Wink et al. (1982)

Wink et al. (1982) also used the 4.9 GHz Altenhoff et al. (1979) continuum survey to select point sources that are relatively well–separated from other continuum emission for further observations. Using the Effeslburg telescope, Wink et al. (1982) observed 91 continuum sources, of which H75α or H90α RRL emission was detected from 50; confirming them as H II regions. H_2CO absorption, observed simultaneously to the RRL, was used to provide KDARs for 50 of the 85 H II regions.

Caswell & Haynes (1987)

The catalogue of Caswell & Haynes (1987) provides hydrogen RRL parameters (and H_2CO absorption) for 316 H II regions, observed with the Parkes 64-m Radio Telescope, over the longitude range $210^\circ < l < 360^\circ$. The majority of H II regions in this study were sourced from this work, the southern counterpart to the Lockman (1989) catalogue (described below).

Despite the use of the same telescope, the Caswell & Haynes (1987) survey extended the Wilson et al. (1970) survey; re-observing more than half of the Wilson et al. (1970) sources and adding approximately 200 new targets, through the use of a more complete catalogue of continuum sources (compiled during 1978-1979). The Caswell & Haynes (1987) survey

contains most H II regions that show 5 GHz continuum brightness temperatures exceeding 1 K (as observed with the $4'$ beam of the Parkes telescope).

Lockman (1989)

This large survey provides RRL velocity detections for 462 H II regions and is the canonical H II region catalogue for the northern sky. The Lockman (1989) survey is estimated to be complete for 5 GHz continuum sources (from Altenhoff et al. 1979) with flux densities ≥ 1 Jy at $\delta \geq -37°$. Lockman (1990a,b) state that the survey probably includes all "Orion A" type nebulae within about 20 kpc of the Sun for $\delta \geq -37°$—although revised (closer) distance estimates to Orion make this unlikely.

Lockman et al. (1996)

The catalogue focused on detecting RRL emission from diffuse (i.e. not classical) H II regions—the Rosette Nebula is the canonical example. This survey aimed to discover diffuse H II regions; therefore, integration times were only as long as required to gain RRL velocity detections and the survey is not complete in any respect. It was discovered that these diffuse H II regions share the same Galactic distribution as their 'classical' counterparts.

Sewilo et al. (2004)

Seventy-two sources were selected that satisfy the infrared Wood & Churchwell colour criteria for ultra-compact H II regions (see Section 6.2.1.2); have 100μm flux densities $\gtrsim 1000$ Jy and lie within the longitude ranges $-20° < l < -10°$ or $10° < l < 30°$; with $|b| < 1°$ (i.e. within the *Spitzer* GLIMPSE survey range—the GLIMPSE survey is described in Section 2.3). H_2CO was simultaneously observed with the RRL transition, and the resulting spectra were used to successfully provide KDARs for 44 of the 72 RRL detected H II regions.

Green Bank Telescope H II Region Discovery Survey

The Green Bank Telescope H II Region Discovery Survey (GBTHRDS, Bania et al. 2010) detected 602 RRL components towards 448 continuum sources in the Galactic plane between $344° < l < 67°$. The survey more than doubled the number of known H II regions within that longitude range - the majority of previously known H II regions were sourced from the Lockman (1989) catalogue. With a 95% detection rate the GBTHRDS selected its target sample from spatially coincident mid-infrared and radio continuum emission. The *Spitzer* MIPSGAL survey (Carey et al. 2009) provided 24μm data, while 21cm continuum emission was sourced from the SGPS, VGPS (Stil et al. 2006) and NVSS (Condon et al. 1998). Complete to 180 mJy at 9 GHz, the Survey is able to detect all H II regions ionized by a single O star to a distance of 12 kpc.

In addition, the GBTHRDS team also compiled a catalogue of known H II regions, as of 2010. The compilation process removed duplicate sources through radio continuum and mid-infrared inspection. However, they note that it is "likely to contain some residual contamination and duplicate entries". The catalogue of 'known' region extends to only $l = 353°$

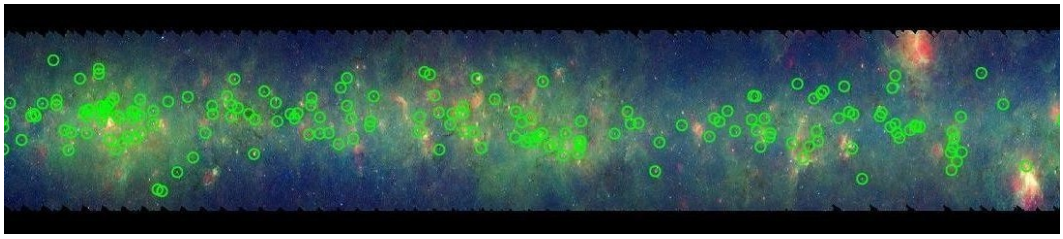

Figure 2.1: H II regions discovered by the GBTHRDS between $15^\circ \lesssim l \lesssim 30^\circ$ and $|b| < 1^\circ$ (green circles) overlaid on an infrared background (red: MIPSGAL 24 μm; green/blue: GLIMPSE 8.0/3.6 μm emission). From the HRDS web portal.

in the Southern sky. Both the GBTHRDS catalogue and the compilation of previously known H II regions is publicly available from the HRDS web portal*.

2.3 Infrared

Infrared data can be used to investigate the location (either Galactic or extragalactic) and classification of a radio continuum emission source—infrared colours have long been used to compile catalogues of H II region candidates (described in detail in Chapter 6). The physical environments probed by the various infrared wavelengths are described in Table 2.3 as well as Sections 1.3.2.2 and 6.2. Anderson et al. (2012b) also provides a discussion of the datasets included in Table 2.4 for the purposes of H II region identification.

IRAS

Launched in 1983, the Infrared Astronomical Satellite (IRAS, Neugebauer et al. 1984) was the first ever space-based observatory to perform a survey of the entire sky at infrared wavelengths. IRAS detected over 350,000 infrared sources, increasing the number of contemporary known sources by 70%. We do not directly use any IRAS data; however, the use of IRAS colours to establish criteria for the identification of H II regions is discussed in Section 6.2.1. Note: the specifications listed in Table 2.4 are for the original IRAS data. The most recent reprocessing of the original data, known as IRIS, corrects for calibration issues and striping—resulting in a factor of five increase in sensitivity.

Spitzer

GLIMPSE

The *Spitzer* Galactic Legacy Infrared Mid-Place Survey Extraordinaire (GLIMPSE I DR5 data release) coverage area includes the ends of the Galactic bar and spiral arms in the inner parts of the first and fourth quadrants. Further data releases cover the Galactic center (GLIMPSE II) and outer Galaxy (GLIMPSE 360), as well as vertical (latitude) extensions for selected longitude ranges (GLIMPSE 3D). GLIMPSE provides 3.6, 4.5, 5.8 and 8 μm images, mosaiced at two pixel scales; 0.6″ (high resolution) and 1.2″ (native resolution).

*www.cv.nrao.edu/hrds

Wavelength (μm)	Survey(s)
Near Infrared	
Stellar Emission:	
2.4	WISE
3.6	GLIMPSE
Ionised and shocked gas:	
4.5	GLIMPSE
4.6	WISE
Mid Infrared	
Photodissociation regions & emission from polycyclic aromatic hydrocarbons:	
5.8	GLIMPSE
8	GLIMPSE
12	IRAS, WISE
Warm dust spatially coincient with the ionized gas:	
22	WISE
24	MIPSGAL
25	IRAS
Far Infrared	
Thermal emission from cooler dust in molecular clouds:	
60	IRAS
70	MIPSGAL
100	IRAS

Table 2.3: The physical environments probed by the wavelengths of surveys outlined in Section 2.3.

However, only the 8μm data are used in analysis. While the presence of co-spatial mid-infrared and radio continuum emission infers a Galactic source (see above), 8μm images can further characterise the source (see Chapter 6).

MIPSGAL

"A 24 and 70 Micron Survey of the Inner Galactic Disk with MIPS", MIPSGAL (Carey et al. 2009), covers 278 square degrees of the inner Galactic plane and provides mosaiced images at resolutions of 6″ and 18″ for 24 μm and 70 μm respectively . The main science goals of MIPSGAL included identification and analysis of massive star formation regions in the inner Galaxy. It complements the shorter wavelength, GLIMPSE survey (above). As with GLIMPSE, the Galactic center region has been mapped as an extension of the original survey—MIPSGAL Version 3 provides coverage of $-8° < l < 9°$ and $|b| < 3°$ at 24μm only.

WISE

The Wide-field Infrared Survey Explorer (WISE, Wright et al. 2010), All-Sky data release (March 14, 2012) covers the whole sky at wavelengths of 2.4, 4.6, 12 and 22 μm. In Chapter 3, WISE 22 μm images are used to confirm that 1.4 GHz continuum emission sources are Galactic—as a source showing both mid-infrared and radio continuum is likely to be Galactic (Anderson et al. 2011b). In a similar manner, the WISE data is also used by Anderson et al. (2014), described in Chapter 6, to produce a catalogue of Galactic H II Region candidates.

Survey & Sky Coverage	Wavelength (μm)	Angular Resolution	Sensitivity (mJy)
Infrared Astronomical Satellite			
IRAS	12	$0.75' \times 4.6'$	500
(96% of sky)	25	$0.75' \times 4.6'$	500
	60	$1.5' \times 4.7'$	500
	100	$3.0' \times 5.0'$	1000
Spitzer Space Telescope			
GLIMPSE I (DR5)	3.6	$1.2''$	0.20
($10^\circ < l < 65^\circ$, $295^\circ < l < 350^\circ$	4.5	$1.2''$	0.20
with $\|b\| < 1^\circ$)			
	5.8	$1.2''$	0.4
	8.0	$1.2''$	0.4
MIPSGAL	**24**	$\mathbf{6}''$	**1.3**
($5^\circ < l < 63^\circ$, $298^\circ < l < 355^\circ$	70	$18''$	73
with $\|b\| < 1^\circ$)			
Wide-field Infrared Survey (WISE)			
All-Sky Release	3.4	$6.1''$	0.08
(all sky)	4.6	$6.4''$	0.11
	12	$6.5''$	1
	22	$\mathbf{12}''$	**6**

Table 2.4: The specifications of the infrared surveys discussed or analysed (bold) in this thesis. The reported sensitivities are indicative of 5σ point source sensitivities in unconfused regions on the ecliptic.

Chapter 3

Kinematic Distance Assignments with H I Absorption

This Chapter includes a co-authored paper.
The bibliographic details of the paper are as follows: Jones, C. and Dickey, JM;, Astrophysical Journal, 753, (1) Article 62, doi:10.1088/0004-637X/753/1/62. The published paper is referenced by this thesis as Jones & Dickey (2012). Please note that Jones is the maiden name of the candidate.

The introductory and methodology sections have been adapted to avoid unnecessary duplication - see Chapters 1 and 2. The individual source descriptions, Section 8 of the published work, are included in Appendix B of this thesis.

Abstract

Using H I absorption spectra from the International Galactic Plane Survey, a new method is implemented to resolve the kinematic distance ambiguity for 75 H II regions with known systemic velocities from radio recombination lines. A further 40 kinematic distance determinations are made for H II region candidates without known systemic velocities through an investigation of the presence of H I absorption around the terminal velocity. New kinematic distance determinations can be used to further constrain spiral arm parameters and the location and extent of other structures in the Milky Way disk. H I absorption toward continuum sources beyond the solar circle is also investigated.

3.1 Introduction

In this work, Kinematic Distance Ambiguity Resolutions (KDARs) are achieved through analysis of H I emission-absorption spectrum pairs from the VLA Galactic Plane Survey (Stil et al. 2006, VGPS) and Southern Galactic Plane Survey (McClure-Griffiths et al. 2005, SGPS). A discussion on the selection of sources appears in Section 3.2. The sum of the H I absorption spectrum over selected velocity intervals, rather than the optical depth of a single

velocity channel, is used to determine the lower limit of the kinematic distance to each H II region. This new method of KDAR is explained in Section 3.3, and results are presented in Section 3.4. The implications of the successful KDAR are discussed in Section 3.6. These include asymmetries in the first and fourth quadrant samples, as well as an investigation of the near:far kinematic distance ratio.

In addition to the KDARs of Section 3.4, the new KDAR method employed in this paper can be extended to investigate absorption in the outer Galaxy. The number of H II regions known to exist beyond the Solar circle, on the far side of the Galactic Center, is extremely limited. Section 3.7 investigates absorption in velocity ranges corresponding to the outer Galaxy in order to prepare a target list of objects suitable for further RRL observations.

Finally, H II regions that are widely discussed in the literature, as well as those that demonstrate significant absorption beyond the Solar Circle, are discussed individually (Appendix B).

3.2 Observations and Data

3.2.1 Archival Data

This paper makes use of radio and infrared archival data (described in Chapter 2). Radio continuum and emission/absorption spectra are extracted from the VGPS and SGPS, while the Wide-field Infrared Survey Explorer (Wright et al. 2010, WISE) and Spitzer Galactic Legacy Infrared Mid-Plane Survey Extradinordinarie (Benjamin et al. 2003, GLIMPSE) surveys provide infrared images used in Section 3.7.

3.2.2 Source Inclusion

In contrast to the majority of KDAR studies in the literature, this work does not start with a target list of H II regions from previous RRL catalogues. Instead, sources were selected through inspection of the VGPS and SGPS continuum maps (see Figure 3.1). As a result, many sources considered here do not have published RRL velocities.

To compare symmetric longitude ranges in the first and fourth Galactic quadrants, two samples of 100 continuum sources were selected in each. Approximately 60 sources of each sample have published RRL velocities. The density of sources in the continuum maps from the SGPS and VGPS are different at the symmetric longitudes ($\pm 25^o$). In order to have the same number of sources in each sample it is necessary to take a broader longitude range in the fourth quadrant than in the first quadrant. This is due both to the lower sensitivity and coarser resolution of the SGPS survey, and to an intrinsic asymmetry in the distribution of continuum sources (Figure 3.1). The longitude ranges chosen were $22.67^o < l < 27.5^o$ and $327.7^o < l < 342.4^o$.

The two longitude ranges give different sample characteristics in their H I absorption profiles as a result of differences in the spiral structure of the Galaxy. For instance, within $22.67^o < l < 27.5^o$ the Bar and Scutum-Centaurus Arm dominate spiral structure at kinematic near distances, while the Perseus and Sagittarius Arms dominate on the far side. The literature on spiral arm locations is too extensive to review here, but for the purpose of vi-

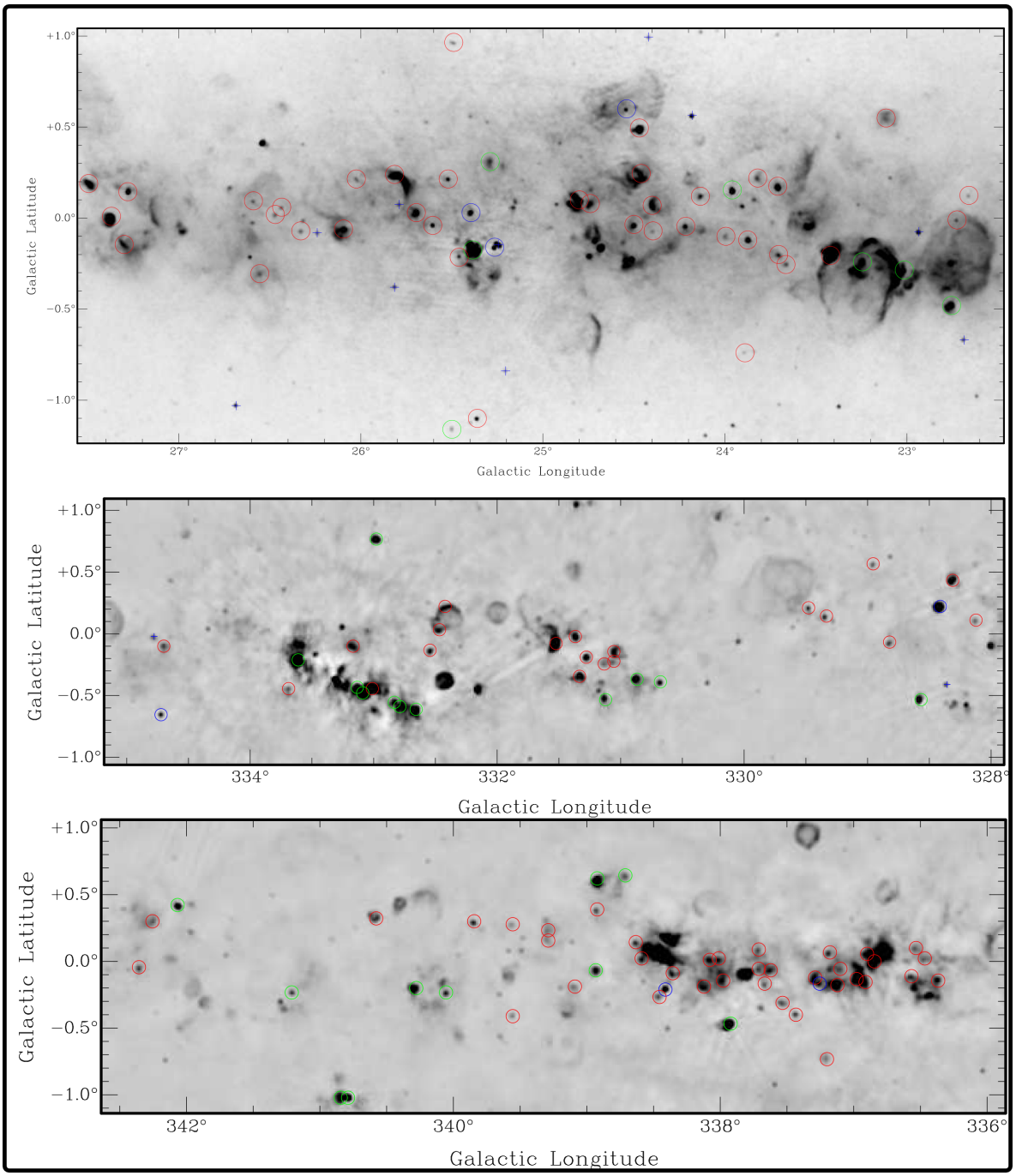

Figure 3.1: The VGPS and SGPS continuum maps showing the location of each radio continuum source with a successful KDAR. Sources are coded as follows: Green - near side; Red - far side; Blue - outer Galaxy or extragalactic (crosses). Note the extent of the longitude range is different in each quadrant.

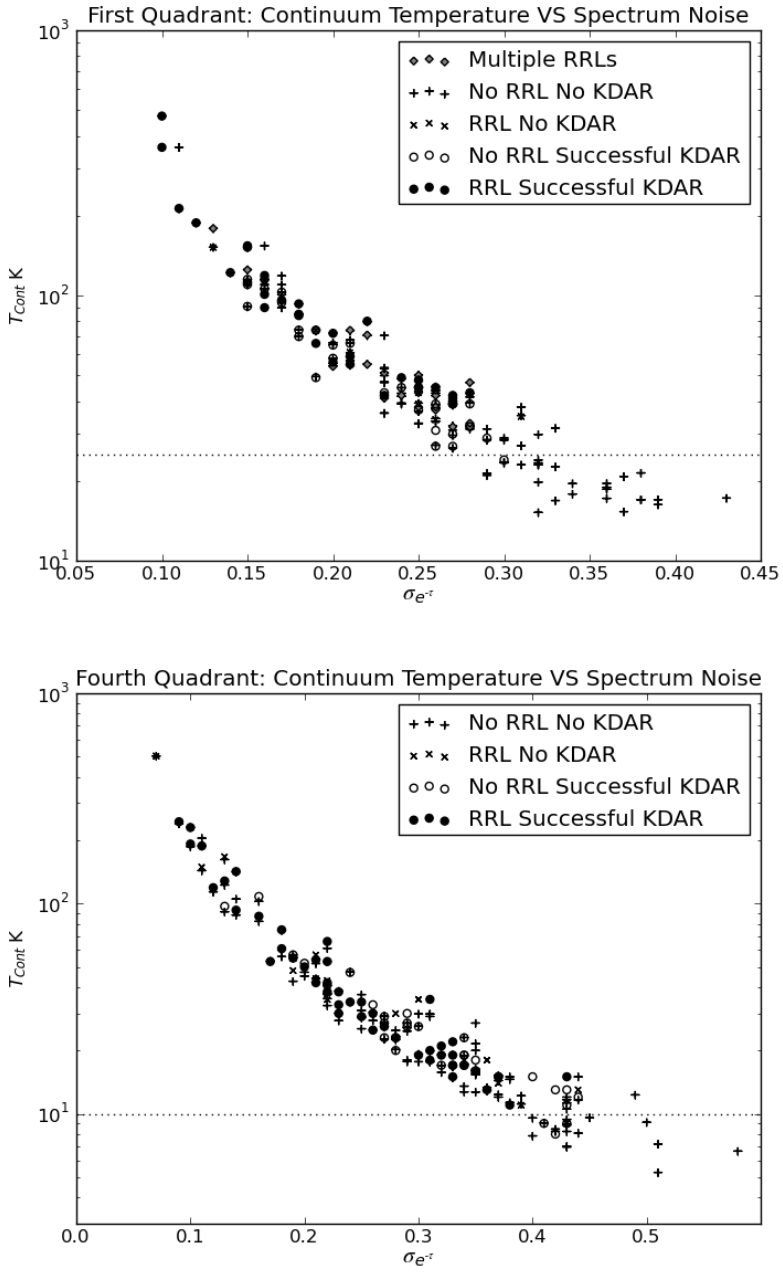

Figure 3.2: The continuum temperature T_{cont} and H I absorption spectrum noise ($\sigma_{e^{-\tau}}$) for the first quadrant (open circles) and fourth quadrant (filled circles) samples.

sualisation of kinematic distances, the face-on Milky Way map of Hurt and Benjamin (2008) using Spitzer data is used throughout this paper.

The KARMA package (Gooch 1996) was used to view each continuum map and catalogue continuum sources. The continuum brightness temperature for which a KDAR is possible was approximately 25 K in the VGPS (first quadrant) and 10 K in the SGPS (fourth quadrant), reflecting the noise levels in the two datasets (Figure 3.2).

3.3 Methodology

The Emission/Absorption (E/A) method has been used for KDARs since the early 1970's Wilson (1972) and has since been employed by many authors. The spectrum extraction and terminal velocity KDAR method are described in Chapter 1 (Sections 1.4.2 and 1.5 respectively).

The Velocity Channel Summation method (Section 3.3.2)—an extension of the E/A method—is used to achieve KDARs for sources with known systemic velocities (Section 3.3.3) and without (Section 3.3.4). Once a kinematic location has been assigned, a kinematic distance can be calculated through the application of the Galactic rotation curve. For all inner Galaxy H II regions (inside the solar circle), the rotation curve of McClure-Griffiths & Dickey (2007) is used.

3.3.1 Emission/Absorption Spectrum Extraction

Absorption spectra were extracted from the VGPS and SGPS, as discussed in Section 1.4.2.

The "on" position is used throughout this Chapter as the "name" of the H II region—designations take the format "G," Galactic longitude, Galactic latitude.

Absorption spectra were verified against data from the literature. Several sources from this analysis are also investigated in Strasser (2006), who also used VGPS continuum and absorption data. The absorption spectra for these sources were compared; in general, the $e^{-\tau}$ values for each velocity channel agree to within 6%.

3.3.2 Velocity Channel Summations

In order to best analyze Galactic structure, data from as many sources as possible (i.e., along the largest number of lines of sight) must be considered. This requires using fainter sources and hence including spectra with higher noise in optical depth, $\sigma_\tau \simeq \sigma_{e^{-\tau}}$. Methods that analyze the absorption in each velocity channel then become problematic (eg. Kolpak et al. 2003; Urquhart et al. 2012), since faint (noisy) sources must demonstrate much stronger absorption than their brighter counterparts to qualify as an absorption detection. A less flux-biased method is to average the absorption over a large number of velocity channels thus reducing the noise level and hence the threshold for detection of absorption (Dickey et al. 2003).

The sum of velocity channels of the absorption spectrum ($S_{\Delta V}$) is computed as:

$$S_{\Delta V} \pm \sigma_S = \sum_{\Delta V}(1 - e^{-\tau}) \pm (\sqrt{N_{\rm ch}}\sigma_{e^{-\tau}}) \tag{3.1}$$

where $N_{\rm ch}$ is the number of velocity channels in the summation interval (ΔV) and $\sigma_{e^{-\tau}}$ is the standard deviation of the noise in the baseine of the $e^{-\tau}$ spectrum—remembering that it is assumed that the E/A spectra sample the same large-scale H I gas (see Section 3.3.1). The measurement of this velocity channel sum is a simple method to quantify the gross absorption along the line of sight for a large sample of sources. For example, for sources with a known RRL velocity, the calculation of $S_{\rm ch}$ between the systemic velocity and terminal velocity, V_T (i.e. $S_{V_{\rm RRL}\text{ to }V_T}$, is a good indicator of whether or not there is significant absorption in this interval, and therefore provides a KDAR. The velocity channel intervals over which $S_{\rm ch}$ is computed must be chosen carefully.

Very few authors make use of velocity integrals, or channel summations, of absorption spectra. Even fewer publish values for specific sources. However, Dickey et al. (2003) published equivalent widths ($EW = \int_{\Delta v} \tau dv$) for 13 H II regions, six of which are held in common with this study. Their absorption spectra were extracted from data from the SGPS Test Region (McClure-Griffiths et al. 2001) and the EW was calculated over all inner Galaxy velocity channels. The EW values agree within 10% for all six H II regions.

3.3.2.1 Velocity Intervals

The velocity intervals for S_{ch} are chosen, in this paper, to avoid the deep absorption often seen in H II regions on both sides of the systemic velocity (Dickey et al. 2003). As a result the default tangent point placement velocity interval (Section 3.3.3 Case A) is required to be within 25 km s^{-1} of the terminal velocity, not 10 to 15 km s^{-1} as with other studies. Consequently, more H II regions are placed at the tangent point location than in other works. This is a conservative approach.

For the same reason, the summation velocity intervals for $S_{V_{RRL}\ to\ V_T}$ start 25km s^{-1} beyond the RRL velocity. In at least one case (eg. G337.922-0.467, see Appendix B) absorption was seen up to 25km s^{-1} beyond the RRL velocity, but no absorption was present within 50 km s^{-1} of the tangent point velocity - therefore it must be on the near side of the tangent point.

The distance errors reported in Table 3.1 correspond to a 15 km s^{-1} uncertainty in velocity. This 15 km s^{-1} accounts for the 5-10 km s^{-1} of uncertainty within the rotation curve as well as the error in the observed RRL velocity (< 5 km s^{-1}), the average of this uncertainty is 10% of the distance for the first quadrant sources and 15% for the fourth quadrant sample. This distance uncertainty is comparable with previous studies that give errors of $10 - 15\%$ (e.g. Roman-Duval et al. (2009); Kolpak et al. (2003)).

See Figures 3.3 and 3.4 for example absorption spectra where the summation intervals are displayed for the analysis in Sections 3.3.3 and 3.3.4 respectively.

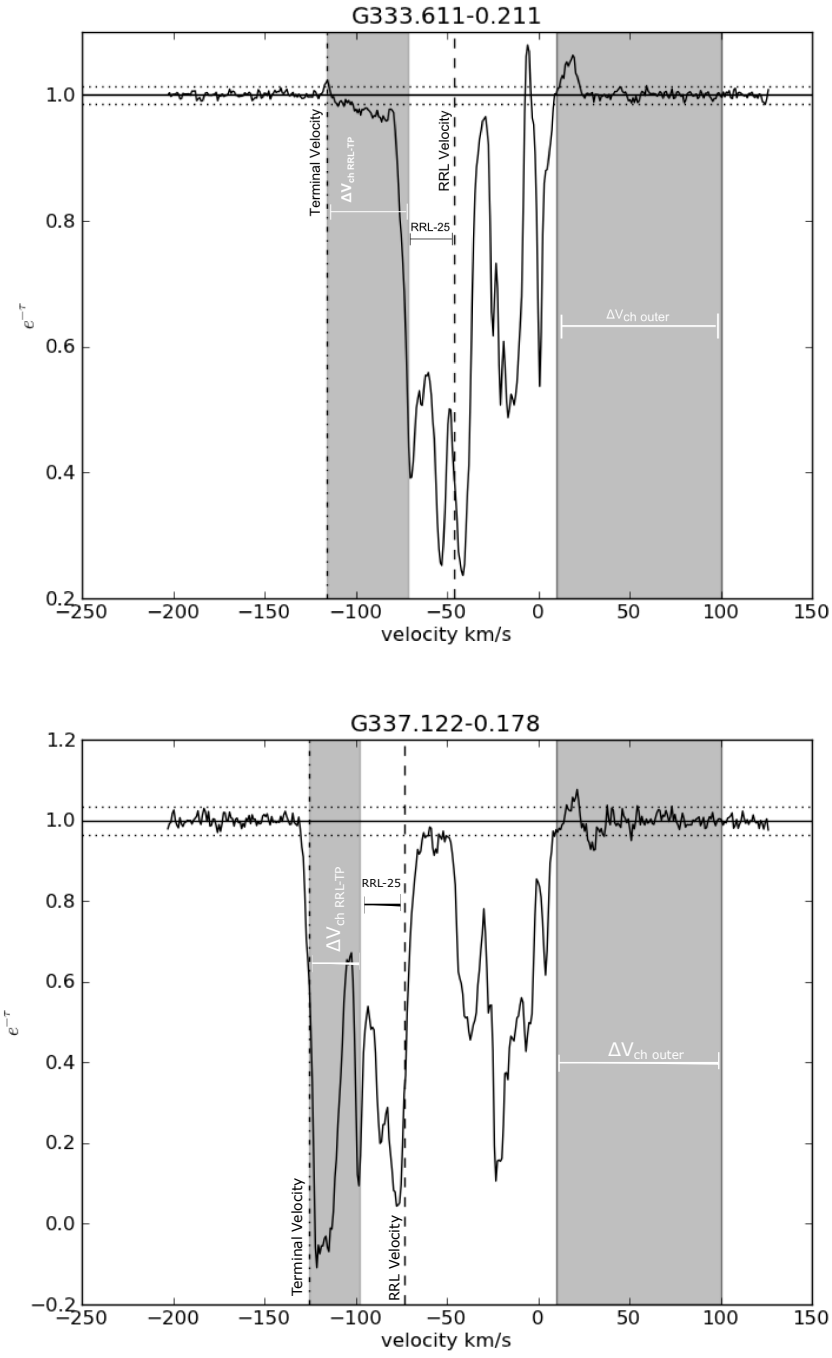

Figure 3.3: Examples of near and far sources (KDARs determined by Paladini et al. (2004) and this work) for H II regions with known RRL velocity. The RRL and terminal velocities are marked by vertical dashed and dot-dashed lines on the absorption spectra. The two intervals of velocity channels used in calculations of ΣAbs_{ch} are also marked: $V_T < V < (V_{RRL} - 25)$ and an interval corresponding to beyond the Solar circle ($10 < V < 100$). The horizontal dotted lines represent $1 \pm 3\sigma$. This work and Paladini et al. (2004) determine the two regions to be at the near (G333.611-0.211) and far (G337.122-0.178) kinematic distances respectively.

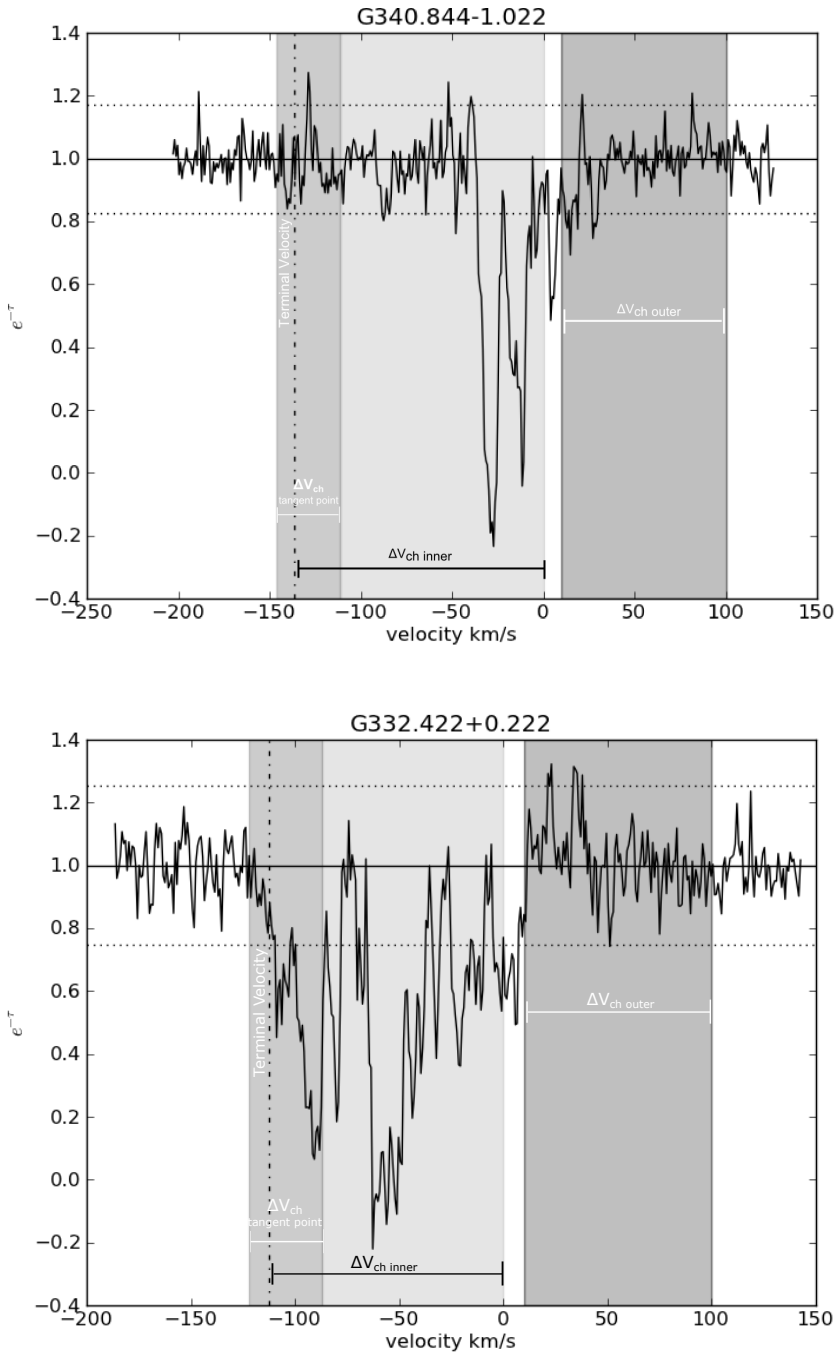

Figure 3.4: Example absorption spectra for sources with no known systemic velocity, one at the near and one at the far kinematic location. The three intervals of velocity channels used in calculations of S_{ch} are marked; NB these differ slightly from those used for sources with known systemic velocity (see Figure 3.3). The terminal velocity is marked by the dot-dashed vertical line. The horizontal dotted lines represent $1 \pm 3\sigma$. G332.422+0.222 is located at least as far as the tangent point, G340.844-1.022 is given a kinematic distance of 2.94kpc based on the velocity of the last absorption feature (-35 km s^{-1}).

3.3.3 H II Regions with Known RRL Velocities

Each H II region was classified into one of three Cases based on its RRL velocity - Case I: default tangent point distance assignment, Case II: no KDAR and Case III: KDAR attempted. Case III is then itself split into three parts, each indicative of the value for $S_{V_{RRL}toV_T}$. These Cases are explained in detail below.

Case I: Default Tangent Point Distance Assignment

The RRL velocity (V_{RRL}) is within 25 km s^{-1} of the terminal velocity. For these H II regions, the tangent point (TP) distance is assigned. See Section 3.3.2.1 for a discussion of the choice of 25 km s^{-1} for the interval.

Case II: No KDAR

No KDAR was achieved if an H II region displays multiple RRL velocities or if the RRL velocity is within the range $(|V_T| - 35) < V_{RRL} < (|V_T| - 25)$. H II regions with RRL velocities in this range are excluded as the summation interval of $S_{V_{RRL}toV_T}$ is <10 km s^{-1} due to the summation interval commencing 25 km s^{-1} from V_{RRL} (see Section 3.3.2.1 and Figure 3.3). For very short intervals ($\delta V < 10$ km s^{-1}) the measurement of $S_{\delta V}$ becomes comparable to the noise. Continuum sources with multiple RRL velocities indicate the presence of two or more separate H II regions blended at the resolution of the RRL surveys. The E/A method is unable to distinguish which HII region has the absorption, and the optical depth scale is biased by the extra continuum of the other regions (Anderson & Bania 2009).

Case III: KDAR Attemped

If the systemic velocity, V_{RRL}, is more than 35 km s^{-1} away from the terminal velocity (i.e. $(V_T + 35) < V_{RRL}$ in the fourth quadrant, or $(V_T - 35) > V_{RRL}$ in the first quadrant), then the absorption summation can be taken over a standard velocity range of V_T to $V_{RRL} - 25$ km s^{-1} in the fourth quadrant or $V_{RRL} + 25$ km s^{-1} to V_T in the first quadrant. This leaves a relatively wide velocity gap between the systemic velocity and the beginning of the velocity interval for the absorption channel sum, to avoid absorption by gas associated with the H II region itself (see Section 3.3.2.1). For regions whose velocities satisfy this criterion, three sub-cases exist based on whether the absorption in the standard velocity range is detected or not, based on the noise expected in the channel sum (σ_S).

Note that a KDAR is not attempted if $\sigma_{e^{-\tau}} > 0.35$, i.e. if the noise in the optical depth spectrum is high (see Figure 3.2). Spectra with noise above this limit often demonstrated large emission fluctuations and resulted in a non-statistically significant S_{ch} measurement.

In a small number of cases, the values for $S_{V_{RRL}toV_T}$ and σ_S were very small (but > 0), these false positive values would lead to incorrect far KDAR assignment. In order to flag these sources, each spectrum was visually inspected and spectra affected by poor baselines were discarded.

Case III Part A: ($S_{RRL\ to\ V_T} - \sigma_S < 0$)

In this case $S_{V_{RRL}\mathrm{to}V_T}$ is negligible. That means there is no evidence for absorption by clouds beyond the near kinematic distance. The H II region is most likely located on the near (N,

Table 3.1) side of the tangent (subcentral) point.

Case III Part B: ($S_{V_{RRL\ to\ V_T}} - 3\sigma_S > 0$)
In this case, there is significant absorption well above the noise. In contrast to Part A, if S_{RRLtoV_T} is significant then the H II region *must* be at the far (F, Table 3.1) kinematic distance.

Case III Part C: Others
If the sum of channels is such that the measured value does not have statistical significance (i.e. not Case III Part A or B), then no conclusion can be drawn about the KDAR. These KDARs are deemed uncertain (?, Table 3.1).

3.3.4 Continuum Sources Without RRL Velocities

While a kinematic *distance* can only be calculated using a systemic velocity, it is possible to attempt a rough KDAR without any RRL detection. In this case the presence or absence of absorption at velocities near the tangent point gives a binary KDAR, either near vs. far relative to the tangent point. A near KDAR is indicated when no absorption is present near the terminal velocity. If absorption near the terminal velocity is present, then the line of sight distance must be at least as far as the tangent point ($d_{los} \geq d_{TP}$).

Values for S_{ch} were measured over the entire inner Galaxy velocity range, and also for a velocity interval around the terminal velocity $(V_T - 25) < V_T < (V_T + 10)$ in the first quadrant (the signs are reversed in the fourth quadrant such that the 10 km s^{-1} range goes beyond the terminal velocity) for analysis of the amount of absorption around the tangent point (S_{TP}). It is expected that these values of S_{TP} will fall into two categories: one where S_{TP} is negligible (i.e. Case III Part A, near side) and one where varying amounts of absorption exist around the terminal velocity (i.e. Case III Part B, far side).

Table 3.1: KDARs from ΣS_{ch} Measurements

1	**2**	**3**	**4**	**5**	**6**[a,b]	**7**[c]	**8**	**9**	**10**	**11**	**12**[d]	**13**	**14**[e,f,g]
l	b	$\sigma_{e^-\tau}$	T_{cont}	V_T	V_{RRL}	Ref.	$S_{\mathrm{RRLtoV_T}}$	S_{inner}	S_{TP}	S_{outer}	KDAR	d_{GR}	d_{los}
342.356	-0.044	0.33	19	-140.86	-13	CH87	24.80 ± 3.41	47.42 ± 3.58	8.60 ± 1.78	-2.21 ± 3.02	F	7.47	$15.11^{+1.47}_{-2.25}$
342.255	0.300	0.33	15	-140.56	-122	L81	-	23.04 ± 3.51	2.51 ± 1.74	-0.13 ± 2.96	TP	2.86	$8.10^{+0.96}_{-1.11}$
342.067	0.422	0.19	55	-140.00	-65	CH87	-0.57 ± 1.52	18.00 ± 2.08	0.01 ± 1.04	1.50 ± 1.76	N	4.25	$4.74^{+0.62}_{-0.74}$
341.967	0.222	0.39	11	-139.70	-8	CH87	12.05 ± 4.08	20.60 ± 4.20	10.91 ± 2.10	5.43 ± 3.56	?	8.09	-
341.267	-0.355	0.36	13	-137.63	-38	CH87	-4.74 ± 3.26	32.48 ± 3.84	-1.52 ± 1.93	-1.51 ± 3.28	?	5.58	-
341.211	-0.233	0.30	19	-137.46	-39	ARM00	-5.13 ± 2.69	13.29 ± 3.18	-1.77 ± 1.60	-0.24 ± 2.58	N	5.53	$3.25^{+0.88}_{-1.14}$
340.844	-1.022	0.24	47	-136.38	-	-	-	21.61 ± 2.54	0.78 ± 1.28	1.61 ± 2.07	N-TP	5.81	$2.94^{+0.94}_{-1.23}$*
340.789	-1.022	0.14	142	-136.21	-25	CH87	-0.43 ± 1.30	14.89 ± 1.44	0.23 ± 0.73	-0.88 ± 1.23	N	6.50	$2.16^{+1.12}_{-1.54}$
340.578	0.322	0.28	20	-135.59	-	-	-	39.69 ± 2.93	8.10 ± 1.48	3.05 ± 2.39	TP-F	-	-
340.278	-0.200	0.21	42	-134.71	-43	GG76	-5.66 ± 1.79	30.58 ± 2.17	-5.50 ± 1.10	0.23 ± 1.87	N	5.41	$3.41^{+0.83}_{-1.05}$
340.055	-0.233	0.26	25	-134.05	-52	CH87	-3.53 ± 2.13	26.97 ± 2.72	-0.20 ± 1.38	-2.58 ± 2.35	N	5.00	$3.91^{+0.74}_{-0.91}$
339.844	0.300	0.28	23	-133.43	-19	CH87	28.15 ± 2.71	53.27 ± 2.93	8.86 ± 1.50	1.52 ± 2.54	F	7.08	$14.43^{+1.24}_{-1.74}$
339.555	-0.411	0.41	9	-132.59	-	-	-	59.24 ± 4.31	11.60 ± 2.21	4.26 ± 3.56	TP-F	-	-
339.555	0.278	0.42	8	-132.59	-	-	-	59.17 ± 4.37	9.45 ± 2.24	1.61 ± 3.61	TP-F	-	-
339.289	0.233	0.38	11	-131.81	-71	CH87	16.75 ± 2.66	65.11 ± 3.92	14.66 ± 2.02	-6.61 ± 3.42	F	4.37	$11.12^{+0.64}_{-0.72}$
339.289	0.156	0.43	9	-131.81	-	-	-	60.86 ± 4.48	11.92 ± 2.30	-2.61 ± 3.71	TP-F	-	-
339.144	-0.400	0.37	14	-131.39	-37	CH87	-8.96 ± 3.23	8.05 ± 3.82	-1.74 ± 1.96	-0.65 ± 3.33	?	5.86	-
339.089	-0.189	0.44	12	-131.22	-	-	-	47.86 ± 4.53	9.21 ± 2.33	-4.91 ± 3.75	TP-F	-	-
338.933	-0.067	0.22	35	-130.77	-43.9	U11	-2.18 ± 1.88	18.04 ± 2.30	-0.03 ± 1.19	1.22 ± 2.01	?(N)	5.51	$3.35^{+0.83}_{-1.03}$ **
338.922	0.622	0.17	53	-130.74	-63	CH87	-0.08 ± 1.28	30.07 ± 1.77	-0.14 ± 0.91	1.30 ± 1.55	N	4.68	$4.38^{+0.68}_{-0.79}$
338.922	0.389	0.31	18	-130.74	-24.7	U11	25.22 ± 2.90	50.16 ± 3.23	3.85 ± 1.66	-1.83 ± 2.68	F	6.69	$13.89^{+1.11}_{-1.49}$
338.711	0.644	0.35	16	-130.12	-62	CH87	1.66 ± 2.60	32.49 ± 3.60	1.18 ± 1.86	2.28 ± 3.16	N	4.74	$4.32^{+0.69}_{-0.80}$
338.633	0.144	0.27	23	-129.90	-	-	-	42.97 ± 2.76	7.44 ± 1.43	-2.12 ± 2.30	TP-F	-	-
338.589	0.022	0.29	26	-129.77	-	-	-	51.50 ± 2.97	18.08 ± 1.53	-2.30 ± 2.47	TP-F	-	-
338.455	-0.267	0.32	17	-129.38	-	-	-	63.32 ± 3.28	11.99 ± 1.70	-6.89 ± 2.74	TP-F	-	-
338.411	-0.211	0.21	54	-129.25	2	CH87	-	63.60 ± 2.21	12.83 ± 1.14	0.56 ± 1.94	O	8.71	$16.03^{+1.67}_{-1.72}$
338.356	-0.089	0.29	27	-129.09	-	-	-	69.11 ± 2.97	17.78 ± 1.54	0.09 ± 2.48	TP-F		-
338.122	-0.189	0.26	30	-128.41	-53	CH87	25.40 ± 2.05	68.11 ± 2.67	12.73 ± 1.39	2.58 ± 2.36	F	5.16	$11.96^{+0.76}_{-0.90}$
338.078	0.011	0.23	38	-128.28	-47	CH87	21.25 ± 1.90	49.87 ± 2.39	9.47 ± 1.25	-1.30 ± 2.11	F	5.44	$12.30^{+0.81}_{-0.98}$
338.011	0.022	0.30	26	-128.09	-	-	-	39.43 ± 3.08	7.46 ± 1.60	2.91 ± 2.58	TP-F	-	-
337.978	-0.144	0.27	27	-127.99	-	-	-	55.49 ± 2.81	12.57 ± 1.46	1.85 ± 2.36	TP-F	-	-
337.922	-0.467	0.10	230	-127.83	-40	CH87	0.75 ± 0.84	23.46 ± 1.01	0.18 ± 0.53	0.46 ± 0.90	N	5.81	$3.02^{+0.88}_{-1.10}$
337.711	-0.056	0.31	20	-127.22	-50	ARM00	16.12 ± 2.48	47.84 ± 3.19	8.39 ± 1.67	-0.87 ± 2.69	F	5.33	$12.12^{+0.79}_{-0.94}$

Continued on next page

Table 3.1 – continued from previous page

l	b	$\sigma_{e^{-\tau}}$	T_{cont}	V_T	V_{RRL}	Ref.	$S_{\mathrm{RRLtoV_T}}$	S_{inner}	S_{TP}	S_{outer}	KDAR	d_{GR}	d_{los}
337.711	0.089	0.33	17	-127.22	-76.7	U11	8.57 ± 2.15	15.00 ± 3.42	9.02 ± 1.79	-1.13 ± 2.88	F	4.35	$10.79^{+0.65}_{-0.71}$
337.667	-0.167	0.35	16	-127.09	-53	U11	21.23 ± 2.70	49.27 ± 3.55	13.32 ± 1.86	-0.46 ± 2.99	F	5.21	$11.95^{+0.76}_{-0.91}$
337.622	-0.067	0.27	26	-126.96	-55	CH87	13.43 ± 2.09	35.79 ± 2.78	11.02 ± 1.45	2.31 ± 2.47	F	5.13	$11.84^{+0.75}_{-0.88}$
337.533	-0.311	0.34	17	-126.71	-101	CH87	0.23 ± 1.55	39.29 ± 3.44	7.06 ± 1.80	-1.72 ± 3.06	TP	3.74	-
337.433	-0.400	0.34	17	-126.42	-	-	-	41.85 ± 3.45	10.43 ± 1.81	-2.11 ± 2.91	TP-F	-	-
337.289	-0.122	0.23	30	-126.00	-54	W70	21.03 ± 1.76	53.85 ± 2.33	14.24 ± 1.22	-0.98 ± 2.08	F	5.20	$11.88^{+0.76}_{-0.90}$
337.255	-0.167	0.27	29	-125.90	-	-	-	31.58 ± 2.76	4.52 ± 1.45	2.28 ± 2.33	O	10.60	$17.92^{+1.57}_{-1.59}$*
337.200	-0.733	0.43	11	-125.74	-	-	-	48.75 ± 4.34	14.19 ± 2.28	0.21 ± 3.68	TP-F	-	-
337.178	0.067	0.28	23	-125.68	-	-	-	56.60 ± 2.82	16.72 ± 1.48	-2.24 ± 2.39	TP-F	-	-
337.122	-0.178	0.11	188	-125.52	-73	CH87	21.45 ± 0.71	65.14 ± 1.10	20.23 ± 0.58	0.17 ± 0.98	F	4.52	$10.92^{+0.67}_{-0.74}$
337.100	-0.056	0.34	19	-125.46	-	-	-	70.48 ± 3.41	17.89 ± 1.79	-3.86 ± 2.89	TP-F	-	-
336.978	-0.133	0.19	57	-125.10	-	-	-	31.02 ± 1.92	8.83 ± 1.01	0.22 ± 1.63	TP-F	-	-
336.911	-0.155	0.22	53	-124.91	-73	W70	7.26 ± 1.40	18.34 ± 2.18	8.69 ± 1.15	-0.81 ± 1.95	F	4.54	$10.90^{+0.68}_{-0.74}$
336.900	0.056	0.22	41	-124.88	-	-	-	18.03 ± 2.21	3.56 ± 1.17	-0.10 ± 1.88	TP-F	-	-
336.844	0.000	0.18	75	-124.72	-79	CH87	17.14 ± 1.10	54.01 ± 1.82	20.76 ± 0.96	0.88 ± 1.63	F	4.37	$10.62^{+0.67}_{-0.71}$
336.567	-0.111	0.34	23	-123.92	-	-	-	47.44 ± 3.42	24.86 ± 1.81	4.40 ± 2.91	TP-F	-	-
336.533	0.100	0.37	15	-123.83	-	-	-	69.99 ± 3.72	19.16 ± 1.97	-9.11 ± 3.17	TP-F	-	-
336.467	0.022	0.37	15	-123.64	-63	CH87	21.64 ± 2.60	38.63 ± 3.72	21.68 ± 1.97	-0.75 ± 3.35	F	4.92	$11.36^{+0.72}_{-0.81}$
336.433	-0.256	0.21	44	-123.54	-93	CH87	4.76 ± 1.05	56.62 ± 2.11	16.19 ± 1.12	-0.06 ± 1.91	?	4.03	-
336.367	-0.144	0.24	34	-123.35	-88	CH87	4.90 ± 1.30	26.07 ± 2.46	12.74 ± 1.30	-1.03 ± 2.21	F	4.16	$10.18^{+0.70}_{-0.69}$
334.778	-0.022	0.36	13	-118.83	-		-	70.31 ± 3.59	15.71 ± 1.94	2.91 ± 3.13	EG	-	-
334.722	-0.655	0.25	29	-118.67	16	CH87	-	39.19 ± 2.42	5.93 ± 1.31	7.19 ± 2.22	O	9.95	$16.95^{+1.44}_{-1.48}$
334.700	-0.100	0.32	19	-118.61	-32	CH87	33.19 ± 2.68	88.46 ± 3.15	12.19 ± 1.71	-1.74 ± 2.89	F	6.53	$13.11^{+0.99}_{-1.22}$
334.522	0.800	0.43	9	-118.11	-77	CH87	-1.97 ± 2.47	48.78 ± 4.22	1.56 ± 2.29	5.81 ± 3.88	?	4.63	-
333.689	-0.444	0.33	17	-115.76	-50	CH87	8.42 ± 2.43	36.97 ± 3.23	7.84 ± 1.77	-2.74 ± 3.00	F	5.68	$11.87^{+0.83}_{-0.95}$
333.611	-0.211	0.07	503	-115.55	-46	CH87	2.53 ± 0.51	31.72 ± 0.66	0.36 ± 0.36	-0.45 ± 0.62	?(N)	5.87	$3.12^{+0.86}_{-1.00}$ **
333.589	-0.089	0.19	55	-115.48	-54	W70	1.59 ± 1.37	9.05 ± 1.88	2.83 ± 1.03	-0.41 ± 1.75	?	5.52	-
333.167	-0.100	0.31	35	-114.30	-91	CH87	-	25.42 ± 2.98	4.18 ± 1.65	-5.26 ± 2.80	TP	4.36	$7.58^{+0.91}_{-1.10}$
333.133	-0.433	0.10	192	-114.21	-52	CH87	-0.01 ± 0.71	5.16 ± 0.97	0.07 ± 0.53	0.05 ± 0.91	N	5.64	$3.45^{+0.82}_{-0.94}$
333.089	-0.478	0.16	108	-114.09	-	-	-	5.23 ± 1.57	0.33 ± 0.87	0.85 ± 1.40	N-TP	6.76	$2.02^{+1.01}_{-1.25}$*
333.011	-0.444	0.13	167	-113.87	-54	W70	2.18 ± 0.92	25.47 ± 1.28	1.64 ± 0.71	0.25 ± 1.20	?(F)	5.56	$11.59^{+0.82}_{-0.92}$ **
332.978	0.767	0.22	66	-113.78	-52	CH87	0.93 ± 1.53	24.32 ± 2.09	0.69 ± 1.15	0.30 ± 1.96	N	5.65	$3.45^{+0.83}_{-0.94}$
332.833	-0.555	0.22	42	-113.38	-57	W70	1.19 ± 1.48	14.22 ± 2.10	1.41 ± 1.16	1.00 ± 1.97	N	5.46	$3.73^{+0.80}_{-0.89}$
332.789	-0.589	0.20	50	-113.25	-57	CH87	1.17 ± 1.33	7.32 ± 1.89	0.71 ± 1.05	1.44 ± 1.78	N	5.46	$3.72^{+0.81}_{-0.89}$
332.656	-0.611	0.13	128	-112.88	-48	CH87	0.38 ± 0.95	13.74 ± 1.25	0.49 ± 0.70	-0.90 ± 1.18	N	5.85	$3.19^{+0.85}_{-0.98}$

Continued on next page

Table 3.1 – continued from previous page

l	b	$\sigma_{e^{-\tau}}$	T_{cont}	V_T	V_{RRL}	Ref.	$S_{\mathrm{RRLtoV_T}}$	S_{inner}	S_{TP}	S_{outer}	KDAR	d_{GR}	d_{los}
332.544	-0.133	0.28	30	-112.57	-50	CH87	4.26 ± 1.97	35.41 ± 2.66	2.50 ± 1.48	1.25 ± 2.50	?(F)	5.77	$11.78^{+0.84}_{-0.96}$ **
332.467	0.033	0.26	33	-112.36	-	-	-	53.82 ± 2.45	15.12 ± 1.36	-0.06 ± 2.20	TP-F	-	-
332.422	0.222	0.29	30	-112.23	-	-	-	52.03 ± 2.80	13.96 ± 1.56	-1.65 ± 2.51	TP-F	-	-
332.156	-0.456	0.11	149	-111.50	-55	CH87	0.93 ± 0.76	22.53 ± 1.06	0.71 ± 0.59	-0.44 ± 1.01	?	5.59	-
331.522	-0.078	0.09	245	-109.75	-89	CH87	-	60.94 ± 0.88	16.73 ± 0.50	-0.24 ± 0.84	TP	4.54	$7.47^{+0.86}_{-1.08}$
331.411	0.022	0.36	18	-109.45	-79	GG76	0.44 ± 1.50	27.88 ± 3.42	13.76 ± 1.93	-4.78 ± 3.11	?	4.82	-
331.367	-0.022	0.20	52	-109.32	-	-	-	50.92 ± 1.90	6.97 ± 1.07	-0.69 ± 1.72	TP-F	-	-
331.356	1.056	0.30	35	-109.29	-79	CH87	0.44 ± 1.50	34.00 ± 2.87	2.60 ± 1.62	0.65 ± 2.75	?	4.82	-
331.333	-0.344	0.21	57	-109.23	-64	CH87	1.79 ± 1.26	29.13 ± 1.97	1.51 ± 1.11	1.16 ± 1.89	?(F)	5.31	$10.86^{+0.82}_{-0.86}$ **
331.278	-0.189	0.18	61	-109.08	-85	CH87	-	34.05 ± 1.73	6.51 ± 0.98	1.10 ± 1.66	TP	4.66	$7.45^{+0.89}_{-1.09}$
331.133	-0.244	0.43	13	-108.69	-	-		109.07 ± 4.06	23.68 ± 2.30	-1.36 ± 3.70	TP-F	-	-
331.122	-0.533	0.23	33	-108.66	-68	CH87	-1.10 ± 1.33	33.08 ± 2.17	-1.41 ± 1.23	3.40 ± 2.09	N	5.19	$4.28^{+0.83}_{-0.85}$
331.055	-0.144	0.25	34	-108.47	-89	CH87	-	69.02 ± 2.38	18.03 ± 1.35	0.50 ± 2.29	TP	4.57	$7.44^{+0.83}_{-1.06}$
331.055	-0.222	0.43	15	-108.47	-89	W70	-	33.57 ± 4.07	-1.70 ± 2.30	3.29 ± 3.91	TP	4.57	$7.44^{+0.83}_{-1.06}$
330.867	-0.367	0.14	93	-107.96	-56	CH87	0.83 ± 0.94	42.75 ± 1.35	0.75 ± 0.77	-0.78 ± 1.31	N	5.64	$3.59^{+0.84}_{-0.92}$
330.678	-0.389	0.22	38	-107.44	-61	CH87	1.00 ± 1.33	38.06 ± 2.02	1.53 ± 1.15	-0.57 ± 1.95	N	5.46	$3.87^{+0.84}_{-0.89}$
330.289	-0.400	0.44	13	-106.38	-76	CH87	1.94 ± 2.15	63.99 ± 4.06	23.51 ± 2.33	9.07 ± 3.95	?	4.99	-
330.044	-0.056	0.34	18	-105.72	-38	CH87	50.00 ± 2.56	95.52 ± 3.20	37.37 ± 1.83	-1.58 ± 3.11	?	6.50	-
329.478	0.211	0.32	21	-104.19	-102	CH87	-	63.53 ± 2.94	24.76 ± 1.70	-0.80 ± 2.89	TP	4.37	$7.32^{+0.92}_{-0.92}$
329.333	0.144	0.33	22	-103.80	-107	CH87	-	50.48 ± 3.03	23.41 ± 1.75	3.33 ± 2.98	TP	4.27	$7.31^{+0.88}_{-0.88}$
328.955	0.567	0.40	15	-102.79	-	-	-	68.66 ± 3.67	32.51 ± 2.14	-1.06 ± 3.45	TP-F	-	-
328.822	-0.067	0.34	19	-102.43	-	-		74.63 ± 3.12	22.45 ± 1.82	-3.67 ± 2.93	TP-F	-	-
328.567	-0.533	0.12	119	-101.75	-51	CH87	0.76 ± 0.77	11.97 ± 1.09	0.94 ± 0.64	0.60 ± 1.08	N	5.99	$3.22^{+0.90}_{-0.97}$
328.411	0.222	0.13	97	-101.33	-	-	-	97.25 ± 1.16	37.22 ± 0.68	5.25 ± 1.09	O	10.49	$16.74^{+1.21}_{-1.24}$*
328.356	-0.411	0.35	18	-101.19	-	-	-	64.17 ± 3.21	14.79 ± 1.88	24.83 ± 3.03	EG	-	-
328.311	0.433	0.16	87	-101.07	-97	CH87	-	43.76 ± 1.44	17.73 ± 0.84	-1.11 ± 1.43	TP	4.56	$7.23^{+0.92}_{-0.92}$
328.122	0.111	0.42	13	-100.57	-	-	-	144.27 ± 3.80	55.10 ± 2.24	-4.33 ± 3.61	TP-F	-	-
327.989	-0.100	0.22	43	-100.21	-51	CH87	2.27 ± 1.45	43.50 ± 1.97	2.87 ± 1.16	-2.50 ± 1.97	?	6.03	-
327.767	-0.355	0.19	48	-99.62	-72	CH87	-0.18 ± 0.91	40.03 ± 1.74	3.40 ± 1.03	-1.83 ± 1.75	?	5.28	-
27.495	0.190	0.14	122	112.5	34	L89	18.05 ± 1.1	34.54 ± 1.33	9.72 ± 0.74	1.16 ± 1.25	F	6.56	$12.80^{+1.17}_{-0.97}$
27.375	1.170	0.20	58	112.8	-	-	-	13.74 ± 1.91	1.47 ± 1.06	2.35 ± 1.80	O-EG	11.86	$18.75^{+1.33}_{-1.35}$*
27.370	0.010	0.15	115	112.8	-	-	-	26.13 ± 1.45	5.12 ± 0.81	-0.62 ± 1.37	TP-F	-	-
27.300	-0.145	0.21	59	113.0	92.3	L89	-	11.17 ± 2.01	1.01 ± 1.12	-0.35 ± 1.90	TP	4.36	$7.55^{+1.95}_{-0.43}$
27.280	0.145	0.15	112	113.1	36.3	L89	18.35 ± 1.2	35.72 ± 1.43	9.54 ± 0.79	-0.25 ± 1.34	F	6.42	$12.66^{+1.13}_{-0.94}$
26.980	-0.070	0.21	57	113.9	79.9	L89	1.18 ± 1.1	15.45 ± 2.02	6.90 ± 1.11	2.40 ± 1.89	?	4.67	-

Continued on next page

Table 3.1 – continued from previous page

l	b	$\sigma_{e^{-\tau}}$	T_{cont}	V_T	V_{RRL}	Ref.	$S_{\mathrm{RRLtoV_T}}$	S_{inner}	S_{TP}	S_{outer}	KDAR	d_{GR}	d_{los}
26.720	0.170	0.24	42	114.6	T	GBT11	-	18.72 ± 2.37	6.89 ± 1.31	1.54 ± 2.21	-	-	-
26.685	-1.030	0.19	49	114.7	-	-	-	11.72 ± 1.81	1.59 ± 0.99	1.44 ± 1.69	EG	-	-
26.610	-0.210	0.20	54	114.9	T	GBT11	-	20.54 ± 1.93	4.27 ± 1.06	5.34 ± 1.80	-	11.58	$18.54^{+1.36}_{-1.38}$*
26.595	-0.025	0.23	41	115.0	T	Sw04	-	19.26 ± 2.25	5.55 ± 1.24	1.47 ± 2.10	-	-	-
26.590	0.095	0.23	42	115.0	102.5	L89	-	11.55 ± 2.19	4.42 ± 1.20	0.00 ± 2.04	TP	4.06	$7.60^{+1.21}_{-0.14}$
26.555	-0.305	0.28	43	115.1	104.2	L89	-	7.03 ± 2.69	0.90 ± 1.48	0.38 ± 2.51	TP	4.02	$7.60^{+1.11}_{-0.21}$
26.540	0.415	0.13	152	115.1	88.4	L89	-	34.55 ± 1.26	12.18 ± 0.70	0.56 ± 1.18	?	4.40	-
26.470	0.020	0.27	40	115.3	100	LPH96	-	4.91 ± 2.58	0.04 ± 1.42	-2.95 ± 2.41	TP	4.11	$7.61^{+1.32}_{-0.07}$
26.435	0.060	0.27	39	115.4	-	-	-	19.91 ± 2.59	3.44 ± 1.42	2.35 ± 2.41	TP-F	-	-
26.330	-0.070	0.27	39	115.7	100.9	GBT11	-	14.88 ± 2.60	4.29 ± 1.42	-1.18 ± 2.41	TP	4.08	$7.62^{+1.24}_{-0.14}$
26.315	-0.010	0.26	37	115.8	D	GBT11	-	12.22 ± 2.53	5.41 ± 1.39	-1.07 ± 2.35	-	-	-
26.240	-0.080	0.27	39	116.0	-	-	-	25.07 ± 2.64	6.19 ± 1.44	4.90 ± 2.45	EG	-	-
26.120	-0.090	0.25	50	116.3	D	L89	-	32.85 ± 2.45	9.02 ± 1.34	3.16 ± 2.28	-	-	-
26.095	-0.060	0.17	94	116.4	-	-	-	38.27 ± 1.67	10.06 ± 0.91	0.73 ± 1.54	TP-F	-	-
26.025	0.215	0.26	39	116.6	-	-	-	15.21 ± 2.54	5.78 ± 1.39	1.19 ± 2.35	TP-F	-	-
25.815	-0.380	0.23	43	117.2	-	-	-	25.73 ± 2.30	7.19 ± 1.25	5.75 ± 2.12	EG	-	-
25.815	0.240	0.17	96	117.2	112.1	Sw04	-	16.69 ± 1.69	-0.82 ± 0.92	0.43 ± 1.56	TP	3.80	$7.65^{+0.55}_{-0.66}$
25.790	0.075	0.24	45	117.2	-	-	-	20.88 ± 2.34	4.83 ± 1.27	4.67 ± 2.16	EG	-	-
25.695	0.030	0.16	106	117.5	-	-	-	37.37 ± 1.57	12.89 ± 0.86	-0.15 ± 1.45	TP-F	-	-
25.605	-0.040	0.18	74	117.7	-	-	-	32.68 ± 1.77	8.56 ± 0.96	6.13 ± 1.63	TP-F	-	-
25.520	0.215	0.20	65	118.0	-	-	-	24.32 ± 1.92	7.76 ± 1.04	0.36 ± 1.77	TP-F	-	-
25.500	-1.160	0.26	27	118.0	-	-	-	7.52 ± 2.57	-0.91 ± 1.39	1.75 ± 2.36	N-TP	5.21	$3.97^{+0.86}_{-0.77}$*
25.490	0.965	0.28	32	118.1	-	-	-	14.34 ± 2.78	3.53 ± 1.51	1.67 ± 2.56	TP-F	-	-
25.470	-0.120	0.26	42	118.1	D	GBT11	-	12.98 ± 2.59	0.01 ± 1.40	1.25 ± 2.38	-	-	-
25.460	-0.215	0.25	45	118.2	D	Sw04	-	17.21 ± 2.47	2.07 ± 1.34	0.03 ± 2.27	-	-	-
25.400	-0.255	0.21	61	118.3	67.6	L89	1.53 ± 1.4	10.30 ± 2.08	0.37 ± 1.13	0.36 ± 1.92	?	4.93	$10.99^{+0.80}_{-0.74}$
25.395	0.030	0.16	101	118.3	-14.4	L89	-	41.02 ± 1.60	8.81 ± 0.87	4.46 ± 1.47	O	9.80	$16.52^{+0.63}_{-0.63}$
25.395	0.560	0.28	32	118.3	D	GBT11	-	13.02 ± 2.78	1.12 ± 1.51	3.86 ± 2.56	-	-	-
25.385	-0.175	0.10	475	118.4	59.1	L89	0.31 ± 0.7	27.08 ± 0.97	0.26 ± 0.52	0.57 ± 0.89	N	5.23	$3.92^{+0.86}_{-0.77}$
25.360	-1.100	0.18	70	118.4	-	-	-	13.85 ± 1.75	3.46 ± 0.95	1.34 ± 1.61	TP-F	-	-
25.290	0.310	0.24	49	118.6	39.6	L89	-0.21 ± 1.9	9.79 ± 2.39	2.36 ± 1.29	-1.21 ± 2.20	N	6.10	$2.78^{+1.09}_{-0.90}$
25.265	-0.160	0.17	103	118.7	-	-	-	47.81 ± 1.68	6.36 ± 0.91	7.37 ± 1.54	O	11.67	$18.78^{+1.42}_{-1.44}$*
25.245	-0.145	0.15	110	118.8	-	-	-	47.63 ± 1.46	8.56 ± 0.79	6.24 ± 1.34	EG?	-	-
25.205	-0.840	0.27	27	118.9	-	-	-	7.83 ± 2.68	-0.16 ± 1.45	2.57 ± 2.46	EG	-	-
25.160	0.060	0.23	51	119.0	D	Sw04	-	19.06 ± 2.30	3.47 ± 1.24	0.94 ± 2.11	-	-	-

Continued on next page

Table 3.1 – continued from previous page

l	b	$\sigma_{e^{-\tau}}$	T_{cont}	V_T	V_{RRL}	Ref.	$S_{\mathrm{RRLtoV_T}}$	S_{inner}	S_{TP}	S_{outer}	KDAR	d_{GR}	d_{los}
25.150	0.090	0.28	47	119.0	D	GBT11	-	15.66 ± 2.73	4.36 ± 1.48	1.49 ± 2.51	-	-	-
24.955	-0.055	0.27	32	119.6	D	GBT11	-	10.08 ± 2.64	1.44 ± 1.43	-0.64 ± 2.42	-	-	-
24.925	0.075	0.26	44	119.7	D	GBT11	-	18.94 ± 2.56	4.64 ± 1.38	0.28 ± 2.34	-	-	-
24.905	0.420	0.25	38	119.7	D	LPH96	-	10.48 ± 2.44	2.78 ± 1.32	1.12 ± 2.23	-	-	-
24.800	0.100	0.11	213	120.0	108.6	L89	-	33.32 ± 1.08	7.01 ± 0.58	0.16 ± 0.99	TP	3.79	$7.72^{+0.49}_{-0.76}$
24.740	-0.205	0.19	74	120.2	T	Sw04	-	23.85 ± 1.86	3.43 ± 1.00	-0.58 ± 1.70	-	-	-
24.740	0.080	0.19	66	120.2	111.3	GBT11	-	12.63 ± 1.93	2.46 ± 1.04	1.53 ± 1.76	TP	3.73	$7.72^{+0.34}_{-0.87}$
24.715	-0.130	0.21	74	120.3	D	GBT11	-	14.66 ± 2.10	2.46 ± 1.13	-0.42 ± 1.92	-	-	-
24.680	-0.160	0.13	179	120.4	D	Sw04	-	38.72 ± 1.31	8.02 ± 0.71	-0.06 ± 1.20	-	-	-
24.540	0.600	0.21	66	120.8	-	-	-	18.77 ± 2.09	4.78 ± 1.12	4.19 ± 1.91	O	12.22	$19.43^{+1.45}_{-1.47}$*
24.510	-0.225	0.15	125	120.8	D	Sw04	-	21.89 ± 1.51	-0.18 ± 0.81	0.34 ± 1.37	-	-	-
24.500	-0.035	0.18	93	120.9	108.1	Sw04	-	20.85 ± 1.75	5.31 ± 0.94	0.49 ± 1.60	TP	3.77	$7.73^{+0.44}_{-0.81}$
24.470	0.495	0.10	362	121.0	99.8	L89	-	30.57 ± 1.01	4.78 ± 0.54	0.12 ± 0.92	TP	3.95	$7.74^{+0.87}_{-0.51}$
24.460	0.245	0.18	85	121.0	98.5	L89	-	23.09 ± 1.80	6.97 ± 0.97	2.02 ± 1.64	TP	3.98	$7.74^{+0.94}_{-0.46}$
24.420	0.995	0.27	30	121.1	-	-	-	4.68 ± 2.65	-0.68 ± 1.42	0.11 ± 2.41	EG	-	-
24.400	0.070	0.16	90	121.2	110	L89	-	22.28 ± 1.57	7.21 ± 0.84	0.22 ± 1.43	TP	3.72	$7.74^{+0.33}_{-0.90}$
24.395	-0.070	0.25	37	121.2	-	-	-	20.81 ± 2.45	5.36 ± 1.32	1.89 ± 2.23	TP-F	-	-
24.215	-0.045	0.20	72	121.7	82	L89	2.69 ± 1.2	22.47 ± 2.03	5.79 ± 1.09	0.25 ± 1.84	?(F)	4.38	$10.40^{+0.72}_{-0.70}$ **
24.200	0.245	0.26	38	121.7	D	GBT11	-	11.80 ± 2.60	2.63 ± 1.39	1.13 ± 2.36	-	-	-
24.180	0.565	0.15	91	121.8	-	-	-	37.76 ± 1.49	8.32 ± 0.80	2.49 ± 1.35	EG	-	-
24.135	0.120	0.20	56	121.9	114.5	L89	-	20.30 ± 1.97	4.18 ± 1.05	1.39 ± 1.79	TP	3.61	$7.76^{+0.05}_{-1.12}$
24.130	1.030	0.29	29	121.9	-	-	-	18.69 ± 2.91	3.34 ± 1.56	3.66 ± 2.64	O-EG	-	$19.34^{+1.47}_{-1.49}$*
24.125	-0.070	0.25	43	121.9	86.9	LPH96	-	15.44 ± 2.50	4.03 ± 1.34	-1.46 ± 2.27	?	4.23	-
23.995	-0.100	0.25	39	122.3	75.8	LPH96	2.20 ± 1.6	19.00 ± 2.55	3.63 ± 1.36	-0.43 ± 2.31	?(F)	4.54	$10.71^{+0.74}_{-0.70}$ **
23.960	0.155	0.12	188	122.4	78.9	L89	0.64 ± 0.7	29.29 ± 1.15	0.84 ± 0.62	0.56 ± 1.04	N	4.44	$4.97^{+0.72}_{-0.69}$
23.905	0.065	0.22	55	122.6	D	L89	-	25.14 ± 2.19	4.62 ± 1.17	1.81 ± 1.98	-	-	-
23.890	-0.740	0.30	24	122.6	-	-	-	9.95 ± 3.05	3.15 ± 1.63	0.13 ± 2.76	TP-F	-	-
23.875	-0.120	0.16	119	122.7	73.8	L89	3.54 ± 1.0	32.22 ± 1.65	4.13 ± 0.88	0.79 ± 1.49	F	4.59	$10.81^{+0.75}_{-0.69}$
23.835	0.100	0.25	43	122.8	D	GBT11	-	16.25 ± 2.53	3.92 ± 1.35	0.53 ± 2.29	-	-	-
23.820	0.220	0.25	48	122.8	107.4	L89	-	15.18 ± 2.52	2.13 ± 1.34	-2.11 ± 2.28	TP	3.73	$7.78^{+0.32}_{-0.94}$
23.735	-0.025	0.28	33	123.1	T	GBT11	-	15.47 ± 2.81	5.06 ± 1.49	0.28 ± 2.53	-	-	-
23.710	0.175	0.15	152	123.1	103.8	L89	-	32.12 ± 1.46	5.76 ± 0.78	0.05 ± 1.32	TP	3.79	$7.78^{+0.47}_{-0.84}$
23.705	-0.200	0.21	55	123.1	76.5	Ar02	1.45 ± 1.3	20.84 ± 2.14	2.42 ± 1.13	-0.60 ± 1.92	?(F)	4.49	$10.70^{+0.73}_{-0.69}$ **
23.665	-0.255	0.27	42	123.3	66.2	GBT11	5.74 ± 1.8	20.46 ± 2.67	3.66 ± 1.42	0.04 ± 2.41	F	4.82	$11.19^{+0.79}_{-0.71}$
23.550	-0.040	0.19	74	123.6	91.3	L89	0.00 ± 1.0	6.12 ± 1.90	-0.31 ± 1.01	0.47 ± 1.72	?	4.07	-

Continued on next page

Table 3.1 – continued from previous page

l	b	$\sigma_{e^{-\tau}}$	T_{cont}	V_T	V_{RRL}	Ref.	$S_{\mathrm{RRLtoV_T}}$	S_{inner}	S_{TP}	S_{outer}	KDAR	d_{GR}	d_{los}
23.420	-0.205	0.15	154	124.0	101.1	Sw04		37.44 ± 1.51	5.23 ± 0.80	-0.41 ± 1.35	TP	3.83	$7.80^{+0.55}_{-0.80}$
23.265	0.075	0.31	35	124.4	78.2	Sw04	-1.23 ± 1.9	7.84 ± 3.08	-0.89 ± 1.63	-0.16 ± 2.77	?	4.40	-
23.245	-0.240	0.22	80	124.5	76.1	L89	0.28 ± 1.4	14.77 ± 2.18	0.39 ± 1.16	0.30 ± 1.96	N	4.46	$4.87^{+0.72}_{-0.68}$
23.115	0.550	0.27	41	124.8	29.5	L89	5.09 ± 2.4	11.21 ± 2.76	2.30 ± 1.45	2.01 ± 2.47	?(F)	6.52	$13.42^{+1.31}_{-1.02}$ **
23.090	0.220	0.26	34	124.9	97.9	LPH96	0.07 ± 1.2	12.33 ± 2.66	1.83 ± 1.40	0.95 ± 2.38	?	3.87	-
23.015	-0.285	0.18	84	125.1	-	-	-	11.08 ± 1.77	-0.53 ± 0.94	0.17 ± 1.59	N-TP	4.29	$5.10^{+0.70}_{-0.67}$*
22.935	-0.075	0.19	74	125.4	-	-	-	39.51 ± 1.89	5.83 ± 0.99	3.09 ± 1.69	EG	-	-
22.755	-0.480	0.16	115	125.9	74.8	L89	0.26 ± 1.0	13.72 ± 1.64	0.34 ± 0.86	-0.29 ± 1.46	N	4.45	$4.83^{+0.72}_{-0.67}$
22.755	-0.245	0.22	71	125.9	D	GBT11		12.54 ± 2.26	0.68 ± 1.19	1.92 ± 2.02	-	-	-
22.725	-0.010	0.26	45	126.0	38.9	GBT11	9.38 ± 2.2	17.80 ± 2.63	3.28 ± 1.39	-0.30 ± 2.35	F	5.93	$12.78^{+1.11}_{-0.90}$
22.685	-0.670	0.28	39	126.1	-	-	-	16.87 ± 2.86	1.34 ± 1.50	3.05 ± 2.55	EG	-	-
22.660	0.125	0.26	31	126.1	-	-	-	14.46 ± 2.69	3.71 ± 1.41	1.49 ± 2.40	TP-F	-	-

[a] Sources with (multiple) double or triple RRL velocity component profiles are denoted 'D' and 'T' respectively.

[b] Velocities from Urq12 are derived from ^{13}CO emission.

[c] References for velocities. Ar02 = Araya et al. (2002); ARM00 = Argon et al. (2000); CH87 = Caswell & Haynes (1987); GG76 = Georgelin & Georgelin (1976); GBT11 = GBTHRDS - Bania et al. (2010); L81 = Lockman (1981); L89 = Lockman (1989); LPH96 = Lockman et al. (1996); Sw04 = Sewilo et al. (2004); Urq12= Urquhart et al. (2012); W70 = Wilson et al. (1970)

[d] N = near side; N-TP = located before the tangent point; TP = tangent point; TP-F = located at least as far as the tangent point; F = far side; O = outer Galaxy; EG = extragalactic; ? = uncertain

[e] Errors are consistent with uncertainties of 15km/s in velocity. See Figure 3.7 for kinematic locations.

[f] Distances marked with an asterisk (*) are based on the last velocity which shows absorption in the outer Galaxy; except in the case of G26.610-0.210 where the GBTHRDS has three RRL velocities listed, one of which is negative (-35.7 km/s). These sources are included in Figures 3.7 and 3.8. See Appendix B.

[g] Distances marked with a double asterisk (**) are based on poor quality KDARs.

3.4 Results

Table 3.1 lists the KDAR information for each source. Columns (1) and (2) contain the Galactic coordinates of the source. Column (3) contains the baseline noise of the absorption spectrum $\sigma_{e^{-\tau}}$. Column (4) lists the continuum temperature of the 'on' source pixel in K. Columns (5)-(7) list the terminal and RRL velocities (in km s^{-1}) with references. Column (8) lists the $S_{RRL\ to\ V_T}$ for Case III H II regions (note S_{RRL-V_T} is not measured for regions located at the tangent point). Columns (8)-(10) list the S_{ch} for the whole inner Galaxy, for the tangent point interval and for the Outer Galaxy. Column (12) contains the KDAR determined in this work. Columns (13) and (14) list the Galactic radius (d_{GR}) and kinematic (d_{los}) distances (both in kpc).

3.4.1 Systemic Velocity Known

A total of 60 first quadrant H II regions had RRL velocities in the literature, however only 35 regions were classified as Case III regions [21 had multiple RRL velocities and 4 had $25 < (V_{TP} - V_{RRL}) < 35$)]. Through an investigation of the total amount of absorption between the known RRL and terminal velocities (S_{RRLtoTP}, Section 3.3.3), the KDAR for 28 of these regions was determined (80% success rate), 5 for the first time. The other 23, of the 28 successful KDARs, had previous kinematic distances in the literature. Comparisons between papers appear in Section 3.5.1 and Table 3.2. In the fourth quadrant, 65 H II regions had known RRL velocities. Of the 59 Case III H II regions, KDARs were determined for 47 (again 80% success rate), 23 for the first time. For the other 24, comparisons between the KDARs from this work and those in the literature appear in Section 3.5.2 and Table 3.3.

3.4.2 Systemic Velocity Unknown

In order to attempt KDARs for H II region candidates without a known systemic velocity, the distribution of S_{TP} values for H II regions with RRL velocities was inspected (see Figure 3.5). Known near side H II regions demonstrate a narrow distribution of S_{TP} values, statistically equivalent to zero, and the distribution of S_{TP} values for the far side sources is much wider (i.e. various amounts of absorption exist around the tangent point). This is also the case for the full sample (Figure 3.6).

Parameters of the known KDAR distribution (Figure 3.5) were used to achieve KDARs from the sample without systemic velocities. If the S_{TP} value of a source is more than the mean minus one standard deviation of the far KDAR distribution (i.e. $S_{TP} > \mu_F - \sigma_F$) then it is most likely on the far side of the tangent point. The reverse applies to the near KDAR distribution; if $S_{TP} < \mu_N + \sigma_N$ then the source is likely to be on the near side of the tangent point. These boundaries are marked on Figures 3.5 and 3.6. H II region candidates with intermediate amounts of absorption at the tangent point (i.e. $\mu_N + \sigma_N < S_{TP} < \mu_F - \sigma_F$) are uncertain and are not considered for KDAR here. Taking the threshold at one sigma on the either side of the mean is a conservative approach for this KDAR method.

A further 40 KDARs were achieved in this way (14 in the first quadrant and 26 in the fourth). In order to confirm that these distributions were applicable to the whole sample,

Table 3.2: Literature Comparisons (First Quadrant)

l (^{o})	b (^{o})	This Work[a]	AB09 E/A[b]	AB09 HISA[b]	K03	Pal04	Sw04	C88	W72
27.495	0.190	F	F	F	-	F	-	-	-
27.300	-0.145	TP	N?	-	-	-	-	-	-
27.280	0.145	F	F	F	-	F	-	F	-
26.980	-0.070	?	F*	N?	-	-	-	-	-
26.590	0.095	TP	-	F	-	-	-	-	-
26.555	-0.305	TP	TP	F	F	-	-	-	-
26.540	0.415	?	F	F	-	-	-	N	-
25.815	0.240	TP	TP	N	-	TP	?	-	TP
25.460	-0.215	-	TP	N	-	F	-	-	-
25.400	-0.255	?	-	F?	N	F	-	-	-
25.385	-0.175	N	N*	F?	N	-	-	-	F
25.290	0.310	N	-	F?	-	N	-	N	-
24.800	0.100	TP	N	N?	-	TP	-	-	TP
24.500	-0.035	TP	F?	F	-	-	N	-	-
24.470	0.495	TP	N	N	F?	TP	-	F	-
24.460	0.245	TP	N?	N?	-	TP	-	-	-
24.400	0.070	TP	TP	F?	-	TP	-	-	-
24.215	-0.045	F?	F	F?	-	-	-	F	-
24.135	0.120	TP	TP	F	-	-	-	-	-
24.125	-0.070	F	F	F	N	-	-	-	-
23.995	-0.100	F?	F	F	-	-	-	-	-
23.960	0.155	N	N*	F?	N	-	-	F	-
23.875	-0.120	F	F	F	F	F	-	-	-
23.820	0.220	TP	N?	F*	-	-	-	-	-
23.710	0.175	TP	N*	F?	-	-	-	-	-
23.705	-0.200	F?	F?	F?	F?	-	F	-	-
23.550	-0.040	?	N	N?	-	F	-	-	-
23.420	-0.205	TP	N*	F?	N?	TP	N	F	N
23.265	0.075	?	-	N?	-	-	F	-	-
23.245	-0.240	N	N	N	-	-	F	-	-
23.115	0.550	F?	N	-	-	N	-	-	-
23.090	0.220	?	-	F?	-		-	-	-
22.755	-0.480	N	N*	F?	-	F	-	-	-

[a] KDAR: N = near side, F = far side, TP = tangent point, O = outer Galaxy, ? = uncertain

[b] Where the E/A and HISA methods have conflicting KDAR, the adopted KDAR is given by the asterisk - note that in most cases the non-adopted method provides a poorer quaility KDAR.

- KDARs with question marks are of poorer quality.

- AB09 = Anderson & Bania (2009); K03 = Kolpak et al. (2003); Pal04 = Paladini et al. (2004); Sw04 = Sewilo et al. (2004); C88 = Clemens et al. (1988); W72 = Wilson (1972).

Table 3.3: Literature Comparisons (Fouth Quadrant)

l (^{o})	b (^{o})	This Work[a,b]	Urq12 [a]	Pal04	Fish03	CH87	KK70	Wilson70
342.067	0.422	N	?	-	-	-	-	-
340.789	-1.022	N	-	N	-	-	-	-
340.278	-0.200	N	?	-	-	-	-	-
338.933	-0.067	N?	N	-	-	-	-	-
338.922	0.622	N	N	N	-	-	-	-
338.922	0.389	F	?	-	-	-	-	-
338.411	-0.211	O	-	-	-	O	-	-
337.922	-0.467	N	F	N	-	-	-	-
337.711	-0.056	F	F	-	F	-	-	-
337.711	0.089	F	F	-	-	-	-	-
337.667	-0.167	F	F	-	-	-	-	-
337.122	-0.178	F	F	F	-	-	-	-
336.844	0.000	F	F	F	-	-	F	-
336.433	-0.256	?	-	N	-	-	-	-
334.722	-0.655	O	F	-	-	O	-	-
333.611	-0.211	N?	?	N	-	-	-	-
333.133	-0.433	N	N	N	-	-	-	-
333.011	-0.444	F?	N	F	-	-	F	N
332.833	-0.555	N	N	-	-	-	-	-
332.789	-0.589	N	-	N	-	-	-	-
332.656	-0.611	N	?	-	-	N?	-	-
332.544	-0.133	F?	?	-	-	-	-	-
332.156	-0.456	?	F	-	-	-	-	-
331.522	-0.078	TP	-	F	-	-	F	-
331.356	1.056	?	N	-	-	-	-	-
331.333	-0.344	F?	-	N	-	N	-	-
331.122	-0.533	N	N	-	-	-	-	-
330.867	-0.367	N	N	N	-	N	-	-
330.289	-0.400	?	F	-	-	-	-	-
329.478	0.211	TP	TP	-	-	-	-	-
328.567	-0.533	N	F	N	-	N?	-	-
328.311	0.433	TP	F	F	-	F	-	-
327.767	-0.355	?	N	-	-	-	-	-

[a] KDAR: N = near side, F = far side, TP = tangent point, O = outer Galaxy, ? = uncertain

[b] KDARs with question marks are of poorer quality.

[-] Urq12 = Urquhart et al. (2012); Pal04 = Paladini et al. (2004); Fish03 = Fish et al. (2003); CH87 = Caswell & Haynes (1987); KK70 = Kerr & Knapp (1970a); W70 = Wilson et al. (1970)

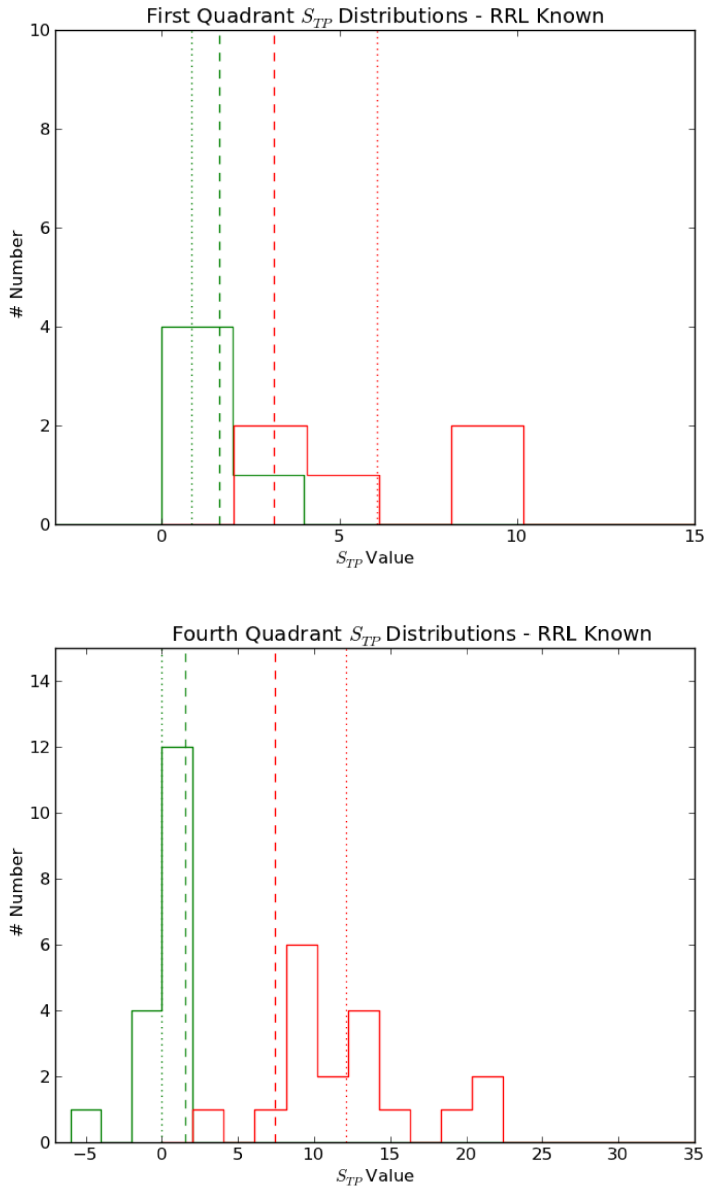

Figure 3.5: Histograms of the S_{TP} values for the first (top) and fourth (bottom) quadrants for sources with systemic velocities. The two dotted lines indicate the mean value of each KDAR group; Near (green) and Far (red). The dashed lines indicate one standard deviation from the mean (i.e. $\mu_N + \sigma_N$ and $\mu_F - \sigma_F$). These dashed lines are used as the boundaries for KDAR for sources without systemic velocities (see Figure 3.6).

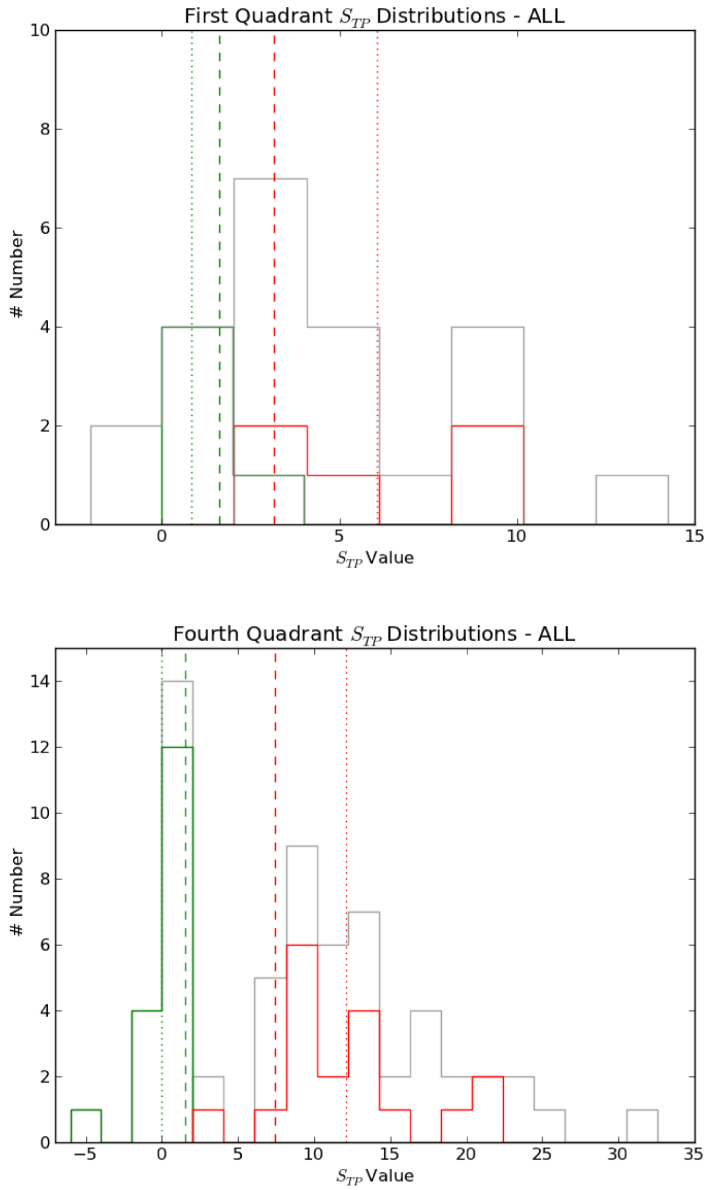

Figure 3.6: The same as Figure 3.5 but for the whole source sample (grey). The dashed (1σ) lines are used as the boundries for KDAR. For example, sources to the right of the red dashed line are most likely to be on the far side, while sources to the left of the green dashed line are most likely to be on the near side of the tangent point. Sources with S_{TP} values between the two dashed lines are uncertain.

Figure 3.5 was redrawn including all S_{TP} values from sources with and without known systemic velocities (see Figure 3.6). The parameters of the distributions are stable, with a slight widening of the far side distribution when the full sample is included.

For sources determined to be located on the near side of the tangent point, a lower limit of the kinematic distance can be determined from the velocity of the last absorption feature - no ambiguity exists. These sources are marked with KDARs of N-TP (near side of the tangent point) in Table 3.1 and their kinematic distances are marked with asterisks. Unfortunately a kinematic distance is unobtainable for H II region candidates assigned to beyond the tangent point (TP-F on Table 3.1).

3.5 Comparisons with the Literature

The results of several studies that all have several H II regions in common with this work, and have used various KDAR methods in order to determine the kinematic distance, are compared to the results of this work. Tables 3.2 and 3.3 summarise these KDAR comparisons for the first and fourth quadrants. It is important to note that sources often have many different KDARs in the literature, for example, G23.420-0.205 has seven previous KDARs that place the H II region at the near, tangent point and far kinematic distance (see Table 3.2). Sources with many, or conflicting, KDARs in the literature are discussed individually in Appendix B. H II regions with a KDAR shared between all previous works (and this paper) are the exception, rather than the rule, and are mostly at the far kinematic distance - as it is simpler to demonstrate that extremely significant absorption exists between the RRL and terminal velocities, than moderate or no H I absorption between the two velocities.

3.5.1 First Quadrant

Lockman (1989) is the canonical RRL velocity catalogue for the northern sky. Consisting of over 450 H II regions, the Lockman (1989) catalogue has been utilised by many modern KDAR works (e.g. Anderson & Bania (2009); Paladini et al. (2004)). Lockman also completed a RRL velocity catalogue of 130 diffuse H II regions in 1996 (Lockman et al. 1996). Other smaller RRL velocity studies have been undertaken (e.g. 72 H II regions in Sewilo et al. (2004)).

Recently, the Green Bank Telescope H II Region Discovery Survey (Bania et al. 2010, GBHRDS) measured RRL velocities from almost 450 previously unknown H II regions in the northern sky. The same work describes the extent of modern H II region RRL velocity surveys that constitutes a complete sample of "known" H II regions as of 2010. A full KDA resolution study of the GBTHRDS catalogue is underway (Anderson et al. 2011a).

Comparison with Anderson & Bania (2009)

Anderson & Bania (2009), resolved the KDA for 266 Galactic H II regions from a sample of 291. Anderson & Bania (2009) used two methods, E/A and H I self absorption (HISA), for their KDARs and found that the HISA method was 'applicable in more cases, but less robust'. The E/A method provided more 'A' confidence level KDARs than HISA for the same source

sample, but could not achieve KDAR for H II regions with multiple RRL velocities or with systemic velocities within 10kms^{-1} of the terminal velocity.

Thirty-one Case III H II regions are shared between this work and Anderson & Bania (2009). The kinematic distance determinations differed between the two analysis methods used by Anderson & Bania (2009) for many cases (see Table 3.2). For these regions, the tangent point distance was often assigned by this work. This is simply due to the wider default tangent point velocity interval in this paper. For the common sources with successful KDARs, there was a 4% disagreement with KDARs achieved using the E/A method of Anderson & Bania (2009) and a 16% disagreement with the HISA method.

It should be noted that for the E/A method, Anderson & Bania (2009) extracted H I absorption and continuum data for sources between $18 < l^o < 67$ from the VGPS. Therefore any differences in KDAR for these sources are due to the differences in methodology only; this is in contrast to all other studies compared. As a result, the very low KDAR disagreement level between Anderson & Bania (2009) and this work (4%) is extremely pleasing.

Comparison with Sewilo et al. (2004)

Sewilo et al. (2004) performed observations of 72 H II regions in order to obtain systemic velocities and investigate formaldehyde absorption (rather than H I) towards each region. KDARs were achieved for 44 of the observed H II regions and for 149 H_2CO clouds. While Sewilo et al. (2004) made observations in both the first and fourth Galactic quadrants ($10 < |l^o| < 65$ - the Spitzer GLIMPSE longitude range), there are no fourth quadrant H II regions held in common with this paper. Of the six common H II regions, only one is assigned the opposite kinematic location in Sewilo et al. (2004) compared to this paper (G23.245-0.240).

Comparison with Kolpak et al. (2003)

Kolpak et al. (2003) resolved the KDA for 49 Galactic H II regions using the E/A method. However, they also presented 22 discrepancies between their kinematic distance designations and the existing literature. Kolpak et al. (2003) required at least three standard deviations of the noise over 5.2 km s^{-1} for absorption to be detected. An 11% disagreement exists for the successful KDARs of this paper and Kolpak et al. (2003).

Comparison with Clemens et al. (1988)

Clemens et al. (1988) estimated the kinematic distance to 50 H II regions through investigation of molecular absorption near the terminal velocity and the density of H_2 at each kinematic distance. This paper shares seven sources in common with the Clemens et al. (1988) work. The H II regions from Clemens et al. (1988) have been analysed in many studies and are disputed throughout the literature (see Table 3.2). For example, Kolpak et al. (2003) assigned the opposite kinematic distance to seven of the eight sources they held in common with Clemens et al. (1988). A discussion of the validity of the method used in the Clemens et al. (1988) study appears in Kolpak et al. (2003). A 17% disagreement exists between the successful KDARs of this work and Clemens et al. (1988).

Comparison with Paladini et al. (2004)

The work of Paladini et al. (2004) provides Galactocentric distance estimates to 550 H II regions in both the first and fourth quadrants, including 294 KDARs. The source catalogue for Paladini et al. (2004) was collated from several existing RRL catalogues (including Caswell & Haynes (1987) and Lockman (1989)). Resolutions were performed by analysis of H I and molecular absorption lines as well as optical counterparts of the sources; the presence of an optical counterpart resulted in a 'near' side distance assignment.

However, identification of these H II regions for comparison with this work is often ambiguous. For example, Paladini et al. (2004) list an H II region at G24.7-0.2, this region could equally refer to the H II region at G24.677-0.160 or the source at G24.742-0.207 (which displays two RRL velocity components).

In the first quadrant, there is a 14% disagreement between successful KDARs for H II regions common to Paladini et al. (2004) and this paper. This is a higher percentage of disagreement than for the H II regions common to both studies in the fourth quadrant (see Section 3.5.2).

3.5.2 Fourth Quadrant

The largest RRL velocity surveys of the fourth Galactic quadrant are those of Caswell & Haynes (1987) (316 H II regions) and Wilson et al. (1970) (130 sources). There is an extreme need for a RRL survey on the scale of the GBTHRDS in the fourth quadrant as the knowledge (and number) of RRL velocities of H II regions in the fourth quadrant is much poorer than for the first quadrant.

Comparison with Paladini et al. (2004)

Fifteen fourth quadrant sources are common between Paladini et al. (2004) and this work (note Section 3.5.1). Disagreement in successful KDAR is lower (7%) for the H II regions in the fourth quadrant than in the first.

Comparison with Urquhart et al. (2012)

Urquhart et al. (2012) performed high resolution H I observations using a target list from the Red MSX Source (RMS) survey, supplemented by H I data from the VGPS and SGPS. Urquhart et al. (2012) achieved KDARs for 102 H II regions, 37 of which are shared with this work, using the same method as Kolpak et al. (2003). However, unlike Kolpak et al. (2003), Urquhart et al. (2012) required the absorption to be stronger than 4σ of the noise level, but do not report the number of consecutive velocity channels with significant absorption required for a 'detection' of absorption. Furthermore, Urquhart et al. (2012) uses ^{13}CO emission velocities to derive systemic velocities for each H II region.

Urquhart et al. (2012) shares the largest number of H II regions with this paper of any of the fourth quadrant studies. The opposite KDAR was provided for 24% of H II regions common to both this paper and Urquhart et al. (2012). This level of disagreement is high compared to that of the other KDAR works, but for each of these H II regions, the Urquhart

et al. (2012) study achieves the opposite KDAR to existing literature; while the KDAR achieved by this work is in agreement with previous determinations (see Table 3.3).

There is some discussion in Urquhart et al. (2012) that use of H I absorption taken from the SGPS is more likely to produce a far side KDAR due to absorption features at velocities close to the tangent velocity that do not appear in their high resolution data sets. There is only one case in which this paper assigns the far kinematic distance while Urquhart et al. (2012) assigns the near, and in both instances H I absorption data was extracted from the SGPS. As a result, the difference in KDAR must be produced by the differences in method only. Furthermore, Urquhart et al. (2012) states that distances assigned by applying their method to the SGPS (and other low resolution data) is far less reliable than for high resolution H I data. This highlights the need for a new KDAR method that can be applied successfully to lower resolution (but existing) data sets as well as for faint sources. Some differences in KDAR might also be the result of using ^{13}CO emission velocities as systemic velocities for each H II region; for example Caswell & Haynes (1987) report an RRL velocity of 16 km s^{-1} for G334.722-0.655, whereas Urquhart et al. (2012) report a source velocity gained from ^{13}CO emission of -44.6 km s^{-1}.

Comparison with Caswell & Haynes (1987)

This canonical survey of recombination line emission provides RRL velocities for fifty-one H II regions in the interval $327.7^o < l < 342.4^o$. Seven of these H II regions were analysed in this work (two of these are automatically assigned to distances beyond the Solar circle due to positive RRL velocities). The kinematic distances of Caswell & Haynes (1987) were based on a model with the Galactic centre located 10 kpc from the Sun and Galactic rotation governed by the Schmidt (1965) curve. Distance assumptions were based on the presence of H I absorption, H_2CO detections or optical counterparts. H II regions with systemic velocities within 5 km s^{-1} of the tangent velocity were assigned to the tangent point distance.

A 14% disagreement exists for H II regions with successful KDARs common to Caswell & Haynes (1987) and this work.

Other

Very few catalogs exist that determine KDARs for fourth quadrant continuum sources, however studies are becoming more common with the availability of high-resolution surveys. Wilson et al. (1970), Fish et al. (2003) and Lockman (1981) provide one common source each, these are discussed in Appendix B.

3.6 Discussion

3.6.1 Galactic Distribution

H II regions, along with giant molecular clouds are among the most important spiral arm tracers (Hou et al. 2009). In order to examine the large scale structure of the Galaxy, H II regions with successful KDARs are superimposed onto the artist's conception face on map of the Milky Way (Churchwell et al. 2009); Figure 3.7. The image has been created using

stellar data as well as H I and CO survey data (Churchwell et al. 2009), Urquhart et al. (2012) provide an extensive explanation of the figure. The H II regions show a good alignment with known spiral arms in the longitude ranges of this study. Figure 3.8 shows close-ups of the near (left panel) and far (right panel) kinematic distance intervals for the fourth quadrant.

There is notably more disagreement in KDARs in the first quadrant than in the fourth (see Tables 3.2 and 3.3). This could be indicative of the amount of literature available for each quadrant, or it could be a result of different spiral structure around the tangent point, where KDARs are inherently more uncertain (and also where authors take various approaches to KDAR assignments). For example, a higher fraction of H II regions in the first quadrant seem to be located near the tangent point distance than in the fourth quadrant in the symmetric longitude ranges.

3.6.2 First Quadrant vs Fourth Quadrant

Another dramatic result of the E/A method is that the average amount of H I absorption differs between the two quadrants. Inspection of Figures 3.5 and 3.6 clearly demonstrates that the there is a greater abundance of cool H I clouds along a typical line of sight in the fourth quadrant sample than in the first quadrant. This can be seen from comparison of the mean and maximum values of the S_{TP} value distributions for sources at the far kinematic distance (see Figures 3.5 and 3.6). Careful study of the calibration of the absorption spectra was conducted to ensure that the high S_{TP} values in the fourth quadrant were not a result of biased data - for example the continuum temperature calibration differences could influence the scale factor of $e^{-\tau}$. Absorption values in each channel, as well as integrals of absorption spectra, were compared to previously published values (Strasser 2006; Dickey et al. 2003), see Section 3.3.1.

While some of the difference between the two quadrant samples must be the result of the parameters of the two IGPS surveys (notably the SGPS has coarser angular resolution than the VGPS), these differences cannot fully account for the differences in total H I absorption. It is interesting that the distribution of S_{TP} values for near side sources in each case is quite similar, suggesting that differences between the absorption in the two longitude ranges exist *only beyond the tangent point.*

3.6.3 Near-Far Asymmetry

There are several effects that could bias the ratio of near to far kinematic distances for the sources in these two samples. Geometrically, there is a bias introduced from the different survey boundaries in longitude and latitude. It should therefore be expected that if sources were distributed uniformly though the Galaxy, more sources would be found on the far kinematic side. The H II region KDAR studies of Kuchar & Bania (1994), Kolpak et al. (2003), Sewilo et al. (2004) and Anderson & Bania (2009) report an average near:far ratio of 1.0:2.3 which could be explained by geometric asymmetry alone, however recent papers (especially those conducted in the fourth quadrant) demonstrate a smaller near:far (see Table 3.4).

Other near:far ratio biases include the effect of flux limits and a non uniformity in the

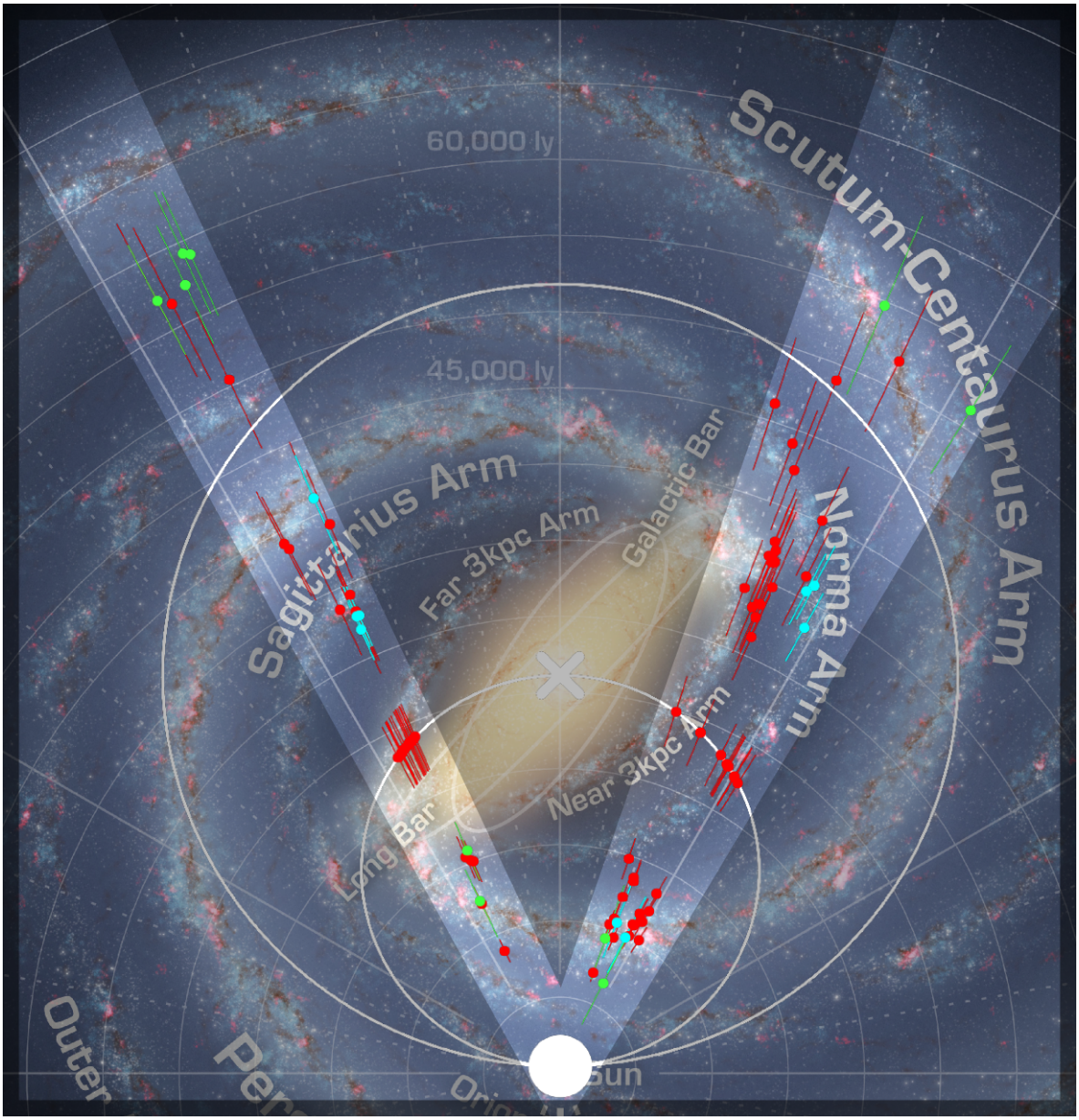

Figure 3.7: Positions of the H II region complexes for which a KDAR was achieved. Also shown are the Solar circle and locus of tangent points (white circles). Errors on the kinematic distances are equivalent to 15 km s^{-1} in each direction. Zoomed in sections for the fourth quadrant appear as Figure 3.8. Cyan markers are those regions with poor quality KDAR. Background image - artists' impression of Milky Way spiral structure from Spitzer Data (Image Credit- Benjamin, Hurt, NASA/JPL-Caltech).

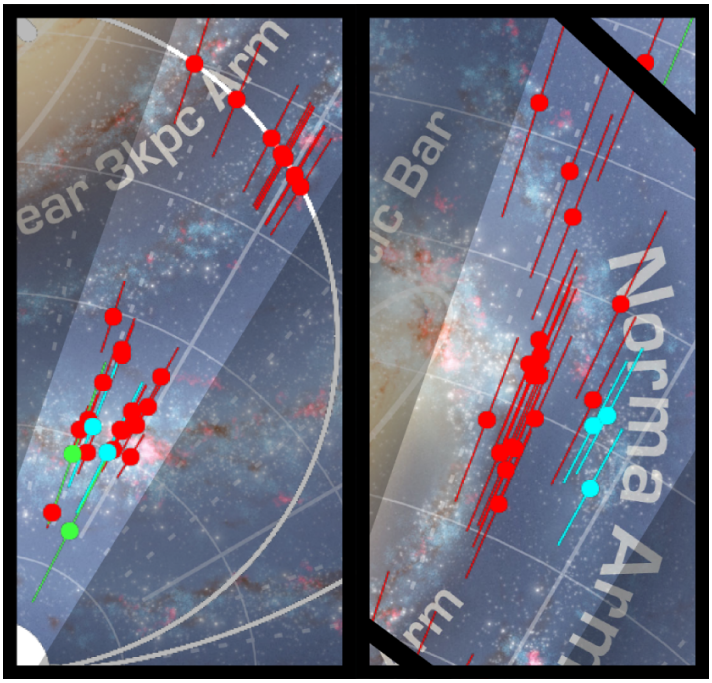

Figure 3.8: The fourth quadrant KDARs, i.e. zoomed portions of Figure 3.7. Left - kinematic near side (the locus of tangent points is visible as the white semi-circle). Right - kinematic far side (the locus of tangent points and Solar circle are defined by the thick black lines).

distribution of H II regions. Paladini et al. (2004) discuss that older, Malmquist-biased surveys often find a ratio in favour of the near side (i.e. Kerr & Knapp (1970a)), hence studies with more complete survey data should result in smaller ratio as fainter H II regions on the far side of the tangent point are included. Furthermore the ratios should differ in each region of the Galaxy as it is well established that H II regions are excellent tracers of massive star formation, and hence of spiral structure. As the spiral arms do not occur symmetrically at both the near and far kinematic distances, the ratio should be dependent on galactic longitude and the spiral structure along a given line of sight.

The near:far kinematic distance ratios produced by this work do not fully reflect the expected biases. In both quadrants the ratio is close to unity; possibly suggesting that the number of near side sources in this longitude range must severely outnumber the far side sources, such that the geometric bias is removed. Indeed this would be the case, in the fourth quadrant, if the bulk of the Scutum-Centaurus Arm is outside the Solar Circle for $l > 330^o$. If the longitude range of this work were extended to $l = 350^o$ then the ratio should change in order to reflect sources at the far end of the Galactic Bar (Churchwell et al. 2009).

However, the number of H II regions used to calculate these ratios is small, the number of near/far/tangent point sources is 5/5/17 for the first quadrant and 17/18/10 for the fourth (NB. only sources with systemic velocities are used to calculate the ratio). Only Fish et al. (2003) find a ratio in favour of the near kinematic distance, however their sample of H II regions was also small (13 only). Anderson & Bania (2009) discuss the different ratios produced by the various categories of H II regions in their sample. However, they also report that the H I E/A KDAR method produces a smaller near:far ratio than their HISA method (near:far is: 1.0:1.9 E/A; 1.0:2.2 HISA, see Table 3.4).

Study	Source	l Range	Near:Far
Kuchar & Bania (1994)	H II	$30 < l^o < 60$	1.0 : 3.6
Fish et al. (2003)	H II	$5 < l^o < 45$	1.5 : 1.0
Kolpak et al. (2003)	H II	$18 < l^o < 49$	1.0 : 2.5
Paladini et al. (2004)	H II	$6 < l^o < 351$	1.0 : 1.5
Sewilo et al. (2004)	H II	$10 < \|l^o\| < 65$	1.0 : 1.5 [a]
Urquhart et al. (2012)	H II	$10 < l^o < 348$	1.0 : 1.5
Anderson & Bania (2009)	H II	$15 < l^o < 54$	1 : 2
	Diffuse H II		1.0 : 3.8
	UC H II		1.0 : 2.2
	Compact H II		1.0 : 1.6
This Work Quadrant I	H II	$22 < l^o < 28$	1 : 1
This Work Quadrant IV	H II	$327 < l^o < 342$	1.0 : 1.1

Table 3.4: KDAR near:far ratios from the literature and this work. NB: Only H II regions that had known RRL velocities are included in this ratio. [a]Only high-quality KDARs are included in this ratio.

Caution is necessary in the interpretation of these ratios; this discussion is based primarily on similar discussions in many other KDAR works. However, the importance of this ratio must depend greatly on the longitude (and latitude) range of the study - and therefore a geometric bias - as well as any imposed flux limits.

3.7 Absorption Beyond the Solar Circle

Before the GBTHRDS there were seven H II regions known in the first quadrant ($l > 10^o$) with negative RRL velocities (Bania et al. 2010). These H II regions therefore lie unambiguously beyond the Solar Circle at a Galactic radius of more than 8.5 kpc. The GBTHRDS added a further 34 negative velocity H II regions to the literature for the first quadrant. Two known outer Galaxy HII regions exist within the first quadrant longitude range of this paper (G25.395+0.030 and G25.477+0.40) and two are known in the fourth quadrant (G334.722-0.655 and G338.411-0.211).

The sample of 200 continuum sources, with extracted absorption spectra, provided a wonderful opportunity to search for additional distant H II regions. An evaluation of the H I absorption in the outer Galaxy was performed for each source. S_{ch} was calculated for velocities pertaining to the outer Galaxy (ΔV =10 to 100 in the fourth quadrant and -10 to -100 in the first). If the measured S_{outer} was not negligible, i.e. either $S_{outer} - 3\sigma_{S_{outer}}$ was bounded above zero or there were at least three velocity channels displaying absorption stronger than a $3\sigma_{e^{-\tau}}$ level, the mid-infrared data for the region was then inspected to ascertain the source type.

For continuum emission targets that display H I absorption at Galactic velocities, infrared data can be used to ascertain the type of object, as well as whether it is Galactic or extragalactic. If the 22μm WISE and radio continuum emission display a source of similar morphology and angular extent, the source is assumed to be either an H II region or a planetary nebula (PN) (see Figure 3.9). 8μm Spitzer GLIMPSE images were inspected in order to attempt to differentiate between H II regions and PNe; point sources at 8μm or non-detections at 8μm

combined with ring-like 22μm morphology are more likely to be PNe (Bania et al. 2010).

For each H II region placed in the outer Galaxy, the line of sight distance was calculated using a flat rotation model $\Theta(d_{GR}) = \Theta_0$ beyond the Solar Circle (see Figure 3.7 and Table 3.1). As a result of this analysis, extragalactic objects (EG) and four new outer Galaxy (O) H II regions were identified (see Table 3.1).

3.8 Summary

H I absorption data from the VGPS and SGPS were used to determine the Kinematic Distance Ambiguity Resolution for 119 radio continuum sources. Kinematic distances were calculated for 86 of these H II regions. These KDAR determinations are mostly in agreement with previous studies ($< 25\%$ disagreement), providing strong evidence that the S_{ch} analysis is an efficient KDAR method.

New RRL velocity surveys (i.e. GBTHRDS) will identify increasingly fainter H II regions increasingly further from the Sun. In order to assess these new H II regions, especially those beyond the Solar circle, a KDAR method that is applicable to faint sources will be required. The S_{ch} KDAR analysis used in this paper can provide that method. The sample of resolved kinematic distances appears to trace Galactic structure components, including spiral arms and possibly the end of the Bar. Existing KDAR methods are more unreliable for existing (low) resolution H I data, including the SGPS used thoughout this work (Urquhart et al. 2012). Therefore, in order to achieve as many KDARs as possible, a method that can be applied to both faint sources - likely to be found in the southern equivalent of the GBTHRDS - as well as exisiting data is paramount. The velocity channel summation KDAR method used in this work can be applied to faint sources in existing low resolution data (i.e. SGPS) and will be applicable to future KDAR works.

Several sources with H I absorption beyond the Solar Circle were identified and flagged for future RRL observations in order to constrain their location. Whole sky infrared image catalogs are now available that will aid the classification of these objects (H II region or PNe). These sources will trace the Outer Arm (McClure-Griffiths et al. 2004) and supplement the general understanding of spiral structure, particularly on the far side of the Milky Way.

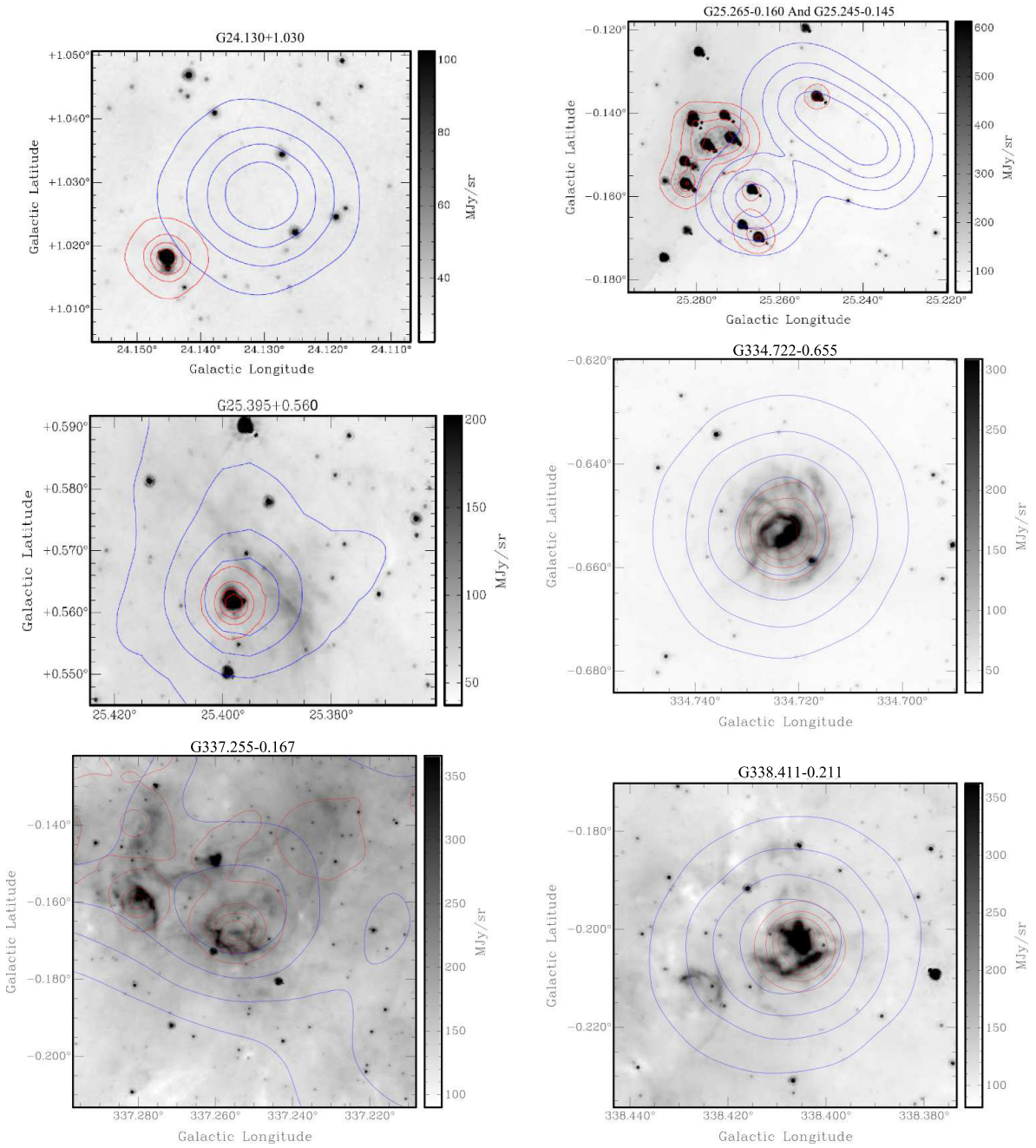

Figure 3.9: SGPS or VGPS radio continuum (blue) and WISE 22μm (red) contours on the Spitzer GLIMPSE 8μm image cutouts for sources which display significant absorption beyond the Solar circle. Note the saturation in the top right panel, appearing as ghosting in the GLIMPSE image.

Chapter 4

H I Absorption Toward H II Regions at Small Galactic Longitudes

This Chapter includes a co-authored paper.
The bibliographic details of the paper, including all authors are: Jones, C.; Dickey, JM; Dawson, JR; McClure-Griffiths, NM; Anderson, LD and Bania, TM, Astrophysical Journal, 774, (2) Article 117. ISSN 0004-637X (2013); doi:10.1088/0004-637X/774/2/117. The published paper is referenced by this thesis as Jones et al. (2013).

The introductory and methodology sections have been adapted to avoid unnecessary duplication - see Chapters 1 and 2. The individual source descriptions, an Appendix of the published work, have been included in this thesis in Appendix B. Figure Set 1, of the published work, has been included in this thesis as part of Appendix C.

Abstract

We make a comprehensive study of H I absorption toward H II regions located within $|l| < 10^o$. Structures in the extreme inner Galaxy are traced using the longitude-velocity space distribution of this absorption. We find significant H I absorption associated with the Near and Far 3kpc Arms, the Connecting Arm, Bania's Clump 1 and the H I Tilted Disk. We also constrain the line of sight distances to H II regions, by using H I absorption spectra together with the H II region velocities measured by radio recombination lines.

4.1 Introduction

The Extreme Inner Galaxy (EIG) has long been the subject of intense astrophysical study as it provides excellent opportunities to explore dynamics, phenomena (from stellar to galactic scales) and physical environments which do not exist in the large-scale Galactic disk.

Throughout this Chapter, we refer to the area inside of, and including, the 3kpc Arms as the EIG (i.e. $R_{Gal} \lesssim 4$kpc). 'Inner Galaxy' is a term already used to describe the areas of the Milky Way inside the Solar Circle, likewise the term 'Galactic Center' (GC) usually refers to the relatively small area with a Galactocentric radius less than a few hundred parsecs.

Useful reviews of the EIG environment include Morris & Serabyn (1996) and Blitz et al. (1993), who discuss the interstellar medium (ISM) and structural components respectively.

Radio observations of the EIG region have been performed since the 1950s (using the Dwingeloo 26 m antenna, van Woerden et al. 1957). These early studies discovered large-scale H I features with non-circular motions (Oort 1977), and concentrated on understanding these individual structures, or particular objects.

The EIG has been extensively observed in CO. Molecular tracers probe denser material than neutral hydrogen (H I) and CO is readily observed; therefore CO observations allow for analysis of regions in which the ISM is concentrated into structures such as arms and bars (Dame et al. 2001). In contrast, observations of atomic gas trace diffuse interstellar clouds.

While H I in the EIG has been well studied at low angular resolution, it is only recently that high-resolution H I data which cover the entire EIG region have become available (i.e. ATCA H I Galactic Center Survey (HIGCS) McClure-Griffiths et al. 2012). These high-resolution H I data allow an analysis of the beginnings of the spiral arms; the transition between orbits associated with the bar; a comparison to high-resolution molecular observations, dynamical models and molecular transitions; as well as investigations into the association of H I with the Galactic wind (McClure-Griffiths et al. 2012).

As a result of the variation in the temperature of interstellar hydrogen, H I emission and absorption spectra probe different phases of the ISM. In most emission spectra it is the warmer components that dominate. However, cool gas is readily observed in absorption against background continuum sources, where it may be disentangled from warmer material along the line of sight. One advantage to studying HI absorption in the EIG is that it probes this predominantly cool material, which tends to be more localised in space, and more closely confined to structural entities such as arms.

Previous H I absorption studies have been vital to our understanding of the structure, rotation and the nature of atomic gas in the EIG region. These include observations of absorption features associated with non-circular velocities, Radio Arc non-thermal filaments as well as particular objects including SgrA* (Lang et al. 2010, and references therein).

While high-resolution H I absorption measurements have been made towards several bright, or otherwise interesting, EIG continuum sources (Uchida et al. 1992; Roy 2003; Lang et al. 2010, and references therein) a complete H I absorption study of the EIG region has not been attempted. This present H I absorption survey constitutes the most complete study of H I absorption against the continuum emission from the entire sample of H II regions known with $|l| < 10^o$. This study is only possible due to recent H II region discovery surveys (which

provide a list of target continuum regions with which to measure absorption against) and improved resolution in H I surveys that include the GC region.

In addition to providing a sample of bright continuum sources against which to measure H I absorption, H II regions themselves are an important tracer of Galactic structure. Galactic H II regions are the formation sites of massive OB stars, which have a main sequence lifetime of ∼tens of millions of years. As a result, Galactic H II regions reveal the locations of current massive star formation, indicate the present state of the ISM, provide a unique probe of Galactic chemical evolution and are the archetypical tracers of Galactic spiral structure (Bania et al. 2010).

In this work we measure HI absorption against only those HII regions with known radio recombination line (RRL) velocities. This sub-sample is discussed in Section 4.2, and the method of HI absorption is described in Section 4.3.

We then summarise the known EIG structures (Section 4.4.1) and their locations in Longitude-Velocity (lv) space. We plot these structures on an 'lv crayon diagram', and use the diagram to consider the EIG lv distribution of H I absorption, in Section 4.5, and later for H II regions (Section 4.6).

We combine the results from Sections 4.5 and 4.6 to explore the Galactic distribution of H II regions (Section 4.7) - through determining the lower limit of the line of sight distance to each H II region based on its H I absorption profile and systemic velocity.

Finally, a discussion of individual sources appears in Appendix B.

4.2 Data & Source Selection

For this work, radio continuum maps were sourced from the NVSS and SGPS. H I absorption spectra were extracted from the two SGPS datasets (SGPS I and SGPS II) and the ATCA HIGCS. More information on these data sets can be found in Chapter 2.

The GBTHRDS team published a list of known H II region (as of 2010) as part of Bania et al. (2010). This list, described in Chapter 2, in addition to the GBTHRDS H II regions provided the target list of H II regions for this work.

4.2.1 H II Regions Selected

There are nearly 200 known H II regions in the range $|l| < 10^o$, $|b| < 1.5^o$ with observed RRL velocities. H I absorption spectra were extracted towards a total of 151 of these H II regions (see Appendix C*). The remaining H II regions were either not visible in the NVSS continuum maps (also used by the GBTHRDS), usually diffuse H II regions from the Lockman et al. (1996) catalog, or H II regions with coordinates that could refer to several continuum sources - see Table 4.1. Therefore this study obtains H I absorption spectra towards over 80% of known H II regions with $|l| < 10^o$. The 'name' for each H II region is taken from the RRL catalog from which it was obtained.

*These spectra appeared as an online only Figure Set in the published work.

4.3 Extraction of the H I Absorption Spectra

The H I emission/absorption method, described in Chapter 1 was used to extract spectra from the H I cubes.

For each absorption spectrum, velocity channels with significant absorption were selected for analysis. Significant absorption is defined to satisfy both:

- significance at the $3\sigma_{e^{-\tau}}$ level, where $\sigma_{e^{-\tau}}$ is calculated from the emission fluctuation envelope (the difference in emission between 'off' sources).
- significance at the $3\sigma_{rms_{e^{-\tau}}}$ level, where $\sigma_{rms_{e^{-\tau}}}$ is the fluctuation in the baseline of the absorption spectrum.

The NVSS continuum maps are biased towards smaller continuum temperatures as they do not include all diffuse continuum emission. However, as T_{cont} acts as a scaling factor for $e^{-\tau}$ (see Equation 1.19), $\sigma_{e^{-\tau}}$ and $\sigma_{rms_{e^{-\tau}}}$ will also scale proportionately with any change in continuum temperature.

Emission and absorption spectrum pairs toward each H II region appear in Appendix C.2.

4.4 Longitude-Velocity Overview of the Extreme Inner Galaxy

Absorption spectra along lines of sight through the Galactic disk within the longitude range $|l| < 10^o$ are complex and difficult to interpret. This longitude region includes structures associated with the GC and EIG ($R_{Gal} \lesssim 4$kpc), with highly non-circular motions; as well as features with velocities consistent with circular disk rotation ($R_{Gal} \gtrsim 4$kpc).

Here we use the summary of EIG structures (§4.4.1) to construct an 'lv crayon plot' (Figure 4.1), marking prominent EIG features based on the integrated intensity of ^{12}CO in the same l, b range (from Dame et al. 2001).

CO traces denser material than H I and therefore picks out the densest features. In the inner Galaxy, atomic gas often acts to shield associated regions of molecular gas from photodissociation (Dickey & Lockman 1990). Therefore H I absorption features may be identified with known EIG molecular emission features using correlations in velocity structure (Lang et al. 2010).

As a result, this plot provides a useful reference, which we use to consider the lv distribution of H I absorption, §4.5, (and later H II region RRL velocities, §4.6).

4.4.1 Structures in the Extreme Inner Galaxy

Structures in the EIG include a long, thin bar, a shorter, boxy-bulge bar, the Near and Far 3 kpc arms, tilted H I inner disk or ring, central molecular zone, and thin twisted 100 pc ring (McClure-Griffiths et al. 2012). In addition to these more prominent structures, recent lv diagrams from H I and CO observations show many 'clumpy' sub-structures, not seen in previous EIG models (Baba et al. 2010).

The angular extent of some of these EIG features is quite large: the Near 3kpc Arm is observed to $l < 348^o$, and to surround all H I emission associated with the EIG region, a

H II Region	Reference	Note
G351.265+01.019	GBTHRDS (2011)	NV
G351.590+00.183	Lockman (1989)	MS
G353.035+00.748	Lockman (1989)	MS
G353.083+00.358	Lockman (1989)	MS
G357.998−00.159	Lockman (1989)	DC
G358.319−00.414	Lockman et al. (1996)	NV
G358.623−00.066	Caswell & Haynes (1987)	DC
G358.661−00.575	Lockman et al. (1996)	NV
G358.664−00.575	Lockman et al. (1996)	NV
G358.974−00.021	Lockman et al. (1996)	NV
G359.186−00.026	Caswell & Haynes (1987)	DC
G359.730−00.407	Downes et al. (1980)	NV
G359.783+00.040	GBTHRDS (2011)	NV
G359.929+00.045	GBTHRDS (2011)	NV
G000.394−00.540	Downes et al. (1980)	NV
G000.521+00.178	Lockman et al. (1996)	NV
G000.605+00.325	Lockman et al. (1996)	NV
G000.656−00.058	Downes et al. (1980)	NV
G000.829+00.193	Downes et al. (1980)	NV
G001.323+00.086	Caswell & Haynes (1987)	DC
G002.303+00.243	Lockman (1989)	MS
G005.049+00.254	Lockman (1989)	NV
G005.332+00.081	Lockman et al. (1996)	MS
G006.616−00.545	Lockman et al. (1996)	NV
G006.667−00.247	Lockman (1989)	NV
G006.979−00.250	Lockman (1989)	NV
G007.002−00.015	Lockman et al. (1996)	NV
G007.299−00.116	Lockman (1989)	NV
G007.387+00.668	Lockman (1989)	NV
G008.415+00.033	Lockman et al. (1996)	NV
G008.786−00.034	Lockman et al. (1996)	NV
G009.176+00.032	Lockman et al. (1996)	DC

Table 4.1: H II regions that were *not* included in this work. Notes - NV: not visible at the SGPS pixel scale; MS: many continuum sources present at this location; DC: duplicate (in both catalogs).

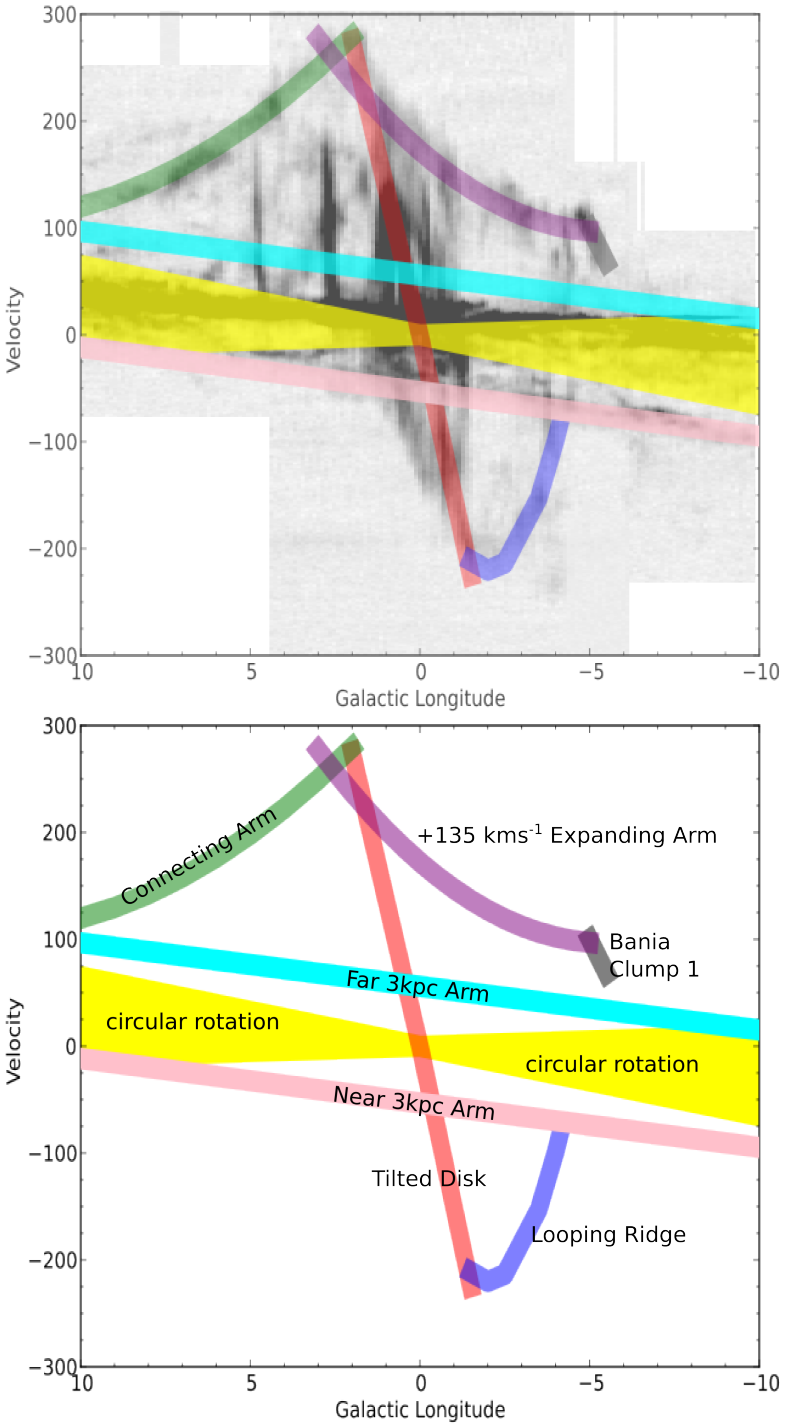

Figure 4.1: Longitude-velocity "crayon" diagram for $l < |10^o|$, $b < |1.5|^o$. Top panel - the 'crayon' features overlaid on CO emission map (Dame et al. 2001). Bottom panel - the 'crayon' features (each with a velocity width of 20 km s^{-1}). The 'crayon' color system is as follows: yellow - circular rotation allowed velocity envelope ; green - Connecting Arm; purple - +135kms^{-1} Expanding Arm; grey - Bania's Clump 1; red - Tilted Disk; cyan - Far 3kpc Arm; yellow - velocities allowed by circular disk rotation; pink - Near 3kpc Arm; blue - Looping Ridge. While not explicitly labeled in the crayon diagram, Bania's Clump 2 can be seen as the thick vertical CO feature at $l \sim 3^o$, $0 \lesssim v \lesssim 200$ km s^{-1} in the top panel.

latitude range of at least $|b| \leq 8^o$ is required (Burton & Liszt 1983) - well beyond the range of known H II regions ($|b| <\sim 2^o$).

Many of these features are not often explicitly discussed in the literature and precise distances are usually unknown (Fux 1999). A summary of the EIG gas structures, many of which are detected in H I absorption spectra appears below. Often these objects have several names in the literature, or several distinct features have been given the same name by different authors.

For a discussion of the evolution of the understanding of H I and CO lv models in the EIG see Baba et al. (2010). Burton & Liszt (1983) provide a series of lv diagrams with prominent features identified.

4.4.1.1 Near and Far 3kpc Arms

Near 3kpc Arm The Near 3kpc Arm or Expanding 3kpc Arm was discovered in the late 1950s and is known to lie in front of the GC (van Woerden et al. 1957). However, it is not yet agreed whether the Near 3kpc Arm is a lateral arm surrounding the bar, or a small arm extending from the end of the bar, or an arm located where the bar meets its co-rotation radius (Rodríguez-Fernández 2011). Stretching over 35^o in longitude, the Near 3kpc Arm exists at 'forbidden' velocities and its discovery provided vital early support for a Galactic bar (Dame & Thaddeus 2008, and references therein). The Near 3kpc Arm appears as the pink line in Figure 4.1.

Far 3kpc Arm Despite the tendency for major anomalous velocity features in the GC to occur in positive and negative velocity pairs (Burton & Liszt 1983), it was originally thought that there was no far side counterpart to the Near 3kpc Arm (Dame & Thaddeus 2008, and references therin). Fux (1999) supposed the 135 km s^{-1} Arm (discussed below) was the feature symmetric to the Near 3kpc Arm - however Fux also noted compositional differences between the +135 km s^{-1} and Near 3kpc Arm, attributing these to an asymmetric spiral structure. Dame & Thaddeus (2008) reported the detection (in CO and then followed up in H I) of the far side counterpart to the Near 3kpc Arm, named the Far 3kpc Arm. The Far 3kpc Arm appears as the cyan line in Figure 4.1.

4.4.1.2 H I Tilted/Nuclear Disk

The H I inner tilted disk, proposed by Liszt & Burton (1980), was the result of a full 3D analysis of all known H I emission in the inner kiloparsec of the Galaxy. It was modeled by a series of closed elliptical gas orbits. The disk is oriented at 23.7^o with respect to the Galactic plane and accounts for positive velocity H I emission at $b < 0^o, l > 0^o$ and negative velocity gas at $b > 0^o, l < 0^o$ (HIGCS). In Figure 4.1, the Tilted Disk appears as the red line crossing through $(l, v) = (0, 0)$.

4.4.1.3 The Expanding Arm(s)

+135kms^{-1} Arm The location of the +135km s^{-1} Arm, or Expanding Arm, is contentious throughout the literature: Fux (1999) assumes it is the far side counterpart to the Near 3kpc

Arm (see §4.4.1.1), Bania (1980) argues that the 3kpc and +135kms^{-1} Arms can not be described together as a kinematic ring, and Baba et al. (2010) model the +135kms^{-1} Arm as part of the end of the bar on the far side.

The +135kms^{-1} Arm is more clumpy than the Near 3kpc Arm (Fux 1999) and extends nearly 30^o in longitude and spans 3^o in latitude near the GC ($-1^o < b < 2^o$ at $l = 359^o$) (Uchida et al. 1992). Distance estimates for the +135kms^{-1} Arm vary; Simonson & Mader (1973) and Bania (1980) give galactocentric radii only (3.4 kpc and 2.8-3.5kpc respectively), whereas Uchida et al. (1992) give a distance estimate of about 2kpc *behind* the GC (i.e. $D_{los} > 10$kpc).

In Figure 4.1, the +135km s^{-1} Expanding Arm appears as the purple curve.

Bania's Clumps The individual emission clumps that comprise the +135kms^{-1} Arm probably either include Bania's Clumps 1 and 2 (Bania 1980; Bania et al. 1986), or the these two clumps are entering the dust lane shock (Liszt 2008). A detailed discussion of the H I properties of Bania's Clump 2 can be found in McClure-Griffiths et al. (2012).

Bania's Clump 1 is seen as the grey line in Figure 4.1, whereas Bania's Clump 2 is seen as the thick vertical CO feature at $l \approx 3^o$, $\sim 0 < v <\sim 200$ km s^{-1} in the CO lv diagram (top panel of Figure 4.1).

-135km s^{-1} Feature Just as the Near 3kpc Arm has a nearly symmetrical velocity and spatial counterpart a -135km s^{-1} Feature is thought to be located in the foreground of the GC, but behind the Near 3kpc Arm, as it is seen in OH absorption (Uchida et al. 1992). This feature is much less distinct than the +135km s^{-1} Arm, indeed Bania (1980) did not detect it. This feature is not included in Figure 4.1.

4.4.1.4 Connecting Arm and Looping Ridge

Two features - the Connecting Arm and Looping Ridge - are visible in CO and H I emission, as well as in near infrared dust extinction (Marshall et al. (2008) and HIGCS). These features lead the bar major axis and are the location of strong shearing shocks, resulting in high velocities (Fux 1999).

The extent of both structures in l, b, v has been explored in detail by Marshall et al. (2008) who use CO data to localise emission to specific lv structures.

Connecting Arm - Positive Velocity Feature The Connecting Arm (at extreme positive velocities and longitudes), was named as it seems to link the nuclear ring/disk to the outer disk (Fux 1999). The Arm was sufficiently prominent in H I to be described as a distinct feature in early EIG surveys (Liszt 2008). The location of the Connecting Arm, in front of or behind the GC, was originally unclear; it has been interpreted as part of the central bar on the far side of the GC, or as an artifact due to velocity crowding along the line of sight, but it is now accepted to be a near side dust lane (Fux 1999, and references therein).

The Connecting Arm appears as the green curve in Figure 4.1.

Looping Ridge - Negative Velocity Feature The corresponding feature to the Connecting Arm (at negative velocities and longitudes) is not always treated as a distinct feature (Liszt 2008) and remains unnamed, however McClure-Griffiths et al. (2012) refer to the negative feature as the "looping" ridge. Liszt (2008) suggests that the Looping Ridge may be (temporarily) starved of gas and hence more difficult to detect and analyse.

In Figure 4.1, the Looping Ridge appears as the blue curve.

4.5 Longitude-Velocity Distribution of H I Absorption Toward the Extreme Inner Galaxy

Figure 4.2 displays the H I absorption in lv space, and compares this distribution with the EIG structures (§4.4.1), H I and CO emission.

Table 4.2 notes if significant H I absorption is associated with any EIG feature for each H II region.

It is immediately obvious that the H I absorption distribution is not random, but closely follows the identified EIG features. This is not surprising as cold H I gas, seen in absorption, is a good tracer of Galactic structure.

H I absorption is associated with the allowed circular rotation velocities (as expected) as well as the Near and Far 3kpc Arms, Connecting Arm and Bania's Clump 1.

4.5.1 H I Absorption Associated with the 3kpc Arms

The CO emission from both the Near and Far 3kpc Arms is contained within $|b| < 1^o$ (Dame & Thaddeus 2008), similar to the Galactic latitude range of the H II regions in this work ($|b| \lesssim 1.5^o$). Furthermore, both 3kpc Arms are thought to span $|l| \lesssim 13^o$, which includes the whole longitude range of this work. Therefore, if an H II region is located behind either of the 3kpc Arms, H I absorption should be detected at velocities pertaining to that arm.

Figure 4.2 demonstrates that significant H I absorption is seen toward the Near 3kpc Arm at all longitudes; although there is a conspicuous gap in absorption at longitudes $\sim 356 < l^o <\sim 358$, consistent with a paucity of H II regions towards which to measure absorption. Indeed 67% H II regions display absorption associated with the Near 3kpc Arm.

Fewer H II regions display absorption associated with the Far 3kpc Arm than with the Near 3kpc Arm ($\sim 1.0 : 3.3$); with the site of greatest absorption for the Far 3kpc Arm centered at $l \approx 7^o$ (see Figure 4.3). This disparity may be an effect of the smaller latitude extent of the Far 3kpc Arm, which is particularly thin in the fourth quadrant (Dame & Thaddeus 2008).

Both the HIGCS and Dame & Thaddeus (2008) report a bifurcation in the velocities of the Far 3kpc Arm (in lv space) at $l < 6^o$. There is limited evidence of this bifurcation at longitudes extending to $\approx 7^o$; the best example of this is in the absorption spectrum of G007.176+00.087 (see Appendix C). The Near 3kpc Arm also displays evidence of bifurcation, in both the H I emission and absorption, near $l = 358^o$ (see, for example, G358.616-00.076, G358.623-00.066, G358.633+00062 and G359.432-00.086 in Appendix C).

Region	N3	CA	TD	+E135	BC1	F3	Region	N3	CA	TD	E135	BC1	F3
G350.004+00.438	N	-	-	-	-	N	G000.284−00.478	Y	-	N	N	-	N
G350.129+00.088	Y	-	-	-	-	N	G000.361−00.780	Y	-	N	N	-	Y
G350.177+00.017	N	-	-	-	-	Y	G000.382+00.017	Y	-	N	Y	-	N
G350.330+00.157	Y	-	-	-	-	Y	G000.510−00.051	Y	-	N	N	-	N
G350.335+00.107	Y	-	-	-	-	N	G000.572−00.628	Y	-	N	N	-	N
G350.524+00.960	N	-	-	-	-	N	G000.640+00.623	Y	-	Y	N	-	Y
G350.769−00.075	N	-	-	-	-	N	G000.729−00.123	Y	-	N	N	-	Y
G350.813−00.019	N	-	-	-	-	Y	G000.838+00.189	Y	-	Y	Y	-	Y
G350.996−00.557	N	-	-	-	-	Y	G001.125−00.105	Y	-	N	Y	-	Y
G351.028+00.155	Y	-	-	-	-	Y	G001.149−00.062	Y	-	Y	N	-	Y
G351.047−00.322	N	-	-	-	-	N	G001.324+00.104	N	-	N	N	-	N
G351.192+00.708	N	-	-	-	-	N	G001.330+00.088	Y	-	N	N	-	Y
G351.201+00.483	N	-	-	-	-	N	G001.488−00.199	Y	-	N	Y	-	Y
G351.358+00.666	N	-	-	-	-	Y	G002.009−00.680	Y	N	-	N	-	N
G351.359+01.014	N	-	-	-	-	N	G002.404+00.068	N	N	-	N	-	N
G351.467−00.462	N	-	-	-	-	N	G002.418−00.611	N	N	-	N	-	N
G351.601−00.348	N	-	-	-	-	Y	G002.510−00.028	Y	N	-	Y	-	N
G351.662+00.518	Y	-	-	-	-	N	G002.611+00.135	Y	N	-	N	-	N
G351.691+00.669	N	-	-	-	-	N	G002.819−00.132	N	N	-	N	-	N
G352.233−00.151	Y	-	-	-	-	N	G002.901−00.006	Y	N	-	N	-	N
G352.313−00.440	Y	-	-	-	-	Y	G002.961−00.053	Y	N	-	N	-	Y
G352.398−00.057	Y	-	-	-	-	N	G003.270−00.101	Y	N	-	-	-	Y
G352.521−00.144	Y	-	-	-	-	N	G003.342−00.079	Y	Y	-	-	-	Y
G352.610+00.177	N	-	-	-	-	N	G003.439−00.349	Y	N	-	-	-	N
G352.611−00.172	Y	-	-	-	-	N	G003.449−00.647	Y	Y	-	-	-	N
G352.866−00.199	Y	-	-	-	-	N	G003.655−00.111	Y	N	-	-	-	N
G353.186+00.887	N	-	-	-	-	N	G003.928−00.116	Y	N	-	-	-	Y
G353.218−00.249	Y	-	-	-	-	N	G003.949−00.100	Y	N	-	-	-	N
G353.381−00.114	Y	-	-	-	-	N	G004.346+00.115	N	N	-	-	-	N
G353.398−00.391	N	-	-	-	-	N	G004.412+00.118	Y	N	-	-	-	Y
G353.557−00.014	Y	-	-	-	-	Y	G004.527−00.136	Y	N	-	-	-	Y
G354.200−00.054	Y	-	-	-	-	N	G004.568−00.118	Y	N	-	-	-	N
G354.418+00.036	N	-	-	-	-	N	G005.193−00.284	Y	Y	-	-	-	N
G354.486+00.085	Y	-	-	-	-	Y	G005.479−00.241	Y	N	-	-	-	Y
G354.588+00.007	Y	-	-	-	N	N	G005.524+00.033	Y	Y	-	-	-	Y
G354.610+00.484	Y	-	-	-	N	Y	G005.633+00.240	N	Y	-	-	-	N
G354.664+00.470	N	-	-	-	N	N	G005.899−00.427	N	Y	-	-	-	N
G354.665+00.247	N	-	-	-	Y	N	G006.014−00.364	Y	N	-	-	-	N
G354.717+00.293	N	-	-	-	Y	N	G006.083−00.117	Y	N	-	-	-	Y
G354.934+00.327	Y	-	-	-	Y	Y	G006.148−00.635	Y	N	-	-	-	N
G354.979−00.528	N	-	-	-	N	N	G006.160−00.608	Y	N	-	-	-	N
G355.242+00.096	Y	-	-	Y	-	Y	G006.225−00.569	N	Y	-	-	-	N
G355.344+00.145	Y	-	-	Y	-	Y	G006.398−00.474	N	Y	-	-	-	N
G355.532−00.100	Y	-	-	Y	-	N	G006.553−00.095	Y	Y	-	-	-	Y
G355.581+00.288	Y	-	-	Y	-	Y	G006.565−00.297	N	Y	-	-	-	Y
G355.661+00.382	Y	-	-	Y	-	N	G007.041+00.176	Y	N	-	-	-	Y
G355.696+00.350	Y	-	-	Y	-	N	G007.176+00.087	Y	N	-	-	-	N
G355.700−00.100	Y	-	-	N	-	N	G007.254−00.073	Y	N	-	-	-	Y
G355.734+00.138	Y	-	-	Y	-	N	G007.266+00.183	Y	Y	-	-	-	N
G355.801−00.253	Y	-	-	N	-	N	G007.299−00.116	N	N	-	-	-	N
G356.230+00.066	Y	-	-	N	-	N	G007.420+00.366	Y	N	-	-	-	Y
G356.235+00.642	Y	-	-	Y	-	N	G007.466−00.279	Y	N	-	-	-	N
G356.307−00.210	Y	-	-	N	-	N	G007.472+00.060	Y	N	-	-	-	Y
G356.470−00.001	Y	-	-	N	-	Y	G007.700−00.079	N	N	-	-	-	N
G356.560−00.086	Y	-	-	N	-	N	G007.768+00.014	Y	Y	-	-	-	N
G356.650+00.129	Y	-	-	Y	-	N	G007.806−00.621	Y	Y	-	-	-	N
G357.484−00.036	N	-	-	N	-	Y	G008.005−00.484	Y	Y	-	-	-	N
G357.970−00.169	Y	-	-	N	-	N	G008.006−00.156	Y	Y	-	-	-	Y
G357.998−00.159	Y	-	-	N	-	N	G008.094+00.085	N	N	-	-	-	N
G358.319−00.414	N	-	-	N	-	N	G008.103+00.340	Y	N	-	-	-	N
G358.379−00.840	N	-	-	N	-	N	G008.137+00.228	N	N	-	-	-	N
G358.530+00.056	N	-	N	N	-	N	G008.362−00.303	Y	N	-	-	-	N
G358.552−00.025	N	-	N	N	-	N	G008.373−00.352	Y	Y	-	-	-	N
G358.616−00.076	Y	-	N	N	-	N	G008.432−00.276	Y	N	-	-	-	Y
G358.623−00.066	Y	-	Y	N	-	N	G008.666−00.351	Y	N	-	-	-	N
G358.633+00.062	Y	-	Y	N	-	N	G008.830−00.715	Y	N	-	-	-	N
G358.652−00.078	N	-	N	N	-	N	G008.865−00.323	Y	N	-	-	-	N
G358.680−00.087	N	-	Y	N	-	N	G009.178+00.043	Y	N	-	-	-	N
G358.694−00.075	N	-	Y	N	-	N	G009.615+00.198	Y	N	-	-	-	N
G358.720+00.011	Y	-	N	N	-	N	G009.682+00.206	N	N	-	-	-	N
G358.797+00.058	Y	-	N	N	-	N	G009.717−00.832	Y	N	-	-	-	N
G358.827+00.085	N	-	N	N	-	N	G009.741+00.842	Y	N	-	-	-	N
G359.159−00.038	Y	-	N	N	-	N	G009.875−00.749	Y	Y	-	-	-	N
G359.277−00.264	N	-	N	N	-	N	G009.925−00.745	Y	N	-	-	-	N
G359.432−00.086	Y	-	N	N	-	N	G009.982−00.752	Y	N	-	-	-	N
G359.467−00.172	Y	-	N	N	-	Y	-	-	-	-	-	-	-

Table 4.2: Presence of significant H I absorption in EIG features for each H II region. EIG features are listed in line of sight order. N3= Near 3kpc Arm, CA= Connecting Arm, TD= H I Tilted Disk, E135= +135km s^{-1} Expanding Arm, BC1= Bania's Clump 1, F3= Far 3kpc Arm.

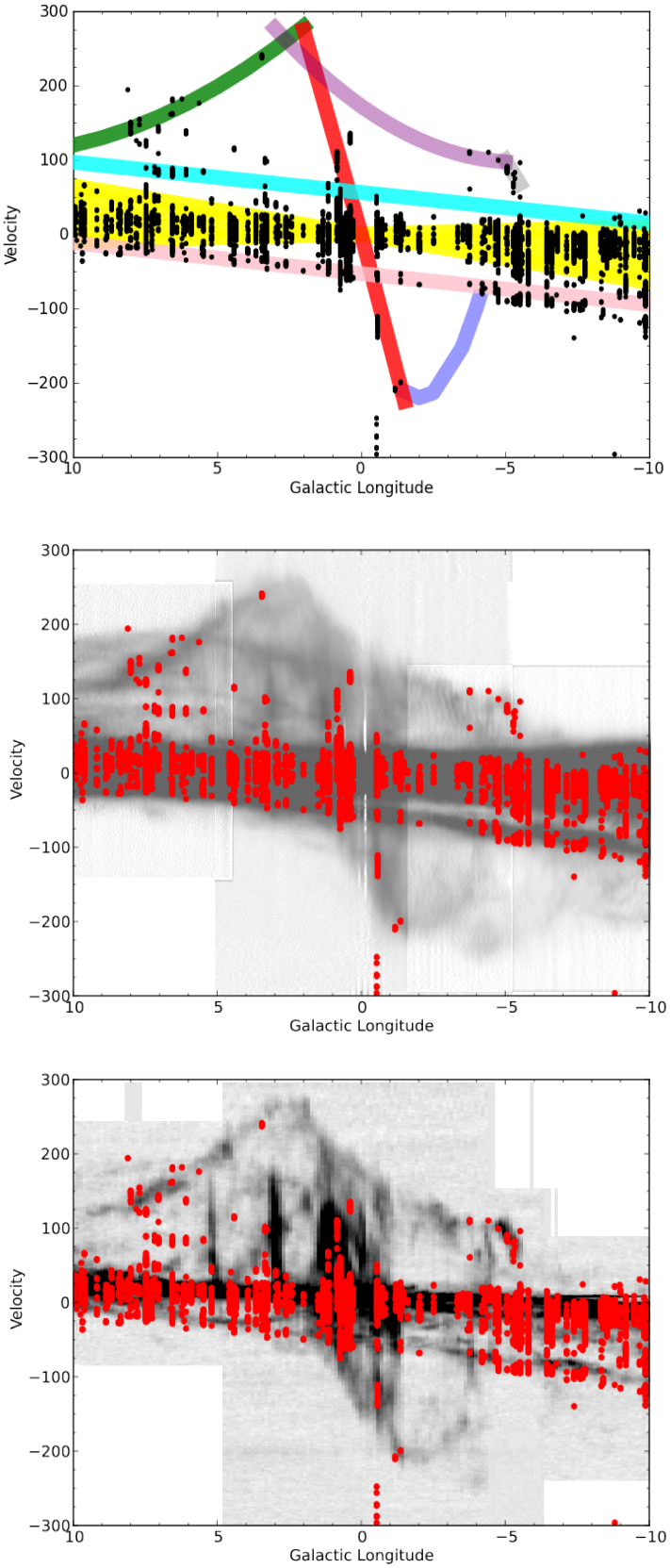

Figure 4.2: *lv* diagrams showing velocity channels with significant absorption for each H II region overlaid onto: top panel - the 'crayon' plot of EIG features (see Figure 4.1); middle panel - H I emission (the intensity map was created from the SGPS I & II and ATCA HIGCS); bottom panel - CO emission (see Figure 4.1).

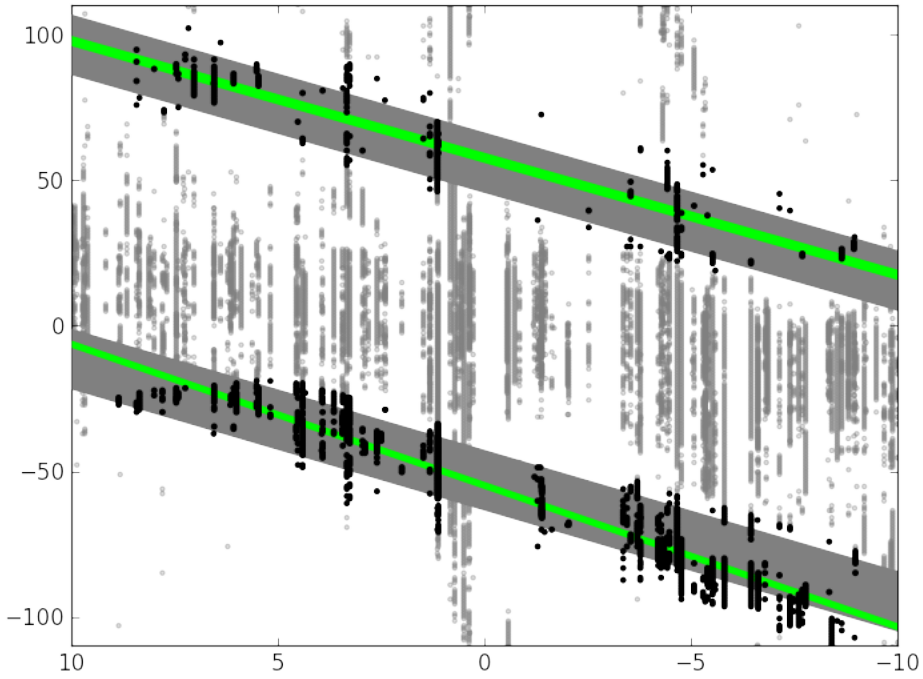

Figure 4.3: Velocity channels of significant H I absorption: those included in the tracing of the 3kpc Arms are shown in black, while those channels which were excluded from the analysis are in grey. The fits of Dame & Thaddeus (2008) are given by the grey bands (see Figure 4.1), the fits from this analysis are displayed in green.

4.5.1.1 The Longitude-Velocity Location of the 3kpc Arms

The locus of each of the 3kpc Arms, as traced by H I absorption, in lv space was also investigated. Dame & Thaddeus (2008) provide lv fits to the Near and Far 3kpc Arms and report a velocity dispersion of 21 km s^{-1} for both Arms. However they excluded large regions of longitude, within $|l| < 10^o$, from the computation of the physical properties of each arm.

In order to investigate the locus of each Arm in lv space, a subset of absorption channels were selected for analysis (see Figure 4.3). We included all channels within $1^o < |l| < 9^o$ (between $9^o < |l| < 10^o$ there is ambiguity between the 3kpc Arms and the circular rotation velocities and for $|l| < 1^o$ there is ambiguity with the Tilted Disk), which had velocities outside the envelope of allowed circular-rotation velocities (i.e. $V_{circular-rotation} < |V| < 110$km s^{-1}) and were not associated with either of Bania's Clumps. Linear least-squares fits to these appear as Equations 4.1 and 4.2 for the Near and Far arms respectively.

$$V_{N3kpc} = -59.2 + 4.12l \pm 8.67 \qquad \text{km s}^{-1} \tag{4.1}$$

$$V_{F3kpc} = +57.7 + 4.02l \pm 15.61 \qquad \text{km s}^{-1} \tag{4.2}$$

In both cases, the linear fits ($\pm$ velocity dispersion) of the structure as given by H I absorption are consistent with the Dame & Thaddeus (2008) fits from CO emission (see Figure 4.3).

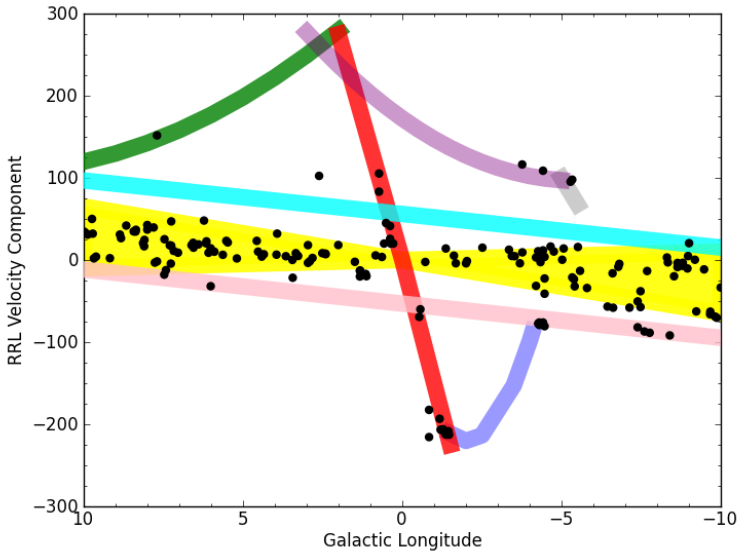

Figure 4.4: Longitude-velocity 'crayon' diagram (see Figure 4.1) showing the distribution of H II region RRL velocity components.

4.6 Longitude-Velocity Distribution of H II Regions Toward the Extreme Inner Galaxy

H II regions provide radio continuum sources to measure H I absorption toward, but they also provide a secondary tracer of the EIG region - their own systemic velocities.

The *lv* distribution of known H II regions has previously been investigated by Anderson et al. (2012a), however all H II regions with highly non-circular motions (i.e. those of interest to this work) were excluded from their analysis. The *lv* distribution of H II region RRL velocity components used in this work is shown in Figure 4.4 - note: for H II regions with multiple velocity components, all are shown.

Just as the distribution of H I absorption was closely associated with known *lv* features in the EIG region (§4.5, Figure 4.2), the systemic velocities of H II regions also trace these structures.

The circular-rotation allowed velocities (yellow envelope in 'crayon plots') account for $\sim$ 85% of the H II region RRL velocity components. Green & McClure-Griffiths (2011), in a study of 6.7 GHz methanol masers near the EIG, find the same velocity range accounts for $\sim$ 79% of their sample. However, only $\sim$ 10% of H II regions with a single RRL velocity component are associated with EIG features. A list of H II regions with RRL velocities associated with an EIG structure appears in Table 4.3.

4.6.1 H II Regions Associated with $R_{Gal} \lesssim 4$

Until recently, it was believed that there are no known H II regions inside of the 3kpc Arms, except in the Tilted Disk (Rodríguez-Fernández 2006). Green & McClure-Griffiths (2011) found no significant 6.7 GHz methanol maser emission towards the +135km s^{-1} Expanding Arm, nor the Connecting Arm; suggesting that the features are primarily associated with gas

that is not undergoing high-mass star formation. This result is in-keeping with observations of other early-type barred galaxies which show star formation in the central nuclear region and at the ends of the bar, but not in the dust lanes along the bar (Rodriguez-Fernandez et al. 2006).

Using the collated H II region catalog of Paladini et al. (2003), Rodriguez-Fernandez et al. (2006) found no H II regions associated with structures outside the Nuclear Disk within $|l| < 2^o$. The GBTHRDS recorded RRL velocity components from 21 previously unknown H II regions within $|l| < 2^o$, many (especially in Quadrant IV) with non-circular velocities - these H II regions are included in the target list of this work. However, as the Rodriguez-Fernandez et al. (2006) study found, these new H II regions are associated (in lv space) with the Nuclear Disk and Looping Ridge intersection. Rodriguez-Fernandez et al. (2006) then investigated a wider longitude range, but could not identify any dust lane associated H II regions. It should be noted that Rodriguez-Fernandez et al. (2006) did not rule out the possibility of undetected ultra-compact H II regions in the dust lanes.

One diffuse H II region, G007.700-0.079 identified by Lockman et al. (1996) (but not included in the Paladini et al. (2003) catalog used in the Rodriguez-Fernandez et al. (2006) study) appears to have one of its RRL velocity components associated with the Connecting Arm. Two 6.7 GHz methanol masers, tracers of current high-mass star formation, are detected in the same part of lv space (see Figure 1 of Green & McClure-Griffiths 2011). In addition, there are four H II region RRL velocity components associated with the $+135\text{kms}^{-1}$ Expanding Arm and/or Bania's Clump 1 (at $l, v =\sim -4^o, \sim 100$ km s^{-1}), as well as two 6.7 GHz methanol masers from the Methanol Multibeam survey (cited in Green & McClure-Griffiths 2011), however only two of these regions have single RRL velocity components (multi-RRL component H II regions are probably the result of blending multiple emission sources along the line of sight). Therefore there is evidence of some recent star formation in these structures.

The other H II region of note is G002.611+0.135 as it is the only H II region that distinctly lies outside the "crayon" lines that delineate EIG structures in Figure 4.2. Rodriguez-Fernandez et al. (2006) suggest that G002.611+0.135 could be associated with either their structure 'J' or Bania's Clump 2 (see Figure 4 of Rodriguez-Fernandez et al. 2006). The latitude of the H II region suggests a stronger association with Clump 2.

4.6.2 H II Regions Associated with the 3kpc Arms

Only recently have significant star formation (Green et al. 2009) and large numbers of H II regions (Bania et al. 2010) in the 3kpc Arms been detected. In emission from molecular clouds the signatures of the 3kpc Arms are clearly seen (Bania 1980), but the GBTHRDS was unable to discover many new H II regions, in either of the Arms. However, both arms host high-mass star formation as traced by about fifty 6.7 GHz methanol masers (Green et al. 2009).

The certainty of associating H II regions with the 3kpc Arms (in lv space) is best in the longitude range of this study ($|l| < 10^o$), as outside this limit the expected velocities of the 3kpc Arms overlap with circular-motion spiral arm models and the association becomes more ambiguous (Green et al. 2009).

Inside $|l| < 10^o$ there are eleven H II region RRL velocity components consistent with

the Near 3kpc Arm and two consistent with the Far 3kpc Arm. This small number of RRL components does not allow for a repetition of the analysis of §4.5.1.1 using H II region RRL components rather than H I absorption.

4.7 Distance Constraints for H II Regions from H I Absorption

The analysis of an H I absorption spectrum towards a H II region can constrain the line of sight distance to the H II itself.

Due to the lack of a reliable rotation model for the inner ∼3kpc of the Milky Way, kinematic distances to objects near, or in, the EIG are the most difficult to ascertain. However, it should be possible to provide distance constraints for H II regions with allowed circular rotation systemic velocities, using H I absorption associated with EIG features as approximate distance indicators.

In the Inner Galaxy, inside the Solar Circle, each velocity corresponds to two degenerate solutions for the kinematic distance - each equidistant from the tangent (subcentral) point. This kinematic distance ambiguity can be resolved in cases where H I absorption is present at the velocity of a known structure - which indicates the H II region must be located behind the absorbing gas.

The distance arrangement of EIG features, listed in §4.4.1, from the literature is assumed to be: Near 3kpc Arm, Connecting Arm, Tilted Disk, Looping Ridge, +135km s^{-1} Expanding Arm (and Bania's Clump 1), Far 3kpc Arm (however not all structures are expected along any single line of sight, see Figure 4.1).

Therefore, if H I absorption is seen at velocities corresponding to a particular feature, the H II region must lie in, or beyond that structure. In this way, we use H I absorption to indicate the *lower limit* of the line of sight distance, D_{los}. The RRL velocity of an H II region also hints at its location, Table 4.3 lists those H II regions with systemic velocities beyond the range expected by circular rotation (see Figure 4.4) and associated with EIG feature(s).

A discussion of each H II region appears in Appendix B.

4.7.1 Kinematic Distances of Selected H II Regions

For H II regions with systemic velocities associated with normal circular disk rotation (i.e. in the yellow envelope in Figure 4.4, $R_{Gal} > 4$kpc), a Kinematic Distance Ambiguity Resolution (KDAR) is attempted. If a KDAR is achieved, the kinematic distance to the H II region can then be calculated.

KDARs were achieved following these rules:

- if the H II region RRL is consistent with normal circular disk rotation, and not with any EIG feature (see Table 4.3) (i.e. no kinematic distances are calculated for regions with $R_{Gal} < 3$kpc).
- FAR: If the H I absorption spectrum displays sufficient absorption associated with EIG features, then the H II region must be located at the 'far' kinematic location - i.e. beyond the tangent point along the line of sight.

H II Region		V_{RRL}	Ref.	Association
Single RRL Velocity Component H II *Regions*				
G350.996 − 00.557		+20.5	2	Far 3kpc Arm
G351.601 − 00.348		−91.8	3	Near 3kpc Arm
G352.233 − 00.151		−88.6	1	Near 3kpc Arm
G352.398 − 00.057		−87.0	2	Near 3kpc Arm
G352.611 − 00.172		−81.9	2	Near 3kpc Arm
G354.665 + 00.247		+97.8	2	Bania's Clump 1?
G354.717 + 00.293		+95.3	1	Bania's Clump 1?
G355.700 − 00.100		−76.1	2	Near 3kpc Arm
G356.235 + 00.642		+116.3	2	+135km s^{-1} Arm
G358.530 + 00.056		−212.6	1	Looping Ridge
G358.552 − 00.025		−208.5	1	Looping Ridge
G358.616 − 00.076		−212.6	1	Looping Ridge
G358.623 − 00.066		−212.0	3	Looping Ridge
G358.652 − 00.078		−211.2	1	Looping Ridge
G358.680 − 00.087		−208.3	1	Looping Ridge
G358.694 − 00.075		−207.8	1	Looping Ridge
G358.720 + 00.011		−206.1	1	Looping Ridge
G358.797 + 00.058		−206.6	2	Looping Ridge
G358.827 + 00.085		−193.3	1	Looping Ridge
G359.432 − 00.086		−60.0	3	Near 3kpc Arm
G359.467 − 00.172		−69.3	1	*blended EIG features*
G000.510 − 00.051		+45.0	4	Far 3kpc Arm
G003.439 − 00.349		−21.6	1	Near 3kpc Arm?
G007.472 + 00.060		−17.8	2	Near 3kpc Arm
Multiple RRL Velocity Component H II *Regions*				
G355.532 − 00.100	a	+3.8	1	-
G355.532 − 00.100	b	−22.5	1	-
G355.532 − 00.100	c	−82.6	1	Near 3kpc Arm
G355.532 − 00.100	d	−41.1	1	-
G355.581 + 00.028	a	108.7	1	+135km s^{-1} Arm
G355.581 + 00.028	b	−76.1	1	Near 3kpc Arm
G355.581 + 00.028	c	11.7	1	-
G355.696 + 00.350	a	+3.0	1	-
G355.696 + 00.350	b	−79.1	1	Near 3kpc Arm
G355.734 + 00.138	a	+10.7	1	-
G355.734 + 00.138	b	−77.4	1	Near 3kpc Arm
G359.159 − 00.038	a	−182.5	1	*blended EIG features*
G359.159 − 00.038	b	−215.6	1	*blended EIG features*
G000.729 − 00.123	a	+105.3	1	Tilted Disk
G000.729 − 00.123	b	+83.2	1	-
G006.014 − 00.364	a	+14.2	1	-
G006.014 − 00.364	b	−31.9	1	Near 3kpc Arm
G007.700 − 00.079	a	−1.7	5	-
G007.700 − 00.079	b	+151.7	5	Connecting Arm

Table 4.3: H II Regions with an RRL velocity associated (in lv space) with known EIG structure(/s) - see Figure 4.4. References for V_{RRL} are as follows: 1 - GBTHRDS (2011), 2 - Lockman (1989), 3 - Caswell & Haynes (1987) and 4 - Downes et al. (1980), 5 - Lockman et al. (1996).

  - if $|V_{RRL}| < 10$km s^{-1} a KDAR is attempted *only* if the H I absorption spectrum displays absorption associated with the Far 3kpc Arm, this is imposed in order to avoid confusion with EIG features at small velocities.
  - Quality 'A' far side KDARs were awarded to H II regions with statistically significant absorption in EIG features including at least the Near and Far 3kpc Arms.
  - Quality 'B' far side KDARs were awarded to H II regions with statistically significant absorption in any EIG feature located on the far side of the GC.
  - Quality 'C' far side KDARs were awarded to H II regions with large uncertainties ($> 50\%$) in their calculated D_{los} value (see §4.7.1.1).

- NEAR: If the H I absorption spectrum displays no absorption associated with any EIG features, then it must be located at the 'near' kinematic location. Here we assume that all the EIG features are detectable within the latitude range of the target H II regions ($|b| < 1.5^o$). Note that the linear scale heights of the Near and Far 3kpc Arms are ~ 103 pc FWHM (Dame & Thaddeus 2008); assuming that the Far 3kpc Arm is at a uniform line of sight distance of 11.5kpc, this scale height corresponds to a latitude range $|b| \lesssim 0.5^o$. As a result, if an H I absorption spectrum towards an H II region located at $|b| > 0.5^o$ displays no absorption associated with any EIG feature, it is awarded a Near KDAR, of Quality 'C'.
  - KDARs of Quality 'A' were given to all near side H II regions, unless
  - the calculated D_{los} value had large uncertainties ($> 50\%$), then a Quality 'C' KDAR was given.

- No KDAR was attempted for H II regions with multiple RRL velocity components, as multiple systemic velocities suggest several ionisation sources along the line of sight. Note: multi-RRL velocity component H II regions account for less than 10% of the H II regions within $|l| < 10^o$, compared with 30% for the Galactic plane in general (GBTHRDS).

H II regions with calculated kinematic distances are listed in Table 4.4.

Four H II regions (G350.177+00.017, G350.330+00.157, G353.557-00.014 and G003.949-00.100) were deemed to lie at the far kinematic location, beyond the EIG, following the rules above. However, these four regions have $R_{Gal} < 3$kpc, i.e. they are outside the bounds of the McClure-Griffiths & Dickey (2007) rotation model and are therefore not included in Table 4.4.

If an H II region is awarded a far side KDAR, based on the above requirements, a kinematic distance can be calculated using a Galactic rotation curve model (which assumes circular rotation). The IAU Galactic Constants have been applied in these calculations: $R_0 = 8.5$ kpc and $\Theta_0 = 220$km s^{-1}.

If an H II region must be located at least as far as the subcentral point, then its location inside, or beyond, the Solar circle is given by its systemic velocity. In the Inner Galaxy, velocities are positive in the first quadrant and negative in the fourth. The signs are reversed

H II Region	V_{RRL}	Ref.	Q	R_{Gal}	D_{los}
KDAR: Far - within rotation model boundaries					
G350.813 − 00.019	+0.3	3	B	8.6	16.9 ±4.2
G351.028 + 00.155	+4.8	1	A	9.7	18.0 ±5.9
G351.358 + 00.666	−3.6	3	B	8.2	16.5 ±3.6
G352.313 − 00.440	−13.4	1	A	5.9	14.3 ±2.6
G354.486 + 00.085	+15.8	3	C	8.8	23.3 ±*
G354.610 + 00.484	−23.4	1	A	3.9	12.3 ±2.2
G354.934 + 00.327	+14	4	C	14.6	23.1 ±*
G355.242 + 00.096	+10.3	3	C	13.3	21.7 ±*
G355.344 + 00.145	+16.4	1	C	16.8	24.8 ±*
G000.640 + 00.623	+3.7	2	C	3.3	11.8 ±*
G000.838 + 00.189	+5.6	1	C	3.0	11.5 ±*
G003.270 − 00.101	+4.9	3	C	6.3	14.7 ±*
G003.342 − 00.079	+8.3	3	A	5.2	13.6 ±6.7
G004.412 + 00.118	+4.1	3	C	7.1	15.6 ±8.9
G004.527 − 00.136	+10.2	1	A	5.4	13.8 ±3.9
G005.479 − 00.241	+21.4	3	A	4.1	12.5 ±2.3
G005.524 + 00.033	+23.3	1	A	4.0	12.3 ±2.2
G006.083 − 00.117	+8.8	3	A	6.3	14.7 ±3.5
G006.553 − 00.095	+15	3	A	5.3	13.7 ±2.5
G006.565 − 00.297	+20.9	3	B	4.6	12.9 ±2.2
G007.041 + 00.176	+8.9	1	A	6.6	14.9 ±3.1
G007.420 + 00.366	−12.3	1	C	12.2	20.6 ±*
G008.006 − 00.156	+42.6	3	A	3.4	11.6 ±1.9
G008.432 − 00.276	+34.8	1	A	4.0	12.2 ±2.0
KDAR: Near					
G351.192 + 00.708	−3.4	3	C	8.2	0.3±*
G353.186 + 00.887	−4.7	3	C	7.6	0.9±*
G359.277 − 00.264	−2.4	5	C	4.5	4.0±*
G005.889 − 00.427	+10.1	3	C	6.0	2.5±*
G008.137 + 00.228	+20.6	3	C	5.1	3.5±2.2
G008.666 − 00.351	+49.1	3	A	4.7	3.9±1.4
G008.830 − 00.715	+26.6	1	C	4.7	3.9±2.0

Table 4.4: H II regions with calculated kinematic distances (in kpc). References for the RRL velocities are as follows: 1) GBTHRDS (2011), 2) Lockman et al. (1996), 3) Lockman (1989), 4) Caswell & Haynes (1987), 5) Wink et al. (1982). Errors in kinematic distances marked with asterisks (*) denote errors which are > 100%; note that while these errors are large, the significance of the KDAR remains.

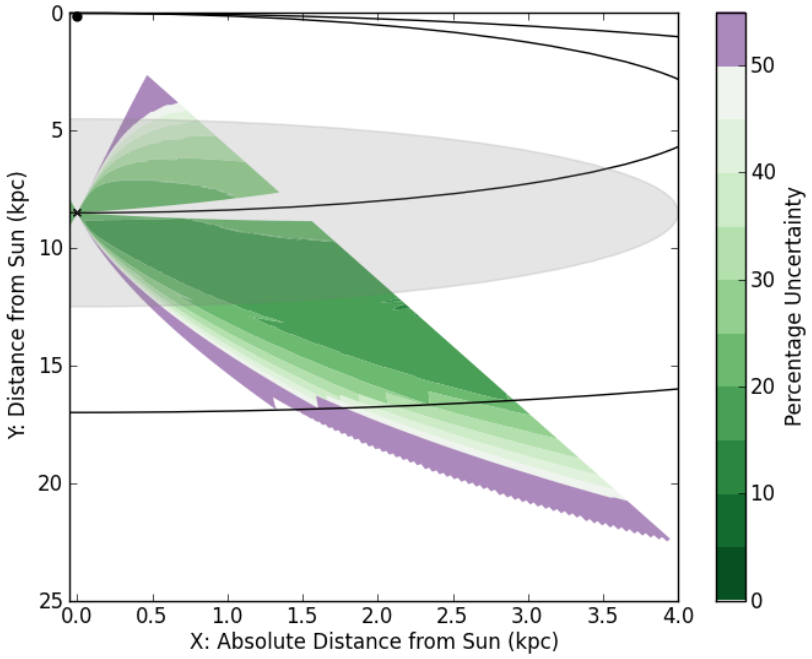

Figure 4.5: Total percentage uncertainty in the line of sight distance D_{los} caused by the choice of rotation curve, non-circular streaming motions of 15 km s^{-1} and by changing the Solar circular rotation speed to Θ_o = 255 km s^{-1}. Blank areas are indicative of $|l| > 10^o$ (where no error analysis was carried out), or percentage uncertainties > 100%. The EIG is shaded grey (no kinematic distances were calculated for this region), and the Solar Circle and Locus of Tangent Points appear as the black circles. The percentage uncertainties are mirrored for lines of sight in the fourth quadrant, here, only $l > 0$ is shown for clarity.

in the Outer Galaxy, such that first quadrant sources located beyond the Solar circle will have negative velocities, and fourth quadrant sources in the Outer Galaxy will have positive velocities.

Throughout this work, the rotation curve of McClure-Griffiths & Dickey (2007) is used for regions within the Solar Circle. In the outer Galaxy, D_{los} was calculated using a flat rotation model $\Theta_{R_{Gal}} = \Theta_0$.

4.7.1.1 Kinematic Distance Uncertainties

We follow the distance uncertainty analysis method of Anderson et al. (2012a), investigating the effects of the choice of rotation curve, streaming motions and Solar rotation speed on kinematic distance calculations. We compare all sources of uncertainty to the distances calculated from the rotation model of McClure-Griffiths & Dickey (2007).

Firstly we compute, for a grid of (l, v) positions, the kinematic distance using the rotation curves of McClure-Griffiths & Dickey (2007); Brand & Blitz (1993) and Clemens (1985). The standard deviation of these distances for each (l, v) is then computed and divided by the McClure-Griffiths & Dickey (2007) distance to obtain the percentage uncertainty due to choice of rotation curve. We assessed a grid of $|l| < 10^o$ and $|v| < 200$km s^{-1} with steps of 0.1 in each unit.

This procedure is then repeated, but instead of varying the Galactic rotation model, the percentage uncertainty due to streaming motions (of 15 km s^{-1}) and an altered circular Solar

rotation speed of 255 km s^{-1} (Reid et al. 2009) are investigated.

The effect of these three sources of error are then added in quadrature for each (l, v) pair, before transformation onto a face-on plot (Figure 4.5).

It should be noted that kinematic distance errors at small Galactic longitudes are intrinsically larger than for other sections of the Galaxy. Equal steps in velocity map to unequal length steps in D_{los}, such that $dD_{los}/dv \propto \sin^{-1} l$. This can be seen in Figure 4.5 where the percentage uncertainty is higher for smaller longitudes.

Uncertainties due to Rotation Curve In addition to larger uncertainties at small longitudes due to the velocity gradient, errors are also larger in the Outer Galaxy due to the uncertainty in the outer Galaxy circular rotation models. Flat, rising and falling rotation curves have been suggested for beyond the Solar circle Brand & Blitz (1993); Honma et al. (2007); Hachisuka et al. (2009). Here we have used the rotation models of McClure-Griffiths & Dickey (2007); Brand & Blitz (1993) and Clemens (1985). Note that the McClure-Griffiths & Dickey (2007) model has an applicable Galactocentric range of $3 \leq R_{Gal} \leq 8$ kpc. As a result the model was extrapolated to the Solar circle, and a flat rotation curve was assumed for $R_{Gal} > R_o$. The largest discrepancy between these three models occurs at $R_{Gal} \sim 10$ kpc, but even at $R_{Gal} < Ro$ the models differ significantly.

Uncertainties due to Non-Circular, Streaming Motions Large non-circular motions have precluded Galactic astronomers from fitting a rotation curve to the EIG. Smaller-scale non-circular motions are ubiquitous in the Galaxy and are the result of systematic velocity fields within a source, or ordered large-scale Galactic streaming motions Anderson et al. (2012a). Bania & Lockman (1984) suggest an uncertainty, due to non-circular motions, of 5 to 10km s^{-1}; whereas Kolpak et al. (2003) assign an estimate of cloud-cloud dispersion of 5 km s^{-1} in addition to contributions from Galactic scale streaming motions of 10 km s^{-1}. Dickey et al. (2003) and Jones & Dickey (2012) find H I absorption components extending to 10-20 km s^{-1} from the systemic velocity of H II regions.

In order to promote a conservative approach to kinematic distance uncertainties, the random uncertainty due to non-circular motions is set to 15 km s^{-1}. The contribution of errors due to streaming motions in relation to the total uncertainty in kinematic distance is high, especially for small longitudes. The errors due to non-circular motions are the standard deviation of the three (l, v) grids,(l, v), $(l, v + 15)$, $(l, v - 15)$ divided by the (l, v) distance, all computed with the McClure-Griffiths & Dickey (2007) rotation model.

Uncertainties due to Solar Rotation Parameters The IAU values for $R_o = 8.5$ kpc and $\Theta_o = 220$km s^{-1} have been used throughout this work. However, here we investigate the significance of an altered Solar rotation speed, as suggested by Reid et al. (2009). Two (l, v) grids were computed with the rotation model of McClure-Griffiths & Dickey (2007), using $\Theta_o = 220, 250$ km s^{-1}. The standard deviation of these two grids, at each locus, was then divided by the standard velocity (i.e. $\Theta_o = 220$ km s^{-1}) to compute the percentage uncertainty due to choice of Solar rotation parameters. Note that the Reid et al. (2009) value for $R_o = 8.4 \pm 0.6$ kpc is consistent with the IAU value, and is therefore not investigated

here.

4.7.2 Galactic Distribution of H II Regions

In order to examine the large-scale structure of the Galaxy, H II regions with successfully calculated kinematic distances were transformed into a face-on map of the Milky Way (left panel of Figure 4.6) and also superimposed onto an artist's conception of the Galaxy (right panel). The background image used in the right panel of Figure 4.6, was created using stellar, H I and CO data (Benjamin et al. 2003) and was reviewed in Urquhart et al. (2012).

In addition, the kinematic distances from Jones & Dickey (2012) are also displayed. Figure 4.6 demonstrates the need for H II region discovery and KDAR studies for Galactic longitudes $340^o < l < 350^o$ in order to further investigate the end of the bar and differentiate the Norma and Near 3kpc Arms, as well as the Sagittarius and Perseus Arms on the far side of the locus of subcentral points (smaller circle in Figure 4.6). At the end of the bar in the first quadrant, H II region KDARs have been made by Anderson & Bania (2009) and Bania et al. (2012) - further encouragement for a fourth quadrant study.

Recently, Dame & Thaddeus (2011) identified an extension of the Scutum-Centaurus Arm at extreme distances from the Sun, in the first Galactic quadrant. However, confirmation of this discovery requires tracing the Arm over its entire longitude range. Dame & Thaddeus (2011) comment that molecular gas which constitutes the section of Scutum-Centaurus Arm behind the Galactic center will be the most difficult to deconvolve. In the longitude range of this Chapter, H II regions with systemic velocities opposite in sign to circular-disk rotation must be located in the EIG or beyond the Solar circle. Using H I absorption features to resolve this ambiguity has allowed for seven H II regions to be unequivocally placed in the outer Galaxy. Several of these outer Galaxy regions (see Figure 4.6) appear to trace the Scutum-Centaurus arm.

4.8 Summary

The EIG remains a difficult section of the Milky Way to study. In terms of Galactic structure, kinematic studies in this region are hampered by a lack of rotation model for $R_{Gal} < 4$kpc (and for the outer Galaxy). In addition, there remains a lack of consensus regarding the number, locations and nomenclature of large-scale structures near the Galactic Centre (these are discussed in Section 4.4.1). Despite this, H I absorption associated with EIG features was successfully used as a distance indicator, allowing for constraints on the line of sight distance for over 80% of the sample of H II regions investigated, or over 60% of all known H II regions with systemic velocities in $|l| < 10^o$.

Over 67% of the H II regions demonstrate H I absorption associated with the Near 3kpc Arm (see Table 4.2) and therefore must be located at line of sight distances of at least $\sim$ 5kpc. A further 16 H II regions show absorption associated with EIG features assumed to lie further along the line of sight than the Near 3kpc Arm, therefore, over 78% of the sample H II regions are located at $D_{los} \gtrsim 5$kpc. This is in keeping with the work of Lang et al. (2010) who find $\sim$ 90% of their sample of 40 EIG continuum sources must be located at least as far as the Near 3kpc Arm.

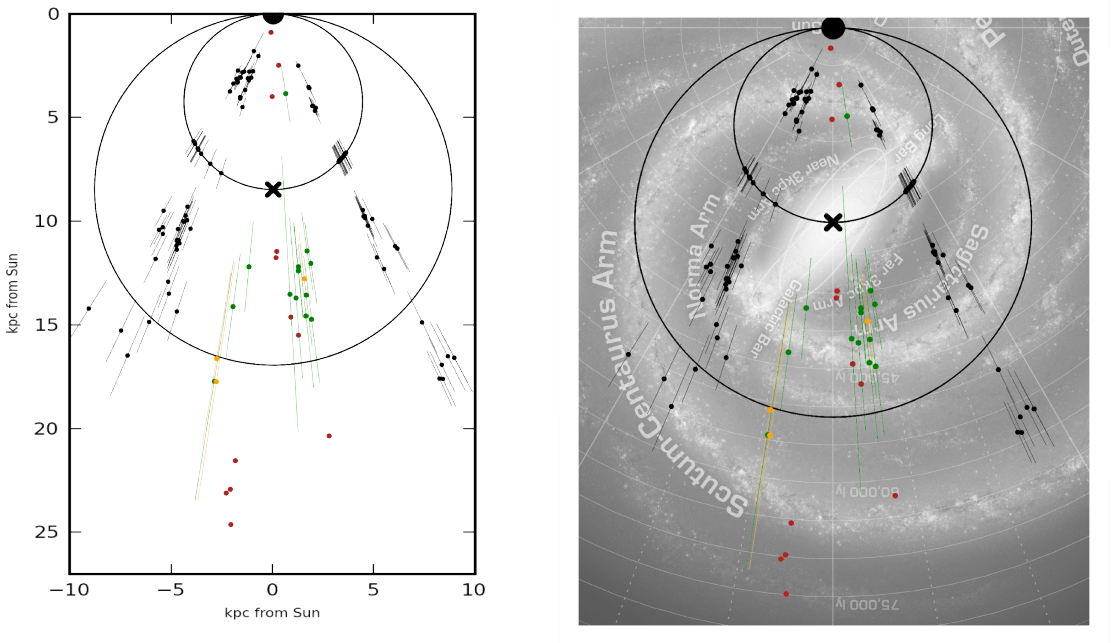

Figure 4.6: Positions of the H II region complexes for which a kinematic distance was calculated (Quality A, B and C shown as green, orange and red markers respectively). Also shown are the Solar Circle and locus of tangent points (black circles) and kinematic distances for H II regions from Jones & Dickey (2012) (black markers). Error bars are calculated according to the analysis of §4.7.1.1; the large uncertainties are not shown for quality C distances. Background image credit [right panel]: Hurt & Benjamin in Churchwell et al. (2009).

Of the 151 H II regions investigated, 54 H II regions display absorption from EIG features assumed to be on the far side of the GC (the +135km s^{-1} Expanding Arm, Bania's Clump 1 or Far 3kpc Arm). Consequently, these H II regions must be located at $D_{los} \gtrsim 8.5$kpc.

After successfully resolving the near/far kinematic distance ambiguity, line of sight distances were calculated for 31 H II regions. These distances suggest locations for the H II regions in known Galactic structures including the Norma, Sagittarius and Perseus spiral Arms (see Figure 4.6). The 7 H II regions beyond the Solar Circle are among the most distant Galactic H II regions known to exist and could be crucial to tracing the Scutum-Centaurus Arm; where identification of star formation with molecular tracers is extremely difficult (Dame & Thaddeus 2011). Errors on these line of sight distances are often large - due to the uncertainty of non-circular streaming motions, and differences in Galactic rotation models - but the near/far KDAR remains both valid and significant.

Using a summary of EIG structures, and the known lv distribution of CO, we construct a 'crayon diagram' with which to investigate the distribution of H I absorption in the EIG (Figure 4.1, Section 4.4). In Section 4.5 we find cold H I clouds, signified by H I absorption, associated with the Near 3kpc Arm, Connecting Arm, Bania's Clump 1, Tilted Disk and Far 3kpc Arm. There was minimal H I absorption associated with either the Looping Ridge or the +135km s^{-1} Expanding Arm. The large amount of H I absorption associated with each of the 3kpc Arms presented an opportunity to fit a model to the lv locus of each Arm (§4.5.1). We find a linear fit (in lv space) that is consistent with the findings of Dame & Thaddeus

(2008), who used CO to trace the Arms.

The lv distribution of the RRL velocities of the 151 H II regions was investigated in Section 4.6. Like the H I absorption distribution, the systemic velocities of the H II regions trace Galactic structures including spiral arms, features located near the Galactic center and possibly the end of the bar. While most H II regions posses RRL velocity components allowed by circular Galactic rotation (suggestive of a location outside the EIG), smaller numbers of H II regions are found to be associated with the H I Tilted Disk, Near 3kpc Arm, +135km s^{-1} Expanding Arm, Bania's Clump 1, Connecting Arm and Far 3kpc Arm. Using the RRL velocity and H I absorption spectrum of each H II region, we were also able to constrain the D_{los} for a further sample of H II regions using only EIG features as a distance indicator.

Chapter 5

A Complete Atlas of H I Absorption toward H II Regions in the Southern Galactic Plane Survey (SGPS I)

This Chapter includes a co-authored paper.
The bibliographic details of the paper, including all authors are: C. Brown, J.M. Dickey, J.R. Dawson and N.M McClure-Griffiths; Astrophysical Journal, 10.1088/0067-0049/211/2/29. The published paper is referenced by this thesis as Brown et al. (2014).

The introductory and methodology sections have been adapted to avoid unnecessary duplication - see Chapters 1 and 2. Figure Set 4, of the published work, is included in Appendix C.

Abstract

We present a complete catalog of H I emission and absorption spectrum pairs, toward H II regions, detectable within the boundaries of the Southern Galactic Plane Survey (SGPS I), a total of 252 regions. The catalog is presented in graphical, numerical and summary formats. We demonstrate an application of this new dataset through an investigation of the locus of the Near 3kpc Arm.

5.1 Introduction

Combining data from the Australia Telescope Compact Array (ATCA) and the Parkes single dish telescopes, the SGPS (SGPS, McClure-Griffiths et al. 2005) provides H I line and 1.4 GHz radio continuum data for the fourth Galactic quadrant, with the best combination of resolution and sensitivity currently available for that line in this area. Using these data, we have measured 21-cm absorption spectra toward a sample of 252 H II regions.

This study produces two distinct data products: a consolidated census of H II regions with known radio recombination line (RRL) velocities, taken from the literature; as well as the H I emission and absorption spectrum pairs towards them - within the bounds of the

SGPS ($255° < l < 353°$). These two resources will enable further study into the structure and dynamics of the neutral interstellar medium (ISM) in the fourth quadrant (on which massive stars and their formation have a significant impact). The catalogs will serve as a data set for numerous studies; including investigations of the spiral structure of the Galaxy (eg. Strasser et al. 2007) and kinematic distance works, both for target regions (eg. Urquhart et al. 2012) as well as for the intervening H I clouds (eg. Roman-Duval et al. 2009).

The sample selection from existing H II region catalogs is described in Section 5.2, while the method of spectrum extraction appears in Section 1.5. The catalog itself appears in Section 5.4, before a discussion of the global properties of H I absorption in Section 5.5 and an illustration of its use: an examination of the distribution of H I absorption in longitude-velocity (lv) space, including the locus of the Near 3kpc Arm.

5.2 Data

In order to avoid repetition, descriptions of the SGPS I and individual H II region RRL catalogs can be found in Chapter 2. The specific details of source selection for this Chapter are discussed below.

5.2.1 H II Regions

Firstly we compiled a list of H II regions from RRL catalogs for the longitude and latitude range of the SGPS. This compilation of H II regions was then over-plotted on the SGPS radio continuum maps using the KARMA software suite (Gooch 1996). Each map was then visually inspected to confirm H II region detection. Target H II regions were included in this catalog (§5.4) if a *single, distinct* emission source was visible in the SGPS continuum map.

Several cataloged H II regions were coincident with multiple radio continuum sources and some targets had coordinates coincident with no continuum source. It is not surprising that the SGPS with angular resolution of $\sim 2'$ detects multiple sources within the larger beam of the early H II region discovery surveys, for instance the Parkes beam of Caswell & Haynes (1987) is $\sim 4'$. Furthermore, there are often clusters of continuum emission sources surrounding a cataloged region's coordinates, such that no successful attempt can be made to distinguish the background emission. Several H II regions are included in more than one H II region RRL velocity catalog (§5.2.1.1) and therefore become duplicate sources when the catalogs are combined. Furthermore, H II regions that did not appear as continuum sources in the SGPS, or had continuum temperatures $T_{\rm cont} < 5$K, were not included in this catalog.

The total number of individual, distinct H II regions, visible in the SGPS continuum is 252. Throughout this work, the name (in form "G longitude ±latitude") reported for each H II region is taken from the catalog from which the region is provided (see §5.2.1.1), hence the inconsistencies in decimal precision.

5.2.1.1 H II Region Catalogs

We use the catalog of Caswell & Haynes (1987) as the basis of our target list, supplementing that catalog with further H II regions sourced from other works. Our final source list is a

compilation of the H II region RRL velocity catalogs of Caswell & Haynes (1987), the Green Bank Telescope H II Region Discovery Survey (Bania et al. 2010), Lockman (1989) and Wilson et al. (1970) (see Table 5.2). We describe each of these works below.

Several other fourth quadrant studies include H II region candidates (Reifenstein et al. 1970; Walsh et al. 1999; Busfield et al. 2006; Urquhart et al. 2012; Foster et al. 2011), but as Hnα emission has not been detected towards these candidates, they are not confirmed H II regions and are therefore excluded from this work.

5.3 Emission/Absorption Method of H I Absorption Spectrum Extraction

In order to avoid duplication, the spectrum extraction method, and the SGPS continuum temperature unit conversion factor, used throughout this thesis, are discussed in Chapters 1 and 2.

The quality assurance tests, which provide the quality factors for individual spectra in the Catalog (Table 5.2), are described below.

5.3.1 Quality of Spectra

As for most emission/absorption studies, the noise level in the absorption spectrum is not dictated by radiometer noise, but rather the precision with which the absorption spectrum can be subtracted from background continuum emission, see Equation 1.19 (Dickey et al. 2003).

A series of five tests were devised to measure the quality of each H I absorption spectrum (see Figure 5.1)—resulting in six quality categories A-F. The quality category for each spectrum included in the catalog is given in Table 5.2. Each spectrum was initially assumed to be at the best quality rating (i.e. category A); the quality factor was then down-graded for each test failed; therefore the spectra in category F failed all five quality tests listed below.

Range This test is designed to demonstrate if the range of calculated absorption values are realistic: theoretically $0 < e^{-\tau} < 1$. Continuum temperature uncertainties or uncertainties in the assumed background emission spectrum will increase the range of $e^{-\tau}$. This test is failed if Range($\exp[-\tau]$)> 1.5.

Maximum Signal to Maximum Noise 'Maximum signal' refers to $1 - min(\exp[-\tau])$ and 'maximum noise' refers to $max(\exp[-\tau]) - 1$, see Figure 5.1. This test is designed to ascertain if emission signals (which should have been removed) overwhelm absorption in the spectrum. This test is failed if (maximum signal/maximum noise)< 3.

Absorption Uncertainty Envelope This test investigates the fluctuations in the absorption envelope (caused by differences between the three emission, off source, spectra). The absorption uncertainty envelope is defined by Equation 1.20.

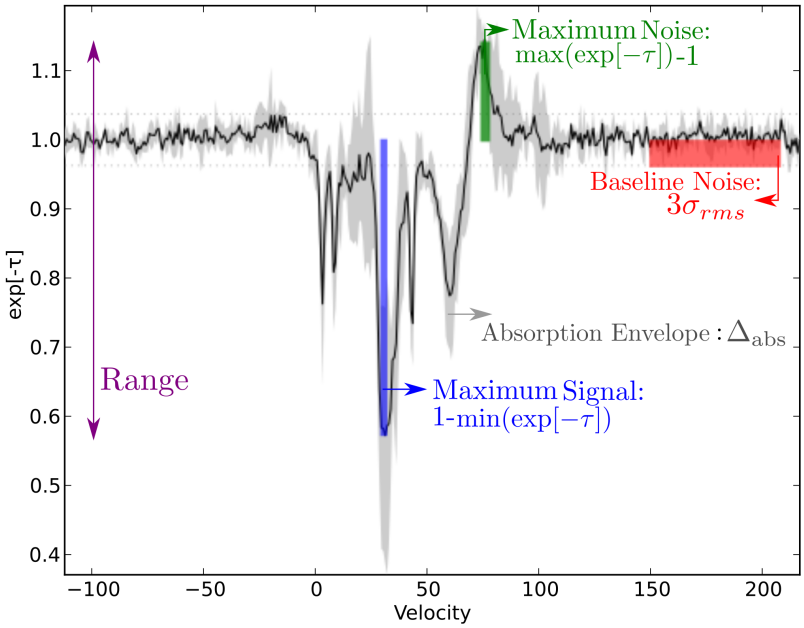

Figure 5.1: Sample absorption spectrum for G254.676+0.229, $e^{-\tau}$ is the solid black line, demonstrating the quality tests. The range (purple), maximum signal (blue) and maximum noise (green), baseline noise (red) and absorption fluctuation envelope (grey) are shown.

This test is failed if the standard deviation of this envelope, over the whole velocity range, is large: i.e. $3\sigma(\Delta_{\rm abs}) > 1$. The absorption uncertainty envelope is shown as grey shading in each H I absorption spectrum panel (see Figures 5.1 and 5.3), while $\pm 3\sigma_{T_{\rm off}}$ is shown as the grey shading in each H I emission spectrum panel (Figure 5.3).

Baseline Noise This test identifies absorption spectra with high levels of baseline noise. This is achieved by investigating the standard deviation of absorption ($\sigma_{\rm rms}$) over the same velocity channel range from which the continuum temperature is determined, i.e. there are no H I emission nor absorption signals. This test is failed if $3\sigma_{\rm rms} > 1$.

Number of Velocity Channels with Significant Absorption The final test is a count of the number of velocity channels with statistically significant absorption signals. That is, the absorption is deeper than a combination of the baseline noise and the absorption envelope uncertainty: $e^{-\tau}(v) < (1 - 3\sigma_{\rm rms} - \sigma(\Delta_{\rm abs}))$. At least 15 channels of statistically significant absorption are required to pass this test. Note that $\sigma(\Delta_{\rm abs}) \propto 3\sigma_{T_{\rm off}}$ (see Absorption Uncertainty Envelope test).

The majority of the poorest quality spectra (category F) come from target regions with $l > 340^\circ$ and were usually sourced from the H II region catalog of the GBTHRDS. This is not particularly surprising as the GBTHRDS avoided previously-observed H II regions; resulting in intrinsically fainter sources compared to Caswell & Haynes (1987).

The bottom panel of Figure 5.2 displays the number of regions in each quality category. The distribution appears to be superficially bimodal, such that the quality categories could be regrouped into 'good' and 'poor' umbrella categories associated with quality factors A-C

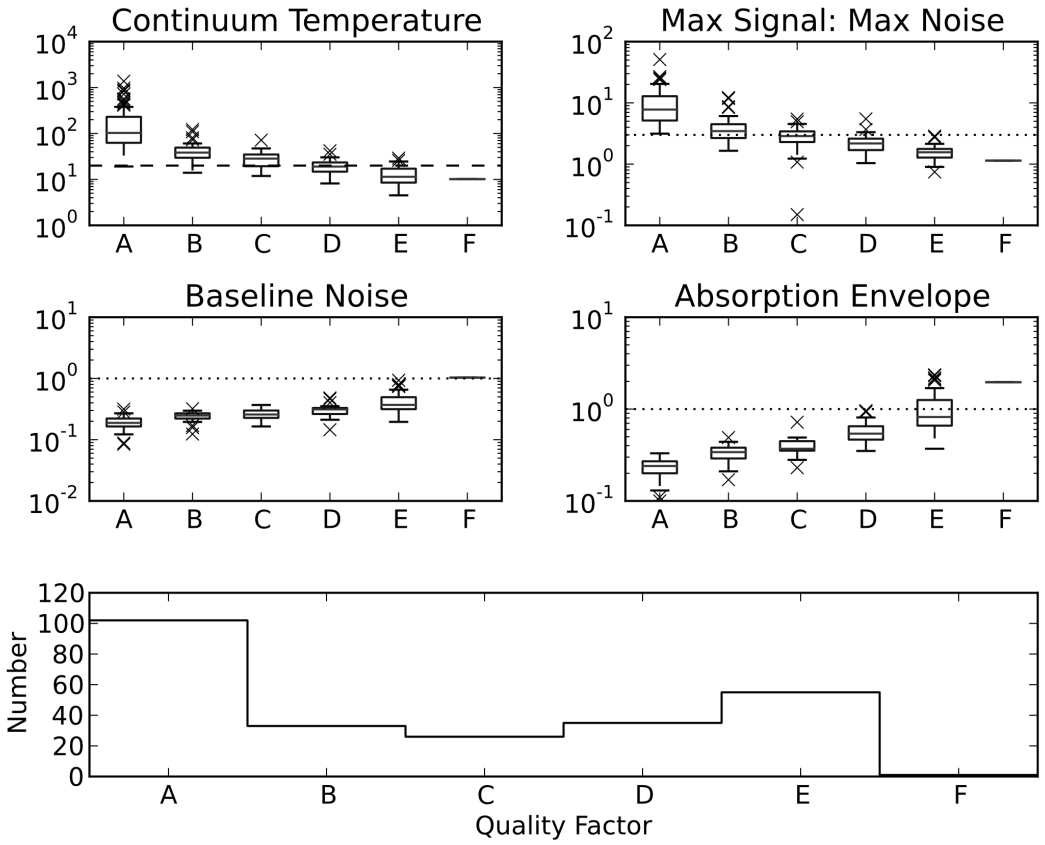

Figure 5.2: Assessment of the quality control variables for each H I absorption spectrum in categories A (best quality) to F (poorest quality). In each panel, the horizontal dotted line signifies the value for which the test is failed (see text). The distribution of continuum temperatures in each quality category is also shown, even though contintuum temperatures do not constitute a formal quality test (§5.3.1); in this case the dashed horizontal line demonstrates the limit in continuum temperature required for resolution of the kinematic distance ambiguity from Jones & Dickey (2012). The bottom panel displays a histogram of the number of H II regions in each quality category.

and D-F respectively. Through the use of these umbrella categories it can be shown that in order to extract a 'good' quality H I absorption spectrum, a continuum temperature greater than $\sim$ 20 K is required—note: while continuum temperature was not used as a quality assurance parameter, stronger sources are associated with higher quality factors (see Figure 5.2).

Jones & Dickey (2012) reported that a continuum temperature of at least 10 K is required to solve the kinematic distance ambiguity for H II regions in the SGPS, using their velocity channel summation technique. This limit approximately corresponds to the median continuum temperature of quality category E (10.4 K). Note that H II regions with continuum temperatures $T_{\rm cont} < 5$ K were not included in the catalog of H I spectra (§5.2.1).

5.4 Catalog

The catalog of H I emission/absorption spectrum pairs is the primary data product of this Chapter. We present it here in three formats: individual spectrum figures, complete data set

[1]	[2]	[3]	[4]	[5]	[6]
-10.718	5.042	3.638	0.803	1.008	0.079
-9.894	4.320	3.266	1.192	1.006	0.067
-9.069	4.932	4.621	0.758	1.002	0.078
-8.245	6.187	4.059	0.850	1.012	0.099
-7.420	6.265	6.871	1.706	0.997	0.100
-6.596	6.783	7.486	0.352	0.996	0.109
-5.771	9.314	7.669	0.612	1.009	0.152
-4.947	8.126	8.502	1.465	0.998	0.132
-4.122	9.135	8.663	0.611	1.003	0.149
-3.298	11.130	11.743	0.890	0.997	0.183
-2.473	10.098	14.215	1.997	0.977	0.165
-1.649	10.418	15.320	0.644	0.972	0.171
-0.824	12.797	16.794	1.634	0.977	0.211
0.000	15.127	20.274	2.506	0.971	0.250
0.825	18.053	23.362	2.692	0.970	0.300
1.649	15.809	28.417	1.363	0.929	0.262
2.474	6.041	33.051	3.283	0.848	0.096
3.298	-2.430	39.661	6.883	0.762	0.047
4.123	17.582	42.043	5.126	0.862	0.292
4.947	28.948	44.790	3.800	0.911	0.484
5.772	33.344	44.136	2.939	0.939	0.559
6.596	36.165	44.364	2.387	0.954	0.607
7.421	28.446	45.145	3.021	0.906	0.476
8.245	10.029	43.982	4.989	0.808	0.164
9.069	15.144	46.651	3.893	0.822	0.251
9.894	30.727	48.985	3.917	0.897	0.515
10.718	37.734	48.884	3.879	0.937	0.633

Table 5.1: Example of spectrum data. Columns are as follows: [1] velocity channel (km s^{-1}); [2] $T_o n$ (K); [3] average T_{off} (K); [4] uncertainty in T_{off}, $3\sigma_{T_{\rm off}}$ (K); [5] absorption, $e^{-\tau}$; [6] uncertainty in absorption, $\Delta_{\rm abs}$. This Table, and similar files for each H II region included in the catalog, are published in entirety in the electronic edition of the journal, a portion is shown here for guidance regarding the form and content of each file.

(in tar format—available via the online version of the published article) and summary table.

Catalog Summary Table 5.2 provides an overview of the entire catalog. The 252 included H II regions are listed, along with their known parameters. The columns list the Galactic coordinates of the H II region (as reported by the original reference); SIMBAD identification; $T_{\rm cont}$ (K), quality factor, RRL velocity and RRL velocity reference respectively.

Spectrum Figures and Data For every included H II region from Table 5.2, the emission and absorption spectra (along with associated uncertainties) are displayed in Figure 5.3. In each Figure, the top panel shows the emission spectra. The emission is shown by the solid line ($T_{\rm off}$, this is the average of the three 'off' positions) and the emission envelope ($3\sigma_{T_{\rm off}}$: standard deviations between the 'off' positions) is shown in grey. Absorption, $e^{-\tau}$, is displayed in the bottom panel. The H I absorption spectrum (see Equation 1.19) is shown by the solid line and the grey envelope signifies $\Delta_{\rm abs}$ (calculated from the emission envelope).

The absorption panel also displays the fluctuation in the baseline of the absorption spectrum (σ_{rms}) (horizontal dotted lines).

The H II region name and reference are shown as well as the expected velocity ranges of spiral arm features with the same 'crayon' color system as Figure 5.4. This color coding provides an accessible method of 'reading' the H I absorption spectra in terms of known Galactic features.

The H I emission/absorption spectra, for each included H II region, are also available in a tar file (in the published online version of this Chapter). We provide an example of this data in Table 5.1. For each velocity channel we provide the on source brightness temperature ($T_{\rm on}$); average of the three off source brightness temperatures (i.e. the emission spectrum, $T_{\rm off}$); the uncertainty in $T_{\rm off}$, caused by the differences in the three off source positions,$3\sigma_{T_{\rm off}}$; the absorption value ($e^{-\tau}$); and the $\Delta_{\rm abs}$ absorption uncertainty envelope.

Table 5.2: H II region catalog

Longitude	Latitude	SIMBAD ID	T_{cont}	Qual	V_{RRL}	Ref
254.676	0.299	NGC 2579	A	134	64	1
263.619	-0.533	GAL 263.62-00.53	A	58	1	1
267.947	-1.066	GAL 267.95-01.07	A	969	1	1
268	-1.1	GAL 268.0-01.1	C	31	1.8	4
268.454	-0.848	GAL 268.45-00.85	A	94	5	1
269.133	-1.137	GAL 269.13-01.14	A	118	15	1
270.294	0.848	GAL 270.29+00.85	D	26	1	1
274.013	-1.141	GUM 26	A	317	39	1
281.595	-0.969	GAL 281.60-00.97	C	30	2	1
282.026	-1.181	GAL 282.03-01.18	A	235	19	1
282.632	-0.853	GAL 282.63-00.85	D	12	0	1
283.131	-0.984	GAL 283.13-00.98	C	35	-1	1
283.312	-0.566	GAL 283.31-00.57	D	20	6	1
283.329	-1.05	GAL 283.33-01.05	B	26	16	1
284.308	-0.334	GUM 29	A	879	0	1
284.559	-0.183	GAL 284.56-00.18	C	29	9	1
284.65	-0.484	GAL 284.65-00.48	D	17	5	1
284.723	0.313	GAL 284.72+00.31	A	72	10	1
285.253	-0.053	GAL 285.25-00.05	A	321	-2	1
286.195	-0.163	GAL 286.20-00.16	B	52	-18	1
286.873	-0.883	GAL 286.87-00.88	D	24	-20	1
287.217	0.053	GAL 287.22+00.05	D	29	-25	1
287.247	0.355	GAL 287.25+00.36	D	22	-18	1
287.393	-0.63	GAL 287.39-00.63	A	415	-17	1
287.55	-0.616	GAL 287.55-00.62	A	344	-39, -14	1
289.063	-0.355	GAL 289.06-00.36	A	88	19	1
289.755	-1.152	GUM 35	B	38	22	1
289.878	-0.792	2MASX J11005954-6050229	A	50	22	1
290.646	0.256	GAL 290.65+00.26	D	10	-28	1
291.059	-0.77	GAL 291.06-00.77	C	41	17	1
291.284	-0.713	OH 291.3 -0.7	A	1377	-25	1
291.466	-0.128	GAL 291.47-00.13	D	22	6	1
291.858	-0.675	GAL 291.86-00.68	A	84	25	1
293.027	-1.031	GAL 293.03-01.03	D	18	66	1
295.76	-0.2	GAL 295.76-00.20	E	5	17	1
296.593	-0.975	GAL 296.59-00.98	E	8	25	1
297.506	-0.765	GAL 297.51-00.77	C	45	23	1
297.655	-0.977	GAL 297.66-00.98	B	41	26	1

Continued on next page

Table 5.2 – continued from previous page

Longitude	Latitude	SIMBAD ID	T_{cont}	Qual	V_{RRL}	Ref
298.187	-0.782	GAL 298.19-00.78	C	14	16	1
298.228	-0.331	GAL 298.23-00.33	A	84	31	1
298.868	-0.432	GAL 298.87-00.43	A	417	25	1
299.016	0.148	GAL 299.02+00.15	D	15	23	1
299.363	-0.257	GAL 299.36-00.26	D	24	-37	1
300.479	-0.192	GAL 300.48-00.19	C	20	26	1
300.956	1.161	GUM 43	A	60	-47	1
301.109	0.969	GAL 301.11+00.97	A	119	-42	1
301.814	1.077	GAL 301.81+01.08	D	11	-42	1
302.025	-0.044	GAL 302.03-00.04	C	19	-27	1
302.504	-0.749	GAL 302.69+00.19	C	19	31	1
302.69	0.19	WR 47b	E	13	-33	1
302.804	1.306	GAL 302.80+01.31	D	8	-32	1
305.173	-0.368	GAL 305.17-00.37	D	20	-45	1
305.202	0.022	GAL 305.20+00.02	A	241	-40	1
305.363	0.179	GAL 305.36+00.18	A	513	-38	1
305.537	0.338	GAL 305.54+00.34	E	72	-39	1
305.551	-0.005	GAL 305.55-00.01	A	117	-45	1
305.787	0.14	GAL 305.79+00.14	E	11	-43	1
306.256	0.066	GAL 306.26+00.07	F	7	-37	1
306.315	-0.361	GAL 306.32-00.36	C	40	-16	1
307.569	-0.616	GAL 307.57-00.62	D	21	-40	1
307.62	-0.32	GAL 307.62-00.32	A	76	-37	1
308.092	-0.432	GAL 308.09-00.43	D	21	-17	1
308.647	0.579	GAL 308.65+00.58	A	42	-50	1
309.057	0.186	GAL 309.06+00.19	E	12	-47	1
309.548	-0.737	GAL 309.55-00.74	B	35	-43	1
309.905	0.373	GAL 309.91+00.37	B	36	-55	1
310.176	-0.131	GAL 310.18-00.13	D	16	4	1
310.796	-0.408	NAME Kes 20A	C	17	+33, -57	1
310.994	0.389	GAL 310.99+00.39	D	11	-51	1
311.114	-0.27	GAL 311.11-00.27	C	24	36	1
311.197	0.752	GAL 311.20+00.75	B	19	-57	1
311.489	0.368	IRAS 14000-6104	C	39	-59	1
311.497	-0.483	GAL 311.50-00.48	C	27	-47	1
311.627	0.27	GAL 311.63+00.27	B	43	-61	1
311.852	-0.222	GAL 311.85-00.22	C	11	-55	1
311.894	0.1	[CH87] 311.894+0.100	A	104	-47	1
311.922	0.229	GAL 311.92+00.23	A	76	-45	1
312.112	0.314	PN G312.1+00.3	B	42	-49	1
312.953	-0.449	GAL 312.95-00.45	C	20	-47	1
313.446	0.176	GAL 313.45+00.18	B	26	-5	1
314.228	0.437	GAL 314.23+00.44	A	66	-63	1
315.312	-0.273	GAL 315.31-00.27	D	10	16	1
316.156	-0.492	GAL 316.16-00.49	A	35	-60	1
316.393	-0.356	GAL 316.39-00.36	B	19	3	1
316.808	-0.037	GAL 316.81-00.04	A	462	-36	1
317.037	0.3	GAL 317.04+00.30	C	40	-49	1
317.291	0.268	GAL 317.29+00.27	C	23	-51	1
317.598	-0.363	GAL 317.60-00.36	D	17	-38	1
317.988	-0.759	GAL 317.99-00.76	D	13	-37	1
318.058	-0.459	IRAS 14518-5925	D	10	-31, +37	1
318.911	-0.181	GAL 318.91-00.18	A	41	-29	1
319.157	-0.423	GAL 319.16-00.42	A	49	-22	1
319.38	-0.025	GAL 319.38-00.03	A	91	-14	1
319.874	0.77	GAL 319.87+00.77	A	35	-38	1
320.109	-0.51	[CH87] 320.109-0.510	C	16	-13	1
320.153	0.78	GAL 320.15+00.78	A	170	-36	1

Continued on next page

Table 5.2 – continued from previous page

Longitude	Latitude	SIMBAD ID	T_{cont}	Qual	V_{RRL}	Ref
320.236	0.417	GAL 320.24+00.42	C	31	-31	1
320.252	-0.332	GAL 320.25-00.33	A	92	-68	1
320.317	-0.208	GAL 320.32-00.21	A	120	-11	1
320.379	0.139	GAL 320.38+00.14	C	30	-3	1
320.706	0.197	GAL 320.71+00.20	C	20	-7	1
321.038	-0.519	GAL 321.04-00.52	A	111	-61	1
321.105	-0.549	GAL 321.11-00.55	A	60	-56	1
321.71	1.157	GAL 321.71+01.16	A	38	-32	1
322.153	0.613	GAL 322.15+00.61	A	281	-52	1
322.407	0.221	GAL 322.41+00.22	C	14	-30	1
324.12	-0.954	GAL 324.12-00.95	E	6	-67	1
324.147	0.231	[CH87] 324.147+0.231	B	31	-91	1
324.192	0.109	[CH87] 324.192+0.109	A	53	-92	1
324.954	-0.584	[CH87] 324.954-0.584	D	10	25	1
326.141	-0.328	[CH87] 326.141-0.328	D	9	-65	1
326.23	0.976	[CH87] 326.230+0.976	D	10	-42	1
326.441	0.914	[CH87] 326.441-0.396	A	161	-39	1
326.645	0.589	[DBS2003] 95	A	425	-44	1
326.959	0.031	GAL 326.96+00.03	C	30	-64	1
327.313	-0.536	[CH87] 327.313-0.536	A	722	-48	1
327.612	-0.354	[CH87] 327.612-0.354	A	46	-72	1
327.759	-0.351	[CH87] 327.759-0.351	A	68	-72	1
327.834	0.113	[CH87] 327.834+0.113	D	18	-100	1
327.985	-0.086	GAL 327.99-00.09	A	59	-45	1
328.31	0.448	GAL 328.31+00.45	D	8	-97	1
328.593	-0.518	GAL 328.59-00.52	A	208	-51	1
328.806	-0.083	GAL 328.81-00.08	B	32	-47	1
328.812	0.637	GAL 328.81+00.64	C	17	-42	1
329.353	0.144	GAL 329.35+00.14	B	34	-107	1
329.489	0.207	GAL 329.49+00.21	C	30	-102	1
330.041	-0.045	GAL 330.04-00.05	C	28	-38	1
330.305	-0.385	GAL 330.31-00.39	B	19	-76	1
330.677	-0.396	GAL 330.68-00.40	A	58	-61	1
330.856	-0.371	GAL 330.86-00.37	A	173	-56	1
331.026	-0.152	GAL 331.03-00.15	C	59	-89	1
331.11	-0.506	GAL 331.11-00.51	A	68	-68	1
331.259	-0.186	GAL 331.26-00.19	A	86	-85	1
331.314	-0.336	GAL 331.31-00.34	A	125	-64	1
331.353	-0.013	GAL 331.35-00.01	A	91	-81	1
331.354	1.072	GAL 331.35+01.07	A	55	-79	1
331.36	0.507	GAL 331.36+00.51	C	19	-46	1
331.517	-0.069	GAL 331.5-00.0	A	466	-89	1
332.148	-0.446	GAL 332.15-00.45	A	275	-55	1
332.541	-0.111	GAL 332.54-00.11	F	10	-50	1
332.662	-0.607	GAL 332.66-00.61	A	149	-48	1
332.978	0.792	GAL 332.98+00.79	A	114	-52	1
333.114	-0.441	GAL 333.11-00.44	A	303	-52	1
333.168	-0.081	GAL 333.17-00.08	A	61	-91	1
333.292	-0.371	GAL 333.29-00.37	A	323	-50	1
333.6	-0.1	GAL 333.6-00.1	A	89	-53.7	4
333.61	-0.208	SNR G333.6-00.2	A	840	-46	1
333.684	-0.457	GAL 333.68-00.46	C	28	-50	1
334.529	0.825	GAL 334.53+00.83	D	11	-77	1
334.684	-0.107	GAL 334.68-00.11	C	24	-32	1
334.714	-0.665	GAL 334.71-00.67	A	30	16	1
335.748	-0.134	GAL 335.75-00.13	B	47	-52	1
335.978	0.185	GAL 335.98+00.19	D	24	-79	1
336.375	-0.131	GAL 336.38-00.13	B	49	-88	1

Continued on next page

Table 5.2 – continued from previous page

Longitude	Latitude	SIMBAD ID	T_{cont}	Qual	V_{RRL}	Ref
336.404	-0.234	GAL 336.40-00.23	A	73	-93	1
336.456	0.038	GAL 336.46+00.04	D	22	-63	1
337.147	-0.181	GAL 337.15-00.18	A	287	-73	1
337.548	-0.304	GAL 337.55-00.30	D	11	-101	1
337.949	-0.476	GAL 337.95-00.48	A	380	-40	1
338.014	-0.121	GAL 338.01-00.12	B	46	-54	1
338.131	-0.173	GAL 338.13-00.17	A	61	-53	1
338.398	0.164	GAL 338.40+00.16	A	121	-29	1
338.407	-0.238	GAL 338.41-00.24	A	98	2	1
338.45	0.061	GAL 338.45+00.06	A	150	-37	1
338.742	0.641	GAL 338.74+00.64	C	23	-62	1
338.921	-0.089	GAL 338.92-00.09	A	60	-40	1
338.943	0.604	GAL 338.94+00.60	A	87	-63	1
339.089	-0.216	GAL 339.09-00.22	D	18	-120	1
339.128	-0.408	SNR G339.2-00.4	C	24	-37	1
339.286	0.163	GAL 339.29+00.16	D	14	-71	1
339.578	-0.124	GAL 339.58-00.12	C	21	-30	1
339.838	0.274	GAL 339.84+00.27	A	35	-19	1
339.955	-0.566	GAL 339.96-00.57	D	10	-89	1
340.047	-0.253	GAL 340.05-00.25	B	34	-52	1
340.24	0.482	GAL 340.24+00.48	C	13	-62	1
340.279	-0.222	GAL 340.28-00.22	A	77	-43	1
340.777	-1.008	GAL 340.78-01.01	A	233	-25	1
341.05	-0.1	GAL 341.05-00.10	E	6	-38	1
341.963	0.205	GAL 341.96+00.21	C	12	-8	1
342.085	0.423	GAL 342.09+00.42	A	85	-65	1
342.3	0.314	GAL 342.30+00.31	D	25	-122	1
342.382	-0.044	GAL 342.38-00.04	C	26	-13	1
345.215	-0.749	GAL 345.22-00.75	D	15	-18	1
345.231	1.035	GAL 345.23+01.04	A	211	-9	1
345.404	1.406	GAL 345.40+01.41	A	27	-15	1
345.45	0.209	GAL 345.45+00.21	B	32	-13	1
345.495	0.326	GAL 345.50+00.33	A	38	-20	1
345.555	-0.042	GAL 345.56-00.04	A	76	-6	1
345.645	0.01	GAL 345.65+00.01	A	81	-10	1
345.722	0.153	HRDS G345.722+0.153	E	6	-77.9	2
345.827	0.041	GAL 345.83+00.04	B	23	-10	1
346.056	-0.021	HRDS G346.056-0.021	C	9	-76.8, -3.4	2
346.077	-0.056	HRDS G346.077-0.056	D	12	-84.7, -7.9	2
346.206	-0.071	GAL 346.21-00.07	C	18	-108	1
346.267	0.128	HRDS G346.267+0.128	E	5	-32.2	2
346.53	-0.013	HRDS G346.530-0.013	E	5	0.6	2
346.539	0.097	GAL 346.54+00.10	B	35	2	1
346.875	0.328	HRDS G346.875+0.328	D	10	4.1	2
347.386	0.266	GAL 347.39+00.27	D	20	-97	1
347.6	0.211	GAL 347.60+00.21	D	19	-96	1
347.772	0.131	HRDS G347.772+0.131	F	6	-88.7	2
347.893	0.044	GAL 347.89+00.04	A	51	-31	1
347.918	-0.761	HRDS G347.918-0.761	F	6	6.1	2
347.964	-0.439	GAL 347.96-00.44	D	27	-97	1
348.061	0.242	HRDS G348.061+0.242	F	5	0.7	2
348.148	0.255	HRDS G348.148+0.255	E	5	-66.3, -1.4	2
348.225	0.459	GAL 348.23+00.46	B	61	-12	1
348.231	-0.982	ESO 333-3	A	237	-18	1
348.557	-0.985	HRDS G348.557-0.985	D	17	-10.5	2
348.715	-1.031	GAL 348.72-01.03	A	562	-13	1
348.891	-0.179	HRDS G348.891-0.179	D	8	10.1	2
349.111	0.105	GAL 349.11+00.11	C	33	-74	1

Continued on next page

Table 5.2 – continued from previous page

Longitude	Latitude	SIMBAD ID	T_{cont}	Qual	V_{RRL}	Ref
349.14	0.02	GAL 349.14+00.02	B	81	-92, +17	1
349.216	0.144	HRDS G349.216+0.144	D	11	-65.7	2
349.579	-0.68	HRDS G349.579-0.680	C	12	-19.4	2
349.84	-0.537	GAL 349.84-00.54	A	110	-25	1
350.004	0.438	HRDS G350.004+0.438	D	13	-33.5	2
350.129	0.088	GAL 350.13+00.09	A	143	-69	1
350.177	0.017	HRDS G350.177+0.017	D	14	-68.9	2
350.33	0.157	HRDS G350.330+0.157	E	11	-62.9	2
350.335	0.107	[KC97c] G350.3+00.1	D	12	-66.1	3
350.524	0.96	GAL 350.52+00.96	A	77	-10	1
350.769	-0.075	HRDS G350.769-0.075	E	5	-62.6	2
350.813	-0.019	GAL 350.81-00.02	B	29	-5	1
350.996	-0.577	GAL 351.00-00.58	D	11	-17	1
351.063	0.662	[L89b] 351.063+00.662	A	150	-3.8	3
351.192	0.708	[L89b] 351.192+00.708	A	224	-3.4	3
351.201	0.483	[L89b] 351.201+00.483	A	157	-7.1	3
351.358	0.666	GAL 351.36+00.67	A	566	-3	1
351.359	1.014	HRDS G351.359+1.014	D	11	-8.6	2
351.467	-0.462	GAL 351.47-00.46	A	80	-21	1
351.601	-0.348	GAL 351.60-00.35	B	20	-94	1
351.617	0.171	GAL 351.62+00.17	A	173	-43	1
351.641	-1.256	GAL 351.60-01.30	A	102	-13	1
351.662	0.518	GAL 351.66+00.52	D	19	-2	1
351.691	0.669	HRDS G351.691+0.669	C	25	3.1	2
351.694	-1.165	GAL 351.69-01.17	A	138	-13	1
352.398	-0.057	GAL 352.40-00.06	C	21	-89	1
352.521	-0.144	HRDS G352.521-0.144	B	61	-57.3, -38.0	2
352.61	0.177	HRDS G352.610+0.177	D	13	-50.4	2
352.611	-0.172	GAL 352.61-00.17	C	21	-82	1
352.676	0.148	GAL 352.68+00.15	D	17	-45	1
353.035	0.748	[L89b] 353.035+00.748	C	44	-9.1	3
353.136	0.66	GAL 353.14+00.66	A	162	-4	1
353.186	0.887	[L89b] 353.186+00.887	A	95	-4.7	3

Columns are as follows: 1) Galactic longitude, 2) Galactic latitude, 3) SIMBAD identification, 4) quality factor, 5) $T_{\rm cont}$ (K), 6) RRL velocity, 7) reference for H II region coordinates and velocity (see below).

References — 1: Caswell & Haynes (1987), 2: Bania et al. (2010), 3: Lockman (1989), 4: Wilson et al. (1970)

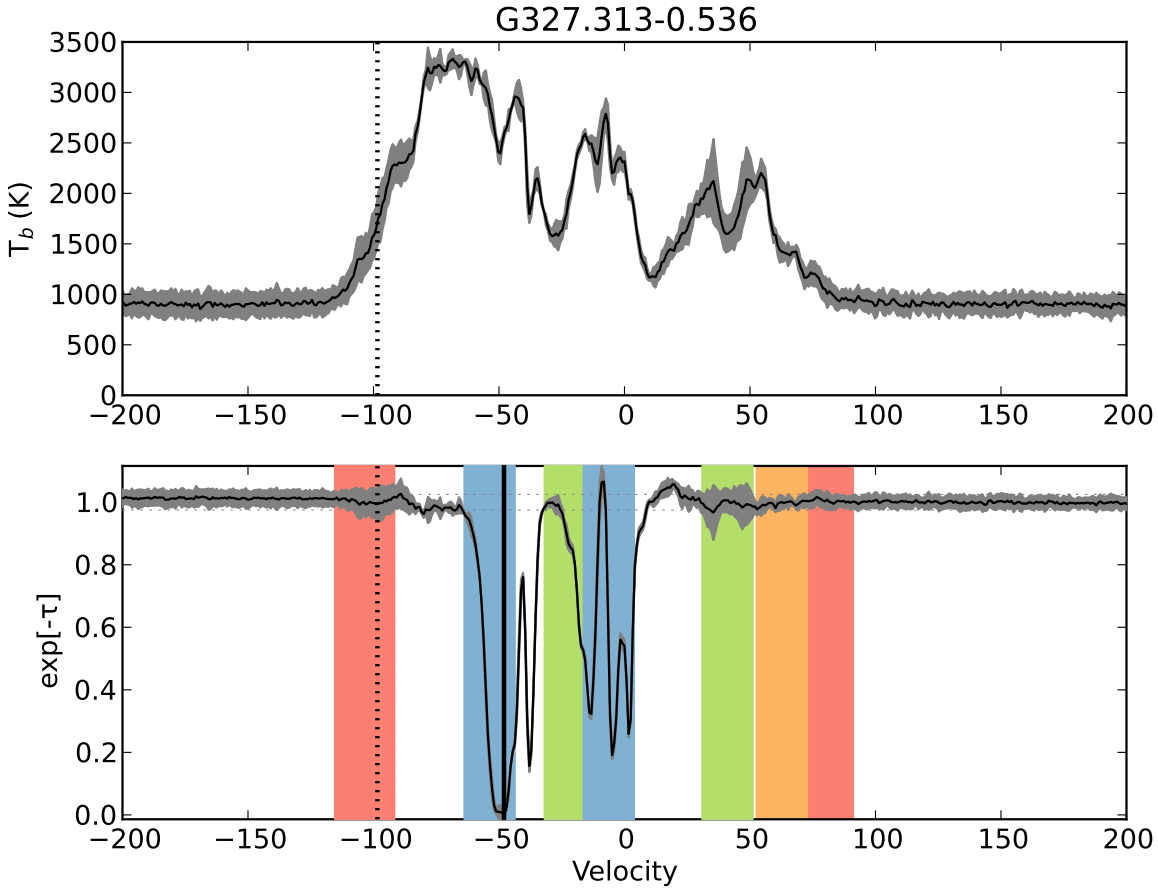

Figure 5.3: H I emission/absorption spectrum pair. The top panel shows the emission spectra: shown by the solid line (this is the average of the three "off" positions) and the emission envelope ($3\sigma_{T_{\rm off}}$) is shown in grey. Absorption, $e^{-\tau}$, is displayed in the bottom panel. The H I absorption spectrum (see Equation 1.19) is shown by the solid line and the grey envelope signifies $\Delta_{\rm abs}$ (calculated from the emission envelope). The absorption panel also displays the fluctuation in the baseline of the absorption spectrum ($\sigma_{\rm rms}$) (horizontal dotted lines). The H II region name and reference are shown as well as the expected velocity ranges of Galactic structure features with the same color system as Figure 5.4.
The published version of this Chapter presented each H I emission/absorption spectrum pair in an online–only Figure Set. This thesis presents each spectrum pair in Appendix C.

5.5 Discussion

Here we briefly discuss the global properties of the H I absorption catalog (§5.5.1), as well as an example of its use - investigating the lv locus of the Near 3kpc Arm (see §5.5.2).

5.5.1 Longitude-Velocity Distribution

One simple application of this catalog is an investigation of the distribution of H I absorption in longitude-velocity (lv) space. Firstly, we construct an 'lv crayon diagram' (Figure 5.4) of known Galactic structures. The Near and Far 3kpc Arm fits are provided by Dame & Thaddeus (2008) and the fourth quadrant spiral arms are taken from Vallée (2008) (who represents the Distant Arm of McClure-Griffiths et al. (2004) as the Cygnus Arm beyond the Solar Circle). The velocity width of each crayon feature is set to 20km s^{-1}.

For each source in the catalog (of quality factor C or better), we plot both the systemic velocity of the H II region and any associated H I absorption (Figure 5.4). It is clear that both the H II regions and their associated H I absorption trace the spiral arm structures, especially in the inner Galaxy. This is in keeping with Jones et al. (2013) who find that $> 90\%$ of their H II region sample is associated with known spiral arm structures. H II regions are considered to be the archetypical tracers of Galactic spiral structure (Bania et al. 2010); but cold, dense gas, traced by H I absorption is also more likely to be located within the spiral arms than in the inter-arm region. Each black marker on the Figure corresponds to five consecutive velocity channels which display significant absorption. It is clear that the H I absorption is also associated with the spiral arms. This is to be expected, as dense, cold gas which is traced by H I absorption is more likely to be located within the spiral arms than in the inter-arm regions. We find H I absorption associated with all inner Galaxy spiral arms.

Figure 5.4 not only demonstrates the suitability of both data-sets (H II region velocities and H I absorption) as spiral arm tracers, but also their inherent velocity uncertainty distributions. Galactic streaming motions are often estimated to be on the order of $\lesssim 15$ km s^{-1} (Bania & Lockman 1984; Kolpak et al. 2003), i.e., within the velocity width of the crayon diagram features. However, H I absorption associated with H II regions can extend ~ 20 km s^{-1} from the systemic velocity of the region (Dickey et al. 2003; Jones et al. 2013).

The association of H I absorption with a Galactic structure feature can be used to infer lower distance limits, or the location of the H II region in our Galaxy (Jones & Dickey 2012; Jones et al. 2013).

5.5.1.1 H I Absorption in the Outer Galaxy

From Figure 5.4 it is evident that this catalog is primarily limited to the inner Galaxy (within the Solar circle); unlike, for example, the work of Strasser et al. (2007).

Strasser et al. (2007) used the SGPS and the E/A spectrum extraction method to study H I absorption towards 111 extragalactic continuum sources - in order to investigate absorption from the outermost arms of the Milky Way. Of these 111 sources, only 17 showed any significant H I absorption at positive velocities, corresponding to a location in the outer Galaxy.

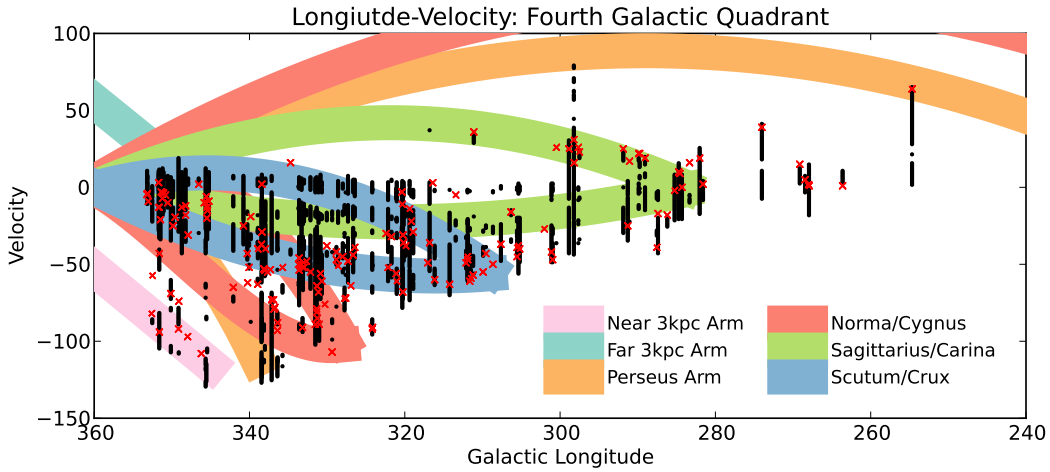

Figure 5.4: H II region RRL velocities (red crosses) and H I absorption (black dots) overlaid on a longitude-velocity 'crayon diagram'. Each dot denotes the central velocity of five adjacent velocity channels ($\sim$ 5km s^{-1}), with each channel demonstrating a statistically significant amount of H I absorption. Only H II regions with H I absorption spectra of Quality 'C' or better are included for use in this figure.

Because the Strasser et al. (2007) source sample included strictly extra-Galactic sources, the H I absorption spectra reflect lines of sight through the entire Galactic plane. Conversely, spectra from this study have systematically shorter lines of sight—towards the H II regions themselves, located within the Galaxy. For this reason, this work is far less likely to identify H I absorption in the outermost spiral arms in the fourth quadrant - as the number of H II regions known (with RRL velocities) is extremely limited in the most distant features.

Nevertheless, for longitudes $l < 300°$ the line of sight distance to the Solar circle is relatively small and investigations of H I absorption in the outer Galaxy become possible; although at these longitudes, there are very few known H II regions (see Figure 5.4). Regions with velocities $\lesssim 15$ km s^{-1} correspond to very short line of sight distances. At $l \approx 250°$ the near-continuous absorption profile is associated with lines of sight through the Local Arm.

5.5.2 Locus of the Near 3kpc Arm

The investigation of the lv distribution of H I absorption (see Figure 5.4) can be further specialized to individual features. In Jones et al. (2013) the locus of the Near and Far 3kpc Arms (in lv space) was investigated using H I absorption. This work presents an opportunity to extend this analysis, by including H I absorption associated with the Near 3kpc Arm at longitudes $l < 350°$. This is a complementary investigation to that first performed by Dame & Thaddeus (2008) using CO 1-0 emission.

Using H I absorption channels from the Near 3kpc Arm analysis of Jones et al. (2013) in addition to those from this work—such that the entire longitude extent $10° > l > 340°$of the Near 3kpc Arm is included—a linear least-squares fit to the lv locus of the Near 3kpc Arm was performed:

$$V = -53.3 + 4.1l \qquad \Delta V = 25.9\text{km s}^{-1} \tag{5.1}$$

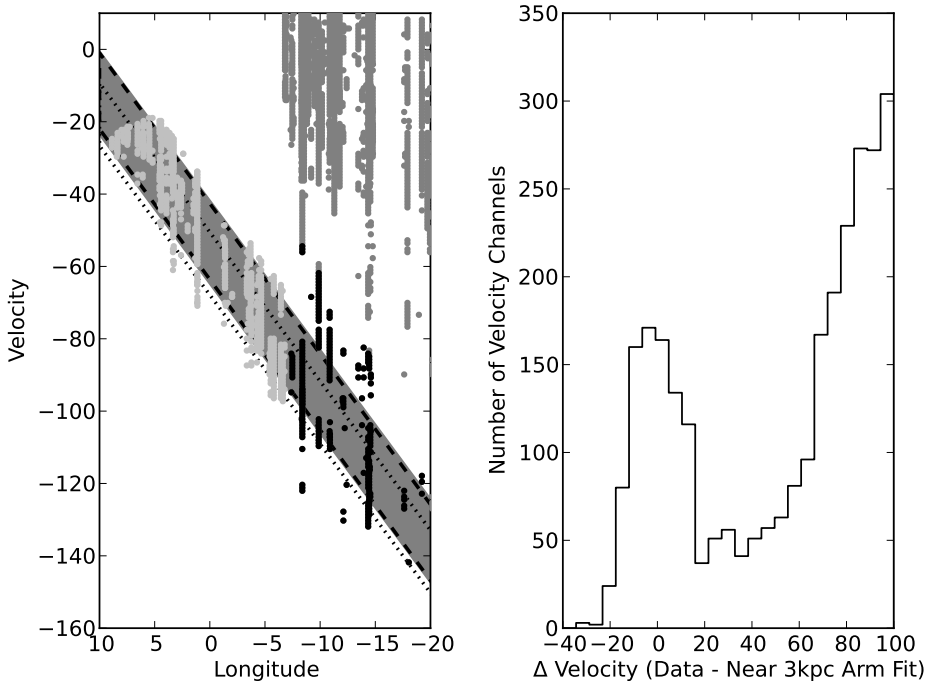

Figure 5.5: H I absorption associated with the Near 3kpc Arm. *Left Panel*: lv diagram of H I absorption corresponding to the Near 3kpc Arm. Light grey dots are data from Chapter 4, dark grey dots are from this Chapter (but were not included in the linear fit analysis as these velocities are probably not associated with the 3kpc Arm), black dots are also from this Chapter (and were used in the analysis of the locus of the Arm). *Right Panel:* fit of data to model (Equation 5.1). The histogram displays the difference in velocity between Equation 5.1 and each channel that displays significant absorption (see Figure 5.4). Note only regions with $l > 340°$ are considered here.

Here ΔV refers to the FWHM of a Gaussian fit to the velocity profile of the Arm model (see right hand panel of Figure 5.5).

With the inclusion of H I absorption from the longitude range $l < 340°$, the model for the locus of the Near 3kpc Arm (Equation 5.1) is extremely consistent with the fit provided by Dame & Thaddeus (2008) from CO observations; $R^2 > 0.97$ and the standard error of the mean difference is 5.4 km s^{-1}, within the FWHM of either fit.

Figure 5.5 demonstrates the location of H I absorption associated with the Arm in lv space, as well as an evaluation of the fit. The left hand panel, supplementary to Figure 5.4, is an lv diagram extended to $l = 10°$ over the velocity range of the Near 3kpc Arm. Channels of significant absorption are shown, in addition to those from Jones et al. (2013). The lv linear fits to the locus of the Near 3kpc Arm from Dame & Thaddeus (2008, $V = -53.1 + 4.6, \Delta V = 19.7$ km s^{-1}), Jones et al. (2013, $V = -59.2 + 4.12, \Delta V = 17.3$ km s^{-1}) and this work (see Equation 5.1) are also shown. In the right hand panel an evaluation of the fit is made. All velocity channels shown in the left-hand panel are compared to the linear Near 3kpc Arm fit (similar to the CO 1-0, Figure 2 of Dame & Thaddeus (2008)). The Near 3kpc Arm is identified as a well defined peak in H I absorption, centered around the fit to the linear model (however, the scale height of the component is exaggerated by the removal of non-Near 3kpc Arm absorption for $360° > l > 353°$). The hump at $\Delta V = 30$ km s^{-1} (i.e. velocities consistent with a line parallel to Equation 5.1 +30 km s^{-1}) may be the signature

of the Norma Arm, which is approximately parallel to the Near 3kpc Arm in lv space for longitudes $l > 340°$ (see Figure 5.4). The broad central peak is the result of the remaining disk rotation, both foreground and background to the Near 3kpc Arm.

For longitudes $l < 350°$, the Far 3kpc Arm is confused in velocity with the other inner Galaxy spiral arms—therefore investigation of the locus of the Far 3kpc Arm, extending the work of Chapter 4, is not possible here.

5.6 Summary

The first attempt to test and interpret H I emission/absorption spectrum pairs from the SGPS (test region) was performed by Dickey et al. (2003). However, until now, no complete census of H I absorption towards Galactic continuum sources in the SGPS has been completed. This paper presents, in graphical, numerical and summary formats, the H I emission and absorption spectrum pairs from every known Galactic H II region distinctly detectable in the SGPS ($255° < l < 353°$, $|b| \lesssim 1°$)—a total of 252 regions.

We have demonstrated one use of this catalog by examining the lv distribution of H I absorption in the Milky Way—including a re-evaluation of the locus of the Near 3kpc Arm in lv space. This catalog has the potential to be an integral data set for numerous works; perhaps even sparking the invigoration of the search for H I spiral arms of the Milky Way in absorption, rather than emission, as Lockman (2002) predicted.

Chapter 6

Preparing for H II Region Discovery

Chapter 5 provided the means to perform KDAR analysis (from Chapter 3) for every *known* H II region in the fourth Galactic quadrant—approximately 250 regions*. According to Anderson et al. (2014) there are currently about 1500 known H II regions (i.e., those with measured RRL velocities) within the Milky Way. Considering the first quadrant only; 900 known H II regions are located within $l < 90^\circ$, along with 700 credible candidate H II regions (see Section 6.2). Thus the first quadrant is expected to host approximately as many H II regions as are currently known in the entire Galaxy.

The first and fourth Galactic quadrants cover the same volume of the inner Galaxy, and while there are asymmetries—for example, the end of the Galactic bar is closer to the Sun in the first quadrant than the fourth—the overall number of H II regions in each quadrant should be similar. We therefore naively expect the actual number of H II regions in the fourth quadrant to be a factor of $\sim 4 - 6$ times greater than the number of confirmed regions known today—indeed Anderson et al. (2014) list over 1000 credible fourth quadrant H II region candidates. This situation is similar to the circumstances of the late 1980s; where only a fifth of the candidate continuum sources had been confirmed as H II regions (Lockman 1990a).

The detection of RRL emission from a H II region candidate source confirms the source as a bona fide H II region. There are two types of RRL observations; targeted and untargeted. Untargeted surveys require no source pre-selection, and can offer a deeper understanding of the overall emission properties within the mapped area. However, blind surveys require substantially longer observation times; but modern radio telescopes can now perform these surveys within a reasonable time. Several such untargeted RRL surveys have already been completed for the southern sky. We investigate resultant source catalogues for the purpose of H II region discovery in Section 6.1. Conversely, targeted surveys require source selection prior to the observations and typically investigate a sample of flux–limited radio continuum sources, with particular infrared morphologies, for RRL emission. The selection of H II region candidates is discussed in Section 6.2.

*The actual number is closer to 400, in that the H II regions investigated in Chapter 5 are those that fall within the latitude ranges of the SGPS I and are distinct continuum emission sources at the angular resolution of the SGPS (approximately $2'$).

6.1 Untargeted RRL Surveys

Targeted surveys are effective in identifying emission from previously categorised objects, but untargeted surveys can offer a deeper understanding by systematically obtaining all emission within the mapped area. The number of untargeted recombination line surveys is extremely limited. Early surveys, hampered by low angular resolution and sensitivity—the surveys of Cersosimo et al. (1989) and Azcarate et al. (1990) had beam sizes $> 30'$ and integration times of 4-6 hours per pointing—could not distinguish individual emission sources. Nevertheless, they were able to investigate the lack of star formation in the Near 3kpc Arm (Lockman 1980), the Galactic warp in ionised gas (Azcarate et al. 1990) and identify the longitude range $25° < l < 35°$, which we now appreciate as the location of the end of the Galactic bar, as the area of strongest emission (Lockman 1979 and Hart & Pedlar 1976 in Cersosimo et al. 1989).

Despite the lack of a targeted southern H II region discovery survey, several modern untargeted surveys have included RRL transitions in their observed frequency ranges. Most notably, the H_2O Southern Galactic Plane Survey (HOPS Walsh et al. 2011) and Millimetre Astronomer's Legacy Team - 45 GHz Galactic Plane Survey (MALT-45 Jordan et al. 2013) have included H69α and H53α surveys of sections of the southern Galactic plane. The Hnα data and catalogues for both works are as yet unpublished. We were however able to obtain the H69α emission source catalogue from the HOPS team via private communication.

Both HOPS and MALT45 cover small portions of the Galactic plane, but their data retains H II region discovery potential. The discovery process has been somewhat simplified through the publication of H II region candidate catalogues (most notably Anderson et al. 2014). Hnα emission maps therefore only need to be cross-referenced with the candidate catalogue in order to establish emission sources as previously known, or new, H II regions.

If these studies do not contain emission from previously unknown H II regions, they still present an opportunity to study RRLs over a large frequency range. Most targeted H II region discovery surveys observe RRL transitions at ∼8 GHz, whereas the transitions observed by HOPS and MALT-45 studies are at much higher frequencies (20 and 45 GHz).

6.1.1 The H_2O Southern Galactic Plane Survey

The H_2O Southern Galactic Plane Survey (HOPS, Walsh et al. 2011) is a southern spectral line survey carried out with the Mopra radio telescope between 2008 and 2010. The survey includes detections of 30 spectral lines between 19591.11 MHz and 27477.943 MHz which trace high mass star formation; including three Hnα lines (n= 69, 65, 62). The HOPS region covers 100 square degrees of the southern Galactic plane, from $290° < l < 30°$ and $|b| < 0.5°$. The size of the Mopra beam at 19.5 GHz (the approximate frequency of the H69α line) is about $2.4'$ (later smoothed to $2.5'$, see below); slightly larger than the SGPS H I beam size of $\sim 2'$.

The HOPS H69α data is as yet unpublished. I had no input, or access, to the data reduction phase of the Survey; however, in the interest of completeness, I will now describe the H69α reduction strategy.

Standard Mopra data reduction (livedata and gridzilla packages) were used to produce the initial data cube. The Duchamp three-dimensional source finding package was then implemented to create a mask of significant emission within the cube. The line cube is then baselined and smoothed to a beam size of $2.5'$ and spectrally smoothed with a hanning filter five channels wide. The Duchamp fitting is then rerun on the smoothed, baselined, data cube - producing a more accurate mask. This mask is in turn subtracted from the smoothed cube, in order to produce a map containing only RMS noise. Finally the baselined cube is divided by the rms noise map to create a signal-to-noise cube. The Duchamp algorithm is run for a final pass, on the signal to noise map, identifying clumps with significant signal to noise ($> 5\sigma$) and determining their properties.

The final Duchamp 5σ catalogue reports the following parameters for the 72 detected clumps: name; the central longitude, central latitude, central velocity (VLSR) based on position of the cloud in $l-v-b$ space, weighted-brightness and peak brightness; the minimum and maximum velocity of the Duchamp mask; the geometric and brightness-weighted centre of emission (l, b position); angle subtended by the emission; integrated intensity of emission, with uncertainty; peak brightness temperature; median RMS noise; and various flags to signal if the cloud touches a l, b or v cube border. Further H69α emission sources, possibly unknown to the literature, may be present in the HOPS dataset; but the detected emission does not meet the 5σ threshold.

The HOPS team cross-referenced twelve of their H69α emission sites with known H II regions from the Caswell & Haynes (1987) catalogue. The mean($\pm\sigma$) difference in line velocity for these twelve H II regions was 2.86 ± 1.52 km s^{-1} (note that the Caswell & Haynes (1987) catalogue detected the H109α and H110α lines) and the difference in centroid l, b position was minimal ($< |0.02|^{\circ}$).

This data reduction is identical to the (published) HOPS water maser and ammonia line reductions (Purcell et al. 2012)) and was completely performed by the HOPS team (namely Dr Andrew Walsh, Dr Steven Longmore and Dr Cormac Purcell). I obtained the HOPS H69α Duchamp source catalogue from the HOPS data server* on June 24, 2013, and performed all the analyses of §6.1.1.1 (including the cross-referencing which populates Table 6.1).

6.1.1.1 Comparing With Known H II Regions

The HOPS H69α catalogue was explored for H II regions previously unknown to the literature (i.e. further to Chapter 5). As previously discussed, the Duchamp catalogue provided by the HOPS team included literature references for 12 of the 72 detected clumps. Based on the catalogue of known H II regions (Chapter 5), it was discovered that all the clumps detected in HOPS were sites of known H II regions.

Of the 72 detected clumps, 68 are coincident with known individual H II regions. The remaining four clumps are associated with multiple confused sources and may not indicate an individual H II region, but rather a group of regions. Of the 68 individual H II regions in HOPS, nearly 70% have been investigated throughout this thesis and over 70% have known KDARs.

*http://awalsh.ivec.org/hops/public/index.php (password required for unpublished data)

Table 6.1 presents the centroid longitude, latitude and velocity of H69α emission clumps from HOPS (columns 1-3). The following columns are the result of my work in cross referencing the clumps with known H II regions. These include the reference for previous RRL detection (i.e. H II region discovery, column 4); SIMBAD identification (column 5); Chapter in which the H II region is investigated in this thesis (column 6); and KDAR, with reference, if known (columns 7-8). Singular identification was not possible for four H69α emission clumps detected by HOPS as these emission sites correspond to multiple known H II regions.

Basic parameters from the HOPS catalogue are consistent with results from previous studies. The absolute average positional differences ($\pm\sigma$) are $0.001 \pm 0.024^\circ$ in Galactic longitude and $0.007 \pm 0.049^\circ$ in latitude. The observed RRL velocities are also well matched to previous detections, with an absolute mean difference of 0.1 ± 3.3 km s^{-1}. Further parameters, such as line to continuum ratios, line widths, and therefore electron temperatures could be investigated. However, as the HOPS catalogue was investigated only for the purpose of identifying new H II regions, these analyses are not performed here.

Table 6.1: Catalogue of H II Regions in HOPS

l	b	v	RRL	SIMBAD	§	KDAR	Ref.
29.937	-0.031	97.5	L89	GAL 029.9-00.0		F	AB09
25.775	0.210	113.0	L89	[WBH2005] G025.765+0.211		N	AB09
25.384	-0.179	66.0	L89	GPSR 025.381-0.181	3	N	3
25.277	-0.324	66.6	L89	[KC97c] G025.3-00.3		F	AB09
24.803	0.095	108.8	L89	GAL 028.81+00.10	3	TP	3
24.475	0.225	114.8	L89	[L89b] 24.460-00.246		F	AB09
24.464	0.491	103.7	L89	GAL 024.47+00.49	3	TP	3
24.388	0.074	108.4	L89	[KC97c] G024.4+00.1	3	TP	3
23.426	-0.202	101.0	L89	GAL 023.46-00.20	3	TP	3
19.619	-0.229	43.3	HRDS	HRDS G019.662-00.305		F	A12
19.058	-0.229	68.6	L89	[KC97c] G019.1-00.3		N	AB09
18.139	-0.289	49.8	L89	GAL 018.14-00.29		N	AB09
14.617	0.073	36.8	L89	[KC97c] G014.6+00.1			
13.887	0.290	52.7	L89	GAL 013.88+0.28			
13.194	0.038	54.0	L89	GAL 013.19+00.05			
12.794	-0.191	39.5	L89	[LB89b] 12.807-00.204			
10.624	-0.369	-2.8	L89	W 31C			
10.311	-0.150	10.4	L89	GPSR 010.332-0.155			
10.158	-0.341	14.4	L89	GAL 010.15-00.34			
8.139	0.227	18.9	L89	[KC97c] G008.3-00.1	4	N	4
6.553	-0.092	11.2	L89	GRS 006.57-00.10	4	F	4
5.893	-0.418	7.7	L89	GAL 005.91-00.43	4	N	4
4.402	0.115	7.6	L89	KC97c G004.4+00.1	4	F	4
3.294	-0.088	8.7	L89	MSX6C G003.2652-00.1035	4	F	4
1.156	-0.077	-20.6	W83	[KC97c] G001.1-00.1	4	EIG	4
0.597	-0.049	54.9	D80	GAL 000.60-00.05	4	F3	4
0.223	-0.080	16.2	W83	GAL 000.18-00.05			
0.095	0.036	-30.3	D80	GAL 000.09+00.01			
359.663	-0.283	13.6	D80	RCW 137			
353.409	-0.372	-13.1	L89	GRS G353.43 -00.37	4	N	4

Continued on next page

Table 6.1 – continued from previous page

l	b	v	RRL	SIMBAD	§[a]	KDAR[b]	Ref.[a]
353.080	0.335	-4.2		multiple sources			
351.585	0.188	-39.7		multiple sources			
351.188	0.456	-8.8	L89	[L89b] 351.201+00.483		N	Q06
350.107	0.090	-66.3	CH87	GAL 350.13+00.09	5	N	4
348.215	0.468	-12.9	CH87	GAL 348.23+00.46	5	N	CH87
347.619	0.197	-96.3	CH87	GAL 347.60+00.21	5		
345.592	-0.019	-4.7	CH87	GAL 345.56-00.04	5	F	CH87
343.474	-0.023	-27.1	CH87	GAL 343.49-00.03			
340.300	-0.201	-47.0	CH87	GAL 340.28-00.22	5	N	3
338.417	0.091	-34.1	CH87	GAL 338.45+00.06	5	O	3
338.098	-0.200	-56.6	CH87	GAL 338.13-00.17			
338.074	0.004	-44.3	CH87	GAL 338.09+00.01	3	F	3
337.968	-0.153	-53.4	CH87	GAL 338.01-0.12	5		
337.931	-0.465	-41.0	CH87	GAL 337.95-00.48	5	N	3
337.659	-0.060	-50.5	CH87	GAL 337.67-00.05	5	F	3
337.117	-0.177	-73.1	CH87	GAL 337.15-00.18	5	F	3
336.917	-0.171	-75.0	W70	[HHB99] 336.934-0.146	5	F	3
336.814	0.046	-76.7	CH87	GAL 336.84+00.05	5	F	3
336.483	-0.216	-88.3	CH87	GAL 336.49-00.15	5		
336.390	-0.136	-85.2	CH87	GAL 336.38-00.13	5	F	3
333.607	-0.191	-47.1	CH87	SNR G333.6-00.2	5	N	3
333.172	-0.095	-91.9	CH87	GAL 333.17-00.08	5	TP	3
333.156	-0.415	-52.6	CH87	GAL 333.11-00.44	5	N	3
332.152	-0.442	-55.0	CH87	GAL 332.15-00.45	5		
331.532	-0.064	-89.7	CH87	GAL 331.5-00.0	5	TP	3
331.354	-0.014	-84.5	CH87	GAL 331.35-00.01	5		
331.335	-0.341	-66.5	CH87	GAL 331.31-00.34	5	F	3
331.271	-0.185	-80.3	CH87	GAL 331.26-00.19	5	TP	3
331.035	-0.148	-89.4	CH87	GAL 331.03-00.15	5	TP	3
330.872	-0.367	-57.0	CH87	GAL 330.86-00.37	5	N	3
328.306	0.440	-97.0	CH87	GAL 328.31+00.45	5	TP	3
319.384	0.006	-11.8	CH87	GAL 319.38-00.03	5	F	CH87
316.780	-0.058	-37.4	CH87	GAL 316.81-00.04	5	N	CH87
311.916	0.214	-45.1	CH87	GAL 311.92+00.23	5	F	CH87
311.887	0.091	-48.9	CH87	[CG2001] G311.90+0.08	5	F	CH87
307.625	-0.296	-36.6	CH87	GAL 307.62-00.32	5		
305.575	0.025	-41.5	CH87	GAL 305.55-00.01	5	N	CH87
305.264	0.142	-37.2	CH87	GAL 305.36+00.18	5	F	CH87
305.054	0.187	-36.3		multiple sources			
298.860	-0.437	24.0	CH87	GAL 298.87-00.43	5	O	CH87
298.220	-0.337	30.8	CH87	GAL 298.23-00.33	5	O	CH87
291.598	-0.468	11.3		multiple sources			

[a] References: numerical references indicate Chapters in this thesis; W70 = Wilson et al. (1970); D80 = Downes et al. (1980); CH87 = Caswell & Haynes (1987); L89 = Lockman (1989); Q06 = Quireza et al. (2006); AB09 = Anderson & Bania (2009); A12 = Anderson et al. (2012a)

[b] KDAR: N = near side, EIG = extreme inner Galaxy ($R_{gal} < 4$ kpc), TP = tangent point, F = far

side, F3 = associated with Far 3kpc Arm, O = outer Galaxy

6.2 H II Region Candidates

The combination of Caswell & Haynes (1987) and Lockman (1989) catalogues represents the quasi-complete census of reasonably strong 5 GHz radio continuum sources; over 750 regions. However, contemporary H II region candidate catalogs (see §6.2.1) suggested that this number represented less than half the of true population.

Not only have new observing techniques been developed since the 1980s, but our understanding of H II region characteristics has also increased significantly. Unlike light at optical wavelengths, infrared and radio waves can pass through the molecular clouds in which star formation (and therefore H II) is located. As a result, a combination of radio and infrared data can be used to infer the presence of H II regions and characterise H II region candidates. Unfortunately, sensitive all-sky surveys in the infrared regime are difficult to complete at ground based observatories—due to obscuration by, and thermal emission from, the Earth's atmosphere. Therefore a cooled space-based telescope is required. Below, we discuss the criteria for H II region candidacy in terms of chronologically listed generations of infrared satellites.

6.2.1 Infrared Astronomical Satellite (IRAS)

The *Infrared Astronomical Satellite* mission (IRAS Neugebauer et al. 1984) observed the infrared wavelengths 12, 25, 60 and 100 μm over 96% of the sky. The *IRAS* point source catalogue contains flux densities for each wavelength for over 250,000 objects. Hughes & MacLeod (1989) and Wood & Churchwell (1989b) present *IRAS* colour criteria for selecting all H II regions, and those associated with more massive stars, respectively.

6.2.1.1 Hughes & MacLeod Criteria

Hughes & MacLeod (1989) compiled a list, and determined the colours, of *IRAS* sources associated with known H II regions, planetary nebulae and reflection nebulae. The colour criteria for *IRAS* sources associated with known H II regions was reported as:

$$\begin{aligned} \log(F_{60\mu m}/F_{25\mu m}) &\geq 0.0 \\ \log(F_{25\mu m}/F_{12\mu m}) &\geq 0.0 \end{aligned} \tag{6.1}$$

Applying this set of criteria to the entire *IRAS* point source catalogue resulted in 2298 H II region candidates. It was estimated that 77% of these were true H II regions; with the remainder made up of planetary and reflection nebulae, stellar sources, supernova remnants and extragalactic sources. Follow up observations of 82 Hughes & MacLeod selected objects demonstrated that 72% were associated with one or more 5 GHz radio sources, and many possessed known maser activity (at various frequencies, Hughes & MacLeod 1994)—reinforcing the inital confidence interval estimate.

6.2.1.2 Wood-Churchwell Criteria

Combining their own interferometric radio continuum survey and the far infrared point source catalogue of *IRAS*, Wood & Churchwell (1989b) presented observations of 75 H II regions. They reported that these regions could be differentiated from the general *IRAS* Point Source Catalogue using colour criteria, know known as the Wood-Churchwell colour criteria for ultra-compact H II regions:

$$\begin{aligned} \log(F_{60\mu m}/F_{12\mu m}) &\geq 1.3 \\ \log(F_{25\mu m}/F_{12\mu m}) &\geq 0.57 \end{aligned} \tag{6.2}$$

These selection criteria, applied to the whole *IRAS* point source catalogue, resulted in the identification of 1717 OB-type star (H II region) candidates (Wood & Churchwell 1989a). Hughes & MacLeod (1994) report that Hughes & MacLeod candidates that possess associated maser emission (OH, H_2O or CH_3OH) have similar colours to the Wood-Churchwell criteria, and, that candidates with larger $\log(F_{25\mu m}/F_{12\mu m})$ values are more likely to be true H II regions.

6.2.2 Spitzer Space Telescope

Compared to *IRAS*, the *Spitzer Space Telescope* provided improved angular resolution factors of ∼25 (at 8/12 μm) and ∼2 (at 24/25 μm), see Table 2.4. Launched in 2003, the most useful data products that *Spitzer* produced, in terms of H II region candidate selection, are "A 24 and 70 Micron Survey of the Inner Galactic Disk with MIPS" (MIPSGAL, Carey et al. 2009) and the "Galactic Legacy Infrared Midplane Survey Extraordinaire" (GLIMPSE, Benjamin et al. 2003). These two surveys are described in Section 2.3.

It is worth noting that the arrival of these *Spitzer* data products coincided with the release of the IGPS (see §2.0.2); that is, there was a simultaneous 'generation leap' in the radio continuum, H I line, and mid-infrared surveys.

6.2.2.1 MIPSGAL 24 μm and Radio Continuum

Coincident MIPSGAL 24 μm and 20 cm radio continuum emission (from various surveys), form the basis for H II region candidate selection criteria used by both the Green Bank and Arecibo H II Region Discovery Surveys (§2.2). This criterion is enough to establish the thermal nature of the source (Bania et al. 2010, and references therein). Known contaminants (planetary nebulae, luminous blue variables, pulsar wind nebulae and supernova remnants) and known H II regions can be removed from the target sample, through SIMBAD database cross referencing. Using this criterion, the GBT and Arecibo HRDS achieved RRL detection rates of 95% and 58% respectively.

However, the presence of coincident 24 μm and radio continuum emission, in conjunction with a successful RRL detection, is insufficient to distinguish H II regions from planetary nebulae. After an RRL detection, a number of methods can be used to estimate the level of planetary nebulae contamination in a sample. Firstly, the *lv* distribution of the targets can indicate the level of planetary nebulae contamination—while H II regions trace Galactic structure, the old stellar population that gives rise to planetary nebulae have well mixed

orbits. The GBTHRDS sample displays significant Galactic structure (in lv space), and therefore it is assumed that the level of contamination by planetary nebulae is minimal (Bania et al. 2010). Secondly, because of their expansion, planetary nebulae have broader line widths compared to those from H II regions (Anderson et al. 2011b).

In order to further improve H II region candidate selection *before* searching for RRL emission, a further parameter is therefore required to remove (or minimise) the H II region/planetary nebula degeneracy. As shown by Hughes & MacLeod (1989, and others), infrared colours can be used to determine object classifications, with the most robust discriminating colour criterion being $\log(F_{12\mu m}/F_{8\mu m}) < 0.3$ (Anderson et al. 2012b). Unfortunately *Spitzer* does not include a 12 μm band, but incorporating the *Spitzer* GLIMPSE 8 μm data does improve the MIPSGAL/radio continuum H II region candidate criterion.

6.2.2.2 GLIMPSE 8 μm Emission and Bubbles

Emission in the *Spitzer* GLIMPSE 8 μm band can occur as the result of either re-radiated emission from heated dust grains (also seen in thermal emission in the MIPSGAL 24 μm band), or as emission from polycyclic aromatic hydrocarbons (PAHs). PAHs provide an excellent tracer of the photodissociation regions of H II regions as these molecules fluoresce when they absorb ultra-violet radiation. In general, PAH emission from planetary nebulae is weaker than from H II regions. This is especially true for oxygen rich planetary nebula for which the PAH emission is weak or absent completely (further discussed in Anderson et al. 2012b). As a result, coincident 8 μm emission can be added to the above criterion (coincident 24 μm and radio continuum emission of a similar morphology and angular extent) to strengthen the likelihood that a candidate is a true H II region.

Rather than rely on the presence of coindcient 8 μm emission, the GBTHRDS team present a candidate selection criterion based on the mid infrared 'signature' of Galactic H II regions—that for angularly resolved regions, the 24 μm (MIPSGAL) emission is enclosed by, or lies interior to, the 8 μm emission (Anderson et al. 2011b). The reported morphological classification of the GBTHRDS H II regions is based upon the target's appearance at 8.0 μm; these classifications include bubble, partial and irregular bubble, bipolar bubble, compact and point source (see Figure 6.1). There is only one source in the GBTHRDS sample which does not demonstrate 8 μm emission extending beyond the 24 μm emission; G005.756-0.932 demonstrates bubble morphology in both the 8 and 24 μm data and was not detected in any RRL transition by the GBTHRDS.

At least 85% of *Spitzer* GLIMPSE 8 μm "bubbles" contain ionised gas (detected by continuum emission at ∼20 cm) and 98% enclose 24 μm emission (Deharveng et al. 2010). The Churchwell et al. (2006) conclusion that 25% of bubbles coincide with known H II regions was based on pre-GBTHRDS literature. Anderson et al. (2011b) conclude that nearly all GLIMPSE bubbles are H II regions and $\sim$ 50% of H II regions have 8 μm (complete) bubble morphology.

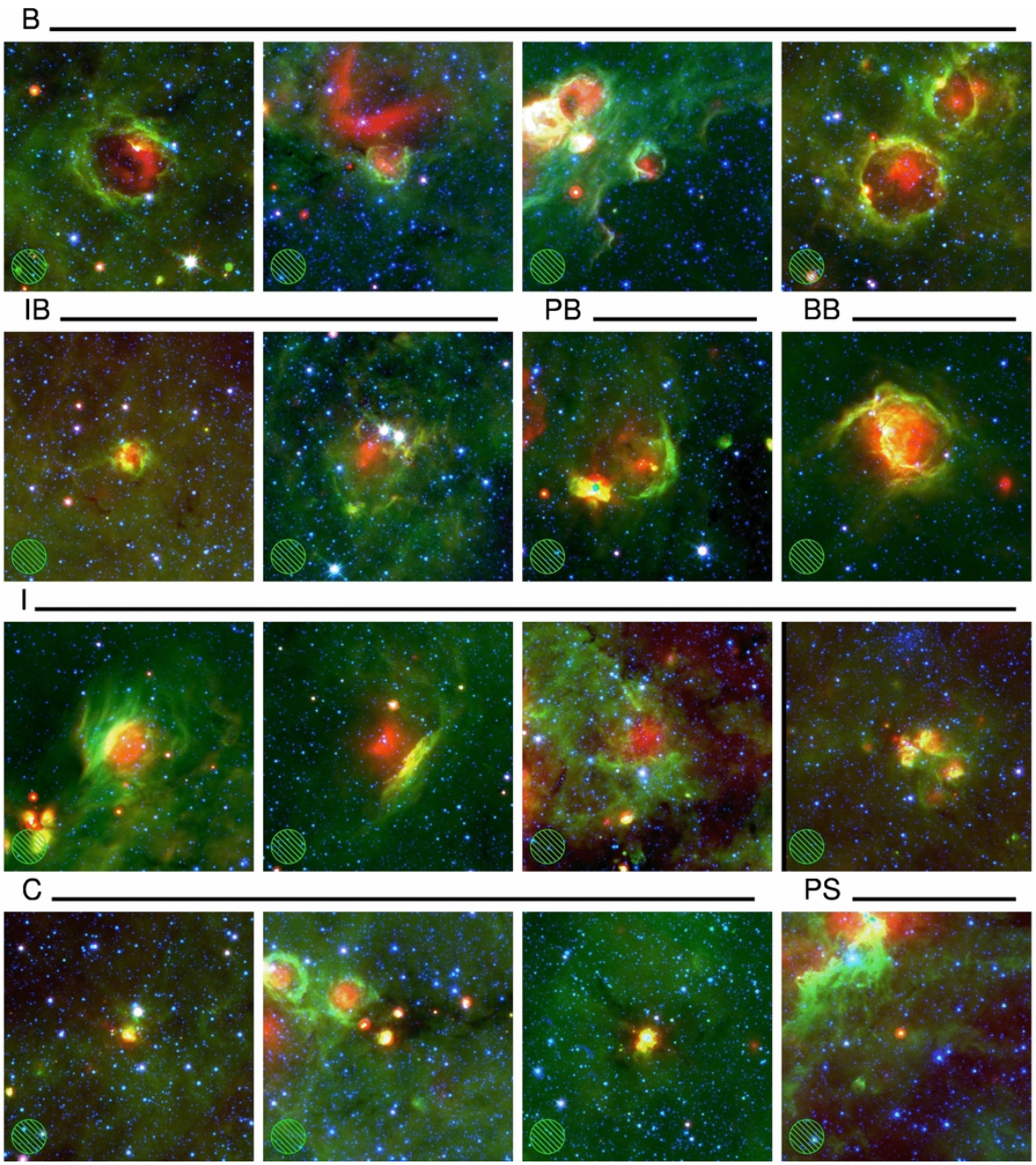

Figure 6.1: Figure 4 from Anderson et al. (2011b). Examples of H II region infrared morphologies from the GBTHRDS. Each panel is 10′square and shows a three-colour image from *Spitzer* 24 μm (red), 8.0 μm (green) and 3.6 μm (blue) data along with the 82″GBT beam. The regions are classified based on their 8.0 μm morphology (which always extends beyond the 24 μm emission). Examples of bubbles (B), irregular bubbles (IB), partial bubbles (PB), broken bubbles (BB), irregular (I) and compact (resolved 8.0 μm emission with no hole in the centre, C) morphologies are shown.

6.2.3 Wide-field Infrared Survey Explorer (WISE)

The angular resolution of the *Spitzer* surveys is finer than for those of the *Wide-field Infrared Survey Explorer (WISE)*, however, GLIMPSE and MIPSGAL are limited in sky coverage (see Table 2.1). Therefore, *WISE* provides the best mid-infrared dataset in which H II region candidates *from the entire Galactic plane* can be selected (Anderson et al. 2014).

The spectral bands of *WISE* differ slightly from those of *Spitzer* (see Table 2.4), but H II regions appear similar in the *WISE* 12 and 22 μm bands, when compared to images created from the *Spitzer* 8 and 24 μm datasets (Anderson et al. 2014). The *WISE* 12 μm band should trace the same dust emission as the *Spitzer* 8 μm band, but will also include PAH features at 7.7, 8.6, 11.2, 12.7 and 16.4 μm (Tielens 2008). The 22/24 μm band-passes are similar between the two telescopes and should trace the same dust emission components (Anderson et al. 2012b, 2014). One major difference between the 22/24 μm band-passes is that the *WISE* 22 μm band saturates for point sources at 12.4 Jy, compared to 2 Jy for the *Spitzer* 24 μm band, and should therefore be less affected by saturation problems (Anderson et al. 2012b).

6.2.4 Current H II Region Candidates

Applying the infrared H II region candidate selection criteria, developed from *Spitzer* data (§6.2.2), to the all-sky data from *WISE* produces the most rigorous catalogue of Galactic H II region candidates currently available (Anderson et al. 2014).

The infrared criteria alone provide $\sim$ 8000 target sources. Approximately 1500 have measured RRL velocities, and are therefore 'known' or confirmed H II regions. Of the remaining candidates, $\sim$ 2500 are coincident with radio continuum emission and a further $\sim$ 500 are positionally associated with known H II region complexes—these 3000 sources therefore have the highest probability of being true H II regions (based on the 95% detection rate of the GBTHRDS). This number may increase if new continuum surveys, beyond the sensitivity limits of existing data, can associate the 'radio quiet' candidates with a continuum source (Anderson et al. 2014).

Compared to the 1980s, the total number of known H II regions has doubled. However, due to the availability of sensitive all-sky surveys and a better understanding of H II region properties, the ratio of credible candidates to known H II regions of the present day is 2:1—the same ratio presented by Lockman (1990a) over two decades ago.

6.3 Preparing for H II Region Discovery Observations

Both existing H II region RRL catalogs, as well as unpublished, untargeted, RRL surveys, have now been exhaustively searched for previously unknown H II regions (see Chapter 5 and Section 6.1, respectively). In order to continue H II region kinematic distance studies in the fourth Galactic quadrant, further (new) H II region discovery, RRL observations must be undertaken.

In preparation for the observations of Chapter 7, the following Sections discuss modern RRL observation methods (Section 6.3.1) and considerations for observing with particular instruments (namely the Australia Telescope Compact Array, Section 6.3.2).

6.3.1 Observing Multiple Hnα Transitions

The line profiles of high-n RRLs are expected to be similar between adjacent lines. Therefore Hnα (or indeed He$n\alpha$ or C$n\alpha$) transitions can be averaged to increase the overall RRL signal to noise ratio. The transitions will be sampled at different velocity resolution (due to differences in frequency), therefore re-sampling onto a common velocity grid is required before the spectra can be averaged (Quireza et al. 2006; Balser 2006).

Simultaneous observations of multiple RRL transitions have been undertaken for many decades. For example, Smirnov et al. (1984) used the 100m Effelsburg telescope, of the Max Planck Institute for Radio Astronomy, to observe pairs of HnΔn transitions ($\Delta n = 1, 2, 3, \ldots \equiv \alpha, \beta, \gamma \ldots$). The individual spectra were added together to increase signal to noise ratios; independent polarisations were also added and averaged to further improve the quality of the overall average spectrum. Receiver upgrades, as forseen by Lockman (1990a), allowed Bell et al. (2000)—who published the data separately as Bell et al. (2011)—to observe HnΔn lines that varied by a factor of 2.7 in n and a factor of 21 in Δn. These studies were primarily concerned with investigating hydrogen to helium abundances, or RRL broadening processes; therefore, while a large number of transitions was observed, the number of target sources was small.

The GBTHRDS is the first study, in recent years, to observe multiple RRL transitions in order to improve signal to noise for the efficiency of discovery. Balser (2006), who was investigating the helium abundance in the outer Galaxy H II region, S206, noticed that eight Hnα transitions (n$= 86 - 93$) could be measured concurrently using the Green Bank Telescope's Auto Correlation Spectrometer (ACS). Unfortunately the H86α line is spectrally compromised by confusing, higher order RRL transitions; nevertheless, the remaining 7 transitions, after re-sampling onto a standard velocity scale and then averaging together, create an extremely sensitive X-band Hnα average spectrum. Wenger et al. (2013) report that the GBTHRDS stacked spectrum represents a factor of five improvement in sensitivity for point sources, compared to the previous most sensitive RRL spectra, taken by Quireza et al. (2006).

	CA02	CA03	CA04	CA05	CA06
CA01	31	77	43	85	4408
CA02		46	31	77	4378
CA03			55	89	4332
CA04				46	4378
CA05					4378

Table 6.2: Spacing between each pair of antennas (m) in the ATCA's H75 configuration. CA06 is fixed in position, and its associated baselines are usually removed from analysis, as the long baselines result in negligable sensitivity.

6.3.2 Considerations for the ATCA

No large–scale H II region discovery surveys have been completed in the fourth quadrant since Caswell & Haynes (1987); a year before the Australia Telescope Compact Array (ATCA) was opened. The ATCA, at the Paul Wild Observatory, is a radio interferometer consisting of six 22m antennas (Frater et al. 1992). Five antennas (CA01 to CA05) can be driven along a 3 km east–west track and 215m north–south spur. The final antenna, CA06, is fixed in position; 3 km from the west end of the track.

The ATCA offers seven 'standard' array configurations, ranging in characteristic baseline length from 75 m (see Table 6.2) to 6 km. The H75m array is the preferred array configuration for confirmation of WISE candidate (Anderson et al. 2014) regions as this configuration is sensitive to emission at the extended scales of H II regions. Baselines to CA06 are therefore excluded from analysis, as the extended emission will be resolved out. The remaining five antennas that make up the H75m configuration provide a synthesised beam size of approximately 105 square arcseconds at 6 GHz, and 65 square arcseconds at 10 GHz—comparable to the most recent RRL surveys of the northern hemisphere (see Table 2.2), and it is the preferred array configuration for confirmation of WISE candidate (Anderson et al. 2014) regions.

6.3.2.1 CABB

Installed in March-April of 2008, the Compact Array Broadband Backend (CABB, Wilson et al. 2011) increased the ATCA's maximum bandwidth from 128 MHz to 2 GHz in each of two, dual polarisation, tuneable intermediate frequency (IF) bands. CABB's C/X (3/6cm) upgrade replaced the previous 3 and 6cm bands with a single 4 cm (4.0-10.8 GHz) band—within which the two 2GHz IFs can be placed. Each 2 GHz (technically 2048 MHz) IF can be split into 2048, 512, 128 or 32 primary channels.

In addition to increased correlator efficiency (lower system temperatures) and digitization levels; CABB also provides "zoom" windows. Up to sixteen of these high velocity resolution windows can be placed in each IF, such that each 2048 channel zoom window corresponds to the width of one 'continuum channel' in the primary IF band. These zoom modes allow for simultaneous observations of multiple spectral lines with fine velocity resolution.

For observation of multiple RRLS, the most useful CABB mode is CFB 64M-32k. The mode provides a bandwidth of 2 GHz with 32 × 64 MHz channels and an optional fine resolution of 32 kHz (2048 channels across 64 MHz) in up to 16 zoom bands *in each IF band*. The CFB 64M-32k observing mode was first made available in the APR2013 semester. Each zoom band is the width of a single channel in the basic 2 GHz spectrum and must be separated from other zoom bands by any integral multiple of half the zoom band width[*]. Sampler birdies are located at 25%, 50% and 75% of the 2048 MHz span, and as such the zooms should not be placed in these locations.

[*] this even allows for the zoom bands to be overlapped and concatenated, resulting in a single, 'wider', zoom facility. But we do not implement this feature here.

Within the 4cm band, centering the two IFs at 9550 and 7350 MHz allows 15 Hnα RRLs to be observed simultaneously between $6-10$ GHz. The H90α transition may be affected by a trapped mode in the ATCA'S 6/3cm horn and, as previously discussed, the H86α suffers from spectral confusion, resulting in 13 non-compromised RRLs. Stacking these 13 transitions provides a factor of $\sqrt{13} \approx 3.5$ improvement in sensitivity. Binning in groups of ~ 5 velocity channels will result in further sensitivity improvement and provide a final average/stacked spectrum velocity resolution of $\sim$ 5km s^{-1}; which allows for the RRLs (which have a typical FWHM of $\sim$ 20km s^{-1}) to be spectrally resolved. This reduction method, that CABB uniquely allows for the southern sky, results in a factor of $\sim$8 improvement in sensitivity. These observations, and their results, are discussed in Chapter 7.

In a second epoch of ATCA observations, C2963 in July 2014, we altered the placement of the two continuum IFs and zoom bands in order to observe 24 simultaneous RRL transitions between $4-8$ GHz. These two epochs of observation are discussed in the next Chapter.

The combination of CABB's zoom capability and the ATCA's compact, hybrid congifurations (which increase surface brightness sensitivity) creates an instrument that is unriveled for H II region discovery potential in the Southern sky.

Chapter 7

Discovery of H II Regions in the Southern Sky

The two ATCA observation projects discussed in this Chapter serve as a 'proof of concept', and more formally, Pilot Study, for a Southern H II Region Discovery Survey. The Candidate, Courtney Brown (nee Jones), is the Principal Investigator for both projects.

Project C2842 requested twenty-four hours with the H75m array configuration of the ATCA during the April 2013 semester. Project C2963 provided a further 24 hours, in the April 2014 semester, again with the H75m configuration. The purpose of both projects was to carry out simultaneous observations of multiple RRL transitions—which would then be stacked to increase signal to noise—for the purpose of H II region discovery. However, there are differences in the observed longitude range, and candidate selection process between the two projects.

7.1 Source Selection

Candidates for both observation epochs were chosen from the WISE catalogue of H II region candidates (Anderson et al. 2014, see Section 6.2.4). This catalogue was unpublished during preparations for C2482 and a list of potential candidates (from the catalogue) was provided by Loren Anderson via private communication.

Specific candidate selection criteria, for each observation epoch, are desribed below.

7.1.1 C2842

For the first round of observations, we decided to investigate H II region candidates in the longitude range $312^\circ < l < 328^\circ$. This is a particularly interesting part of the fourth Galactic quadrant as it avoids non-circular motions caused by the end of the bar, but provides lines of sight along the Norma-Cygnus and Scutum-Crux arms, in the inner Galaxy, and perpendicular to the Scutum-Centaurus and Sagittarius Arms, in the outer Galaxy.

A sub-set of $\sim$ 100 H II region candidates from the as yet unpublished *WISE* Catalog

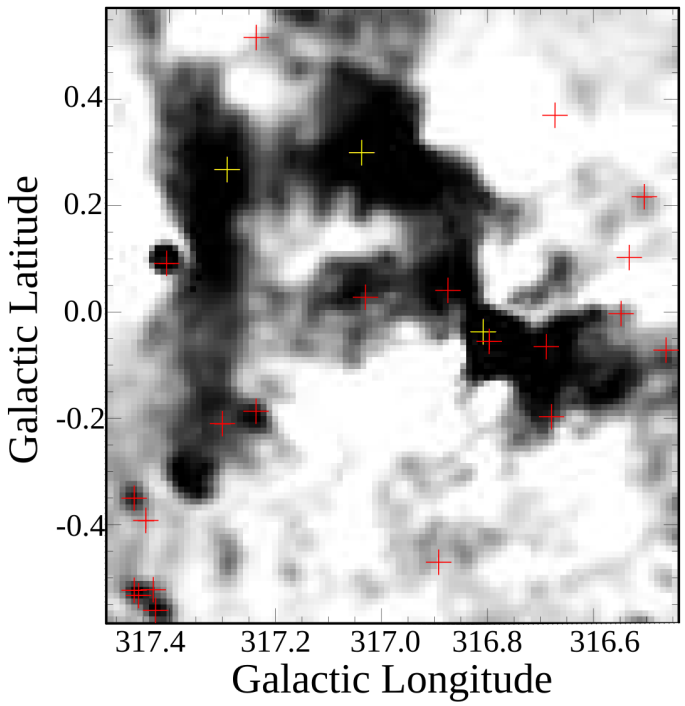

Figure 7.1: A small segment of the SGPS continuum map (T>10 K, $l \approx 317°$, $b \approx 0°$) overlaid with H II regions from Chapter 5 (yellow crosses) and candidates from Anderson et al. (2014), red crosses. Note that some continuum sources are associated with several candidates, and other candidates are associated with continuum emission that was not detected by the SGPS.

of H II region candidates (Anderson et al. 2014) was provided by Loren Anderson*. These candidates were then overlaid on the SGPS continuum maps and visually inspected (see Figure 7.1).

H II region candidates were selected for observation if they were visible in the continuum maps of the SGPS. The availability of the associated SGPS H I data allows for emission and absorption spectra to be extracted (as per Chapter 5), and therefore a KDAR to be attempted (see Section 7.4.4).

Figure 7.2 describes the analysis process, from selection of H II region candidates to unambiguous line of sight distance. As H I data is available for each of the C2842 obseration targets, the detection of RRL velocities are the *only new* data required to attempt KDARs.

Upon visual inspection of the SGPS continuum maps, see Figure 7.1, twenty-two candidate regions were confirmed as single, distinct, sources with brightness temperatures > 4 K. These twenty-two candidate H II regions form the basis of our observations. In addition to these 22 candidates, two known H II regions *GAL 315.31-00.27* and *GAL 327.30-00.60*, both from the Caswell & Haynes (1987) catalogue, were included in the observation schedule.

Despite being listed as candidate regions by Anderson et al. (2014) (i.e. with no known RRL velocity), two sources (G313.790+00.706 and G323.464-00.079) were observed in RRL transitions by Misanovic et al. (2002) and are therefore "known" H II regions. These previous RRL detections were discovered after observations had taken place. Therefore the C2842 observation sample included 20 H II region candidates and 4 known H II regions.

*The total number of candidate regions in Anderson et al. (2014) between $312° < l < 328°$ is 201. There are also 62 known H II regions in this longitude range.

Individual source descriptions, providing a summary of the literature for each target can be found in Appendix B.1.

7.1.2 C2963

As with C2842, the candidates for C2963 were selected from (the published version of) the WISE H II region candidate catalogue (Anderson et al. 2014). Unlike the previous observations, the limit on observed longitude range ($213^\circ < l < 301^\circ$) resulted from the LST range of our scheduled telescope time. This presented an excellent opportunity to explore H II regions in the outer Galaxy, as the majority of the Galactic volume between $213^\circ < l < 301^\circ$ is beyond the Solar Circle. Hence any H II regions discovered during these observations will intrinsically have galactocentric radii $\gtrsim 8.5$ kpc—even if the line of sight distance to the region is small—currently only 15.6% of known H II regions are located in the outer Galaxy.

This longitude range is also relatively poorly studied—there are fewer than 100 known H II regions between $213^\circ < l < 301^\circ$. Therefore the discovery of even a modest number of H II regions will significantly increase our understanding of this part of the Milky Way—including tracing the Sagittarius Arm in the outer Galaxy and connecting known features at the boundary of Galactic quadrants III and IV.

Candidates were selected if they had no known velocity information—either RRL or molecular velocities, as reported by Anderson et al. (2014)—and were a 'typical' size for candidates in the catalogue (WISE radii between $60'' - 150''$). We selected all thirty-three H II region candidates between $213^\circ < l < 240^\circ$ and $290^\circ < l < 300^\circ$ that fulfilled these criteria. This selection process acts as a 'typical' representative sample from Anderson et al. (2014) and therefore is an excellent target list for the purpose of a Southern H II Region Discovery Survey Pilot Study.

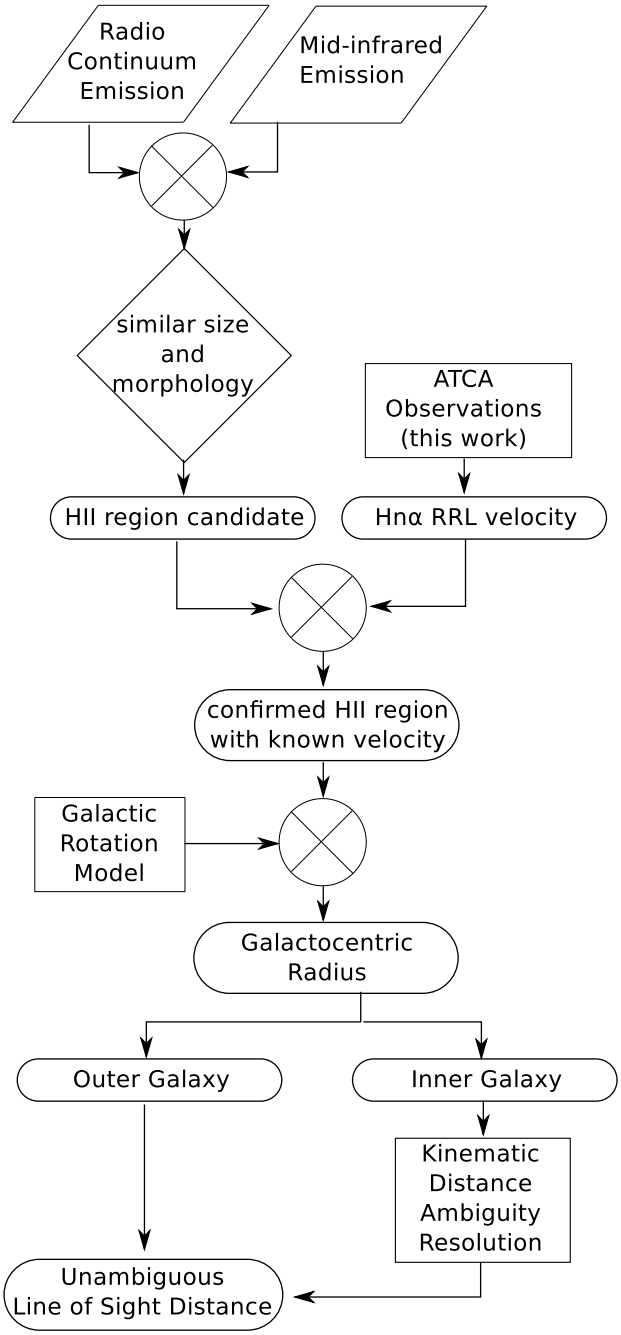

Figure 7.2: A flowchart demonstrating the process of H II region identification through to a calculated unambiguous line of sight distance. The work of Anderson et al. (2014) is represented by the upper left branch; while the observations of this Chapter are represented by the upper right branch. Previous Chapters have relied on catalogues of known H II regions and therefore have performed analysis based on the lower section only.

7.2 Observations

The observation strategy for both C2842 and C2963 was identical—*except* that the observed RRL transitions differ (see Tables 7.1 and 7.2). Both observation epochs were conducted on the ATCA, in the H75m configuration (see Table 6.2); with each epoch consisting of two twelve-hour blocks.

All observations included at least 13 simultaneous RRL transitions, which can then be averaged (after re-sampling onto a common velocity scale) to significantly increase the RRL signal-to-noise ratio (as detailed by Balser 2006). Figure 7.3 presents a graphical schematic of the frequency set-up for both observation epochs. Each project used 1934-638 as a flux calibrator and phase calibration was performed every ∼20 minutes. Each source was observed in several (typically 6-8) *uv* cuts over the twelve hours.

In each case the CABB schedules were prepared by myself. The specifications of the ATCA's CABB system are described in Chapter 6; including the details of the two compromised RRL transitions, H86α and H90α, which were not included in the analysis of this Chapter. The specific details of each project's observation parameters are below.

7.2.1 C2842

Observations were performed by Chris Jordan (a fellow PhD candidate at the University of Tasmania), John Dickey and I, remotely from the University of Tasmania, on June 30 and July 1, 2013, in two blocks of twelve hours. For these observations, 1934-638 was used as both a flux and bandpass calibrator and a single phase calibrator, 1421-490, was chosen. As each target was successfully detected, the observed source list appears in the table of results, Table 7.4.

Centering the 2GHz CABB bands at 7000 MHz and 9900 MHz allows for thirteen Hnα RRLs to be observed *simultaneously*, see Table 7.1. This choice includes three of the RRL transitions observed by the GBTHRDS, and an additional ten transitions.

7.2.2 C2963

Observations were performed by Chris Jordan, who was located at the ATCA, on July 26 and 27, 2014; again in two lots of twelve hours. The target list appears as Table 7.3.

The frequency set up was slightly different to C2842 in that the centres of the two broadband IFs were moved to 5000 and 7100 MHz in order to simultaneously observe a greater number of RRL transitions—fifteen in the lower band and ten in the higher band—see Table 7.2.

Hnα $n =$	ν rest MHz	ν central MHz	ΔV km s^{-1}
85	10522.04	10508	0.9
87	9816.864	9804	1.0
88	9487.821	9484	1.0
89	9173.321	9164	1.0
94	7792.871	7800	1.2
95	7550.614	7544	1.2
96	7318.296	7320	1.3
97	7095.411	7096	1.3
98	6881.486	6872	1.4
99	6676.076	6680	1.4
100	6478.760	6488	1.4
101	6289.144	6296	1.5
102	6106.855	6104	1.5

Table 7.1: Hnα transition and rest frequency, alongside the central frequency and velocity resolution of the 32 kHz zoom band for observations performed in 2013.

Hnα $n =$	ν rest MHz	ν central MHz	ΔV km s^{-1}	Hnα $n =$	ν rest MHz	ν central MHz	ΔV km s^{-1}
93	8045.603	8060	1.2	103	5931.544	5928	1.6
94	7792.871	7804	1.2	104	5762.88	5768	1.6
95	7550.614	7548	1.2	105	5600.55	5608	1.7
96	7318.296	7324	1.3	106	5444.26	5448	1.7
97	7095.411	7100	1.3	107	5293.732	5288	1.8
98	6881.486	6876	1.4	108	5148.703	5160	1.8
99	6676.076	6684	1.4	109	5008.923	5000	1.9
100	6478.76	6492	1.4	110	4874.157	4872	1.9
101	6289.144	6300	1.5	111	4744.776	4744	2.0
102	6106.855	6108	1.5	112	4618.789	4616	2.0
				113	4497.776	4488	2.1
				114	4380.954	4392	2.1
				115	4268.142	4264	2.2
				116	4159.171	4168	2.2
				117	4053.878	4040	2.3

Table 7.2: Hnα transition and rest frequency, alongside the central frequency and velocity resolution of the 32 kHz zoom band for observations performed in 2014.

Day 1		Day 2	
g213.833+00.618	g291.596-00.239	g230.354-00.597	g297.248-00.754
g214.250-02.461	g292.722+00.157	g237.232-01.066	g300.519-00.409
g217.497-00.008	g292.889-00.831	g295.275-00.255	g234.762-00.277
g217.640-00.057	g293.483-00.903	g298.669+00.064	*g294.656-00.438*
g222.096-01.981	g293.936-00.873	g234.267-01.496	g297.626-00.906
g222.159-02.163	g293.994-00.934	g237.257-01.281	g300.972+00.994
g290.012-00.867	*g294.656-00.438*	g295.748-00.207	g235.696-01.243
g290.323-02.984	*g294.988-00.538*	g299.505+00.025	*g294.988-00.538*
g290.385-01.042		g234.673-00.243	g298.473+00.104
g290.674-00.133		g239.332-02.738	g300.983+01.117

Table 7.3: Target H II Region Candidates for C2963. Sources that were observed both days are emphasised.

As with C2842, 1934-638 was used as the flux calibration source. Other calibration sources are as follows:

- *bandpass calibration:* 1934-638 was observed for the dual purpose of flux and bandpass calibration. However, a secondary bandpass calibration source was also observed — 0823-500 on day 1 (July 26) and 0537-441 on day 2 (July 27).
- *phase calibration:* as the target H II region candidates fell into two longitude groups ($l \approx 220°$ and $l \approx 295°$) two phase calibration sources were chosen each day: 0723-008 and 1129-58 on day 1 and 0727-115 and 1148-671 on day 2.

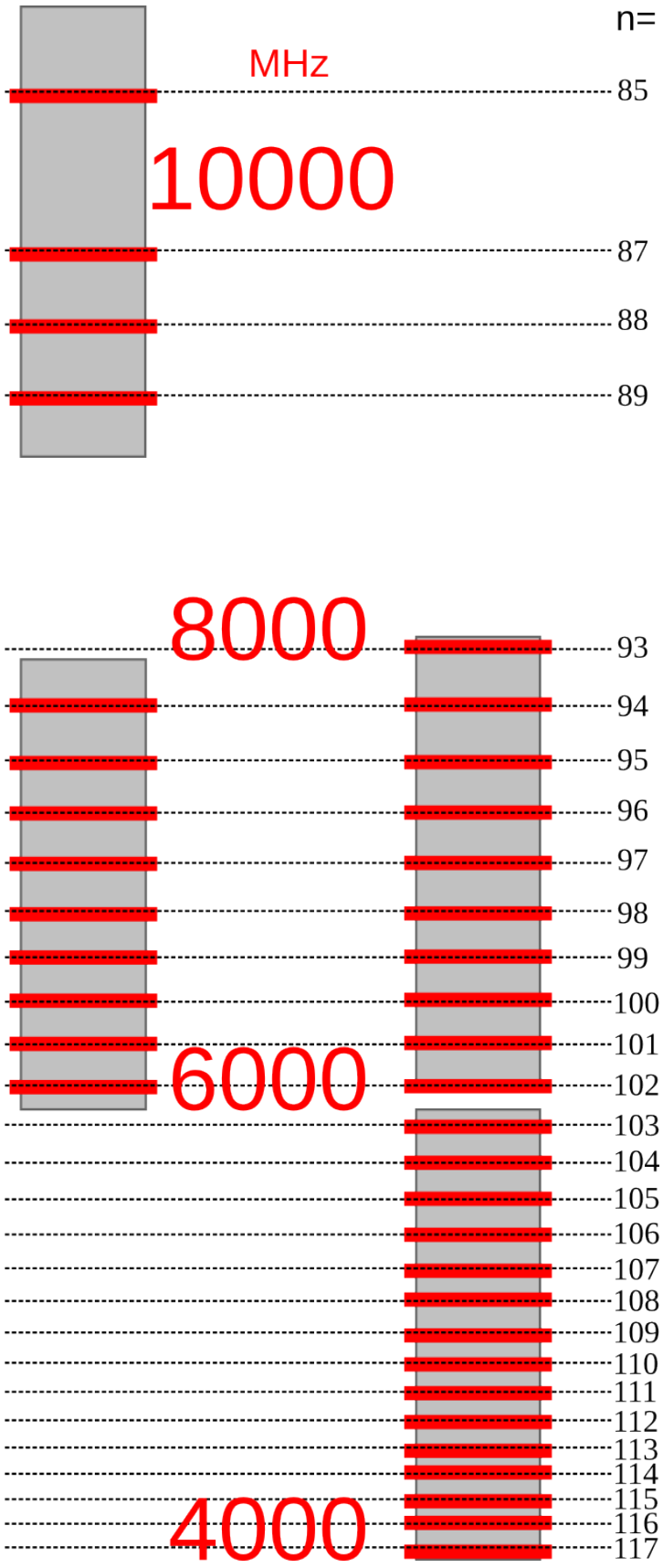

Figure 7.3: Schematic of CABB zooms for C2862 (left) and C2963 (right). A frequency scale, from 4,000 to 10,000 MHz is shown in red and each observed Hnα line is labeled. For each observation epoch, the chosen zoom bands (red) are positioned within the two 2 GHz continuum bands (grey) .

7.3 Data Reduction

A similar, standard MIRIAD (Sault et al. 1995), data reduction process was used for both observation epochs, allowing the development of a data reduction 'pipeline' for any future Southern H II Region Discovery Survey.

For each zoom band, the data are transferred into Miriad format (using the *atlod* task) implementing automatic flagging of channels which suffer from known interference or CABB self-interference. The task *qvack* is used to flag the first six seconds of data at the start of each new source (this ensures that data are flagged where the telescope may not have had time to settle correctly). The data for each source are then extracted through *uvsplit*, removing all baselines to antenna 6, before the data are flagged. Each source (including calibrators) is interactively flagged through inspection of visibilities (i.e., amplitude vs time) in each of the stokes parameters *xx, yy, xy, yx, i, q, u, v* using *blflag*.

Calibration corrections for the flux calibrator are determined through *mfcal* and then copied to the bandpass (if the flux and bandpass calibrators differ) and phase calibrators with *gpcopy*. *Gpcal* is then implemented to determine the gain and phase calibration corrections—the polirisation leakage characteristics are ignored. Gain, flux and phase corrections are then applied to the entire source list (*gpboot*, *mfboot*, *gpcopy*).

We extract the RRL spectrum for each source (per zoom) from the time averaged spectrum of the visibility dataset (*uvspec*). For C2842, the average transition spectrium is weighted, per baseline, by continuum flux. However, no weighting is implemented for the C2963 reductions so far. This individual transition spectrum is then recorded for use in calculating the combined <H$n\alpha$> spectrum for each source, see Section 7.3.3.

Data reduction for C2842 was performed by John Dickey. That process was streamlined and modified by Chris Jordan for the C2963 observations. All further analysis (below) was performed by myself.

Any specific considerations for each project's data reduction are detailed below.

7.3.1 C2842

Only the second 12 hour block of observations were reduced for analysis so far. This was sufficient for detections from *every* target source, including statistically significant detections of over 75% of the individual transitions—such that stacking and averaging the transitions was not required for the purpose of H II region discovery.

7.3.2 C2963

The data reduction process for C2963 is still under way. At present four zoom bands from the first twelve-hour block (H$n\alpha$ for n =93,94,95 and 103) and two zooms from the second block of observations (H$n\alpha$ for n =93 and 94) have been reduced—Day 1 and Day 2 reductions, and flagging, were performed by myself and Chris Jordan, respectively. The <H$n\alpha$> spectra are

of sufficient signal for detection of, and therefore discovery of, eight H II regions. We expect as more zooms are reduced, increasing the signal in the <Hnα> spectrum, more discoveries will ensue.

7.3.3 Calculating the average RRL spectrum, <Hnα>

The spectrum averaging procedure was identical for both C2842 and C2963. First, the individual RRL transition (zoom band) spectra were re-grided to a common velocity scale, corresponding to the coarsest raw velocity resolution in the sample ($\Delta V \approx 2$ km s^{-1}, see Tables 7.1 amd 7.2).

No smoothing was performed to account for the difference in synthesised beam FWHM. For C2842 the range of synthesised beam sizes is $\sim$ 104 square arcseconds (for the zoom band covering H85α) to $\sim$ 127 square arcseconds (for the H102α zoom). As the range of observed frequencies for C2963 is extended, compared to C2842, the resulting range of synthesised beam FWHMs is also wider (from $\sim$ 79 square arcseconds for the H93α zoom and $\sim$ 175 arcseconds for the H117α zoom). The GBTHRDS did not scale to a common beam size—which varied by 20% (Anderson et al. 2011b), about the same as our beam range for C2842. Based on comparisons between the GBTHRDS and Quireza et al. (2006) studies, Balser (2006) notes that the detected RRL velocity is not altered by differences in beam size.

These spectra can be seen as the top panel of each figure in Figure 7.9—for most of the C2842 targets, the RRL can be identified 'by eye' in several of the individual transitions. The spectra from each RRL transition were then averaged, for each velocity channel. The contribution to the average RRL spectrum (<Hnα>) from each transition is weighted by that transition's continuum flux. At this stage, individual zooms which weakened the average spectrum's signal to noise were removed from analysis. These removed spectra appear in red in the top panel of each figure in Figure 7.9, and were not included in the final <Hnα> spectrum (the second panel in each figure of Figure 7.9).

7.3.4 Calculating Line Parameters

A Gaussian fit was applied to each <Hnα> spectrum, see the dotted line in second panel of each figure in Figure 7.9. From this fit, the RRL velocity and FWHM were calculated. For the regions observed in C2842, the transitions were detected in each zoom—such that the velocity, FWHM, line and continuum flux, as well as electron temperature could be calculated for each RRL. These are shown in the lower left panel of each figure in Figure 7.9.

For each source, the line parameters listed in Table 7.4 are derived from the <Hnα> spectrum, *except* for the (frequency dependent) electron temperature, which is derived from the average electron temperature in each transition. A discussion of each line parameter can be found in Section 7.4.

7.4 Results

The individual results from each observing project are detailed in Sections 7.4.1 and 7.4.2 before the properties of the H II region sample are discussed (Section 7.4.3).

7.4.1 C2842

A total of 240 RRL transitions were independently detected from the 24 observation targets—twenty of these are confirmed as H II regions for the first time. On average, of the thirteen RRL transitions simultaneously observed, 12 RRLs were independently detected from each source—the minimum was 8 transitions, see Table 7.4. For previously identified H II regions, the derived parameters are consistent with previous RRL detections. In the case of candidate regions, successful RRL detections confirm the targets as H II regions.

WISE Name	$V \pm \sigma$ km s^{-1}		$\Delta V \pm \sigma$ km s^{-1}		$T_e \pm \sigma$ K		SNR	RRL known?	Other known?	Rgal kpc	QF	KDAR	Dlos kpc
313.671 − 00.105	−54.1	0.9	22.4	0.9	6760	80	15	N	Y	6.5	E	TP*	5.9
313.790 + 00.706	−56.5	0.7	22.8	0.7	6980	10	17	Y	Y	6.5	A	TP	5.9
314.219 + 00.344	−62.9	0.4	21.0	0.4	6310	120	28	N	N	6.2	D	TP	5.9
315.312 − 00.273	+14.7	1.2	25.0	1.2	7630	150	10	Y	Y	10.5	D	O*	13.3
316.516 − 00.600	−45.5	0.6	19.5	0.6	6140	70	22	N	N	6.8	E	?	-
317.861 + 00.160	+1.1	0.5	23.6	0.5	7460	120	32	N	Y	9.3	C	O	12.7
318.248 + 00.151	−39.6	1.1	19.5	1.1	6180	120	10	N	N	7.0	D	?	-
319.229 + 00.225	−66.3	1.4	25.1	1.4	6760	120	9	N	N	5.9	E	TP	6.4
323.449 + 00.095	−74.6	1.0	21.5	1.0	6120	80	12	N	Y	5.5	E	TP*	6.8
323.464 − 00.079	−68.6	1.0	35.4	1.0	11100	100	26	Y	Y	5.6	E	TP	6.8
323.743 − 00.249	−47.6	0.5	19.6	0.5	6020	80	21	N	Y	6.4	E	?*	-
323.806 + 00.020	−59.2	0.7	25.1	0.7	6870	110	19	N	N	5.9	C	?	> 3.7
323.936 − 00.037	−52.9	2.6	26.3	2.6	5060	140	6	N	N	6.2	E	?	-
324.642 − 00.321	−48.5	0.9	23.2	0.9	7000	120	10	N	N	6.3	C	F	10.9
325.108 + 00.054	−67.7	1.6	20.8	1.6	6650	110	7	N	Y	5.6	E	?	-
325.354 − 00.035	−61.8	1.1	30.1	1.1	7020	100	12	N	N	5.8	E	?	-
326.721 + 00.773	−40.2	0.7	22.3	0.7	6510	160	15	N	Y	6.6	D	N*	2.5
326.890 − 00.277	−44.7	0.4	18.8	0.4	6350	120	28	N	Y	6.4	E	F	> 11.3
326.916 − 01.100	−49.6	1.0	21.9	1.0	6040	100	12	N	Y	6.1	E	?	-
327.313 − 00.536	−49.3	0.4	29.6	0.4	6210	60	39	Y	Y	6.1	A	N*	3.1
327.401 + 00.484	−77.4	1.3	19.7	1.3	6280	130	10	N	Y	5.1	D	TP	7.2
327.555 − 00.829	−37.6	1.9	22.4	2.0	7140	210	6	N	Y	6.7	D	?	-
327.714 + 00.576	−48.5	1.3	24.1	1.3	5860	80	9	N	N	6.2	E	?	-
327.763 − 00.163	−92.9	0.9	21.6	0.9	7180	130	12	N	N	4.7	D	TP	7.2

Table 7.4: Overview of the 24 H II regions observed during C2842. The WISE Name (Anderson et al. 2014), LSR velocity with error (km s^{-1}), line width with error (km s^{-1}), electron temperature of the region with error (K) and signal to noise ratio of the final stacked RRL spectrum are reported. In addition, we report if this paper marks the first instance of the source being confirmed as an H II region (by way of RRL detection), as well as whether other source velocities (maser or molecular line) are known. Finally we report the galactocentric radius (kpc), Quality Factor of the H I absorption spectrum (see rating scheme in Brown et al. 2014), the KDAR (N=Near, TP=Tangent Point, F=Far, O=Outer) and line of sight distance (kpc) for each source. Sources with previously known KDARs are marked with *.

7.4.1.1 Comparison to Previous Velocity Detections

Several of our observational targets are known H II regions, with previously detected RRLs. These targets can be used to confirm the calibration of our observations, and in each case, our

observations extend the number of observed RRL transitions for each region. Other targets have been observed in molecular lines. A comparison between the RRL velocities observed in this work, and previously detected velocities, appears in Figure 7.4. The "90 GHz" tracers are sourced from the MALT90 Survey (Foster et al. 2011; Jackson et al. 2013) and include N_2H^+, HNC, HCO^+, HCN, C_2H, SiO, $H^{13}CO^+$ and $H^{13}CN$. The other molecular tracers include observations of several transitions. These are all detailed in Appendix B.1.

For a single, isolated, star formation region, the theoretical velocity difference between gas traced by RRLs and molecular lines should be small (< 10 km s^{-1}, Immer et al. 2014). For the total sample of previously detected velocities in Figure 7.4, the average $\Delta V_{(\mathrm{RRL\text{-}other})} = 0.2 \pm 5.6$ km s^{-1}, and the absolute difference is always < 13 km s^{-1}. This compares well to the mean absolute difference between the molecular and ionized gas velocities of Anderson et al. (2014), 3.1 ± 2.3 km s^{-1}. On average, our RRL observations are closest to previous Hnα detections with residuals of 1.5 ± 1.0 km s^{-1}; see Figure 7.4.

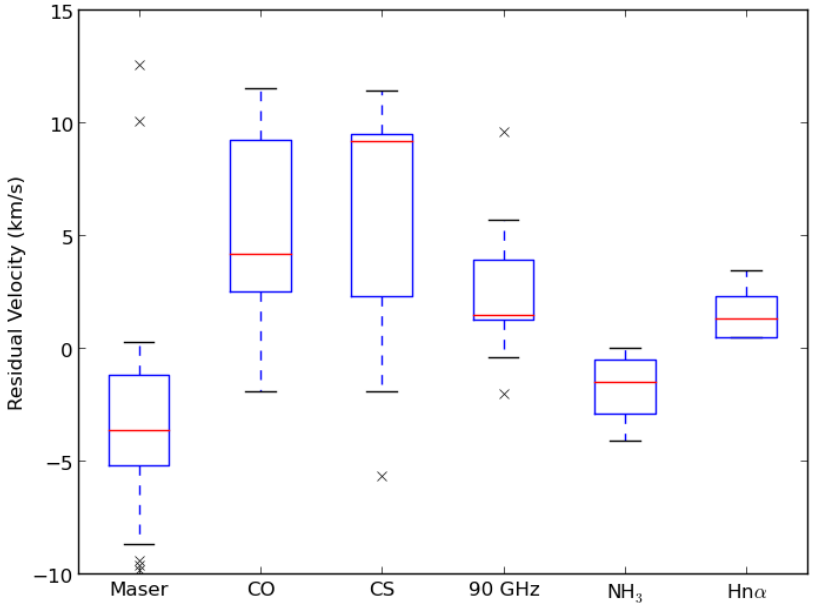

Figure 7.4: A box and whisker plot of the residual velocities between RRL detections from this work and previously detected velocities. Maser velocities are mostly associated methanol and OH masers from Green et al. (2012) or Caswell (1998), while the '90 GHz' tracers are sourced from the MALT90 Pilot survey—these previous detections are detailed for each region in Appendix B.1.

7.4.2 C2963

The results from C2963 are preliminary, as data reduction and analysis is still underway. However the reduction and analysis of a small number of zoom bands is sufficient to detect RRL emission from eight H II region candidates—confirming their categorisation as *bona fide* H II regions for the first time.

The uncertainty in the results of Table 7.5 should improve as more transitions are added to the <Hnα> spectrum. Note that the electron temperatures reported in Table 7.5 are

calculated from the <Hnα> spectrum, rather than a fit to the electron temperature calculated from each individual transition (as was performed for C2842). This is due to the fact that the number of individual transitions reduced is low $(2-4)$ and the lines may not be detectable in the individual RRL spectra.

WISE Name	V	$\pm\sigma$	ΔV	$\pm\sigma$	SNR	T_e	$\pm\sigma$	R_{gal}	KDAR	Dlos
	km s^{-1}		km s^{-1}			km s^{-1}		kpc		kpc
$293.936-00.873$	30.1	11.1	33.4	11.3	0.6	10900	700	9.8	O	8.9
$293.994-00.934$	48.3	2.9	25.0	3.0	3.2	8900	500	10.5	O	10.1
$294.998-00.538$	39.6	8.5	25.3	8.7	1.9	10900	400	10.2	O	9.8
$295.748-00.207$	17.9	7.7	14.9	7.8	2.0	8800	500	9.3	O	8.9
$297.248-00.754$	21.1	18.5	31.0	18.8	3.7	7200	700	9.4	O	9.5
$297.626-00.906$	29.1	13.5	24.4	13.7	2.5	7700	700	9.8	O	10.2
$298.473+00.104$	27.2	9.7	22.0	9.8	1.6	9400	500	9.7	O	10.2
$300.983+01.117$	-36.8	18.4	14.6	18.6	5.6	7100	1000	10.6	-	-

Table 7.5: Preliminary results from C2963. The magnitude of uncertainty will decrease as more transitions are added to the <Hnα> spectrum. Column headings are the same as Table 7.4.

7.4.3 Properties of Observed H II Regions

7.4.3.1 Velocity Widths of Detected RRLs

The velocity width of H II region RRLs is typically $\sim$ 25km s^{-1}. Since this is considerably broader than the $\sim$ 10km s^{-1} line width derived purely from the $\sim 10,000$K H II plasma; turbulent and ordered motions act to broaden the line (discussed in Anderson et al. 2011b). The reported velocity full-width-half-maximum (see Tables 7.4 and 7.5) is obtained from a Gaussian fit to the stacked spectrum - however the FWHM values obtained for each individual RRL transition for C2842 sources are shown in Figure 7.9.

Figure 7.5 displays the velocity line width distribution for the 28 detected H II regions from our observations (solid histogram) and the H II regions from Caswell & Haynes (1987, shown as the dashed histogram). The distribution from our observations favours slightly narrower line widths than that of Caswell & Haynes (1987) with mean $\pm$ standard deviation of 21.5 ± 5.8 and 27.3 ± 6.7 km s^{-1} respectively.

A similar difference in line width distributions was found between the northern hemisphere GBTHRDS and Lockman (1989) RRL surveys. The GBTHRDS team compared the two northern hemisphere works with a two-sided asymptotic Kolmogorov-Smirnov test; determining the two distributions are statistically distinct. The same test, applied to the FWHM distributions of our observations, and the Caswell & Haynes (1987) line widths, determines that the two southern hemisphere distributions are also statistically distinct (see Figure 7.5). In the northern hemisphere, this difference was attributed to the smaller spectral resolution and smaller beam size of the more recent survey (Anderson et al. 2011b). The same arguments could be applied to the differences between this work and Caswell & Haynes (1987)—however, for the two common H II regions (*GAL 315.31-00.27* and *GAL 327.30-00.60*), the values of ΔV from the ATCA <Hnα> spectra are wider than the line widths reported by Caswell &

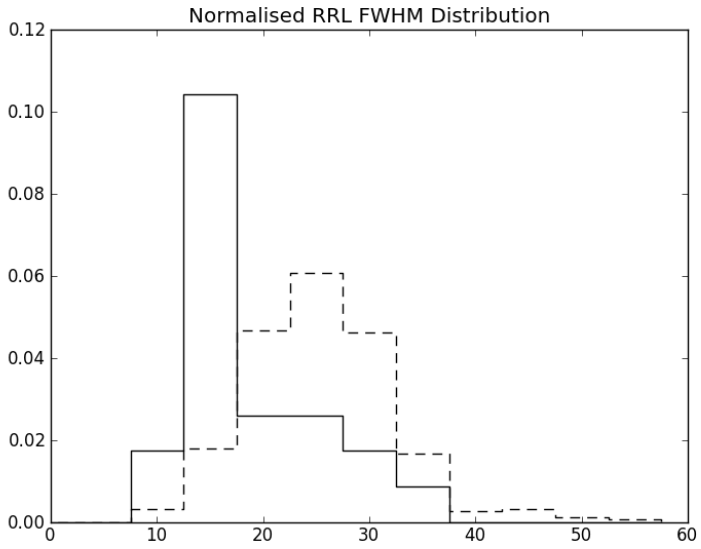

Figure 7.5: The RRL velocity line width distribution from C2842: solid histogram, and regions from Caswell & Haynes (1987): dashed histogram.

Haynes (1987). We will continue to refine the RRL velocity width distribution as we increase our sample size (after reduction and analysis of C2963).

7.4.4 Galactic Distribution of H II Regions

The longitude-velocity (lv) distribution of the observed H II regions can be investigated directly. Figure 7.6 is an lv 'crayon' diagram (see Chapter 5) for Galactic longitudes $240° < l < 360°$ and LSR velocities $|V| < 150$ km s^{-1}. The H II regions from Caswell & Haynes (1987) are also displayed. From this Figure, it is evident that most of the observed regions are probably associated with the Scutum/Crux and Sagittarius/Carina spiral arms.

The galactocentric radius of an H II region can be calculated via a Galactic rotation model and the systemic velocity of the region. We remind the reader that throughout this thesis, the McClure-Griffiths & Dickey (2007) rotation model is implemented for inner Galaxy distances, $R_{gal} < R_0$. For outer Galaxy distances, $R_{gal} > R_0$, a flat rotation model $\Theta(R) = \Theta_0$ is employed. In all cases, the IAU Galactic constants ($R_0 = 8.5$ kpc and $\Theta_0 = 220$km s^{-1}) are applied.

The calculated galactocentric radii are displayed in Figure 7.8 and recorded in Tables 7.4 and 7.5. The sign of the detected RRL LSR velocity indicates the location of the region in relation to the Solar circle. For C2842, twenty-two of the twenty-four observed H II regions must be located in the inner Galaxy; whereas for C2963, all but one of the confirmed H II regions are located in the outer Galaxy.

While galactocentric radii are unambiguous; the kinematic distance ambiguity results in bi-valued line of sight distances for the inner Galaxy. Kinematic Distance Ambiguity Resolutions (KDARs) can be achieved through an investigation of the H I emission/absorption spectrum pairs (Anderson et al. 2012a; Jones & Dickey 2012; Jones et al. 2013). We follow the procedures from Chapter 3, investigating the total amount of H I over particular velocity

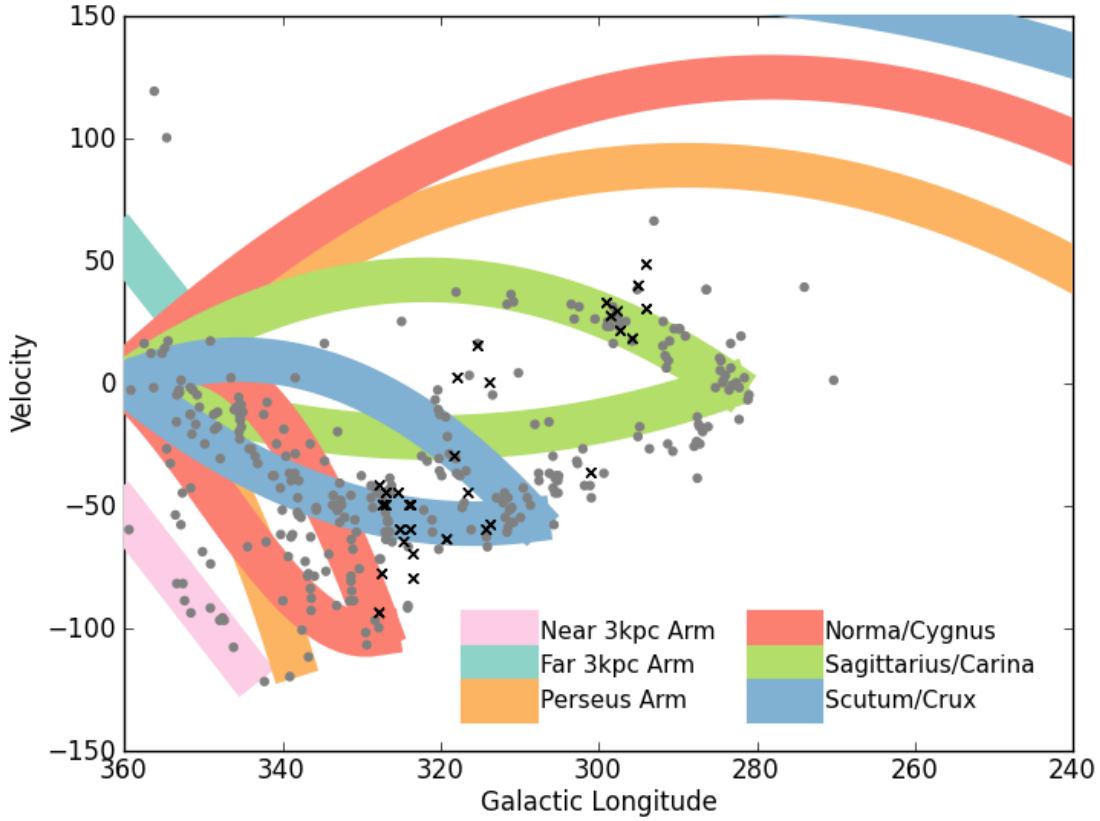

Figure 7.6: Longitude-Velocity 'crayon' diagram, as in Chapter 5, the spiral arm model is taken from Vallée (2008). H II regions observed with the ATCA appear as black crosses, while H II regions sourced from Caswell & Haynes (1987) appear as grey dots.

intervals, to attempt KDARs for each of our absorbed sources.

From the C2842 sample, eight H II regions are assigned to the tangent point distance. There are two C2842 H II regions which possess positive RRL velocities and therefore must be located in the outer Galaxy (denoted 'O' in Table 7.4), beyond the Solar Circle ($R_{Gal} > 8.5$ kpc). Of the C2963 confirmed H II region sample, all but one lies unambiguously in the outer Galaxy. This leaves 15 regions for which a KDAR could be attempted.

As the C2842 sources were chosen based on the availability of SGPS data, KDARs (following the method of Chapter 3) can be performed. H I emission/absorption spectrum pairs were extracted from the SGPS following the procedures of Brown et al. (Chapter 5 2014). Applying the spectrum quality tests of Chapter 6, the SGPS provides H I absorption spectra of rank C-E for most sources (see Table 7.4)—note that the spectra for G315.312-00.273 and G327.313-00.536 are taken directly from the Chapter 6 catalogue. In Chapter 6 we noted that spectra of qualities 'E' and below are unlikely to have an achievable KDAR using the velocity channel summation technique of Chapter 3. Where the H I absorption spectrum is too poor a quality to provide a KDAR, we can use individual absorption features as indicators of lower limits on the line of sight distance (i.e. method of Chapter 4).

From C2963, there is one H II region with an inner Galaxy velocity: G300.983+01.117. However, this source does not have a continuum brightness temperature sufficient to perform the terminal–velocity H I emission/absorption KDAR analysis.

Comparison to Previous KDARs Sources with KDARs marked with an asterisk in Table 7.4 have previously determined kinematic distances. The KDARs of this work do not disagree with any of the previous determinations; however, we report the more conservative TP location for G313.671-0.104 and G323.449+0.095 (previously determined as far and near side respectively). The sources from C2963 have no reported velocity information (from RRL or other transitions; Anderson et al. 2014) and therefore we present the first distance estimates for those sources in Table 7.5.

7.4.4.1 Electron Temperatures

Traditionally, optical transitions are used to compute the electron temperatures (T_e) of H II regions. However, high temperatures are required to excite the forbidden lines of nitrogen and oxygen (> 7000 K), such that these transitions can only be used to measure the T_e for a subset of (hot, bright) H II regions. As no such limitation exists for RRLs, they provide one of the simplest ways to calculate the electron temperature of an H II region (Gordon & Sorochenko 2002).

The FWHM (ΔV), along with the line (T_L) and continuum (T_C) temperatures for each RRL detection, can be used to estimate the electron temperature (T_e) of each H II region:

$$\left(\frac{T_e}{K}\right) \approx \left[\frac{7.0 \times 10^3}{1.08}\left(\frac{\nu}{\mathrm{GHz}}\right)^{1.1}\left(\frac{\mathrm{km\ s^{-1}}}{\Delta V}\right)\left(\frac{T_C}{T_L}\right)\right]^{0.87} \tag{7.1}$$

Equation 7.1, discussed in Quireza et al. (2006), assumes LTE, a typical He^+/H^+ ratio of 0.08, and that the line frequency (ν) is high enough so that free-free continuum emission is optically thin.

For C2842 we calculated the T_e for each detected Hnα RRL transition, with the reported electron temperature in Table 7.4 for the region taken from a linear least-squares fit across the different Hnα transitions - see bottom right panel for each H II region in Figure 7.9. For confirmed H II regions from C2963, we compute the electron temperature from the <Hnα> spectrum (using the average of the RRL frequencies in place of ν).

A galactic temperature gradient (low T_e in the Galactic centre, increasing with galactocentric radius) was first observed in external galaxies in the 1970s. Radio continuum emission and optical [O III] observations confirmed a similar temperature gradient within the Milky Way (discussed in Quireza et al. 2006).

Shaver et al. (1983) explained this temperature gradient through a corresponding (inversely related) Galactocentric metallicity gradient. As heavy elements (particularly oxygen and nitrogen) cool photoionised gas, the T_e of an H II region directly relates to the heavy-element abundance—such that low electron temperatures correspond to high metallicities and vice versa.

The exact form of this temperature gradient is still controversial. Proponents exist for

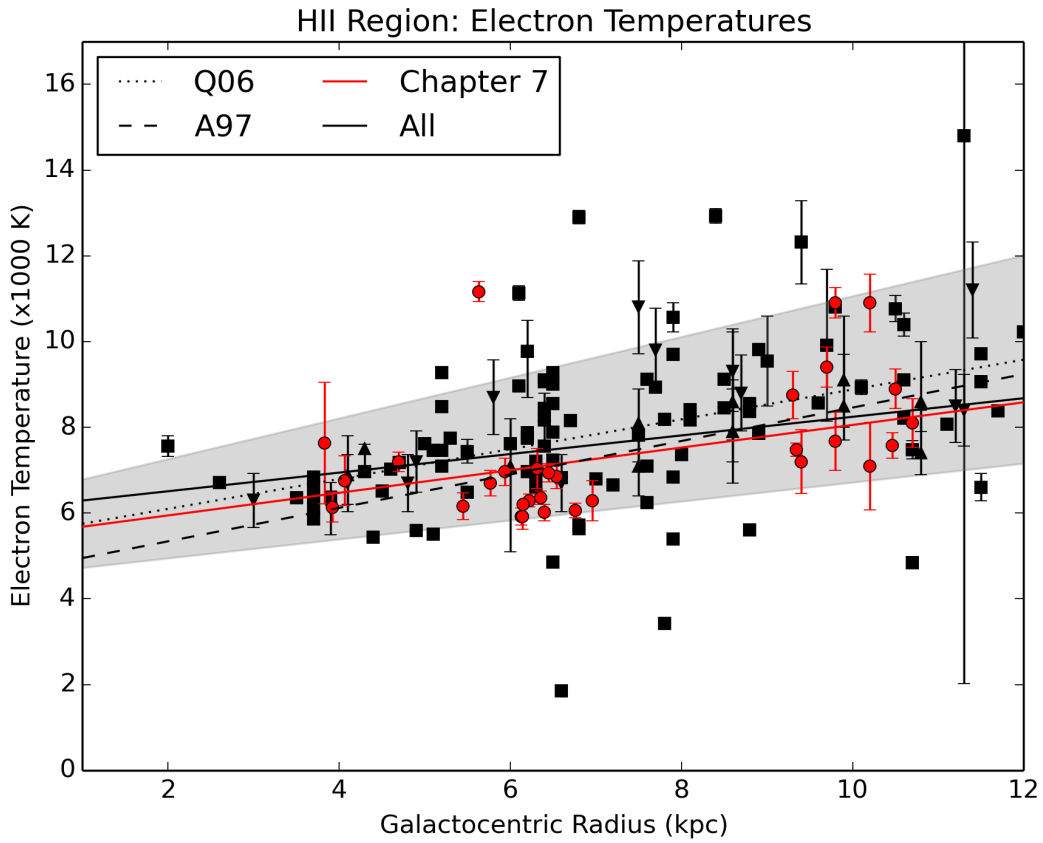

Figure 7.7: Electron Temperature vs Galactocentric Radii. Markers are as follows: circles–from the observations in this Chapter; squares–Quireza et al. (2006), triangles–Afflerbach et al. (1996, pointing up) and Afflerbach et al. (1997, pointing down). Linear least–squares fits are also shown: red solid–regions from this Chapter; dotted–Quireza et al. (2006); dashed–Afflerbach et al. (1997); solid black line, $\pm\sigma$ grey envelope–combined fit to all regions.

a increasing and decreasing gradient with respect to galactocentric radius*. Furthermore, there is evidence for flat gradients over all (Kaufer et al. 1994) or parts of the Milky Way ($R_{\rm gal} > 10$ kpc, Fich & Silkey 1991; Simpson 1975), and in some external galaxies (Zaritsky et al. 1994).

Derived Galactic Disk Electron Temperature Gradient The H II regions discovered by the observations in this Chapter span ~ 8 kpc in galactocentric radius, providing an excellent opportunity to derive an independent estimate of the Galactic disk electron temperature gradient and compare it to previous works—namely those of Afflerbach et al. (1997) and Quireza et al. (2006).

Afflerbach et al. (1997), building on the work by Afflerbach et al. (1996), present a unique approach to the derivation of a Milky Way electron temperature gradient. They construct highly detailed statistical and ionisation equilibrium models, from infrared fine–structure lines and high-resolution radio continuum maps, for thirty-four compact H II regions between

*increasing gradients vary between approximately 250 to 440 K kpc^{-1}]Shaver83, Mezger79, Churchwell-Walmsley75, Afflerbach97, Quireza06, while **?** supports a decreasing electron temperature gradient (between 6–17 kpc)

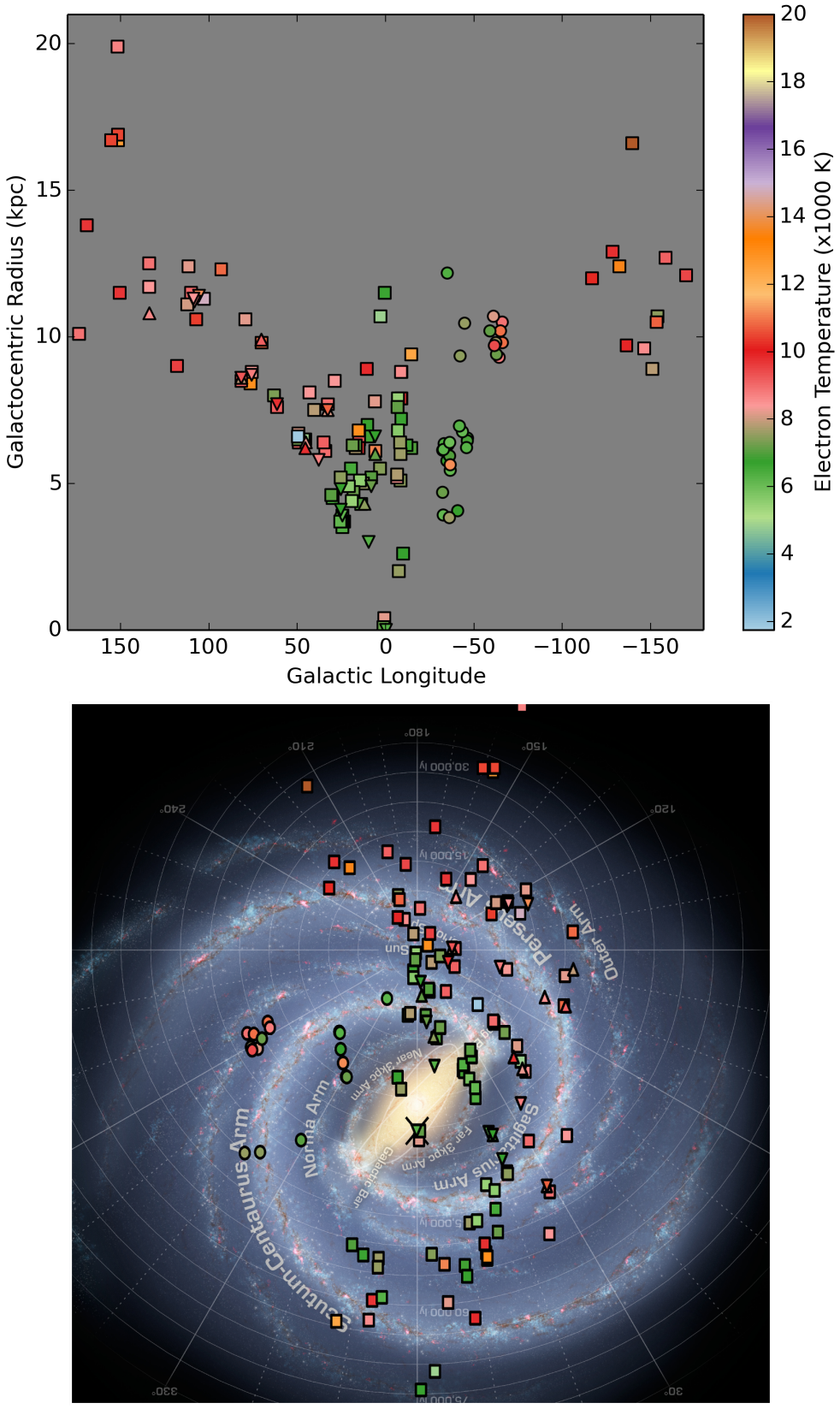

Figure 7.8: Top: H II regions from Figure 7.7, in terms of galactocentric radius vs longitude. Bottom: Face on map for H II regions with known line of sight distances. The same T_e colour scale is used in both panels. Markers: circles–from the observations in this Chapter; squares–Quireza et al. (2006), triangles–Afflerbach et al. (1996, pointing up) and Afflerbach et al. (1997, pointing down).

$0 < R_{\rm gal} < 12$ pc. Thus, they can derive independent estimates of the metallicity abundance gradient, and the inversely proportional electron temperature gradient (see Equation 7.3). This electron temperature gradient is shown as the dashed line in Figure 7.7, while the individual H II region temperatures are displayed as triangles pointing upwards Afflerbach et al. (1996) and downwards Afflerbach et al. (1997).

Quireza et al. (2006) present a Galactic electron temperature gradient from a sample of high quality RRL spectra from over 100 H II regions, spanning $0 - 17$ kpc in galactocentric radius (see Equation 7.2). Their method of electron temperature derivation is identical to the method used in this Chapter (i.e., Equation 7.1), except that Quireza et al. (2006) derive the He^+/H^+ ratio for each region (rather than assuming $He^+/H^+ = 0.08$). In Figure 7.7, the electron temperatures and temperature gradient derived by Quireza et al. (2006) are shown as the black squares and dotted line, respectively.

A least-squares linear electron temperature gradient is fit to the H II region electron temperatures from the observations of this Chapter, shown as the red circles and fit in Figure 7.7, resulting in Equation 7.4. This gradient is comparable to the results of Afflerbach et al. (1997) and Quireza et al. (2006), although it is slightly flatter. This could be attributed to the concentration of inner Galaxy sources.

$$\text{Quireza et al. (2006)}\, T_e = 287 R_{\rm gal} + 5780 \tag{7.2}$$

$$\text{Afflerbach et al. (1997)}\, T_e = 390 R_{\rm gal} + 4560 \tag{7.3}$$

$$\text{(New)}\, T_e = 346 R_{\rm gal} + 5417 \tag{7.4}$$

$$\text{(All)}\, T_e = 348(\pm 127) R_{\rm gal} + 5392(\pm 909) \tag{7.5}$$

Indeed over 43% of the H II regions in Figure 7.7 are located between $5 < R_{\rm gal} < 8$ kpc. A bootstrapping Monte Carlo analysis is used to investigate any bias this concentration of regions may cause to the T_e gradient fit. From the entire sample size (N) of 171 H II regions, in Figure 7.7, 10,000 simulated samples are selected. Each simulated sample, of size N, is generated by drawing regions from the observed sample, independently, with replacement.

The average fit (Equation 7.5) is computed from the individual T_e gradients from each of the 10,000 simulations. This method provides the 1σ grey envelope shown on Figure 7.7. The uncertainty of the fit suggests that the radial concentration may significantly effect the electron temperature gradient. This effect should be mitigated as we continue to discover new H II regions.

As well as the galactocentric radial distribution, the longitude ranges of previous works are also limited. The only fourth quadrant regions surveyed by Quireza et al. (2006) have longitudes greater than $l > 330°$, while the confirmed regions of this Chapter are confined to $295° < l < 327°$. We investigate the effects of this longitude clumping in Figure 7.8.

The top panel of Figure 7.8 is a modification of Figure 7.7, using Galactic longitude as an additional axis. While the bias towards regions with galactocentric radii $4 - 8$ kpc is

particularly striking, the plot is insufficient for the purposes of deducing any longitudinal bias. The plot does however, highlight the paucity of H II regions with measured electron temperatures in the fourth Galactic quadrant.

The bottom panel of Figure 7.8 displays H II regions with known electron temperatures and line of sight distances. As this Figure is further populated by future studies, we will perhaps see the electron temperature signals of the ends of the Bar, or across (rather than along) the spiral arms themselves.

7.5 Individual Source Overview

The following section provides an image panel for each observed H II region or H II region candidate (now all confirmed as H II regions). In each case we report with the WISE name from Anderson et al. (2014). Each Figure provides an overview of the observations and analysis for each source. The top panel provides the individual RRL spectra, while the second panel displays the <Hnα> spectrum - here the flux scale has been adjusted to remove any contribution from the continuum and therefore demonstrates the average line flux from the stacked RRL transitions only. The solid line indicates the stacked spectrum, while the dotted line shows a Gaussian model.
For sources from C2842, the figures also include:
- the H I absorption spectrum (solid line) with uncertainty (grey envelope). In this panel, the terminal velocity from McClure-Griffiths & Dickey (2007) is shown as the vertical dotted line. The velocity ranges for the spiral arm components shown in Figure 7.6 are also shown.
- a three-color WISE image (bottom left panel); blue, green, red mapped by 3.4, 12 and 22 μm respectively. Contours of SGPS 1.4GHz continuum are also shown; indicating levels of 10%, 30%,...,90% of the peak value.
- individual Hnα RRL overview (bottom right panel).The central velocity, line width and computed electron temperature is shown for each detected RRL.

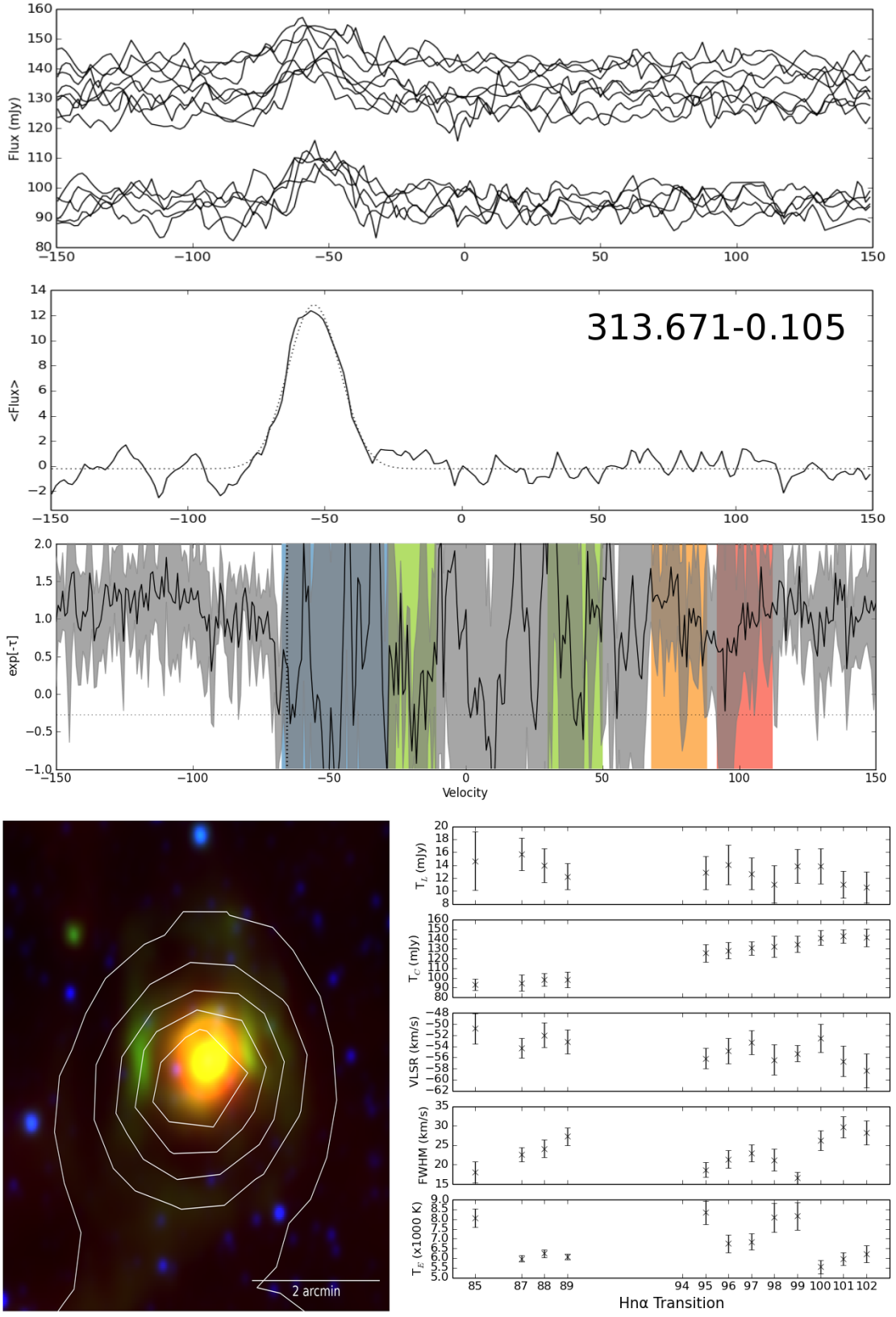

Figure 7.9: Overview of each source. The stacked Hnα RRL and H I absorption spectra are shown; along with an infrared three color image, overlaid with radio continuum contours; and an overview of the parameters for each detected Hnα transition.

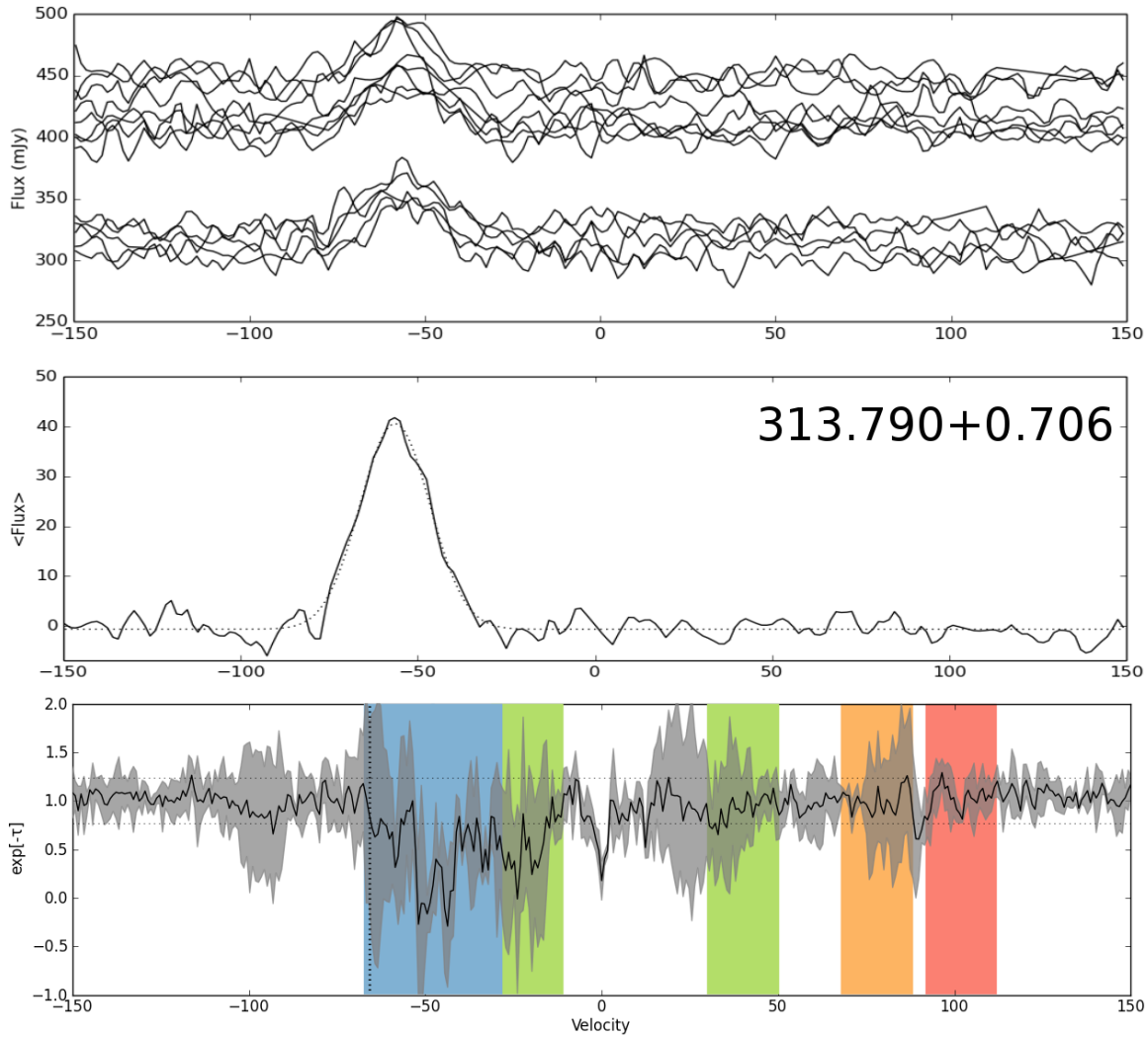
Flux (mJy)
313.790+0.706
<Flux>
exp[-τ]
Velocity

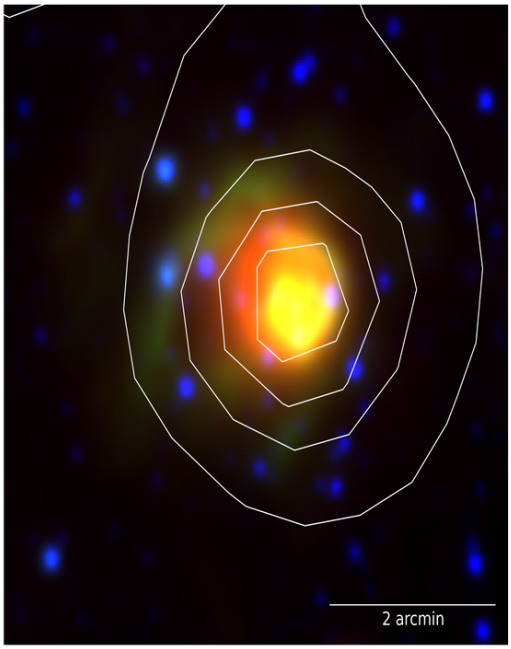
2 arcmin

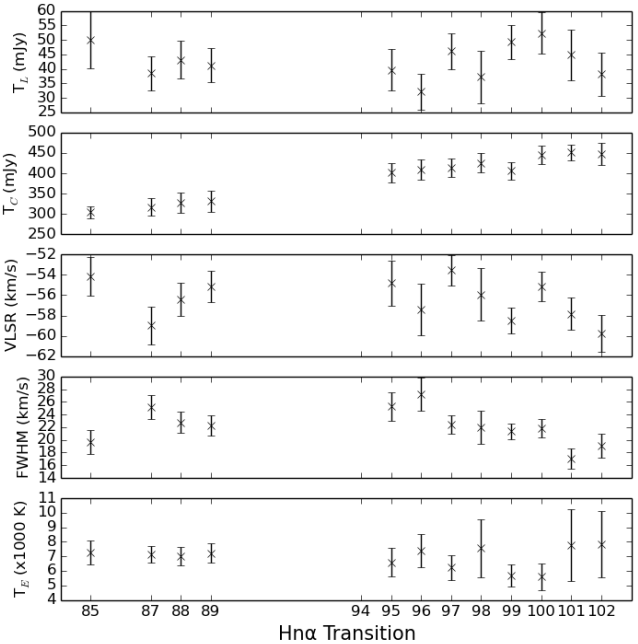
T_L (mJy)
T_C (mJy)
VLSR (km/s)
FWHM (km/s)
T_E (x1000 K)
Hnα Transition

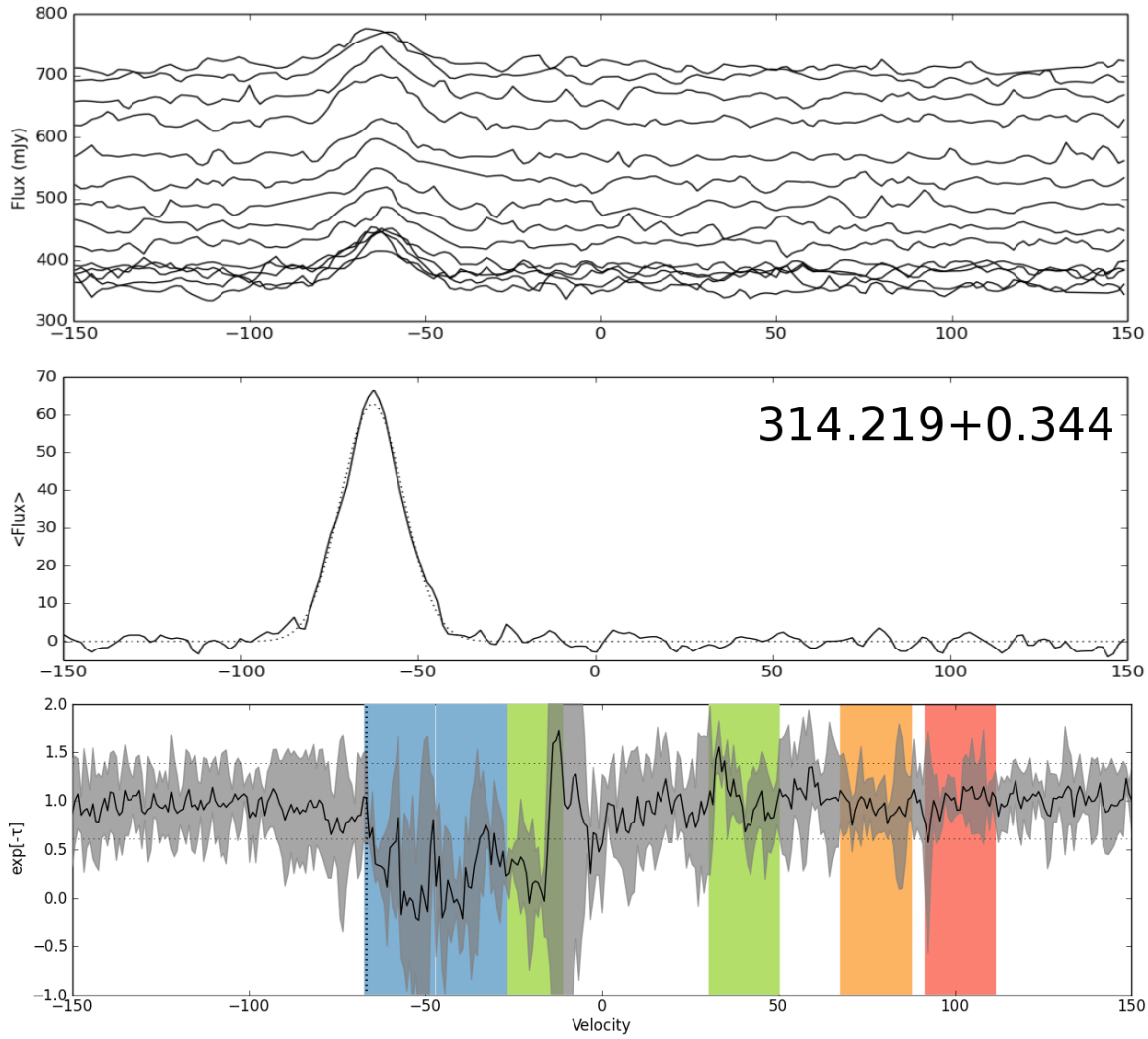
Flux (mJy)
<Flux>
314.219+0.344
exp[-τ]
Velocity

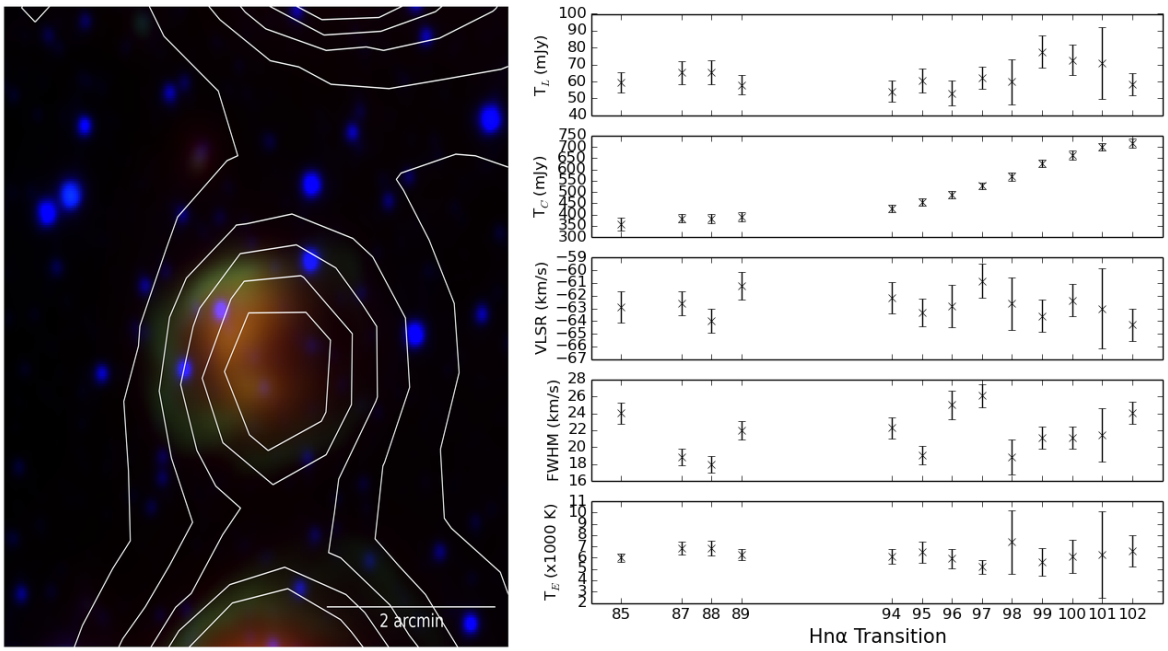
2 arcmin
T_L (mJy)
T_C (mJy)
VLSR (km/s)
FWHM (km/s)
T_E (x1000 K)
Hnα Transition

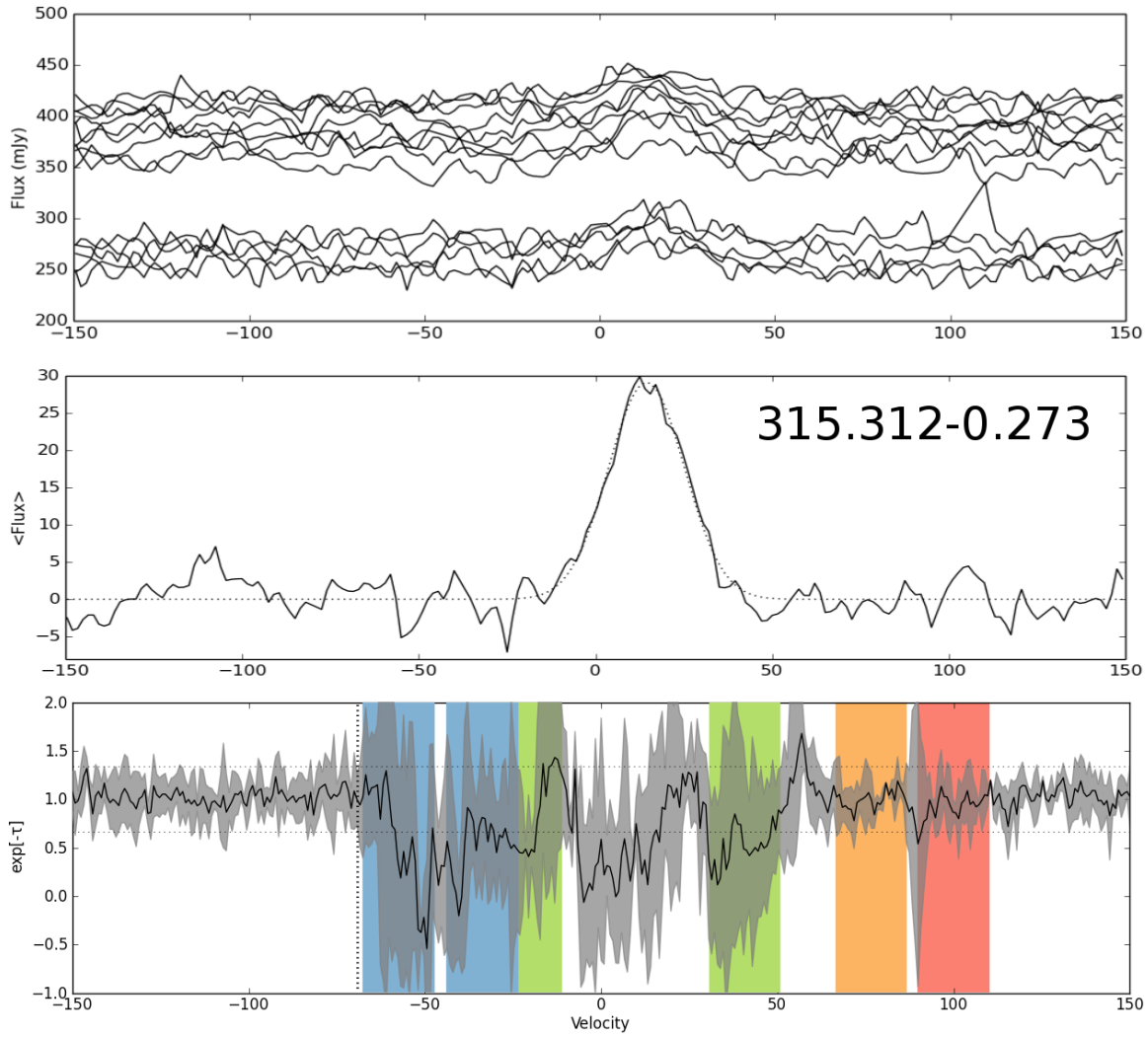
Flux (mJy)
315.312-0.273
<Flux>
exp[-τ]
Velocity

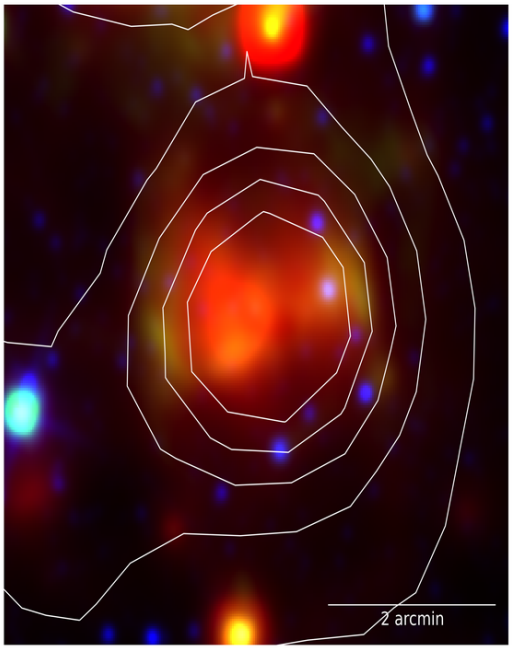
2 arcmin

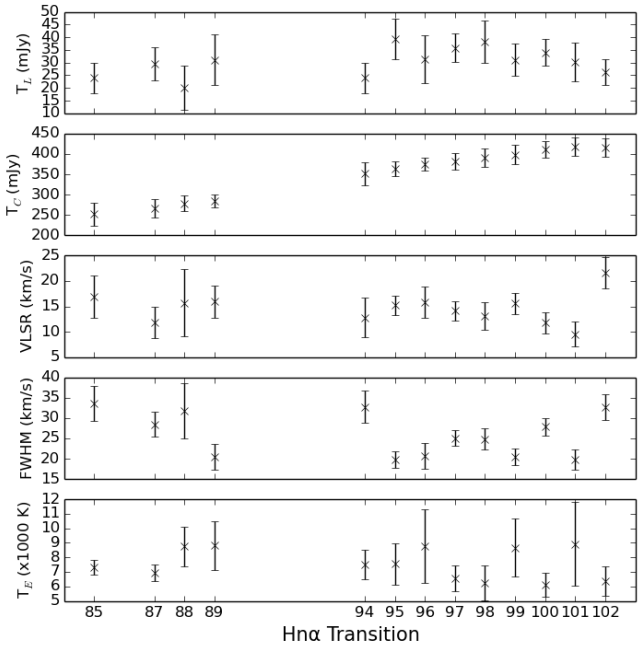
T_L (mJy)
T_C (mJy)
VLSR (km/s)
FWHM (km/s)
T_E (x1000 K)
Hnα Transition

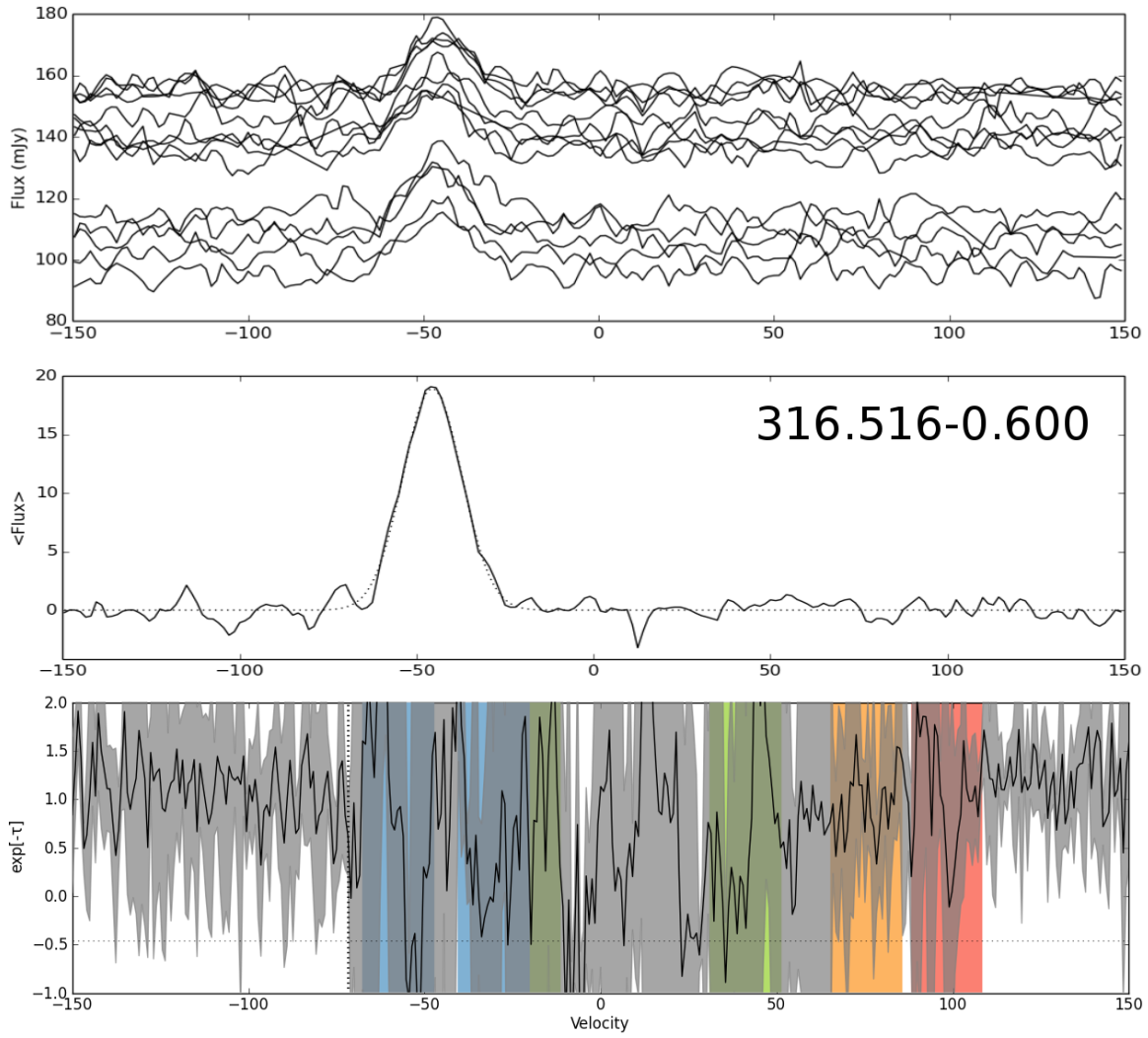
Flux (mJy)
<Flux>
316.516-0.600
exp[-τ]
Velocity

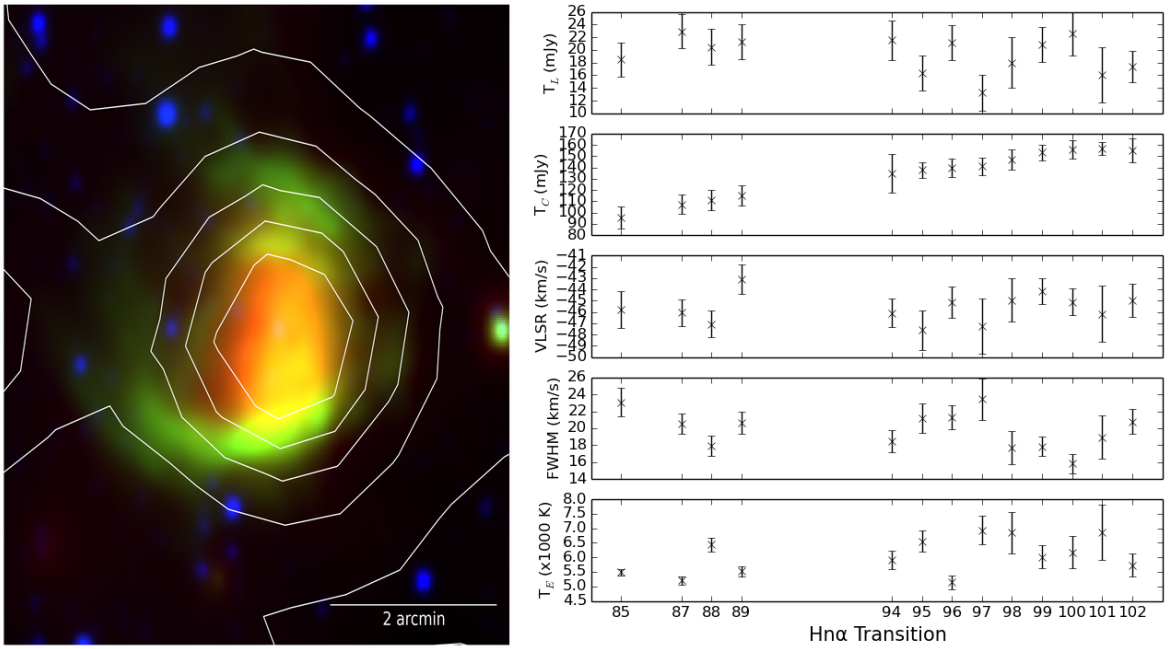
2 arcmin
T_L (mJy)
T_C (mJy)
VLSR (km/s)
FWHM (km/s)
T_E (x1000 K)
Hnα Transition

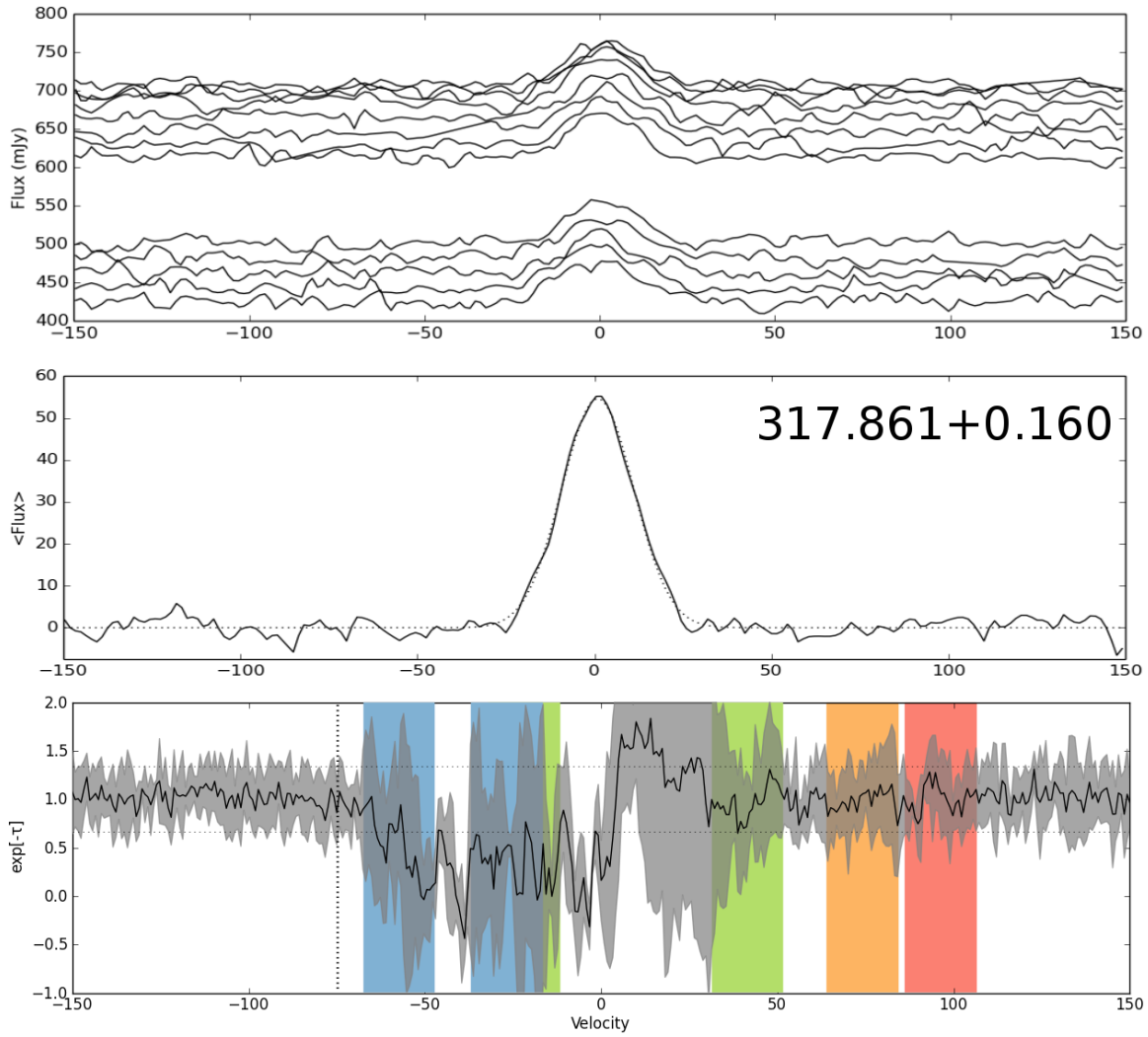
Flux (mJy)
<Flux>
317.861+0.160
exp[-τ]
Velocity

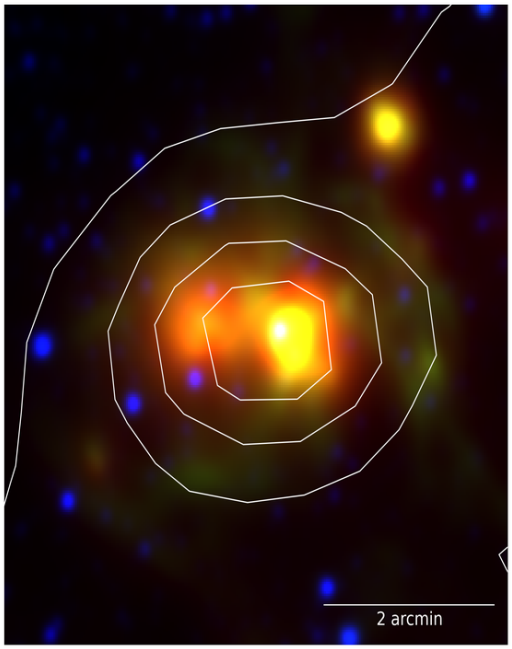
2 arcmin

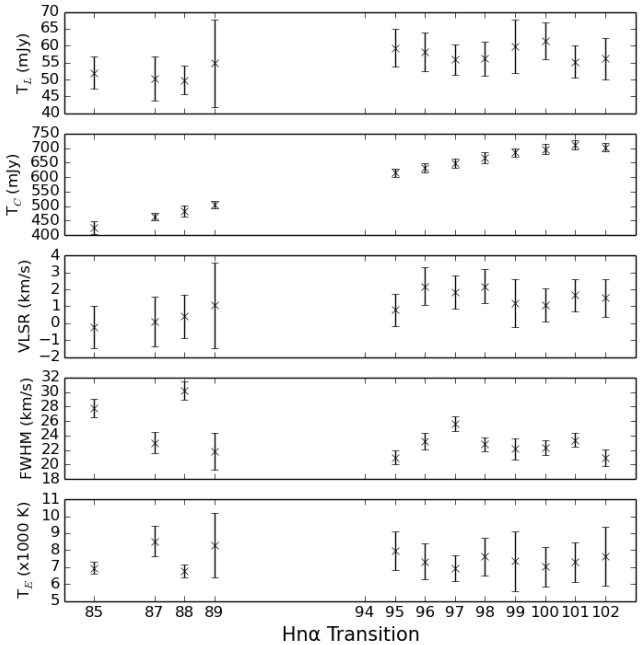
T_L (mJy)
T_C (mJy)
VLSR (km/s)
FWHM (km/s)
T_E (x1000 K)
Hnα Transition

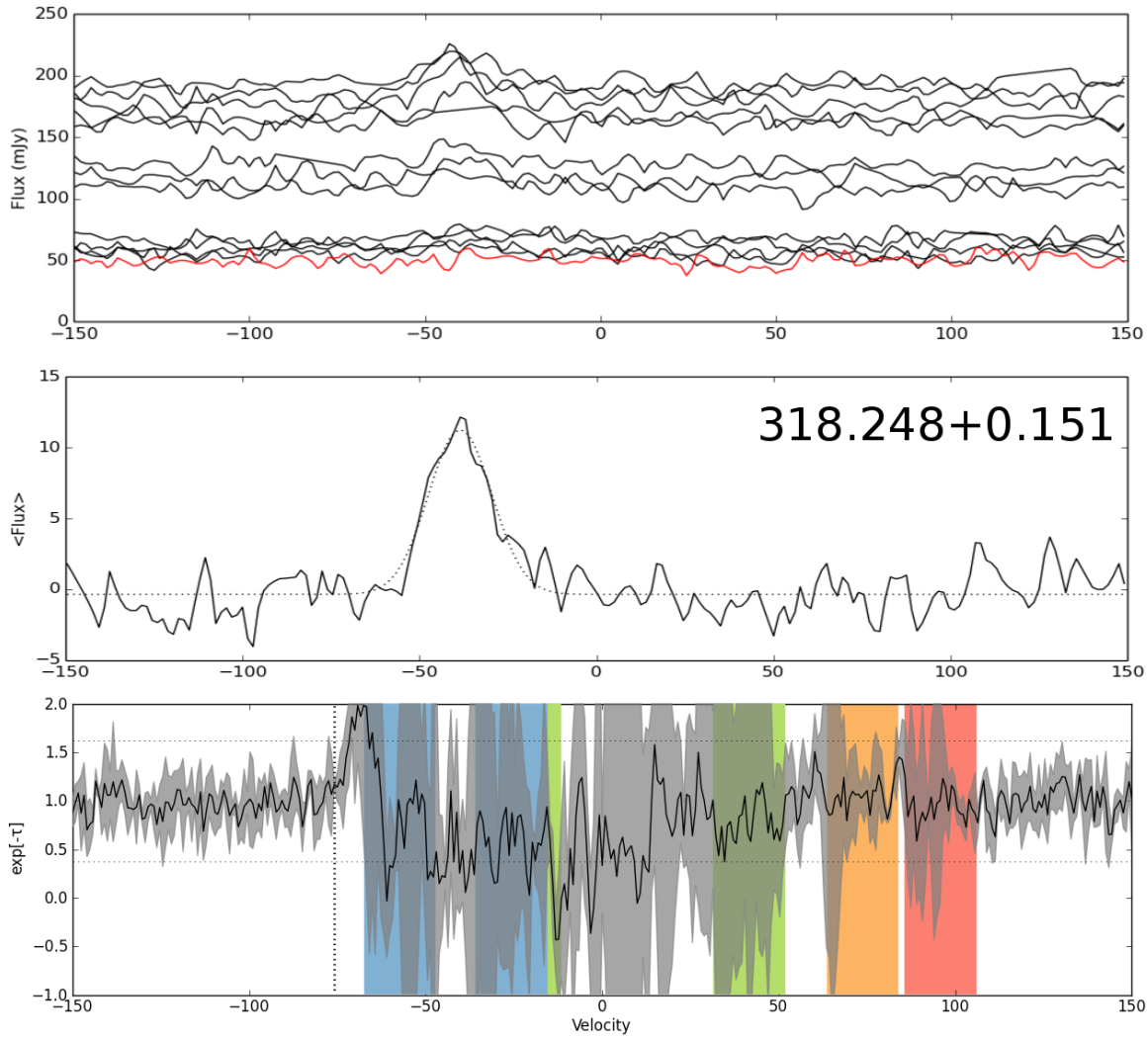
Flux (mJy)
<Flux>
318.248+0.151
exp[-τ]
Velocity

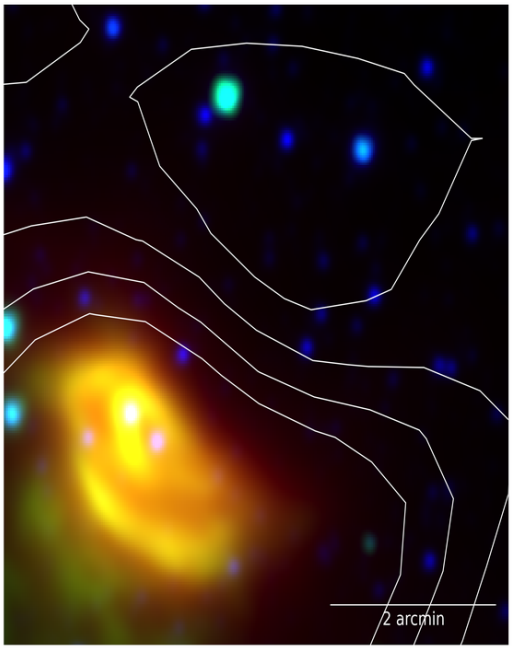
2 arcmin

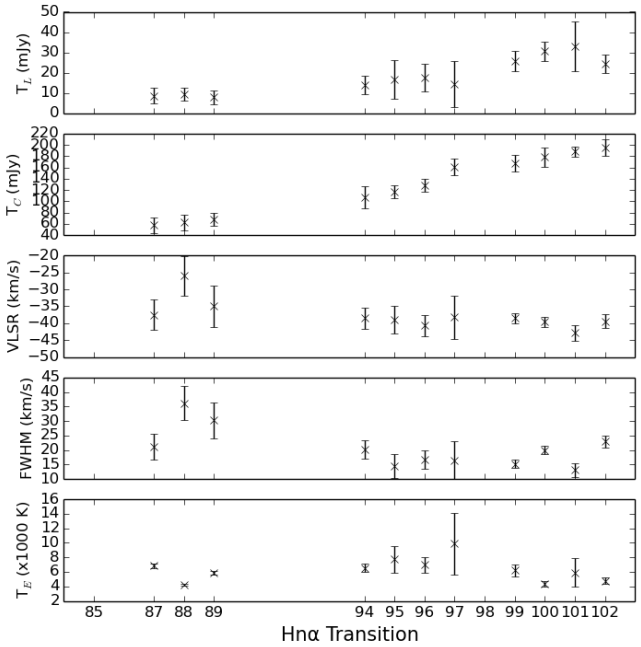
T_L (mJy)
T_C (mJy)
VLSR (km/s)
FWHM (km/s)
T_E (x1000 K)
Hnα Transition

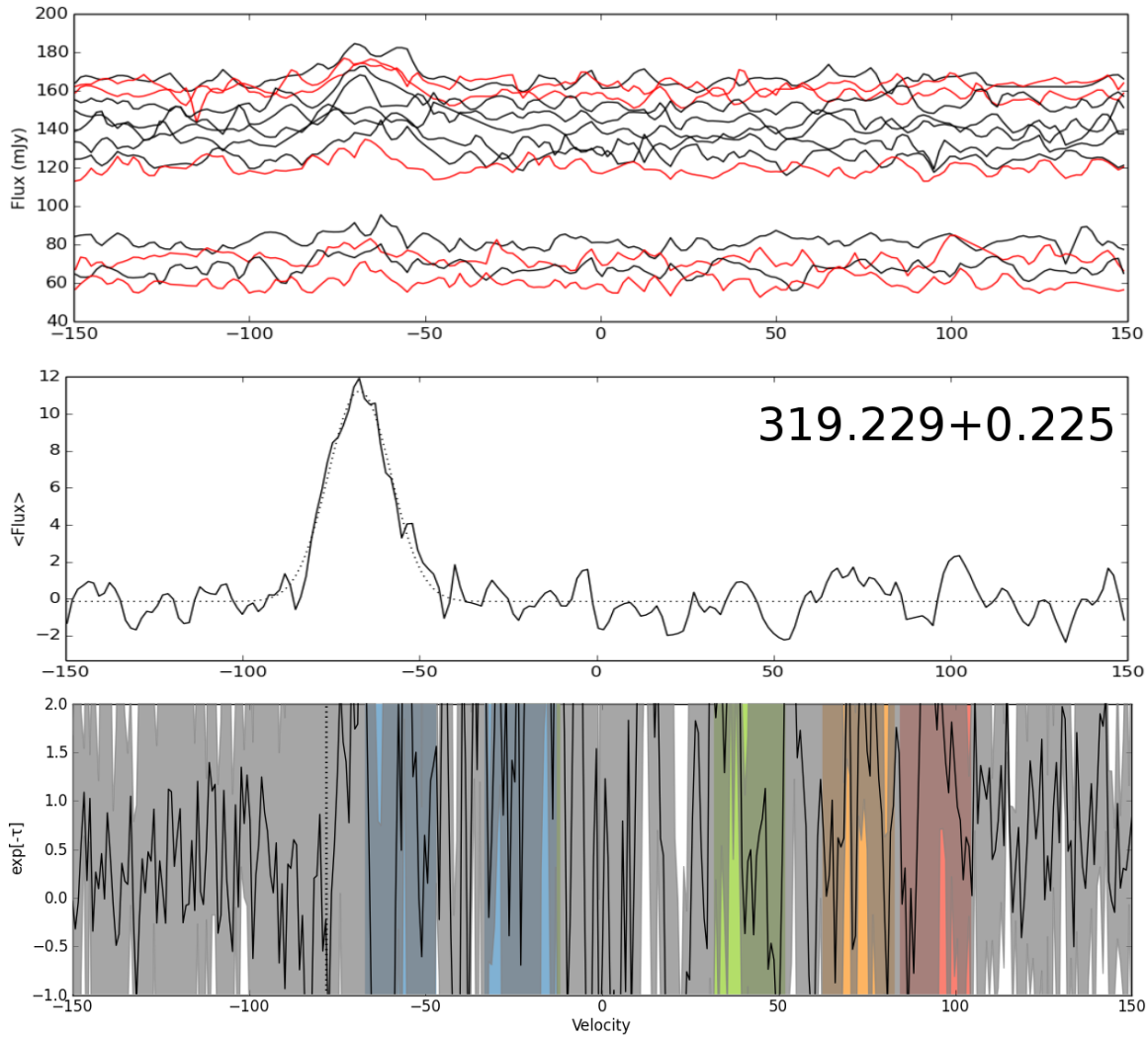
Flux (mJy)
<Flux>
319.229+0.225
exp[-τ]
Velocity

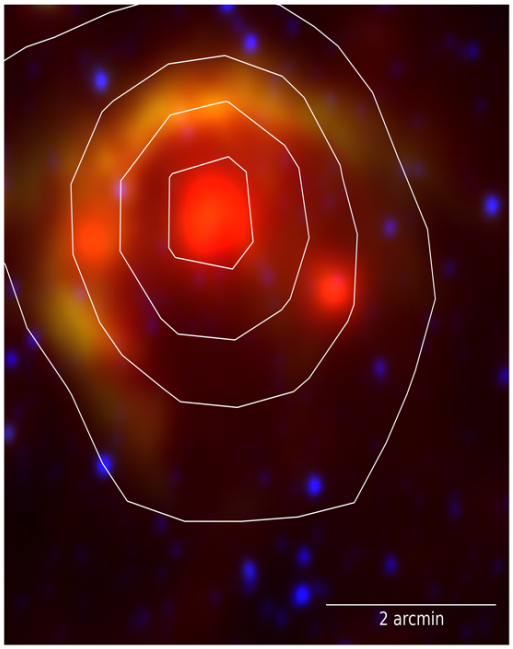
2 arcmin

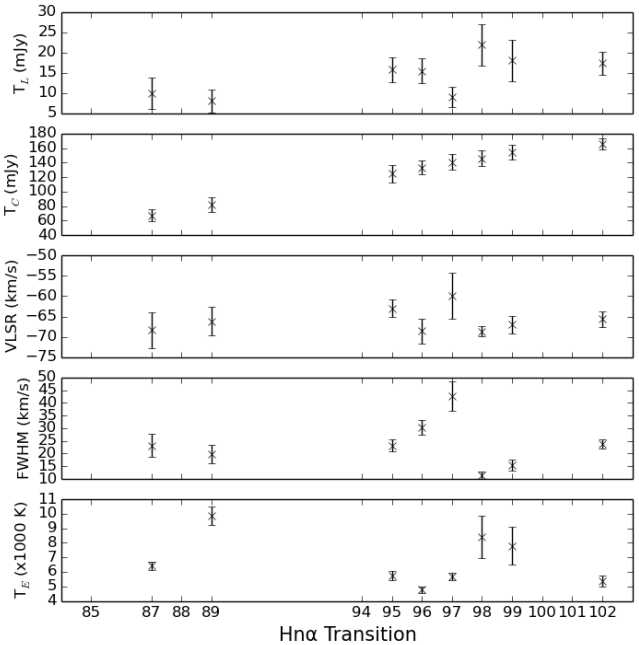
T_L (mJy)
T_C (mJy)
VLSR (km/s)
FWHM (km/s)
T_E (x1000 K)
Hnα Transition

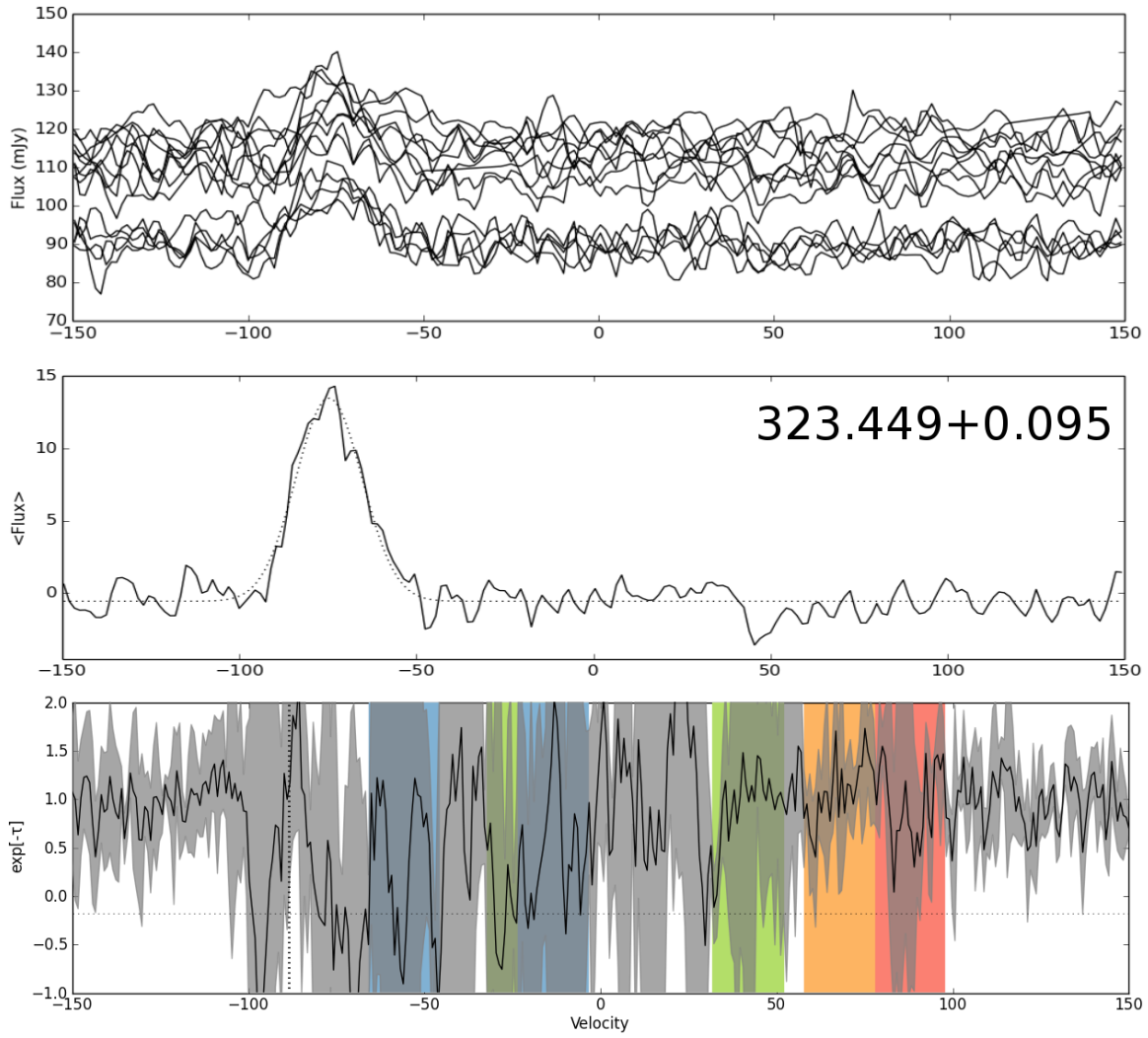
Flux (mJy)
<Flux>
323.449+0.095
exp[-τ]
Velocity

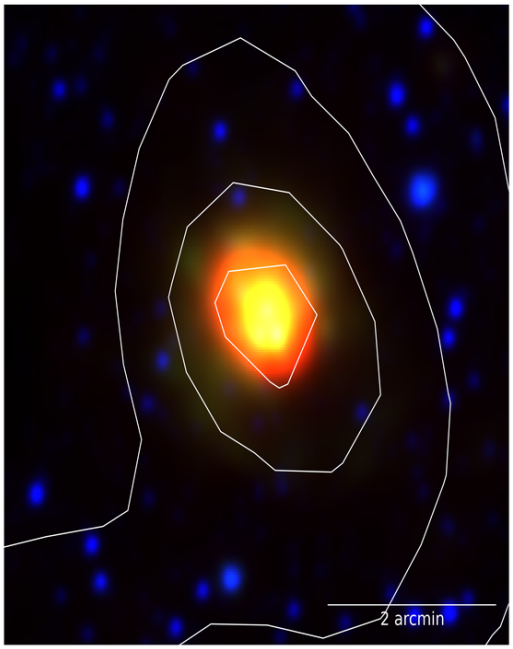
2 arcmin

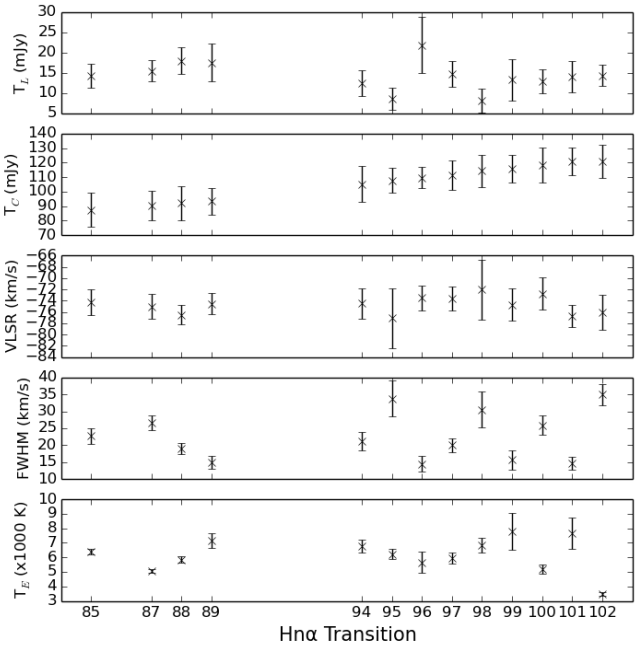
T_L (mJy)
T_C (mJy)
VLSR (km/s)
FWHM (km/s)
T_E (x1000 K)
Hnα Transition

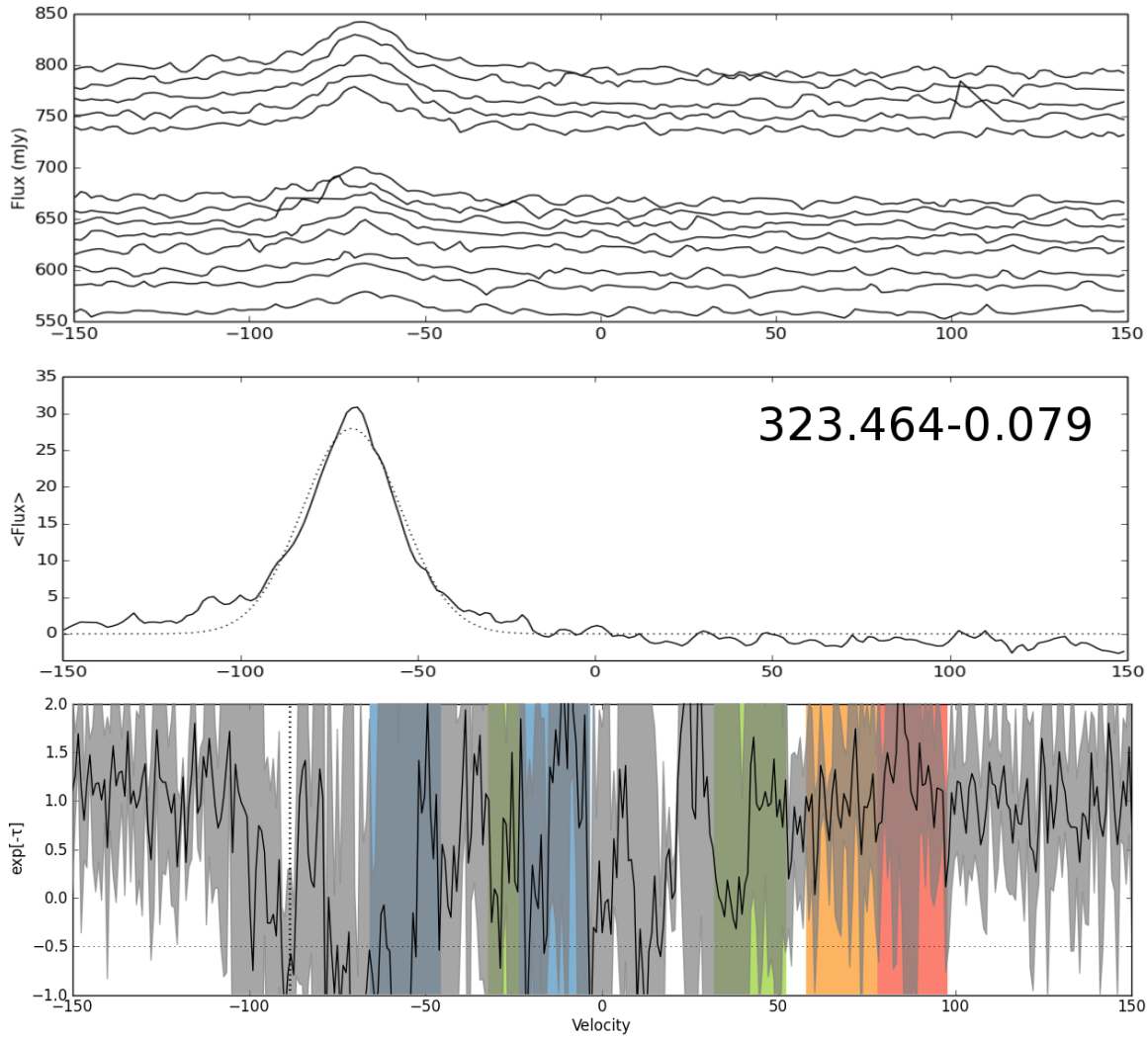
Flux (mJy)
<Flux>
323.464-0.079
exp[-τ]
Velocity

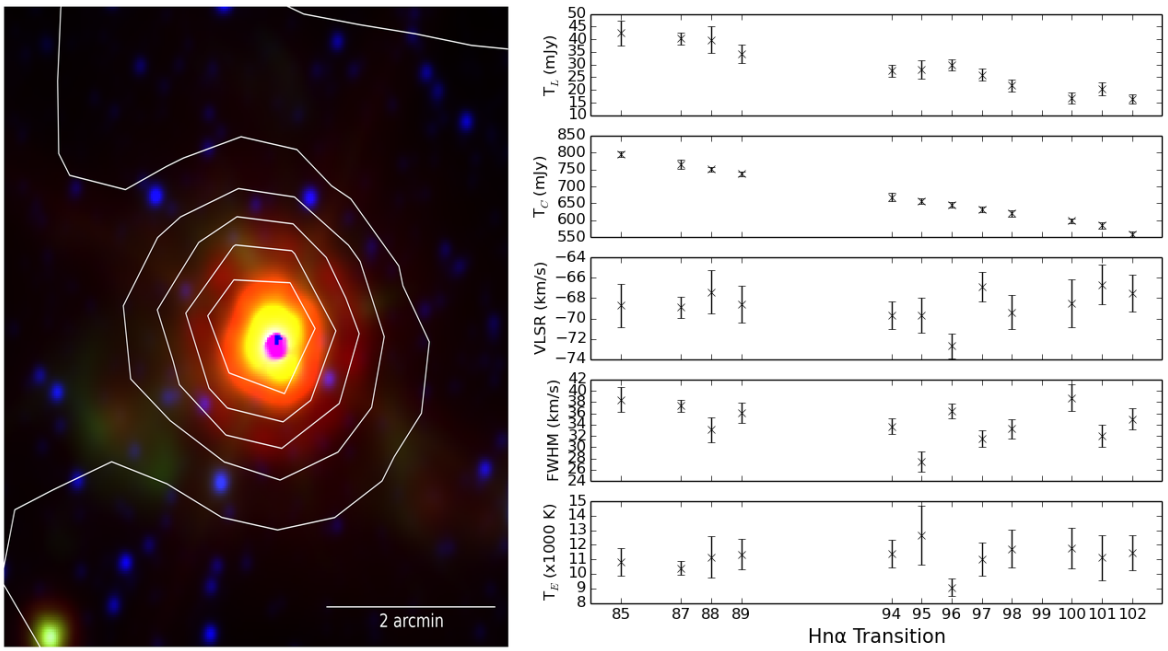
2 arcmin
T_L (mJy)
T_C (mJy)
VLSR (km/s)
FWHM (km/s)
T_E (x1000 K)
Hnα Transition

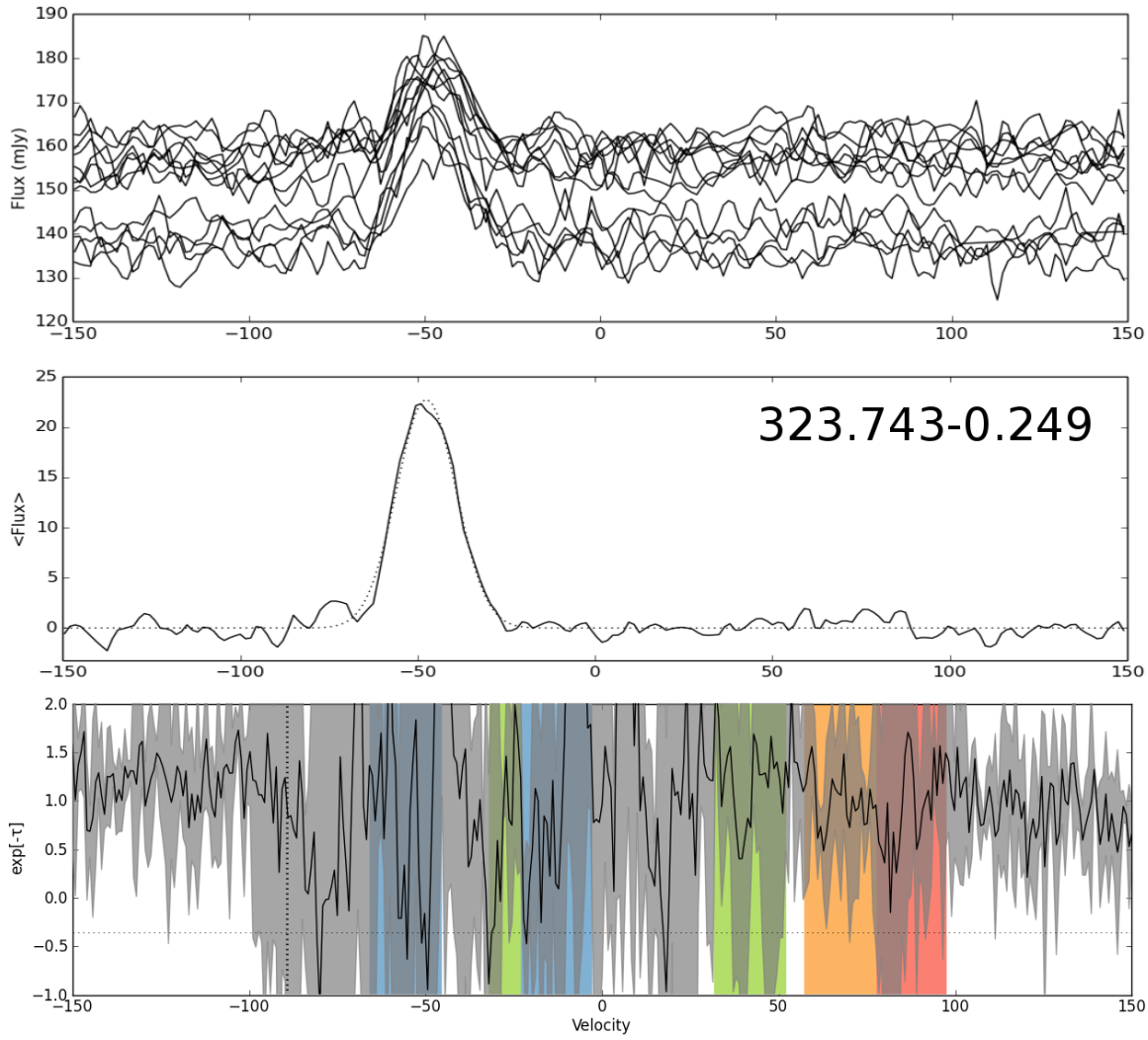
Flux (mJy)
<Flux>
323.743-0.249
exp[-τ]
Velocity

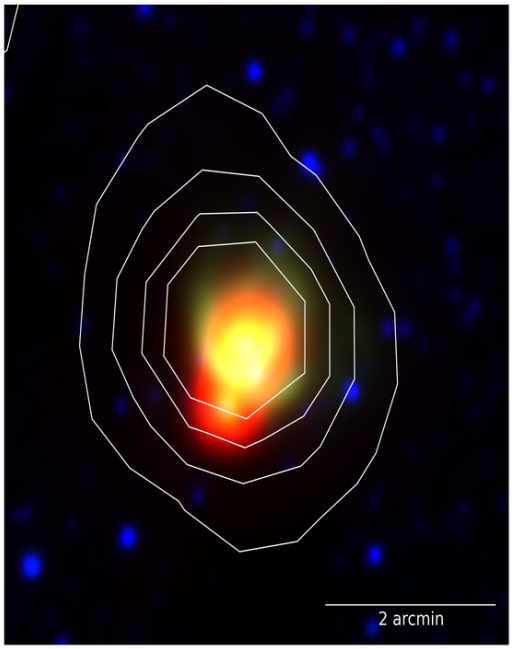
2 arcmin

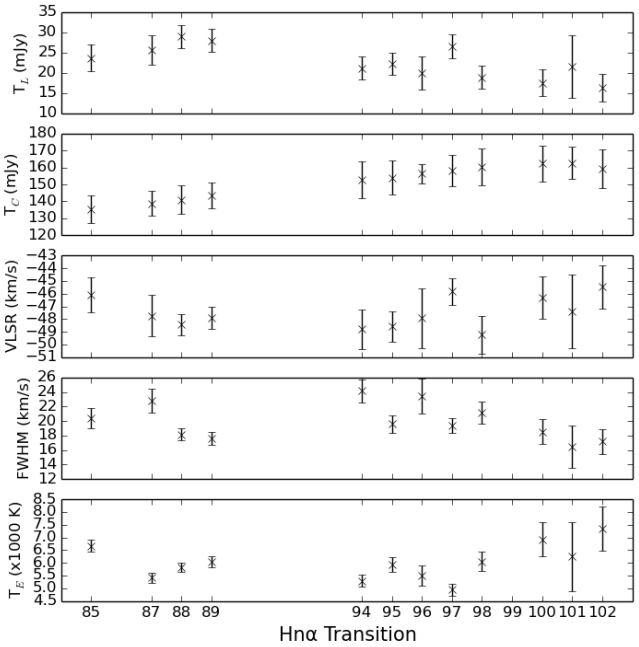
T_L (mJy)
T_C (mJy)
VLSR (km/s)
FWHM (km/s)
T_E (x1000 K)
Hnα Transition

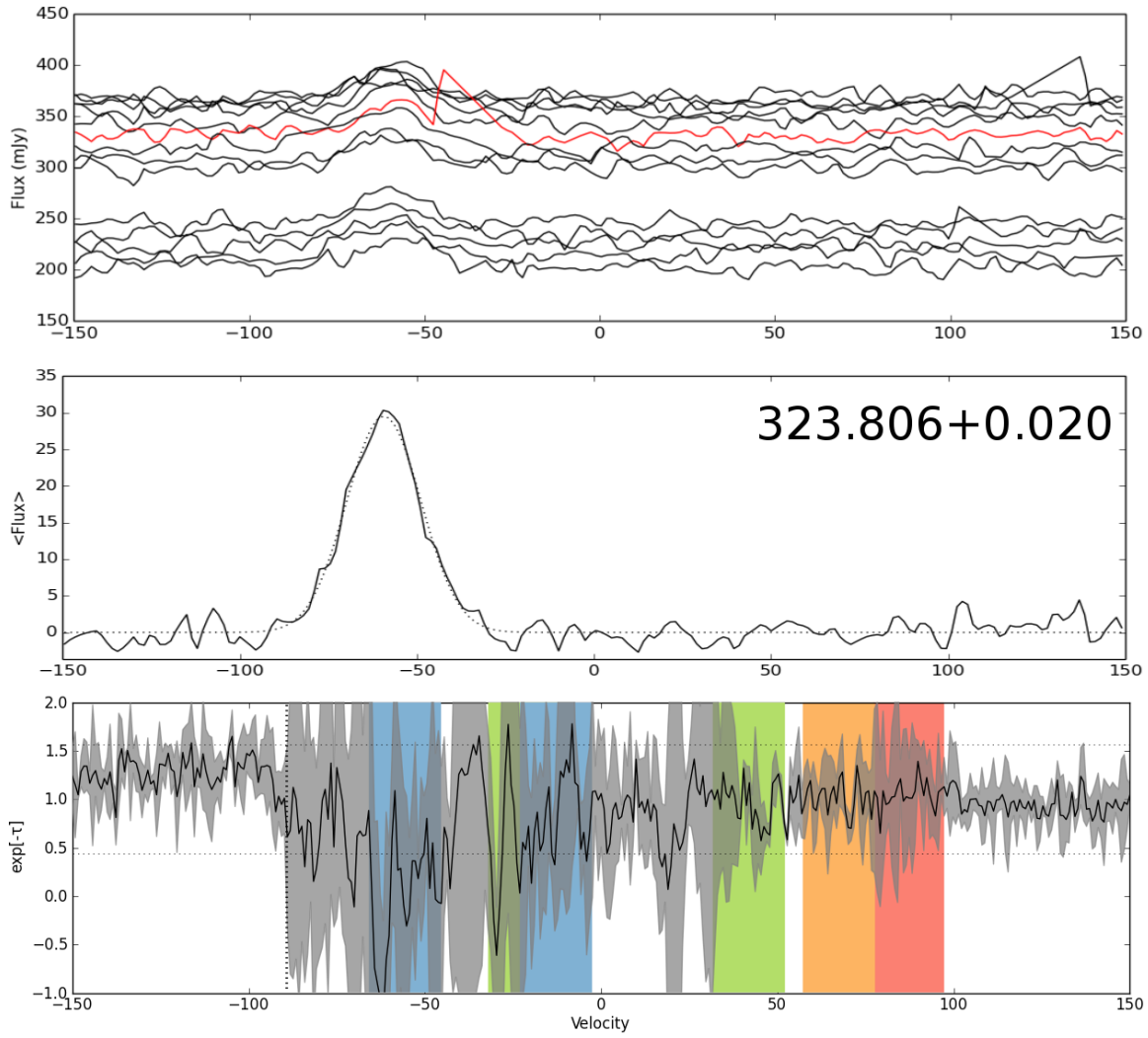
Flux (mJy)
<Flux>
323.806+0.020
exp[-τ]
Velocity

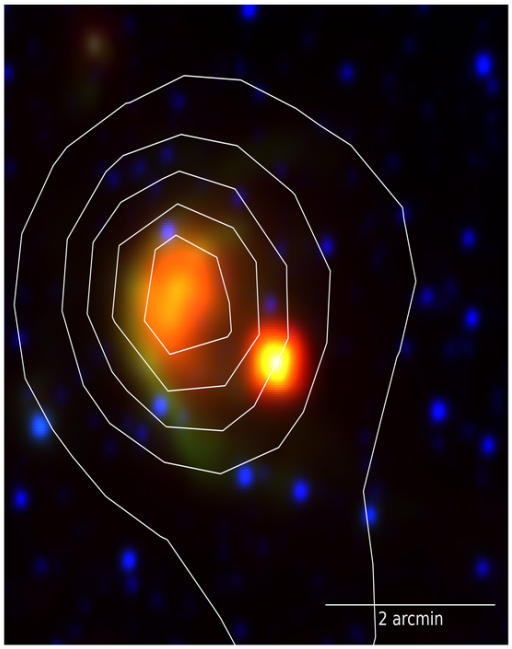
2 arcmin

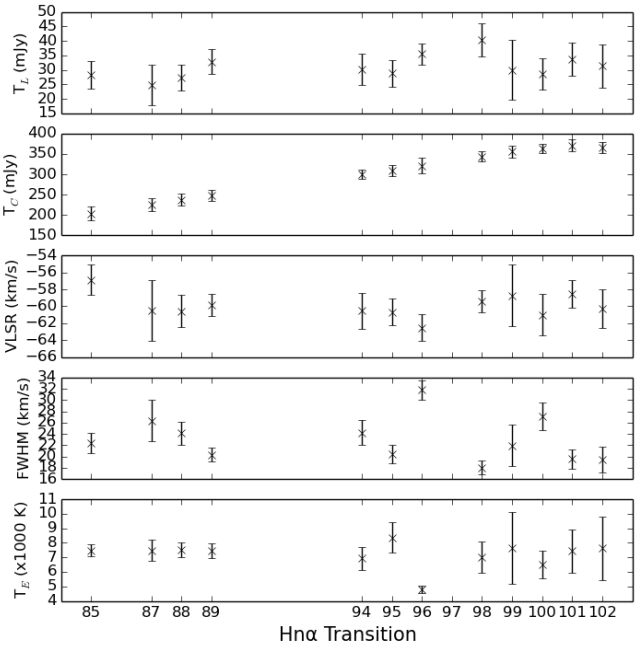
T_L (mJy)
T_C (mJy)
VLSR (km/s)
FWHM (km/s)
T_E (x1000 K)
Hnα Transition

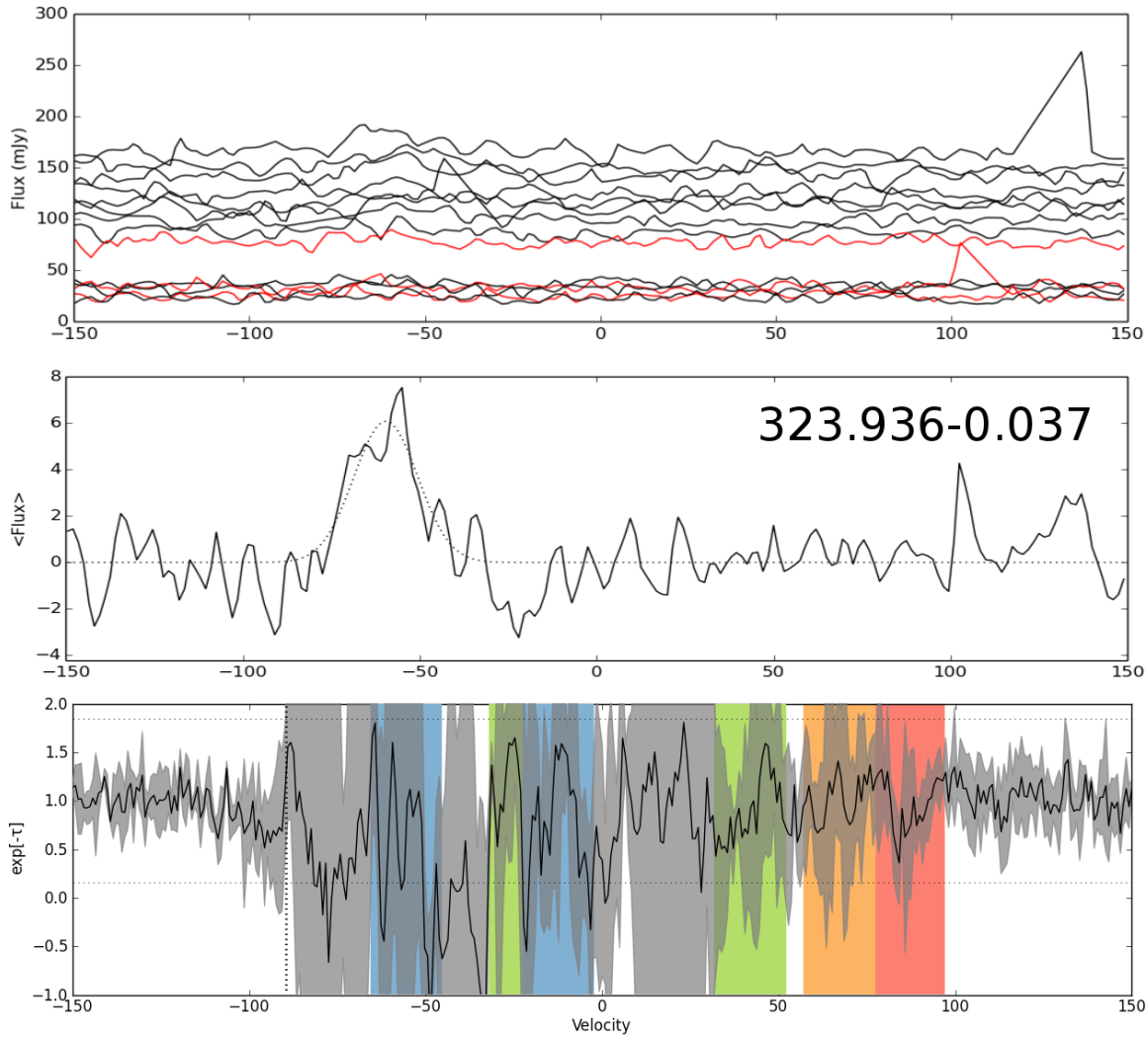
Flux (mJy)
<Flux>
323.936-0.037
exp[-τ]
Velocity

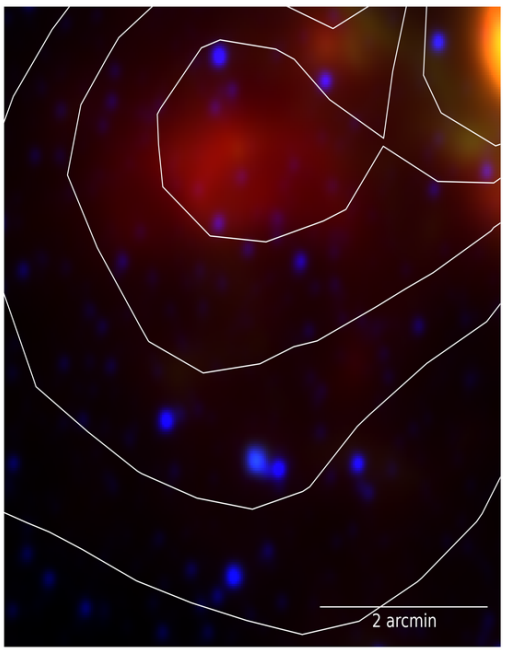
2 arcmin

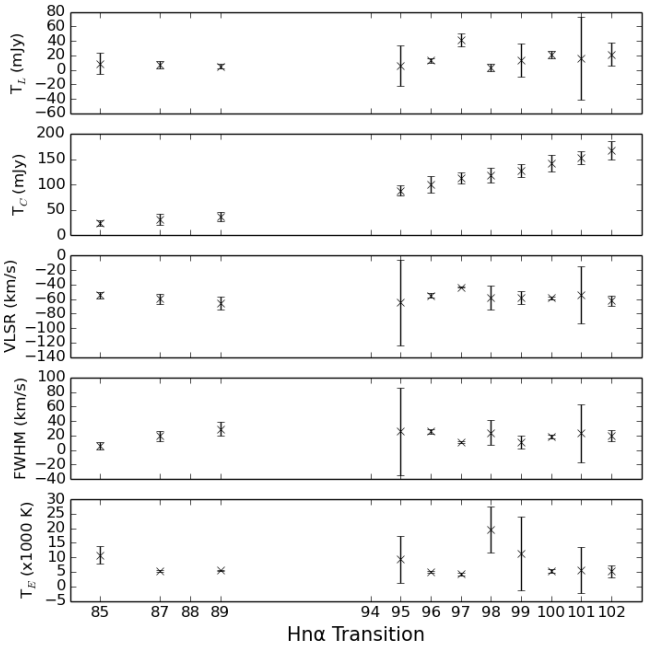
T_L (mJy)
T_C (mJy)
VLSR (km/s)
FWHM (km/s)
T_E (x1000 K)
Hnα Transition

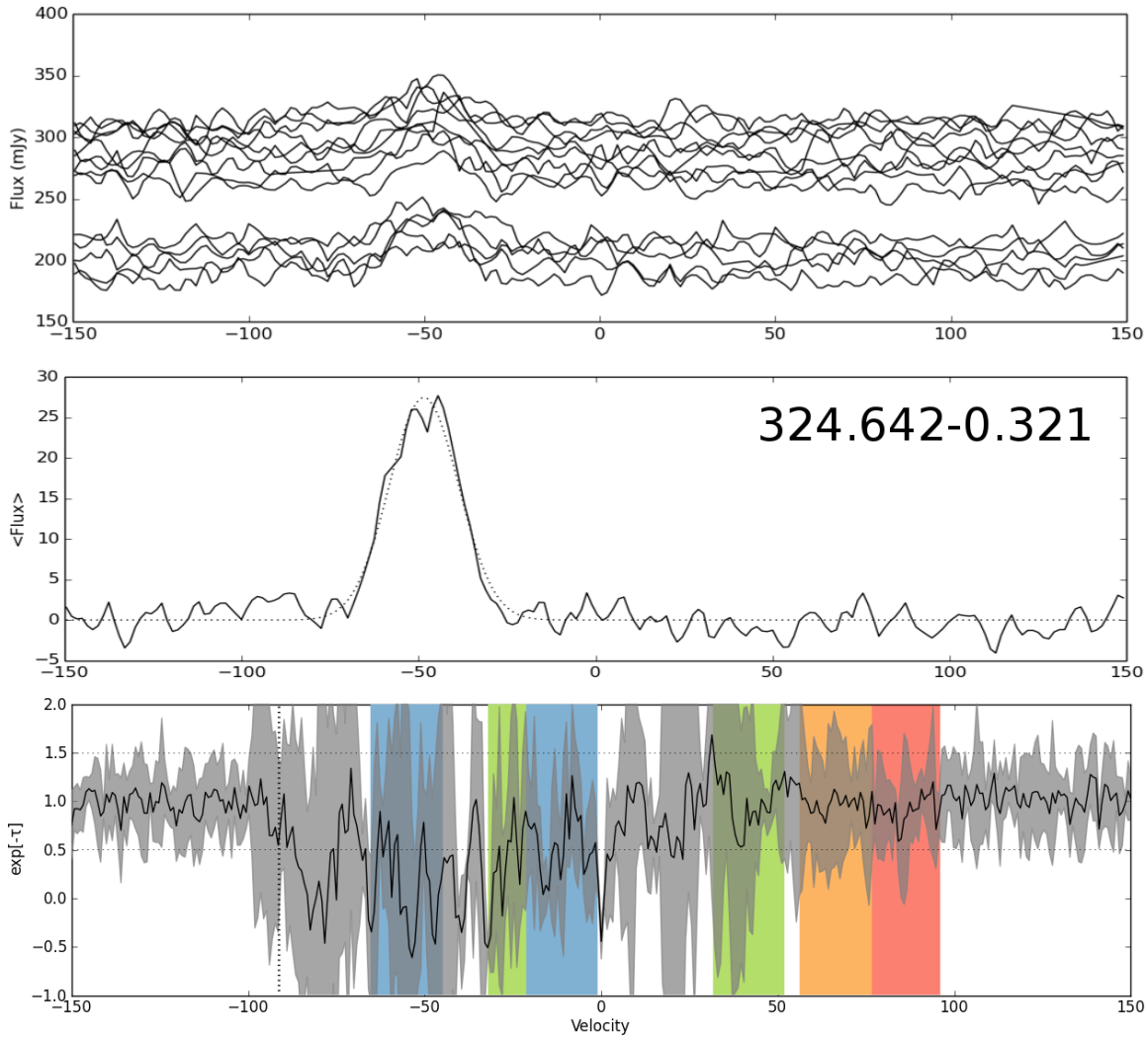
Flux (mJy)
<Flux>
324.642-0.321
exp[-τ]
Velocity

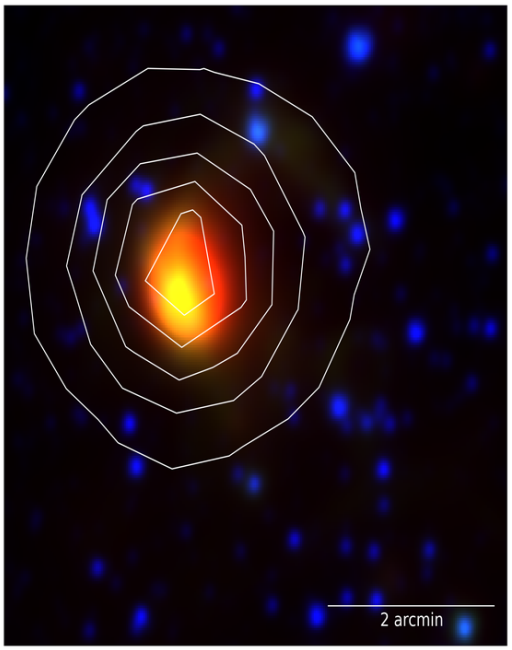
2 arcmin

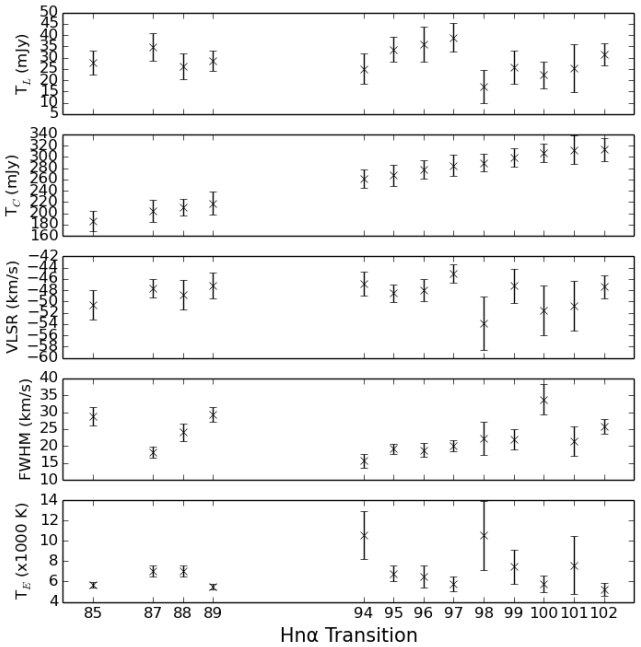
T_L (mJy)
T_C (mJy)
VLSR (km/s)
FWHM (km/s)
T_E (x1000 K)
Hnα Transition

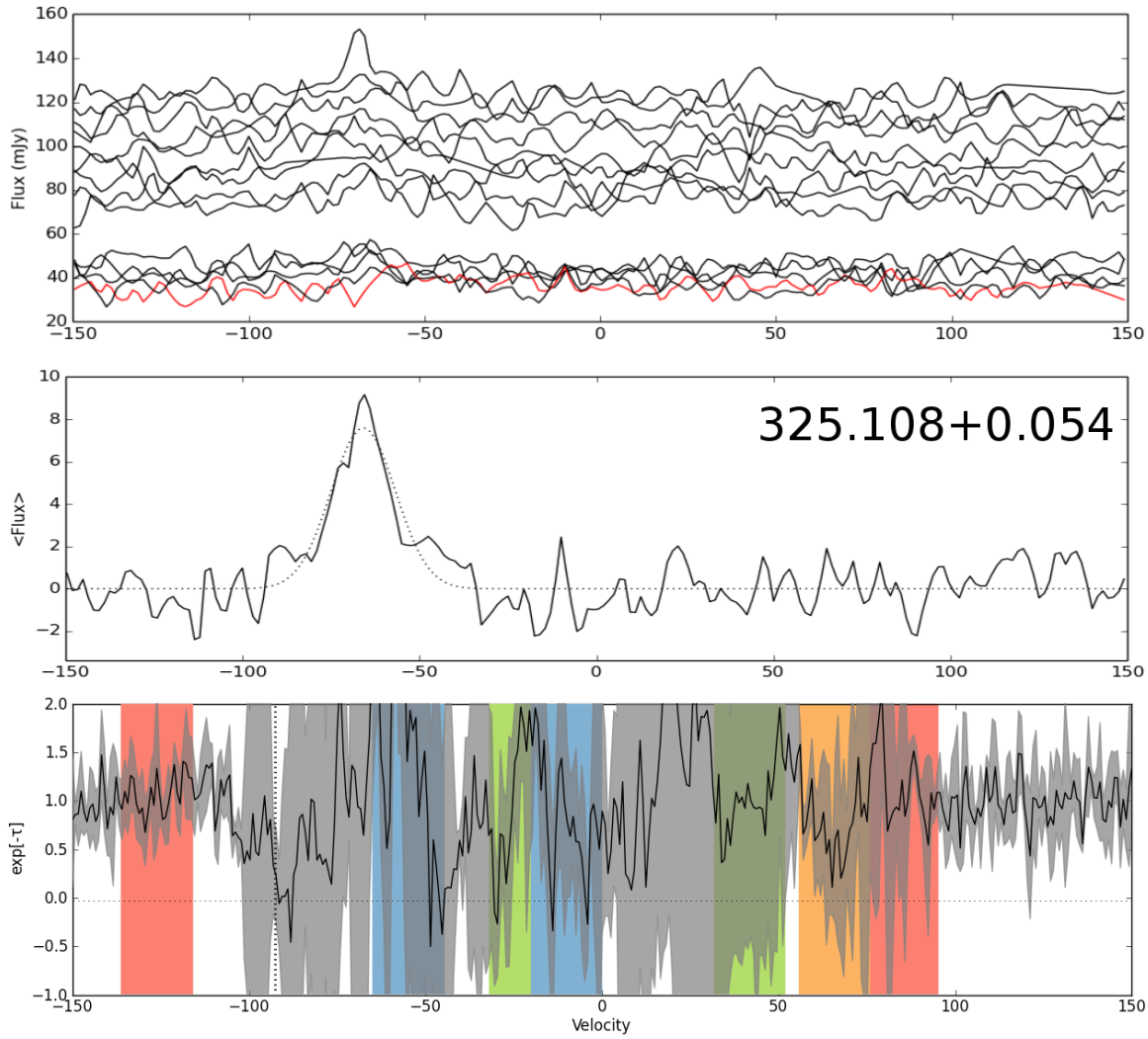
Flux (mJy)
<Flux>
325.108+0.054
exp[-τ]
Velocity

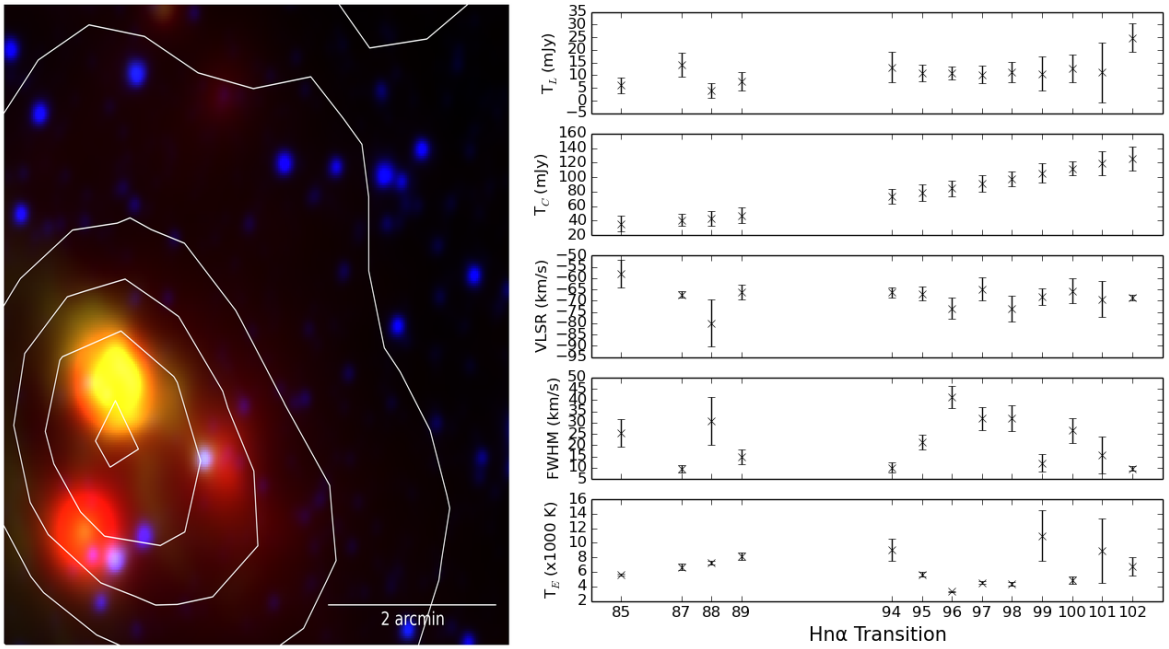
2 arcmin
T_L (mJy)
T_C (mJy)
VLSR (km/s)
FWHM (km/s)
T_E (x1000 K)
Hnα Transition

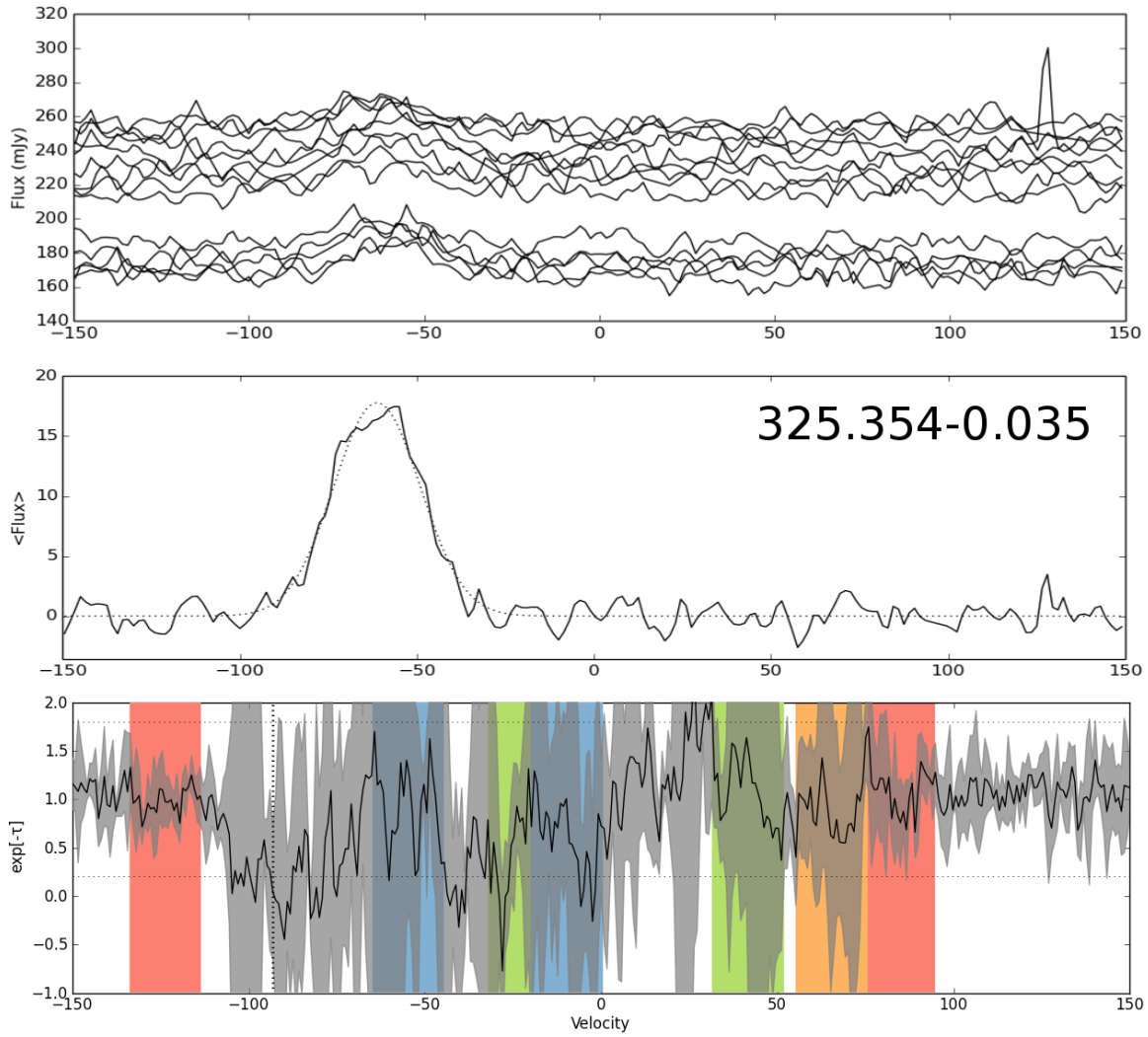
Flux (mJy)
<Flux>
325.354-0.035
exp[-τ]
Velocity

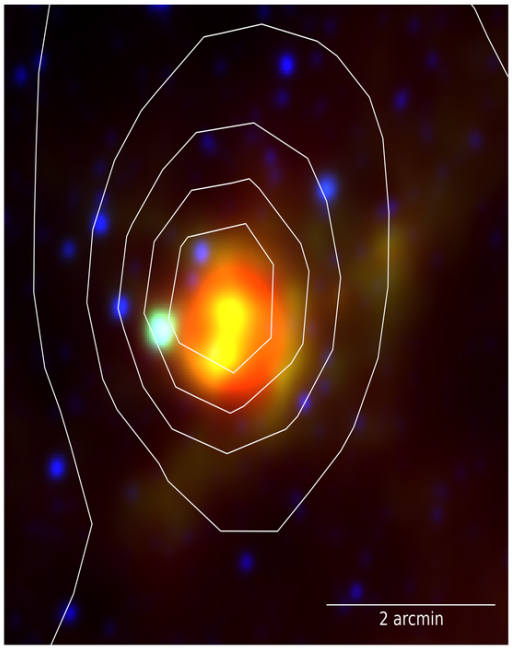
2 arcmin

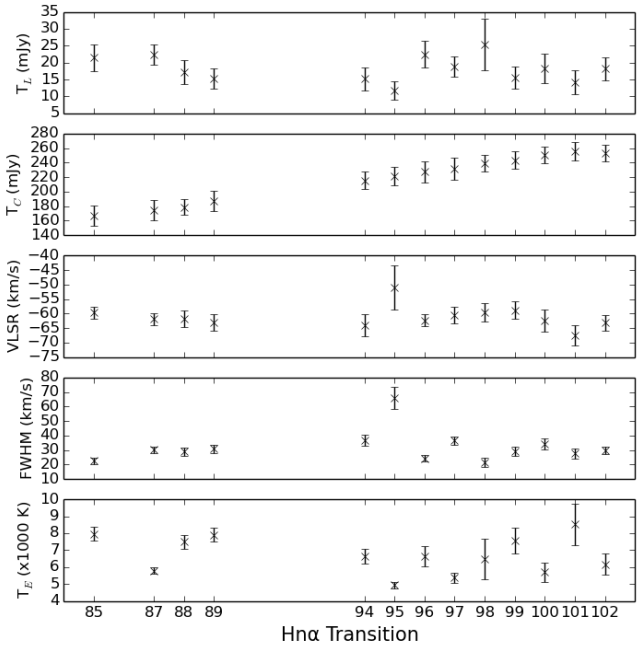
T_L (mJy)
T_C (mJy)
VLSR (km/s)
FWHM (km/s)
T_E (x1000 K)
Hnα Transition

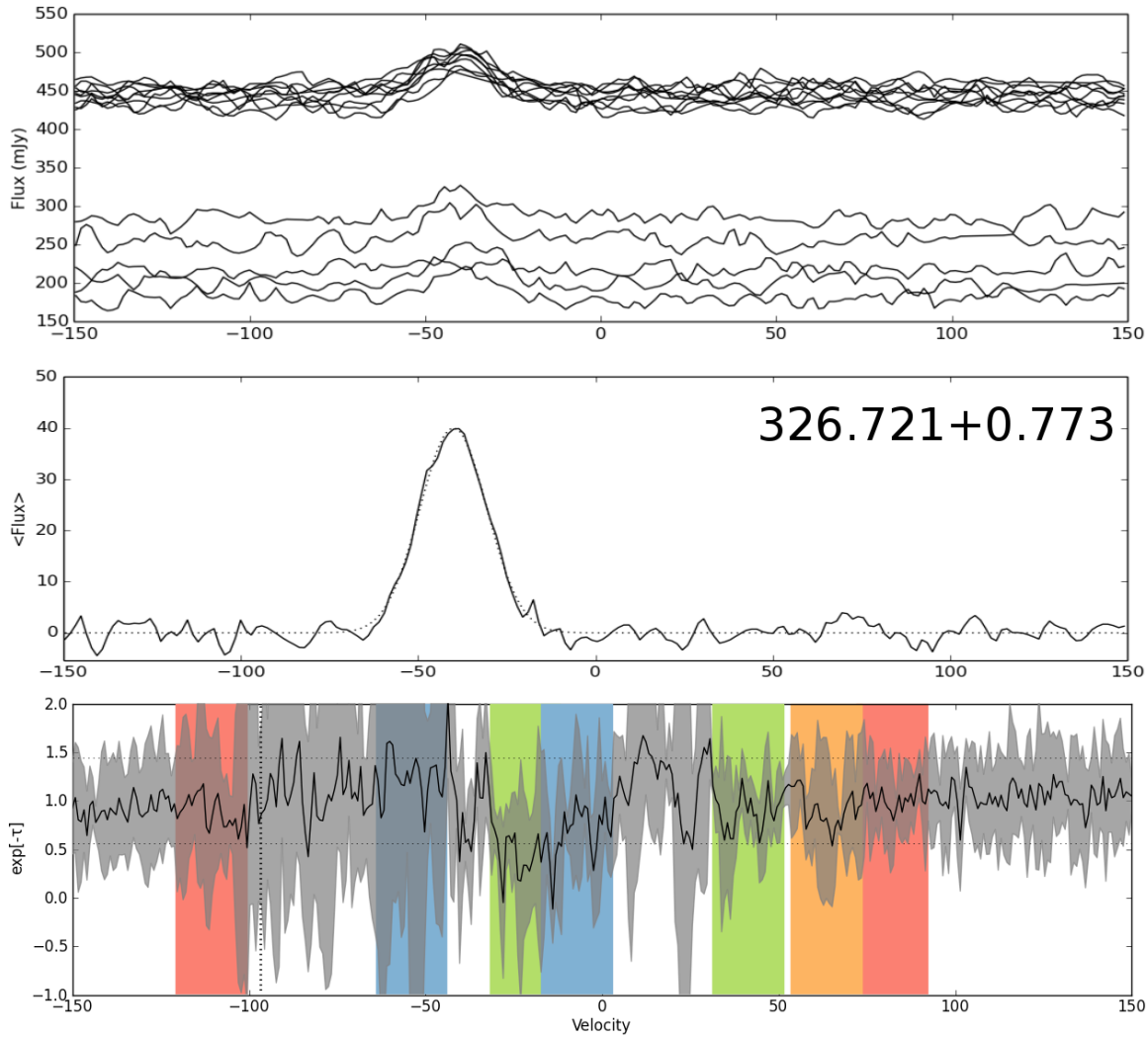
Flux (mJy)
<Flux>
326.721+0.773
exp[-τ]
Velocity

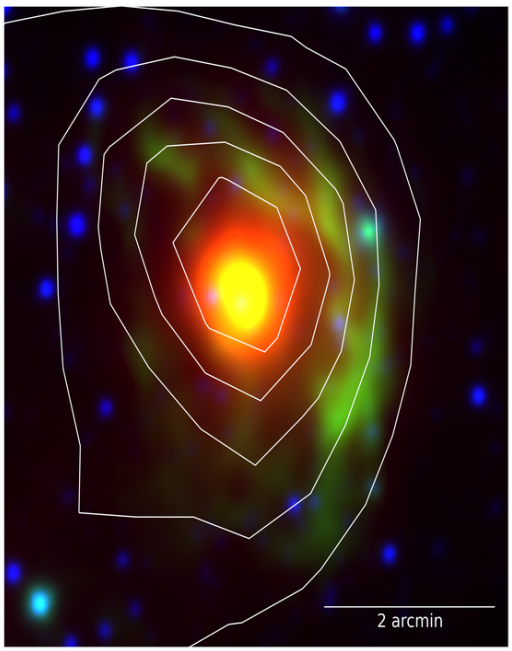
2 arcmin

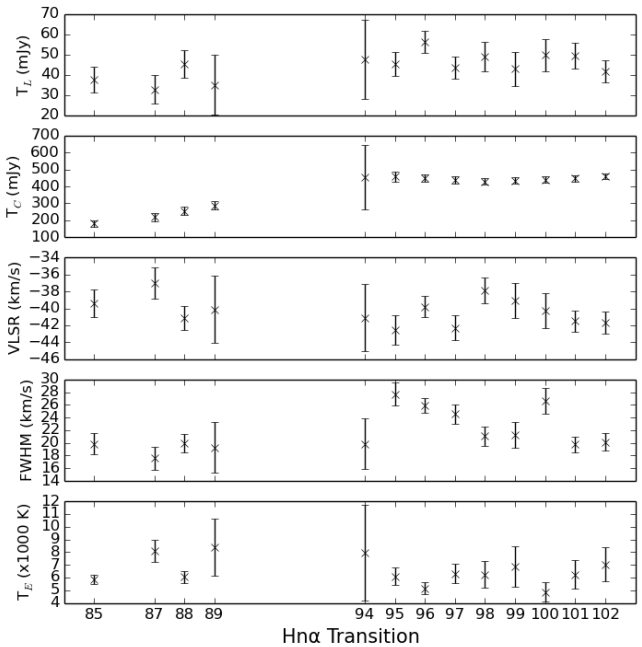
T_L (mJy)
T_C (mJy)
VLSR (km/s)
FWHM (km/s)
T_E (x1000 K)
Hnα Transition

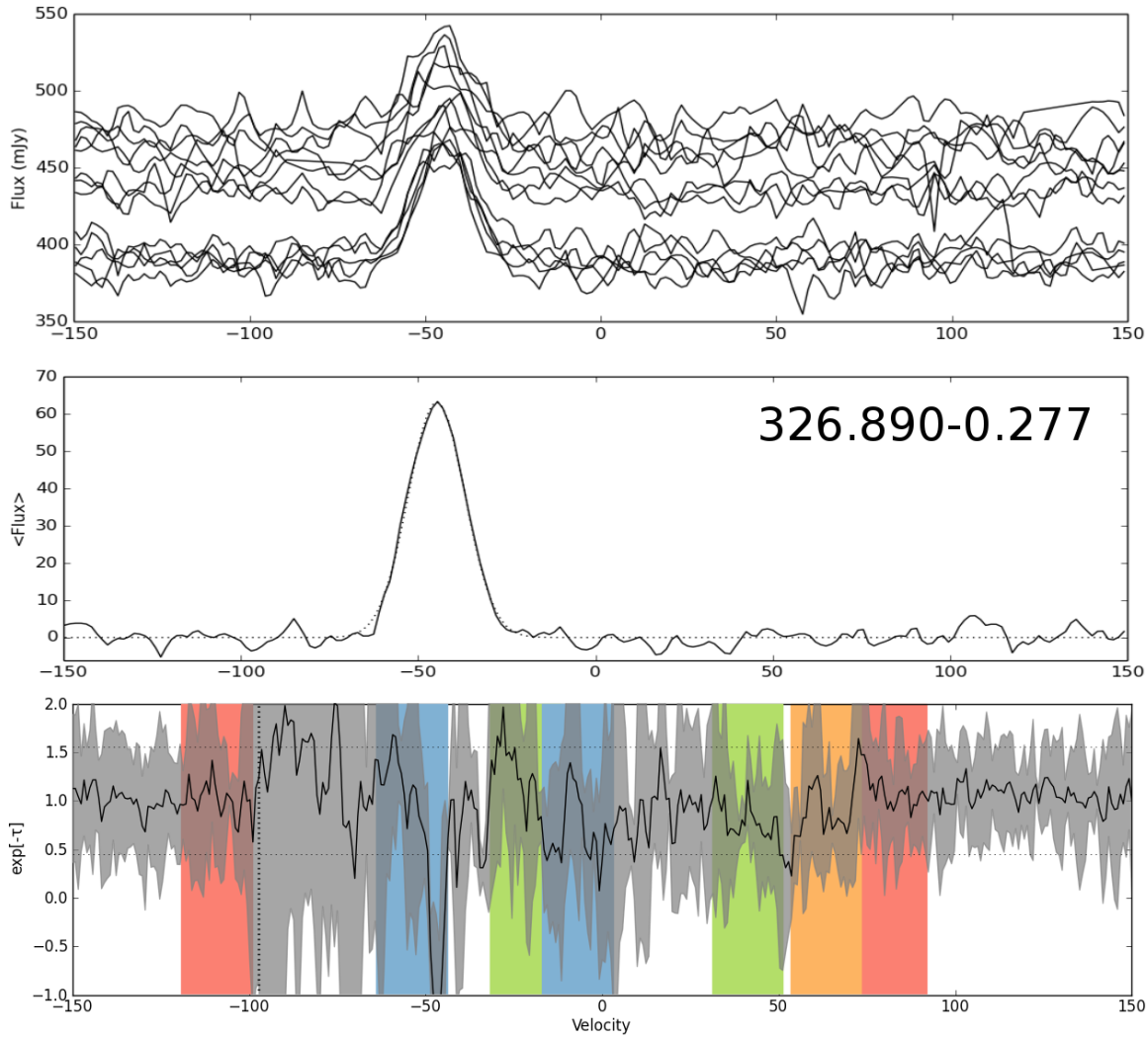
Flux (mJy)
<Flux>
326.890-0.277
exp[-τ]
Velocity

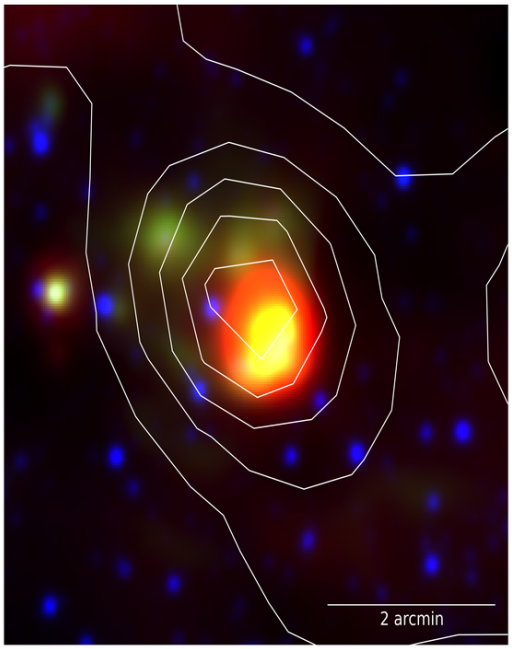
2 arcmin

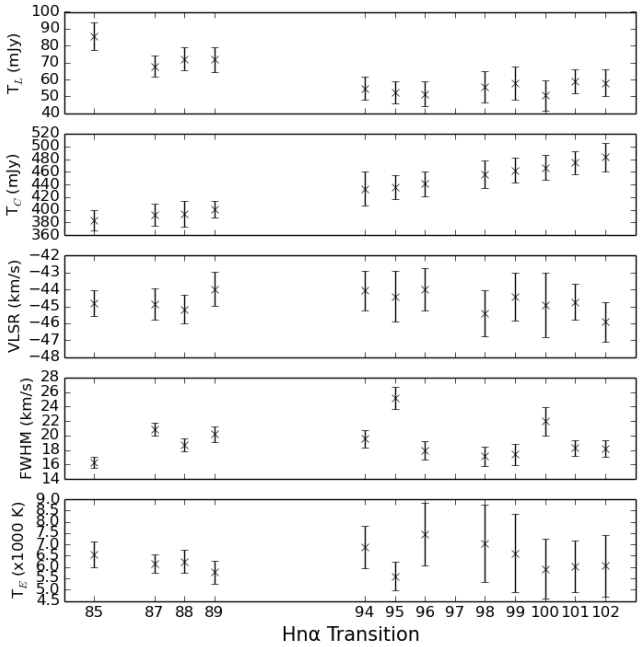
T_L (mJy)
T_C (mJy)
VLSR (km/s)
FWHM (km/s)
T_E (x1000 K)
Hnα Transition

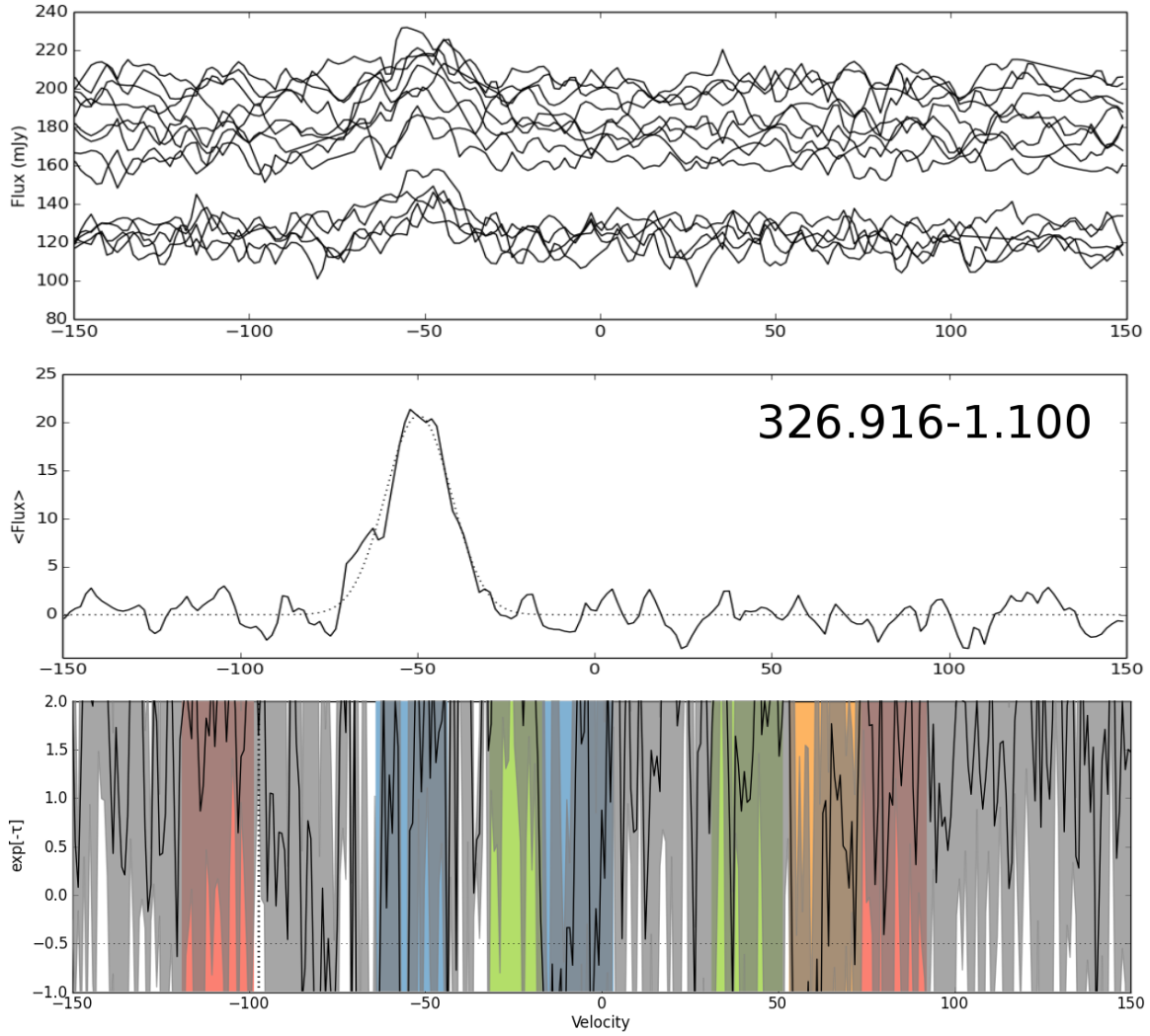
Flux (mJy)
<Flux>
326.916-1.100
exp[-τ]
Velocity

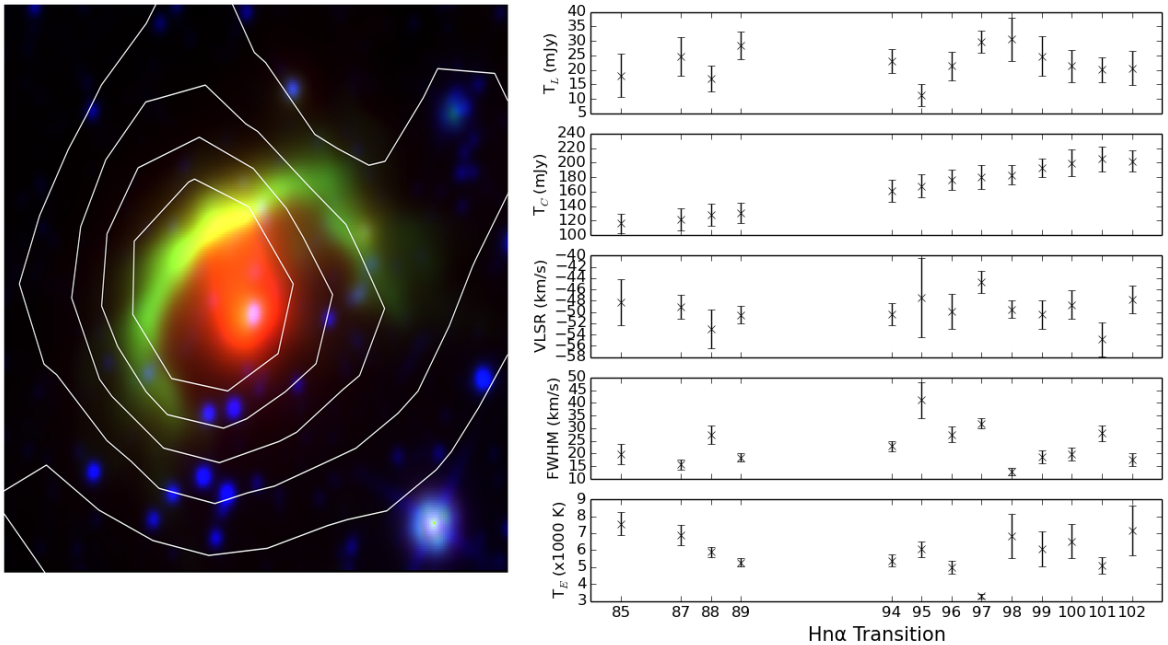
T_L (mJy)
T_C (mJy)
VLSR (km/s)
FWHM (km/s)
T_E (x1000 K)
Hnα Transition

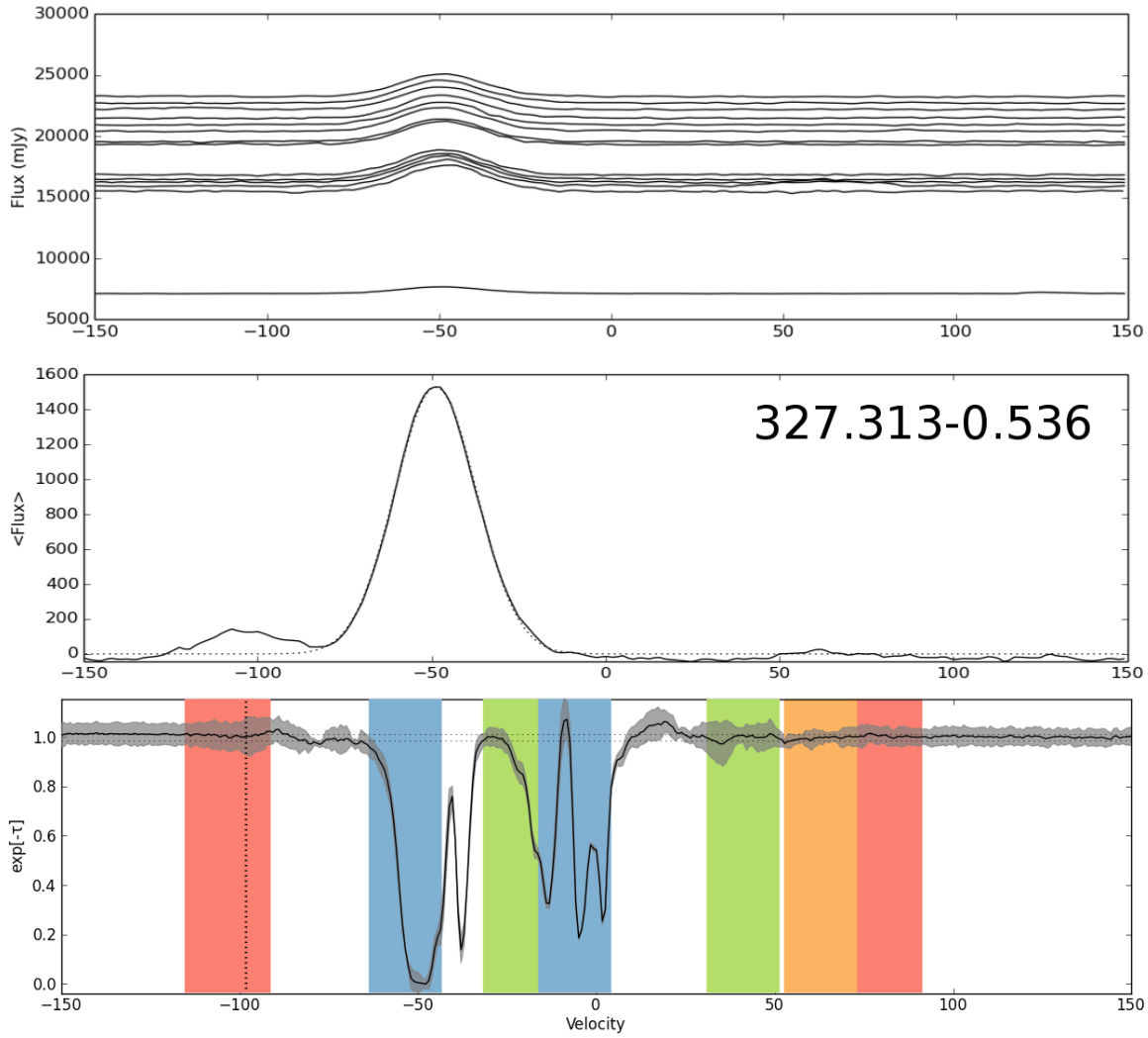
Flux (mJy)
<Flux>
327.313-0.536
exp[-τ]
Velocity

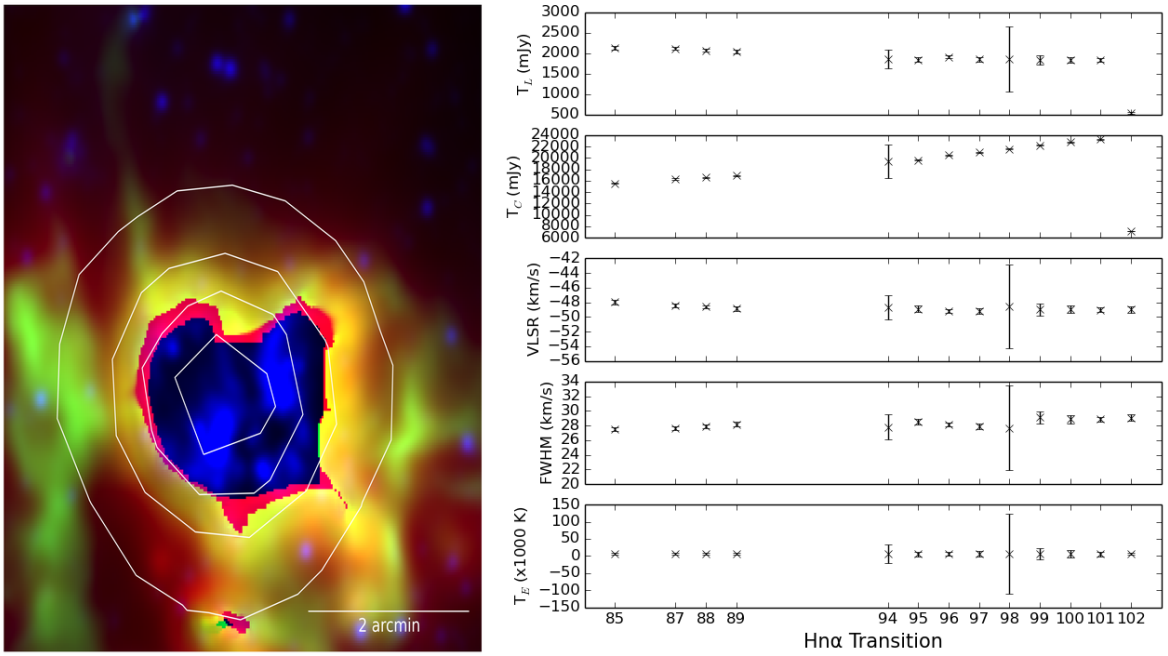
2 arcmin
T_L (mJy)
T_C (mJy)
VLSR (km/s)
FWHM (km/s)
T_E (x1000 K)
Hnα Transition

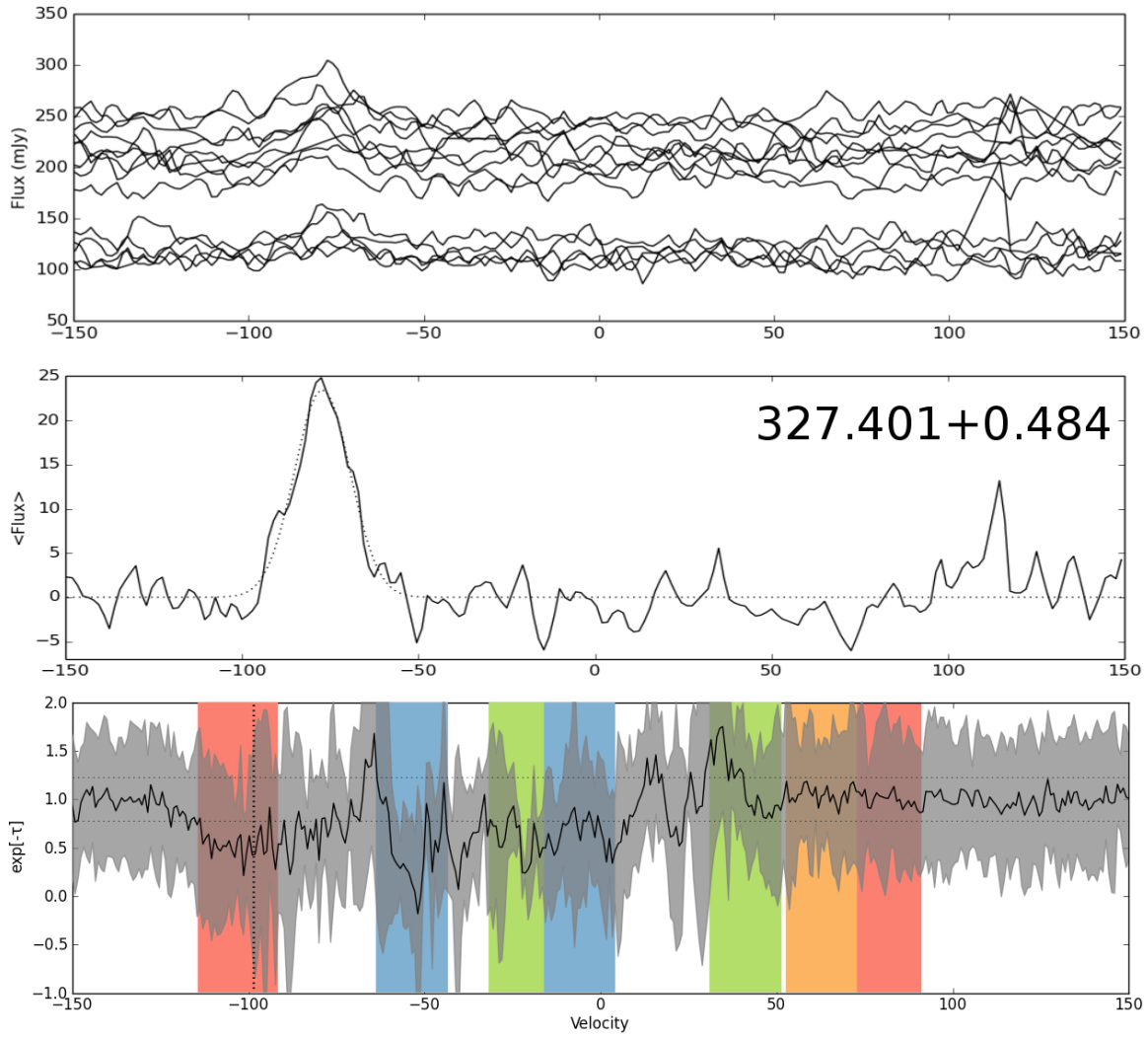
Flux (mJy)
<Flux>
327.401+0.484
exp[-τ]
Velocity

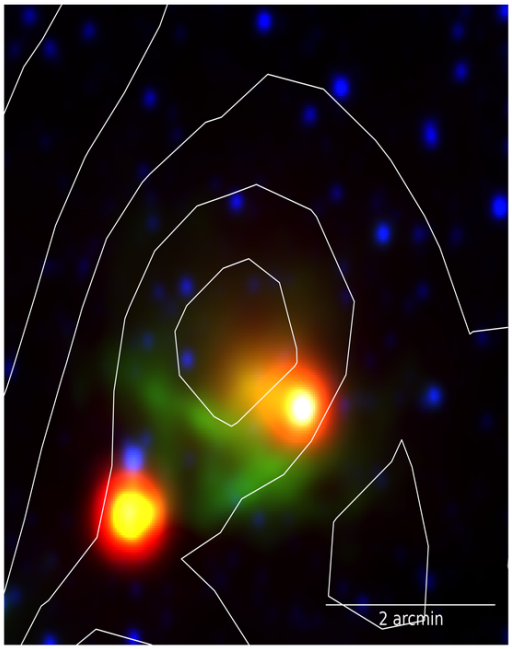
2 arcmin

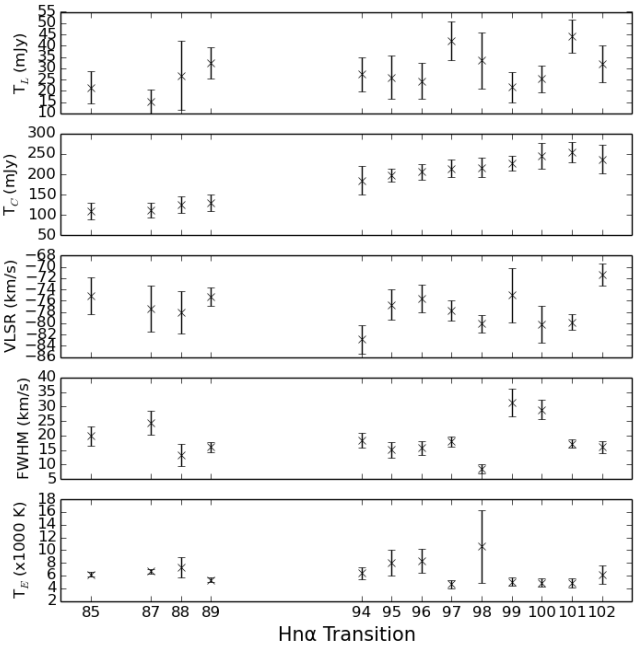
T_L (mJy)
T_C (mJy)
VLSR (km/s)
FWHM (km/s)
T_E (x1000 K)
Hnα Transition

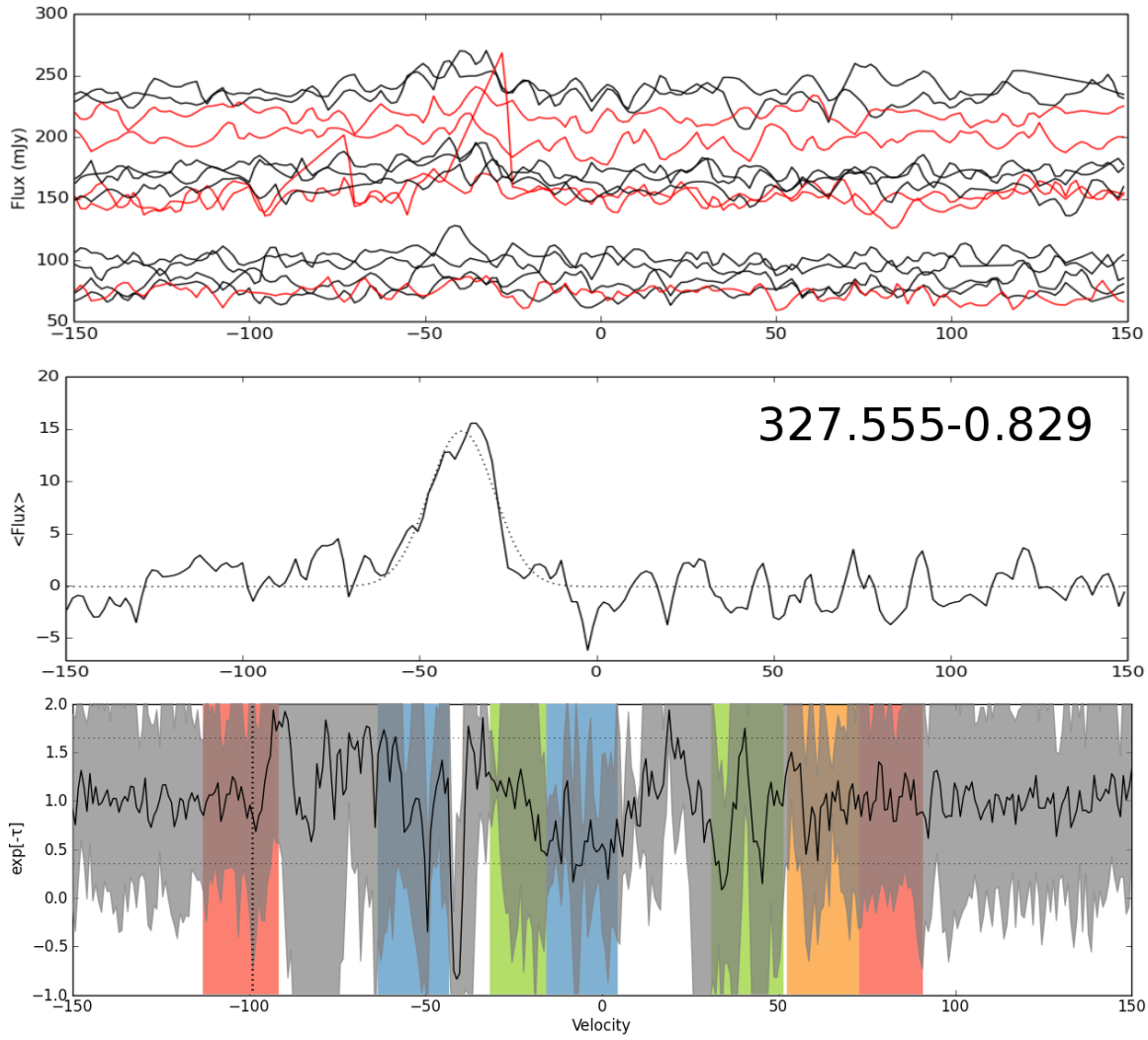
Flux (mJy)
<Flux>
327.555-0.829
exp[-τ]
Velocity

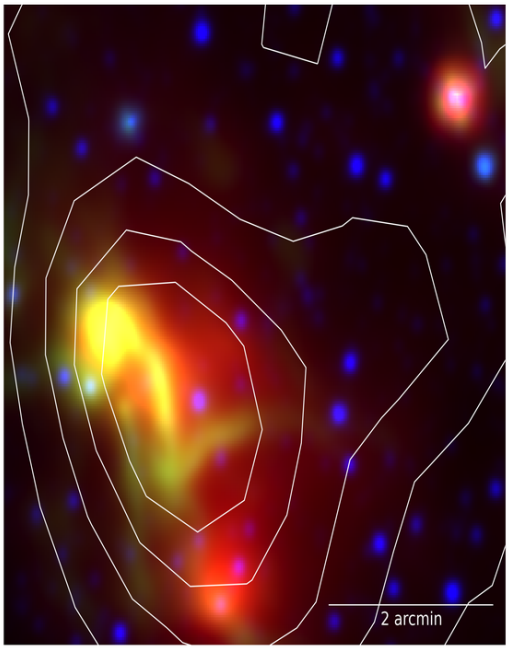
2 arcmin

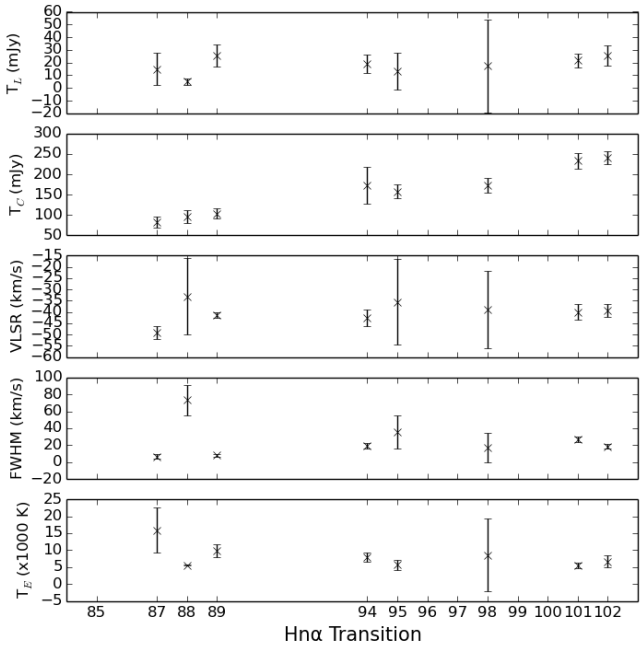
T_L (mJy)
T_C (mJy)
VLSR (km/s)
FWHM (km/s)
T_E (x1000 K)
Hnα Transition

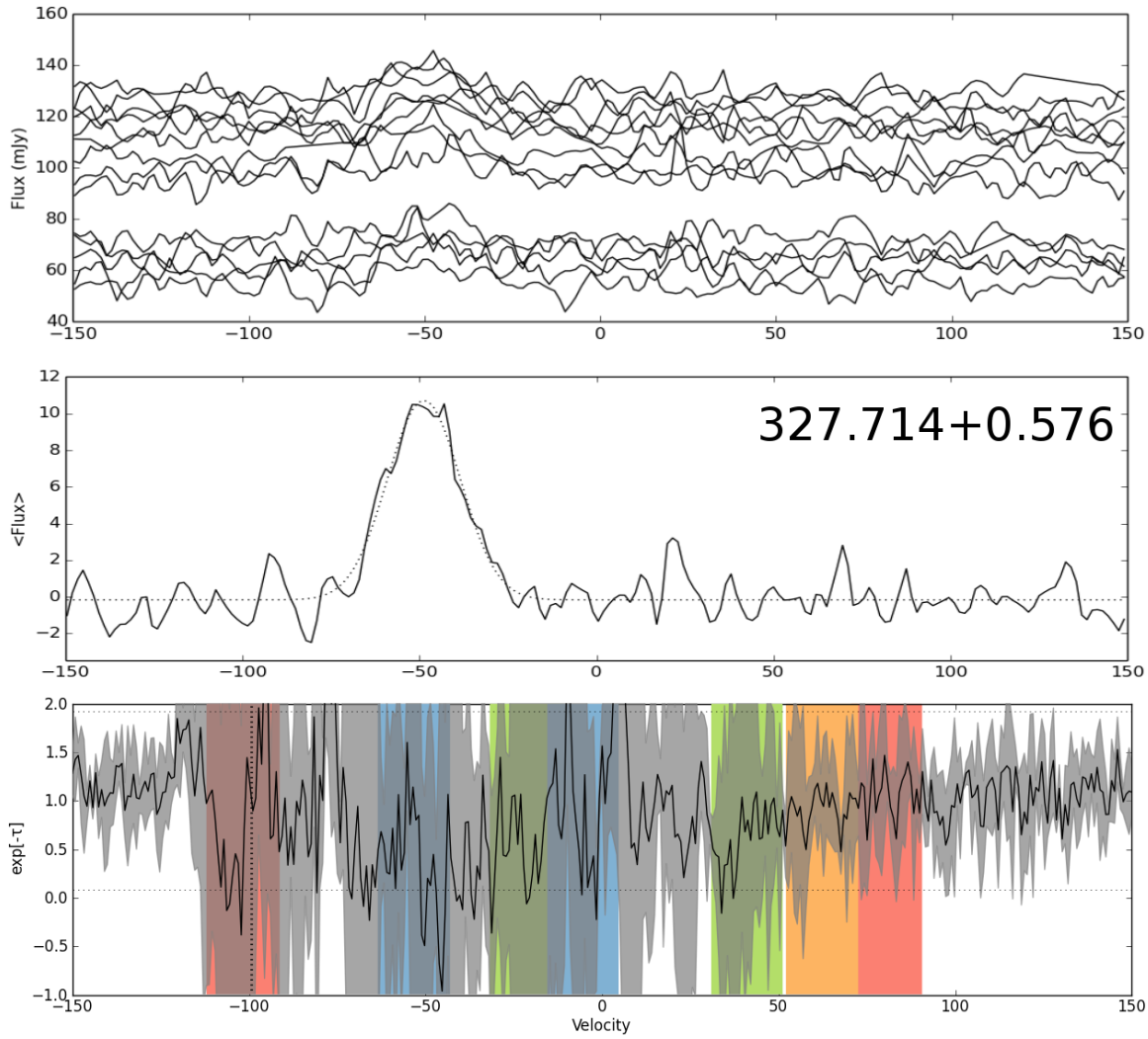
Flux (mJy)
<Flux>
327.714+0.576
exp[-τ]
Velocity

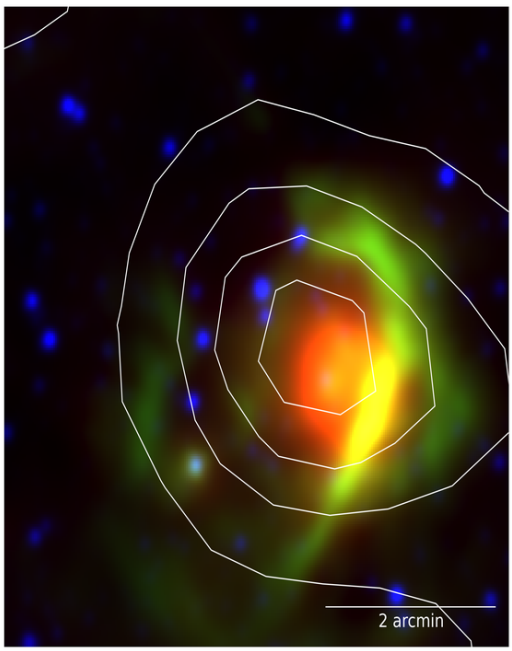
2 arcmin

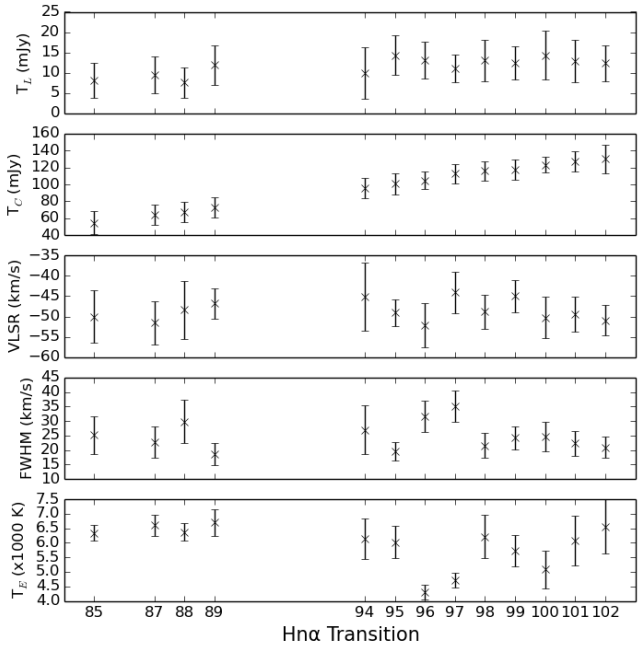
T_L (mJy)
T_C (mJy)
VLSR (km/s)
FWHM (km/s)
T_E (x1000 K)
Hnα Transition

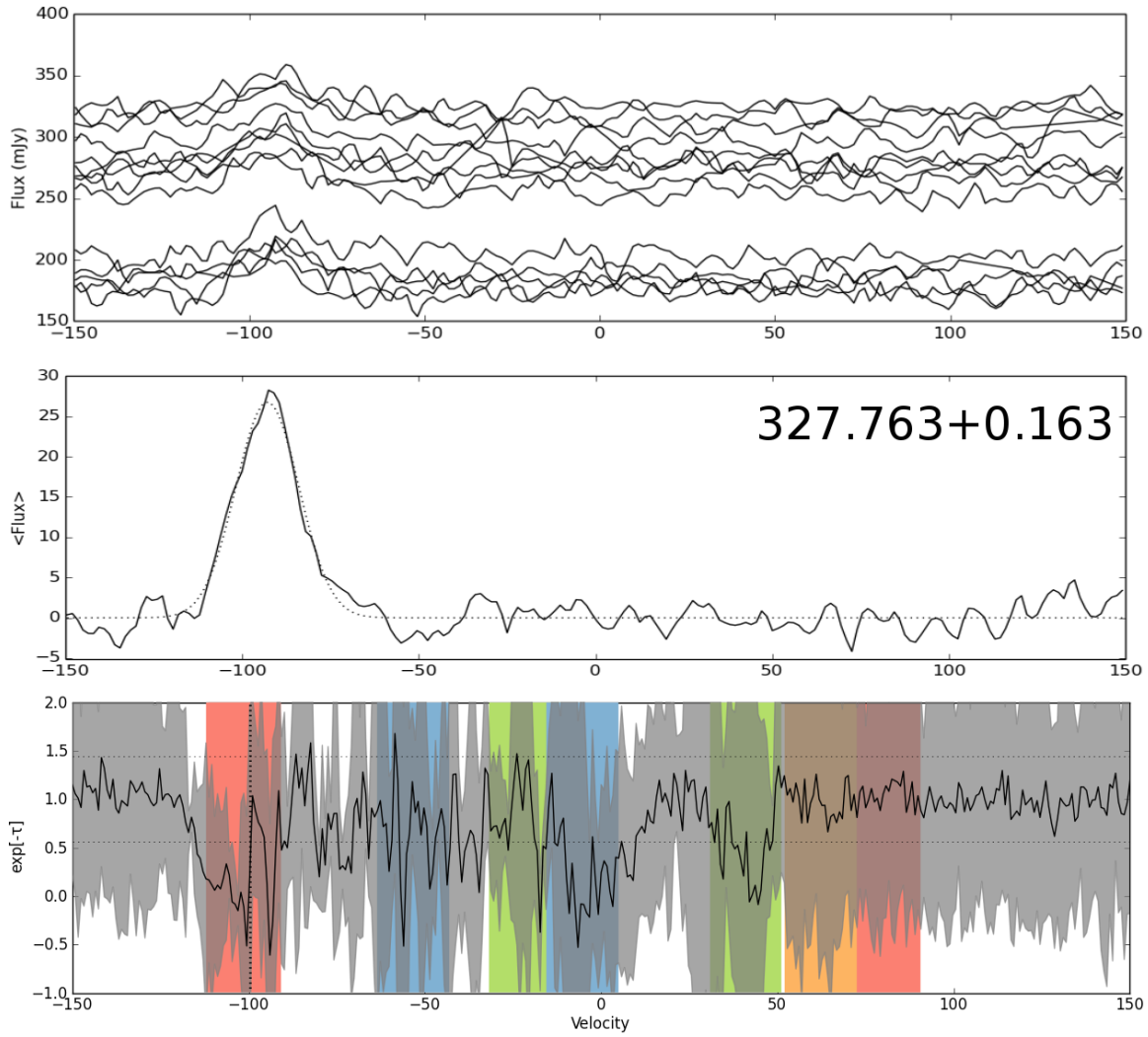
Flux (mJy)
<Flux>
327.763+0.163
exp[-τ]
Velocity

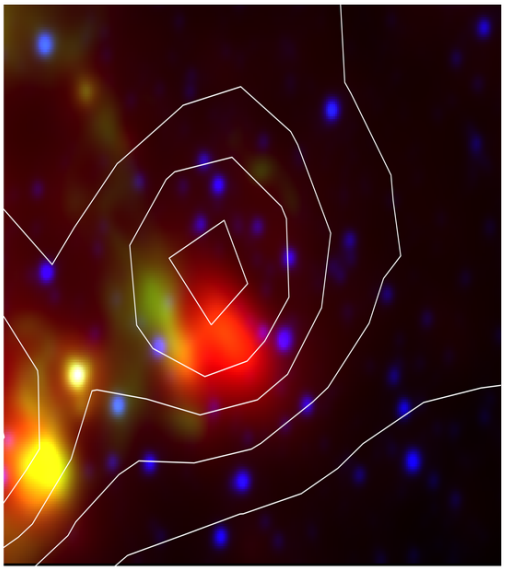

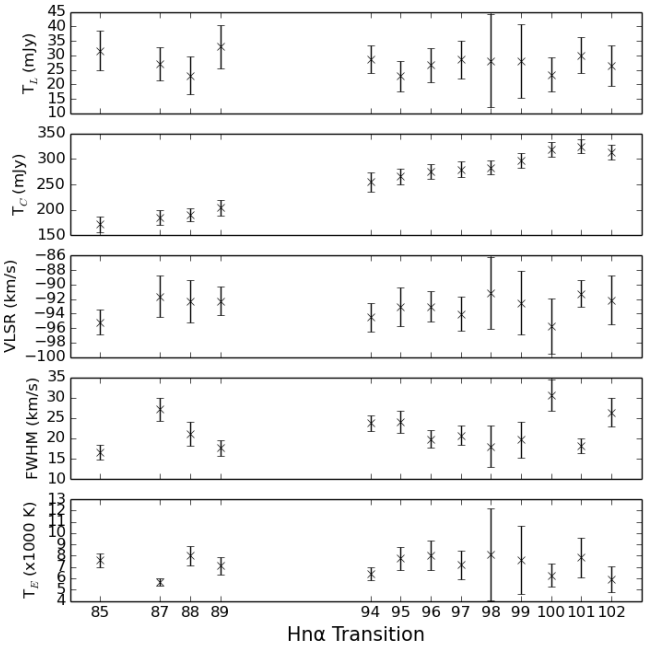
T_L (mJy)
T_C (mJy)
VLSR (km/s)
FWHM (km/s)
T_E (x1000 K)
Hnα Transition

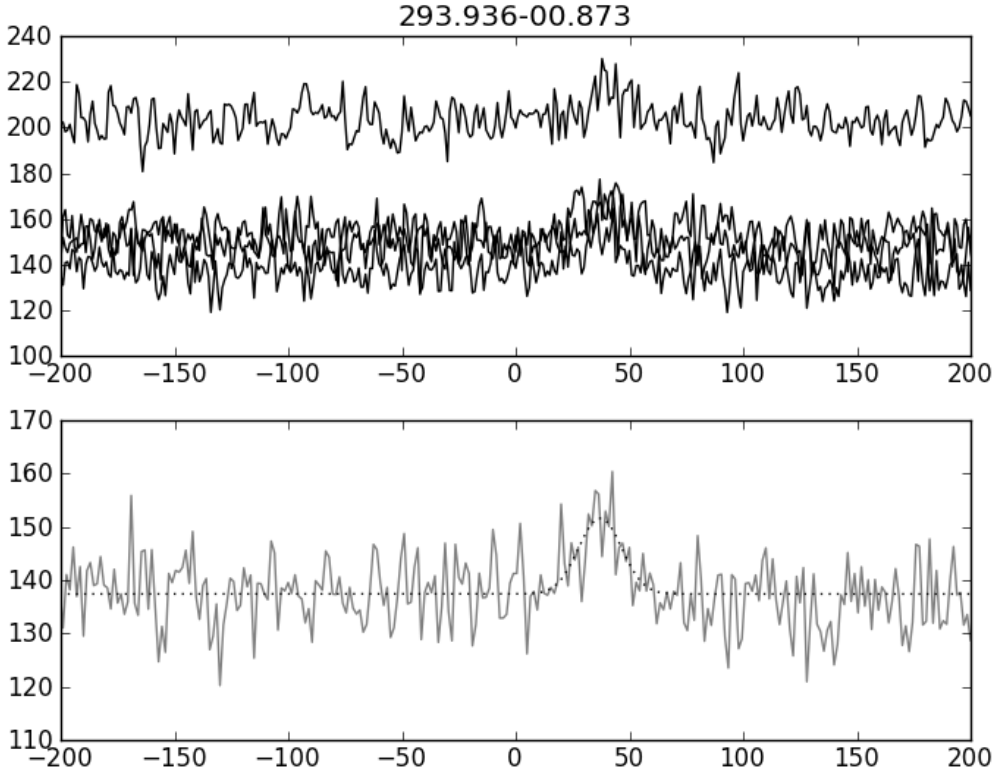
293.936-00.873
240
220
200
180
160
140
120
100
−200
−150
−100
−50
0
50
100
150
200
170
160
150
140
130
120
110
−200
−150
−100
−50
0
50
100
150
200

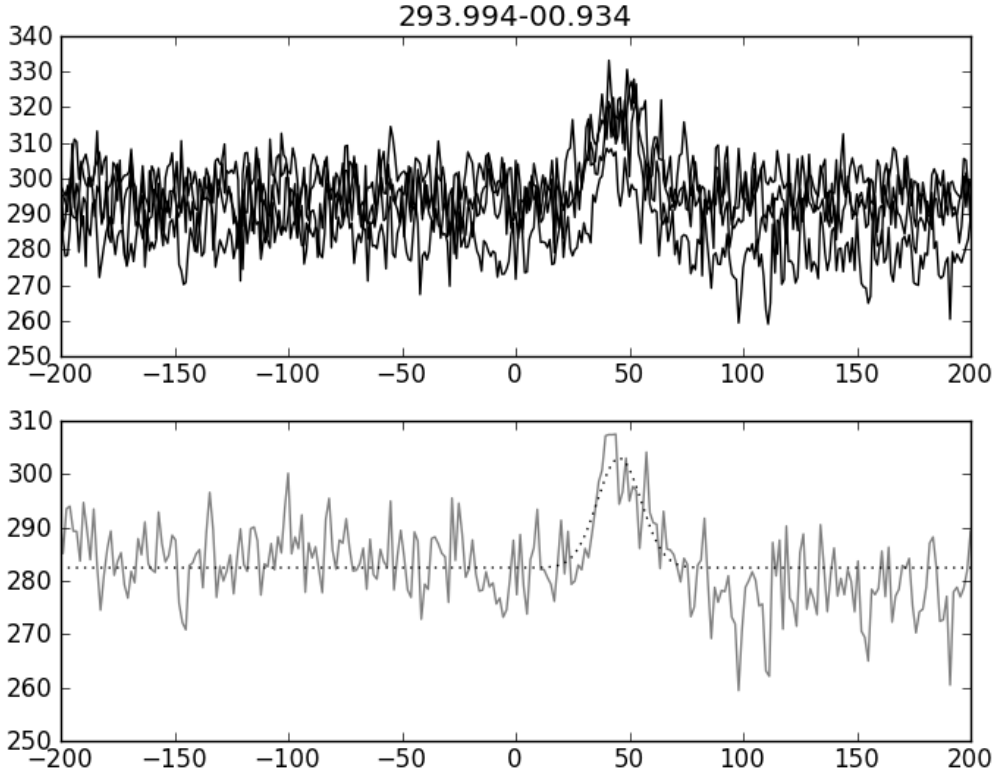
293.994-00.934
340
330
320
310
300
290
280
270
260
250
−200
−150
−100
−50
0
50
100
150
200
310
300
290
280
270
260
250
−200
−150
−100
−50
0
50
100
150
200

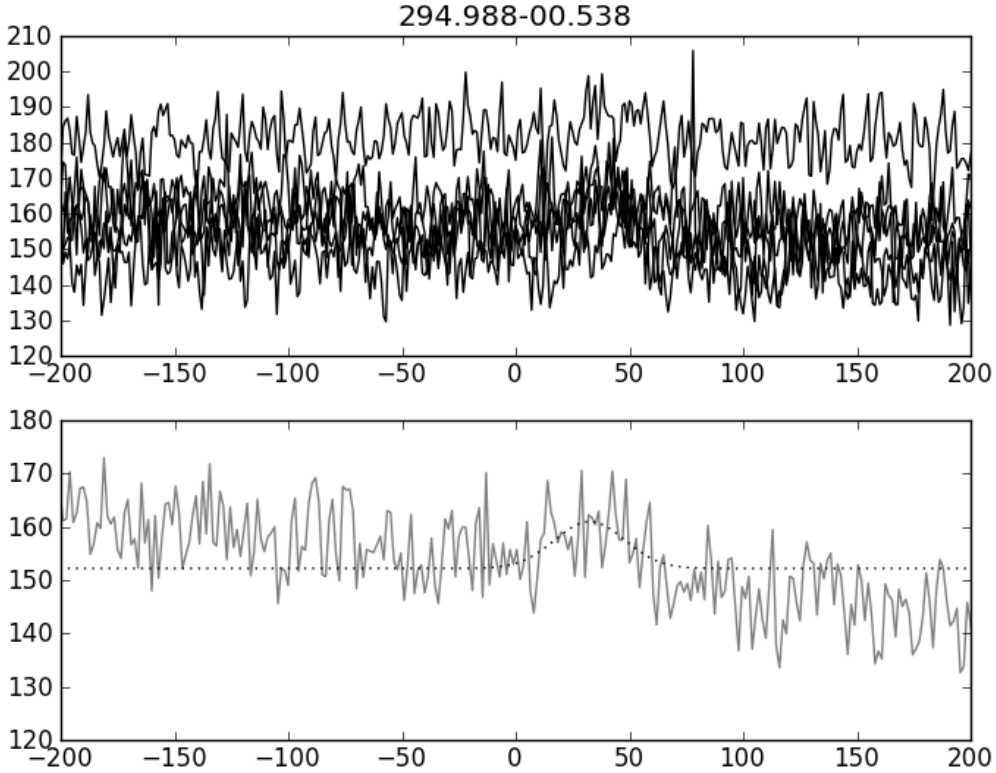
294.988-00.538
210
200
190
180
170
160
150
140
130
120
−200
−150
−100
−50
0
50
100
150
200
180
170
160
150
140
130
120
−200
−150
−100
−50
0
50
100
150
200

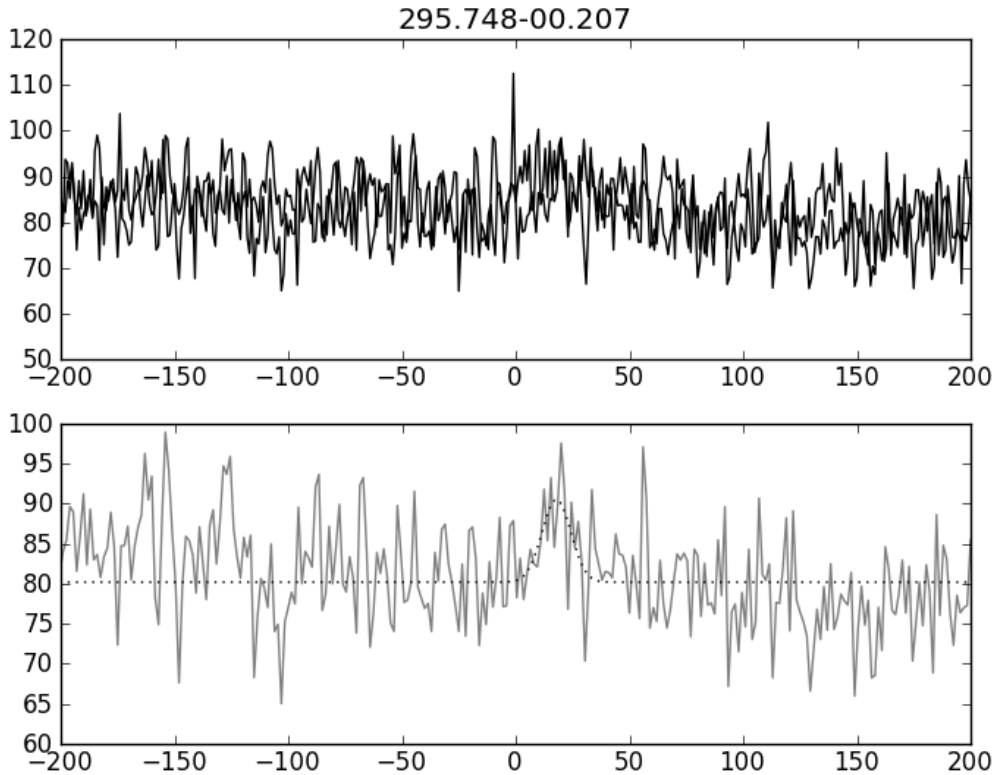
295.748-00.207
120
110
100
90
80
70
60
50
−200
−150
−100
−50
0
50
100
150
200
100
95
90
85
80
75
70
65
60
−200
−150
−100
−50
0
50
100
150
200

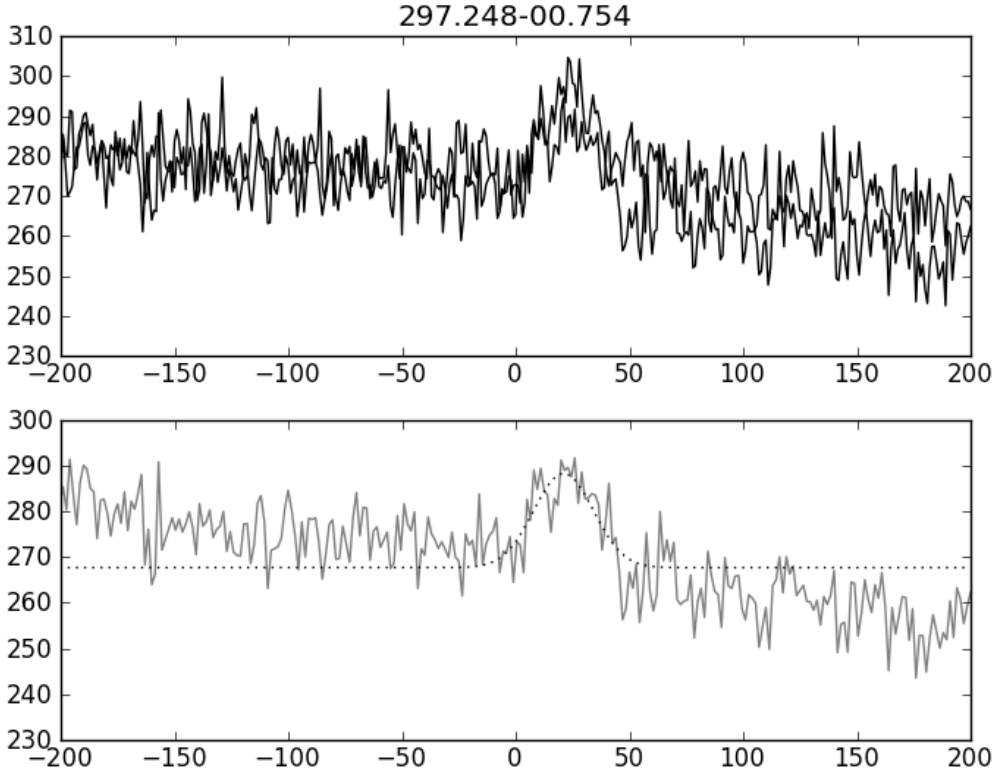
297.248-00.754
310
300
290
280
270
260
250
240
230
−200
−150
−100
−50
0
50
100
150
200
300
290
280
270
260
250
240
230
−200
−150
−100
−50
0
50
100
150
200

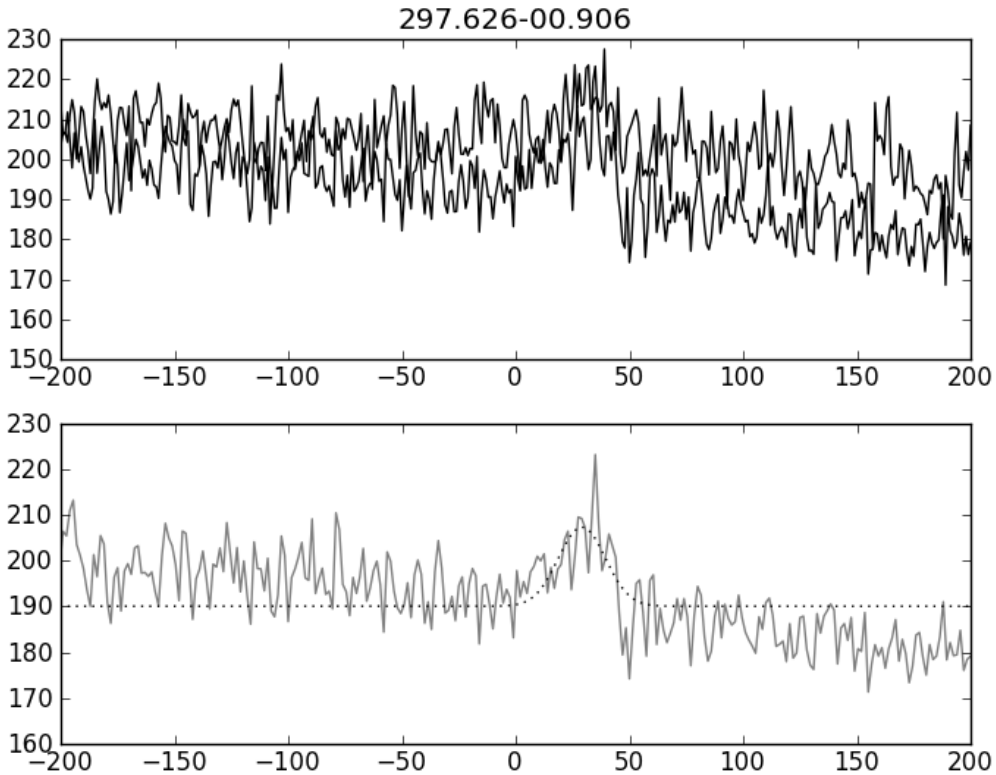
297.626-00.906
230
220
210
200
190
180
170
160
150
−200
−150
−100
−50
0
50
100
150
200
230
220
210
200
190
180
170
160
−200
−150
−100
−50
0
50
100
150
200

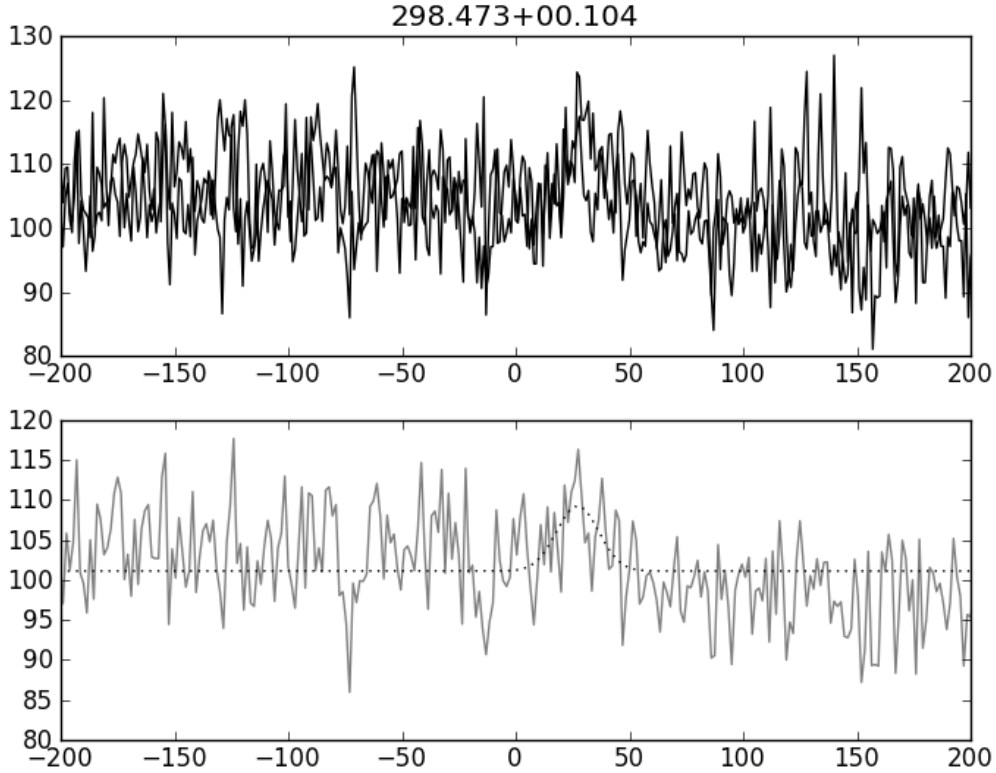
298.473+00.104
130
120
110
100
90
80
−200
−150
−100
−50
0
50
100
150
200
120
115
110
105
100
95
90
85
80
−200
−150
−100
−50
0
50
100
150
200

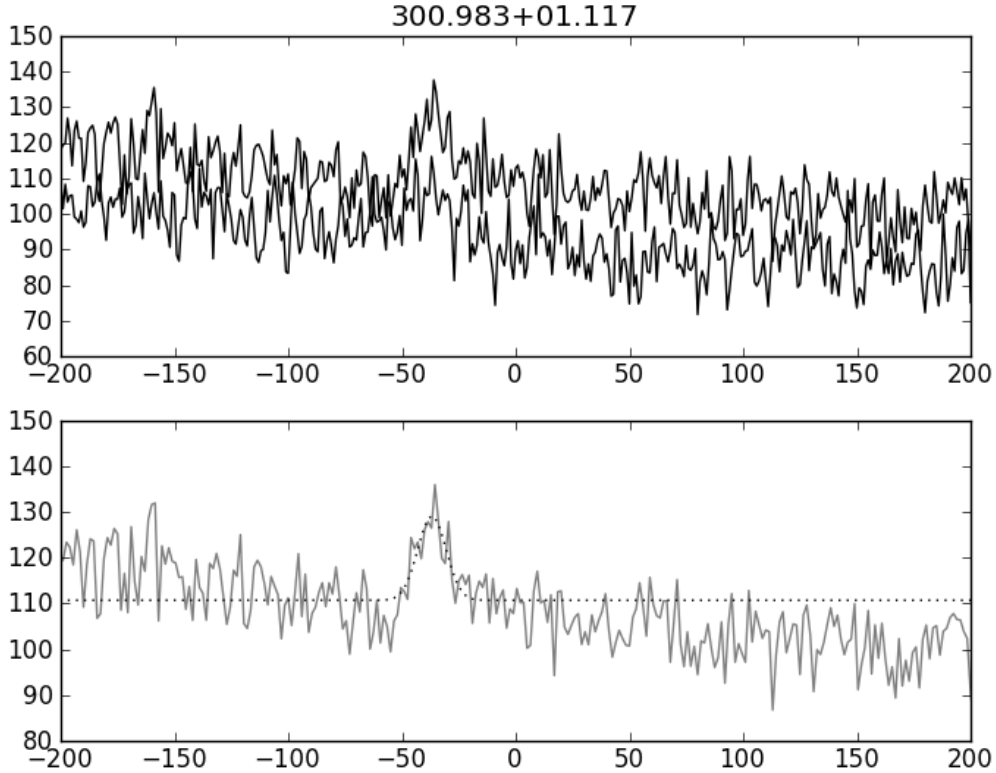
300.983+01.117
150
140
130
120
110
100
90
80
70
60
−200
−150
−100
−50
0
50
100
150
200
150
140
130
120
110
100
90
80
−200
−150
−100
−50
0
50
100
150
200

7.6 Summary

We have successfully used the ATCA to observe and detect RRL emission from H II region candidates—confirming these targets as *bona fide* H II reigons. These studies demonstrate the feasibility of a Southern H II Region Discovery Survey on the scale (and modelled after) the GBTHRDS.

Where applicable, the RRL velocities are in keeping with previous detections, or velocities gained from other lines; we also find the same bias towards smaller line widths as the GBTHRDS. Electron temperatures computed from the RRL parameters are also adhere to the expected Galaxy gradient.

As the sources for C2842 were selected based on the availability of 21 cm, H I, data, and many of the C2963 regions are unambiguously in the outer Galaxy, we were able to ascertain the line of sight distances to over 70% of our detected H II regions.

These observations have resulted in at least 28 newly discovered H II regions; increasing the number of known H II regions in the observed longitude ranges by over 36%. Many of the newly discovered H II regions are located in the outer Galaxy - beyond the Solar Circle - where the census of H II regions is least complete. Analysis of C2963 is ongoing and we expect additional H II region discoveries.

Chapter 8

Conclusions and Future Work

This thesis explores H II regions and the H I absorption towards them; with a focus on the fourth Galactic quadrant. Here we briefly summarise the major findings of the previous Chapters and discuss projects for further study.

2014 marks ninety years since humanity's realisation that the Milky Way is a distinct galactic system; separate from other observed (spiral) nebulae. Chapter 1 explores the historical progression of our understanding of our own home Galaxy, including the discovery of the H I transition, properties of the ISM, and the first attempts to use H II regions as spiral arm tracers

This thesis is largely based on publicly available data from large (all-sky) surveys—indeed no new data was taken until the observations of Chapter 7. These data sets are described in Chapter 2.

The principle of the terminal–velocity H I emission/absorption KDAR method is that H I absorption can be linked to known features along the line of sight (i.e. the tangent point). The presence or absence of H I absorption in these features constrain the line of sight distance to the region. Chapters 3 and 4 presented modifications of this method for the purposes of poor quality H I spectra and H II regions within the extreme inner Galaxy, respectively—these spectra are traditionally deemed especially difficult to analyse.

These two Chapters constrained the line of sight distance to over 200 H II regions. Furthermore, an investigation of the lv locus of the Near and Far 3kpc Arms was performed. This is the first time the Arms have been traced via H I absorption, and the fits from our analysis are consistent with the CO fits of Dame & Thaddeus (2008).

Chapters 3 and 4 have provided distances to a large sample of H II regions between $10^\circ < l < 342^\circ$, for the first time since Caswell & Haynes (1987). This distance data has been collated with other H II region distance studies to provide a greatly improved view of the H II region distribution in, and therefore structure of, the Galaxy (García et al. 2014; Hou & Han 2014; Vallée 2014).

Unlike the previous Chapters, Chapter 5 does not provide a KDAR analysis and the

resulting line of sight distances; but rather presents a complete 'atlas' of H I absorption toward known fourth quadrant H II regions. The Atlas provides the foundations for a KDAR analysis, but also introduces the opportunity to investigate Galactic spiral structure via the longitude–velocity loci of H I absorption features. For example, Vallée (2014) claim that the H I absorption distribution of Chapter 5 is well aligned with their four–arm model for the Milky Way.

As a result of Chapter 5, kinematic distance studies have either been prepared, or carried out, for every *known* H II region in the fourth quadrant (within the bounds of the SGPS I). Despite this achievement, within the longitude range $260^\circ < l < 353^\circ$ (i.e. outside the observable sky for the GBT) for every confirmed H II region, 2.5 candidate regions exist.*

Chapter 6 prepares for H II region discovery in the southern sky: searching for new regions in existing untargeted RRL survey data, selecting "H II region candidate" criteria, and discussing particular considerations for ATCA observations.

In 2013, we obtained 24 hours of observing time with the ATCA in the H75 array configuration for the purposes of H II region discovery (project ID: C2842). Chapter 7 presents those observations, in which 14 RRL transitions were observed toward 24 H II regions—20 of which were confirmed as bona fide H II regions for the first time during this experiment. A further 24 hours of observations in 2014 resulted in the discovery of at least eight new H II regions (data reduction is still under way). These observations serve as the Pilot Study required to propose for a Southern H II Region Discovery Survey (see Section 8.1.3).

8.1 Future Work

Answers to many of the questions facing the first Galactic astronomers are still being sought today: Where are the spiral arms? How many arms does the Milky Way have? What does the outer Galaxy look like? And what's happening in the Galactic centre? Just like the early twentieth century, the vital datum for solving these problems is *distance*.

The analyses of this thesis were only possible due to a 'generation leap' in H I, radio continuum and infrared surveys (namely the IGPS and Spitzer/WISE). The unprecedented sky–coverage and resolution of these surveys produced a resurgence in the H I emission/absorption terminal–velocity KDAR analysis; resulting in hundreds of new kinematic distances for H II regions—indeed, the number of Galactic structure tracers, with known distances, has almost doubled between 2009 and 2014 (including H II regions, Giant Molecular Clouds and 6.7 GHz methanol masers, Hou & Han 2014). One of the main features of this thesis is a complete census of H I spectra towards known H II regions in the fourth quadrant (Chapter 5). While this may appear to be an 'end point' for the field, it is merely a beginning.

*The known:candidate ratio for the whole Galaxy is 1.0:1.3. For the first quadrant—as a direct result of the GBTHRDS, which approximately doubled the number of known H II regions within its longitude range—the ratio is now in favour of known H II regions 1.4:1.0. All ratios are calculated from the 'known' and 'candidate' lists prepared by Anderson et al. (2014), available online at http://astro.phys.wvu.edu/wise/

8.1.1 Immediate Science

This thesis provides the ground work for science results in several distinct projects:

- *HOPS RRL catalogue:* So far the HOPS team have published their H_2O and NH_3 [(1,1) and (2,2)] catalogues. Chapter 6 provides a complete literature cross–referenced catalogue of the HOPS RRL 5σ detections.

- H II *region discovery with the ATCA:* We have now completed two epochs of observations with the ATCA for the purposes of H II region discovery. The results of the first observing run are presented in Chapter 7, while the second epoch is presently undergoing data reduction. These two epochs constitute the Pilot Study for a Southern H II Region Discovery Survey (see Section 8.1.3).

- H I *Absorption in the Fourth Quadrant:* Dickey et al. (2003) present an investigation of H I emission and absorption spectrum pairs towards H II regions in the SGPS test region. In their concluding remarks, Dickey et al. (2003) state that *"extending these techniques to the full survey area will indicate whether [our] conclusions apply to the inner Galaxy as a whole and also give a much better determination of the distribution of cool cloud temperatures"*. Combining the results of Chapter 5 with the published spectra of Strasser et al. (2007, towards extragalactic continuum sources) provides an opportunity to investigate the mean opacity (as a function of galactocentric radius), temperature of cool H I clouds, peak brightness temperature of H I emission and catalog H I self absorption over the *entire* fourth quadrant.

8.1.2 Long Term

In addition to immediate science opportunities; the projects required to extend the analysis of this thesis are already in the planning stages.

8.1.2.1 H I, radio continuum and infrared data

Just as the 'generation leap' of H I and infrared surveys spurred the H II region studies of the last ten years; advanced plans for the next generation of H I, radio continuum and infrared surveys are underway.

The Galactic ASKAP (Australian Square Kilometre Array Pathfinder) Survey (GASKAP, Dickey et al. 2013) will achieve about an order of magnitude improvement in brightness sensitivity and angular resolution compared with current H I (and OH) surveys and will be complete for the entire sky south of $\delta = +40°$, $|b| < 10°$. GASKAP is a monumental survey which brings together over 75 investigators from 42 institutions in 11 countries - a testament to the continued importance of the H I transition to Galactic studies. The successor to GASKAP, H I science with the Square Kilometre Array (SKA), is overseen by the SKA Working Group 1 (Milky Way and Nearby Galaxies), Level 1 science team.

Radio continuum surveys are also planned science activities of the SKA and SKA–Pathfinder telescopes. Pathfinder 1.4 GHz radio surveys (i.e. EMU) will provide a factor of ∼100 improvement in 5σ sensitivity compared to the NVSS and SUMSS (Norris et al. 2013).

The James Webb Space Telescope is the science successor to the Spitzer Space Telescope* (and Hubble Space Telescope); with an expected eight fold increase in resolution. In planning since 1996, the telescope was originally intended for launch in 2007; however, as of 2013, launch is expected to take place in 2018.

These surveys should enable all the H II regions in the Milky Way to be discovered, and line of sight distances to the entire sample established.

8.1.3 The Southern H II Region Discovery Survey

In 1987, Felix Lockman presented *Recombination Line Searches for Galactic* H II *Regions* at a NRAO Workshop entitled *Large-scale surveys of the sky.* The conference paper begins with the words:

> *WHY MAKE A NEW RECOMBINATION LINE SURVEY?*
> *Because so little is known about the Galaxy. (Lockman 1990a)*

Despite nearly three decades of intervening science, that statement still holds true. Furthermore, we find ourselves in a similar situation to the H II region discoverers of the 1980s—in that there currently exist two candidate regions for every known H II region.

Anderson et al. (2014) have catalogued ∼8000 H II region candidates based on WISE mid-infrared morphology. Of these ∼ 2000 are confirmed (i.e. have detected RRL emission) and ∼ 2000 have co-spatial radio continuum. The distribution of known H II regions is dominated by Northern Hemisphere detections (in no small part due to the recent GBTHRDS), with the greatest number of remaining H II region candidates located between the longitudes $300^\circ < l < 340^\circ$.

There is an acute requirement for a Southern Hemisphere H II *Region Discovery Survey; both to complement existing Northern Hemisphere surveys, as well as to investigate fourth quadrant Galactic features.*

To this end, we have submitted a proposal seeking 900 hours with the ATCA for the purposes of a Southern H II Region Discovery Survey.

*That is the operational wavelengths are similar. Webb's wavelength range is 0.6 to 28.5 μm.

Bibliography

Afflerbach, A., Churchwell, E., Acord, J. M., Hofner, P., Kurtz, S., & Depree, C. G. 1996, ApJS, 106, 423

Afflerbach, A., Churchwell, E., & Werner, M. W. 1997, ApJ, 478, 190

Airy, G. B. 1848, MNRAS, 9, 18

Alexander, S. 1852, AJ, 2, 97

Altenhoff, W. J., Downes, D., Pauls, T., & Schraml, J. 1979, A&AS, 35, 23

Anderson, L. D. & Bania, T. M. 2009, ApJ, 690, 706

Anderson, L. D., Bania, T. M., Balser, D. S., Cunningham, V., Wenger, T. V., Johnstone, B. M., & Armentrout, W. P. 2014, ApJS, 212, 1

Anderson, L. D., Bania, T. M., Balser, D. S., & Rood, R. T. 2011a, in Bulletin of the American Astronomical Society, Vol. 43, American Astronomical Society Meeting Abstracts 217, 132.02

Anderson, L. D., Bania, T. M., Balser, D. S., & Rood, R. T. 2011b, ApJS, 194, 32

—. 2012a, ApJ, 754, 62

Anderson, L. D., Bania, T. M., Jackson, J. M., Clemens, D. P., Heyer, M., Simon, R., Shah, R. Y., & Rathborne, J. M. 2009, ApJS, 181, 255

Anderson, L. D., Zavagno, A., Barlow, M. J., García-Lario, P., & Noriega-Crespo, A. 2012b, A&A, 537, A1

Araya, E., Hofner, P., Churchwell, E., & Kurtz, S. 2002, ApJS, 138, 63

Argon, A. L., Reid, M. J., & Menten, K. M. 2000, ApJS, 129, 159

Azcárate, I. N., Cersosimo, J. C., & Colomb, F. R. 1987, Revista Mexicana de Astronomia y Astrofisica (RMxAA), 15, 3

Azcarate, I. N., Cersosimo, J. C., & Colomb, F. R. 1990, Revista Mexicana de Astronomia y Astrofisica (RMxAA), 20, 75

Baade, W. 1944, Contributions from the Mount Wilson Observatory / Carnegie Institution of Washington, 696, 1

Baade, W. & Gaposchkin, C. H. P. 1963, Evolution of stars and galaxies. (Cambridge, Harvard University Press)

Baba, J., Saitoh, T. R., & Wada, K. 2010, PASJ, 62, 1413

Bailey, M. E., Butler, C. J., & McFarland, J. 2005, Astronomy and Geophysics, 46, 26

Baldwin, J. A., Ferland, G. J., Martin, P. G., Corbin, M. R., Cota, S. A., Peterson, B. M., & Slettebak, A. 1991, ApJ, 374, 580

Balser, D. S. 2006, AJ, 132, 2326

Bania, T. M. 1980, ApJ, 242, 95

Bania, T. M., Anderson, L. D., & Balser, D. S. 2012, ApJ, 759, 96

Bania, T. M., Anderson, L. D., Balser, D. S., & Rood, R. T. 2010, ApJLett, 718, L106

Bania, T. M. & Lockman, F. J. 1984, ApJS, 54, 513

Bania, T. M., Stark, A. A., & Heiligman, G. M. 1986, ApJ, 307, 350

Beichman, C. A., Neugebauer, G., Habing, H. J., Clegg, P. E., & Chester, T. J., eds. 1988, Infrared astronomical satellite (IRAS) catalogs and atlases. Volume 1: Explanatory supplement, Vol. 1

Belkora, L. 2003, Minding the heavens : the story of our discovery of the Milky Way (UK: Institute of Physics Publishing)

Bell, M. B., Avery, L. W., MacLeod, J. M., & Vallée, J. P. 2011, Ap&SS, 333, 377

Bell, M. B., Avery, L. W., Seaquist, E. R., & Vallée, J. P. 2000, PASP, 112, 1236

Benjamin, R. A., Churchwell, E., Babler, B. L., Bania, T. M., Clemens, D. P., Cohen, M., Dickey, J. M., Indebetouw, R., Jackson, J. M., Kobulnicky, H. A., Lazarian, A., Marston, A. P., Mathis, J. S., Meade, M. R., Seager, S., Stolovy, S. R., Watson, C., Whitney, B. A., Wolff, M. J., & Wolfire, M. G. 2003, PASP, 115, 953

Bertin, G. 2000, Dynamics of Galaxies (Cambridge University Press)

Beuther, H., Walsh, A. J., & Longmore, S. N. 2009, ApJS, 184, 366

Bickerton, A. 1879, Origin of the Visible Universe ("Press" Company, New Zealand)

Binney, J. & Tremaine, S. 2011, Galactic Dynamics: (Second Edition), Princeton Series in Astrophysics (Princeton University Press)

Blitz, L., Binney, J., Lo, K. Y., Bally, J., & Ho, P. T. P. 1993, Nature, 361, 417

Bohlin, K. 1907, Astronomische Nachrichten, 176, 205

Brand, J. 1986, PhD thesis, Leiden Univ., Netherlands.

Brand, J. & Blitz, L. 1993, A&A, 275, 67

Breen, S. L., Ellingsen, S. P., Johnston-Hollitt, M., Wotherspoon, S., Bains, I., Burton, M. G., Cunningham, M., Lo, N., Senkbeil, C. E., & Wong, T. 2007, MNRAS, 377, 491

Bronfman, L. 2008, Ap&SS, 313, 81

Bronfman, L., Nyman, L.-A., & May, J. 1996, A&AS, 115, 81

Brown, C., Dickey, J. M., Dawson, J. R., & McClure-Griffiths, N. M. 2014, ApJS, 211, 29

Brown, J. C., Haverkorn, M., Gaensler, B. M., Taylor, A. R., Bizunok, N. S., McClure-Griffiths, N. M., Dickey, J. M., & Green, A. J. 2007, ApJ, 663, 258

Brown, R. L. 1987, in Spectroscopy of Astrophysical Plasmas, ed. A. Dalgarno & D. Layzer, 35–58

Burbidge, E. M., Burbidge, G. R., Fowler, W. A., & Hoyle, F. 1957, Rev. Mod. Phys., 29, 547

Burton, W. B. & Liszt, H. S. 1983, A&AS, 52, 63

Busfield, A. L., Purcell, C. R., Hoare, M. G., Lumsden, S. L., Moore, T. J. T., & Oudmaijer, R. D. 2006, MNRAS, 366, 1096

Carey, S. J., Noriega-Crespo, A., Mizuno, D. R., Shenoy, S., Paladini, R., Kraemer, K. E., Price, S. D., Flagey, N., Ryan, E., Ingalls, J. G., Kuchar, T. A., Pinheiro Gonçalves, D., Indebetouw, R., Billot, N., Marleau, F. R., Padgett, D. L., Rebull, L. M., Bressert, E., Ali, B., Molinari, S., Martin, P. G., Berriman, G. B., Boulanger, F., Latter, W. B., Miville-Deschenes, M. A., Shipman, R., & Testi, L. 2009, PASP, 121, 76

Caswell, J. L. 1998, MNRAS, 297, 215

Caswell, J. L., Fuller, G. A., Green, J. A., Avison, A., Breen, S. L., Brooks, K. J., Burton, M. G., Chrysostomou, A., Cox, J., Diamond, P. J., Ellingsen, S. P., Gray, M. D., Hoare, M. G., Masheder, M. R. W., McClure-Griffiths, N. M., Pestalozzi, M. R., Phillips, C. J., Quinn, L., Thompson, M. A., Voronkov, M. A., Walsh, A. J., Ward-Thompson, D., Wong-McSweeney, D., Yates, J. A., & Cohen, R. J. 2010, MNRAS, 404, 1029

Caswell, J. L. & Haynes, R. F. 1987, A&A, 171, 261

Caswell, J. L., Haynes, R. F., Goss, W. M., & Mebold, U. 1981, Australian Journal of Physics, 34, 333

Caswell, J. L. & Reynolds, J. E. 2001, MNRAS, 325, 1346

Cersosimo, J. C., Azcarate, I. N., & Colomb, F. R. 1989, Revista Mexicana de Astronomia y Astrofisica (RMxAA), 17, 91

Choudhuri, A. R. 2010, Astrophysics for Physicists (Cambridge University Press)

Churchwell, E., Babler, B. L., Meade, M. R., Whitney, B. A., Benjamin, R., Indebetouw, R., Cyganowski, C., Robitaille, T. P., Povich, M., Watson, C., & Bracker, S. 2009, PASP, 121, 213

Churchwell, E., Povich, M. S., Allen, D., Taylor, M. G., Meade, M. R., Babler, B. L., Indebetouw, R., Watson, C., Whitney, B. A., Wolfire, M. G., Bania, T. M., Benjamin, R. A., Clemens, D. P., Cohen, M., Cyganowski, C. J., Jackson, J. M., Kobulnicky, H. A., Mathis, J. S., Mercer, E. P., Stolovy, S. R., Uzpen, B., Watson, D. F., & Wolff, M. J. 2006, ApJ, 649, 759

Churchwell, E. & Walmsley, C. M. 1975, A&A, 38, 451

Clark, D. 2004, Measuring the Cosmos: How Scientists Discovered the Dimensions of the Universe (Rutgers University Press)

Clemens, D. P. 1985, ApJ, 295, 422

Clemens, D. P., Sanders, D. B., & Scoville, N. Z. 1988, ApJ, 327, 139

Cohen, R. J., Baart, E. E., & Jonas, J. L. 1988, MNRAS, 231, 205

Condon, J. J., Cotton, W. D., Greisen, E. W., Yin, Q. F., Perley, R. A., Taylor, G. B., & Broderick, J. J. 1998, AJ, 115, 1693

Croswell, K. 1999, Magnificent universe (Simon & Schuster)

Crowe, M. J. 1994, Modern theories of the universe : from Herschel to Hubble (Dover Publications)

Culverhouse, T., Ade, P., Bock, J., Bowden, M., Brown, M. L., Cahill, G., Castro, P. G., Church, S., Friedman, R., Ganga, K., Gear, W. K., Gupta, S., Hinderks, J., Kovac, J., Lange, A. E., Leitch, E., Melhuish, S. J., Memari, Y., Murphy, J. A., Orlando, A., Pryke, C., Schwarz, R., O'Sullivan, C., Piccirillo, L., Rajguru, N., Rusholme, B., Taylor, A. N., Thompson, K. L., Turner, A. H., Wu, E. Y. S., Zemcov, M., & QUaD Collaboration. 2011, ApJS, 195, 8

Curtis, H. D. 1917, PASP, 100, 6

—. 1920, JRASC, 14, 317

Dame, T. M., Hartmann, D., & Thaddeus, P. 2001, ApJ, 547, 792

Dame, T. M. & Thaddeus, P. 2008, The Astrophysical Journal Letters, 683, L143

Dame, T. M. & Thaddeus, P. 2011, ApJLett, 734, L24

Deguchi, S., Nakada, Y., & Sahai, R. 1990, A&A, 230, 339

Deharveng, L., Schuller, F., Anderson, L. D., Zavagno, A., Wyrowski, F., Menten, K. M., Bronfman, L., Testi, L., Walmsley, C. M., & Wienen, M. 2010, A&A, 523, A6

Dickey, J. M. & Lockman, F. J. 1990, ARA&A, 28, 215

Dickey, J. M., McClure-Griffiths, N., Gibson, S. J., Gómez, J. F., Imai, H., Jones, P., Stanimirović, S., Van Loon, J. T., Walsh, A., Alberdi, A., Anglada, G., Uscanga, L., Arce, H., Bailey, M., Begum, A., Wakker, B., Bekhti, N. B., Kalberla, P., Winkel, B., Bekki, K., For, B.-Q., Staveley-Smith, L., Westmeier, T., Burton, M., Cunningham, M., Dawson, J., Ellingsen, S., Diamond, P., Green, J. A., Hill, A. S., Koribalski, B., McConnell, D., Rathborne, J., Voronkov, M., Douglas, K. A., English, J., Ford, H. A., Lockman, F. J., Foster, T., Gomez, Y., Green, A., Bland-Hawthorn, J., Gulyaev, S., Hoare, M., Joncas, G., Kang, J.-H., Kerton, C. R., Koo, B.-C., Leahy, D., Lo, N., Migenes, V., Nakashima, J., Zhang, Y., Nidever, D., Peek, J. E. G., Tafoya, D., Tian, W., & Wu, D. 2013, Publications of the Astron. Soc. of Australia, 30, 3

Dickey, J. M., McClure-Griffiths, N. M., Gaensler, B. M., & Green, A. J. 2003, ApJ, 585, 801

Dickey, J. M., McClure-Griffiths, N. M., Stanimirović, S., Gaensler, B. M., & Green, A. J. 2001, ApJ, 561, 264

Dickey, J. M., Strasser, S., Gaensler, B. M., Haverkorn, M., Kavars, D., McClure-Griffiths, N. M., Stil, J., & Taylor, A. R. 2009, ApJ, 693, 1250

Downes, D., Wilson, T. L., Bieging, J., & Wink, J. 1980, A&AS, 40, 379

Dravskikh, A. F. & Dravskikh, Z. V. 1967, Soviet Ast., 11, 27

Dreyer, J. L. E. 1888, MmRAS, 49, 1

Dupree, A. K. & Goldberg, L. 1970, ARA&A, 8, 231

Easton, C. 1900, ApJ, 12, 136

Ellingsen, S. P., von Bibra, M. L., McCulloch, P. M., Norris, R. P., Deshpande, A. A., & Phillips, C. J. 1996, MNRAS, 280, 378

Ewen, H. I. & Purcell, E. M. 1951, Nature, 168, 356

Ferrière, K. M. 2001, Reviews of Modern Physics, 73, 1031

Fich, M. & Silkey, M. 1991, ApJ, 366, 107

Fish, V. L., Reid, M. J., Wilner, D. J., & Churchwell, E. 2003, ApJ, 587, 701

Fontani, F., Beltrán, M. T., Brand, J., Cesaroni, R., Testi, L., Molinari, S., & Walmsley, C. M. 2005, A&A, 432, 921

Ford, H. A., McClure-Griffiths, N. M., Lockman, F. J., Bailin, J., Calabretta, M. R., Kalberla, P. M. W., Murphy, T., & Pisano, D. J. 2008, ApJ, 688, 290

Foster, J. B., Jackson, J. M., Barnes, P. J., Barris, E., Brooks, K., Cunningham, M., Finn, S. C., Fuller, G. A., Longmore, S. N., Mascoop, J. L., Peretto, N., Rathborne, J., Sanhueza, P., Schuller, F., & Wyrowski, F. 2011, ApJS, 197, 25

Foster, T. J. & Brunt, C. M. 2014, ArXiv e-prints

Frater, R. H., Brooks, J. W., & Whiteoak, J. B. 1992, Journal of Electrical and Electronics Engineering Australia, 12, 103

Fux, R. 1999, A&A, 345, 787

Gaensler, B. M., Dickel, J. R., & Green, A. J. 2000, ApJ, 542, 380

García, P., Bronfman, L., Nyman, L.-Å., Dame, T. M., & Luna, A. 2014, ApJS, 212, 2

Gardner, F. F. & Whiteoak, J. B. 1978, MNRAS, 183, 711

Gelfand, J. D., Gaensler, B. M., Slane, P. O., Patnaude, D. J., Hughes, J. P., & Camilo, F. 2007, ApJ, 663, 468

Georgelin, Y. M., Amram, P., Georgelin, Y. P., Le Coarer, E., & Marcelin, M. 1994, A&AS, 108, 513

Georgelin, Y. M. & Georgelin, Y. P. 1976, A&A, 49, 57

Gibson, S. J. 2010, in Astronomical Society of the Pacific Conference Series, Vol. 438, Astronomical Society of the Pacific Conference Series, ed. R. Kothes, T. L. Landecker, & A. G. Willis, 111

Gibson, S. J., Taylor, A. R., Higgs, L. A., Brunt, C. M., & Dewdney, P. E. 2005, ApJ, 626, 195

Gooch, R. 1996, in Astronomical Society of the Pacific Conference Series, Vol. 101, Astronomical Data Analysis Software and Systems V, ed. G. H. Jacoby & J. Barnes, 80

Gordon, M. A. & Sorochenko, R. L., eds. 2002, Astrophysics and Space Science Library, Vol. 282, Radio Recombination Lines. Their Physics and Astronomical Applications

Grave, J. M. C. & Kumar, M. S. N. 2009, A&A, 498, 147

Green, D. A. 1993, MNRAS, 262, 327

Green, J. A., Caswell, J. L., Fuller, G. A., Avison, A., Breen, S. L., Ellingsen, S. P., Gray, M. D., Pestalozzi, M., Quinn, L., Thompson, M. A., & Voronkov, M. A. 2012, MNRAS, 420, 3108

Green, J. A., Caswell, J. L., McClure-Griffiths, N. M., Avison, A., Breen, S. L., Burton, M. G., Ellingsen, S. P., Fuller, G. A., Gray, M. D., Pestalozzi, M., Thompson, M. A., & Voronkov, M. A. 2011, ApJ, 733, 27

Green, J. A. & McClure-Griffiths, N. M. 2011, MNRAS, 417, 2500

Green, J. A., McClure-Griffiths, N. M., Caswell, J. L., Ellingsen, S. P., Fuller, G. A., Quinn, L., & Voronkov, M. A. 2009, ApJLett, 696, L156

Griffith, M. R. & Wright, A. E. 1993, AJ, 105, 1666

Hachisuka, K., Brunthaler, A., Menten, K. M., Reid, M. J., Hagiwara, Y., & Mochizuki, N. 2009, ApJ, 696, 1981

Hagen, J. P., Lilley, A. E., & McClain, E. F. 1955, ApJ, 122, 361

Harrison, T. G. 1984, QJRAS, 25, 65

Haverkorn, M., Gaensler, B. M., McClure-Griffiths, N. M., Dickey, J. M., & Green, A. J. 2006, ApJS, 167, 230

Henderson, A. P., Jackson, P. D., & Kerr, F. J. 1982, ApJ, 263, 116

Henning, T. & Launhardt, R. 1998, A&A, 338, 223

Herschel, W. 1784, Philosophical Transactions of the Royal Society of London, 437

—. 1785, Philosophical Transactions of the Royal Society of London, 75, pp. 213

Herschel, W. 1786, Royal Society of London Philosophical Transactions Series I, 76, 457

Hollenbach, D. J. & Tielens, A. G. G. M. 1999, Reviews of Modern Physics, 71, 173

Honma, M., Bushimata, T., Choi, Y. K., Hirota, T., Imai, H., Iwadate, K., Jike, T., Kameya, O., Kamohara, R., Kan-Ya, Y., Kawaguchi, N., Kijima, M., Kobayashi, H., Kuji, S., Kurayama, T., Manabe, S., Miyaji, T., Nagayama, T., Nakagawa, A., Oh, C. S., Omodaka, T., Oyama, T., Sakai, S., Sato, K., Sasao, T., Shibata, K. M., Shintani, M., Suda, H., Tamura, Y., Tsushima, M., & Yamashita Kazuyoshi. 2007, PASJ, 59, 889

Hoskin, M. 1989, Proceedings of the American Philosophical Society, 133, pp. 427

Hoskin, M. A. 1976, Journal for the History of Astronomy, 7, 47

Hou, L. G. & Han, J. L. 2014, A&A, 569, A125

Hou, L. G., Han, J. L., & Shi, W. B. 2009, A&A, 499, 473

Hubble, E. 1936, The Realm of the Nebulae, Mrs. Hepsa Ely Silliman memorial lectures (New Haven and London : Yale University Press)

Hubble, E. P. 1925, Popular Astronomy, 33, 252

—. 1926, ApJ, 64, 321

Hughes, V. A. & MacLeod, G. C. 1989, AJ, 97, 786

—. 1994, ApJ, 427, 857

Immer, K., Cyganowski, C., Reid, M. J., & Menten, K. M. 2014, A&A, 563, A39

Jackson, J. M., Rathborne, J. M., Foster, J. B., Whitaker, J. S., Sanhueza, P., Claysmith, C., Mascoop, J. L., Wienen, M., Breen, S. L., Herpin, F., Duarte-Cabral, A., Csengeri, T., Longmore, S. N., Contreras, Y., Indermuehle, B., Barnes, P. J., Walsh, A. J., Cunningham, M. R., Brooks, K. J., Britton, T. R., Voronkov, M. A., Urquhart, J. S., Alves, J., Jordan,

C. H., Hill, T., Hoq, S., Finn, S. C., Bains, I., Bontemps, S., Bronfman, L., Caswell, J. L., Deharveng, L., Ellingsen, S. P., Fuller, G. A., Garay, G., Green, J. A., Hindson, L., Jones, P. A., Lenfestey, C., Lo, N., Lowe, V., Mardones, D., Menten, K. M., Minier, V., Morgan, L. K., Motte, F., Muller, E., Peretto, N., Purcell, C. R., Schilke, P., Bontemps, S.-N., Schuller, F., Titmarsh, A., Wyrowski, F., & Zavagno, A. 2013, Publications of the Astron. Soc. of Australia, 30, 57

Jones, C. & Dickey, J. M. 2012, ApJ, 753, 62

Jones, C., Dickey, J. M., Dawson, J. R., McClure-Griffiths, N. M., Anderson, L. D., & Bania, T. M. 2013, ApJ, 774, 117

Jordan, C. H., Walsh, A. J., Lowe, V., Lo, N., Purcell, C. R., Voronkov, M. A., & Longmore, S. N. 2013, MNRAS, 429, 469

Joy, A. H. 1939, ApJ, 89, 356

Kalberla, P. M. W. & Kerp, J. 2009, ARA&A, 47, 27

Kantharia, N. G., Goss, W. M., Roshi, D. A., Mohan, N. R., & Viallefond, F. 2007, Journal of Astrophysics and Astronomy, 28, 41

Kapteyn, J. 1922, Astrophys.J., 55, 302

Karachentsev, I. D., Karachentseva, V. E., Huchtmeier, W. K., & Makarov, D. I. 2004, AJ, 127, 2031

Kardashev, N. S. 1959, Soviet Ast., 3, 813

Kaufer, A., Szeifert, T., Krenzin, R., Baschek, B., & Wolf, B. 1994, A&A, 289, 740

Kavars, D. W., Dickey, J. M., McClure-Griffiths, N. M., Gaensler, B. M., & Green, A. J. 2005, ApJ, 626, 887

Kemball, A. J., Gaylard, M. J., & Nicolson, G. D. 1988, ApJLett, 331, L37

Kerr, F. J. 1969, ARA&A, 7, 39

Kerr, F. J. & Knapp, G. R. 1970a, Australian Journal of Physics Astrophysical Supplement, 18, 9

—. 1970b, Australian Journal of Physics Astrophysical Supplement, 18, 9

Kolpak, M. A., Jackson, J. M., Bania, T. M., Clemens, D. P., & Dickey, J. M. 2003, ApJ, 582, 756

Kothes, R. & Dougherty, S. M. 2007, A&A, 468, 993

Krishnan, V., Ellingsen, S. P., Voronkov, M. A., & Breen, S. L. 2013, MNRAS, 433, 3346

Kuchar, T. A. & Bania, T. M. 1994, ApJ, 436, 117

Kuchar, T. A. & Clark, F. O. 1997, ApJ, 488, 224

Kurtz, S. 2005, in IAU Symposium, Vol. 227, Massive Star Birth: A Crossroads of Astrophysics, ed. R. Cesaroni, M. Felli, E. Churchwell, & M. Walmsley, 111–119

Lallement, R., Quémerais, E., Bertaux, J.-L., Sandel, B. R., & Izmodenov, V. 2011, Science, 334, 1665

Lang, C. C., Goss, W. M., Cyganowski, C., & Clubb, K. I. 2010, ApJS, 191, 275

Lee, J.-K., Walsh, A. J., Burton, M. G., & Ashley, M. C. B. 2001, MNRAS, 324, 1102

Lilley, A. E. & Palmer, P. 1968, ApJS, 16, 143

Lindblad, B. 1927, MNRAS, 87, 553

Liszt, H. S. 2008, A&A, 486, 467

Liszt, H. S. & Burton, W. B. 1980, ApJ, 236, 779

Lockman, F. J. 1980, ApJ, 241, 200

—. 1981, ApJ, 245, 459

—. 1989, ApJS, 71, 469

Lockman, F. J. 1990a, in Large-Scale Surveys of the Sky, ed. J. J. Condon & F. J. Lockman, 107

Lockman, F. J. 1990b, in Astrophysics and Space Science Library, Vol. 163, IAU Colloq. 125: Radio Recombination Lines: 25 Years of Investigation, ed. M. A. Gordon & R. L. Sorochenko, 225

Lockman, F. J. 2002, in Astronomical Society of the Pacific Conference Series, Vol. 276, Seeing Through the Dust: The Detection of HI and the Exploration of the ISM in Galaxies, ed. A. R. Taylor, T. L. Landecker, & A. G. Willis, 107

Lockman, F. J., Pisano, D. J., & Howard, G. J. 1996, ApJ, 472, 173

Longair, S. 2006, The Cosmic Century: A History of Astrophysics and Cosmology (Cambridge University Press)

Longmore, S. N., Burton, M. G., Barnes, P. J., Wong, T., Purcell, C. R., & Ott, J. 2007, MNRAS, 379, 535

Maciel, W. J. & Koppen, J. 1994, A&A, 282, 436

MacLeod, G. C., van der Walt, D. J., North, A., Gaylard, M. J., Galt, J. A., & Moriarty-Schieven, G. H. 1998, AJ, 116, 2936

Marshall, D. J., Fux, R., Robin, A. C., & Reylé, C. 2008, A&A, 477, L21

McClure-Griffiths, N. M. & Dickey, J. M. 2007, ApJ, 671, 427

McClure-Griffiths, N. M., Dickey, J. M., Gaensler, B. M., & Green, A. J. 2004, ApJLett, 607, L127

McClure-Griffiths, N. M., Dickey, J. M., Gaensler, B. M., Green, A. J., Green, J. A., & Haverkorn, M. 2012, ApJS, 199, 12

McClure-Griffiths, N. M., Dickey, J. M., Gaensler, B. M., Green, A. J., Haverkorn, M., & Strasser, S. 2005, ApJS, 158, 178

McClure-Griffiths, N. M., Green, A. J., Dickey, J. M., Gaensler, B. M., Haynes, R. F., & Wieringa, M. H. 2001, ApJ, 551, 394

McKee, C. F. & Ostriker, J. P. 1977, ApJ, 218, 148

Mercer, E. P., Clemens, D. P., Meade, M. R., Babler, B. L., Indebetouw, R., Whitney, B. A., Watson, C., Wolfire, M. G., Wolff, M. J., Bania, T. M., Benjamin, R. A., Cohen, M., Dickey, J. M., Jackson, J. M., Kobulnicky, H. A., Mathis, J. S., Stauffer, J. R., Stolovy, S. R., Uzpen, B., & Churchwell, E. B. 2005, ApJ, 635, 560

Mezger, P. G., Pankonin, V., Schmid-Burgk, J., Thum, C., & Wink, J. 1979, A&A, 80, L3

Misanovic, Z., Cram, L., & Green, A. 2002, MNRAS, 335, 114

Mohr, P. J., Taylor, B. N., & Newell, D. B. 2008, Reviews of Modern Physics, 80, 633

Moisés, A. P., Damineli, A., Figuerêdo, E., Blum, R. D., Conti, P. S., & Barbosa, C. L. 2011, MNRAS, 411, 705

Morris, M. & Serabyn, E. 1996, ARA&A, 34, 645

Mottram, J. C., Hoare, M. G., Lumsden, S. L., Oudmaijer, R. D., Urquhart, J. S., Sheret, T. L., Clarke, A. J., & Allsopp, J. 2007, A&A, 476, 1019

Muller, C. A. & Oort, J. H. 1951, Nature, 168, 357

Murphy, T., Cohen, M., Ekers, R. D., Green, A. J., Wark, R. M., & Moss, V. 2010, MNRAS, 405, 1560

Nakanishi, H. & Sofue, Y. 2003, PASJ, 55, 191

—. 2006, PASJ, 58, 847

Neugebauer, G., Habing, H. J., van Duinen, R., Aumann, H. H., Baud, B., Beichman, C. A., Beintema, D. A., Boggess, N., Clegg, P. E., de Jong, T., Emerson, J. P., Gautier, T. N., Gillett, F. C., Harris, S., Hauser, M. G., Houck, J. R., Jennings, R. E., Low, F. J., Marsden, P. L., Miley, G., Olnon, F. M., Pottasch, S. R., Raimond, E., Rowan-Robinson, M., Soifer, B. T., Walker, R. G., Wesselius, P. R., & Young, E. 1984, ApJLett, 278, L1

Neugebauer, G., Morton, D., Oke, J. B., Becklin, E., Daltabuit, E., Matthews, K., Persson, S. E., Smith, A. M., Soifer, B. T., Torres-Peimbert, S., & Wynn-Williams, C. G. 1980, ApJ, 238, 502

Nichol, J. P. 1846, Thoughts on some important points relating to the system of the world. (William Tait, Edinburgh)

Nilsson, K. K. 2007, PhD thesis, Dark Cosmology Centre, Niels Bohr Institute Faculty of Science, University of Copenhagen

Normandeau, M. 1999, AJ, 117, 2440

Norris, R. P., Afonso, J., Bacon, D., Beck, R., Bell, M., Beswick, R. J., Best, P., Bhatnagar, S., Bonafede, A., Brunetti, G., Budavári, T., Cassano, R., Condon, J. J., Cress, C., Dabbech, A., Feain, I., Fender, R., Ferrari, C., Gaensler, B. M., Giovannini, G., Haverkorn, M., Heald, G., Van der Heyden, K., Hopkins, A. M., Jarvis, M., Johnston-Hollitt, M., Kothes, R., Van Langevelde, H., Lazio, J., Mao, M. Y., Martínez-Sansigre, A., Mary, D., Mcalpine, K., Middelberg, E., Murphy, E., Padovani, P., Paragi, Z., Prandoni, I., Raccanelli, A., Rigby, E., Roseboom, I. G., Röttgering, H., Sabater, J., Salvato, M., Scaife, A. M. M., Schilizzi, R., Seymour, N., Smith, D. J. B., Umana, G., Zhao, G.-B., & Zinn, P.-C. 2013, Publications of the Astron. Soc. of Australia, 30, 20

Oort, J. H. 1927, Bull. Astron. Inst. Netherlands, 4, 79

—. 1972, Annals of the New York Academy of Sciences, 198, 255

—. 1977, ARA&A, 15, 295

Oort, J. H., Kerr, F. J., & Westerhout, G. 1958, MNRAS, 118, 379

Oort, J. H. & Muller, C. A. 1952, Monthly Notes of the Astronomical Society of South Africa, 11, 65

Paladini, R., Burigana, C., Davies, R. D., Maino, D., Bersanelli, M., Cappellini, B., Platania, P., & Smoot, G. 2003, A&A, 397, 213

Paladini, R., Davies, R. D., & De Zotti, G. 2004, MNRAS, 347, 237

Paul, E. 1993, The Milky Way Galaxy and Statistical Cosmology, 1890-1924 (Cambridge University Press)

Paul, E. R. 2006, The Milky Way Galaxy and Statistical Cosmology, 1890-1924 (Cambridge University Press)

Pavlyuchenkov, Y. N., Kirsanova, M. S., & Wiebe, D. S. 2013, Astronomy Reports, 57, 573

Penfield, H., Palmer, P., & Zuckerman, B. 1967, ApJLett, 148, L25

Peng, R. S. & Whiteoak, J. B. 1992, MNRAS, 254, 301

Pradhan, A. & Nahar, S. 2011, Atomic Astrophysics and Spectroscopy (Cambridge University Press)

Proctor, R. 1902, Other worlds than ours (Longmans, Green, and Co.)

Proctor, R. A. 1872, Essays on astronomy (Longmans, Green and Co., London)

—. 1880, Our place among infinities; a series of essays contrasting our little abode in space and time with the infinities around us (Chatto & Windus, London)

Purcell, C. R., Longmore, S. N., Walsh, A. J., Whiting, M. T., Breen, S. L., Britton, T., Brooks, K. J., Burton, M. G., Cunningham, M. R., Green, J. A., Harvey-Smith, L., Hindson, L., Hoare, M. G., Indermuehle, B., Jones, P. A., Lo, N., Lowe, V., Phillips, C. J., Thompson, M. A., Urquhart, J. S., Voronkov, M. A., & White, G. L. 2012, MNRAS, 426, 1972

Quireza, C., Rood, R. T., Balser, D. S., & Bania, T. M. 2006, ApJS, 165, 338

Radhakrishnan, V., Goss, W. M., Murray, J. D., & Brooks, J. W. 1972, ApJS, 24, 49

Reber, G. 1940, ApJ, 91, 621

Reber, G. & Greenstein, J. L. 1947, The Observatory, 67, 15

Reid, M. J., Menten, K. M., Zheng, X. W., Brunthaler, A., Moscadelli, L., Xu, Y., Zhang, B., Sato, M., Honma, M., Hirota, T., Hachisuka, K., Choi, Y. K., Moellenbrock, G. A., & Bartkiewicz, A. 2009, ApJ, 700, 137

Reifenstein, E. C., Wilson, T. L., Burke, B. F., Mezger, P. G., & Altenhoff, W. J. 1970, A&A, 4, 357

Rodríguez-Fernández, N. J. 2006, Journal of Physics Conference Series, 54, 35

—. 2011, Memorie della Societa Astronomica Italiana Supplementi, 18, 195

Rodriguez-Fernandez, N. J., Combes, F., Martin-Pintado, J., Wilson, T. L., & Apponi, A. 2006, A&A, 455, 963

Roman-Duval, J., Jackson, J. M., Heyer, M., Johnson, A., Rathborne, J., Shah, R., & Simon, R. 2009, ApJ, 699, 1153

Roy, S. 2003, A&A, 403, 917

Sandage, A., Brown, L., Craig, P., Maienschein, J., Glitz, M., & Allen, G. 2004, Centennial History of the Carnegie Institution of Washington: Volume 1, The Mount Wilson Observatory: Breaking the Code of Cosmic Evolution, Centennial History of the Carnegie Institution of Washington (Cambridge University Press)

Sanna, A., Reid, M. J., Moscadelli, L., Dame, T. M., Menten, K. M., Brunthaler, A., Zheng, X. W., & Xu, Y. 2009, ApJ, 706, 464

Sault, R. J., Teuben, P. J., & Wright, M. C. H. 1995, in Astronomical Society of the Pacific Conference Series, Vol. 77, Astronomical Data Analysis Software and Systems IV, ed. R. A. Shaw, H. E. Payne, & J. J. E. Hayes, 433

Scalise, Jr., E., Rodriguez, L. F., & Mendoza-Torres, E. 1989, A&A, 221, 105

Schutte, A. J., van der Walt, D. J., Gaylard, M. J., & MacLeod, G. C. 1993, MNRAS, 261, 783

Sestokas Filho, B. & Scalise, Jr., E. 1990, Revista Mexicana de Astronomia y Astrofisica (RMxAA), 21, 481

Sewilo, M., Watson, C., Araya, E., Churchwell, E., Hofner, P., & Kurtz, S. 2004, ApJS, 154, 553

Shapley, H. 1918, PASP, 30, 42

Shapley, H. 1968, Through Rugged Ways to the Stars (Charles Scribner's Sons, New York)

Shapley, H. & Curtis, H. D. 1921, Bulletin of the National Research Council, Vol. 2, Part 3, No. 11, p. 171-217, 2, 171

Shaver, P. A., McGee, R. X., Newton, L. M., Danks, A. C., & Pottasch, S. R. 1983, MNRAS, 204, 53

Shu, F. 1982, The Physical Universe: An Introduction to Astronomy, A Series of books in astronomy (University Science Books)

Simonson, III, S. C. & Mader, G. L. 1973, A&A, 27, 337

Simpson, J. P. 1975, A&A, 39, 43

Smirnov, G. T., Sorochenko, R. L., & Pankonin, V. 1984, A&A, 135, 116

Smith, R. W. 1985, in IAU Symposium, Vol. 106, The Milky Way Galaxy, ed. H. van Woerden, R. J. Allen, & W. B. Burton, 43

Sofue, Y. & Rubin, V. 2001, ARA&A, 39, 137

Sorochenko, R. 1990, in Astrophysics and Space Science Library, Vol. 163, Radio Recombination Lines: 25 Years of Investigation, ed. M. Gordon & R. Sorochenko (Springer Netherlands), 1–18

Sorochenko, R. L. & Borodzich, É. V. 1966, Soviet Physics Doklady, 10, 588

Sorochenko, R. L., Puzanov, V. A., Salomonovich, A. E., & Shteinshleger, V. B. 1969, Astrophys. Lett., 3, 7

Stil, J. M., Taylor, A. R., Dickey, J. M., Kavars, D. W., Martin, P. G., Rothwell, T. A., Boothroyd, A. I., Lockman, F. J., & McClure-Griffiths, N. M. 2006, AJ, 132, 1158

Strasser, S. T. 2006, PhD thesis, University of Minnesota, Minnesota, USA

Strasser, S. T., Dickey, J. M., Taylor, A. R., Boothroyd, A. I., Gaensler, B. M., Green, A. J., Kavars, D. W., Lockman, F. J., Martin, P. G., McClure-Griffiths, N. M., Rothwell, T. A., & Stil, J. M. 2007, AJ, 134, 2252

Strömgren, B. 1939, ApJ, 89, 526

Struve, F. G. W. 1847, Etudes d'astronomie stellaire (St. Pétersbourg : Impr. de l'Académie impériale des sciences)

Sullivan, W. 2005, The Early Years of Radio Astronomy: Reflections Fifty Years After Jansky's Discovery (Cambridge University Press)

Swaters, R. A., Sancisi, R., & van der Hulst, J. M. 1997, ApJ, 491, 140

Taylor, A. R., Gibson, S. J., Peracaula, M., Martin, P. G., Landecker, T. L., Brunt, C. M., Dewdney, P. E., Dougherty, S. M., Gray, A. D., Higgs, L. A., Kerton, C. R., Knee, L. B. G., Kothes, R., Purton, C. R., Uyaniker, B., Wallace, B. J., Willis, A. G., & Durand, D. 2003, AJ, 125, 3145

Tielens, A. 2005, The Physics and Chemistry of the Interstellar Medium (Cambridge University Press)

Tielens, A. G. G. M. 2008, ARA&A, 46, 289

Trimble, V. 1995, PASP, 107, 1133

Trumpler, R. J. 1930, Lick Observatory Bulletin, 14, 154

Uchida, K., Morris, M., & Yusef-Zadeh, F. 1992, AJ, 104, 1533

Urquhart, J. S., Hoare, M. G., Lumsden, S. L., Oudmaijer, R. D., Moore, T. J. T., Mottram, J. C., Cooper, H. D. B., Mottram, M., & Rogers, H. C. 2012, MNRAS, 420, 1656

Vallée, J. P. 2008, AJ, 135, 1301

—. 2014, MNRAS, 442, 2993

van de Hulst, H. C. 1945, Nederlands Tijdschrift voor Natuurkunde, 11, 210

van de Hulst, H. C., Muller, C. A., & Oort, J. H. 1954, Bull. Astron. Inst. Netherlands, 12, 117

van der Walt, D. J., Gaylard, M. J., & MacLeod, G. C. 1995, A&AS, 110, 81

van Woerden, H., Rougoor, G. W., & Oort, J. H. 1957, Academie des Sciences Paris Comptes Rendus, 244, 1691

van Woerden, H. & Strom, R. G. 2006, Journal of Astronomical History and Heritage, 9, 3

Vlemmings, W. H. T., Torres, R. M., & Dodson, R. 2011, A&A, 529, A95

Walsh, A. J., Bertoldi, F., Burton, M. G., & Nikola, T. 2001, MNRAS, 326, 36

Walsh, A. J., Breen, S. L., Britton, T., Brooks, K. J., Burton, M. G., Cunningham, M. R., Green, J. A., Harvey-Smith, L., Hindson, L., Hoare, M. G., Indermuehle, B., Jones, P. A., Lo, N., Longmore, S. N., Lowe, V., Phillips, C. J., Purcell, C. R., Thompson, M. A., Urquhart, J. S., Voronkov, M. A., White, G. L., & Whiting, M. T. 2011, MNRAS, 416, 1764

Walsh, A. J., Burton, M. G., Hyland, A. R., & Robinson, G. 1999, MNRAS, 309, 905

Walsh, A. J., Hyland, A. R., Robinson, G., & Burton, M. G. 1997, MNRAS, 291, 261

Walsh, A. J., Lee, J.-K., & Burton, M. G. 2002, MNRAS, 329, 475

Wendker, H. J. & Wrigge, M. 1996, A&A, 305, 592

Wendt, H., Orchiston, W., & Slee, B. 2008, Journal of Astronomical History and Heritage, 11, 185

Wenger, T. V., Bania, T. M., Balser, D. S., & Anderson, L. D. 2013, ApJ, 764, 34

Wild, J. P. 1952, ApJ, 115, 206

Wilson, T. L. 1972, A&A, 19, 354

Wilson, T. L. 1980, in Astrophysics and Space Science Library, Vol. 80, Radio Recombination Lines, ed. P. A. Shaver, 205–223

Wilson, T. L., Mezger, P. G., Gardner, F. F., & Milne, D. K. 1970, A&A, 6, 364

Wilson, W. E., Ferris, R. H., Axtens, P., Brown, A., Davis, E., Hampson, G., Leach, M., Roberts, P., Saunders, S., Koribalski, B. S., Caswell, J. L., Lenc, E., Stevens, J., Voronkov, M. A., Wieringa, M. H., Brooks, K., Edwards, P. G., Ekers, R. D., Emonts, B., Hindson, L., Johnston, S., Maddison, S. T., Mahony, E. K., Malu, S. S., Massardi, M., Mao, M. Y., McConnell, D., Norris, R. P., Schnitzeler, D., Subrahmanyan, R., Urquhart, J. S., Thompson, M. A., & Wark, R. M. 2011, MNRAS, 416, 832

Wink, J. E., Altenhoff, W. J., & Mezger, P. G. 1982, A&A, 108, 227

Wood, D. O. S. & Churchwell, E. 1989a, ApJ, 340, 265

—. 1989b, ApJS, 69, 831

Wright, E. L., Eisenhardt, P. R. M., Mainzer, A. K., Ressler, M. E., Cutri, R. M., Jarrett, T., Kirkpatrick, J. D., Padgett, D., McMillan, R. S., Skrutskie, M., Stanford, S. A., Cohen, M., Walker, R. G., Mather, J. C., Leisawitz, D., Gautier, III, T. N., McLean, I., Benford, D., Lonsdale, C. J., Blain, A., Mendez, B., Irace, W. R., Duval, V., Liu, F., Royer, D., Heinrichsen, I., Howard, J., Shannon, M., Kendall, M., Walsh, A. L., Larsen, M., Cardon, J. G., Schick, S., Schwalm, M., Abid, M., Fabinsky, B., Naes, L., & Tsai, C.-W. 2010, AJ, 140, 1868

Wright, T. & Hoskin, M. 1734, An Original Theory Or New Hypothesis of the Universe, 1750: A Facsimile Reprint Together with the First Publication of A Theory of the Universe, 1734, History of science library (Macdonald & Co.).: Primary sources (Macdonald and Company)

Wynn-Williams, C. G. 1984, in Astrophysics and Space Science Library, Vol. 108, Galactic and Extragalactic Infrared Spectroscopy, ed. M. F. Kessler & J. P. Phillips, 133–144

Xu, Y., Reid, M. J., Menten, K. M., & Zheng, X. W. 2006, ApJS, 166, 526

Zaritsky, D., Kennicutt, Jr., R. C., & Huchra, J. P. 1994, ApJ, 420, 87

Zavagno, A., Cox, P., & Baluteau, J.-P. 1992, A&A, 259, 241

Appendices

Appendix A

Historical Overview of Hydrogen Lines

Following from the discussion in Section 1.1, this Appendix presents a historical overview of the hydrogen transitions used within this thesis; the H I line and RRLs.

A.1 H I: A Historical Perspective

During World War II, Grote Reber (the "father of radio astronomy") published a paper entitled *Cosmic Static* (Reber 1940), which presented confirmation of Galactic radio waves. This sparked the interest of Jan Oort, a Dutch astronomer, who had previously derived rough estimates for differential Galactic rotation from stellar motions (Oort 1927, see Section 1.2). Oort postulated that radio waves, not impaired by Galactic extinction in the same way as optical lines, may provide an unprecedented, unhindered, view of the entire Galactic system.

Of particular interest would be a method with which to observe hydrogen—the most plentiful element in the Galaxy. The Lyman series of hydrogen emission lines ($n \geq 2 \rightarrow n = 1$), and more specifically the Lyman-alpha line (Ly-α, $n = 2 \rightarrow n = 1$) should be the intrinsically strongest transition. However, the wavelength of the Ly-α transition is in the ultraviolet regime, and is therefore unobservable from the surface of the Earth due to atmospheric opacity[*].

Further development of these ideas was severely hampered by the Second World War, however Oort managed to run several colloquia on behalf of the *Netherlands Astronomer's Club* at the Leiden Observatory (as discussed in van Woerden & Strom 2006). At one such colloquium, *Radio Waves from Space* (April 15, 1944), Dr C.J. Bakker of the Phillips Physical Laboratory spoke on the reception of these radio waves, while van de Hulst discussed their origin (van de Hulst 1945). Modifying earlier work by Henyey and Keenan, van de Hulst calculated the continuous spectrum expected from a layer of ionised hydrogen and further

[*]Note that the line can be observed in distant galaxies, beyond a red shift of ∼2, such that the transition is shifted into the visible spectrum (Nilsson 2007). Closer to home, the first detection of the Ly-α transition from the Milky Way was made in 2011 by *Voyager 1* in its transition through the heliosphere; where confusion from Solar emission is minimised (Lallement et al. 2011).

suggested that the spin-flip transition of ground state hydrogen ($\lambda \approx 21$ cm) may prove to be the most promising radio spectral line candidate. He also noted, however, that the sensitivity of contemporary radio receivers required a factor of 100 improvement in order for the predicted emission to be detected (Wendt et al. 2008). Publication of the colloquium's papers was delayed until the end of the War. Unaware of the Dutch efforts, Shklovskii, independently established the possibility of cosmic radio emission (Shklovskii 1956, cited in van Woerden & Strom 2006).

The development of radio astronomy, as a science, was also severely hampered by the Second World War; and yet arguably, would not have been possible without it. Australian and English radio-astronomical research started almost immediately after the War, by radio engineers and physicists with extensive radar experience. Furthermore, especially in Australia, surplus equipment became available for re-appropriation for science in 1945 (van Woerden & Strom 2006). The Dutch circumstances were not as bountiful; Nazi occupation had closed universities and van de Hulst's visits to Leiden could only be approved whilst his supervisor, M.G.J. Minnaert, was on temporary leave from detention camp (Wendt et al. 2008).

Just as the efforts of the Dutch and Soviet theoretical groups were unknown to each other, the Dutch attempts to detect the 21 cm hydrogen emission line were unknown to Harvard researchers. It was coincidence then, that when Harold Ewen and Edward Purcell first detected the H I transition, at the Lyman Laboratory of Harvard University on March 25, 1951, that van de Hulst should be visiting (van Woerden & Strom 2006). This initial detection was quickly confirmed by both the Dutch and Australian observing groups, with the results of each team published in the same edition of *Nature*[*].

The Tenth General Assembly of the International Union of Radio Science was held in Sydney, in August, 1972—in recognition of the growing contribution of Australian researchers to the new field of radio astronomy. This allowed all involved in the initial detections of the 21cm line to meet for the first time (Wendt et al. 2008). The "21cm Astronomers" (nominally the American, Dutch and Australian teams) continued their co-operation, even exchanging a regular "1420 Mc/s newsletter" (van de Hulst et al. 1954).

The discovery of the 21 cm, spin–flip transition of hydrogen, redefined Galactic astronomy studies:

> *The present evidence shows conclusively what has so far only been suspected from indirect evidence, that the interstellar gas is concentrated in the spiral arms. …By these observations, which are now being made, it may well become possible to unravel considerable further structure.* (Oort & Muller 1952)

[*]The American and Dutch papers (Ewen & Purcell 1951; Muller & Oort 1951) were published alongside a note mentioning that the Australian team (Christiansen and Hindman) had also succeeded in detecting the emission line

A.2 RRLs: A Historical Perspective

The suggestion of transitions between high-excitation levels of the hydrogen atom was presented by van de Hulst (1945), at the colloquium *Radio waves from space* (alongside discussion of the H I line; see Section A.1). However, he overestimated the effect of Stark broadening (due to a substitution error, discussed in van Woerden & Strom 2006) and concluded that the line would be observationally effaced*.

American astronomers were also pessimistic regarding the detectability of these lines. Reber & Greenstein (1947) predicted that H II regions would present an opportunity to observe transitions from ionised hydrogen. However, they dismissed hydrogen RRLs from follow up investigations due to the supposed difficulty of detection as *"it can be shown that these [lines] have small intensity"*. Wild (1952) confirmed that emission lines arising between the main levels of high quantum number are *of no particular interest in the study of discrete lines because they are so numerous that, without the presence of some selective excitation mechanism, they may be regarded merely as contributing toward a continuous spectrum"*.

Soviet astronomers, unaware of these pessimistic calculations (due to the disruption of scientific communication during World War II; Gordon & Sorochenko 2002), re-computed the expected line widths and intensities of hydrogen RRLs from Galactic ionised nebulae. Kardashev (1959) predicted not only that hydrogen (and possibly helium) RRLs would be detectable from far infrared to decimetre wavelengths, but that the H$n\alpha$ ($n \rightarrow n-1$) transition would be simplest to detect due to a relatively high transition probability.

The first attempt to detect excited hydrogen RRLs took place in 1958 without success (Egorova & Ryzkov (1960): cited in Gordon & Sorochenko 2002). The first 'semi-successful' attempt was carried out in 1963 (Dravskikh & Dravskikh 1967). These observations resulted in spectra of the H104α RRL from the Omega and Orion Nebulae, but with poor signal to noise due to strong winds on the antenna. Sorochenko & Borodzich (1966) succeeded in detecting the H90α transition on April 27, 1964 from the Omega Nebula. Within a month, the Lebedev group had also succeeded in detecting the H104α RRL from the Omega nebula; (Dravskikh, Dravskikh, Kolbasov et al. (1965): cited in Gordon & Sorochenko 2002).

The results from both teams were presented at the XII General Assembly of the International Astronomical Union on August 31, 1964. The unambiguous detection of two RRLs from the same source, within month of each other, which also overlapped in measured Doppler shift, prompted both groups of astronomers to set the day of the IAU General Assembly as the official date of discovery of radio emission from excited hydrogen atoms (Gordon & Sorochenko 2002).

Within only a few years, numerous hydrogen RRLs were confirmed; including transitions between H253α at 404 MHz (Penfield et al. 1967) and H56α at 36.5 GHz (Sorochenko et al.

*Van de Hulst's original derivation was that the Stark broadening, $\Delta\nu_S \propto \lambda^{3/5}$; the index had been incorrectly inverted and should have been $\Delta\nu_S \propto \lambda^{5/3}$. At 5 GHz this inversion makes over six orders of magnitude difference for $\Delta\nu_S/\nu$ and as a result, Van de Hulst assumed that the lines would be too broad, and therefore too weak, to observe.

1969) as well as helium and carbon RRLs. RRLs have also revealed ultra-low density regions of the Galaxy, where an atom can exist with very high quantum levels (up to $n \approx 1000$) and correspondingly, huge diameters approaching 0.1mm (Gordon & Sorochenko 2002).

Appendix B

Discussion of Individual H II Regions

B.1 Discussion of Individual H II Regions, $313^\circ < l < 327^\circ$

The following section provides a literature review of each observed H II region or H II region candidate (now all confirmed as H II regions) from Chapter 7. In each case we report with the WISE name from Anderson et al. (2014).

G313.671-00.105 G313.671-00.105 (IRAS 14183-6050) has been observed in several transitions. These include CS(2-1) with a peak velocities of -42.64±1.10 and -42.7±1.9 km s^{-1} as measured by Fontani et al. (2005) and Henning & Launhardt (1998) respectively; CS (3-2) at -42.65±1.43 km s^{-1} (Fontani et al. 2005); and ^{12}CO(2-1) at -42.5±2.7 km s^{-1}. MacLeod et al. (1998) did not detect any methanol masers towards the region, however Green et al. (2012) catalogued a 6.6 GHz methanol maser at G313.705-0.190 (-41.5 km s^{-1}). The maser site also exhibits OH emission at -44km s^{-1} (Caswell OH 313.705-00.190 in Caswell 1998). Using the CS line velocities, the region has previously been associated with the far side kinematic distance at $\sim$ 3 kpc (Fontani et al. 2005). As this work represents the first detections of RRL velocities towards the region, G313.671-00.105 is now confirmed as an H II region. The H I absorption spectrum is of poor quality, due to the low continuum brightness ($\sim$ 5 K). Despite this, as the difference in observed systemic velocity and calculated velocity is less than 25 km s^{-1}, the H II region is placed, by default, at the tangent point distance.

G313.790+00.705 This source was confirmed as an H II region (PMN J1420-6015) by Misanovic et al. (2002), who detected the H107α RRL transition at -53±5.4 km s^{-1}. The associated infrared source (IRAS 14170-6002) adheres to the Wood-Churchill criteria for ultracompact H II regions, but is not associated with any known methanol, nor hydroxyl, maser emission (van der Walt et al. 1995; Walsh et al. 1997). In addition, no CS(2-1) was detected towards the source by Bronfman et al. (1996). The infrared bubble with which this source is associated has a complete, or closed, morphology with enclosed star cluster (S121 in Churchwell et al. 2006). Mercer et al. (2005) confirmed the internal star cluster ([MCM2005b] 51), with 38 members. For G313.790+00.705, the difference between terminal and systemic velocities is $<$ 10 km s^{-1}. As a result, the H II region is designated as being at the tangent point distance.

G314.219+00.343 Our RRL detections confirm G314.219+00.343 as an H II region, although molecular line velocities are known (-60.76 km s^{-1} from N_2H^+, HNC, HCO^+, HCN, C_2H, $H^{13}CO^+$ and $H^{13}CN$ in Jackson et al. 2013). The associated mid-infrared bubble has a complete or closed ring morphology with enclosed star cluster (S117 in Churchwell et al. 2006). Mercer et al. (2005) confirmed the internal star cluster ([MCM2005b] 52), with 41 members.

A known giant molecular cloud (GMC), at G314.250+0.250, has an angular radius of 48 parsecs and includes three associated UC H II sources (Cloud 15 in García et al. 2014). Two of these are known H II regions, GAL 314.18+00.31 and G314.228+0.473, which both demonstrate H_2CO absorption at -61 km s^{-1} and RRL emission at -62 km s^{-1} and -63 km s^{-1} respectively (García et al. 2014). We assume that G314.219+00.343 is the third UC H II source within the cloud.

The CO velocity of the GMC is -57.6 km s^{-1} and it is assumed to be in the foreground of the two known H II regions - which themselves are assumed to be at either the near or tangent point kinematic distances. We place the newly confirmed H II region at the tangent point distance, as the difference between the RRL and rotation model's terminal velocities is < 25 km s^{-1}.

G315.312-00.273 This known H II region (GAL 315.31-00.27) is catalogued by Caswell & Haynes (1987). Superimposed on a supernova remnant (G315.4-0.3 in Caswell et al. 1981), the H II region has a positive RRL velocity, unambiguously placing the region in the outer Galaxy.

G316.516-00.600 G316.516-00.600 is associated with a complete/closed ring infrared bubble with probable enclosed star cluster (S114 in Churchwell et al. 2006). As this study marks the first detected RRL transitions, we are able to confirm this candidate as an H II region.

MALT90 provides several molecular velocities for the ATLASGAL source at G316.514-00.576 (IRAS 14412-6013); with detections of C_2H(1-0), HCN and HCO^+ at -44 km s^{-1}, HNC at -45 km s^{-1} and N_2H^+ at -43 km s^{-1}*.

The H I absorption spectrum is not of a sufficient quality to allow for an attempt of a KDAR.

G317.861+00.160 These coordinates are known to host both a radio (PMN J1452-5910) and infrared source (IRAS 14482-5857). The source has been observed in many transitions, but no known hydroxyl or methanol maser (Schutte et al. 1993), nor CS(2-1) (Bronfman et al. 1996) emission has been detected. However, a water maser was detected by Walsh et al. (2011) at -3.3 km s^{-1}. The IRAS colors satisfy the Wood-Churchill criteria for ultra-compact H II regions (Walsh et al. 1997; Culverhouse et al. 2011). We are the first to confirm that the target is an H II region, through the detection of several RRL transitions. The RRL velocities are positive, indicative of a position near the Solar circle, in the outer Galaxy.

*Note that MALT90 data is not yet published, they are however, available through the Australia Telescope Online Archive (ATOA) http://atoa.atnf.csiro.au/MALT90

G318.248+00.151 This source has been identified as a Massive Young Stellar Object (MYSO) in the Mid-course Space Experiment point source catalog (G318.2650+00.1269 1 in Mottram et al. 2007). Our Hnα RRL detections, confirm, for the first time, that the source is an H II region. The H I absorption spectrum is not of a sufficient quality to allow for an attempt of a KDAR.

G319.229+00.225 Our Hnα RRL observations are the first to confirm that the candidate is an H II region. The infrared bubble with which this source is associated (S99 in Churchwell et al. 2006) is indicative of a broken or incomplete ring morphology.

The source does not meet the continuum temperature requirements for a KDAR suitable H I absorption spectrum. However, as the difference in terminal and systemic velocities is less than 25 km s^{-1}, we place the H II region at the tangent point distance.

G323.449+00.095 Grave & Kumar (2009) describe G323.499+00.095 (IRAS 15246-5612) as an alpha-magnitude (based on IRAC bands spectral index) point source surrounded by an infrared nebula which looks like a dense core irradiated by central star. The source also satisfies the infrared color criteria from Hughes & MacLeod (1989) for H II regions, but does not fulfil the Wood-Churchil criteria for ultra-compact H II regions (MacLeod et al. 1998). Our detections of several Hnα RRL transitions confirm the presence of an H II region.

This source has been observed by Fontani et al. (2005) in many molecular transitions: CS(2-1) -65.44 km s^{-1}; CS(3-2) -65.35km s^{-1}; C^{17}O(1-0) -65.32 km s^{-1} and C^{17}O(2-1) at -65.4 km s^{-1} and is also detectable at 1.2 mm. MALT90 observations of C_2H (-66 km s^{-1}), H^{13}CO$^+$ (-62 km s^{-1}), HCN (-67 km s^{-1}), HCO$^+$ (-64 km s^{-1}), HNC (-64 km s^{-1}) and N_2H^+ (-65 km s^{-1}) towards IRAS 15246-5612 at G323.444+00.094 are inkeeping with previous molecular velocities and our new detections of Hnα RRL emissions.

The source is placed at the tangent point distance due to the proximity of the observed RRL velocity tp the calculated terminal velocity.

G323.464-00.079 This known H II region was confirmed by the detection of the H70α RRL by Murphy et al. (2010). This source demonstrates the broadest Hnα line widths of all of our targets - with wide wings not well fitted by the Gaussian model (see overview Figure Set 7.9)— Murphy et al. (2010) also report a broad FWHM (50 km s^{-1}).

The giant molecular cloud which includes this region, as the single UC H II source, has a CO velocity of -65.5 km s^{-1} (García et al. 2014). They adopt the near kinematic distance for the cloud, due to the line of sight distance to the embedded maser, Caswell CH3OH 323.459-00.079, of 4.5 kpc (Caswell & Reynolds 2001). We take a more conservative apporach, placing the H II region at the tangent point distance.

G323.743-00.249 The observational history of the source includes OH, methanol and water maser detections (Cohen et al. 1988; Kemball et al. 1988; Scalise et al. 1989; Sestokas Filho & Scalise 1990; Walsh et al. 2011); no detectable CO or SiO emission (Deguchi et al. 1990) and characterisation as a reflection nebula with a line of sight distance of 3 kpc (Zavagno et al. 1992). During the 1990s, Walsh et al. performed a series of observations that

determined 15 maser spots (at ~ -51 km s^{-1}); two sites of methanol masers, with coincident near infrared sources, and one OH maser site were located to the south-east of the nebulous emission; a line of sight distance of 3.6 kpc; fan shaped H_2 emission to the north-west of the maser sites; and the likelyhood that the H II region was powered by a B0 star (Walsh et al. 1997, 1999, 2001; Lee et al. 2001; Walsh et al. 2002). The star forming region is reviewed, as the sole focus of Walsh et al. (2002). The SGPS H I abosrption spectrum is insufficient for a KDAR attempt, so we adopt the findings of the previous targeted works.

Since the 1990s, the source has been observed in the (1,1), (2,2), (4,4) and (5,5) transitions of NH_3 (Longmore et al. 2007; Beuther et al. 2009; Purcell et al. 2012) and has been targeted by maser observations (Vlemmings et al. 2011; Krishnan et al. 2013; Walsh et al. 2011). In addition the source was detected at multiple tracers at 90 GHz, including N_2H^+, HNC, HCO^+, HCN, C_2H, SiO, $H^{13}CO^+$ and $H^{13}CN$ (Jackson et al. 2013).

Despite this extensive history of observations, and satisfaction of the Wood-Churchill criteria for ultracompact H II regions (Culverhouse et al. 2011), G323.743-00.249 has not observed in Hnα RRLs before this work. Our observations add 13 detected Hnα RRL transitions to the extensive list of known line emissions for this source.

G323.806+00.020 Misanovic et al. (2002) observed the source in the H197α RRL, but were unable to detect emission above a 3σ level. However, Misanovic et al. (2002) also report that the source exhibits the Wood-Churchill criteria for H II regions. Therefore, this is the first work to detect any RRL statistically significant emission, and the first to confirm the source as an H II region. The infrared bubble associated with this H II region is complete in its morphology (Churchwell et al. 2006).

Using absorption signatures from known features along the line of sight (i.e. the methodology of Jones et al. 2013), the H II region must have a line of sight lower limit distance of 3.7 kpc due to absorption consistent with the near side components of the Saggitarius and Scutum-Crux spiral arms.

G323.936-00.037 We are the first to detect G323.936-00.037 in Hnα RRL transitions, confirming the presence of an H II region. We were, however, only able to detect five transitions, the lowest number for any target source in this work. The quality of the H I absorption spectrum is also poor.

G324.624-00.321 Walsh et al. (1997) suggest that the source has infrared colors usually associated with ultra-compact H II regions, but could not detect any defining H II region characteristics, nor 6.7 GHz methanol maser emission. Bronfman et al. (1996) did not detect any CS(2-1) emission towards the source. Therefore, our observations are the first to confirm the presence of an H II region, and provide a velocity for the source.

Following the Jones & Dickey (2012) KDAR method, we place the H II region at the far kinematic distance.

G325.108+00.054 Observed by the Pilot study of MALT90, the source has been detected at ~ -67.7 km s^{-1} in N_2H^+, HNC, HCO^+, HCN and C_2H. Our observations provide a

similar source velocity to those detected by molecular transitions and are the first to detect Hnα RRLs, confirming the presence of an H II region.

G325.354-00.035 We are the first to make targeted observations of this source. Our detection of several Hnα RRL transitions determine the presence of an H II region. The H I absorption spectrum is of insufficient quality to attempt a KDAR.

G326.721+00.773 This H II region is located in the complex including RCW95, RCW96, RCW98 as well as other large star forming regions. The parent giant molecular cloud includes 7 ultra-compact H II sources and exhibits a CO velocity of -42.1 km s^{-1} (Cloud 29 in García et al. 2014). Despite this association with well studied star formation regions, this work marks the first isolated observations of G326.721+00.773; providing a velocity and evidence for a presence of an H II region.

The near kinematic distance is adopted for several of the H II regions and IRAS sources on the basis of H I and OH absorption (García et al. 2014, and references therein). As a result, the distance of the newly confirmed H II region is assumed to be similar to the surrounding complex; $\sim$ 3.3 kpc (Georgelin et al. 1994). We determine the H II region is located at the kinematic near side distance - in agreement with previous determinations.

G326.890-00.277 This source has been observed in CS(2-1) with a velocity of -46.1±2.5 km s^{-1} (Bronfman et al. 1996) as well as NH_3(1,1) and (2,2) by Purcell et al. (2012). Our observations provide a similar source velocity to those detected by molecular transitions and are the first to detect Hnα RRLs, confirming the presence of an H II region. The H I spectrum indicates the presence of absorption at velocities associated with the Scutum/Crux sprial arm. As a result the H II region must be located at least that far along the line of sight (11.3 kpc).

G326.916-01.100 The associated infrared source, IRAS 15457-5429, has colors which infer an ultra-compact H II region. Bronfman et al. (1996) detect CS(2-1) emission at -46.1±2.5 km s^{-1} and MALT90 observations detect three molecular transitions; HCN (-52 km s^{-1}), HCO^+ (-50 km s^{-1}) and HNC (-51 km s^{-1}). These velocity detections are supported by our observed RRL velocity of -46.6 ± 1.0 km s^{-1}. Our detection of several RRL transitions confirm the presence of an H II region for the first time.

The morphology of the associated infrared bubble is indicative of a broken or incomplete ring with probable enclosed stellar cluster (S77 in Churchwell et al. 2006).

G327.313-00.536 This known H II region (GAL 327.30-00.60) has been extensively observed, especially over a range of Hnα transitions: H41α (-48 km s^{-1} Jackson et al. 2013); H109α (-48.8 ± 5.4 km s^{-1} Wilson et al. 1970); H109α/H110α (-48 km s^{-1} Caswell & Haynes 1987), H159α (detected by Cersosimo et al. 1989) and H166α (-47 km s^{-1} Azcárate et al. 1987). Gardner & Whiteoak (1978, and references therein) present and summarise observations in CO (-47 km s^{-1}), CS (-46.8 km s^{-1}) and H_2CO (-48.6 km s^{-1}). Our observations add a further 14 detected RRL transitions.

The source is also the site of a hydroxyl maser at −54.5 (Caswell 1998) and 12.2 GHz methanol maser at −49 km s^{-1} (Peng & Whiteoak 1992). MALT90 provides, in addition the the Hnα RRL transition above, a further nine molecular transitions with velocities between −44 and −48 km s^{-1}.

Associated with the optical object RCW97, the H II region, and associated giant molecular cloud (Cloud 30 in García et al. 2014), are assumed to lie at the near kinematic distance. Using the Jones & Dickey (2012) KDAR method, we also determine the near-side kinematic distance.

It should be noted that G327.323-00.536 was our strongest source; RRL emission became detectable in *each* observed transitition within several seconds of integration time.

G327.401+00.484 The colors of the associated infrared source, IRAS 15457-5429, infer an ultra-compact H II region (Beichman et al. 1988). Multiple molecular transitions have been detected from the soruce, including CS(2-1) at -83 km s^{-1} (Bronfman et al. 1996), NH_3 (2,2) at -80.4 km s^{-1} (Purcell et al. 2012); as well as OH, H_2O, 6.7 and 12.2 GHz methanol maser emission (Walsh et al. 1997; Ellingsen et al. 1996; Walsh et al. 2011; Caswell 1998). Our observations provide a similar source velocity to those detected by molecular transitions and are the first to detect Hnα RRLs, confirming the presence of an H II region. We place the H II region at the tangent point line of sight distance due to the similarities between the systemic and terminal velocities.

G327.555-00.829 Observed by the Pilot study of MALT90, the source has been detected at ~ -36.77 km s^{-1} in N_2H^+, HNC, HCO^+, HCN and C_2H. Our observations provide a similar source velocity to those detected by molecular transitions and are the first to detect Hnα RRLs, confirming the presence of an H II region. The H I absorption spectrum is insufficient to provide a KDAR.

G327.714+00.576 The infrared bubble associated with this source has a broken morphology (S79 in Churchwell et al. 2006). Our observations confirm the presence of an H II region; however the H I spectrum cannot provide a KDAR.

G327.763+00.163 Our observations are the first to provide velocity and classification evidence for the presence of an H II region. The region is located near the tangent point line of sight distance—the difference between systemic and terminal velocities is ~ 5 km s^{-1}.

B.2 Discussion of Individual H II Regions, $327^\circ < l < 345^\circ$

The following appeared as a Section in the published version of Chapter 3. In order to conserve the Galactic longitude order throughout Appendix B, only the sources $328 < l < 340^\circ$ are discussed here, the other sources ($l > 0^\circ$) can be found in Section B.4.

G331.333-0.344, V_{RRL}=-64 km/s, V_T=-109.2 km/s, KDA Assignment = Far Side (poor quality) Paladini et al. (2004) and Caswell & Haynes (1987) assign this strong, diffuse H II region to the near kinematic distance, however this work finds in favour of the far location, but with poor quality. The region is surrounded by diffuse emission in the SGPS continuum map and H I absorption is seen up to and including the terminal velocity, well above than the 3σ noise threshold (and even possibly at velocities beyond the Solar circle).

G331.522-0.078, V_{RRL}=-89 km/s, V_T=-109.8 km/s, KDA Assignment = Tangent Point This giant H II region was assigned to the near kinematic distance by Caswell & Haynes (1987), but is assigned to the 'tangent point' distance by default in this work. Bronfman (2008) performed continuum observations with the Australia Telescope Compact Array toward G331.50-0.1 revealing four distinct compact radio sources within a field of 10'. This region would benefit from an intensive RRL velocity investigation to resolve all four sources (Caswell & Haynes (1987) provide only one RRL velocity, -89 km/s). The SGPS continuum map indeed displays at least four continuum emission sources in the region, often with blended morphology.

Kerr & Knapp (1970b) give a distance estimate of 11 kpc, placing the H II region in the far part of the Sagittarius Arm. It should be noted that Kerr & Knapp (1970b) chose distances in relation to a known inner spiral arm pattern (Kerr 1969). Therefore, while the kinematic distance chosen by Kerr & Knapp (1970b) is significantly larger than that derived by this paper, the position of the H II region, in terms of a modern understanding of Galactic structure, is not dissimilar.

RCW 106; G333.011-0.444, V_{RRL}=-54 km/s, V_T=-113.9 km/s, KDA Assignment = Far Side (poor quality) Located close to RCW 106, this H II region is assigned to the far kinematic distance by this work and Paladini et al. (2004). However Wilson et al. (1970) (from whom the RRL velocity is sourced) and Urquhart et al. (2012) assign the near kinematic distance. H I absorption is present both at the terminal velocity and even possibly at positive velocities, indicating that the source is located at least as far along the line of sight as the tangent point.

RCW 106, G333.133-0.433, V_{RRL}=-52 km/s, V_T=-114.2 km/s, KDA Assignment = Near Side Also associated with RCW106, the SGPS continuum map displays several sources in an extremely crowded field rich in both OH and water masers (Breen et al. 2007).

G336.844+0.000, V_{RRL}=-79 km/s, V_T=-124.72 km/s, KDA Assignment = Far Side This H II region is possibly associated with G336.789+0.044 and another strong continuum source. Both this work and Paladini et al. (2004) determine the far kinematic location (10.5 kpc). Kerr & Knapp (1970b) acknowledge that the RRL velocity as well as H I and OH absorption profiles confirm a far kinematic location in the Norma-Scutum Arm and give a line of sight distance estimate of 12 kpc (see G331.522-0.078 (above) for a discussion of the distances in Kerr & Knapp (1970b)).

G337.711-0.056, V_{RRL}=-50 km/s, V_T=-127.2 km/s, KDA Assignment = Far Side This is the only H II region held in common with this paper and the work of Fish et al. (2003). Both works establish that the region is located at the far kinematic distance.

G337.922-0.467, V_{RRL}=-40 km/s, V_T=-127.8 km/s, KDA Assignment = Near Side This H II region is common between this work and Urquhart et al. (2012) and it demonstrates the utmost importance of both visual inspection of spectra and defining an appropriate detection threshold. Absorption appears up to 25 km/s beyond the RRL velocity, highlighting the necessity of a carefully chosen RRL interval (see Section 3.3.2.1). However no absorption is present within 50 km/s of the tangent point velocity - the E/A definition of a near side source.

B.2.1 Sources beyond the Solar Circle

The following sources all display significant H I absorption at velocities corresponding to distances beyond the Solar Circle. All of these objects would benefit from observations aimed at RRL velocity measurement in order to ascertain their location. While the sources in the outer Galaxy seem to align themselves with spiral structure (based on a flat rotation model beyond the Solar circle, see Figure 3.8), it is possible that the absorption lines at these velocities are products of cool H I clouds in the Solar neighbourhood with anomalous velocities.

G328.411+0.222, Last V_{Abs}=27 km/s Appearing as a discrete source on the SGPS continuum map, Gelfand et al. (2007) conclude that the source is pulsar wind nebula inside a Crablike supernova remnant (Gaensler et al. 2000). G328.411+0.222 is listed as an H II region by Kuchar & Clark (1997) and the Parkes-MIT-NRAO Survey (Griffith & Wright 1993), however, no mid-infrared counterpart is detected. The kinematic distance, 16.7 ± 1.2 kpc, (see Table 3.1 and Figure 3.7) is based on the velocity of the last absorption feature (+27 km/s) and is in good agreement with Gaensler et al. (2000) who assign G328.411+0.222 to the outer Galaxy - at a distance of approximately 17kpc .

G333.011-0.444, Last V_{Abs}=65 km/s In the area of an extensively studied Giant Molecular Cloud, the mid-infrared data for this region is saturated both in the 22μm WISE and 24μm Spitzer MIPSGAL archives. A well known H II region RCW 106 (with RRL velocity of about -55km/s) is located nearby. Significant H I absorption on the far side of the tangent point as well as beyond the Solar circle (to 65km/s) in conjunction with a confused radio continuum suggest that there are several sources in the region - at least one of which is at a large distance from the Sun. Kerr & Knapp (1970b) observe an H I absorption component at 38 km/s but consider that it is probably not reliable given large emission fluctuations in their spectrum.

G334.722-0.655, V_{RRL}=16 km/s A known outer Galaxy H II region, G334.722-0.655 has an RRL velocity of 16km/s (Caswell & Haynes (1987)), H I absorption is seen to approximately 20 km/s. A Spitzer GLIMPSE "bubble" source surrounds a compact co-spatial 22μm and

radio continuum source (see Figure 3.9). However, Urquhart et al. (2012) report a source velocity, derived from ^{13}CO emission, of -44.6 km/, suggesting that the absorption at low positive velocities is local (in the Solar neighbourhood).

G337.255-0.167, Last V_{Abs}=21 km/s This region is very crowded in both the radio and mid-infrared, see Figure 3.9. The 8μm image displays both a central compact and outer partial-shell components. Multiple-component RRL velocity measurements would probably arise from this region due to the crowded and confused nature of the radio continuum. Significant H I absorption is seen to 21km/s, this feature is used to calculate the kinematic distance (17.9$\pm$1.6 kpc). Unusually, no NED or SIMBAD radio source is listed within a five arcminute radius, however an infrared source is known from the IRAS catalogue (IRAS 16334-4719).

G338.411-0.211, $-4.3 \pm 3.6 < V_{RRL} < 2 \pm 2$ km/s The spectrum for G338.411-0.211 does not show significant absorption at velocities higher than the listed RRL velocity (2 km/s, Caswell & Haynes (1987)). As expected for an H II region, the mid-infrared emission exists co-spatially with the radio SGPS continuum. The 8μm GLIMPSE data shows a compact source as well as significant partial shell structure, spatially consistent with the 22μm and radio sources (see Figure 3.9). It should however be noted that Wilson et al. (1970) and Georgelin & Georgelin (1976) both recorded a RRL velocity of $-4.3(\pm 3.6)$ km/s for this H II region, which would indicate the far kinematic distance (with local clouds accounting for the H I absorption about 0km/s).

B.2.2 Southern Extragalactic Sources

The following continuum sources did not exhibit co-spatial mid-infrared components and are therefore likely to be extragalactic: G328.356-0.411 (Brown et al. 2007, see), G328.411+0.222 and G334.778-0.022.

B.3 Discussion of Individual H II Regions, $|l| < 10°$

The following appeared as an appendix in the published version of Chapter 4.

G350.004+00.438 The H I absorption spectrum does not give a clear indication of any absorption associated with any EIG feature. At this longitude, the velocity range of the Far 3kpc Arm is not clearly distinct from velocities expected by normal circular rotation.

GAL 350.13+00.09 G350.129+00.088 The H I absorption spectra clearly demonstrates absorption either side of the velocities expected by an association with the Near 3kpc Arm. Quireza et al. (2006) place the H II region at a line of sight distance of 6.2 kpc (i.e. on the near side of the GC).

G350.177+00.017 Evidence of absorption in the Far 3kpc Arms suggests a far KDAR. As with G350.330+00.157 (below), the calculated R_{Gal} and D_{los} for the region are outside the bounds of the McClure-Griffiths & Dickey (2007) rotation model.

G350.330+00.157 While the H I absorption spectrum suffers from emission fluctuations around the RRL velocity (~ -60km s^{-1}), there is evidence of absorption associated with the Near 3kpc Arm. Assuming a far side KDAR, the calculated R_{Gal} and D_{los} are outside the bounds of the McClure-Griffiths & Dickey (2007) rotation model.

G350.335+00.107 Evidence of H I absorption is seen either side of the velocities associated with the Near 3kpc Arm (see G350.129+00.088 above), and is therefore located at least as far as the Near 3kpc Arm along the line of sight.

G350.524+00.960 G350.524+00.960 does not demonstrate any H I absorption outside the velocities expected by normal circular rotation. If the near kinematic distance is therefore assumed, the H II region has a calculated $D_{los} \approx 1.9$kpc.

G350.769-00.075 The H I absorption spectrum of G350.769-00.075 does not give conclusive evidence for either a near, nor far, KDAR.

G350.813-00.019 As the H I absorption spectrum of G350.813-00.019 demonstrates absorption in velocities associated with the Far 3kpc Arm, the H II region must be on the far side of the GC. The positive (small) RRL velocity then locates the H II region at a line of sight distance beyond (but close to) the Solar Circle.

G350.996-00.557 Strong absorption is seen in the Far 3kpc Arm, but not in the Near 3kpc Arm. The RRL velocity suggests a location within the Far 3kpc Arm.

G351.028+00.155 The H I absorption spectrum of G351.028+00.155 demonstrates significant absorption at velocities corresponding to both the Near and Far 3kpc Arms, and therefore must be located at least as far as the Far 3kpc Arm along the line of sight. The positive RRL velocity then requires that G351.028+00.155 is located in the outer Galaxy.

G351.047-00.322 The H I absorption spectrum of G351.047-00.322 does not give conclusive evidence for either a near, nor far, KDAR.

G351.192+00.708 H I absorption is evident in circular rotation allowed velocities only. If the near kinematic distance is therefore assumed, the H II region has a calculated $D_{los} \approx$ 0.3kpc. Moisés et al. (2011) assumes the near kinematic distance, however Quireza et al. (2006) place the H II region at a line of sight distance of 17.1 kpc.

G351.201+00.483 The H I absorption spectrum of G351.201+00.483 does not give conclusive evidence for either a near, nor far, KDAR. Quireza et al. (2006) place the object at 1.4 kpc, at the near kinematic location.

G351.358+00.666 Quireza et al. (2006) assumes a near KDAR for G351.358+00.666, but H I absorption associated with velocities expected of the Far 3kpc Arm suggest that the H II region is located at the far kinematic location.

G351.359+01.014 The H I absorption spectrum of G351.359+0.1014 does not give conclusive evidence for either a near, nor far, KDAR.

G351.467-00.462 Quireza et al. (2006) give G351.467-00.462 a near side KDAR, but the H I absorption spectrum from this paper does not give conclusive evidence for a KDAR.

GAL 351.60-00.35 G351.601-00.348 The RRL velocity for this H II region (-91.8 km s^{-1}, Lockman (1989)) is associated with the Near 3kpc Arm. Green et al. (2011) also position a nearby 6.7 GHz maser ($l, b = 351.581, -0.353$)in the Near 3kpc arm.

G351.662+00.518 G351.662+00.518 has a near zero RRL velocity (-2.9km s^{-1}, Lockman (1989)) which is associated with locations inside the EIG region, near the Solar Cirle, or at a very small line of sight distance from the Sun. Absorption at velocities associated with the Near 3kpc Arm imply a $D_{los} > 5$kpc. As there is no H I absorption associated with other EIG features (only the Far 3kpc Arm is expected at this longitude), a location within $R_{Gal} \lesssim 3$kpc is assumed.

G351.691+00.669 No H I absorption falls outside the circular rotation envelope of allowed velocities, suggesting a near KDAR. However, the positive RRL velocity suggests a location in either the EIG or outer Galaxy.

G352.233-00.151 This H II region has an RRL velocity associated with the Near 3kpc Arm (-88.6km s^{-1}, GBTHRDS). Strong absorption in the allowed circular rotation velocities and at velocities associated with the Near 3kpc Arm, reaffirm the location in the Arm.

G352.313-00.440 Evidence of H I absorption in both the Near and Far 3kpc Arms suggests a far side KDAR for G351.313-00.440.

GAL 352.40-00.06 G352.398-00.057 Absorption is seen at the expected velocities of the Near 3kpc Arm, which is also where the RRL velocity for this H II region lies (-87km s^{-1}, Lockman (1989)). Absorption up to 25 km s^{-1} beyond the RRL velocity of an H II region is not uncommon (Dickey et al. 2003; Jones & Dickey 2012), therefore it is assumed that the H II region is located in the Near 3kpc Arm.

G352.521-00.144 Two RRL velocities have been recorded for G352.521-00.144 (-57.3 and -38 km s^{-1}, GBTHRDS), suggestive of multiple emission sources along the line of sight.

G352.610+00.177 The H I absorption spectrum for G352.610+00.177 suffers from emission fluctuations. As a result the poor quality spectrum does not give conclusive evidence for a KDAR.

G352.611-00.172 G352.611-00.172 displays strong absorption at $\sim$ 100km s^{-1}, approximately 20km s^{-1} beyond the known RRL velocity of the H II region (-81.9km s^{-1}, Lockman (1989)). As with G352.398-00.057 (above), G352.611-00.172 is assumed to lie in the Near 3kpc Arm. This location, in the Near 3kpc Arm, is approximately the same as the line of sight distance given by Quireza et al. (2006) (6.7 kpc).

G352.866-00.199 Evidence of absorption at velocities corresponding to the Near 3kpc Arm suggest a $D_{los} \geq$ 5kpc. Green et al. (2011) position a nearby 6.7 GHz methanol maser $(l, b = 352.855, -0.201)$ at the far kinematic location ($D_{los} \approx$ 11kpc).

G353.186+00.887 H I absorption is evident in circular rotation allowed velocities only, G353.186+00.887. If the near kinematic location is then assumed, the H II region has a calculated $D_{los} \approx$ 0.9kpc. Quireza et al. (2006) provide a near side KDAR for this H II region.

G353.218-00.249 Also the source of a variable maser (Caswell et al. 2010), G353.218-00.249 has a small RRL velocity (-8.3 km s^{-1}, GBTHRDS) and absorption present at Near 3kpc Arm, but not Far 3kpc Arm, velocities. These are evidence for a location near the EIG, and as such $D_{los} \geq$ 5kpc, $R_{gal} <$ 3kpc is assumed.

G353.381-00.114 The H I absorption spectrum of G353.381-00.114 displays strong H I absorption associated with the Near 3kpc Arm, suggesting that the H II region must lie behind the feature.

G353.398-00.391 H I absorption is evident in circular rotation allowed velocities only, if, therefore, a near side KDAR is assumed, the calculated $D_{los} \approx$ 5.2kpc.

G353.557-00.014 H I absorption is present at velocities corresponding to both 3kpc Arms, suggestive of a far side KDAR. However, like the H II regions G350.330+00.157 and G350.177+00.017, the calculated R_{Gal} and D_{los} fall outside the boundaries of the McClure-Griffiths & Dickey (2007) rotation model.

G354.200-00.050 Strong absorption is centered at velocities to the negative side of those expected for the Near 3kpc Arm (see G352.611-00.172 and G352.398-0.057 above).Green et al. (2011) were unable to determine a KDAR for a nearby 6.7 GHz methanol maser $(l, b = 354.206, -0.038)$. Due to the H I absorption associated with the Near 3kpc Arm $D_{los} \geq$ 5kpc is assumed.

G354.418+0.036 The H I absorption spectrum of G354.418+0.036 does not give conclusive evidence for either a near, nor far, KDAR.

G354.486+00.085 Caswell et al. (2010) places a nearby 6.7 GHz methanol maser $(l, b = 354.496, 0.083)$ in the Far 3kpc Arm. The RRL velocity of the H II region (15.8km s^{-1}, Lockman (1989)) is slightly smaller than that expected for the Far 3kpc Arm, but the absorption

indicates the H II region must be located at least as far along the line of sight as the feature. Due to the positive RRL velocity, we assume that G354.486+00.085 is located beyond the Solar Circle (see Table 4.4).

G354.588+00.007 A line of sight along the longitude of 354.588^o intersects the Near and Far 3kpc Arms as well as the assumed position of Bania's Clump 1. The H I absorption spectrum of G354.588+00.007 does not give conclusive evidence for either a near, nor far, KDAR; but absorption associated with the Near 3kpc Arm suggests $D_{los} \geq 5$kpc.

G354.610+00.484 Significant H I absorption is present before and after the velocities expected of the Near 3kpc Arm, as well as at Far 3kpc Arm velocities. A known strong 6.7 GHz methanol maser is also in the region (Caswell et al. 2010), with a velocity equivalent to the RRL velocity (maser velocity: -23km s^{-1}, RRL velocity: -23.4km s^{-1} (GBTHRDS)). Green et al. (2011) suggest a poor quality near side KDAR for the associated maser, but a far kinematic distance is assumed here.

GAL 354.66+00.47 G354.664+00.470 H I absorption is evident in circular rotation allowed velocities only, assuming a near side KDAR the calculated $D_{los} \approx 4.5$kpc.

GAL 354.67+00.25 G354.665+00.247 No absorption is seen at the RRL velocity of the H II region (97.8km s^{-1}, Lockman (1989)), nor at velocities corresponding to the Near 3kpc Arm. However, significant absorption is seen at $\sim$ 70km s^{-1}, possibly associated with Bania's Clump 1. No KDAR is given here, however the high RRL velocity is suggestive of a location in the EIG (Caswell et al. 2010).

G354.717+00.293 As with G354.665+00.247, the high RRL velocity of G354.717+00.293 suggests a location in the EIG. The H I absorption spectrum suffers from emission fluctuations at the RRL velocity (95.3km s^{-1}, GBTHRDS) and no absorption is present at Near 3kpc Arm velocities. At least two masers with high velocities ($\sim$ 100km s^{-1}) are known to exist in the area (Caswell et al. 2010).

GAL 354.93+00.33 G354.934+00.327 G354.934+00.327 shares a similar absorption profile to that of G354.717+00.293 and G354.665+00.247, however it does not share a highly non-circular RRL velocity (14km s^{-1}, Caswell & Haynes (1987)). Absorption velocities corresponding to all expected EIG features requires the H II region to be located at least as far along the line of sight as the Far 3kpc Arm. Due to the positive RRL velocity, the H II region must then be located in the outer Galaxy, beyond the Solar circle along the line of sight.

G354.979-00.528 The H I absorption spectrum of G354.979-00.528 does not give conclusive evidence for either a near, nor far, KDAR.

G355.242+00.096 H I absorption is present at velocities corresponding to the Near 3kpc Arm on the near side of the GC, and there is evidence of absorption on the far side of the GC

due to the Far 3kpc Arm and +135km s^{-1} Expanding Arm. A far side KDAR is given, but due to the positive RRL velocity, the H II region must be located beyond the Solar Circle.

G355.344+00.145 Absorption at the Near 3kpc Arm, +135km s^{-1} Expanding Arm and Far 3kpc Arm infer that the H II region is located beyond the EIG along the line of sight. The positive RRL velocity then places the H II region beyond the Solar circle. There are several masers in the region which are assumed to lie within 3 kpc of the GC (see $(l, b) = (355.343, +0.148), (355.344, +0.147)$ and $(355.346, +0.149)$ in Green et al. 2011).

G355.532-00.100 This region has four known RRL velocities (3.8, -22.5, -80.6 and -41.1 km s^{-1}, GBTHRDS), a strong indication that there are several emission sources along the line of sight. Note that the RRL velocity -80.6km s^{-1} is associated with velocities expected of the Near 3kpc Arm. No KDAR is given.

G355.581+00.288 Three RRL velocities are known towards the H II region (+108.7, -76.1 and +11.7 km s^{-1}, GBTHRDS). As with G355.532-00.100 (above), this is an indication of several sources along the line of sight. No KDAR is given, however the RRL velocity -76.1km s^{-1} is associated with the Near 3kpc Arm and the RRL velocity component +108.7km s^{-1} is associated with the +135km s^{-1} Expanding Arm.

G355.611+00.382 The near zero RRL velocity (-2.6 km s^{-1}, GBTHRDS) is indicative of a EIG location, or a location near the Solar circle (either very close or at a great distance from the Sun). Absorption in velocities associated with the Near 3kpc Arm and +135km s^{-1} Expanding Arm, but not at velocities corresponding to far side EIG features prompts $D_{los} \geq 8.5$kpc, $R_{gal} < 3$ kpc to be given as a distance limit for the H II region. In contrast, Green et al. (2011) presents a far side KDAR for a 6.7 GHz methanol maser at $l, b = 355.666, +0.398$ which has a systemic velocity of ~ -2km s^{-1}.

G355.696+0.350 Two RRL velocities (3 and -79.1 km s^{-1}, GBTHRDS) suggest multiple emission sources along the line of sight, at least one of which is associated with the Near 3kpc Arm (-79.1km s^{-1} RRL association). At this longitude, the velocities of the Near 3kpc Arm and the Looping Ridge (on the far side of the GC) overlap. No KDAR is given.

G355.700-00.100 G355.700-00.100 has an absorption profile and RRL velocity (-76.1 km s^{-1}, Lockman (1989)) suggestive of a location within the Near 3kpc Arm or Looping Ridge (as the expected velocities of these features overlap at this longitude). No KDAR is given.

G355.734+0.138 There are multiple RRL velocities associated with G355.734+0.138 (10.7 and -77.4 km s^{-1}, GBTHRDS). No KDAR is given, but the RRL velocity component at -77.4km s^{-1} is associated with the velocities expected of the Near 3kpc Arm or Looping Ridge.

G355.801-00.253 The velocity ranges of the Near 3kpc Arm and Looping Ridge continue to overlap at this longitude. Two RRL velocities are known (-31.5, 3.1 km s^{-1}, GBTHRDS), suggestive of multiple sources along the line of sight. No KDAR is given.

G356.230+00.066 At this longitude the expected velocities of the Near 3kpc Arm and Looping Ridge are distinct (see above). However, the H I absorption spectrum of G356.230+00.066 does not give conclusive evidence for either a near, nor far, KDAR.

G356.235+00.642 Absorption is seen at velocities corresponding to the Near 3kpc Arm and Looping Ridge. It is assumed that the H II region is located in the +135km s^{-1} Expanding Arm (due to the RRL velocity (116.3km s^{-1}, Lockman (1989)). This is supported by absorption at velocities corresponding to the Looping Ridge (on the far side of the GC, but closer to the GC than the +135km s^{-1} Expanding Arm).

G356.307-00.210 A near zero RRL velocity (-4km s^{-1}, Lockman (1989)) and absorption concurrent with Near 3kpc Arm velocities suggests $R_{gal} < 3$ kpc for this H II region.

G356.470-0.001 The H I absorption spectrum of G356.470-0.001 does not give conclusive evidence for either a near, nor far, KDAR.

G356.560-00.086 The H I absorption spectrum of G356.560-00.086 does not give conclusive evidence for either a near, nor far, KDAR.

G356.650+00.129 H I absorption is present in velocities corresponding to the Near 3kpc Arm. As such $D_{los} > 5$kpc is assumed.

G357.484-00.036 The H I absorption spectrum suffers from emission fluctuations in the velocity ranges associated with the Near 3kpc Arm and Looping Ridge. As such the poor quality spectrum does not allow a KDAR to be given for this H II region.

G357.970-00.169 The H I absorption spectrum of G357.970-00.169 displays absorption at velocities associated with the Near 3kpc Arm. As a result, $D_{los} > 5kpc$ is assumed. The small RRL velocity, and lack of absorption corresponding to other EIG features suggests a further constraint, $R_{Gal} < 3$kpc.

G357.998-00.159 The H I absorption spectrum of G357.998-00.159 displays absorption at velocities associated with the Near 3kpc Arm. As a result, $D_{los} > 5kpc$ is assumed. The small RRL velocity, and lack of absorption corresponding to other EIG features suggests a further constraint, $R_{Gal} < 3$kpc.

G358.319-00.414 The H I absorption spectrum of G358.319-0.414 does not give conclusive evidence for either a near, nor far, KDAR.

G358.379-00.840 The H I absorption spectrum of G358.379-00.840 does not give conclusive evidence for either a near, nor far, KDAR.

G358.530+00.056 This H II region has an RRL associated with the Looping Ridge or Tilted Disk(-208.5km s^{-1}, GBTHRDS), however the spectrum is of poor quality and no absorption is seen at velocities pertaining to any EIG feature.

G358.552-00.025 This H II region has an RRL associated with the Looping Ridge or Tilted Disk(-208.5km s^{-1}, GBTHRDS), however the spectrum is of poor quality and no absorption is seen at velocities pertaining to EIG features in front of the GC along the line of sight.

G358.616-00.076 The H II region has an RRL association with the Tilted Disk or Looping Ridge. The H I absorption spectrum confirms absorption at velocities corresponding to the Near 3kpc Arm only; further supporting a location in the EIG. Absorption is also seen at velocities either side of the expected velocity range of the Tilted Disk.

GAL 358.62-00.07 G358.623-00.066 Like G358.616-00.076 (above), G358.623-00.066 demonstrates significant absorption associated with the Near 3kpc Arm and Tilted Disk. The RRL association with the Looping Ridge/Tilted Disk suggests a location in the EIG. Note the bifurcation in the Near 3kpc Arm absorption profile, see §4.4.

G358.633+00.062 H I absorption is seen at velocities corresponding to the Near 3kpc Arm and the H I Tilted Disk. The positive RRL velocity suggests either a EIG or near Solar circle location: absorption corresponding to near-side EIG features discounts the near-kinematic distance; and if the H II region was located near the Solar cirlce on the far side, there should be evidence of absorption associated with the Far 3kpc Arm. As a result it is assumed that the H II region is located within the EIG, i.e. $R_{Gal} < 3$kpc, $D_{los} > 8.5$kpc. Note the bifurcation in the Near 3kpc Arm absorption profile (see G358.623-00.066 above).

G358.652-00.078, G358.680-00.087, G358.694-00.075, G358.720+00.011, G358.797+00.058, G358.827+00.085 and G359.159-00.038 The H I absorption profiles of these H II regions are all similar. And all have highly non-circular RRL velocities which correspond to the Tilted Disk - G359.159-00.038 has two known RRL velocities (-182.5 and -215.6 km s^{-1}). The H I absorption spectra suffer from emission fluctuations and are generally of poor quality.

G359.277-00.264 G359.277-00.264 demonstrates no absorption at velocities corresponding to EIG features, a near side KDAR is given.

G359.432-00.086 G359.432-00.086 has a known RRL velocity associated with the Near 3kpc Arm. The H I absorption spectrum towards the region demonstrates absorption associated with the Near 3kpc Arm (and also at ~ -120km s^{-1}).

G359.467-00.172 At this longitude the expected velocity ranges of the Near 3kpc Arm and Tilted Disk overlap. The H I absorption spectrum demonstrates absorption at velocities corresponding to the Near 3kpc Arm, but suffers from emission fluctuations at the overlap. The H II region has an RRL velocity consistent with either the Tilted Disk or Near 3kpc Arm.

G000.284-00.478 Absorption is present at velocities corresponding to the Near 3kpc Arm, but not at the expected velocities of other EIG features. It is assumed that the H II region is located in the EIG, beyond the Near 3kpc Arm; $R_{Gal} < 3$kpc, $D_{los} > 8.5$kpc.

KC97c G000.4-00.8 G000.361-00.780 G000.361-00.780 demonstrates H I absorption at velocities associated with the Near 3kpc Arm, but no absorption at other EIG lv features. It is therefore assumed, as with G000.284-00.478 above that the H II region is located within $R_{Gal} < 3$kpc, $D_{los} > 8.5$kpc.

G000.382+00.107 With two RRL velocities (25.7 and 41.4 km s^{-1}, GBTHRDS), the absorption spectrum is likely to have contributions from at least emission two sources along the line of sight. Absorption at the Near 3kpc Arm and +135km s^{-1} Expanding Arm velocities suggests that at least one of the emission sources is located on the far side of the GC. No KDAR is given. Note also that at this longitude, the expected velocity ranges of the H I Tilted Disk and Far 3kpc Arm are nearly indistinguishable.

G000.510-00.051 H I absorption is present at velocities corresponding to the Near 3kpc Arm, but not at the velocities of other EIG features. The RRL velocity (45km s^{-1}, Downes et al. (1980)) suggests an association with the Far 3kpc Arm.

G000.572-00.628 The H I absorption spectrum of G000.572-00.628 does not give conclusive evidence for either a near, nor far, KDAR.

LPH96 000.640+0.623 G000.640+00.623 A far-side KDAR is assumed for G000.640+00.623 due to absorption at velocities corresponding to both 3kpc Arms (and the Tilted Disk).

G000.729-00.103 G000.729-00.123 has two recorded RRL velocities (105.3 and 83.2 km s^{-1}, GBTHRDS), both forbidden by circular Galactic rotation. The region was studied by Downes et al. (1980) who found an RRL velocity of 102 km s^{-1}. Caswell & Haynes (1987) discussed the H II region as being clearly located near the EIG, but not delineating the outer boundary of the Galactic bar. The GBTHRDS find that of their nine H II regions associated (in lv space) with the Nuclear Disk, G000.729-0.103 is the only source that could be located on the red-shifted side. The H I spectrum demonstrates statistically significant absorption at velocities corresponding to both 3kpc Arms, but not for the Nuclear Disk nor +135km s^{-1} Expanding Arm. No H I absorption is present at either of the RRL velocities. No KDAR is given.

G000.838+00.189 The H I absorption spectrum, which is of poor quality due to emission fluctuations, demonstrates absorption consistent with the velocities expected of each of the EIG features (Near 3kpc Arm, H I Tilted Disk, +135km s^{-1} Expanding Arm and Far 3kpc Arm). A far-side KDAR is therefore awarded to the H II region.

G001.125-00.105 Wink et al. (1982) remarked that the non-circular RRL velocity (-19.7 km s^{-1}) and H_2CO at 84 and 123 km s^{-1} was typical of a EIG source; Quireza et al. (2006) also give D_{los} = 8.5kpc. THe H II region must be located within the EIG, as absorption at EIG features negates the near-side kinematic location and if the H II region must have a non-realistic $R_{Gal} > 45$kpc.

G001.149-00.062 G001.149-00.062 displays absorption at velocities corresponding to both the Near and Far 3kpc Arms. Assuming a distance of at least the Far 3kpc Arm, G001.149-00.062 must lie in the outer Galaxy, beyond the Solar Circle (due to the negative systemic velocity). However, using a flat rotation model for the outer Galaxy, the calculated D_{los} is unrealistic ($\sim$ 50kpc). Therefore the H II region must lie in the EIG region, but behind the Far 3kpc Arm.

G001.324+00.104 No H I absorption is seen at velocities corresponding to EIG features, suggesting a near KDAR. However, the negative RRL velocity (-12.7 km s^{-1}, GBTHRDS) suggests a location in either the EIG or in the outer Galaxy - locations that each would imply absorption by the Near 3kpc Arm, which is not seen. No KDAR is given.

GAL 001.32+00.09 G001.330+00.088 G001.330+00.088 has a similar H I absorption profile as G001.324+00.104. A EIG location is assumed.

G001.488-0.199 Caswell et al. (2010) assigns a 6.7 GHz methanol maser at the same velocity to $R_{gal} < 3$ kpc due to the negative systemic velocity. Absorption at velocities corresponding to the Near 3kpc Arm supports the $R_{gal} < 3$ kpc placement.

G002.009-0.680 $D_{los} > 5$ kpc is assumed due to absorption at Near 3kpc Arm velocities.

G002.404+0.068 The H I absorption spectrum of G002.404+0.068 does not give conclusive evidence for either a near, nor far, KDAR.

G002.418-0.611 The H I absorption spectrum of G002.418-0.611 does not give conclusive evidence for either a near, nor far, KDAR.

G002.510-00.028 $D_{los} > 5$kpc is assumed due to absorption at velocities corresponding to the Near 3kpc Arm.

G002.611+00.135 For a 6.7 GHz methanol maser at the same coordinates, Caswell et al. (2010) discuss that the large positive systemic velocity is most readily attributed to a location within the Galactic bar. Absorption is seen at Near 3kpc Arm velocities, and at velocities slightly lower than the RRL velocity (102.4 km s^{-1}, Lockman (1989)), but not at +135km s^{-1} Expanding Arm velocities; therefore $R_{gal} < 3$kpc is assumed. See Section 4.6 for a previous discussion of this H II region.

G002.819-00.132 The H I absorption spectrum of G002.819-00.132 does not give conclusive evidence for either a near, nor far, KDAR.

G002.901-00.006 The negative RRL velocity suggests a EIG or outer Galaxy location. Absorption at Near 3kpc Arm velocities infers a $D_{los} > 5$kpc; but a lack of absorption associated with any other EIG feature does not allow the EIG/outer Galaxy location degeneracy to be resolved. Quireza et al. (2006) give a location in the Outer Galaxy.

G002.961-0.053 The H I absorption spectrum is most likely a confusion of multiple H II regions - there are two RRL velocities (18.1 and -3.5 km s^{-1}, GBTHRDS). No KDAR is given.

G003.270-00.101 Absorption at velocities corresponding to both 3kpc Arms suggests a kinematic location in, or beyond, the Far 3kpc Arm. The near zero systemic velocity then suggests a location near the Solar circle. Quireza et al. (2006) give a line of sight distance to G003.270-00.101 of 14 kpc.

G003.342-00.079 Significant absorption is seen at both the Near and Far 3kpc Arms (and at $\sim$ 100km s^{-1}). Using this absorption as a distance indicator, G003.342-00.079 is given a far KDAR.

G003.439-0.349 G003.439-0.349 is assumed to be located in the Near 3kpc Arm, due to RRL and maser velocities (GBTHRDS, Caswell et al. (2010)), as well as H I absorption, at velocities expected of the Near 3kpc Arm.

G003.449-0.647 With H I absorption at Near 3kpc Arm velocities, $D_{los} > 5$kpc is assumed. As the H II region has a near zero systemic velocity, and no absorption associated with the Far 3kpc Arm, then $R_{Gal} < 3$kpc should also apply.

PWN J1754-25551 G003.655-00.111 Absorption at velocities corresponding to the Near 3kpc Arm and a near zero RRL velocity (4.6 km s^{-1}, Lockman (1989)) suggests $R_{gal} < 3$kpc.

G003.928-00.116 Evidence of absorption is present at velocities corresponding to both the Near and Far 3kpc Arms. As a result, G003.928-00.116 is given a far side KDAR.

LPH96 00.3949-0.100 G003.949-00.100 The H I absorption spectrum is of poor quality, typical of the diffuse regions of the Lockman et al. (1996) catalog. No KDAR is given, however the small RRL velocity (6.5km s^{-1}) suggests a possible EIG location.

G004.346+00.115 The H I absorption spectrum of G004.346+00.115 does not give conclusive evidence for either a near, nor far, KDAR.

G004.412+00.118 Absorption is present at velocities corresponding to the Near and Far 3kpc Arms. This suggests a location of $R_{gal} > 3$kpc on the far side of the GC; i.e. a far side KDAR.

G004.527-00.136 Absorption at Near 3kpc Arm velocities and evidence of absorption at Far 3kpc Arm velocities suggests a far KDAR.

G004.568-00.118 Absorption at velocities associated with the Near 3kpc Arm suggest $D_{los} > 5$kpc.

G005.193-00.284 Absorption at Near 3kpc and Connecting Arm velocities suggests $D_{los} >$ 7kpc; that is, the H II region must be located behind the Connecting Arm along the line of sight.

G005.479-00.241 Significant absorption is present at velocities associated with both the Near and Far 3kpc Arms, resulting in a far side KDAR.

KKL96 Compact 2 G005.524+00.033 Absorption is present at velocities associated with the Near and Far 3kpc Arms, suggesting a far side KDAR.

G005.633+00.240 The H I absorption spectrum of G005.633+00.240 does not give conclusive evidence for either a near, nor far, KDAR.

G005.889-00.427 Absorption is not seen towards any EIG features, suggesting a near side KDAR. Downes et al. (1980) also provided a near side KDAR, however, Quireza et al. (2006) give a line of sight distance of 14.5 kpc, placing the H II region on the far side of the GC.

G006.014-00.364 There are two RRL velocities reported for G006.014-00.364 (14.2 and -31.9 km s^{-1}, GBTHRDS) suggesting that there are multiple sources along the line of sight. No KDAR is given.

G006.083-00.117 Absorption at the $3\sigma_e{}^{-\tau}$ level is seen at velocities associated with the Near and Far 3kpc Arms, suggesting a far side KDAR. In addition, absorption at $\sim +135$ is present.

G006.148-00.635 The H I absorption spectrum of G006.148-00.635 does not give conclusive evidence for either a near, nor far, KDAR. However, absorption is present at velocities associated with the Near 3kpc Arm; suggestive of $D_{los} > 5$kpc.

G006.160-00.608 H I absorption is present at velocities corresponding to the Connecting Arm, but not the Near 3kpc Arm (possibly due to emission fluctuations).

G006.225-00.569 The H I absorption spectrum of G006.225-00.569 does not give conclusive evidence for either a near, nor far, KDAR. As with G006.160-00.608, absorption is seen at velocities corresponding with the Connecting Arm, but not the Near 3kpc Arm (which precedes the Connecting Arm along the line of sight).

KC97c G006.4-00.5 G006.398-00.474 Absorption is present at velocities corresponding to the Connecting Arm, but not the Near 3kpc Arm (see above).

G006.553-00.095 Perhaps the most well behaved absorption spectrum in this work; significant absorption is seen in the Near and Far 3kpc Arms as well as the Connecting Arm, strongly indicative of a far side KDAR.

G006.565-00.297 Again there is no absorption seen at velocities corresponding to the Near 3kpc Arm (see G006.160-00.60, G006.225-00.569 and G006.398-00.474 above), but in this case the lack of absorption is probably due to emission fluctuations. Absorption at velocities corresponding to the Connecting and Far 3kpc Arms suggests a far side KDAR.

G006.616-00.545 The H I absorption spectrum of G006.616-00.545 does not give conclusive evidence for either a near, nor far, KDAR.

G007.041+00.176 Significant absorption is present at velocities corresponding to the Near and Far 3kpc Arms, a far side KDAR is given.

G007.176+00.086 The H I absorption spectrum of G006.616-00.545 does not give conclusive evidence for either a near, nor far, KDAR.

G007.254-00.073 G007.254-00.073 has two known RRL velocities (47 and 17.5 km s^{-1}, GBTHRDS), suggesting multiple sources along the line of sight.

G007.266+00.186 The H I absorption spectrum of G007.266+00.186 demonstrates absorption at velocities associated with the Near 3kpc and Connecting Arms, which suggests a location $D_{los} > 7$kpc. In addition, a near zero RRL velocity (-4.4 km s^{-1}, GBTHRDS), and a lack of absorption at Far 3kpc Arm velocities suggests $R_{gal} < 3$kpc.

G007.299-00.116 The H I absorption spectrum of G007.299-00.116 does not give conclusive evidence for either a near, nor far, KDAR.

G007.420+00.366 The H I absorption spectrum of G007.420+00.366 shows absorption at velocities associated with the Near and Far 3kpc Arms,as a result the H II region is given a far side KDAR.

G007.466-00.279 Absorption is present at velocities associated with the Near 3kpc Arm, but no further evidence for a KDAR is forthcoming from the H I absorption spectrum.

G007.472+00.060 Significant absorption at velocities corresponding to both the Near and Far 3kpc Arms strongly suggests a far side KDAR, however the RRL velocity (-17.8km s^{-1}, Lockman (1989)) is indicative of a location in the Near 3kpc Arm. The H II region also presents significant absorption at $\sim$ +135km s^{-1} (see G006.083-00.117, above).

G007.700-00.079 The H II region has two observed RRL velocities, one of which is associated with the velocity expected of the Connecting Arm. No KDAR is given.

G007.768+00.014 The H I absorption spectrum of G007.768+0.014 does not give conclusive evidence for either a near, nor far, KDAR.

G007.806-00.621 Evidence of absorption at velocities corresponding to the Near 3kpc Arm, Connecting Arm implies a distance along the line of sight as least as far as the Connecting Arm.

G008.005-00.484 Absorption is present at velocities consistent with the Near 3kpc and Connecting Arms, but with no other EIG features. The lower line of sight distance limit is therefore $D_{los} > 7$kpc.

G008.006-00.156 Evidence of absorption at velocities corresponding to the Near 3kpc Arm, Connecting Arm and Far 3kpc Arm strongly implies a far side KDAR.

G008.094+00.085 The H I absorption spectrum of G008.094+00.085 does not give conclusive evidence for either a near, nor far, KDAR.

G008.103+00.340 The H I absorption spectrum of G008.103+00.340 does not give conclusive evidence for either a near, nor far, KDAR. However absorption is present at velocities corresponding to the Near 3kpc Arm.

G008.137+00.228 Absorption is not seen towards any EIG features, suggesting a near side KDAR in agreement with Wink et al. (1982) and Quireza et al. (2006).

G008.362-00.303 The H I absorption spectrum of G008.362-00.303 does not give conclusive evidence for either a near, nor far, KDAR. However absorption is present at velocities corresponding to the Near 3kpc Arm.

G008.373-00.352 Absorption is present at velocities consistent with the Near 3kpc and Connecting Arms, but with no other EIG features.

G008.432-00.276 Evidence of absorption due to both the Near and Far 3kpc Arms suggests a far side KDAR

G008.666-00.351 Green et al. (2011) and Downes et al. (1980) both give a near side KDAR for the H II region. A near side KDAR is also given by this work - note that at this longitude the expected velocity range of the Near 3kpc Arm overlaps the expected velocities of general circular rotation.

G008.830-00.715 Absorption is not seen towards any EIG features, suggesting a near side KDAR.

G008.865-00.323 The H I absorption spectrum of G008.362-00.303 does not give conclusive evidence for either a near, nor far, KDAR.

G009.178+00.043 There H I absorption spectrum suffers from emission fluctuations, the H II region must be located at least as far as the Near 3kpc Arm along the line of sight.

G009.615+00.198 Kinematic distance analyses can be greatly affected by velocity crowding and a decrease of cold, dense H I in the EIG. For example, Sanna et al. (2009) thoroughly investigated the high mass star formation region G9.62+0.20 - comprised of several H II regions - and find from trigonometric parallax that it has a distance of 5.2 ± 0.6 kpc, placing it in the 3 kpc Arm. This distance is at odds with the kinematically determined distances for the region (0.36 and 16.4 kpc, based on the systemic velocity of the region, 4.1 km s^{-1}). Inspection of the H I absorption spectrum of G009.615+00.198 rules out the far kinematic distance as there is no significant absorption at the velocities of far side EIG features (i.e. the Far 3kpc Arm).

G009.925-00.745, G009.682+00.206, G009.717-00.832, G009.741+00.842, G009.875-00.749 and G009.982-00.752 At this longitude the velocities associated with the Near 3kpc Arm and normal circular rotation overlap. No KDARs are given.

B.4 Discussion of Individual H II Regions, $22° < l < 28°$

The following appeared as a Section in the published version of Chapter 3. In order to conserve the Galactic longitude order throughout Appendix B, only the sources $l > 0°$ are discussed here, the other sources ($l < 360°$) can be found in Section B.2.

G23.245-0.240, V_{RRL}=76.1 km/s, V_T=124.5 km/s, KDA Assignment = Near Side Near side assignments are provided by this work as well as both methods employed by Anderson & Bania (2009). However, Sewilo et al. (2004) give the far kinematic distance as the location of this H II region, as they find a H_2CO cloud along the line of sight at a distance of

10.5 kpc; as this cloud must be between the H II region and the observer, Sewilo et al. (2004) assume that the region is located at the far kinematic distance.

G23.420-0.205, V_{RRL}=101.1 km/s, V_T=124.0 km/s, KDA Assignment = Tangent Point The VGPS continuum map about this location is very crowded; two continuum sources appear centred on G23.435-0.21 and G23.42-0.22 with diffuse emission between them. The near side assignment is preferred by the E/A analysis of Anderson & Bania (2009) and by Kolpak et al. (2003). However the far kinematic location is given by C88 and by the HISA analysis of Anderson & Bania (2009). Reid et al. (2009) provide a distance from parallax measurements of 5.88 kpc - at the near kinematic distance.

G24.460+0.245, V_{RRL}=98.5 km/s, V_T=121.0 km/s, KDA Assignment = Tangent Point The continuum map shows a crowded field with at least three extended sources in the region of G24.46+0.245. While Anderson & Bania (2009) assign the H II region to the near kinematic distance, this work assigns the 'tangent point' distance by default.

G24.470+0.495, V_{RRL}=99.8 km/s , V_T=121.0 km/s, KDA Assignment = Tangent Point Kolpak et al. (2003) discuss the differences in KDARs for this H II region that probably arise from the use of various rotation curves. Wilson (1980) who uses the Schmidt (1965) Galactic rotation model, places the region at the tangent point, as do Paladini et al. (2004) and this work; Kolpak et al. (2003) find in favour of the far kinematic distance. Anderson & Bania (2009) find in favour of the near distance through both E/A and HISA analysis.

G24.740-0.205, V_{RRL} = Multiple Component, KDA Assignment = N/A The VGPS continuum map displays a faint extended source in a generally bright crowded field. Lockman (1989) observed three velocity components, but reported two radio recombination line velocities. The non-reported RRL velocity is associated with a nearby nebula (G24.677-0.160). Kantharia et al. (2007) give a kinematic distance of 6 kpc, however no KDAR is achived by this work as the source displays a multiple component RRL velocity profile.

G25.290+0.310, V_{RRL}=39.6 km/s, V_T=118.6 km/s, KDA Assignment = Near Side This diffuse H II region is designated to the near kinematic distance by this work and Paladini et al. (2004). However, Anderson & Bania (2009)'s HISA analysis determines that the H II region is at the far kinematic distance (but with a poor confidence parameter). Anderson & Bania (2009) were unable to achieve a KDAR using the E/A method for this region.

W42; G25.385-0.175, V_{RRL}=59.1 km/s, V_T=118.4 km/s, KDA Assignment = Near Side This giant H II region has been extensively studied in the literature. This star forming region is the location of a giant molecular cloud and several red supergiant stars. The source is also studied in Kolpak et al. (2003) and Wilson (1972). Kolpak et al. (2003) discuss the difference between this source and G25.397-0.141; initially thought to be parts of the same H II region. The distinct sources were separated through their 21cm absorption spectra; the absorption spectrum of G25.397-0.141 exhibits absorption to 100km/s whereas G25.385-0.175 displays absorption to a maximum velocity of 67km/s. Wilson (1972) designates the far

kinematic distance to the H II region on the basis of OH and H_2CO data, however reference is made to the near assignment of Radhakrishnan et al. (1972) on the basis that H I absorption is seen to only 66 km/s. Anderson & Bania (2009)'s HISA analysis is also in favour of the far distance but they chose to adopt the near kinematic distance gained from their E/A analysis. Kolpak et al. (2003) place the source at the near side of the tangent point - reasoning that no absorption occurs within at least 25 km/s of the tangent point velocity. The spectrum extracted from the VGPS for this study has an extremely low $\sigma_{e^{-\tau}}$ and agrees with the near kinematic distance determination of Anderson & Bania (2009), Kolpak et al. (2003) and Radhakrishnan et al. (1972).

B.4.1 Sources beyond the Solar Circle

The following sources all display significant H I absorption at velocities corresponding to distances beyond the Solar Circle. All of these objects would benefit from observations aimed at RRL velocity measurement in order to ascertain their location. While the sources in the outer Galaxy seem to align themselves with spiral structure (based on a flat rotation model beyond the Solar circle, see Figure 3.8), it is possible that the absorption lines at these velocities are products of cool H I clouds in the Solar neighbourhood with anomalous velocities.

G24.130+1.030, Last V_{Abs}=-38 km/s The mid-infrared and radio sources are spatially slightly offset. Significant H I absorption is seen to -38km/s.

G24.540+0.600, Last V_{Abs}=-40 km/s Absorption is seen at -40km/s; the radio and mid-infrared sources are slightly offset.

G24.905+0.420 and G25.395+0.560 These sources display significant H I absorption at velocities corresponding to the outer Galaxy. However, both have known (multiple) RRL velocities that would place each source inside the Solar Circle. G25.395+0.56 has RRL velocities of +12 and +41 km/s (GBTHRDS). Co-spatial radio and mid-infrared sources exist (see Figure 3.9), however the radio source is quite weak (resulting in very low signal to noise in absorption) and exhibits extended morphology. G24.905+0.42 has RRL velocities of +43.8 and +104.6 km/s (Lockman et al. 1996). The radio continuum emission is confused and diffuse mid-infrared emission exists throughout the area. The negative velocity neutral hydrogen absorption, combined with a lack of mid-infrared source co-located with the radio source seems to suggest that this object is extragalactic, however, the presence of measured RRL velocities is unsettling.

G25.245-0.145 and G25.265-0.160 The location of a young red supergiant cluster RSGC1, and supernova remnant W33, this region has been extensively studied in the literature. The two radio sources share diffuse continuum emission and while there is 22μm emission nearby it is not necessarily associated with either object, see Figure 3.9. Xu et al. (2006) class G25.265-0.160 as 'most likely an extragalactic object', however, of the two sources G25.265-0.16 has the best mid-infrared association, and is therefore the more likely of the two to be Galactic.

The 8μm Spitzer GLIMPSE images for the region display numerous point sources that suffer severe ghosting, this region is an especially strong candidate for RRL observations.

G25.395+0.030, V_{RRL}=-14.4 km/s This H II region has a known negative RRL velocity and therefore can be unambiguously placed in the outer Galaxy. Unusually, the 22μm emission shows two blended sources, see Figure 3.9.

G26.610-0.210, V_{RRL}=103.9, 69.9, -35.7 km/s The GBTHRDS reports three RRL velocities for this H II region, one of which is negative (also the RRL with the highest line temperature) . Absorption is seen to -39 km/s. The line of sight distance in Figure 3.7 and Table 3.1 is based on this RRL velocity.

G27.375+1.170, Last V_{Abs}=-40 km/s As the radio and 22μm emission are not completely co-spatial, there is no definitive evidence to place this object in either the outer Galaxy, or as an extragalactic object. Absorption by cool H I is seen to about -40km/s.

B.4.2 Northern Extragalactic sources

The following continuum sources do not exhibit co-spatial mid-infrared and radio continuum components and are therefore likely to be extragalactic: G22.685-0.670, G22.935-0.075 (Xu et al. (2006)), G24.180+0.565, G25.205-0.84., G25.815-0.380 and G26.240-0.080.

Appendix C

H I Emission & Absorption Spectra

In this Appendix we present the H I absorption spectra for the H II regions investigated in Chapters 3, 4 and 5. The spectra have been ordered such that the H II regions are sequential in longitude, from $l \approx 30^\circ$ in §C.1 through the Galactic centre to $l \approx 255^\circ$ in §C.3.

C.1 Emission/Absorption Spectrum Pairs from Chaper 3

Absorption spectra for each first quadrant H II region from Chapter 3. The terminal velocity, as determined by the rotation curve of McClure-Griffiths & Dickey (2007) is shown as the vertical red line. Below each panel the H II region name, continuum temperature and RMS noise in the spectrum's baseline is displayed. Fourth quadrant regions are included later in the Appendix, such that the fourth quadrant catalog appears complete, and in longitude order.

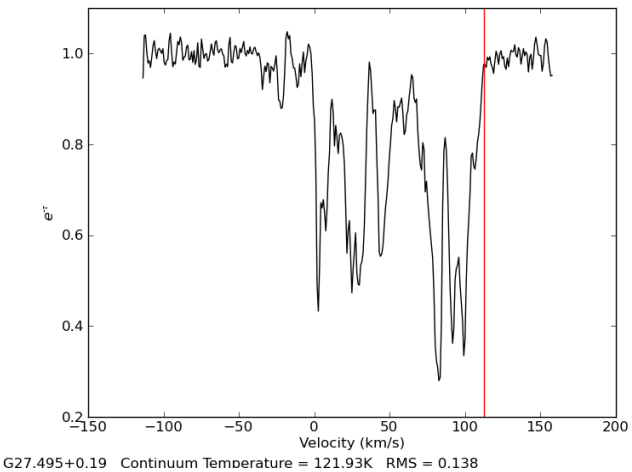

G27.495+0.19 Continuum Temperature = 121.93K RMS = 0.138

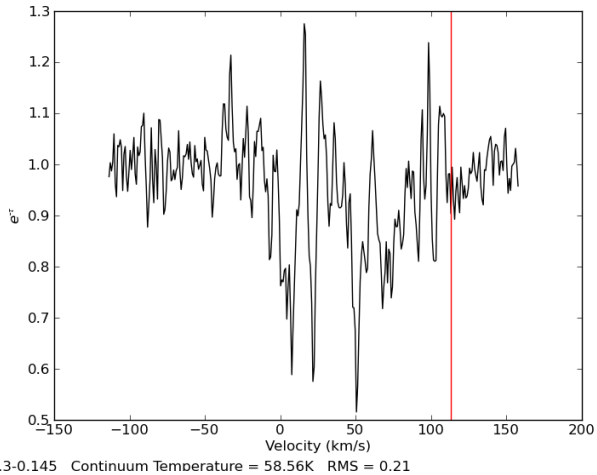

G27.3-0.145 Continuum Temperature = 58.56K RMS = 0.21

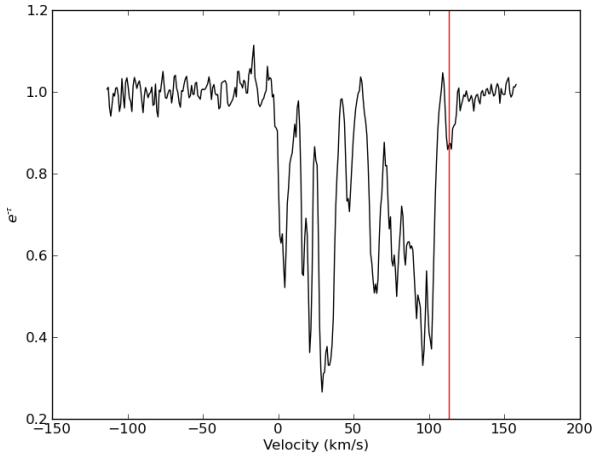

G27.28+0.145 Continuum Temperature = 112.28K RMS = 0.149

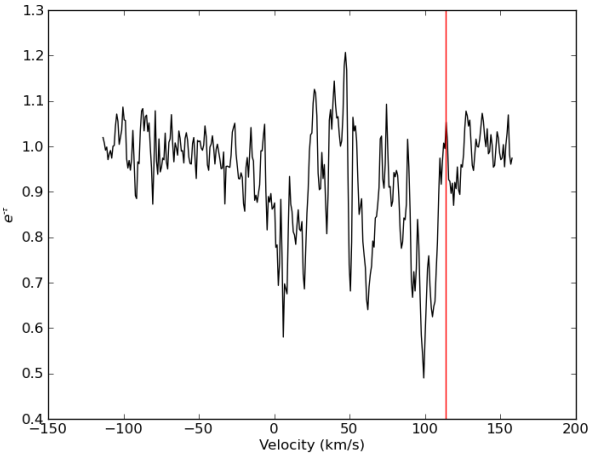

G26.98-0.07 Continuum Temperature = 56.83K RMS = 0.209

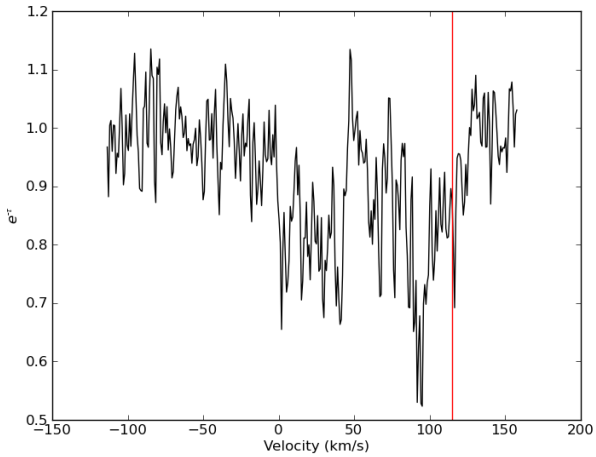

G26.72+0.17 Continuum Temperature = 41.67K RMS = 0.244

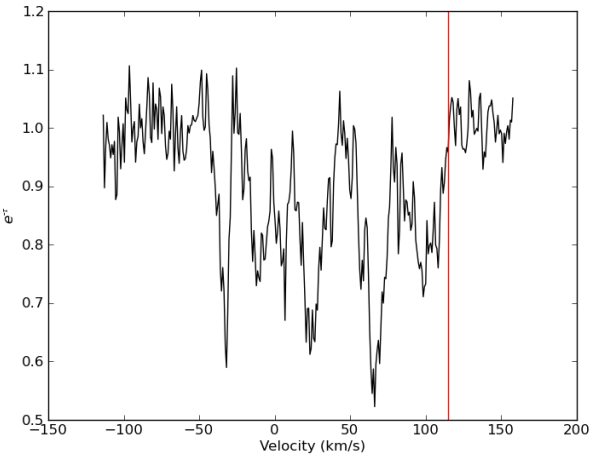

G26.61-0.21 Continuum Temperature = 54.3K RMS = 0.199

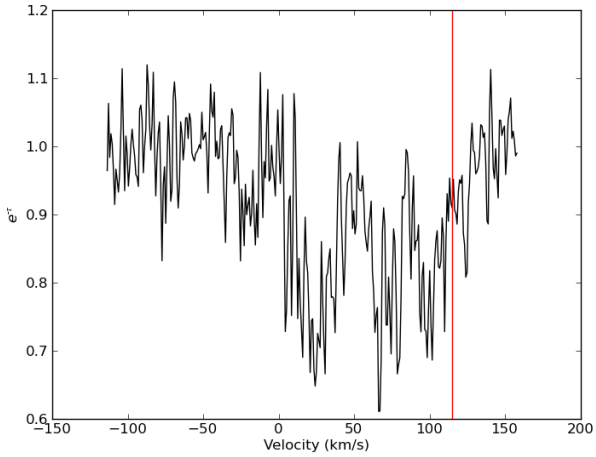

G26.595-0.025 Continuum Temperature = 41.13K RMS = 0.231

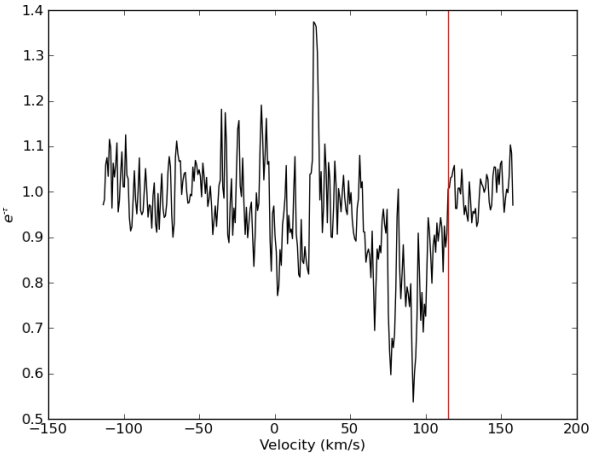

G26.59+0.095 Continuum Temperature = 42.03K RMS = 0.225

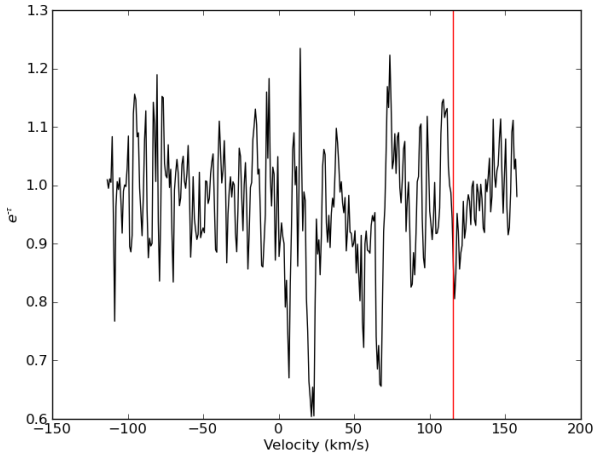

G26.555-0.305 Continuum Temperature = 42.74K RMS = 0.277

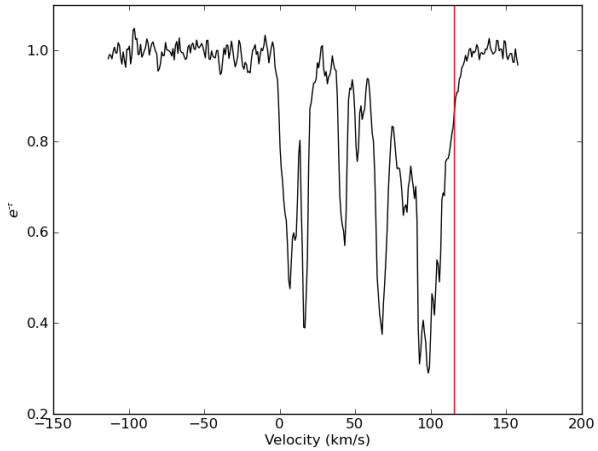

G26.54+0.415 Continuum Temperature = 152.15K RMS = 0.13

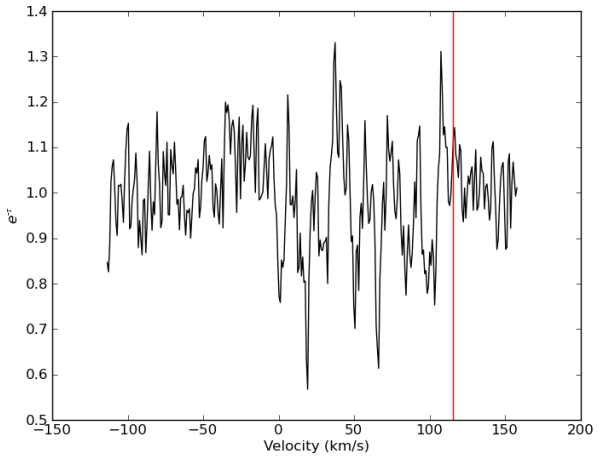

G26.47+0.02 Continuum Temperature = 39.92K RMS = 0.266

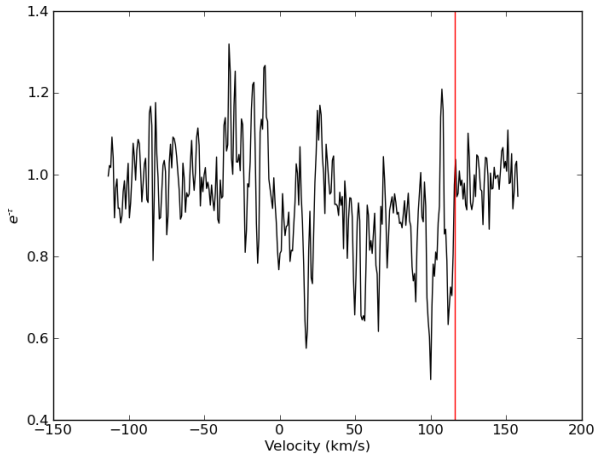

G26.33-0.07 Continuum Temperature = 39.04K RMS = 0.267

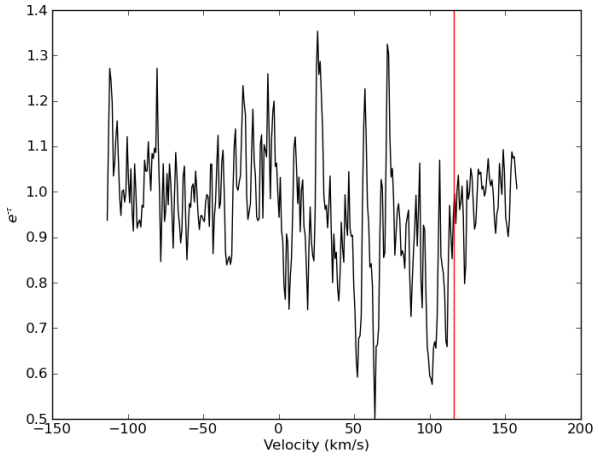

G26.315-0.01 Continuum Temperature = 37.46K RMS = 0.259

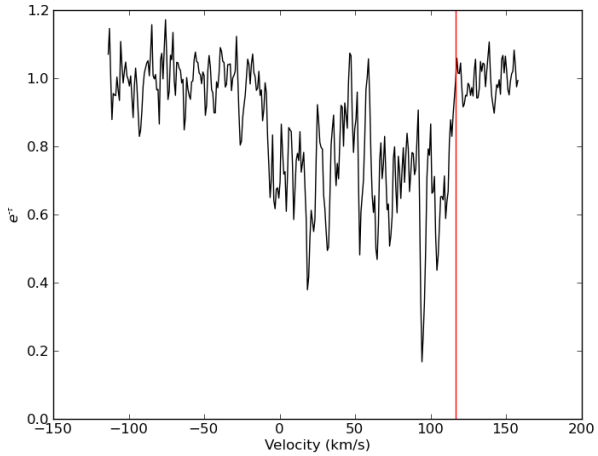

G26.12-0.09 Continuum Temperature = 50.23K RMS = 0.252

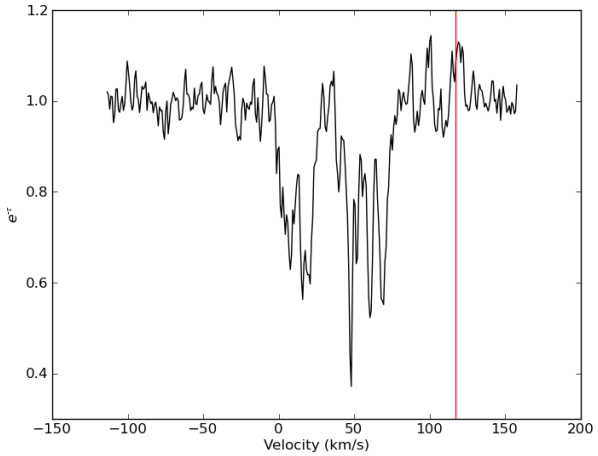

G25.815+0.24 Continuum Temperature = 95.79K RMS = 0.173

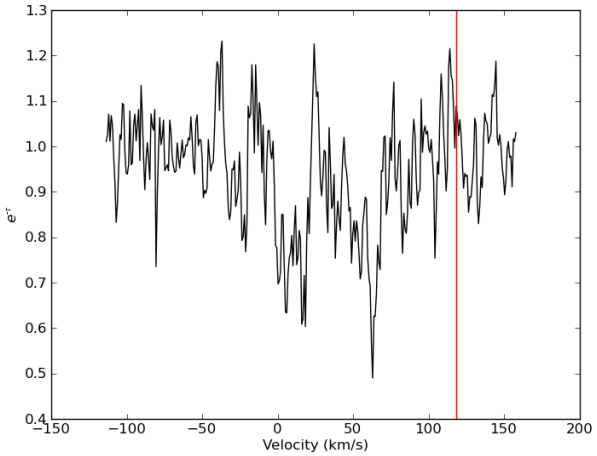

G25.47-0.12 Continuum Temperature = 41.91K RMS = 0.263

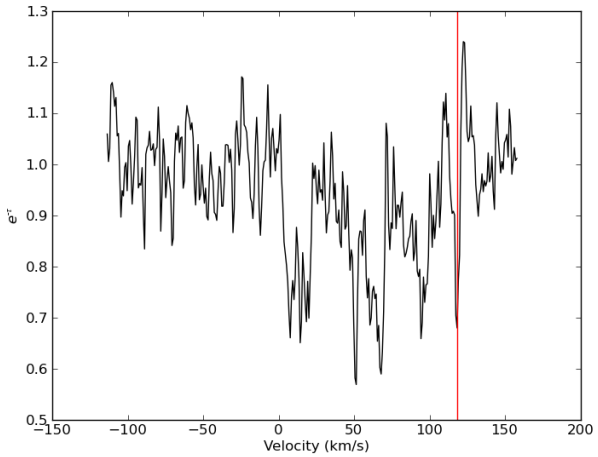

G25.46-0.215 Continuum Temperature = 45.28K RMS = 0.251

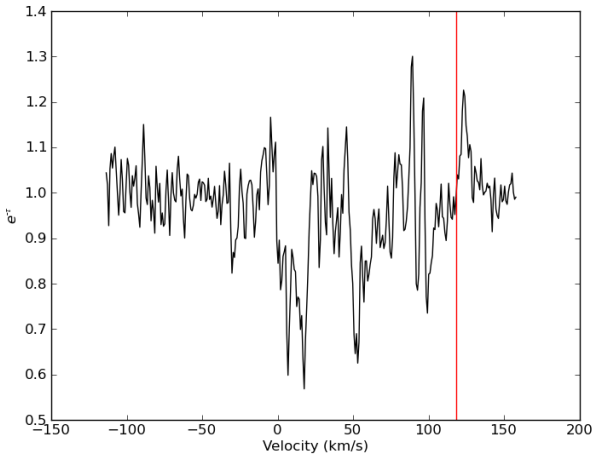

G25.4-0.255 Continuum Temperature = 60.84K RMS = 0.211

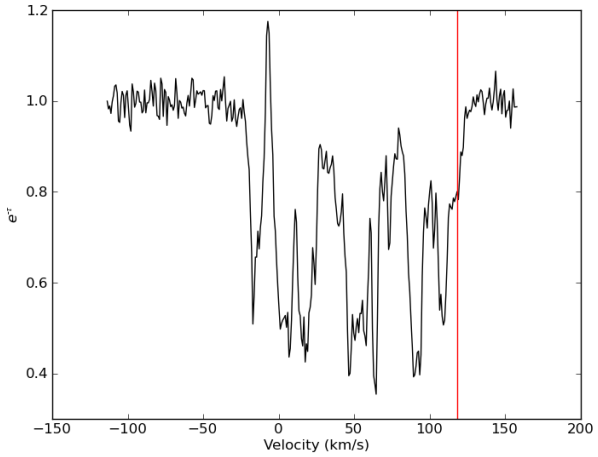

G25.395+0.03 Continuum Temperature = 100.57K RMS = 0.162

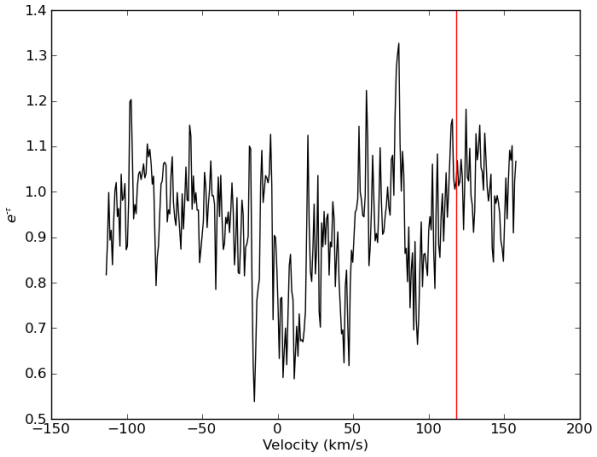

G25.395+0.56 Continuum Temperature = 32.41K RMS = 0.282

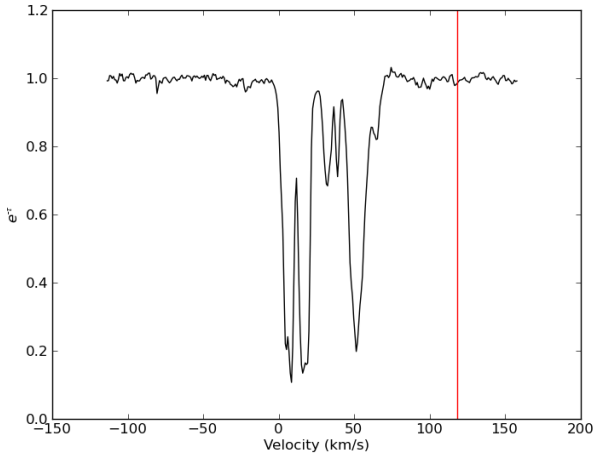

G25.385-0.175 Continuum Temperature = 475.35K RMS = 0.098

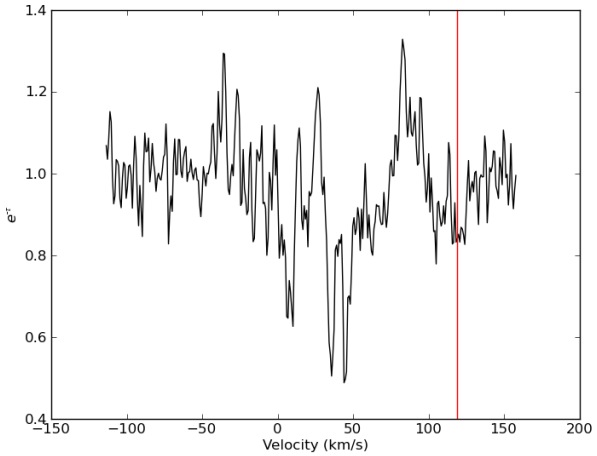

G25.29+0.31 Continuum Temperature = 48.55K RMS = 0.242

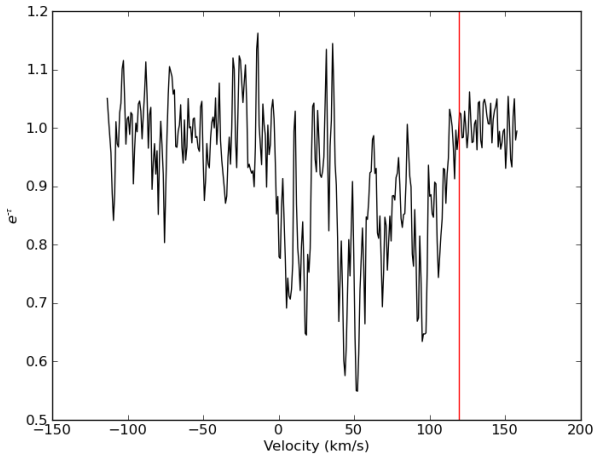

G25.16+0.06 Continuum Temperature = 51.14K RMS = 0.233

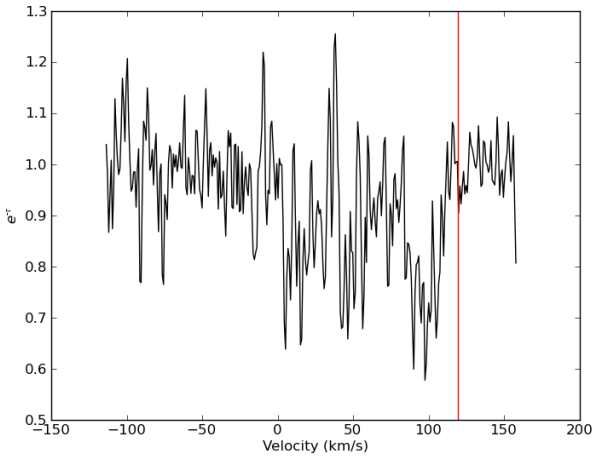

G25.15+0.09 Continuum Temperature = 46.97K RMS = 0.277

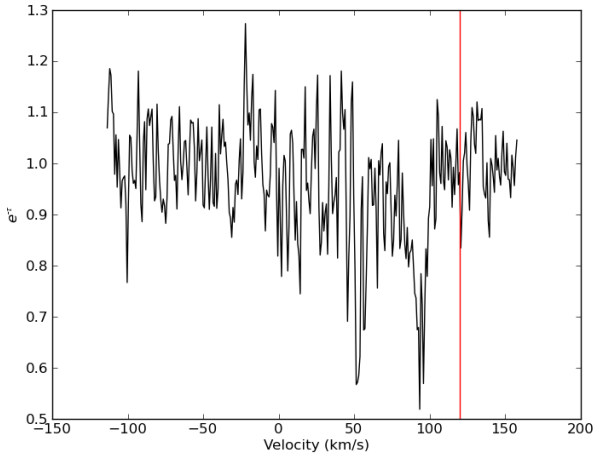

G24.955-0.055 Continuum Temperature = 32.29K RMS = 0.267

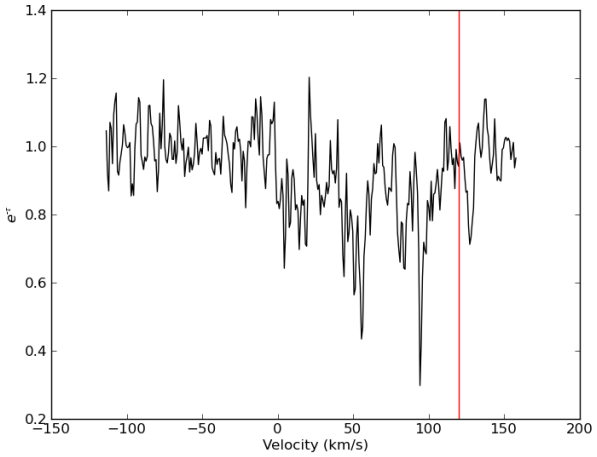

G24.925+0.075 Continuum Temperature = 43.77K RMS = 0.259

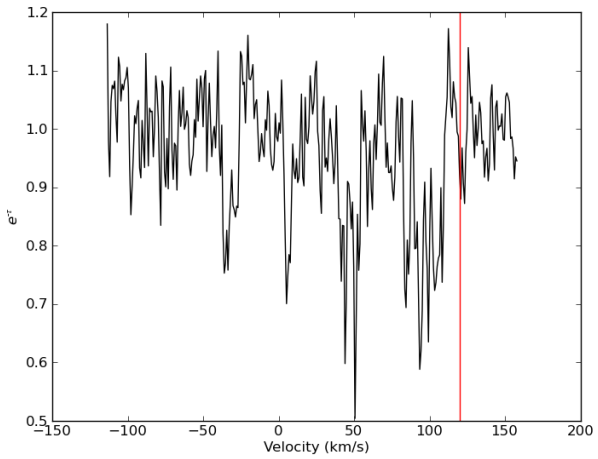

G24.905+0.42 Continuum Temperature = 37.83K RMS = 0.246

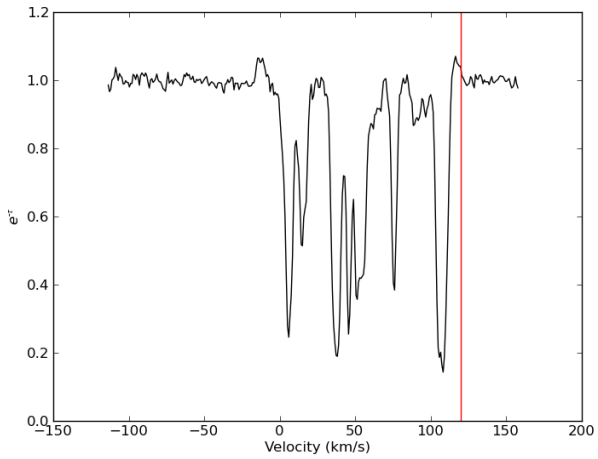

G24.8+0.1 Continuum Temperature = 212.57K RMS = 0.109

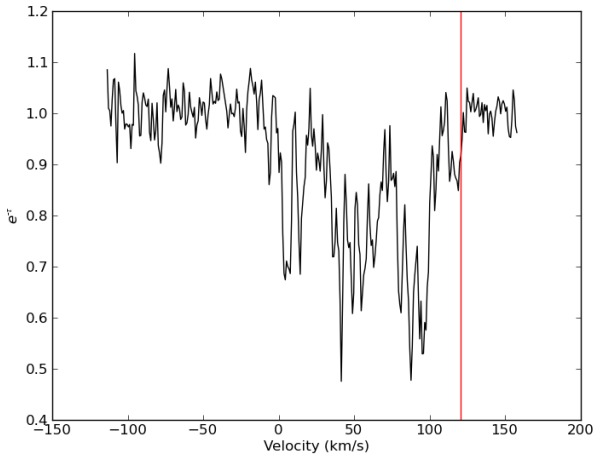

G24.74-0.205 Continuum Temperature = 73.55K RMS = 0.187

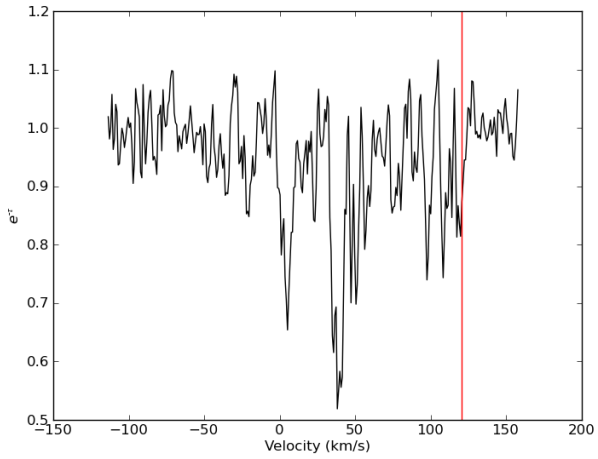

G24.74+0.08 Continuum Temperature = 66.36K RMS = 0.195

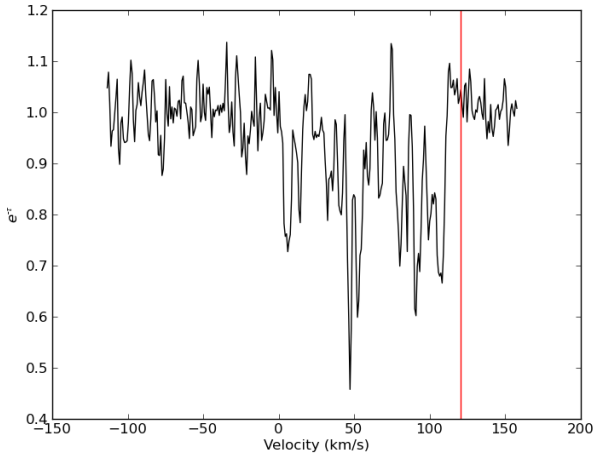

G24.715-0.13 Continuum Temperature = 73.78K RMS = 0.212

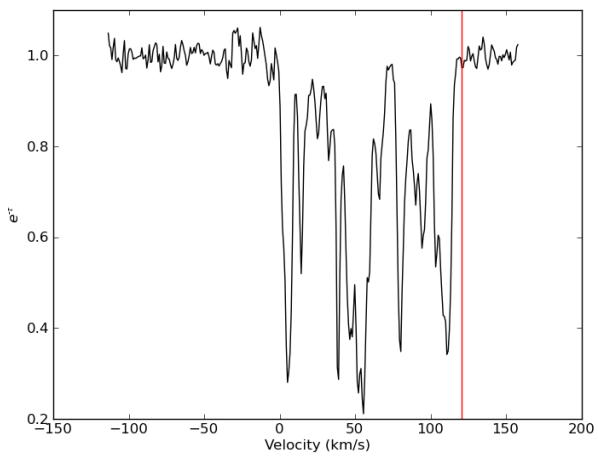

G24.68-0.16 Continuum Temperature = 179.12K RMS = 0.132

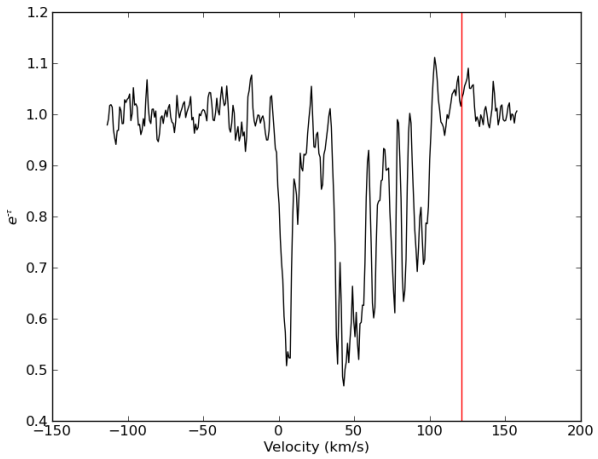

G24.51-0.225 Continuum Temperature = 125.38K RMS = 0.152

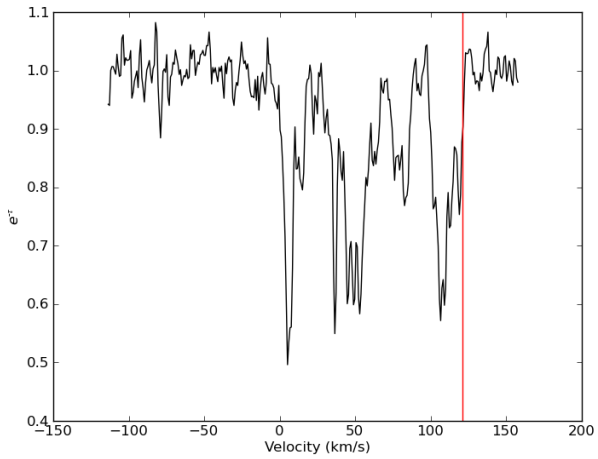

G24.5-0.035 Continuum Temperature = 93.02K RMS = 0.177

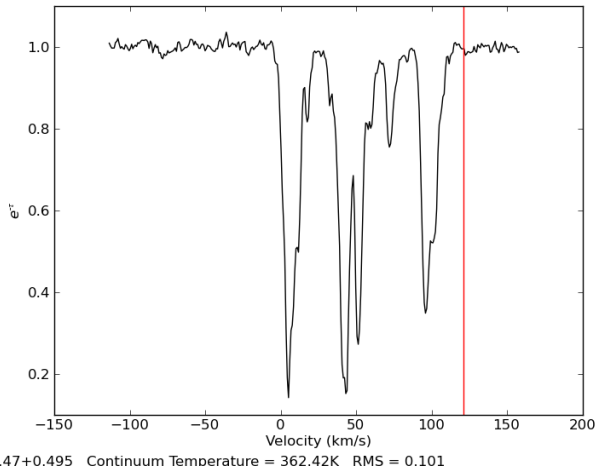

G24.47+0.495 Continuum Temperature = 362.42K RMS = 0.101

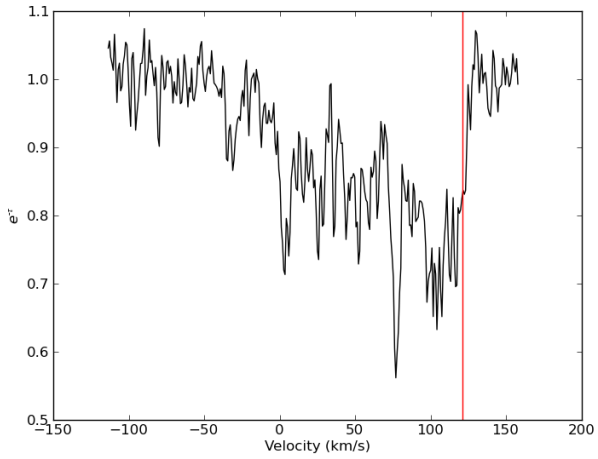

G24.46+0.245 Continuum Temperature = 85.32K RMS = 0.181

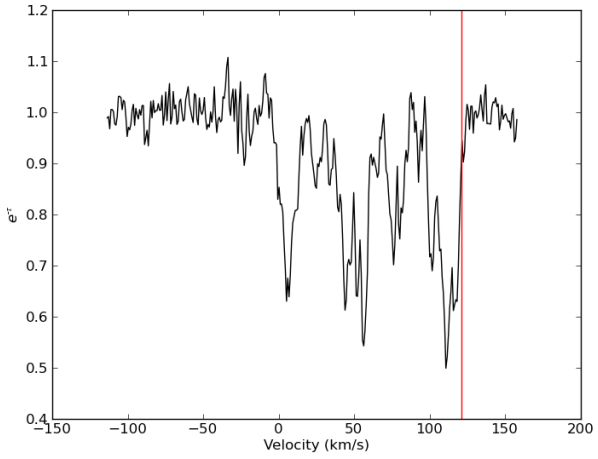

G24.4+0.07 Continuum Temperature = 89.95K RMS = 0.157

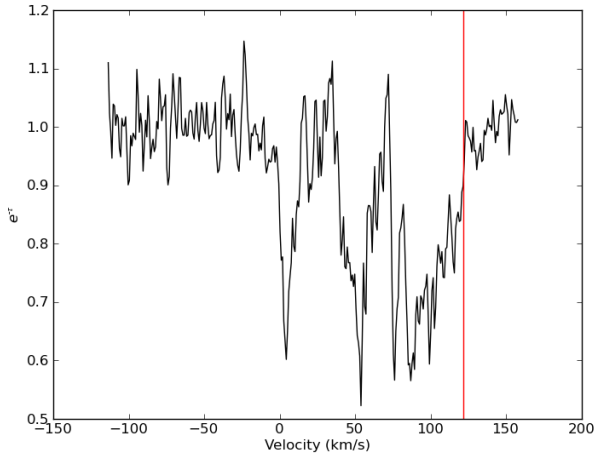

G24.215-0.045 Continuum Temperature = 72.16K RMS = 0.204

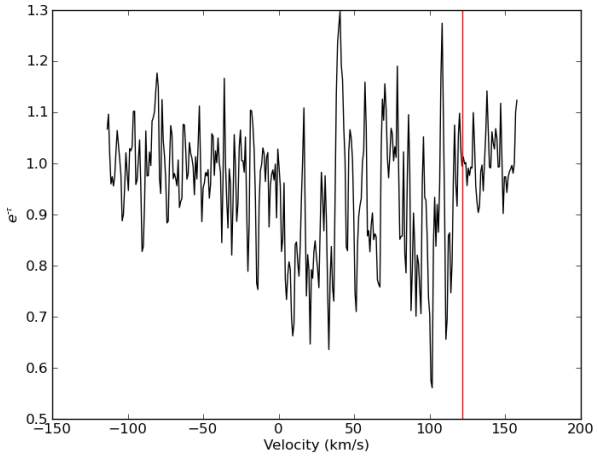

G24.2+0.245 Continuum Temperature = 37.69K RMS = 0.261

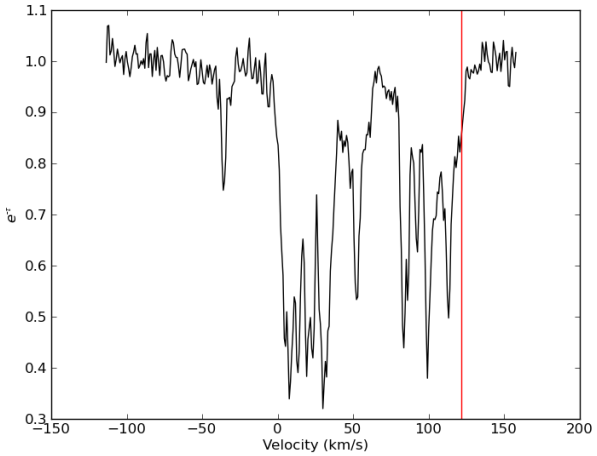

G24.18+0.565 Continuum Temperature = 90.7K RMS = 0.149

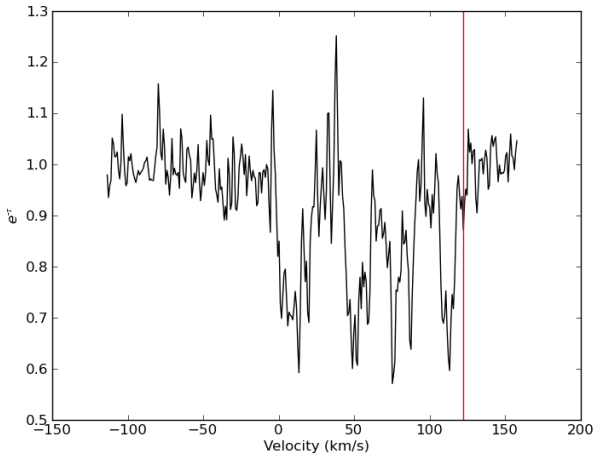

G24.135+0.12 Continuum Temperature = 55.51K RMS = 0.198

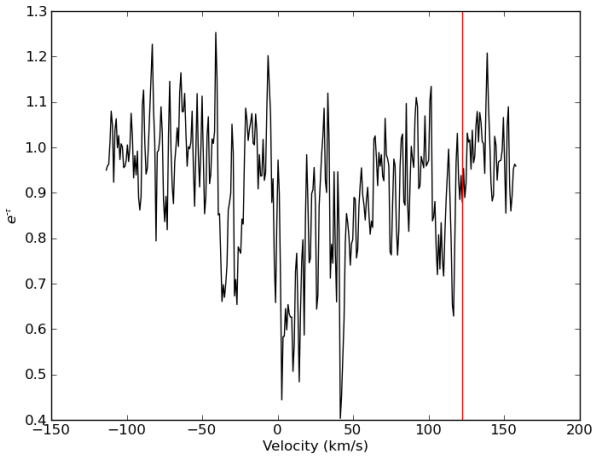

G24.13+1.03 Continuum Temperature = 28.59K RMS = 0.292

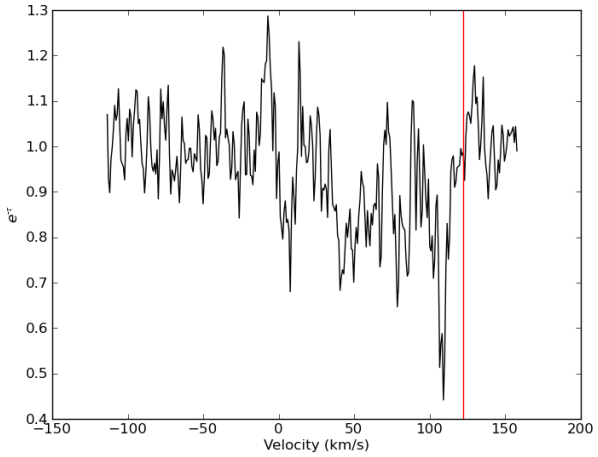

G24.125-0.07 Continuum Temperature = 43.42K RMS = 0.25

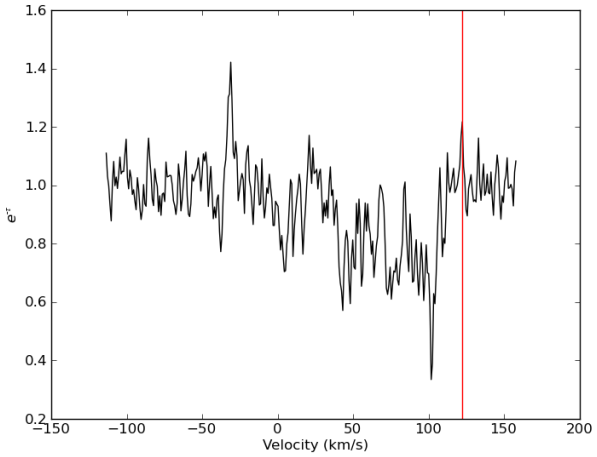

G23.995-0.1 Continuum Temperature = 38.67K RMS = 0.255

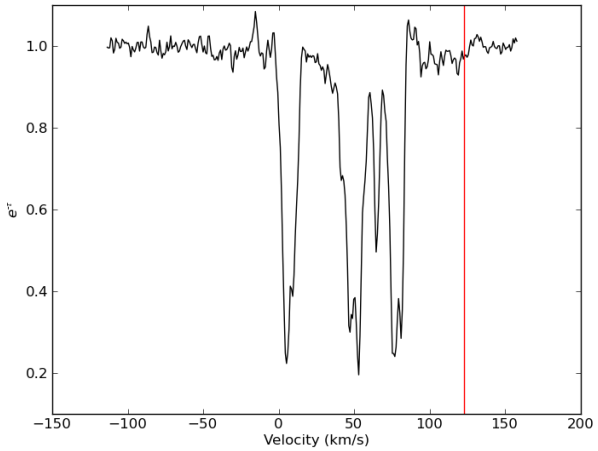

G23.96+0.155 Continuum Temperature = 188.0K RMS = 0.115

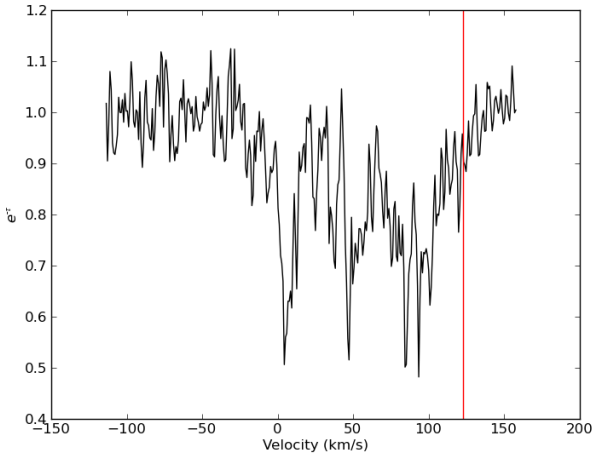

G23.905+0.065 Continuum Temperature = 55.17K RMS = 0.219

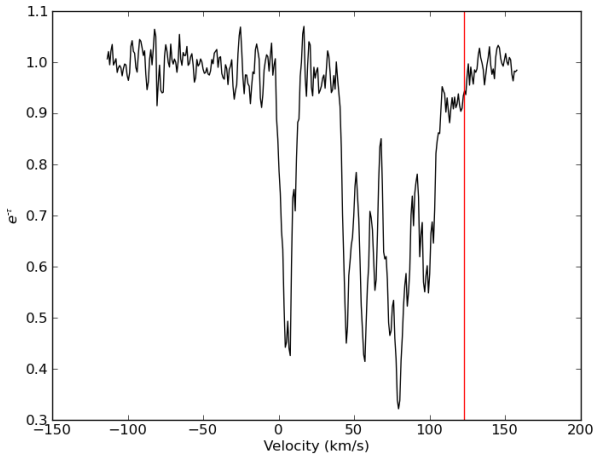

G23.875-0.12 Continuum Temperature = 118.6K RMS = 0.164

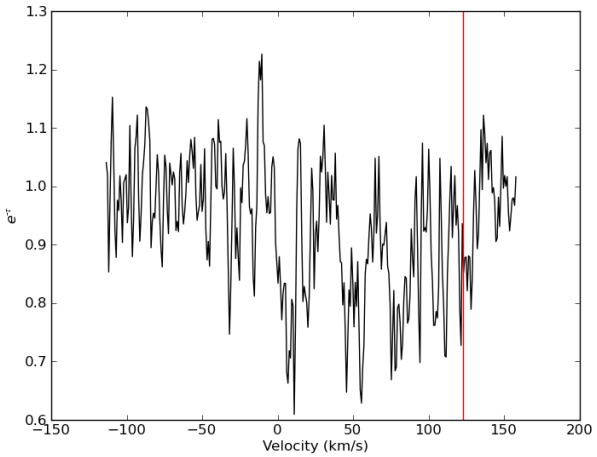

G23.835+0.1 Continuum Temperature = 42.86K RMS = 0.253

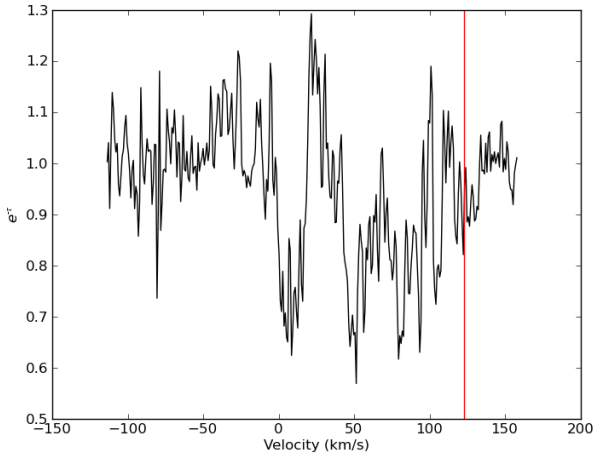

G23.82+0.22 Continuum Temperature = 47.54K RMS = 0.252

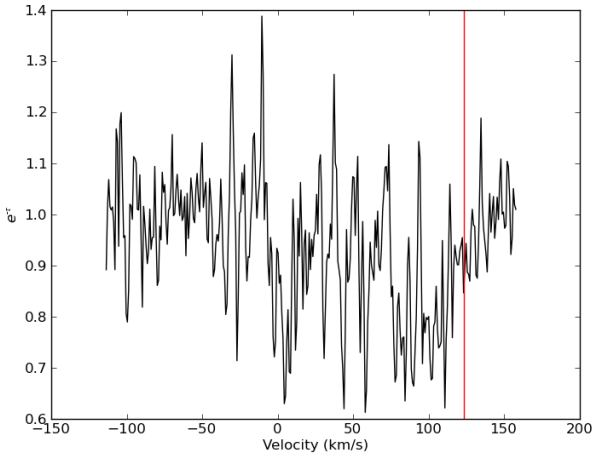

G23.735-0.025 Continuum Temperature = 32.53K RMS = 0.28

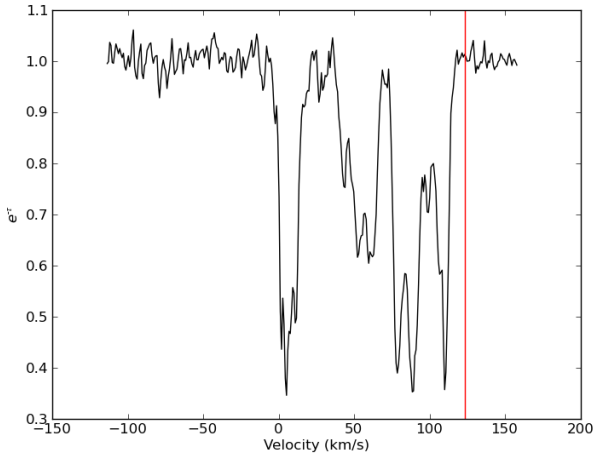

G23.71+0.175 Continuum Temperature = 151.87K RMS = 0.146

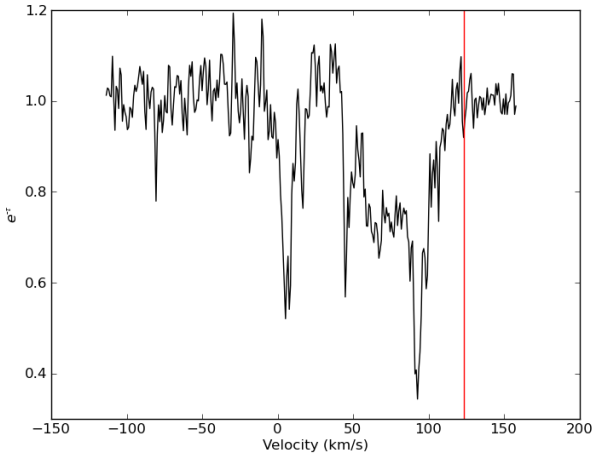

G23.705-0.2 Continuum Temperature = 54.59K RMS = 0.212

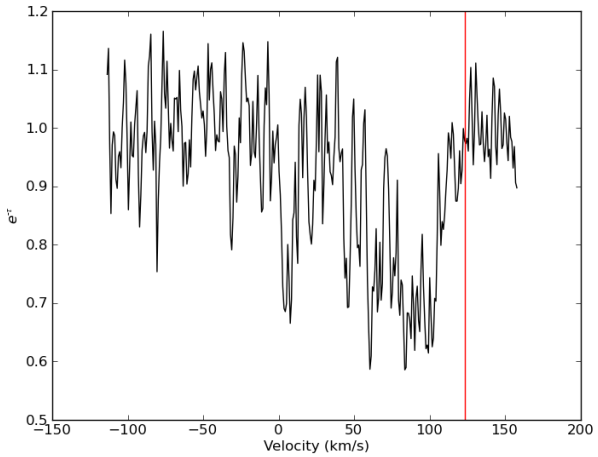

G23.665-0.255 Continuum Temperature = 42.07K RMS = 0.266

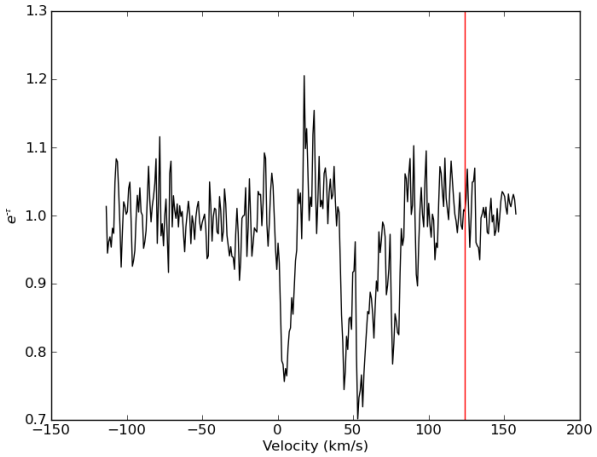

G23.55-0.04 Continuum Temperature = 74.41K RMS = 0.189

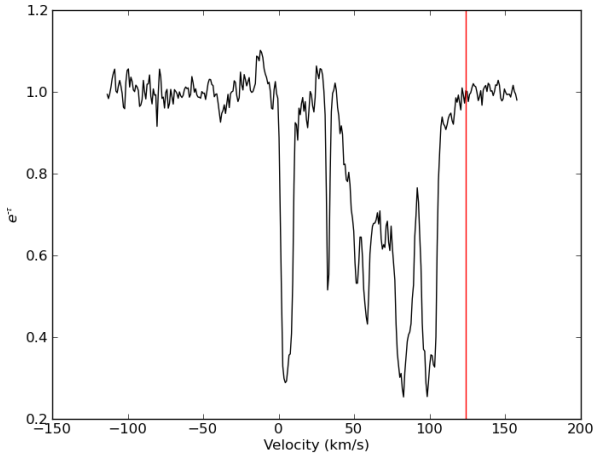

G23.42-0.205 Continuum Temperature = 153.93K RMS = 0.15

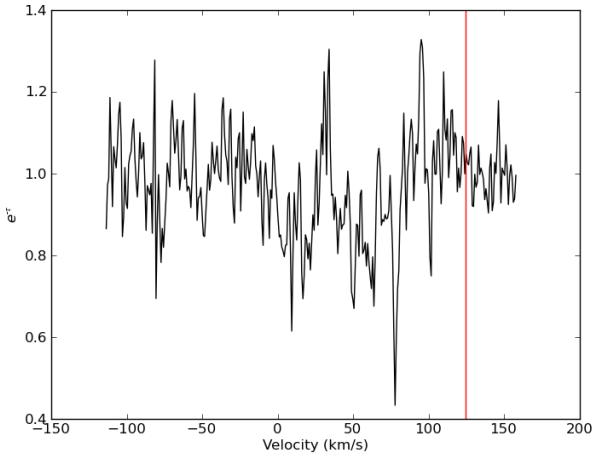

G23.265+0.075 Continuum Temperature = 35.27K RMS = 0.306

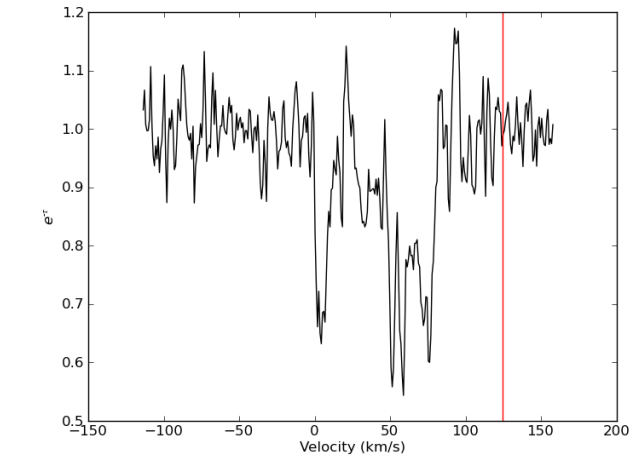

G23.245-0.24 Continuum Temperature = 79.66K RMS = 0.216

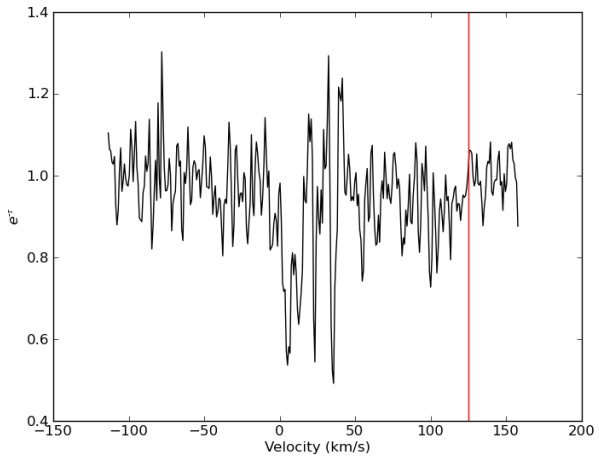

G23.115+0.55 Continuum Temperature = 41.43K RMS = 0.272

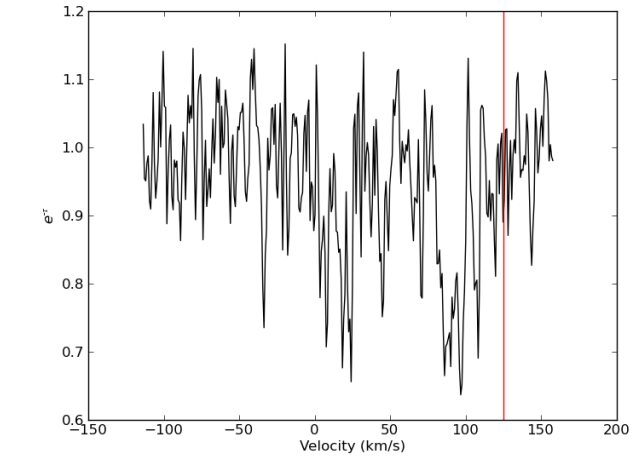

G23.09+0.22 Continuum Temperature = 34.35K RMS = 0.263

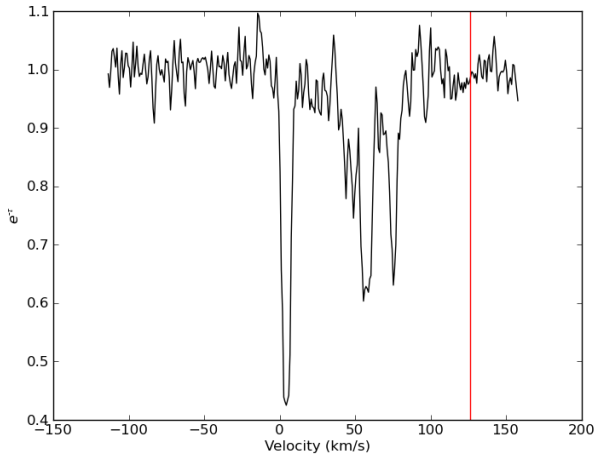

G22.755-0.48 Continuum Temperature = 114.64K RMS = 0.161

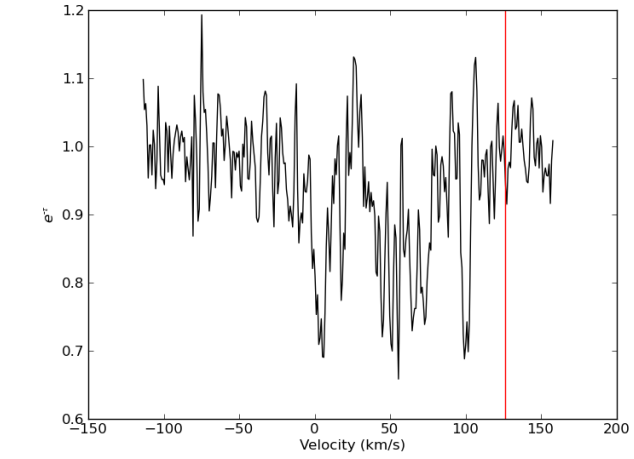

G22.755-0.245 Continuum Temperature = 70.65K RMS = 0.222

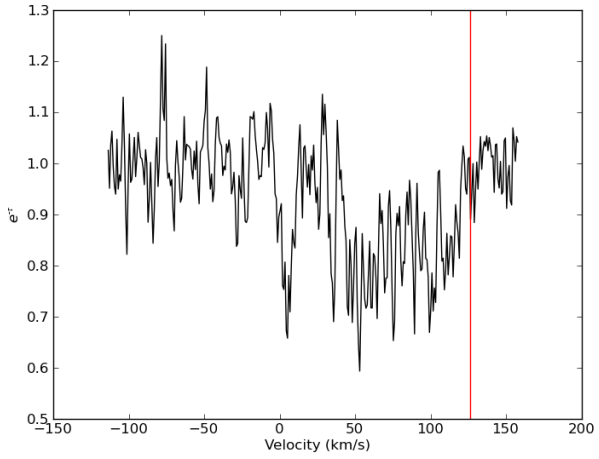

G22.725-0.01 Continuum Temperature = 45.37K RMS = 0.26

C.2 Emission/Absorption Spectrum Pairs from Chapter 4

The following appeared as a Figure Set in the the published version of Chapter 4.

In each figure, the top panel shows the emission spectra. The emission is shown by the solid line (this is the average of the three 'off' positions) and the emission envelope (difference between the 'off' positions) is shown in grey. Absorption, $e^{-\tau}$, is displayed in the bottom

panel. The H I absorption spectrum is shown by the solid line and the grey envelope signifies $3\sigma_{e^{-\tau}}$ (calculated from the emission envelope). The absorption panel also displays the RRL velocities of the H II region (solid vertical lines) and the fluctuation in the baseline of the absorption spectrum ($3\sigma_{rms_{e^{-\tau}}}$) (horizontal dotted lines). The H II region name, RRL velocity and reference are shown as well as the expected velocity ranges of EIG features with the same color system as Figure 4.1.

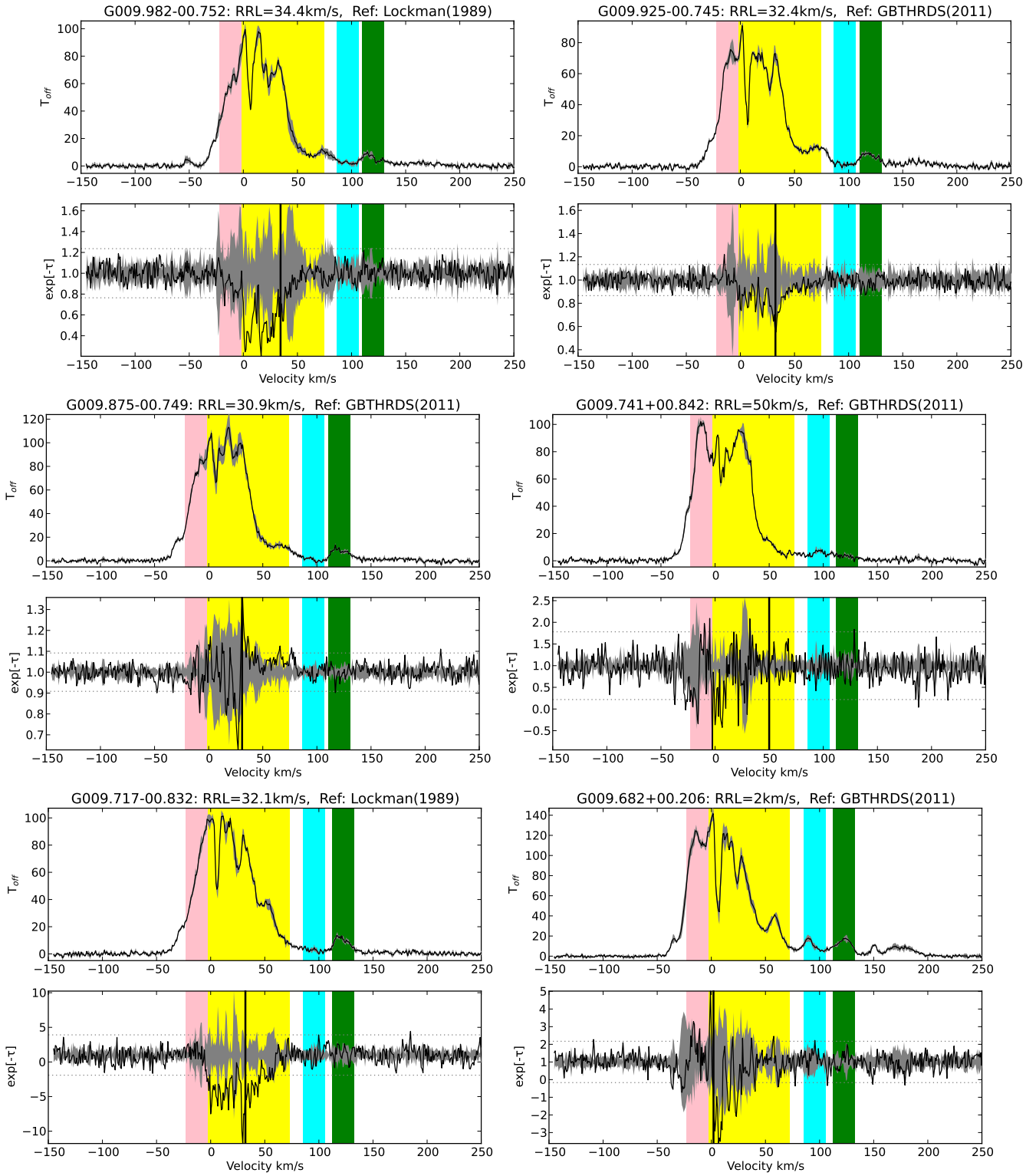

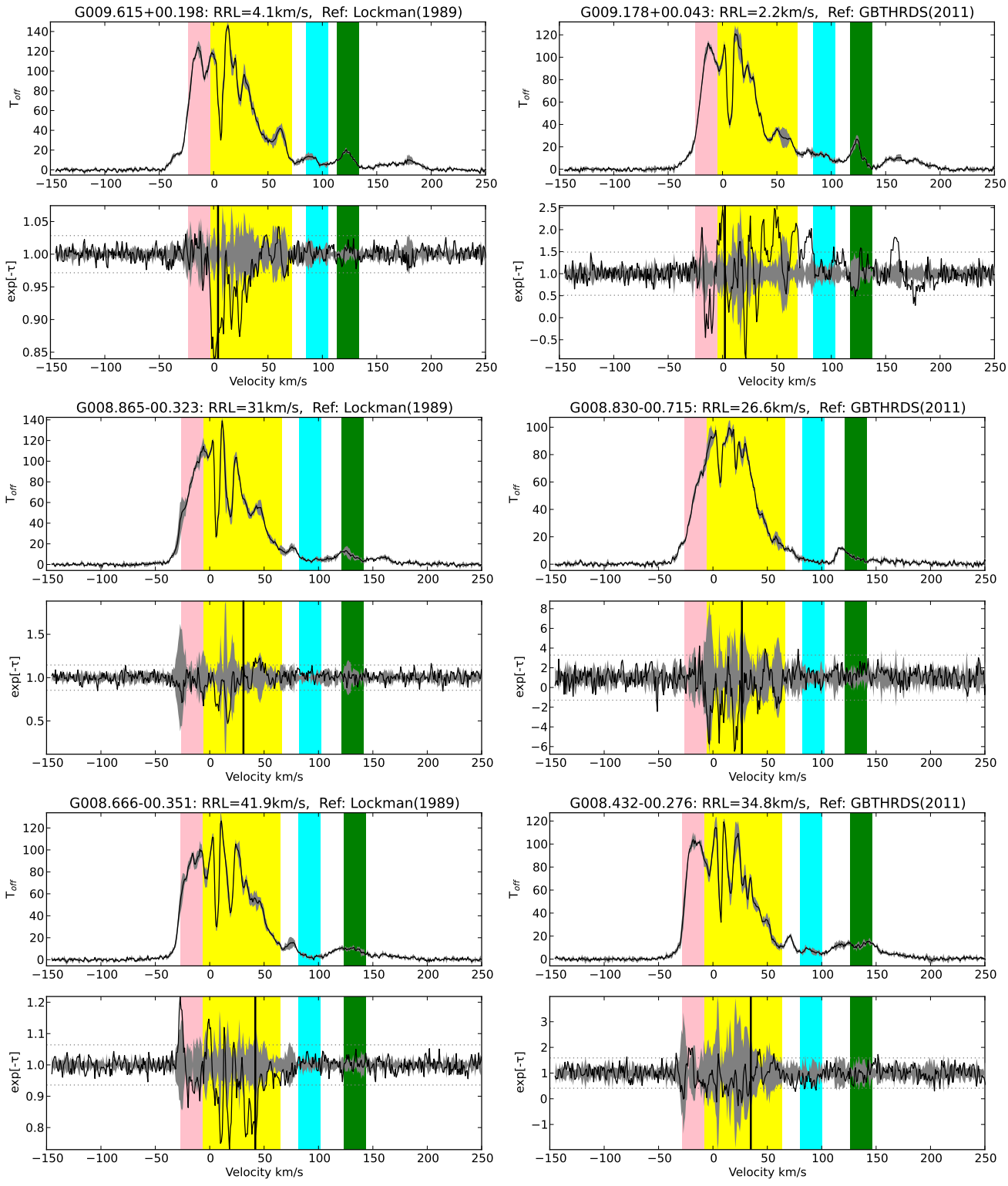
G009.615+00.198: RRL=4.1km/s, Ref: Lockman(1989)
G009.178+00.043: RRL=2.2km/s, Ref: GBTHRDS(2011)
G008.865-00.323: RRL=31km/s, Ref: Lockman(1989)
G008.830-00.715: RRL=26.6km/s, Ref: GBTHRDS(2011)
G008.666-00.351: RRL=41.9km/s, Ref: Lockman(1989)
G008.432-00.276: RRL=34.8km/s, Ref: GBTHRDS(2011)
T_off
exp[-τ]
Velocity km/s

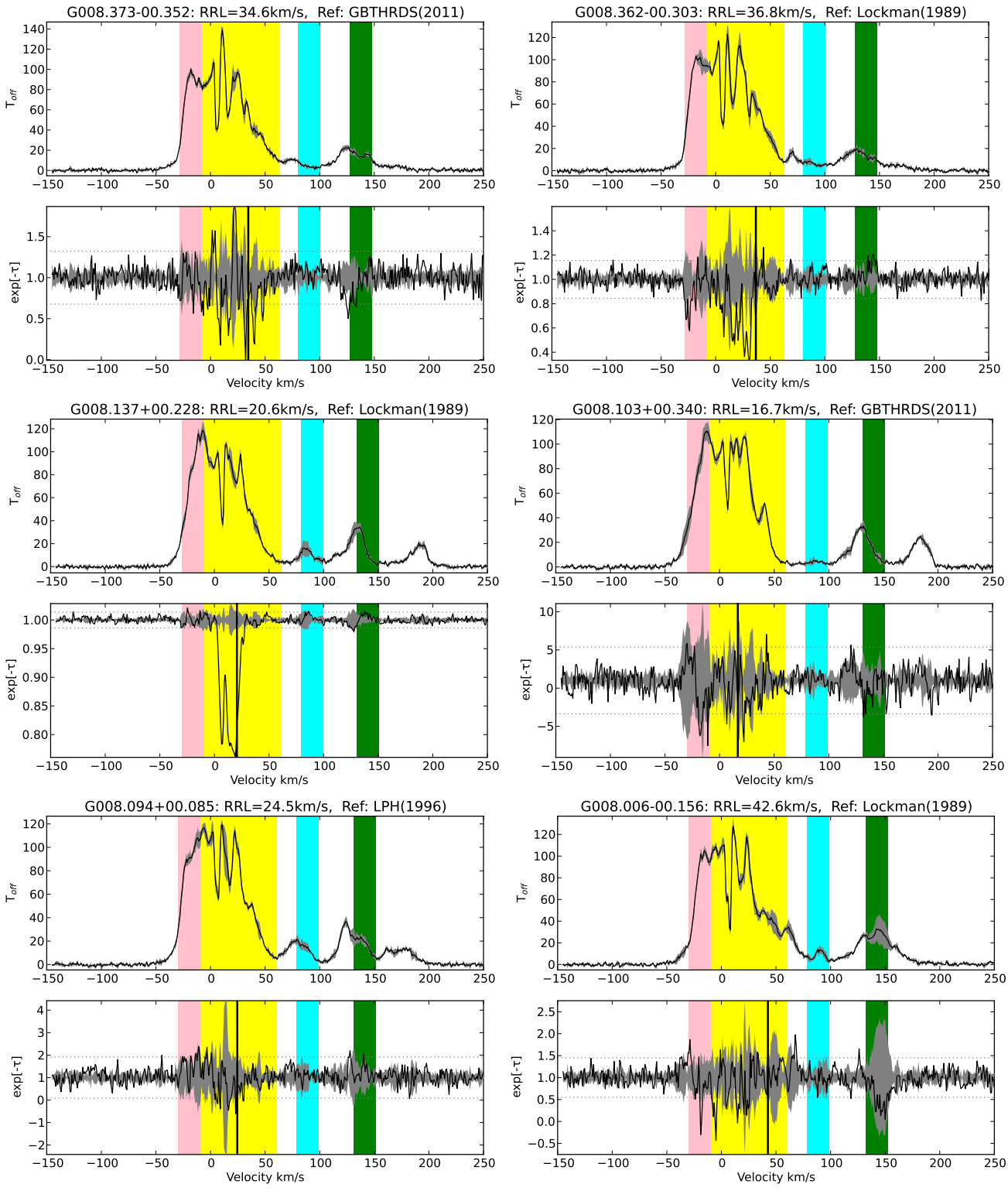
G008.373-00.352: RRL=34.6km/s, Ref: GBTHRDS(2011)
G008.362-00.303: RRL=36.8km/s, Ref: Lockman(1989)
G008.137+00.228: RRL=20.6km/s, Ref: Lockman(1989)
G008.103+00.340: RRL=16.7km/s, Ref: GBTHRDS(2011)
G008.094+00.085: RRL=24.5km/s, Ref: LPH(1996)
G008.006-00.156: RRL=42.6km/s, Ref: Lockman(1989)
T_off
exp[-τ]
Velocity km/s

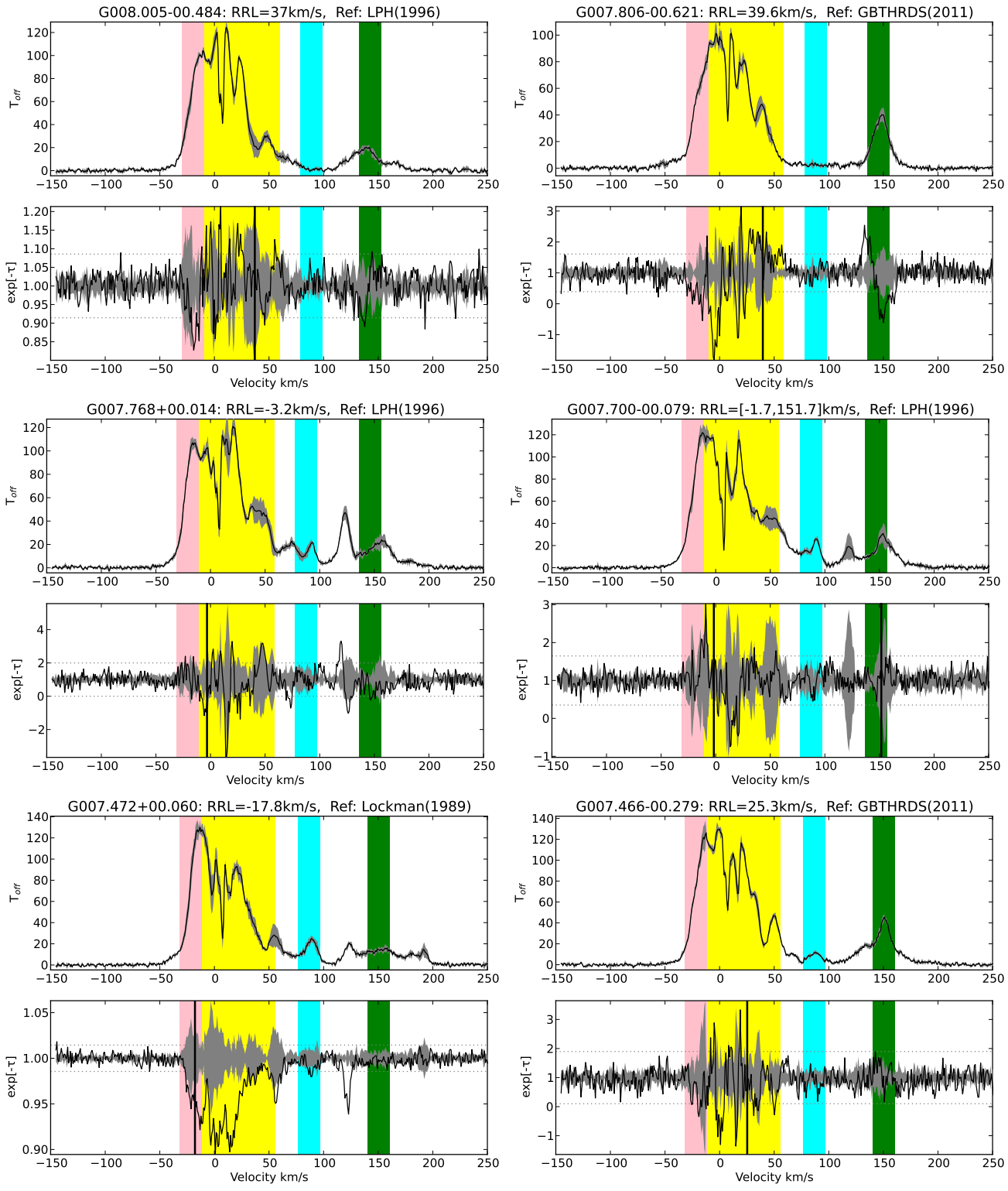
G008.005-00.484: RRL=37km/s, Ref: LPH(1996)
G007.806-00.621: RRL=39.6km/s, Ref: GBTHRDS(2011)
G007.768+00.014: RRL=-3.2km/s, Ref: LPH(1996)
G007.700-00.079: RRL=[-1.7,151.7]km/s, Ref: LPH(1996)
G007.472+00.060: RRL=-17.8km/s, Ref: Lockman(1989)
G007.466-00.279: RRL=25.3km/s, Ref: GBTHRDS(2011)
T_off
exp[-τ]
Velocity km/s

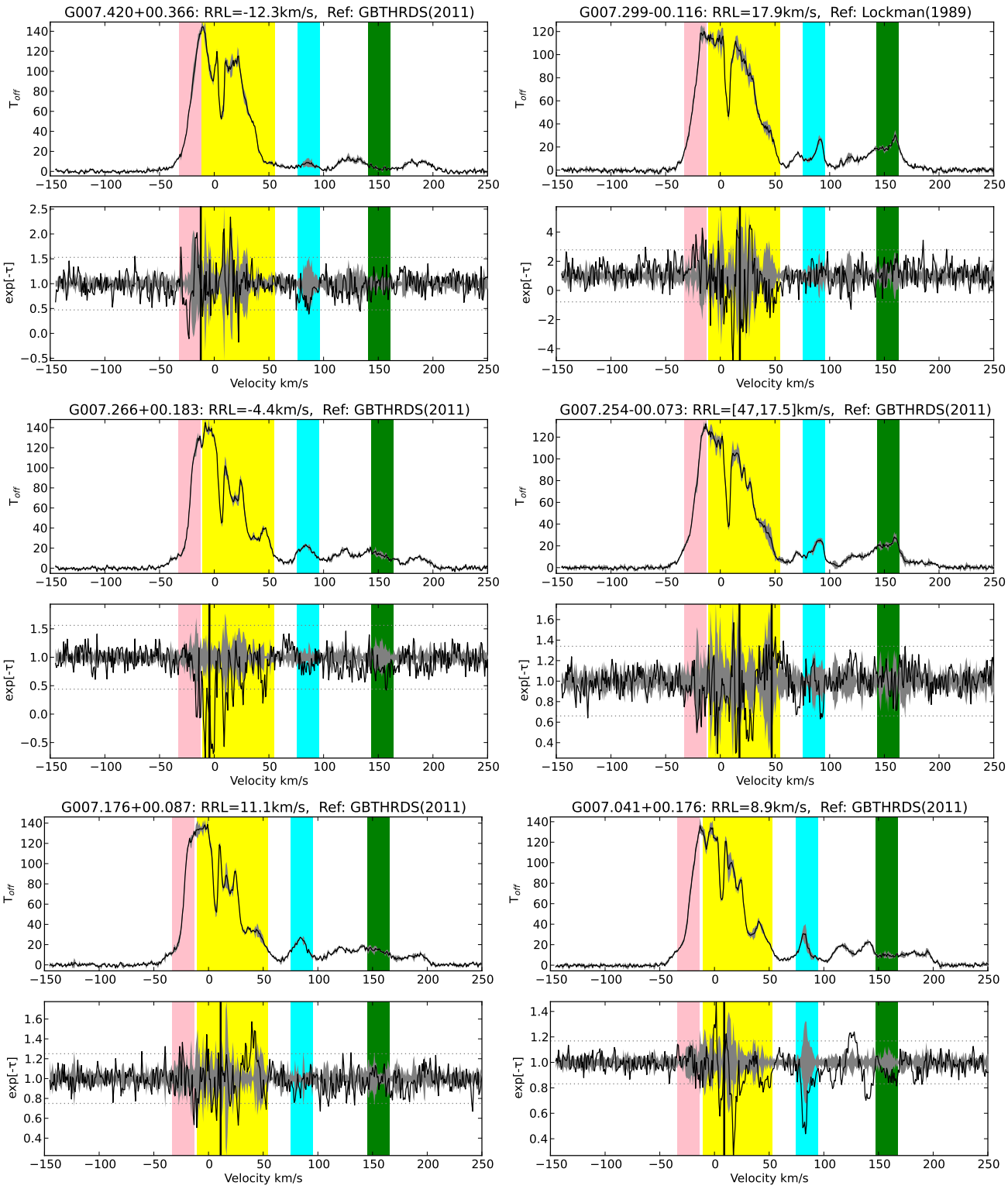
G007.420+00.366: RRL=-12.3km/s, Ref: GBTHRDS(2011)
G007.299-00.116: RRL=17.9km/s, Ref: Lockman(1989)
G007.266+00.183: RRL=-4.4km/s, Ref: GBTHRDS(2011)
G007.254-00.073: RRL=[47,17.5]km/s, Ref: GBTHRDS(2011)
G007.176+00.087: RRL=11.1km/s, Ref: GBTHRDS(2011)
G007.041+00.176: RRL=8.9km/s, Ref: GBTHRDS(2011)
T_off
exp[-τ]
Velocity km/s

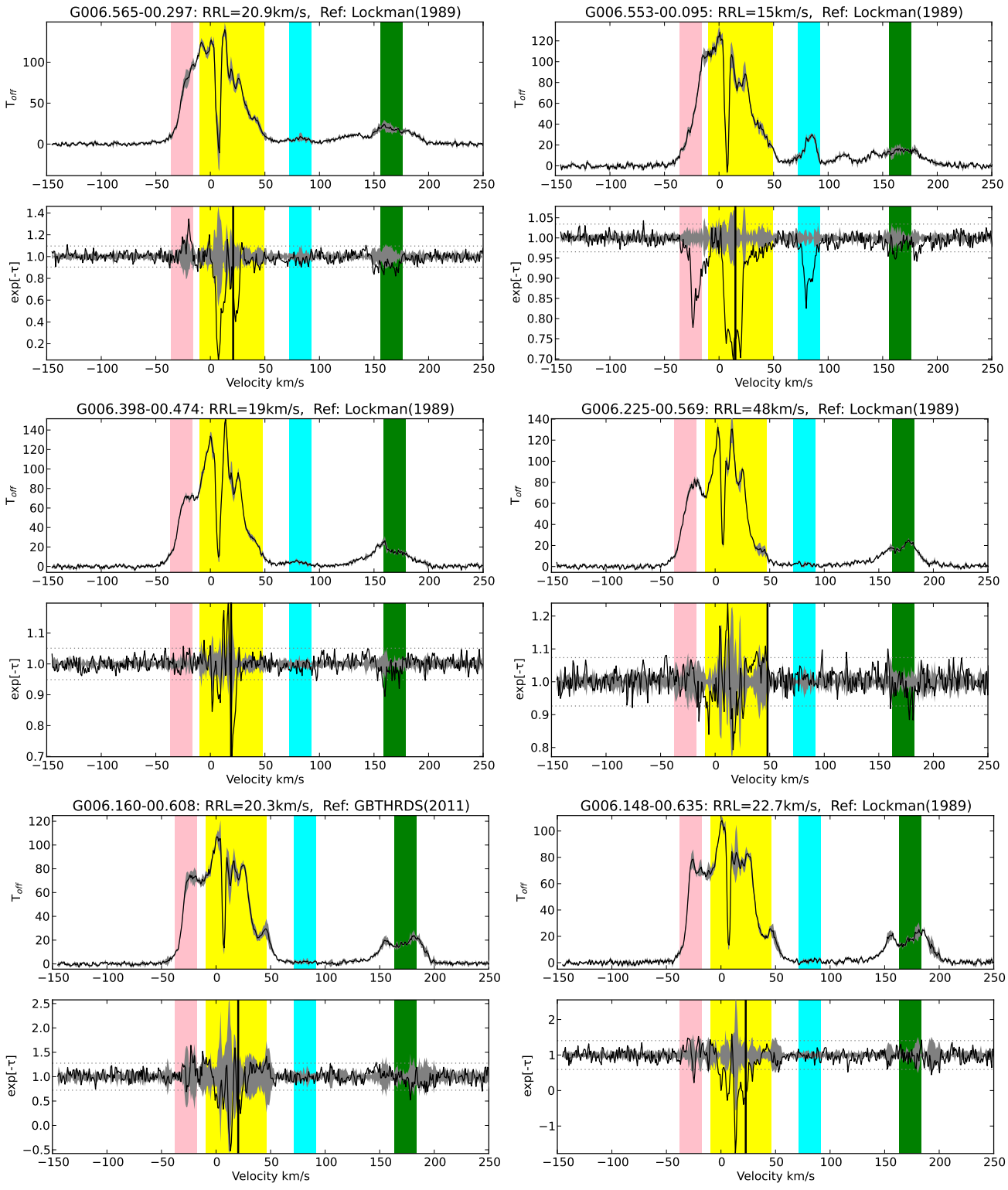
G006.565-00.297: RRL=20.9km/s, Ref: Lockman(1989)
G006.553-00.095: RRL=15km/s, Ref: Lockman(1989)
G006.398-00.474: RRL=19km/s, Ref: Lockman(1989)
G006.225-00.569: RRL=48km/s, Ref: Lockman(1989)
G006.160-00.608: RRL=20.3km/s, Ref: GBTHRDS(2011)
G006.148-00.635: RRL=22.7km/s, Ref: Lockman(1989)
T_off
exp[-τ]
Velocity km/s

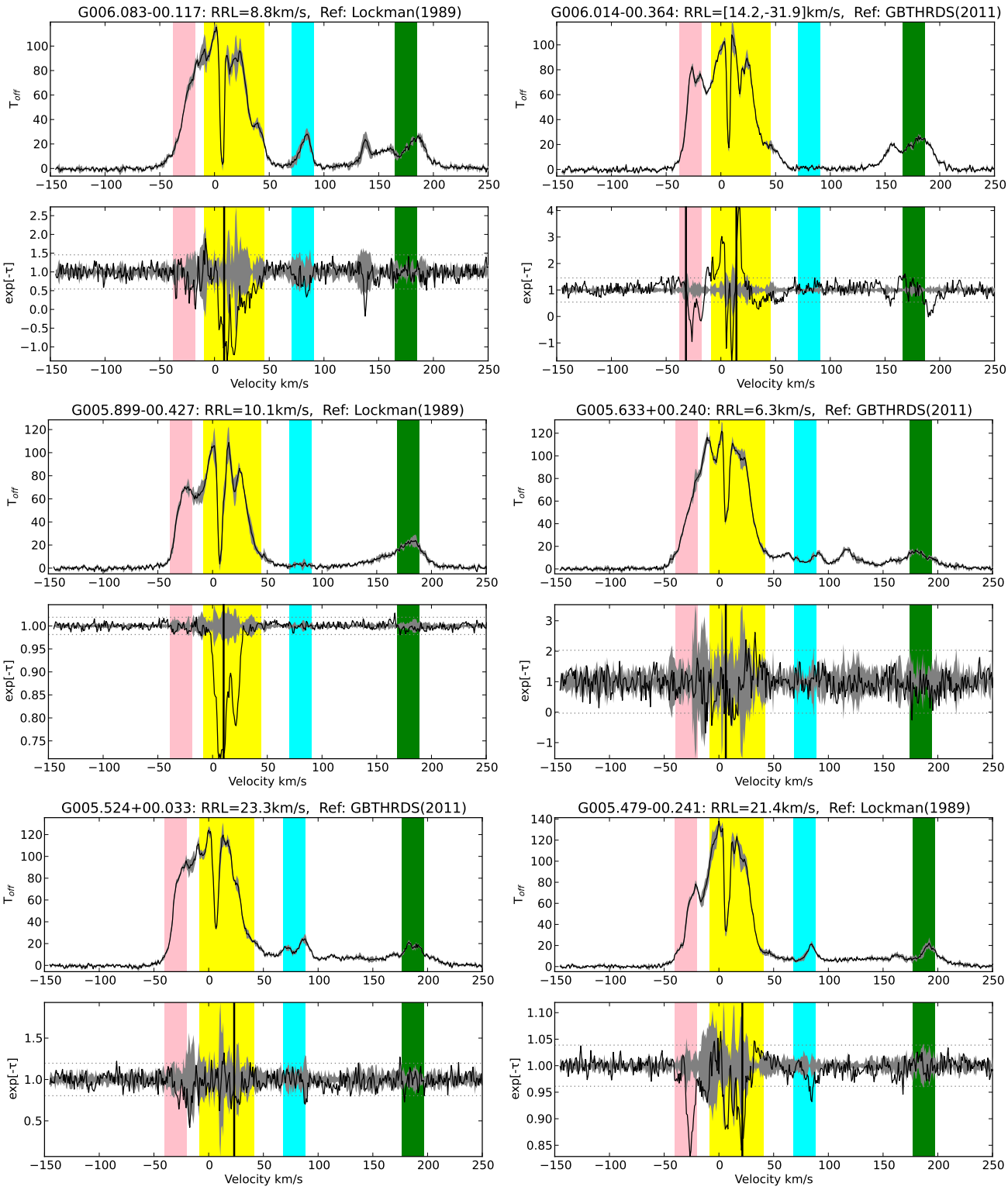
G006.083-00.117: RRL=8.8km/s, Ref: Lockman(1989)
G006.014-00.364: RRL=[14.2,-31.9]km/s, Ref: GBTHRDS(2011)
G005.899-00.427: RRL=10.1km/s, Ref: Lockman(1989)
G005.633+00.240: RRL=6.3km/s, Ref: GBTHRDS(2011)
G005.524+00.033: RRL=23.3km/s, Ref: GBTHRDS(2011)
G005.479-00.241: RRL=21.4km/s, Ref: Lockman(1989)
T_off
exp[-τ]
Velocity km/s

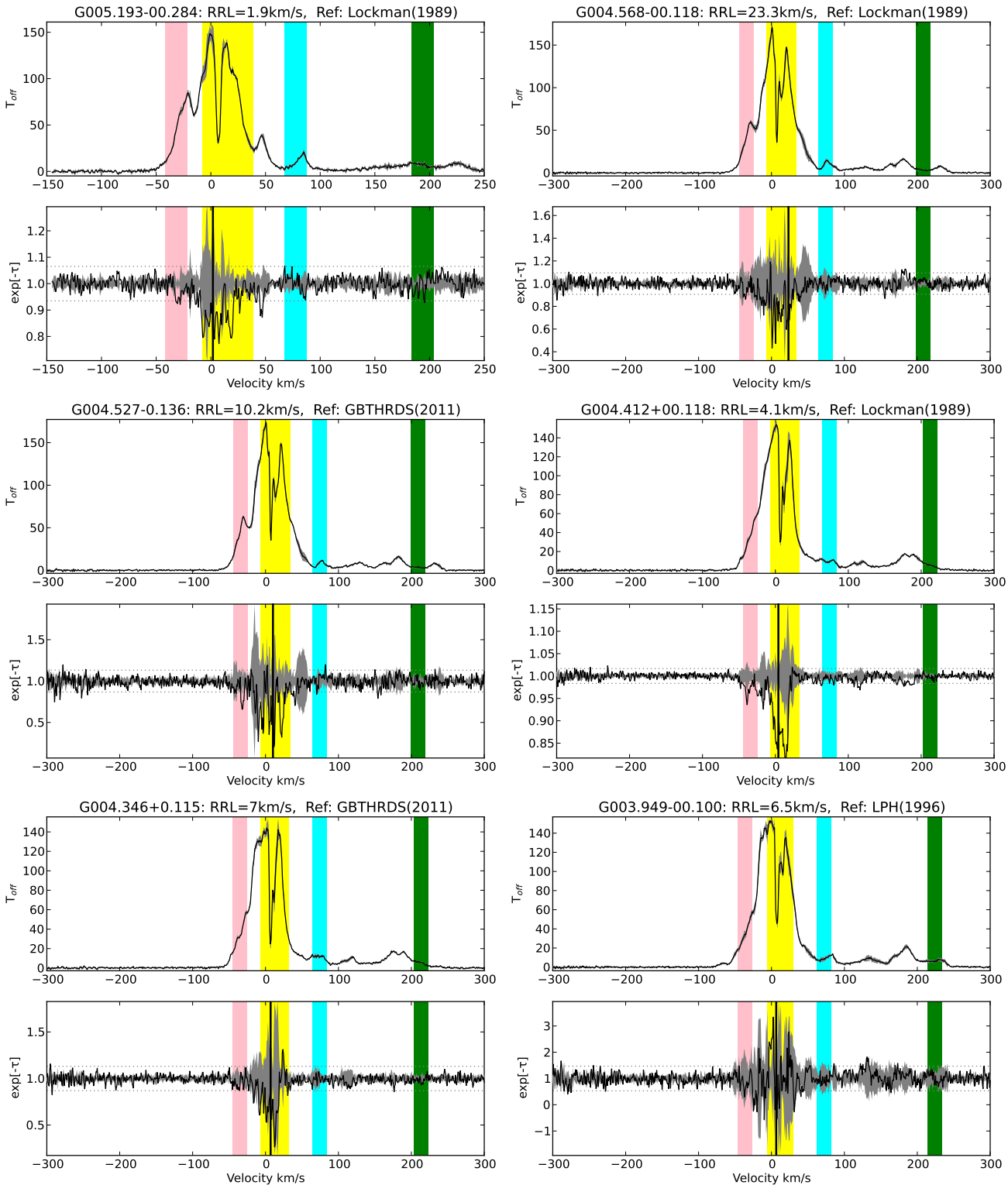
G005.193-00.284: RRL=1.9km/s, Ref: Lockman(1989)
G004.568-00.118: RRL=23.3km/s, Ref: Lockman(1989)
G004.527-0.136: RRL=10.2km/s, Ref: GBTHRDS(2011)
G004.412+00.118: RRL=4.1km/s, Ref: Lockman(1989)
G004.346+0.115: RRL=7km/s, Ref: GBTHRDS(2011)
G003.949-00.100: RRL=6.5km/s, Ref: LPH(1996)
T_off
exp[-τ]
Velocity km/s

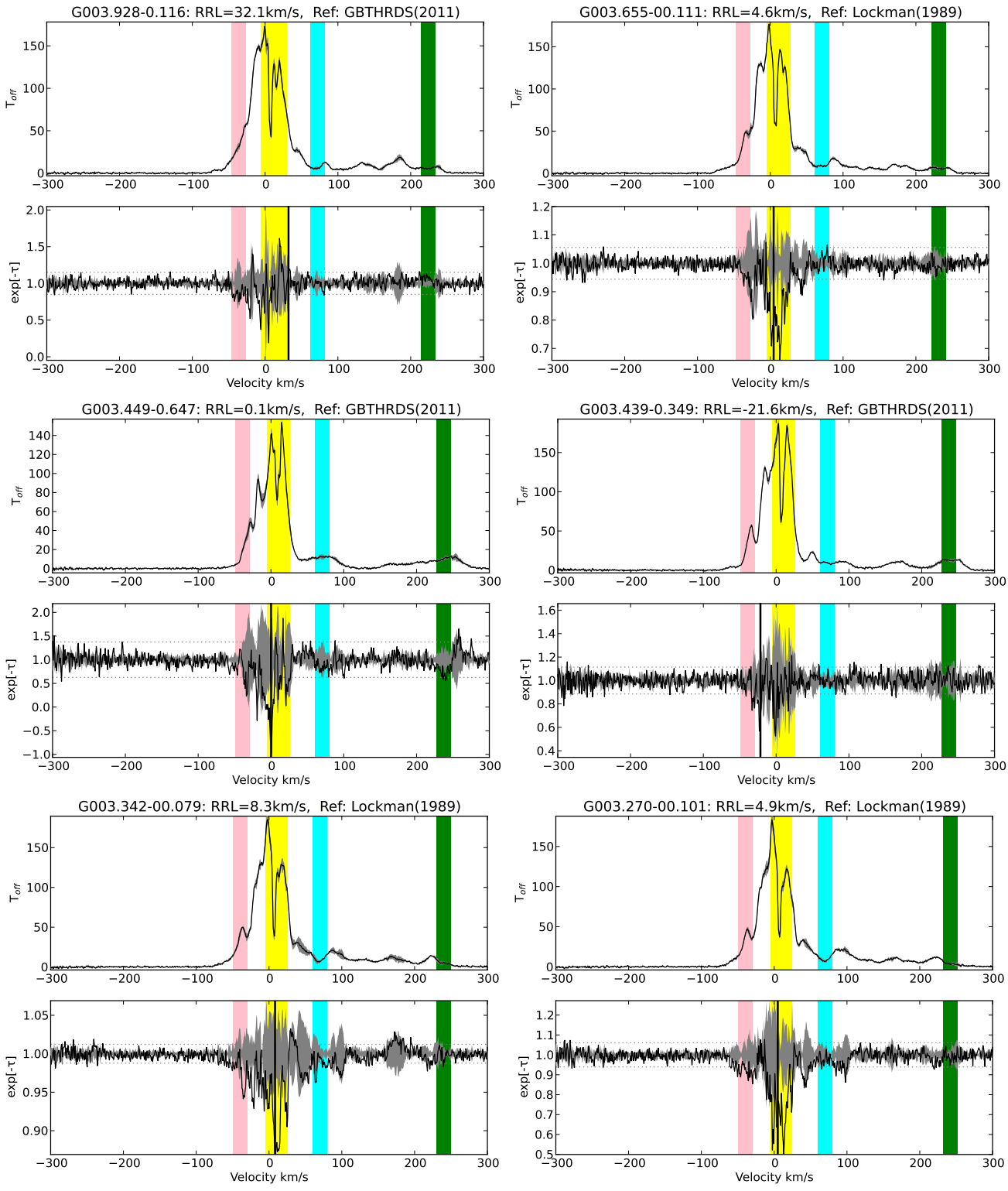
G003.928-0.116: RRL=32.1km/s, Ref: GBTHRDS(2011)
G003.655-00.111: RRL=4.6km/s, Ref: Lockman(1989)
G003.449-0.647: RRL=0.1km/s, Ref: GBTHRDS(2011)
G003.439-0.349: RRL=-21.6km/s, Ref: GBTHRDS(2011)
G003.342-00.079: RRL=8.3km/s, Ref: Lockman(1989)
G003.270-00.101: RRL=4.9km/s, Ref: Lockman(1989)
T_off
exp[-τ]
Velocity km/s

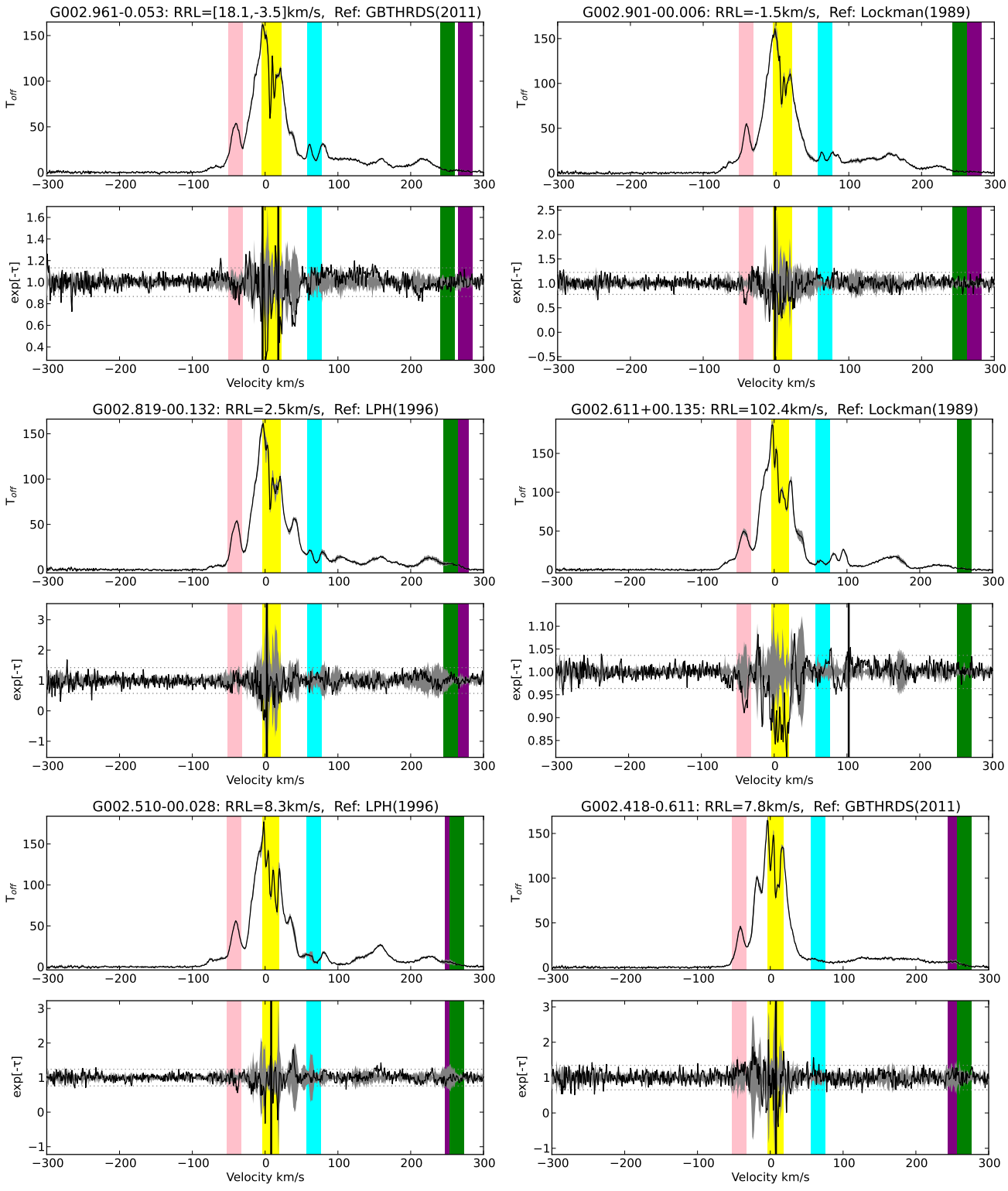
G002.961-0.053: RRL=[18.1,-3.5]km/s, Ref: GBTHRDS(2011)
G002.901-00.006: RRL=-1.5km/s, Ref: Lockman(1989)
G002.819-00.132: RRL=2.5km/s, Ref: LPH(1996)
G002.611+00.135: RRL=102.4km/s, Ref: Lockman(1989)
G002.510-00.028: RRL=8.3km/s, Ref: LPH(1996)
G002.418-0.611: RRL=7.8km/s, Ref: GBTHRDS(2011)
T_off
exp[-τ]
Velocity km/s

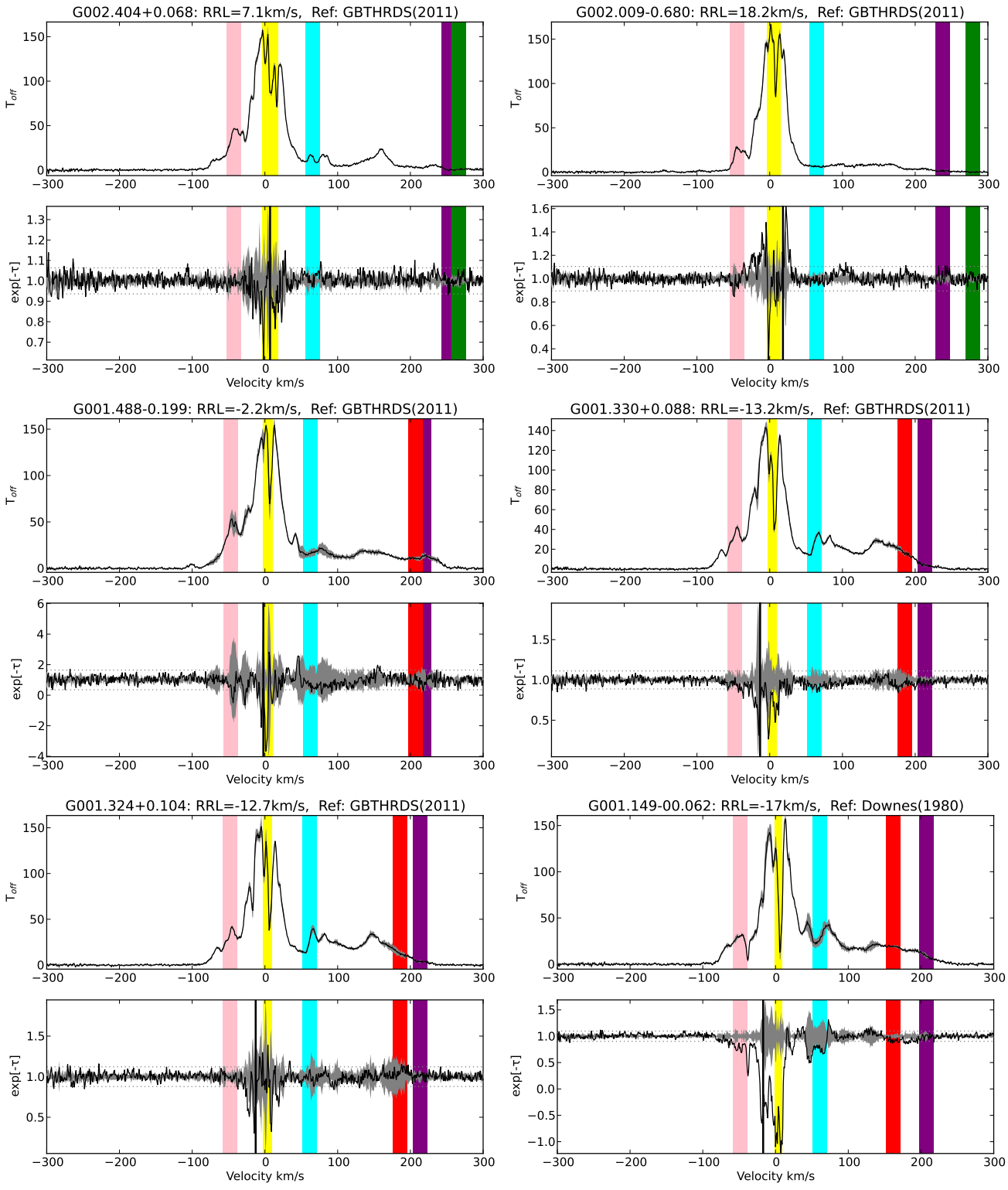
G002.404+0.068: RRL=7.1km/s, Ref: GBTHRDS(2011)
G002.009-0.680: RRL=18.2km/s, Ref: GBTHRDS(2011)
G001.488-0.199: RRL=-2.2km/s, Ref: GBTHRDS(2011)
G001.330+0.088: RRL=-13.2km/s, Ref: GBTHRDS(2011)
G001.324+0.104: RRL=-12.7km/s, Ref: GBTHRDS(2011)
G001.149-00.062: RRL=-17km/s, Ref: Downes(1980)
T_off
exp[-τ]
Velocity km/s

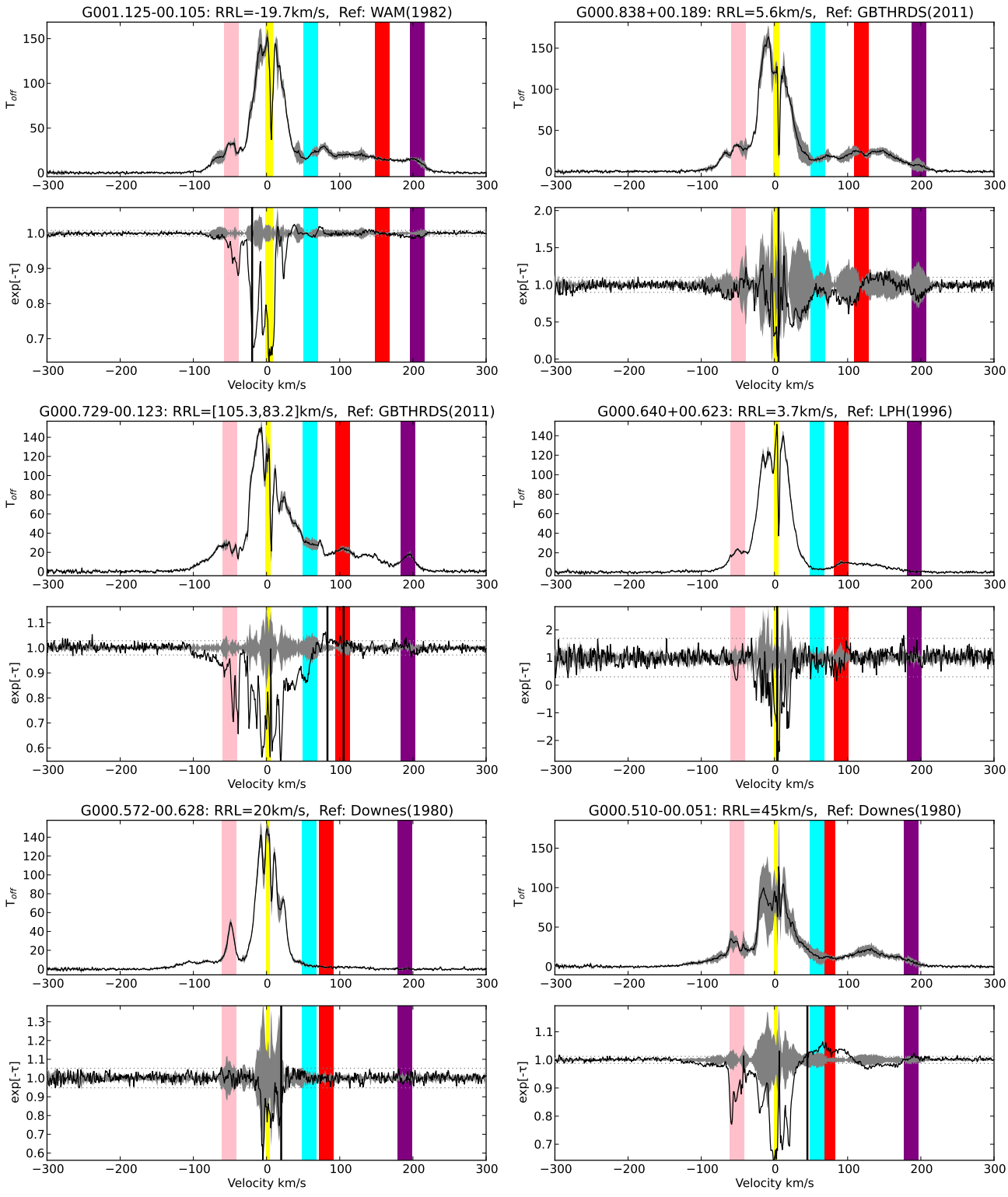
G001.125-00.105: RRL=-19.7km/s, Ref: WAM(1982)
G000.838+00.189: RRL=5.6km/s, Ref: GBTHRDS(2011)
G000.729-00.123: RRL=[105.3,83.2]km/s, Ref: GBTHRDS(2011)
G000.640+00.623: RRL=3.7km/s, Ref: LPH(1996)
G000.572-00.628: RRL=20km/s, Ref: Downes(1980)
G000.510-00.051: RRL=45km/s, Ref: Downes(1980)
T_off
exp[-τ]
Velocity km/s

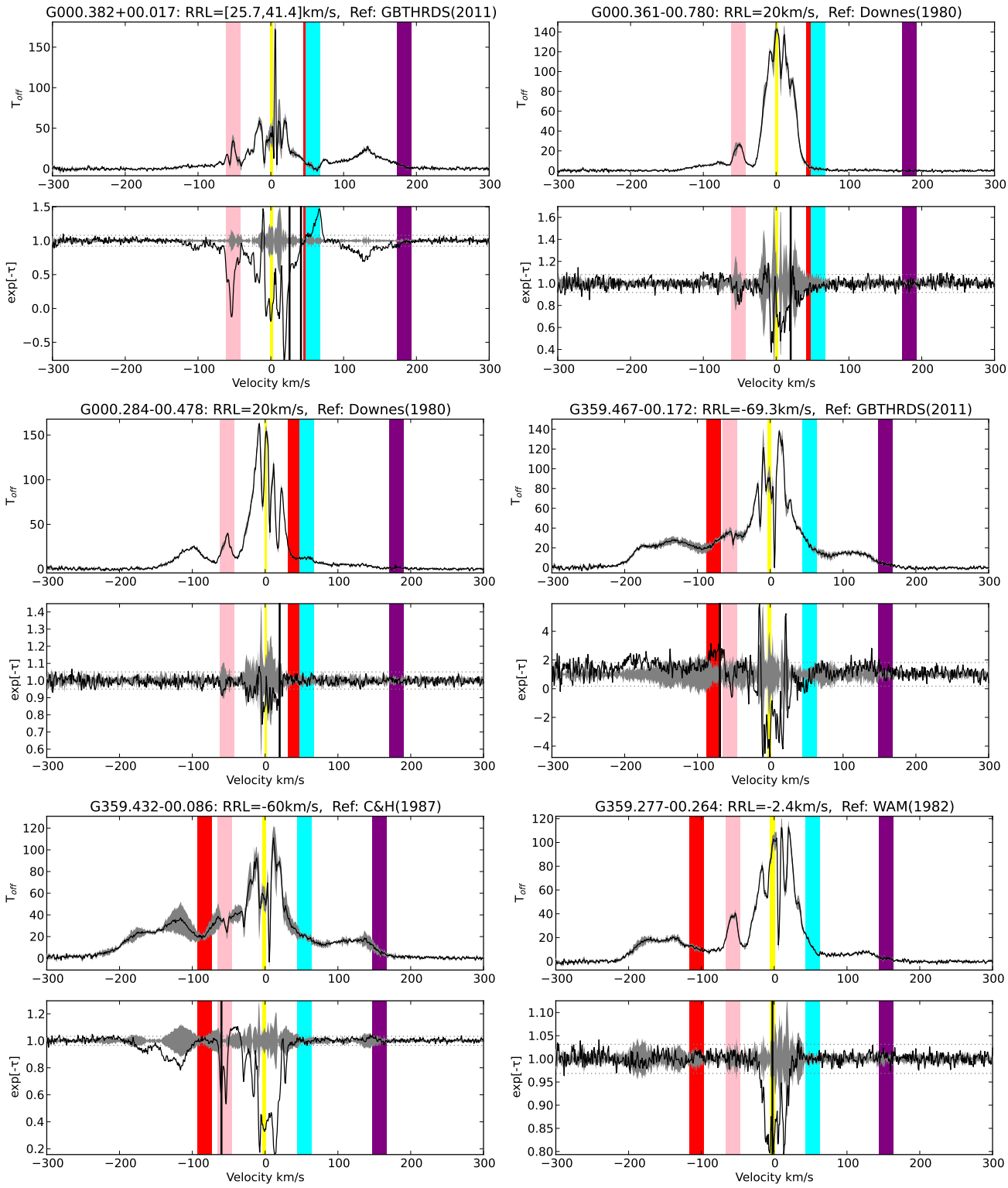
G000.382+00.017: RRL=[25.7,41.4]km/s, Ref: GBTHRDS(2011)
G000.361-00.780: RRL=20km/s, Ref: Downes(1980)
G000.284-00.478: RRL=20km/s, Ref: Downes(1980)
G359.467-00.172: RRL=-69.3km/s, Ref: GBTHRDS(2011)
G359.432-00.086: RRL=-60km/s, Ref: C&H(1987)
G359.277-00.264: RRL=-2.4km/s, Ref: WAM(1982)
T_off
exp[-τ]
Velocity km/s

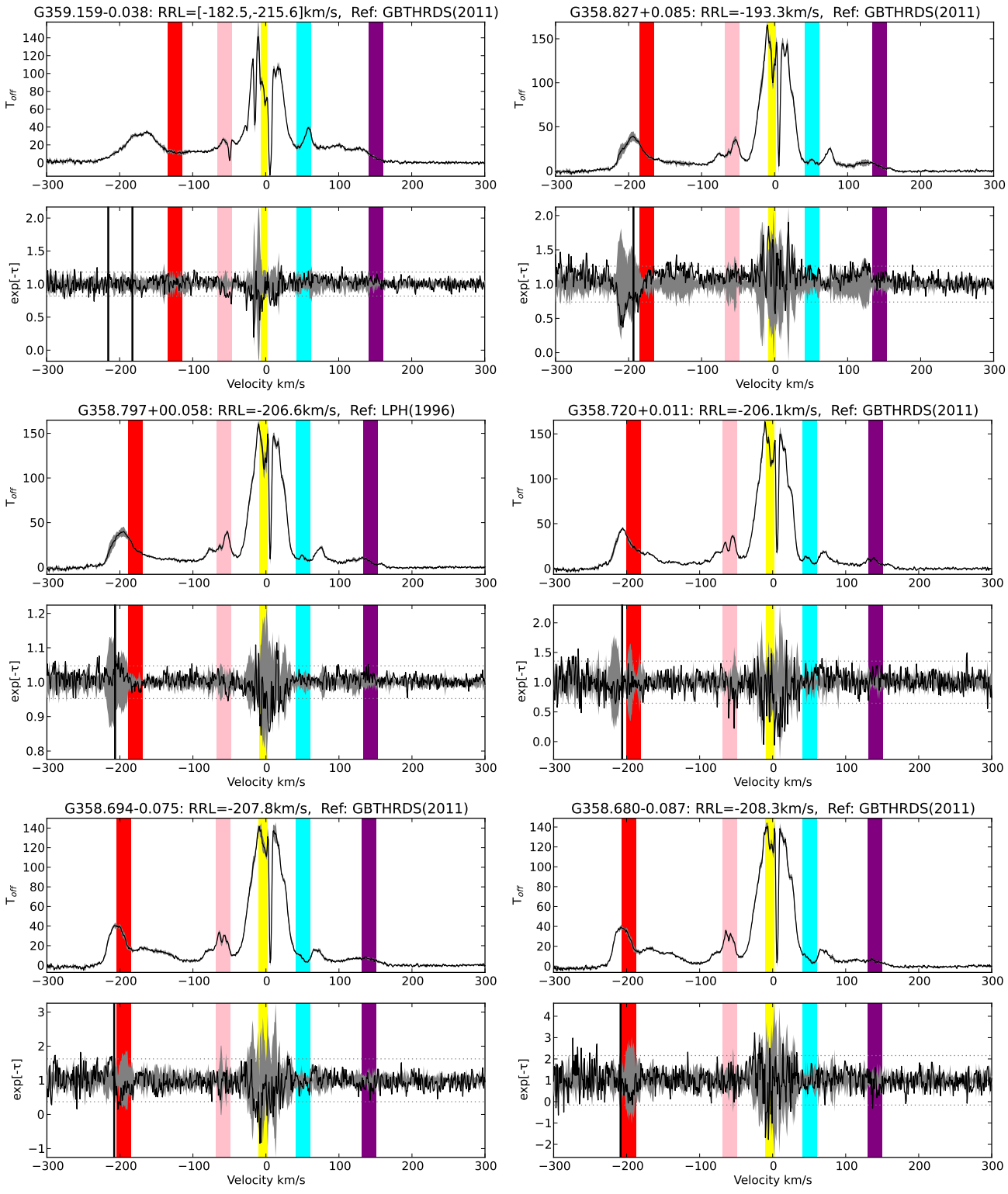
G359.159-0.038: RRL=[-182.5,-215.6]km/s, Ref: GBTHRDS(2011)
G358.827+0.085: RRL=-193.3km/s, Ref: GBTHRDS(2011)
G358.797+00.058: RRL=-206.6km/s, Ref: LPH(1996)
G358.720+0.011: RRL=-206.1km/s, Ref: GBTHRDS(2011)
G358.694-0.075: RRL=-207.8km/s, Ref: GBTHRDS(2011)
G358.680-0.087: RRL=-208.3km/s, Ref: GBTHRDS(2011)
T_off
exp[-τ]
Velocity km/s

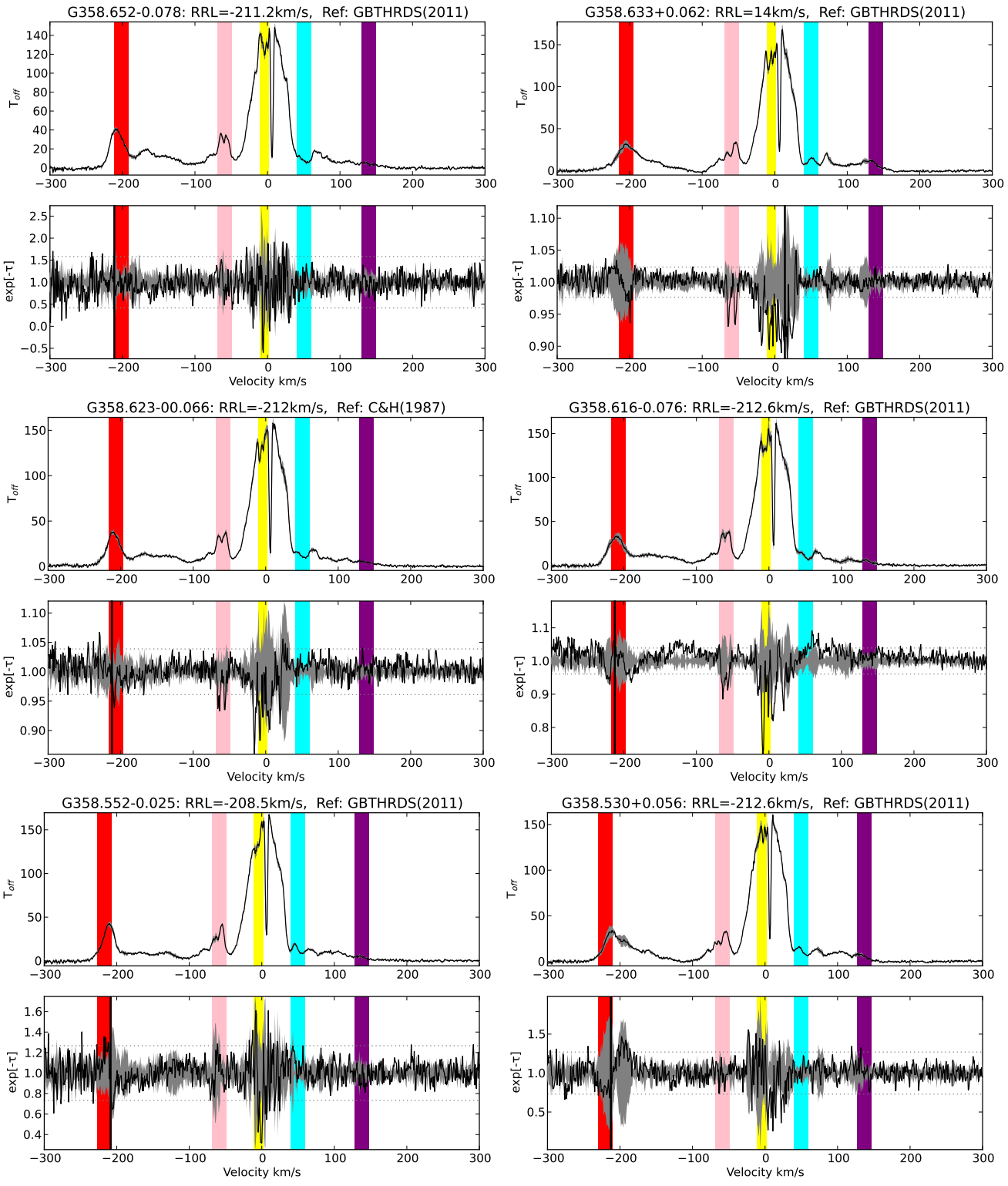
G358.652-0.078: RRL=-211.2km/s, Ref: GBTHRDS(2011)
G358.633+0.062: RRL=14km/s, Ref: GBTHRDS(2011)
G358.623-00.066: RRL=-212km/s, Ref: C&H(1987)
G358.616-0.076: RRL=-212.6km/s, Ref: GBTHRDS(2011)
G358.552-0.025: RRL=-208.5km/s, Ref: GBTHRDS(2011)
G358.530+0.056: RRL=-212.6km/s, Ref: GBTHRDS(2011)
T_off
exp[-τ]
Velocity km/s

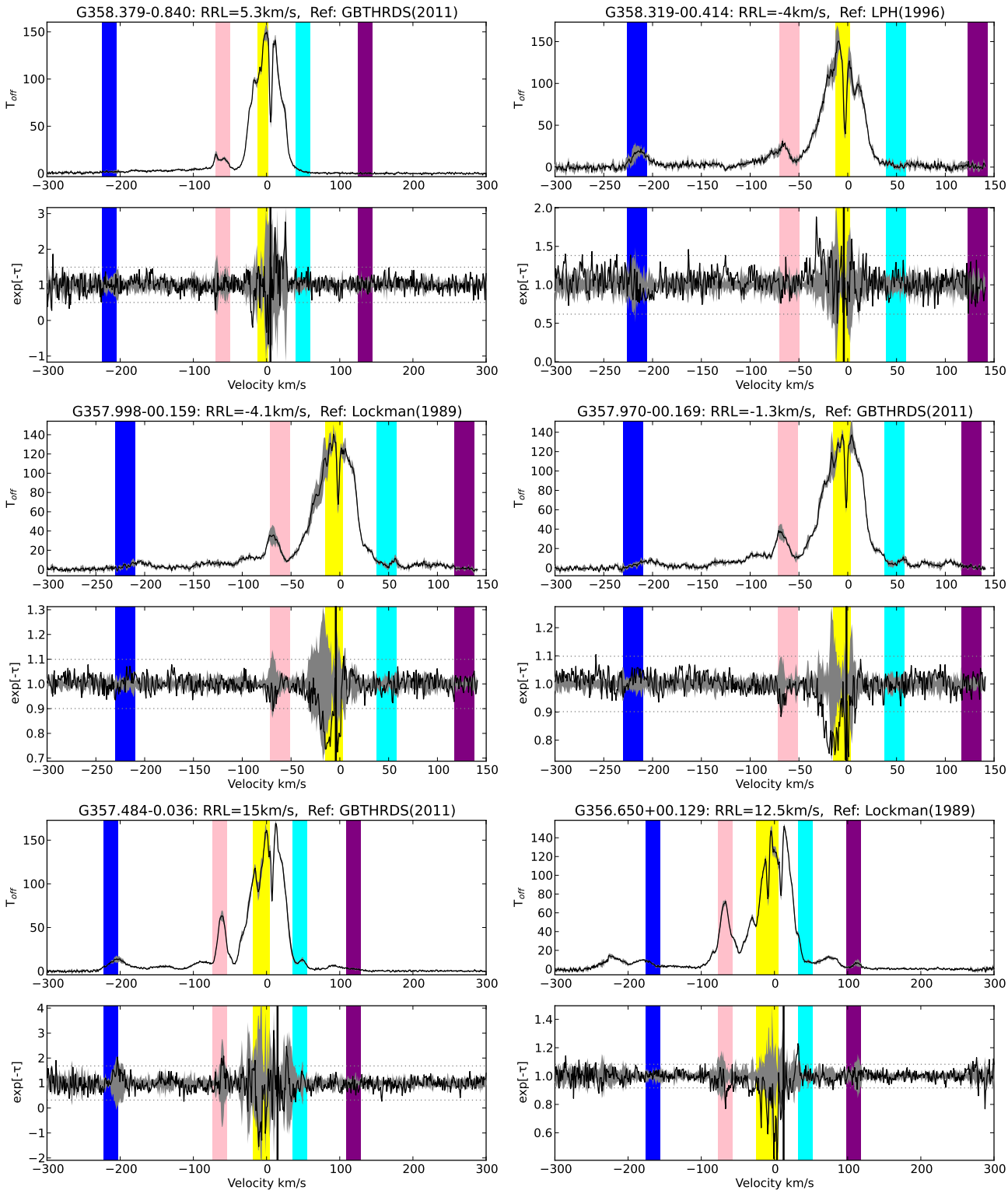
G358.379-0.840: RRL=5.3km/s, Ref: GBTHRDS(2011)
G358.319-00.414: RRL=-4km/s, Ref: LPH(1996)
G357.998-00.159: RRL=-4.1km/s, Ref: Lockman(1989)
G357.970-00.169: RRL=-1.3km/s, Ref: GBTHRDS(2011)
G357.484-0.036: RRL=15km/s, Ref: GBTHRDS(2011)
G356.650+00.129: RRL=12.5km/s, Ref: Lockman(1989)
T_off
exp[-τ]
Velocity km/s

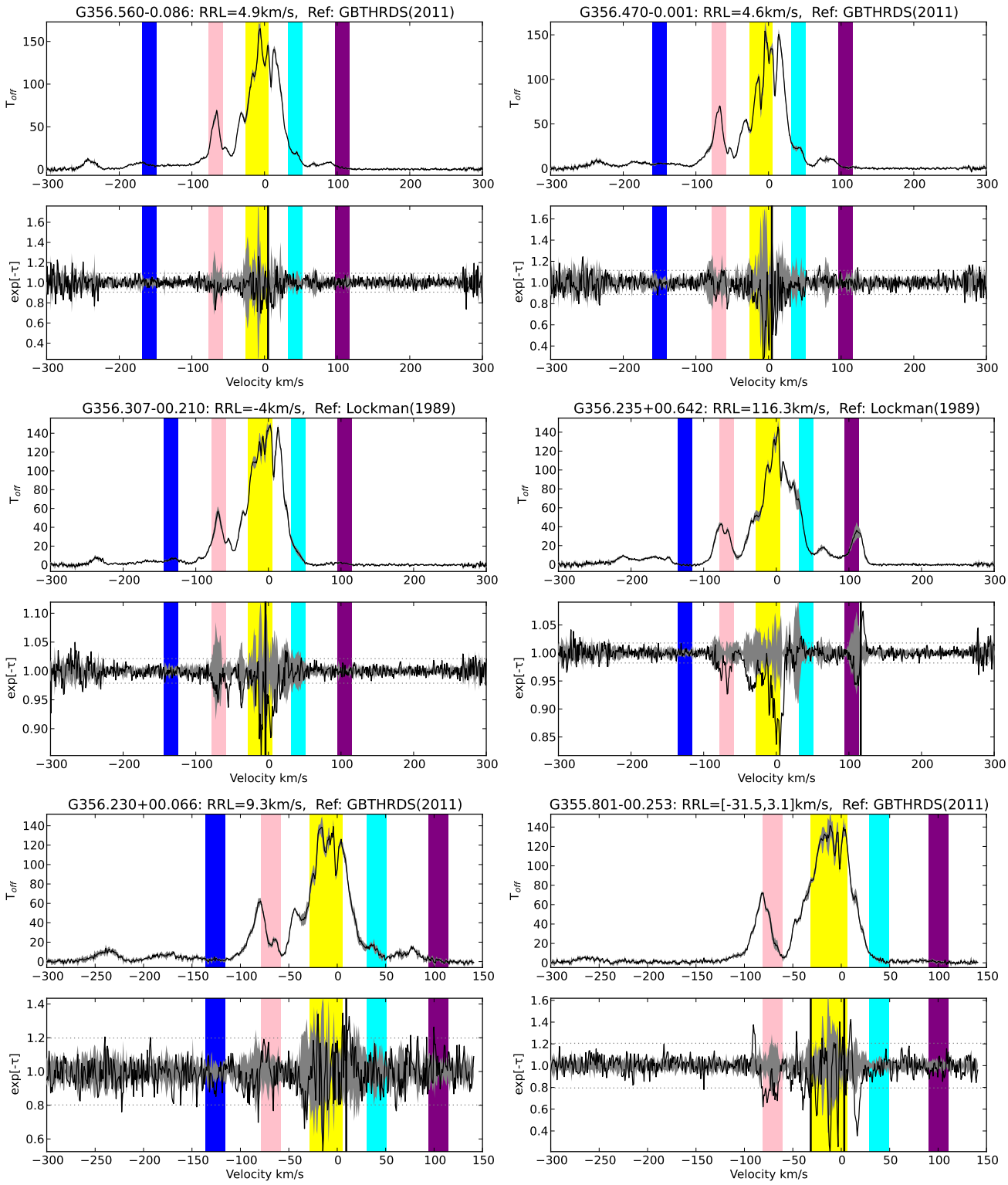
G356.560-0.086: RRL=4.9km/s, Ref: GBTHRDS(2011)
G356.470-0.001: RRL=4.6km/s, Ref: GBTHRDS(2011)
G356.307-00.210: RRL=-4km/s, Ref: Lockman(1989)
G356.235+00.642: RRL=116.3km/s, Ref: Lockman(1989)
G356.230+00.066: RRL=9.3km/s, Ref: GBTHRDS(2011)
G355.801-00.253: RRL=[-31.5,3.1]km/s, Ref: GBTHRDS(2011)
T_off
exp[-τ]
Velocity km/s

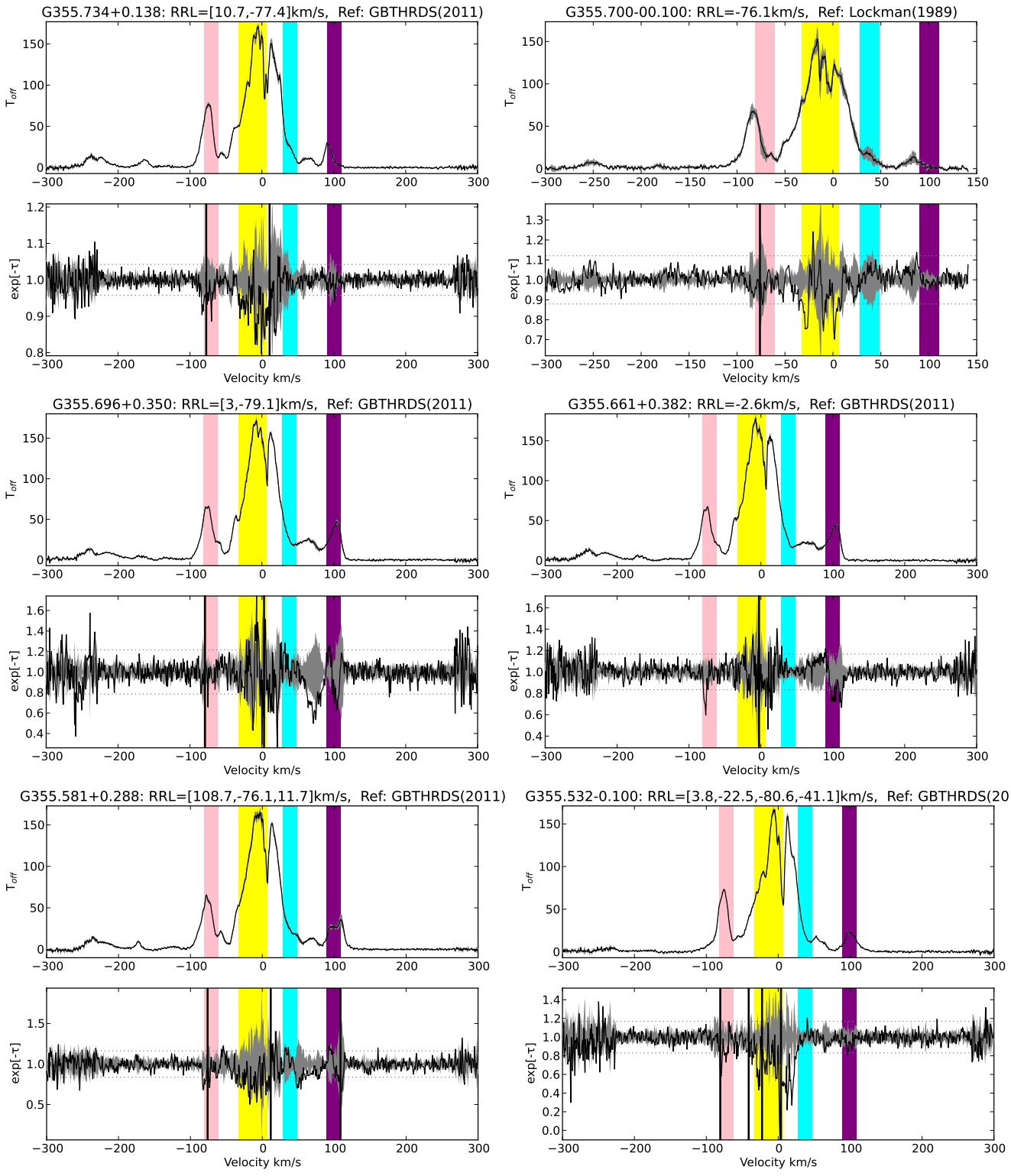
G355.734+0.138: RRL=[10.7,-77.4]km/s, Ref: GBTHRDS(2011)
G355.700-00.100: RRL=-76.1km/s, Ref: Lockman(1989)
G355.696+0.350: RRL=[3,-79.1]km/s, Ref: GBTHRDS(2011)
G355.661+0.382: RRL=-2.6km/s, Ref: GBTHRDS(2011)
G355.581+0.288: RRL=[108.7,-76.1,11.7]km/s, Ref: GBTHRDS(2011)
G355.532-0.100: RRL=[3.8,-22.5,-80.6,-41.1]km/s, Ref: GBTHRDS(2011)
T_off
exp[-τ]
Velocity km/s

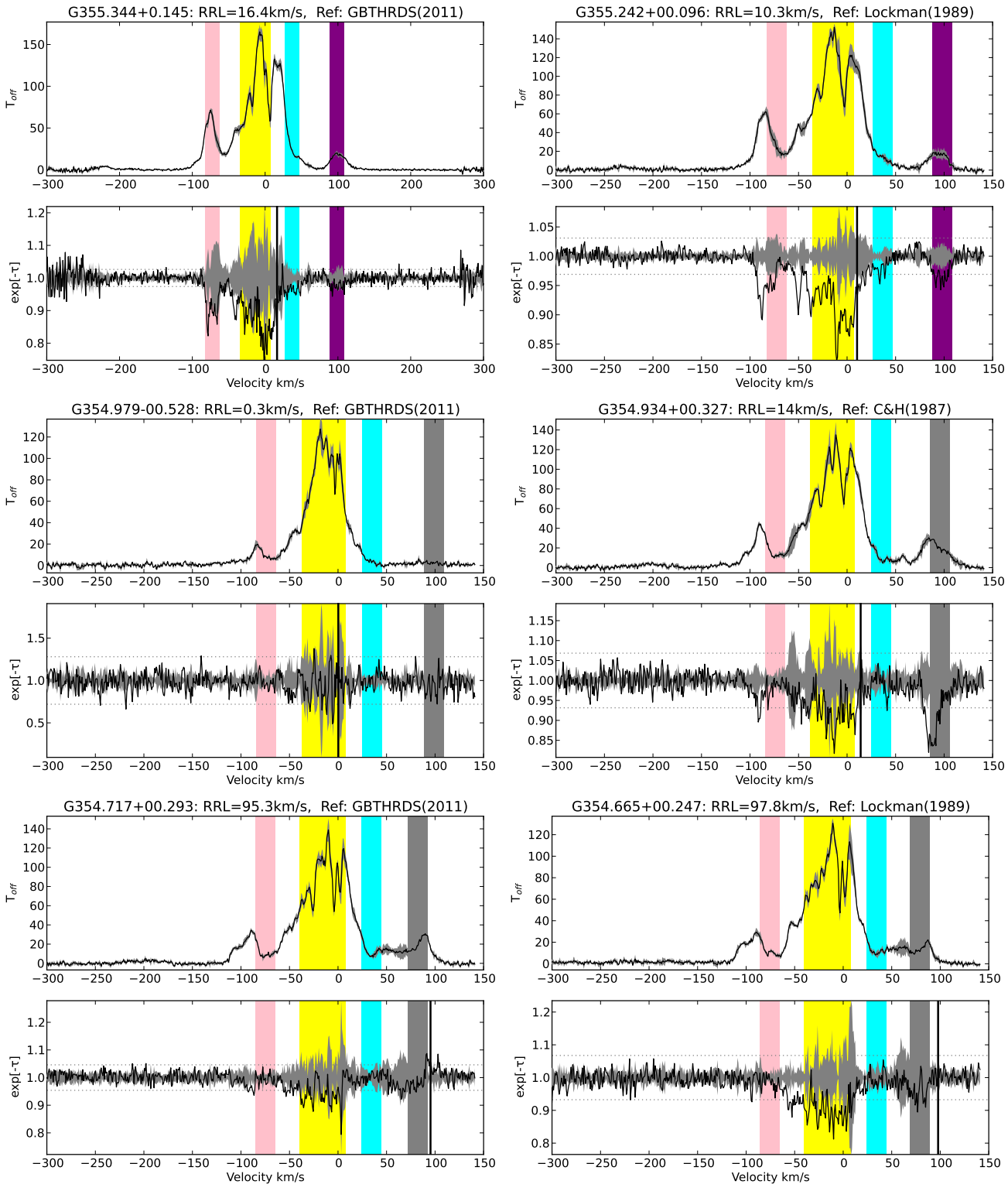
G355.344+0.145: RRL=16.4km/s, Ref: GBTHRDS(2011)
G355.242+00.096: RRL=10.3km/s, Ref: Lockman(1989)
G354.979-00.528: RRL=0.3km/s, Ref: GBTHRDS(2011)
G354.934+00.327: RRL=14km/s, Ref: C&H(1987)
G354.717+00.293: RRL=95.3km/s, Ref: GBTHRDS(2011)
G354.665+00.247: RRL=97.8km/s, Ref: Lockman(1989)
T_off
exp[-τ]
Velocity km/s

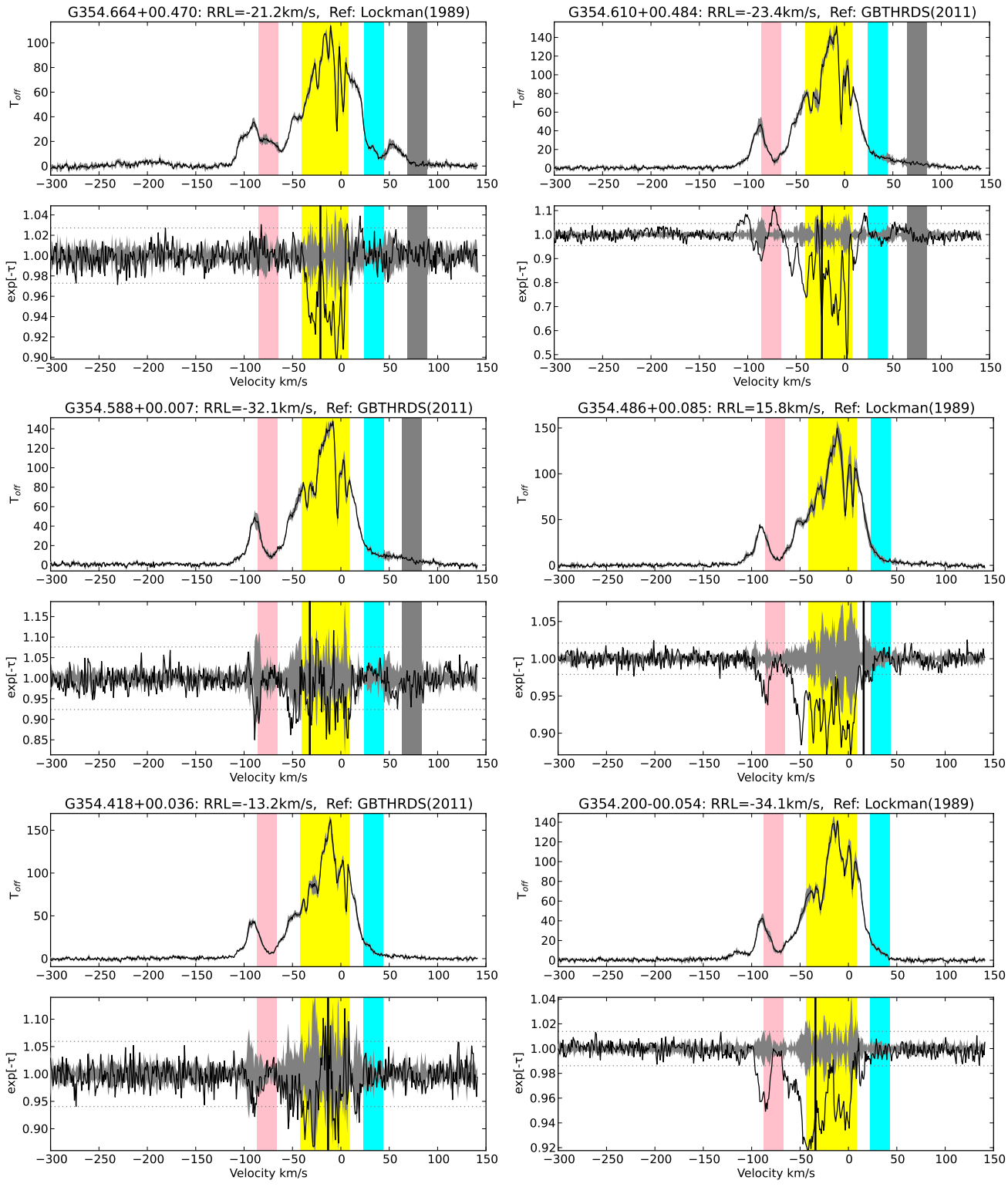
G354.664+00.470: RRL=-21.2km/s, Ref: Lockman(1989)
G354.610+00.484: RRL=-23.4km/s, Ref: GBTHRDS(2011)
G354.588+00.007: RRL=-32.1km/s, Ref: GBTHRDS(2011)
G354.486+00.085: RRL=15.8km/s, Ref: Lockman(1989)
G354.418+00.036: RRL=-13.2km/s, Ref: GBTHRDS(2011)
G354.200-00.054: RRL=-34.1km/s, Ref: Lockman(1989)
T_off
exp[-τ]
Velocity km/s

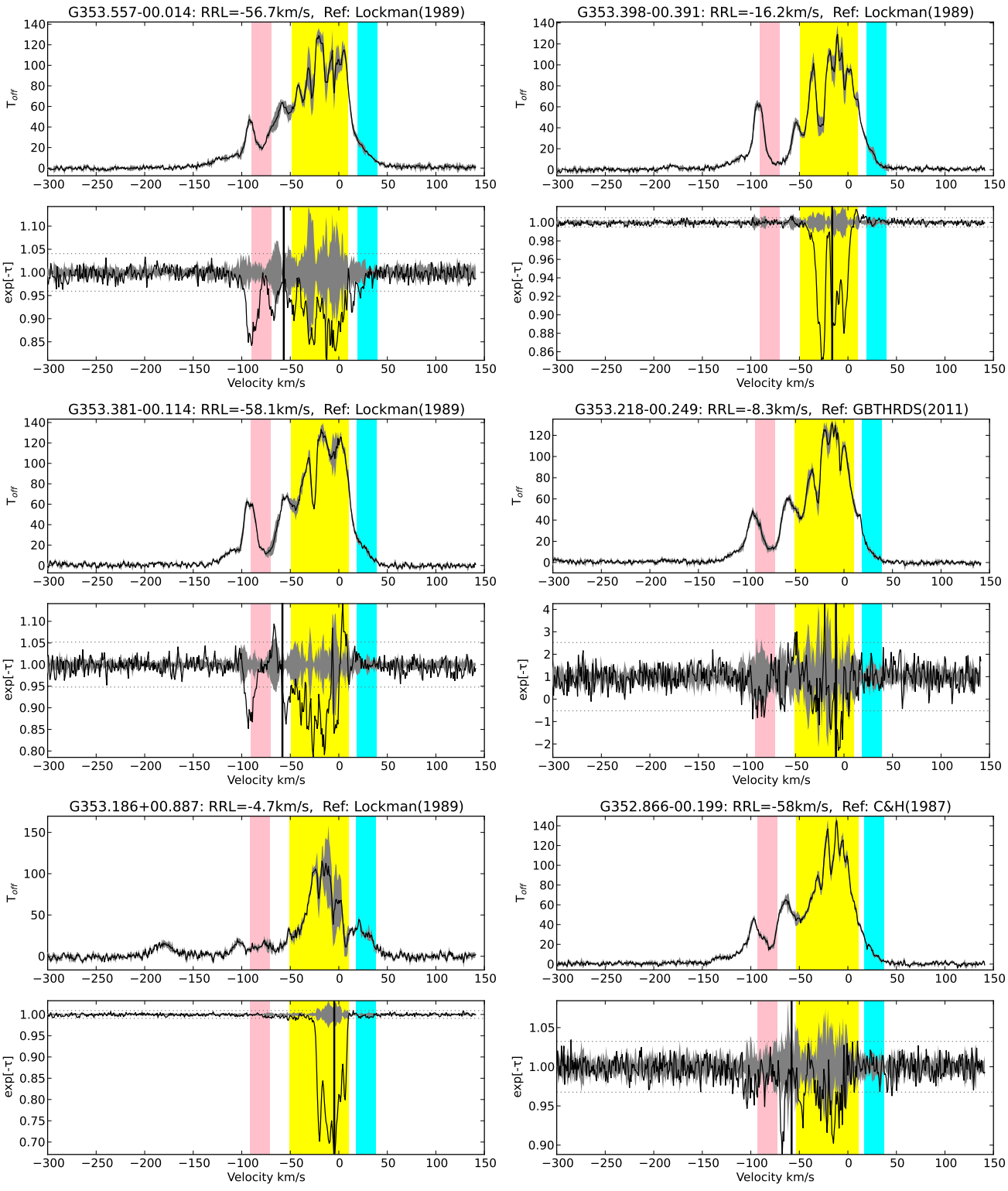
G353.557-00.014: RRL=-56.7km/s, Ref: Lockman(1989)
G353.398-00.391: RRL=-16.2km/s, Ref: Lockman(1989)
G353.381-00.114: RRL=-58.1km/s, Ref: Lockman(1989)
G353.218-00.249: RRL=-8.3km/s, Ref: GBTHRDS(2011)
G353.186+00.887: RRL=-4.7km/s, Ref: Lockman(1989)
G352.866-00.199: RRL=-58km/s, Ref: C&H(1987)
T_off
exp[-τ]
Velocity km/s

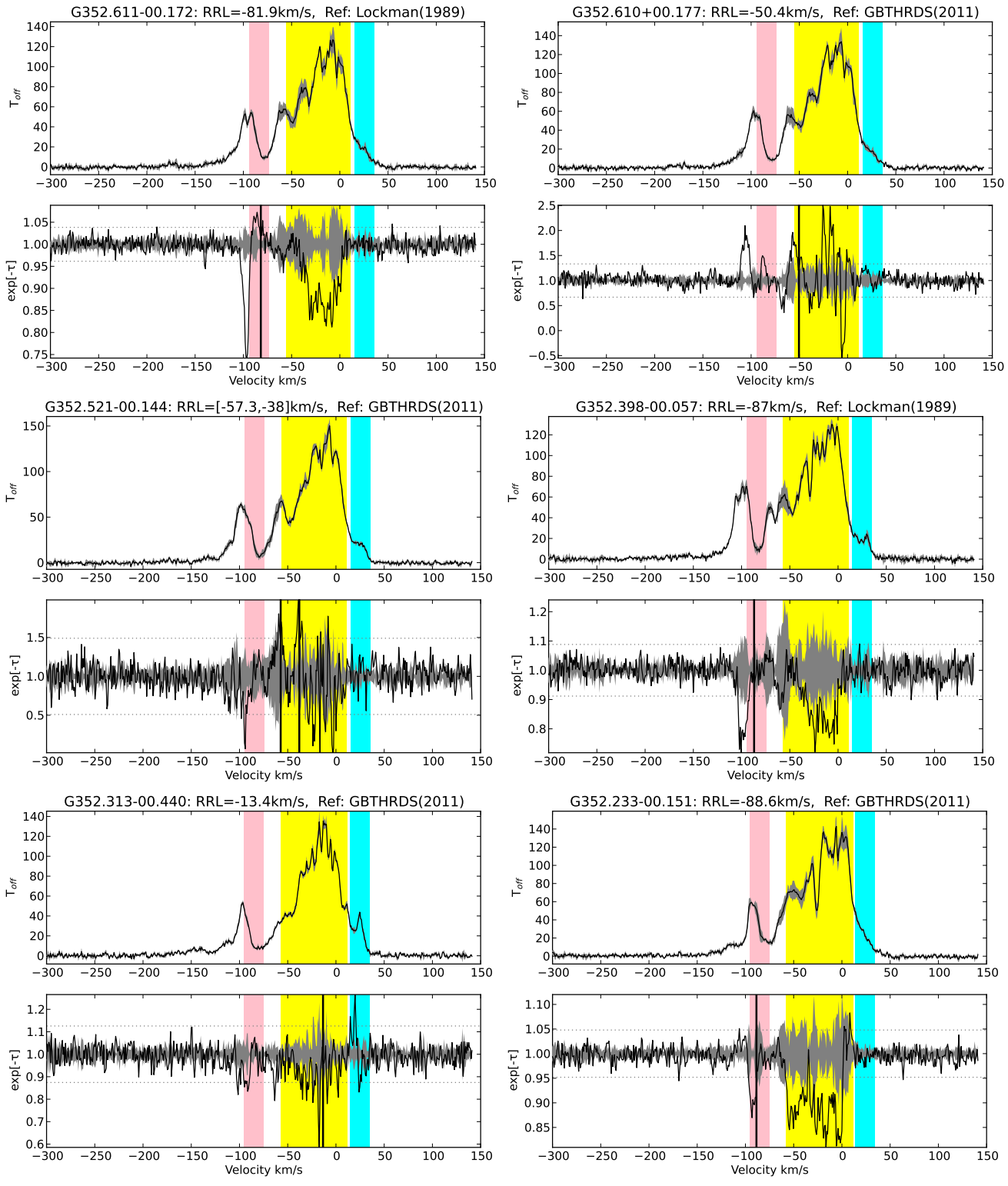
G352.611-00.172: RRL=-81.9km/s, Ref: Lockman(1989)
G352.610+00.177: RRL=-50.4km/s, Ref: GBTHRDS(2011)
G352.521-00.144: RRL=[-57.3,-38]km/s, Ref: GBTHRDS(2011)
G352.398-00.057: RRL=-87km/s, Ref: Lockman(1989)
G352.313-00.440: RRL=-13.4km/s, Ref: GBTHRDS(2011)
G352.233-00.151: RRL=-88.6km/s, Ref: GBTHRDS(2011)
T_off
exp[-τ]
Velocity km/s

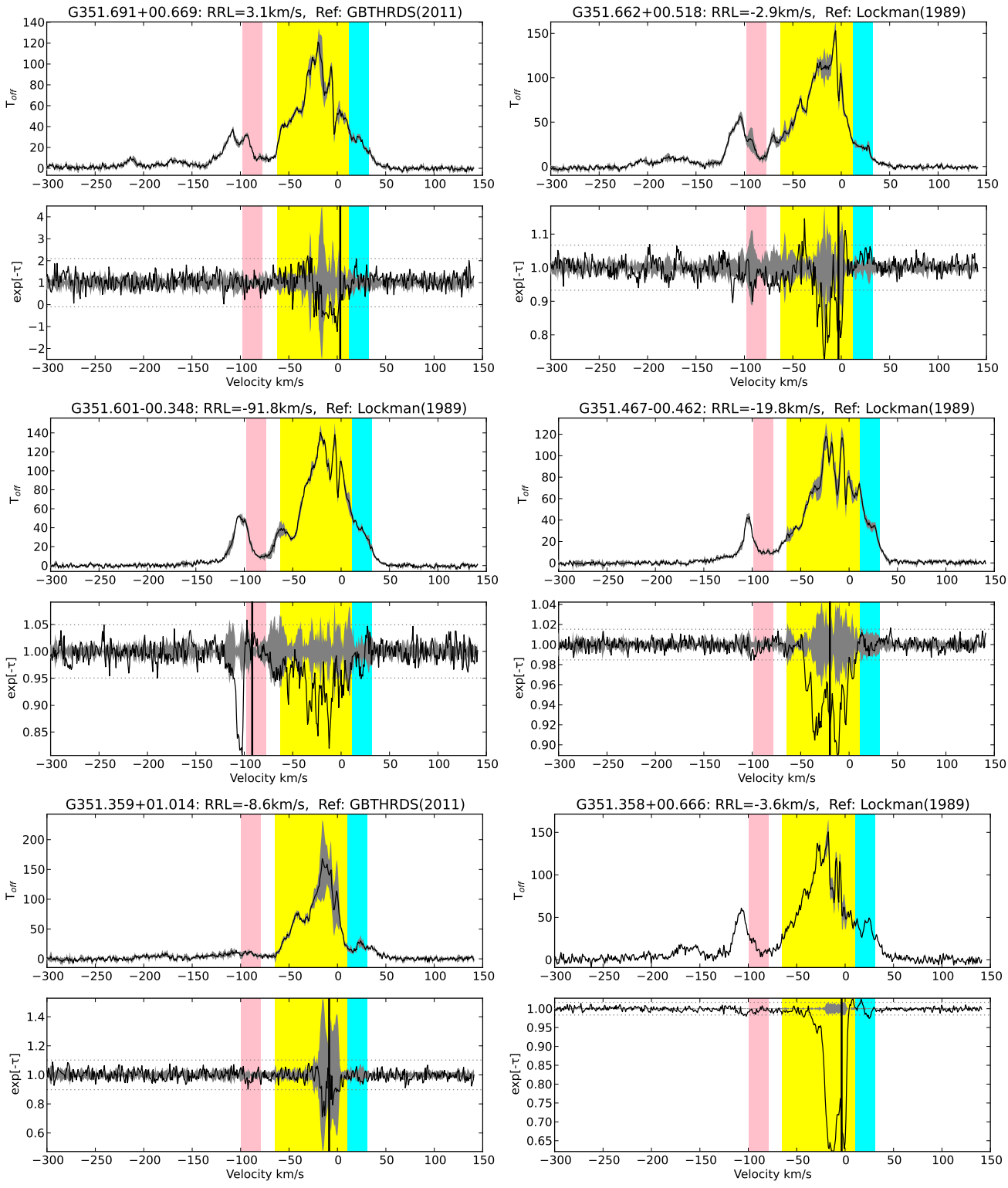
G351.691+00.669: RRL=3.1km/s, Ref: GBTHRDS(2011)
G351.662+00.518: RRL=-2.9km/s, Ref: Lockman(1989)
G351.601-00.348: RRL=-91.8km/s, Ref: Lockman(1989)
G351.467-00.462: RRL=-19.8km/s, Ref: Lockman(1989)
G351.359+01.014: RRL=-8.6km/s, Ref: GBTHRDS(2011)
G351.358+00.666: RRL=-3.6km/s, Ref: Lockman(1989)
T_off
exp[-τ]
Velocity km/s

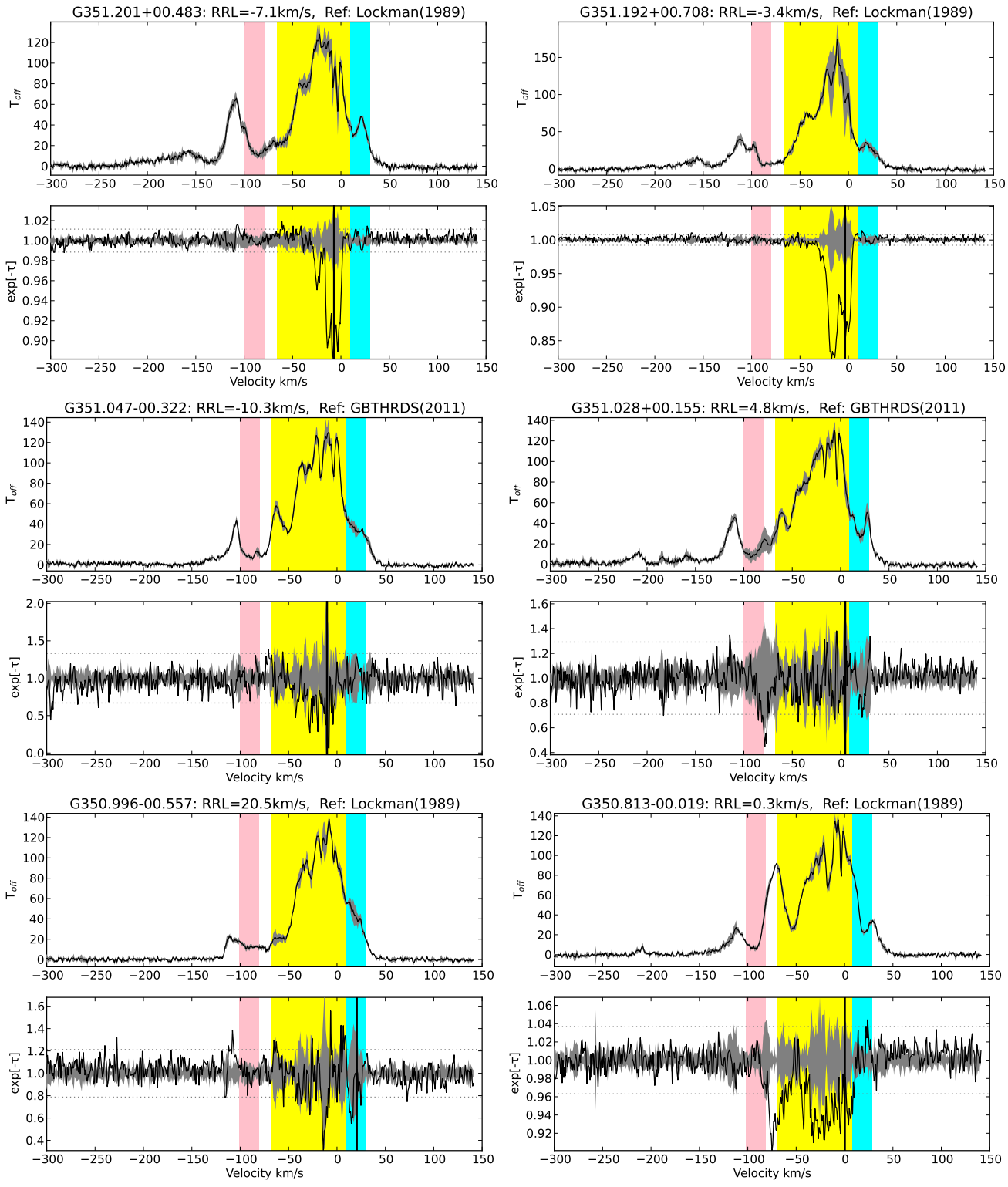
G351.201+00.483: RRL=-7.1km/s, Ref: Lockman(1989)
G351.192+00.708: RRL=-3.4km/s, Ref: Lockman(1989)
G351.047-00.322: RRL=-10.3km/s, Ref: GBTHRDS(2011)
G351.028+00.155: RRL=4.8km/s, Ref: GBTHRDS(2011)
G350.996-00.557: RRL=20.5km/s, Ref: Lockman(1989)
G350.813-00.019: RRL=0.3km/s, Ref: Lockman(1989)
T_off
exp[-τ]
Velocity km/s

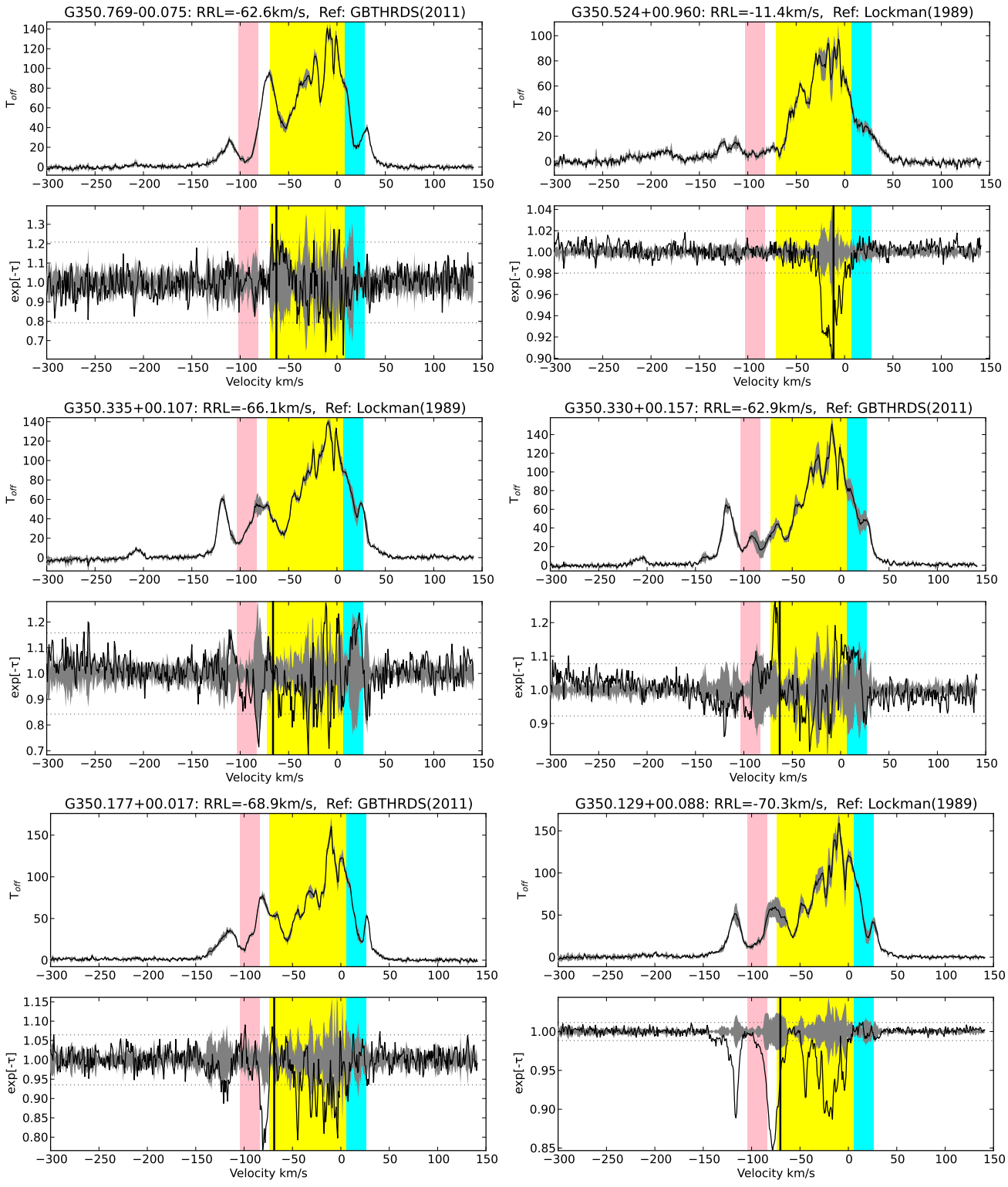
G350.769-00.075: RRL=-62.6km/s, Ref: GBTHRDS(2011)
G350.524+00.960: RRL=-11.4km/s, Ref: Lockman(1989)
G350.335+00.107: RRL=-66.1km/s, Ref: Lockman(1989)
G350.330+00.157: RRL=-62.9km/s, Ref: GBTHRDS(2011)
G350.177+00.017: RRL=-68.9km/s, Ref: GBTHRDS(2011)
G350.129+00.088: RRL=-70.3km/s, Ref: Lockman(1989)
T_off
exp[-τ]
Velocity km/s

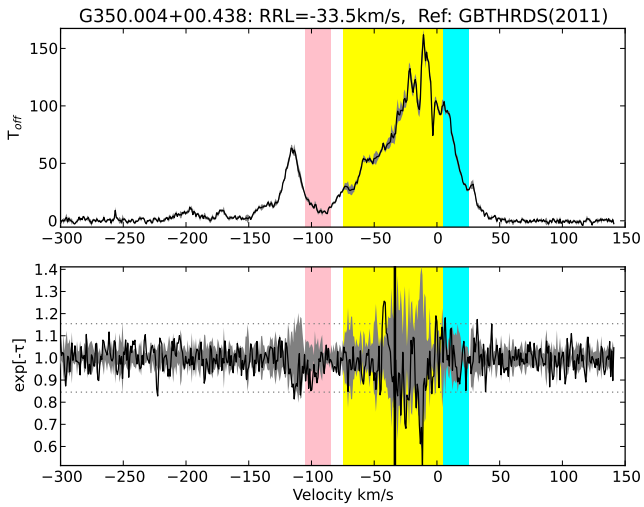

C.3 Emission/Absorption Spectrum Pairs from Chapter 5

The following H I emission/absorption spectrum pairs appeared as a Figure Set in the the published version of Chapter 5. The only modifications made to the published version of this Figure Set are the excusion of any H II regions between $350° < l < 360°$—as those regions were included in the previous section; and that the ordering of spectra has been reversed, such that the entirety of Appendix C is in longitude order.

In each figure, the top panel shows the emission spectra. The emission is shown by the solid line (this is the average of the three off positions, see Section 1.4.2.1) and the emission envelope ($3\sigma_{T_{\rm off}}$) is shown in grey. Absorption, $e^{-\tau}$, is shown in the bottom panel. The H I absorption spectrum is shown as the solid line and the grey envelope signifies $\Delta_{\rm abs}$ (calculated from the emission envelope). The absorption panel also displays the fluctuation in the baseline of the absorption spectrum ($\sigma_{\rm rms}$, horizontal dotted lines). The H II region name and reference are shown as well as the expected velocity ranges of Galactic structure features with the same colour system as Figure 5.4.

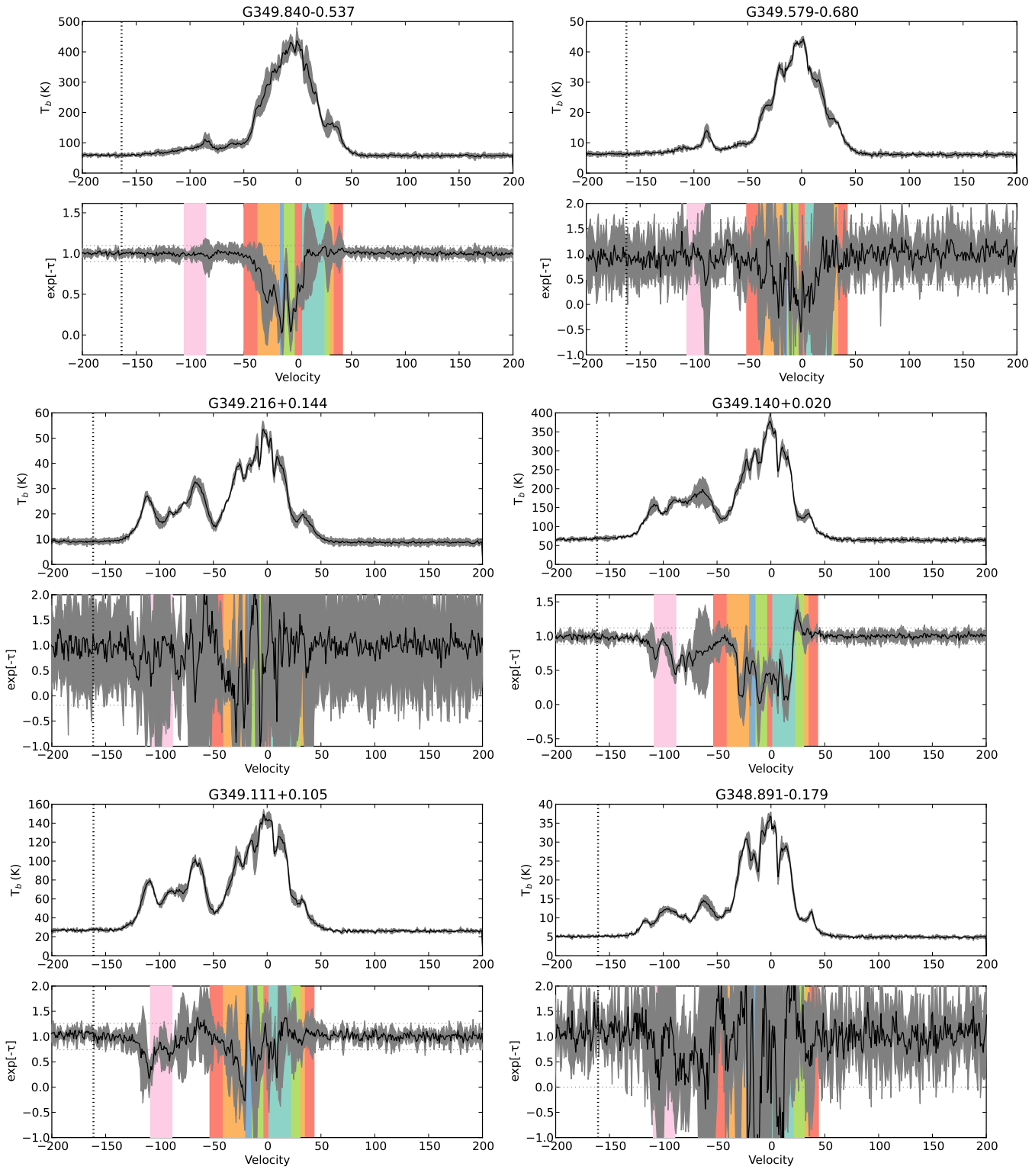
G349.840-0.537
G349.579-0.680
G349.216+0.144
G349.140+0.020
G349.111+0.105
G348.891-0.179
T_b (K)
exp[-τ]
Velocity

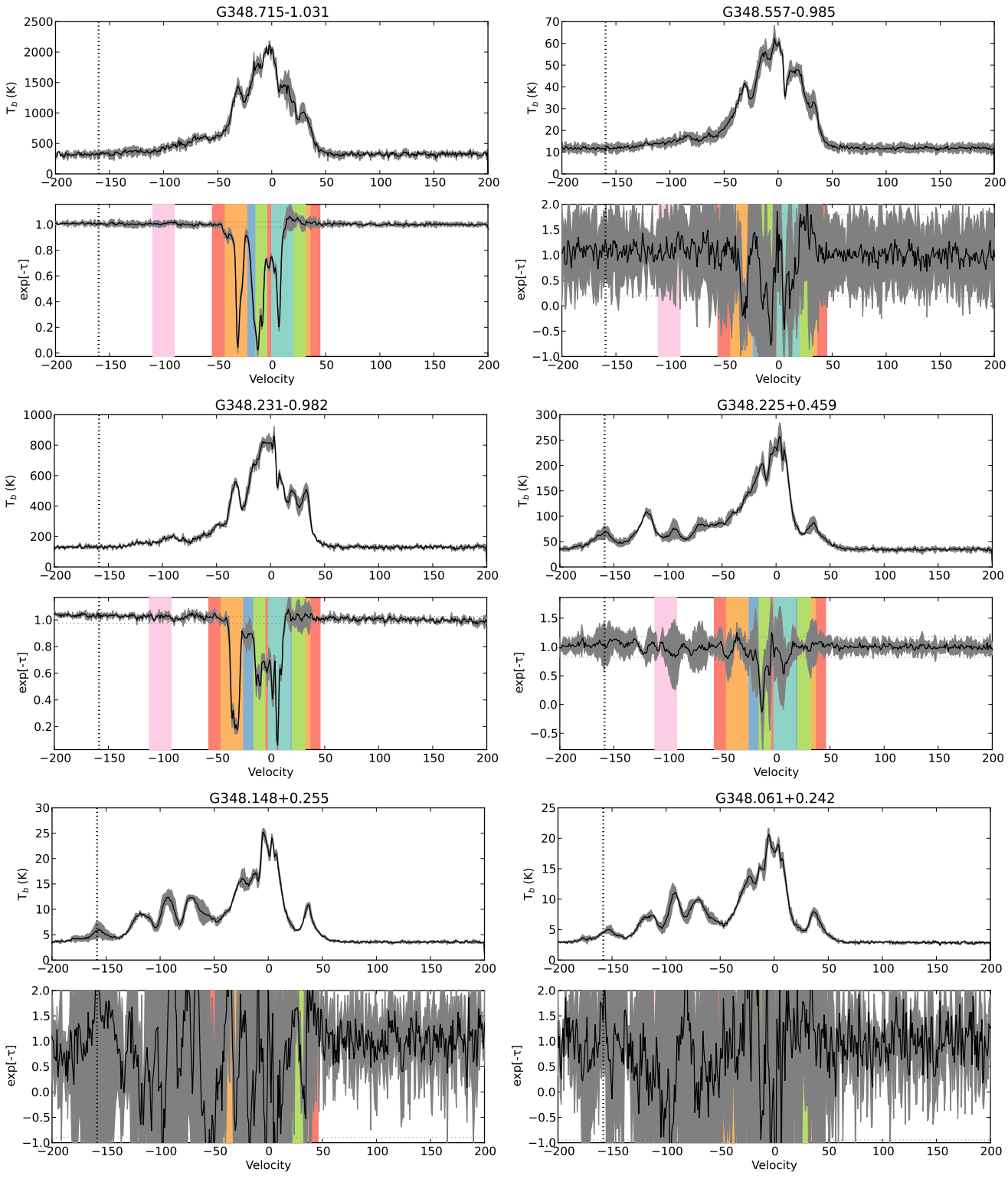
G348.715-1.031
G348.557-0.985
G348.231-0.982
G348.225+0.459
G348.148+0.255
G348.061+0.242
T_b (K)
exp[-τ]
Velocity

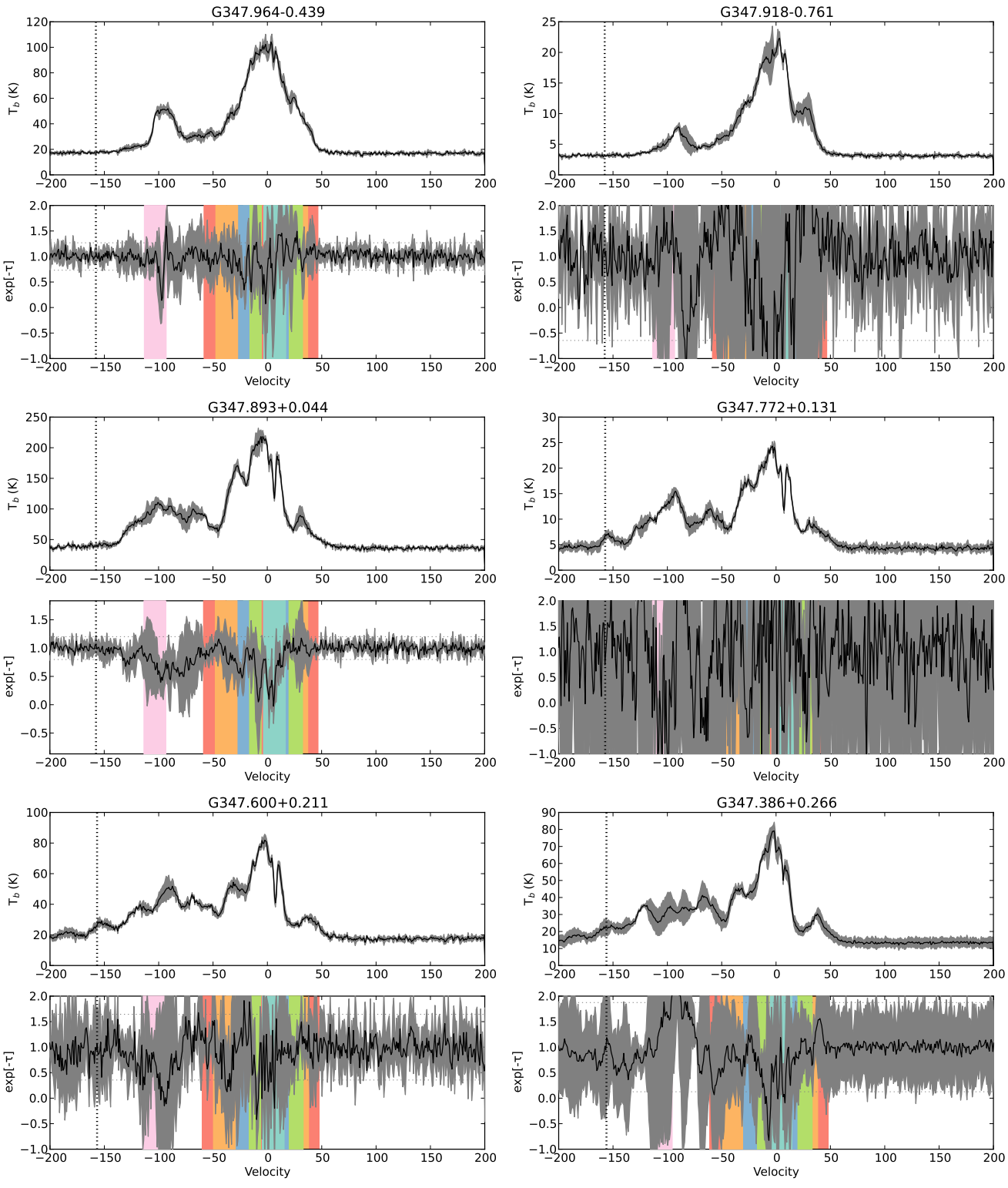
G347.964-0.439
G347.918-0.761
G347.893+0.044
G347.772+0.131
G347.600+0.211
G347.386+0.266
T_b (K)
exp[-τ]
Velocity

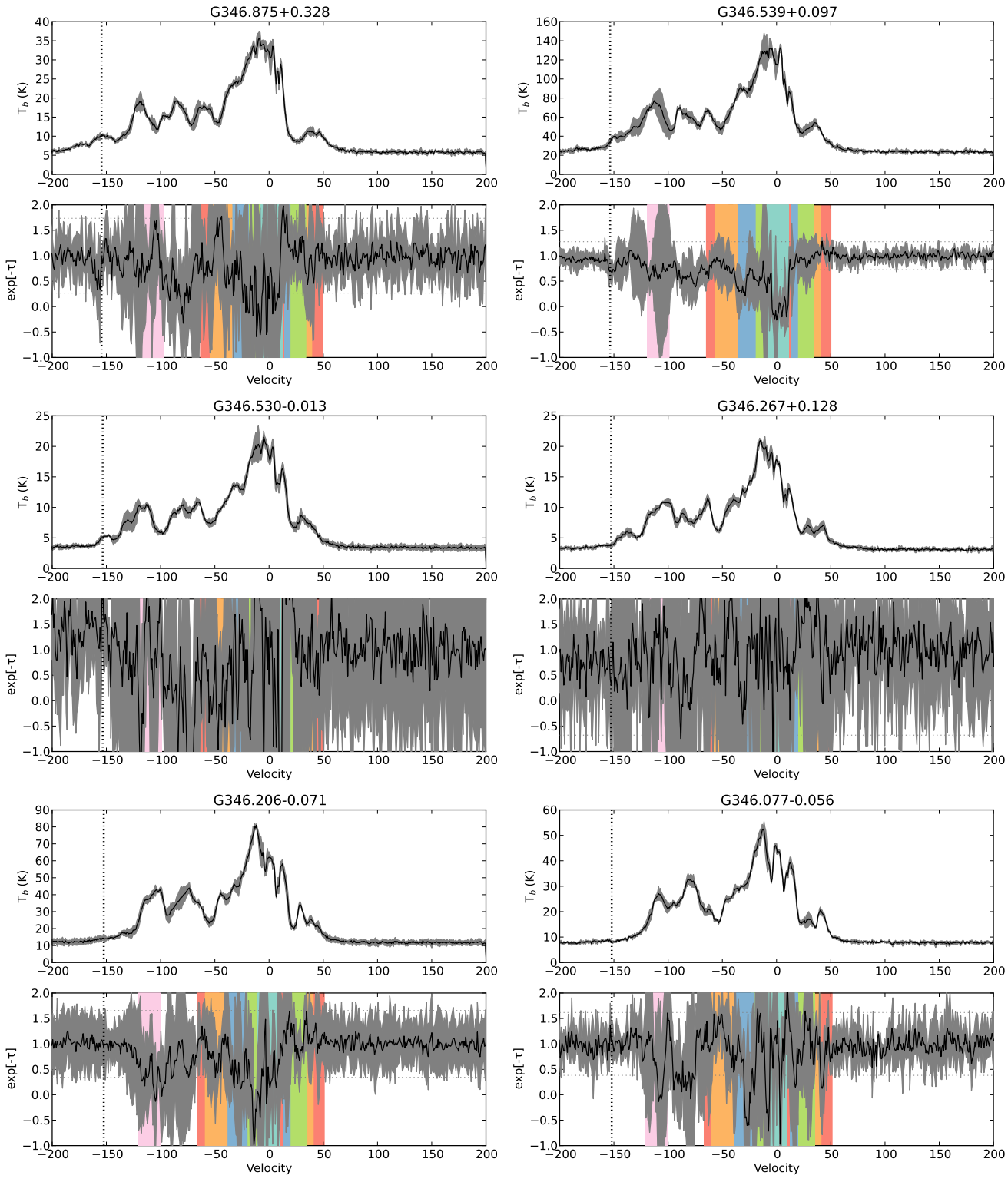
G346.875+0.328
G346.539+0.097
G346.530-0.013
G346.267+0.128
G346.206-0.071
G346.077-0.056
T_b (K)
exp[-τ]
Velocity

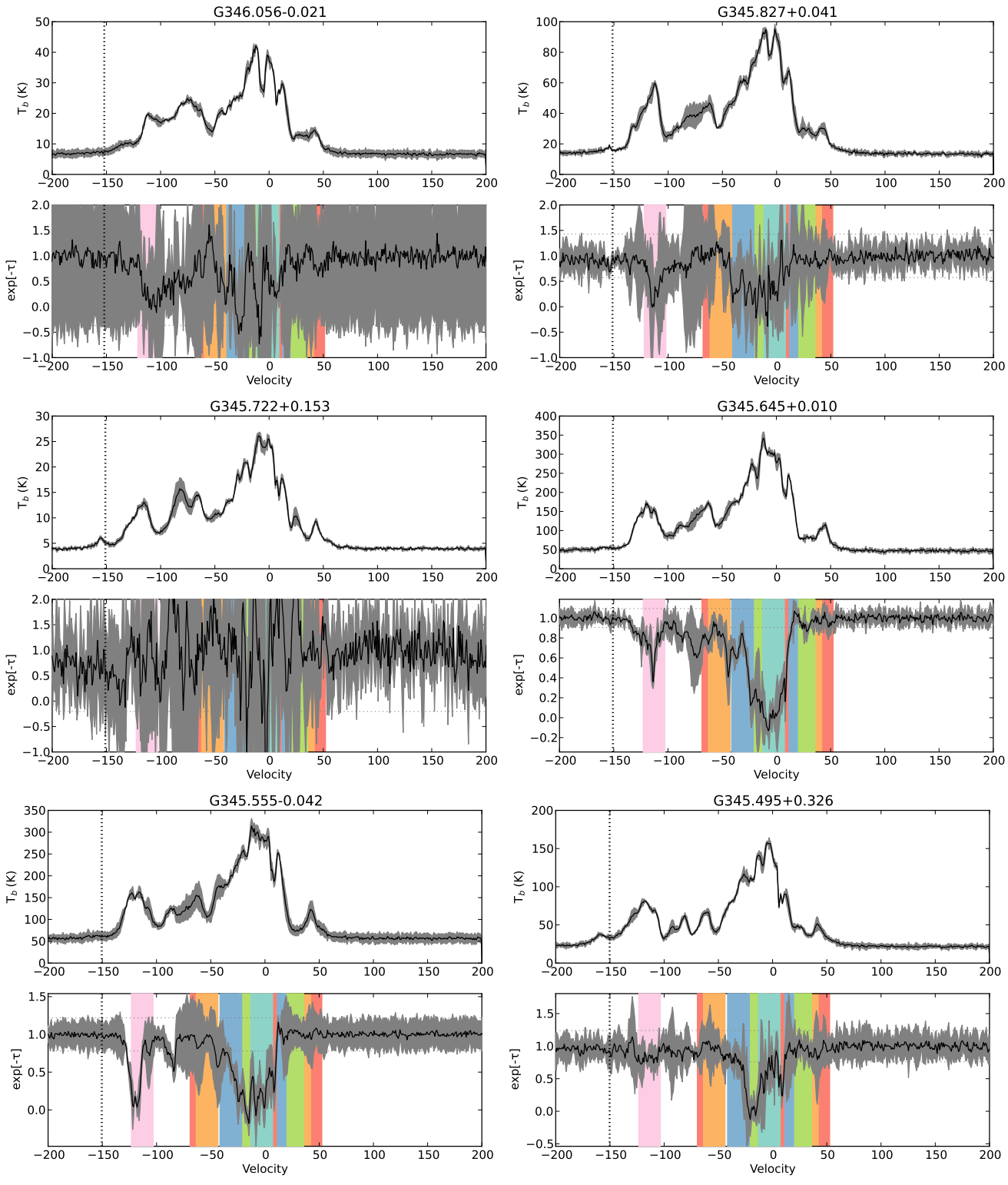
G346.056-0.021
G345.827+0.041
G345.722+0.153
G345.645+0.010
G345.555-0.042
G345.495+0.326
T_b (K)
exp[-τ]
Velocity

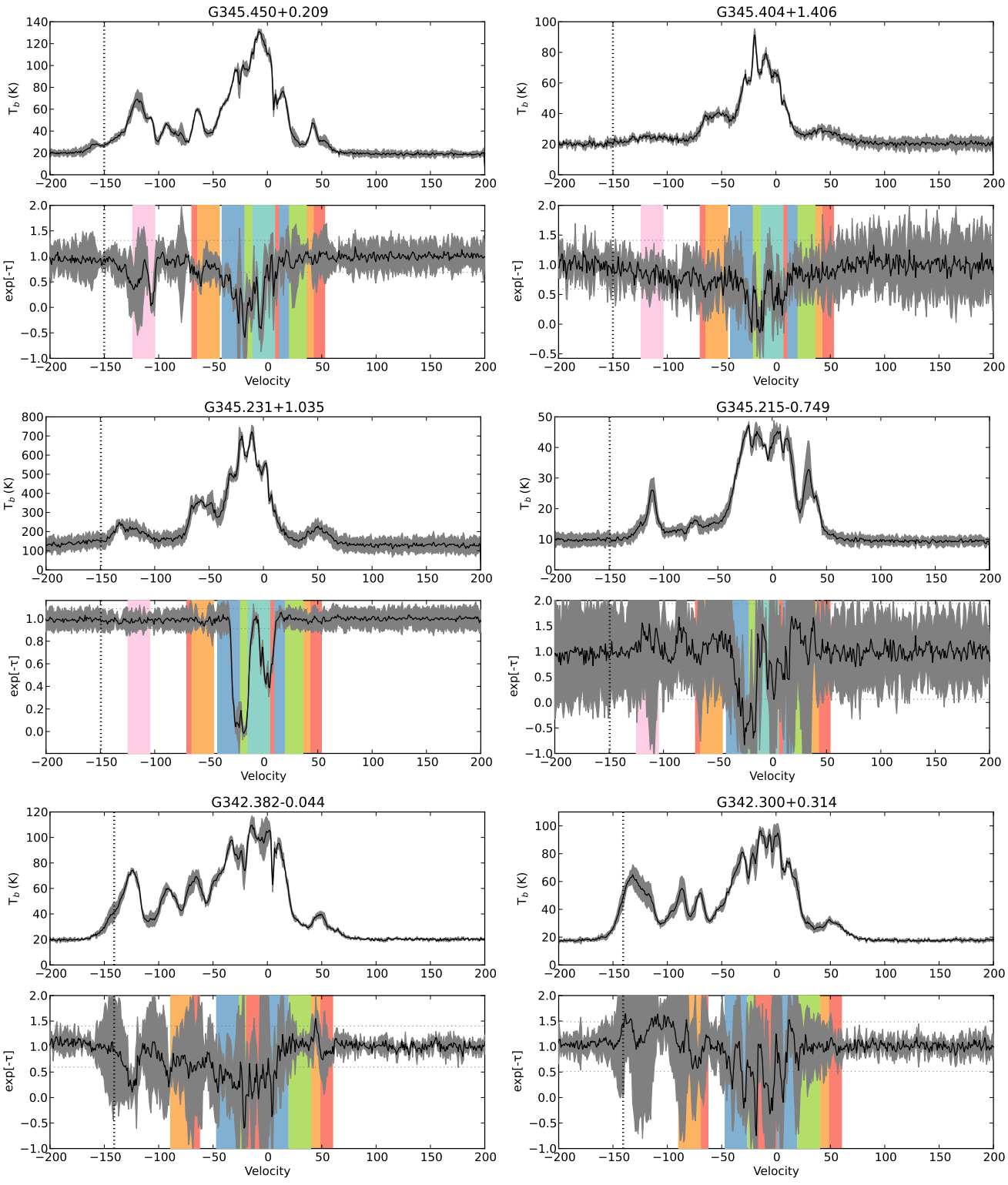
G345.450+0.209
G345.404+1.406
G345.231+1.035
G345.215-0.749
G342.382-0.044
G342.300+0.314
T_b (K)
exp[-τ]
Velocity

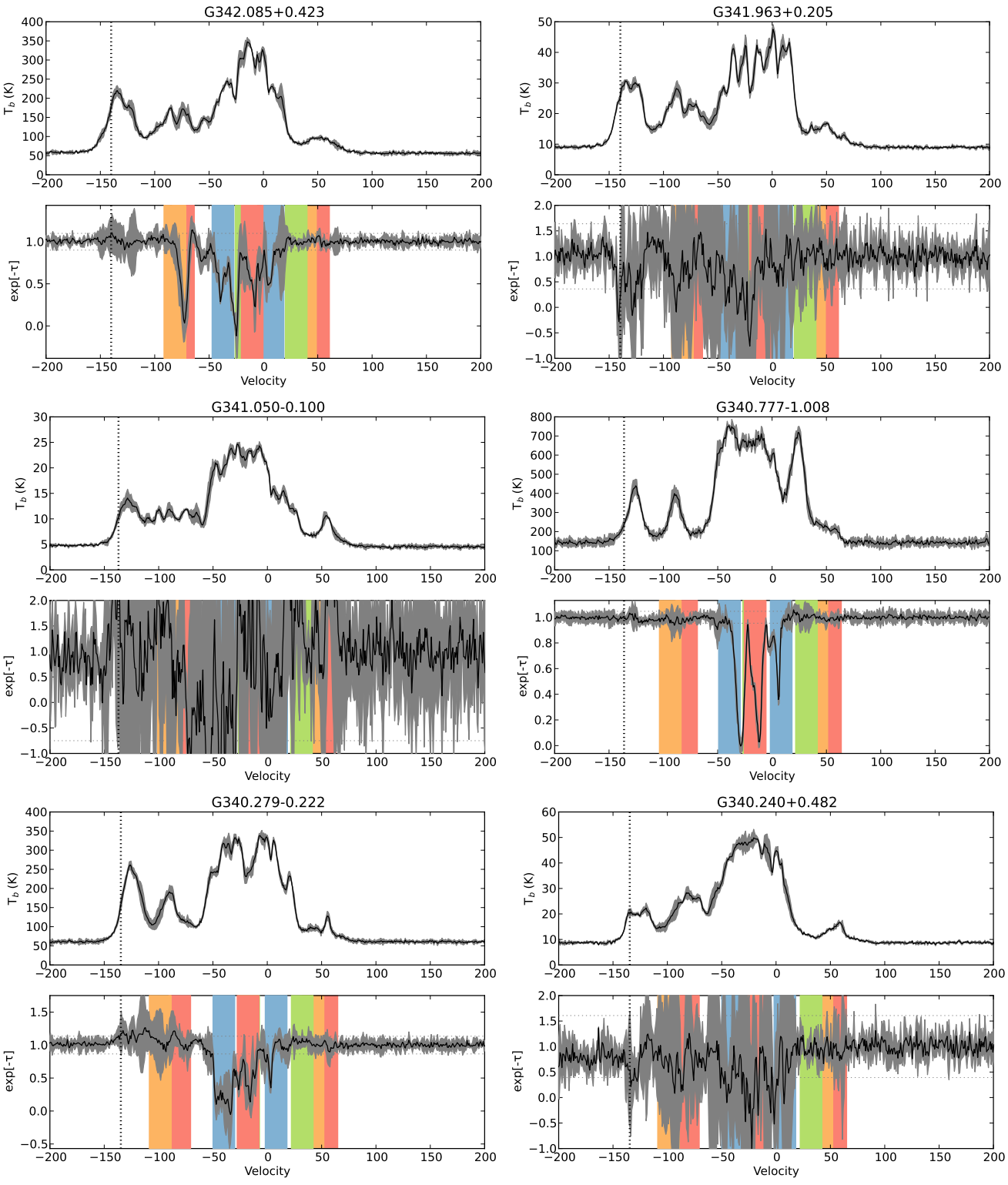
G342.085+0.423
G341.963+0.205
G341.050-0.100
G340.777-1.008
G340.279-0.222
G340.240+0.482
T_b (K)
exp[-τ]
Velocity

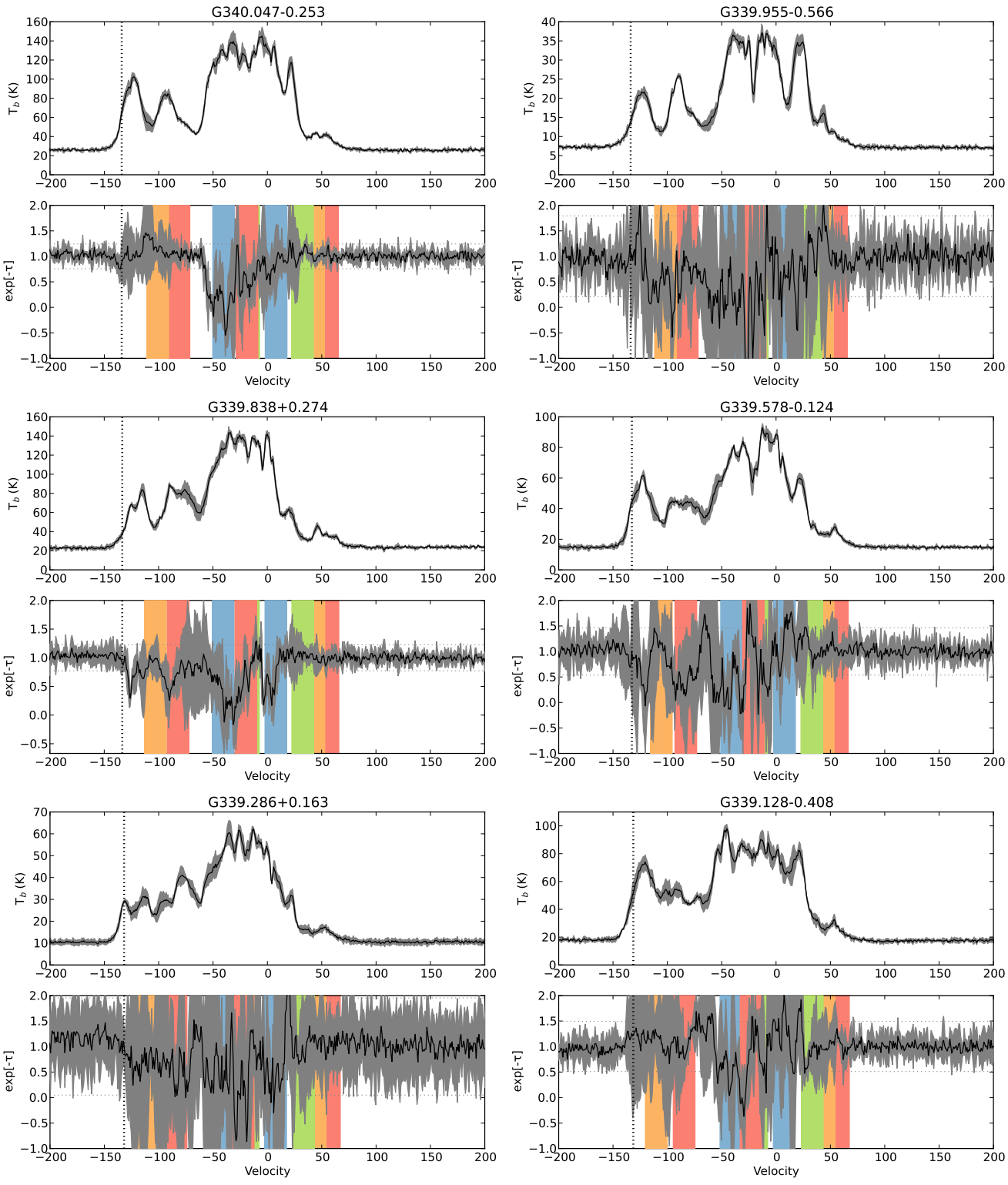
G340.047-0.253
G339.955-0.566
G339.838+0.274
G339.578-0.124
G339.286+0.163
G339.128-0.408
T_b (K)
exp[-τ]
Velocity

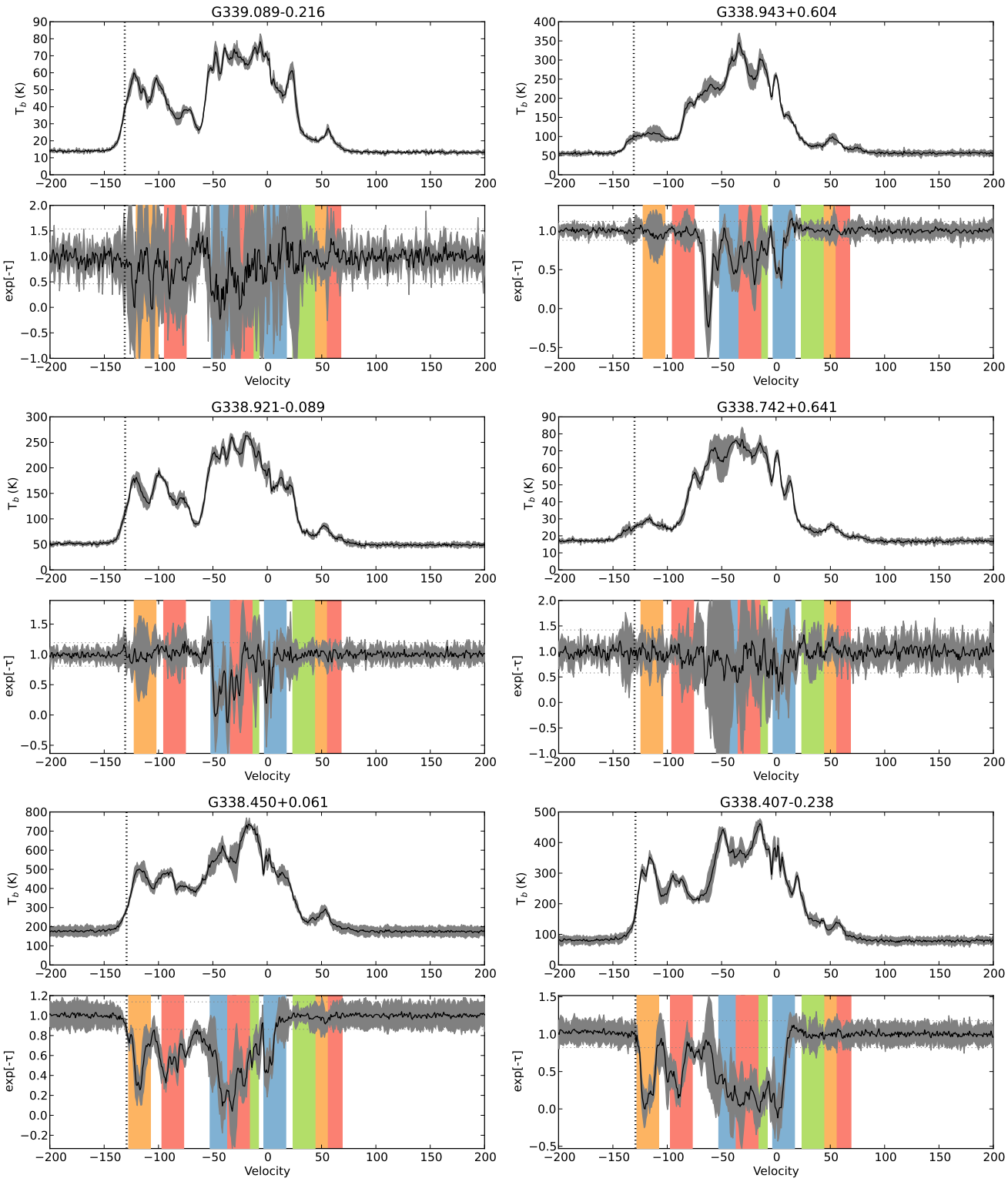
G339.089-0.216
G338.943+0.604
G338.921-0.089
G338.742+0.641
G338.450+0.061
G338.407-0.238
T_b (K)
exp[-τ]
Velocity

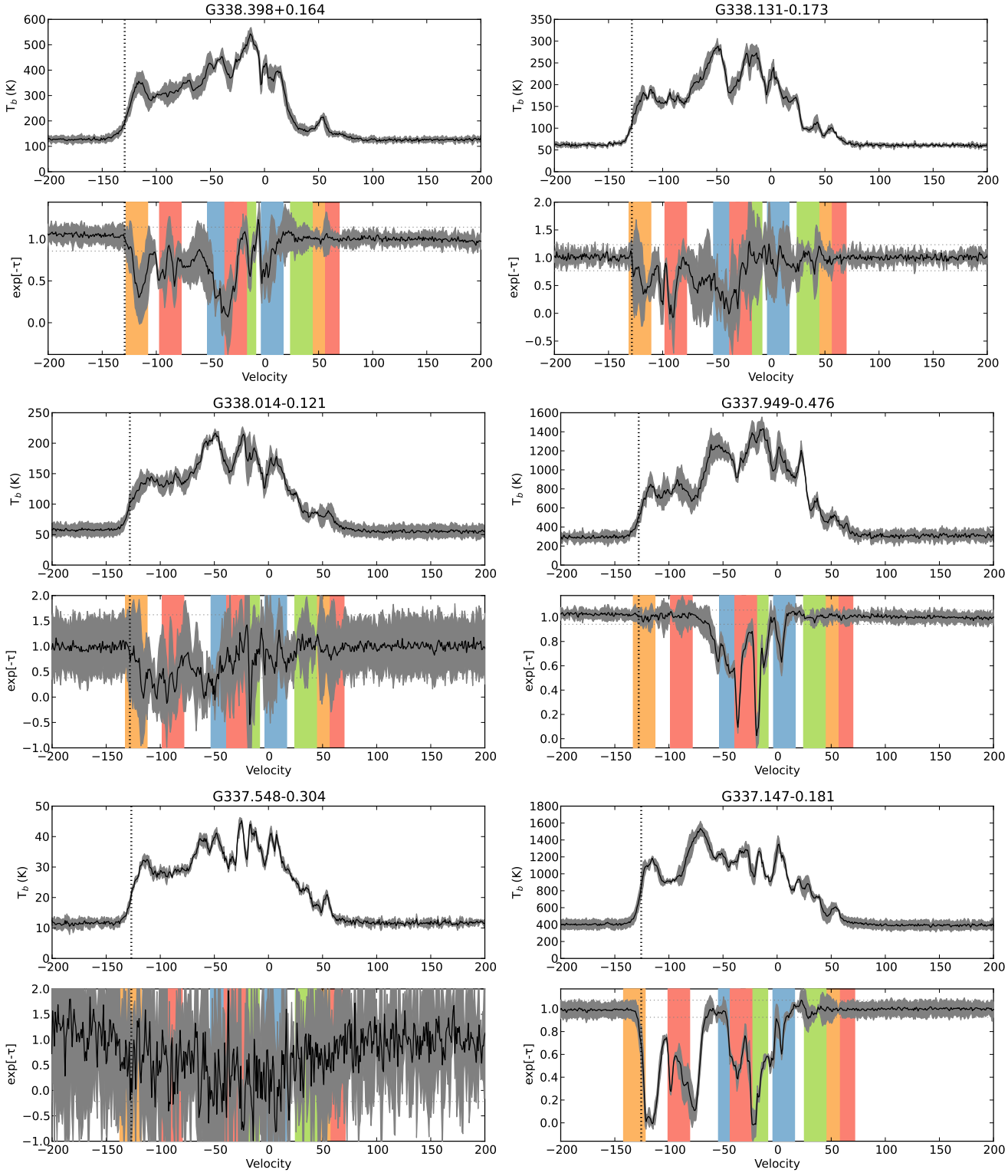
G338.398+0.164
G338.131-0.173
G338.014-0.121
G337.949-0.476
G337.548-0.304
G337.147-0.181
T_b (K)
exp[-τ]
Velocity

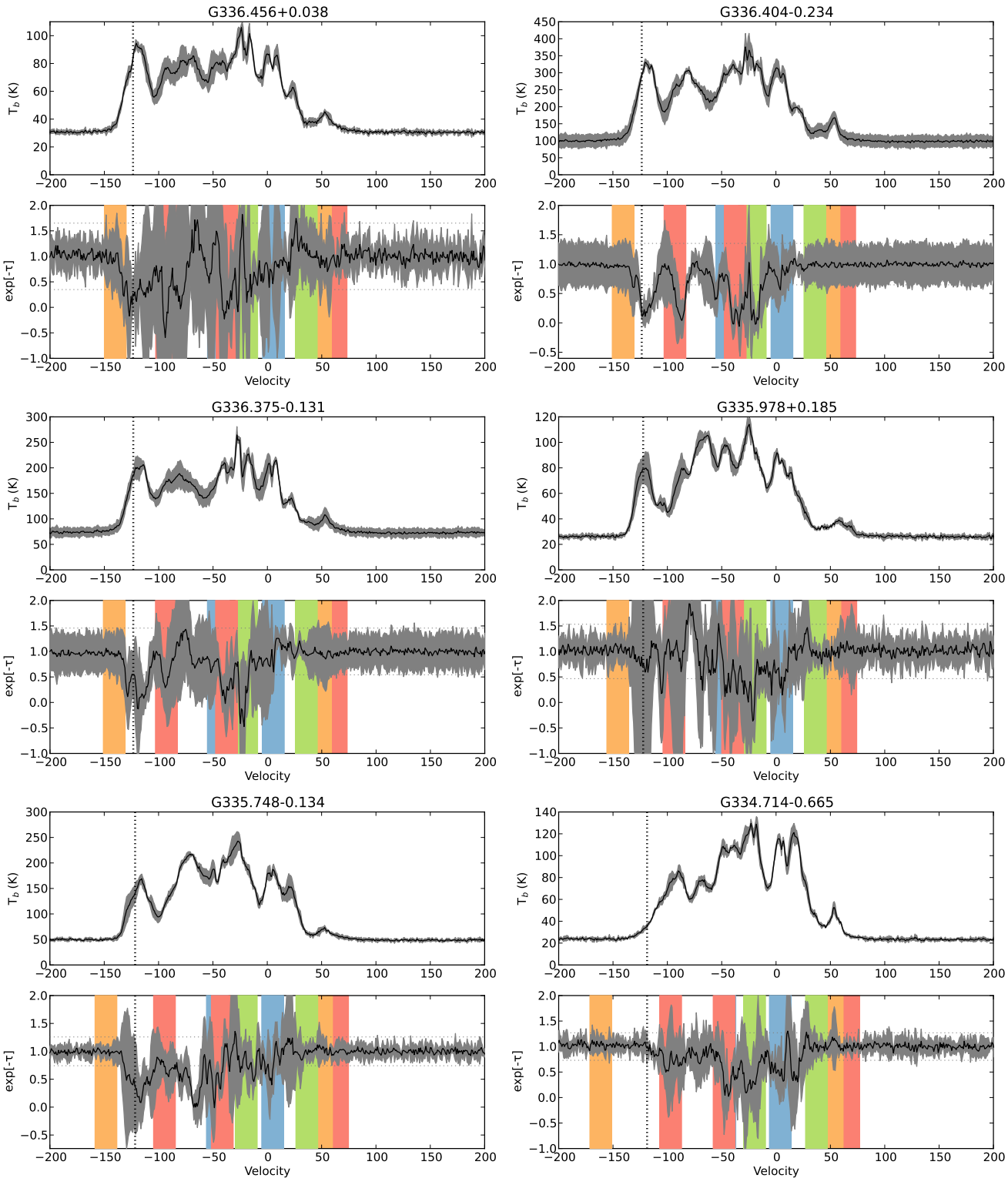
G336.456+0.038
G336.404-0.234
G336.375-0.131
G335.978+0.185
G335.748-0.134
G334.714-0.665
T_b (K)
exp[-τ]
Velocity

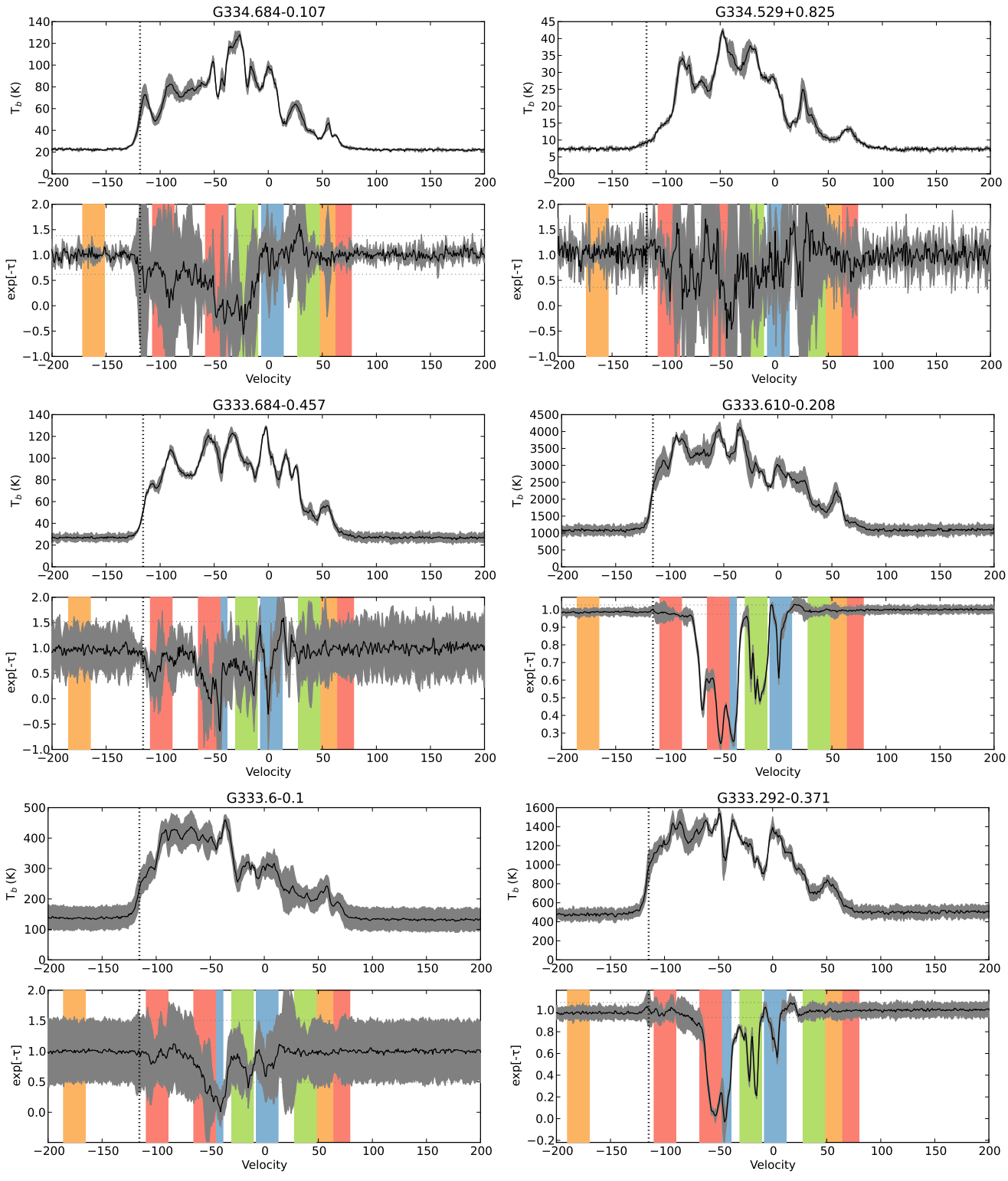
G334.684-0.107
G334.529+0.825
G333.684-0.457
G333.610-0.208
G333.6-0.1
G333.292-0.371
T_b (K)
exp[-τ]
Velocity

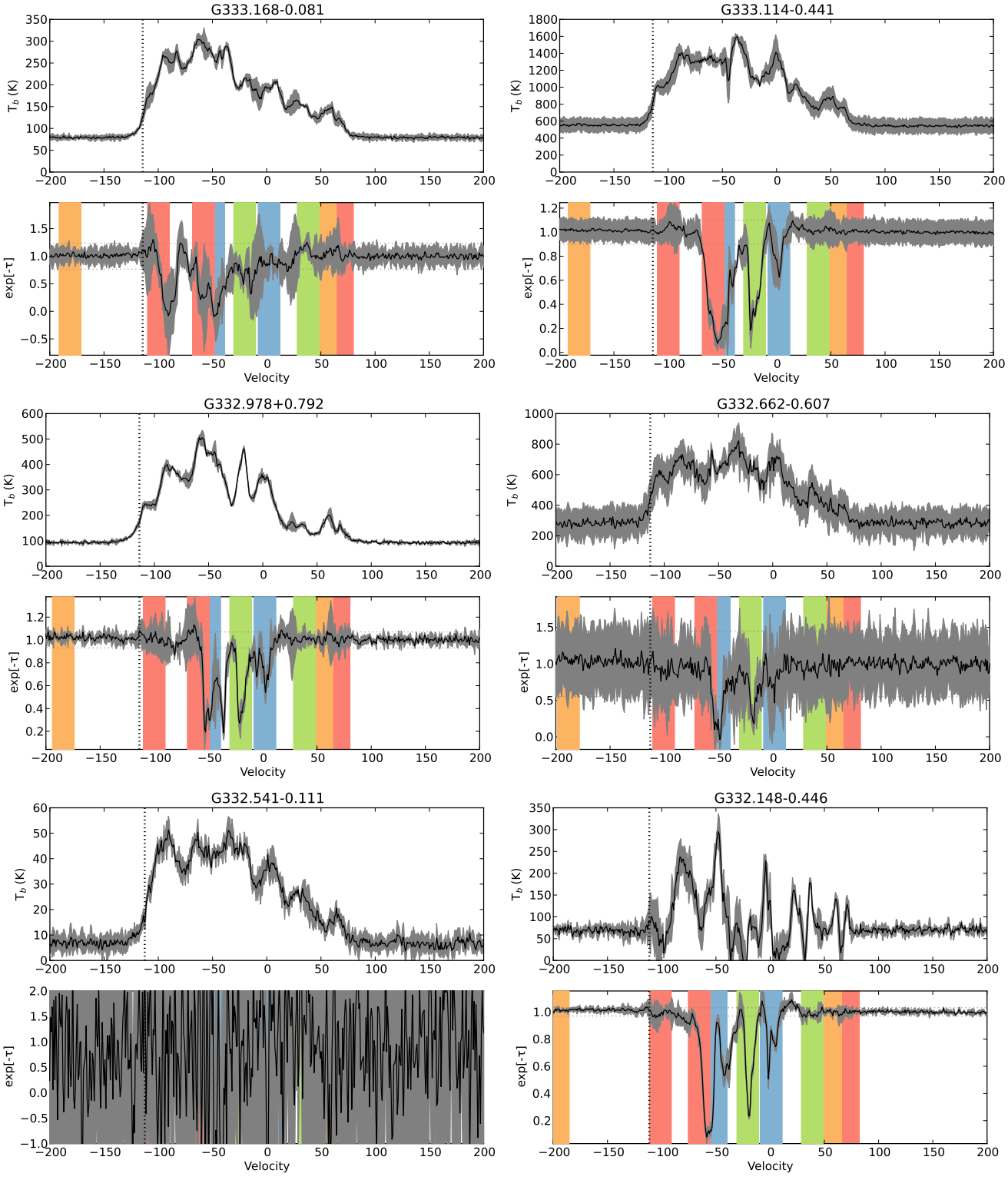
G333.168-0.081
G333.114-0.441
G332.978+0.792
G332.662-0.607
G332.541-0.111
G332.148-0.446
T_b (K)
exp[-τ]
Velocity

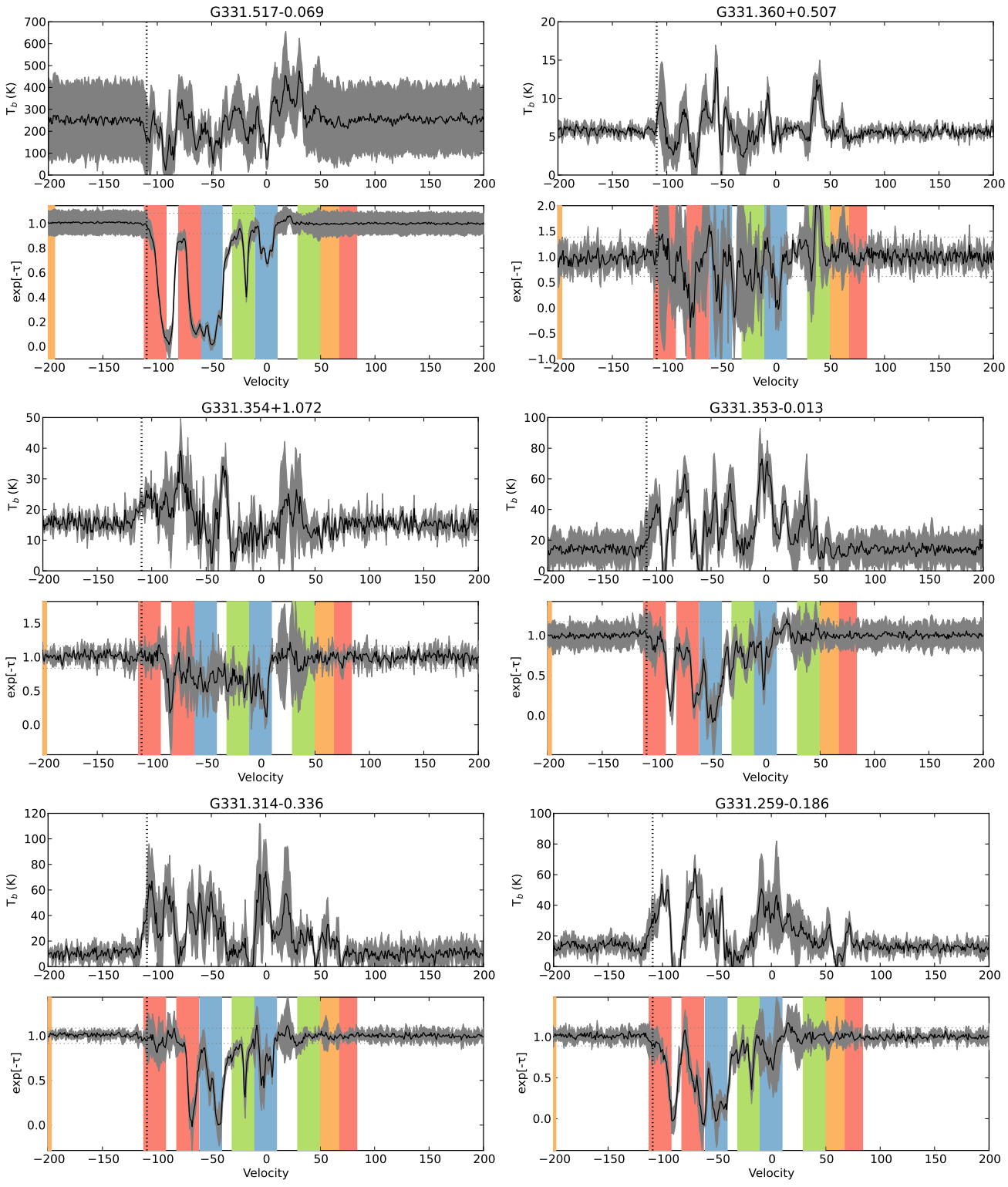
G331.517-0.069
G331.360+0.507
G331.354+1.072
G331.353-0.013
G331.314-0.336
G331.259-0.186
T_b (K)
exp[-τ]
Velocity

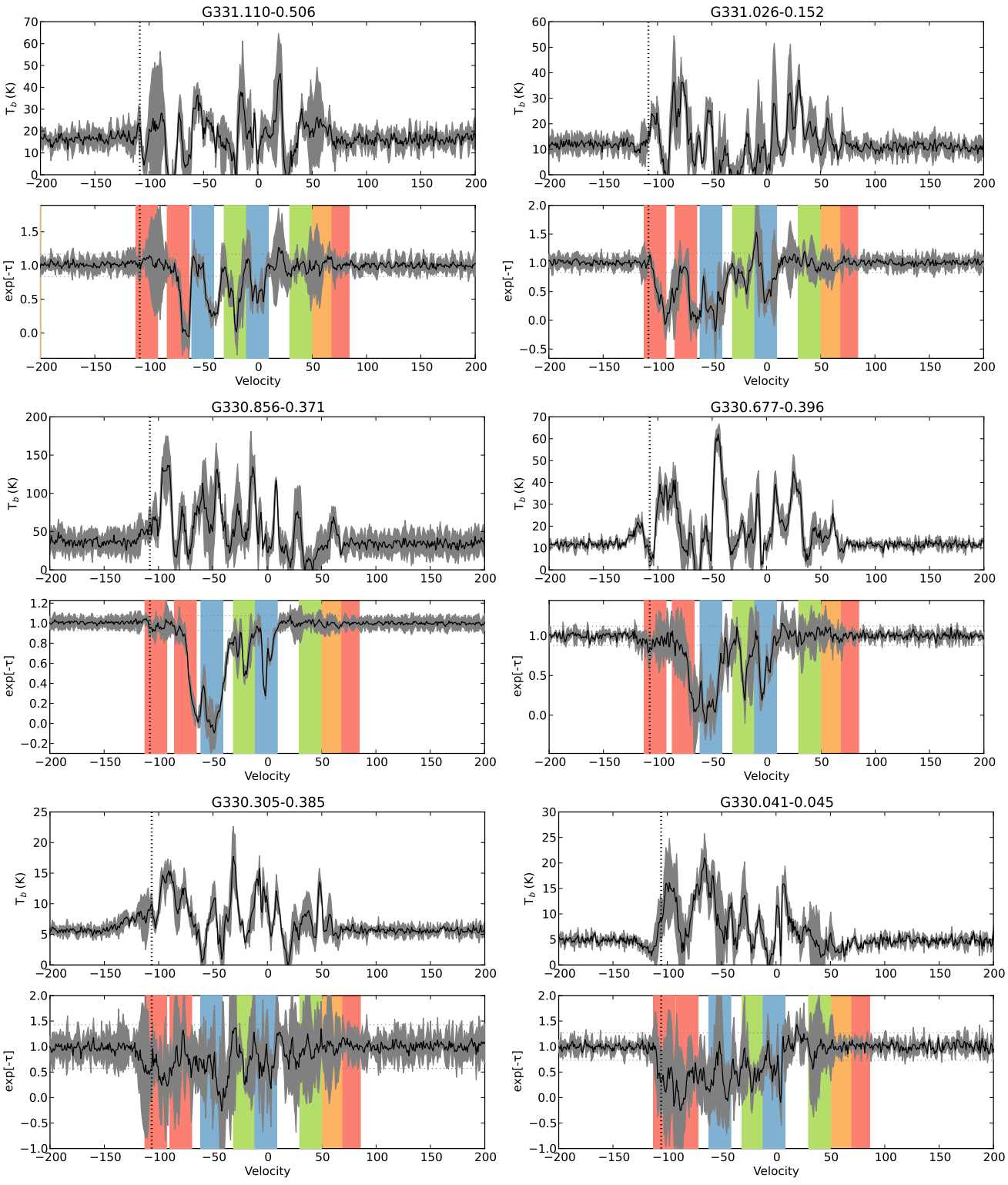
G331.110-0.506
G331.026-0.152
G330.856-0.371
G330.677-0.396
G330.305-0.385
G330.041-0.045
T_b (K)
exp[-τ]
Velocity

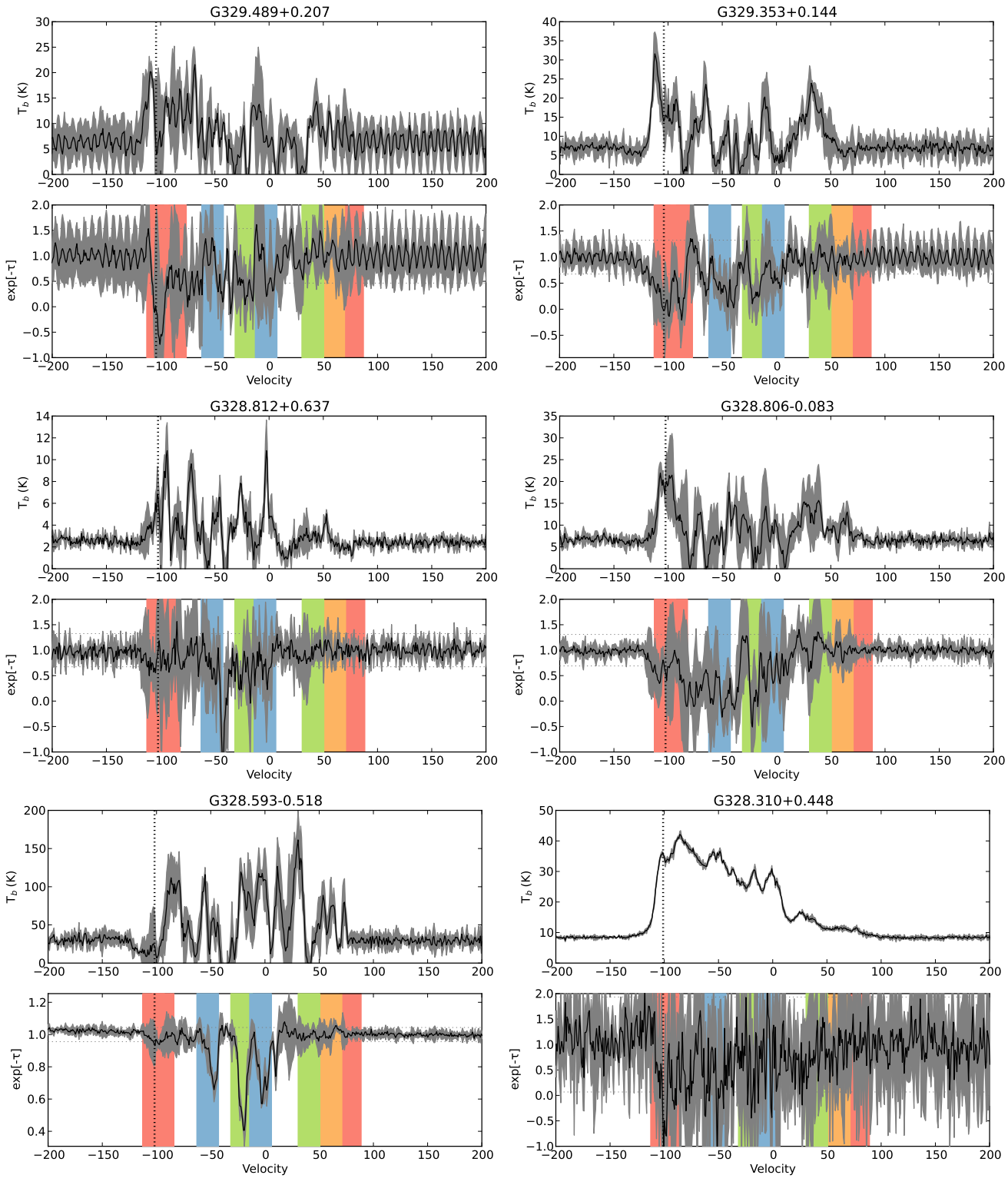
G329.489+0.207
G329.353+0.144
G328.812+0.637
G328.806-0.083
G328.593-0.518
G328.310+0.448
T_b (K)
exp[-τ]
Velocity

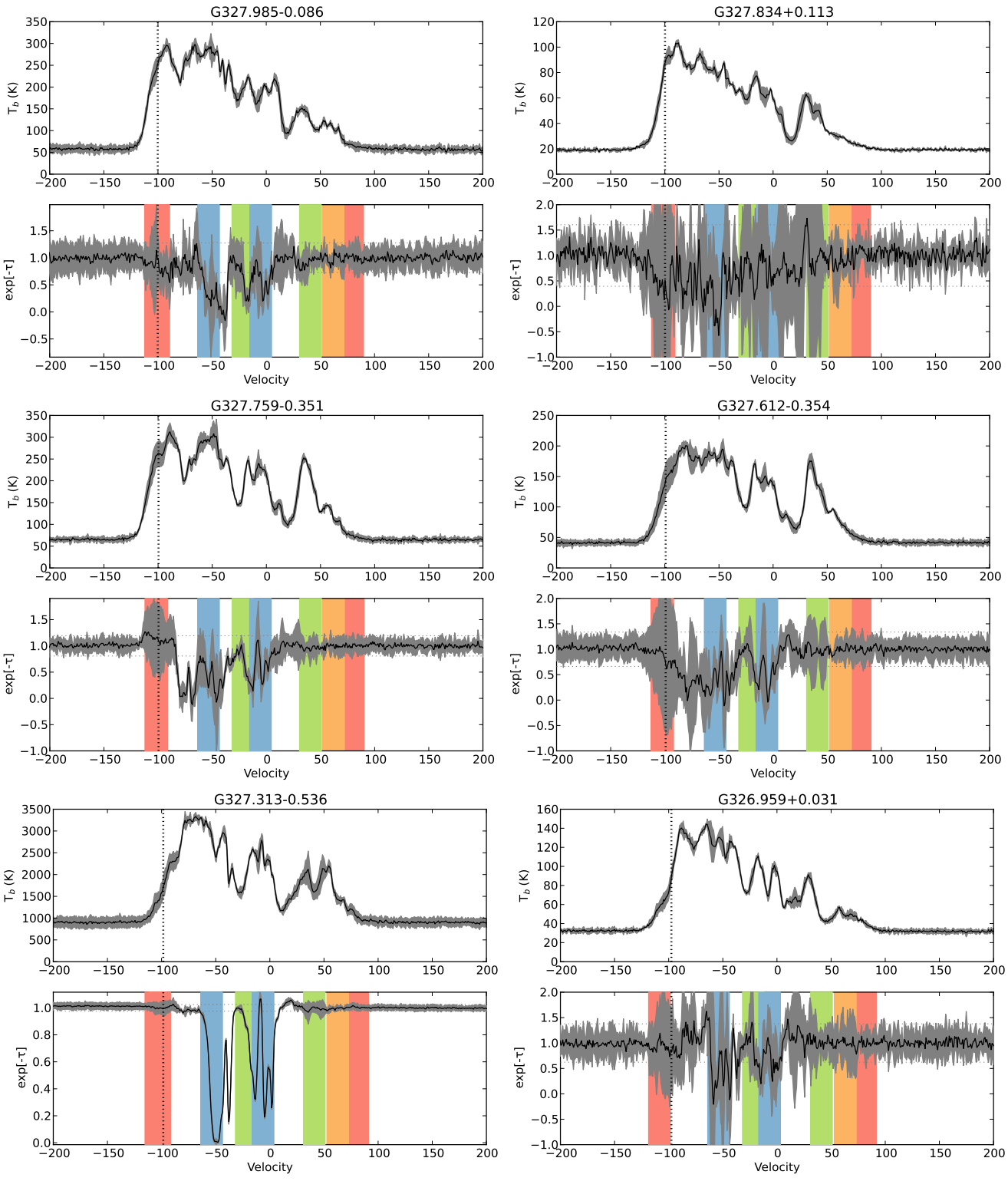
G327.985-0.086
G327.834+0.113
G327.759-0.351
G327.612-0.354
G327.313-0.536
G326.959+0.031
T_b (K)
exp[-τ]
Velocity

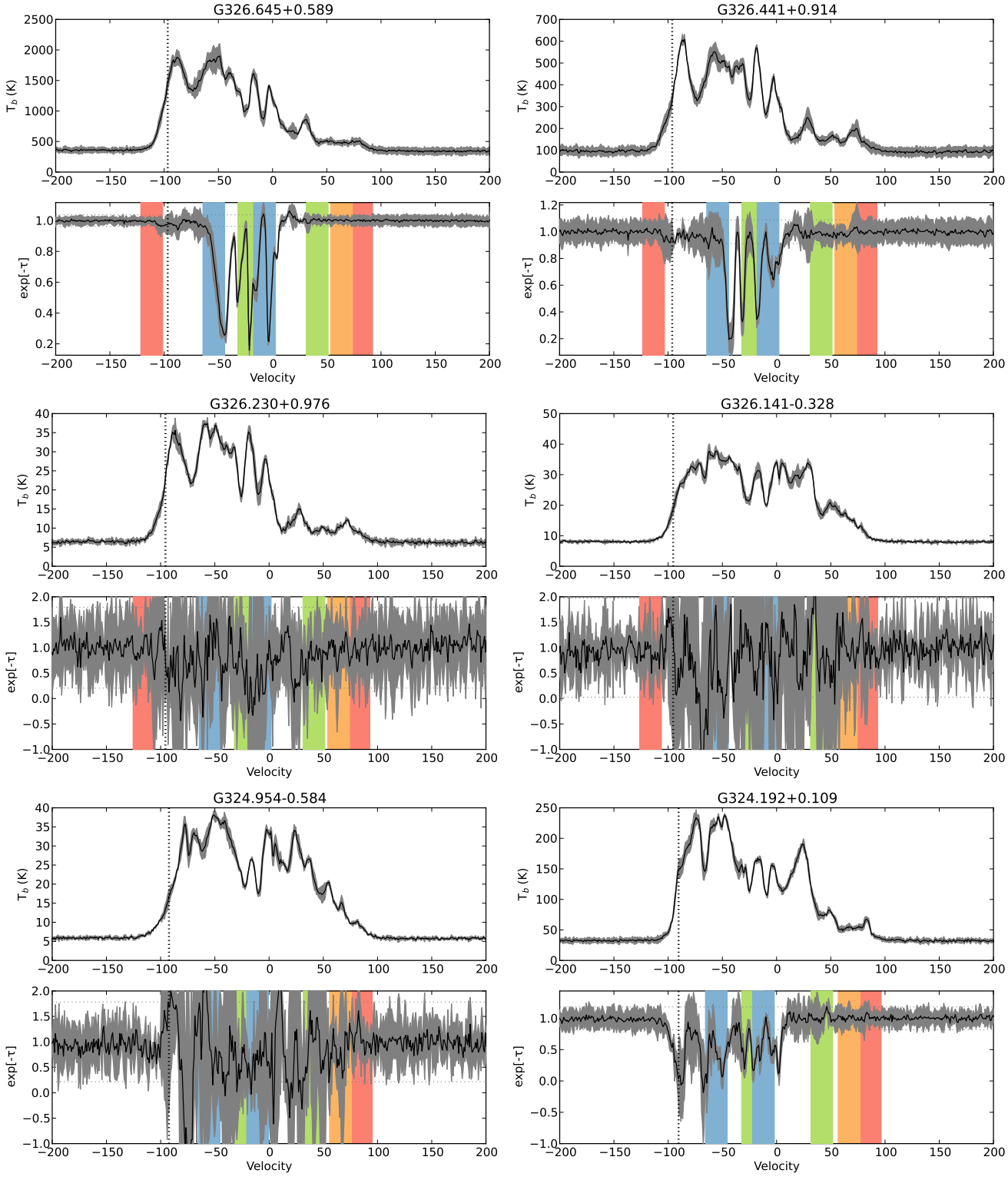
G326.645+0.589
G326.441+0.914
G326.230+0.976
G326.141-0.328
G324.954-0.584
G324.192+0.109
T_b (K)
exp[-τ]
Velocity

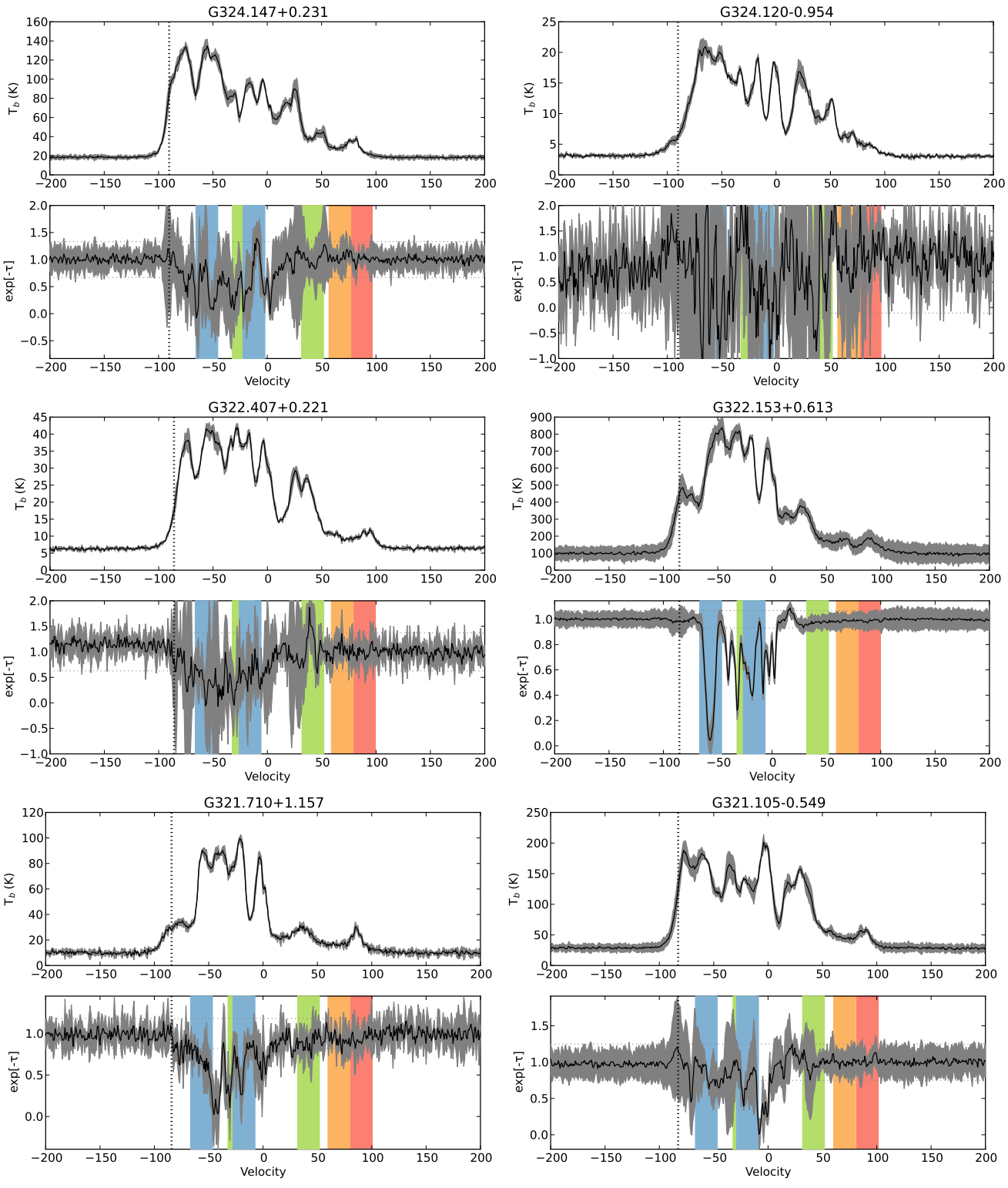
G324.147+0.231
G324.120-0.954
G322.407+0.221
G322.153+0.613
G321.710+1.157
G321.105-0.549
T_b (K)
exp[-τ]
Velocity

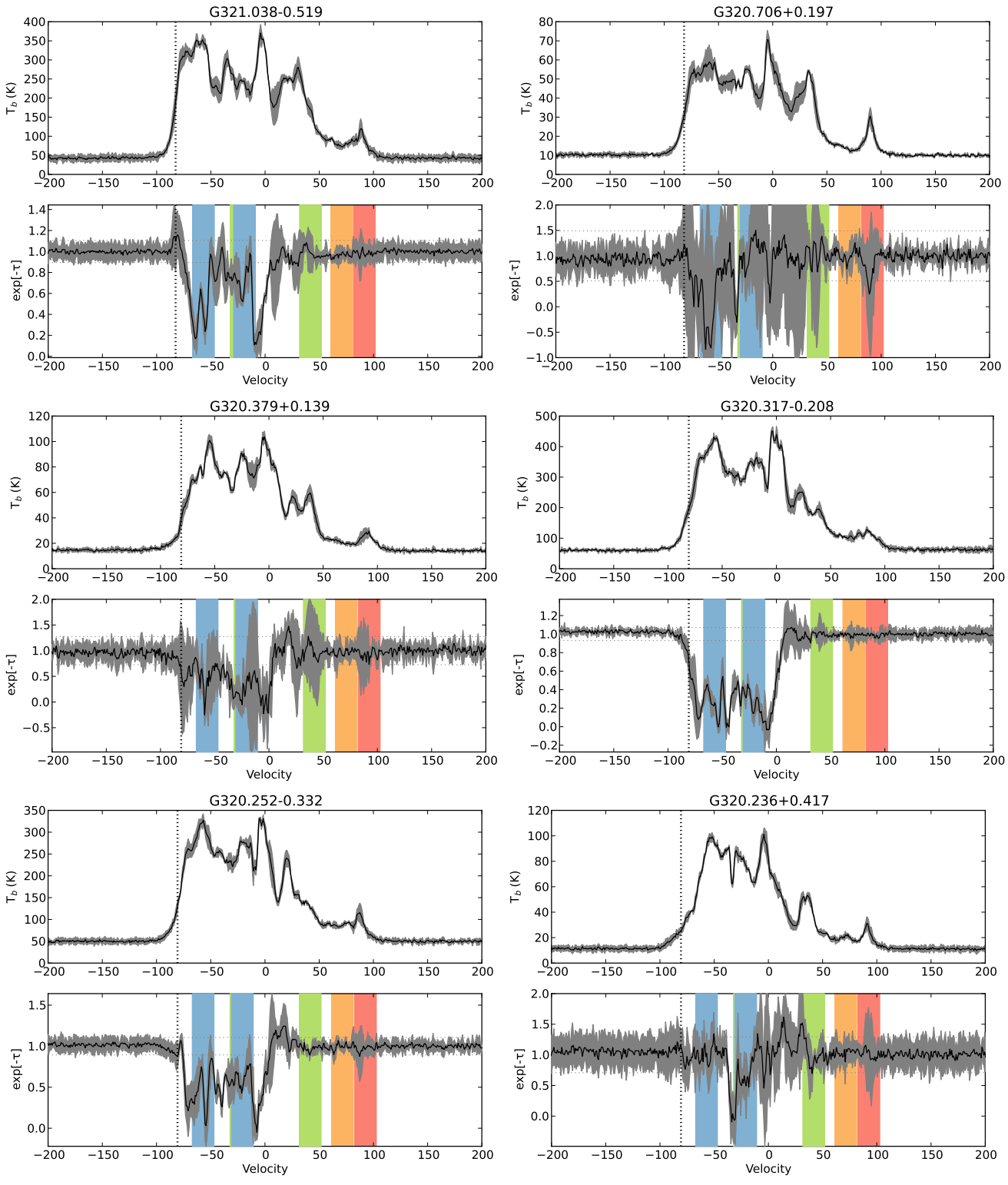
G321.038-0.519
G320.706+0.197
G320.379+0.139
G320.317-0.208
G320.252-0.332
G320.236+0.417
T_b (K)
exp[-τ]
Velocity

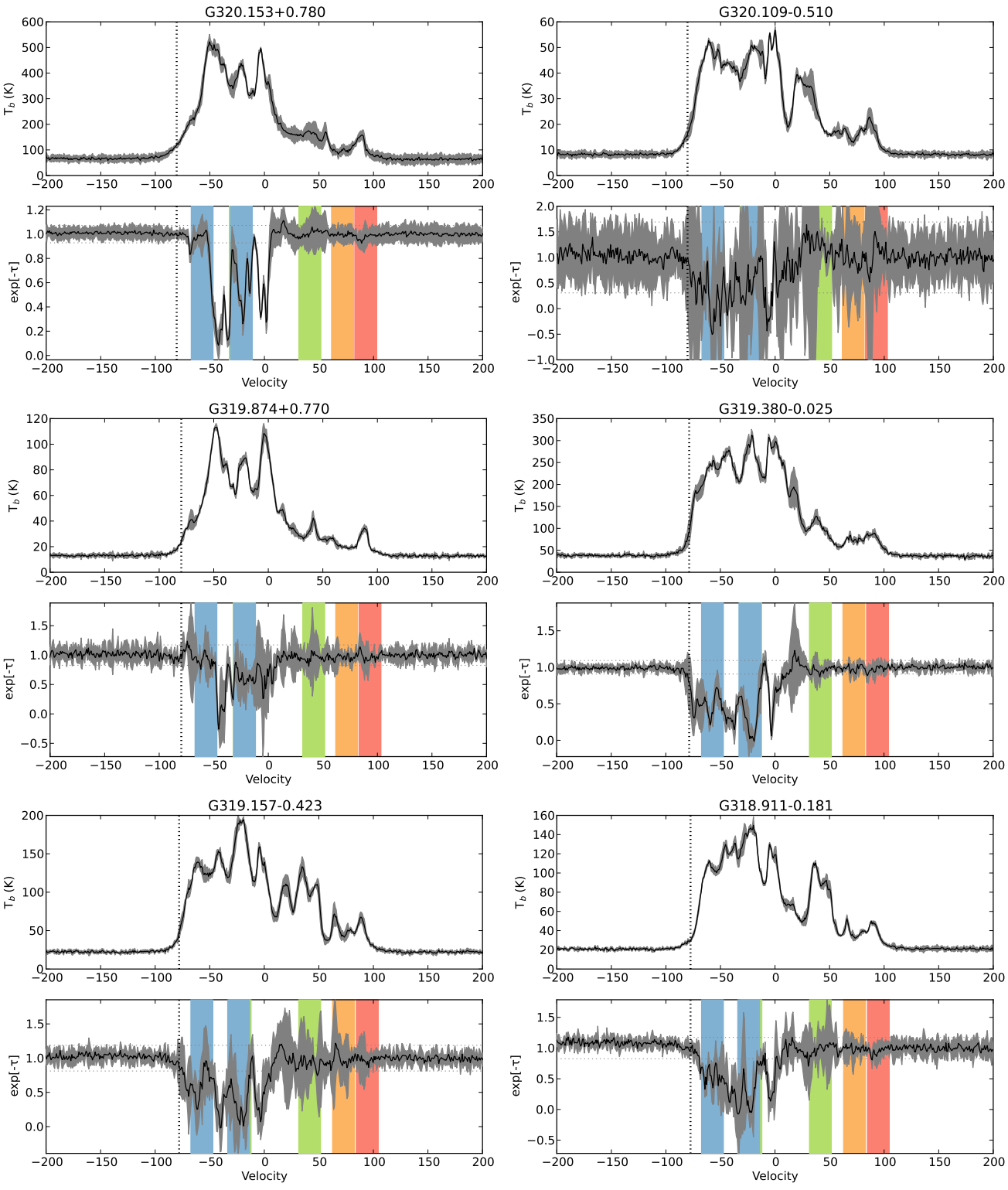
G320.153+0.780
G320.109-0.510
G319.874+0.770
G319.380-0.025
G319.157-0.423
G318.911-0.181
T_b (K)
exp[-τ]
Velocity

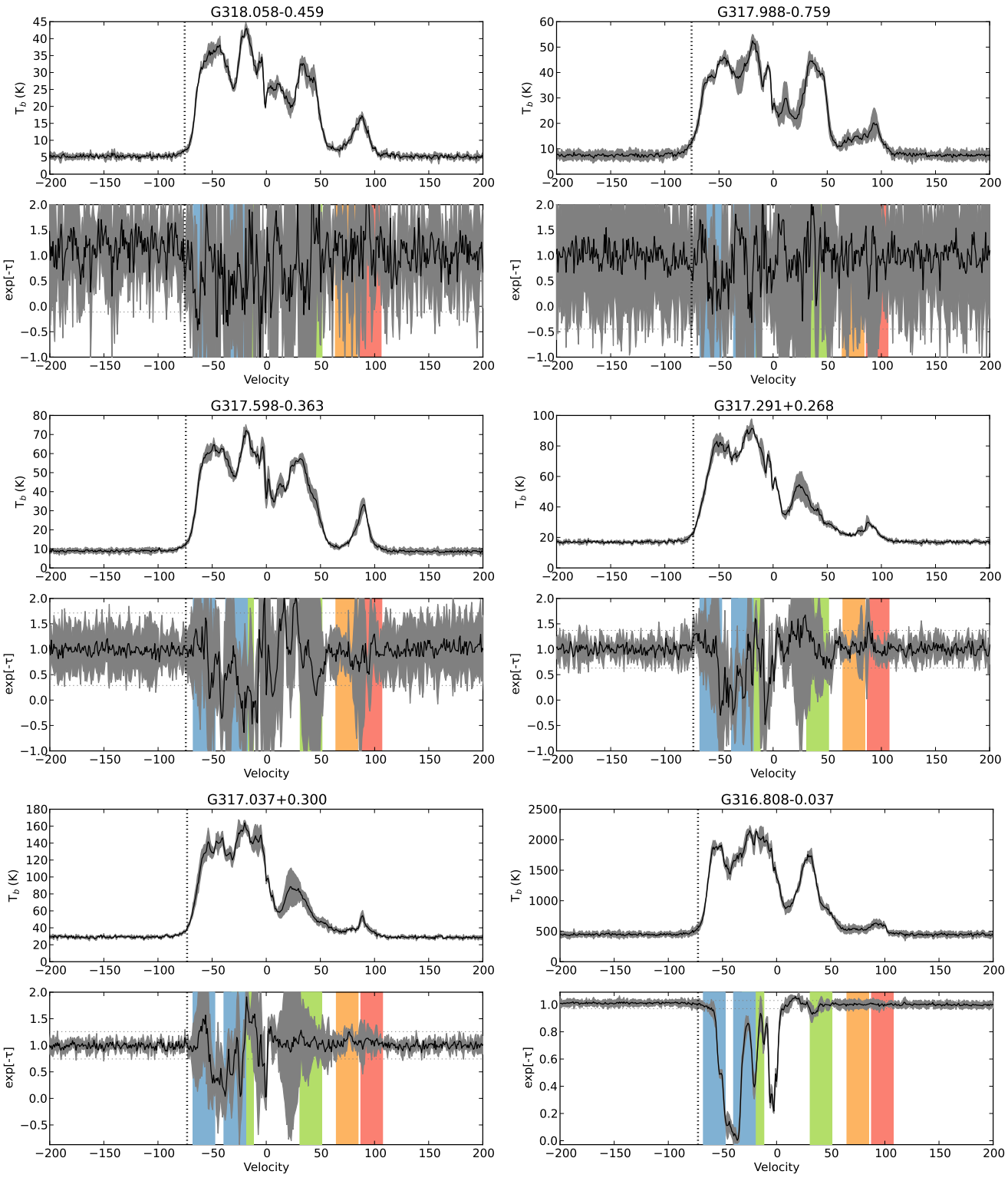
G318.058-0.459
G317.988-0.759
G317.598-0.363
G317.291+0.268
G317.037+0.300
G316.808-0.037
T_b (K)
exp[-τ]
Velocity

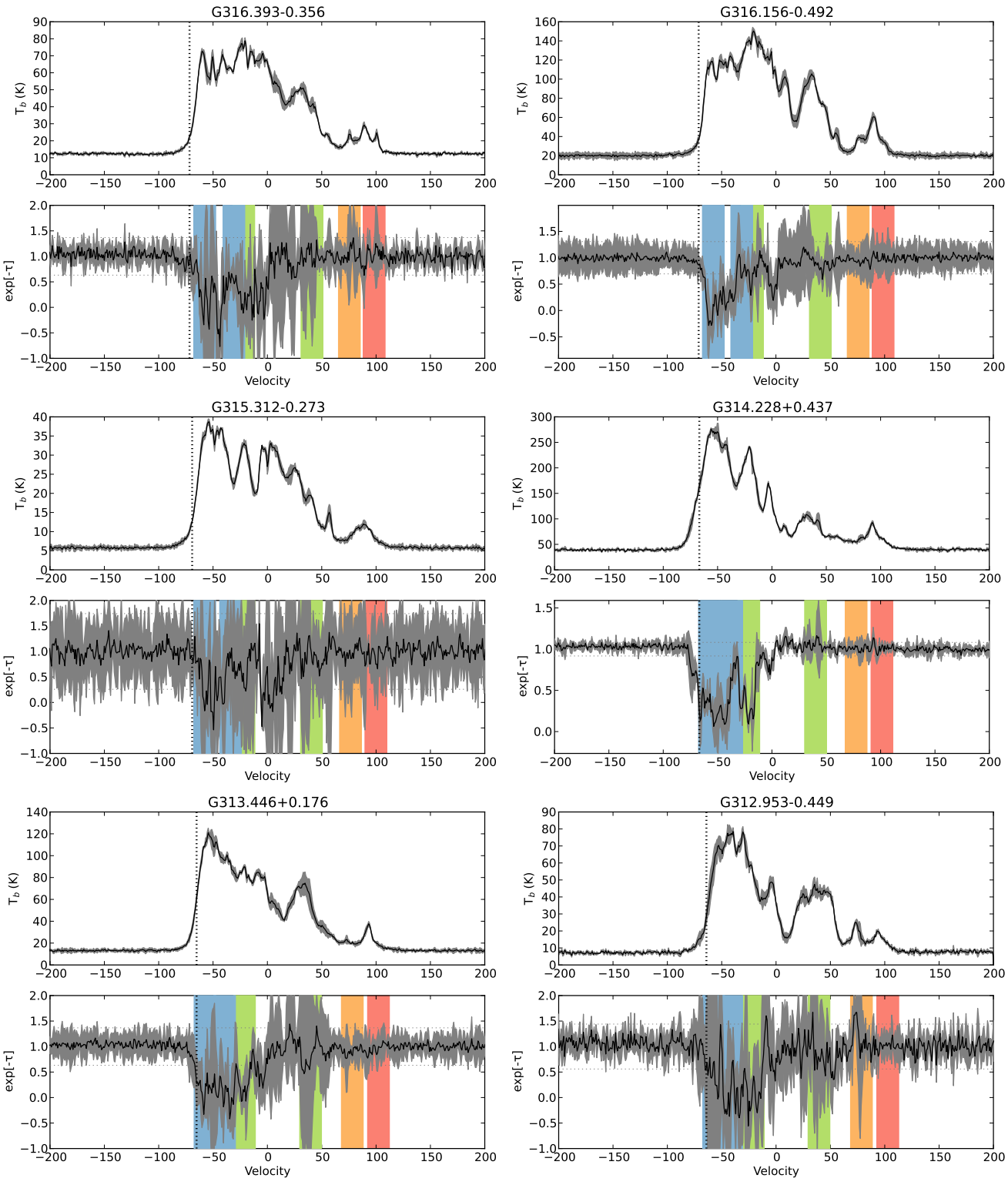
G316.393-0.356
G316.156-0.492
G315.312-0.273
G314.228+0.437
G313.446+0.176
G312.953-0.449
T_b (K)
exp[-τ]
Velocity

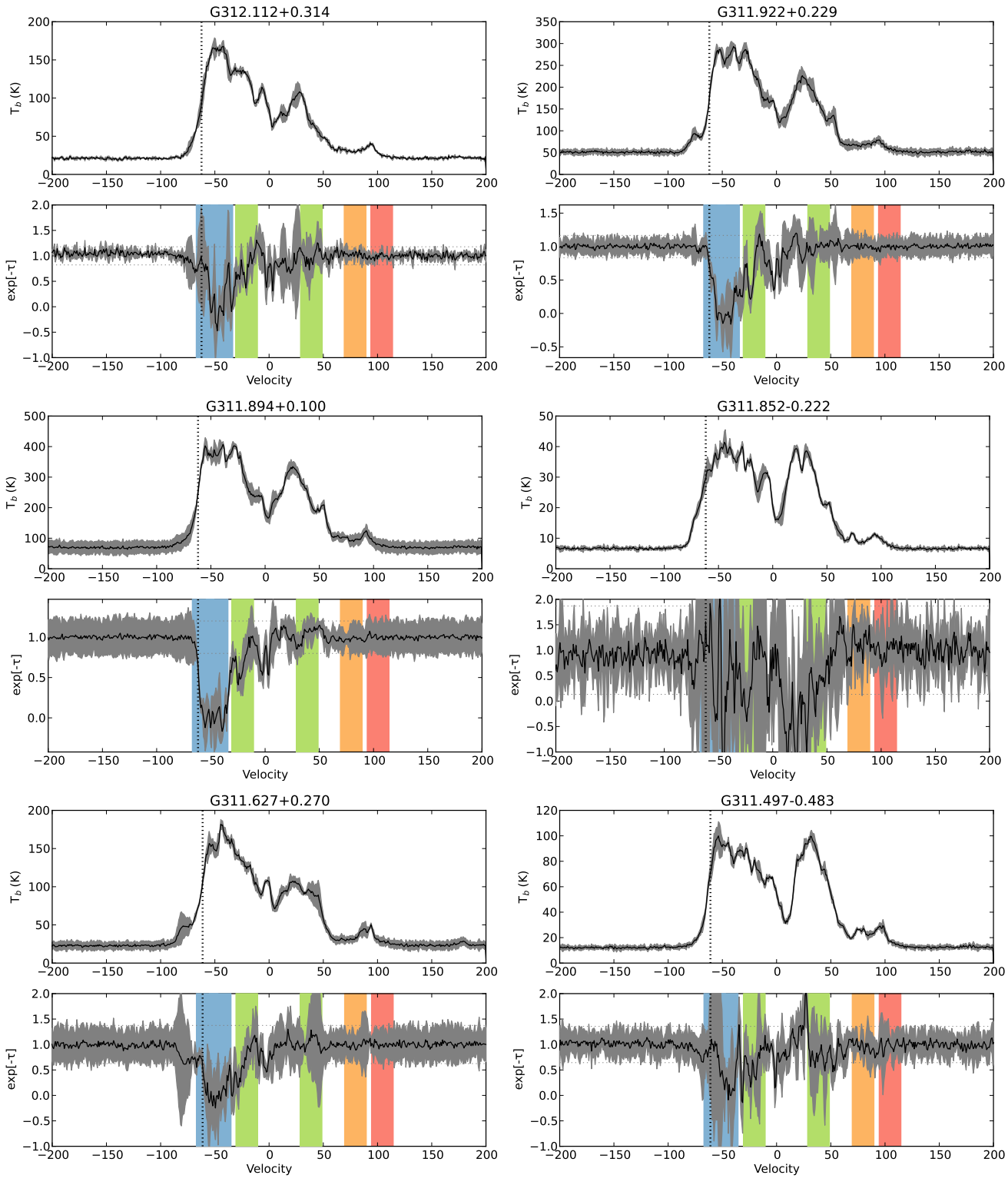
G312.112+0.314
G311.922+0.229
G311.894+0.100
G311.852-0.222
G311.627+0.270
G311.497-0.483
T_b (K)
exp[-τ]
Velocity

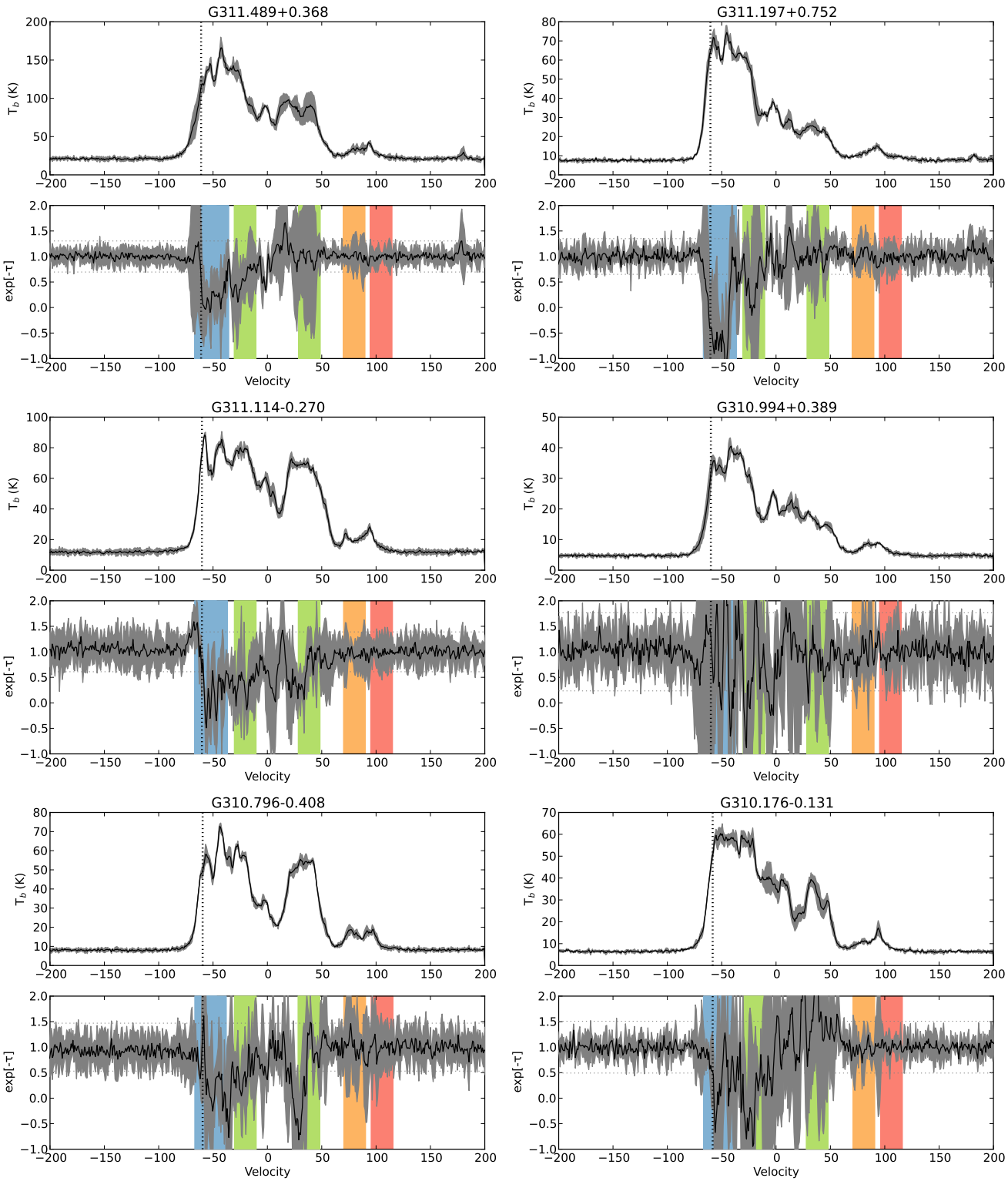
G311.489+0.368
G311.197+0.752
G311.114-0.270
G310.994+0.389
G310.796-0.408
G310.176-0.131
T_b (K)
exp[-τ]
Velocity

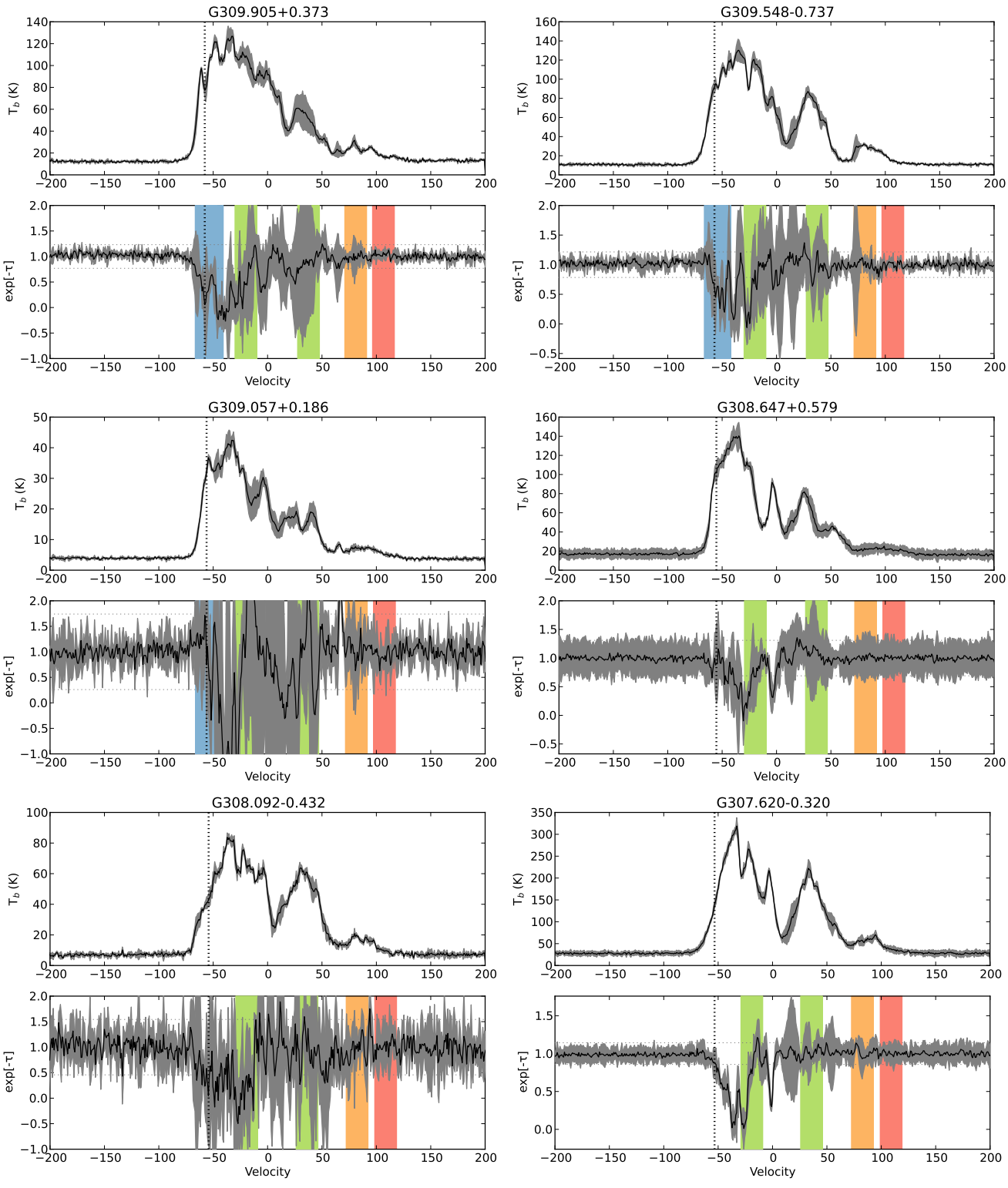
G309.905+0.373
G309.548-0.737
G309.057+0.186
G308.647+0.579
G308.092-0.432
G307.620-0.320
T_b (K)
exp[-τ]
Velocity

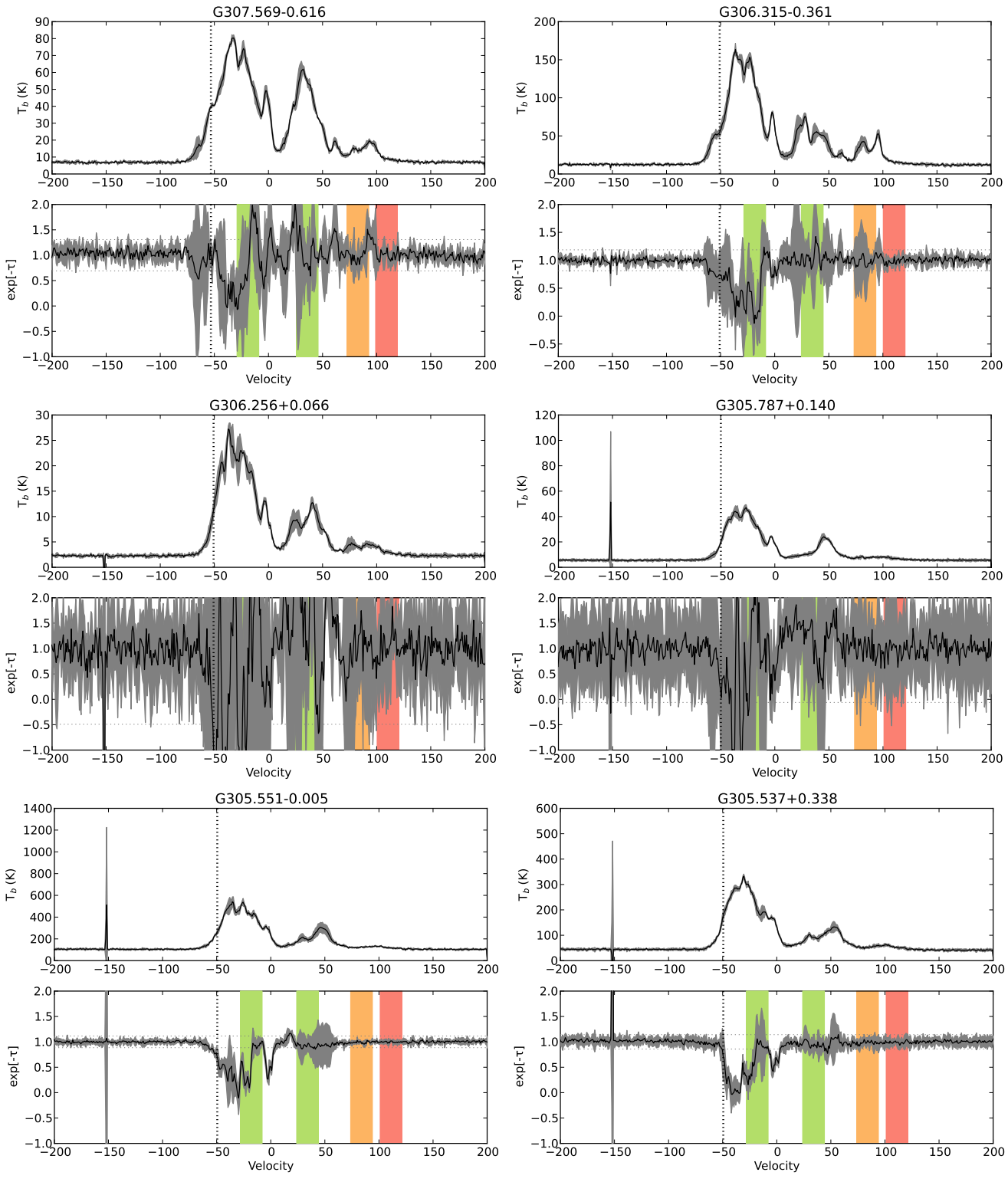
G307.569-0.616
G306.315-0.361
G306.256+0.066
G305.787+0.140
G305.551-0.005
G305.537+0.338
T_b (K)
exp[-τ]
Velocity

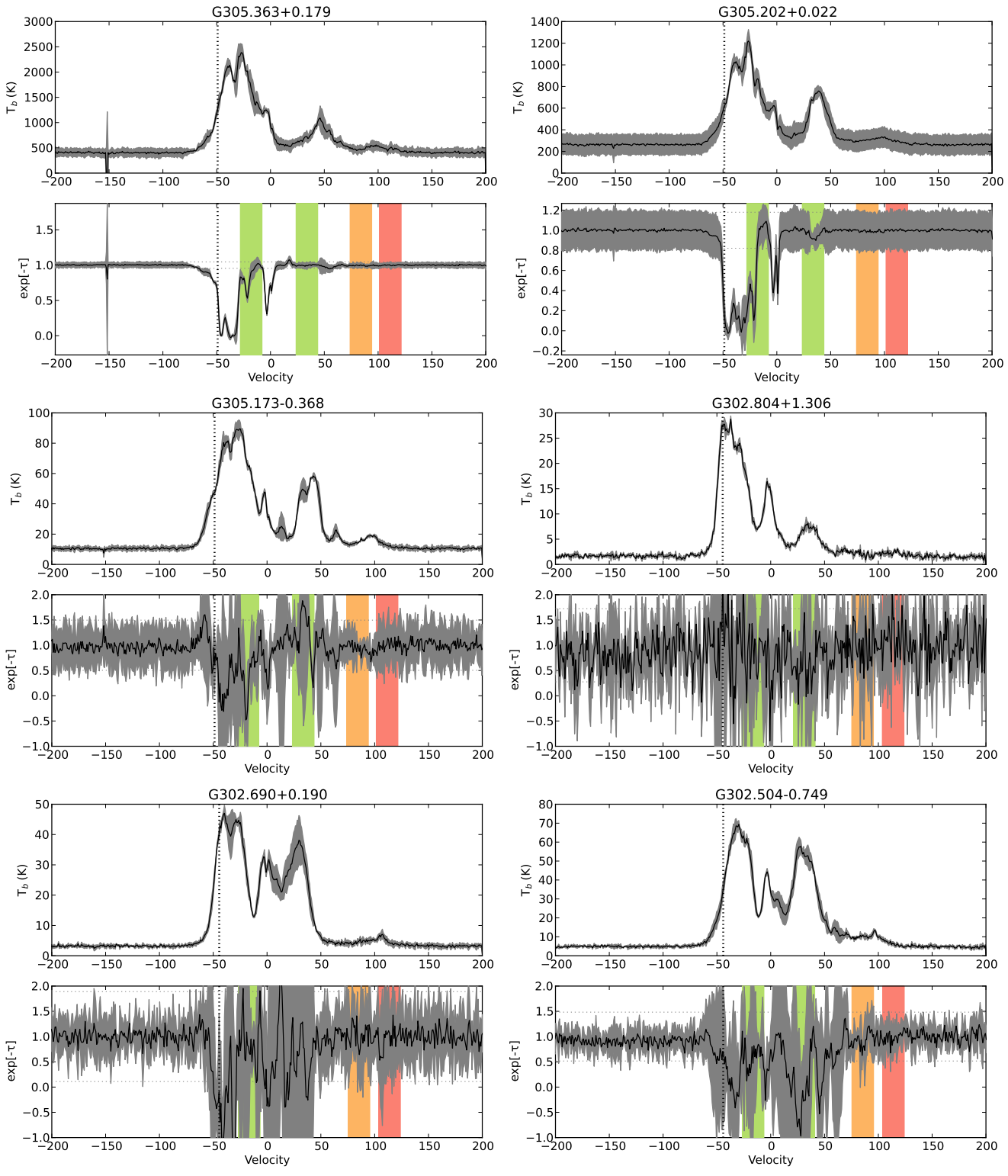
G305.363+0.179
G305.202+0.022
G305.173-0.368
G302.804+1.306
G302.690+0.190
G302.504-0.749
T_b (K)
exp[-τ]
Velocity

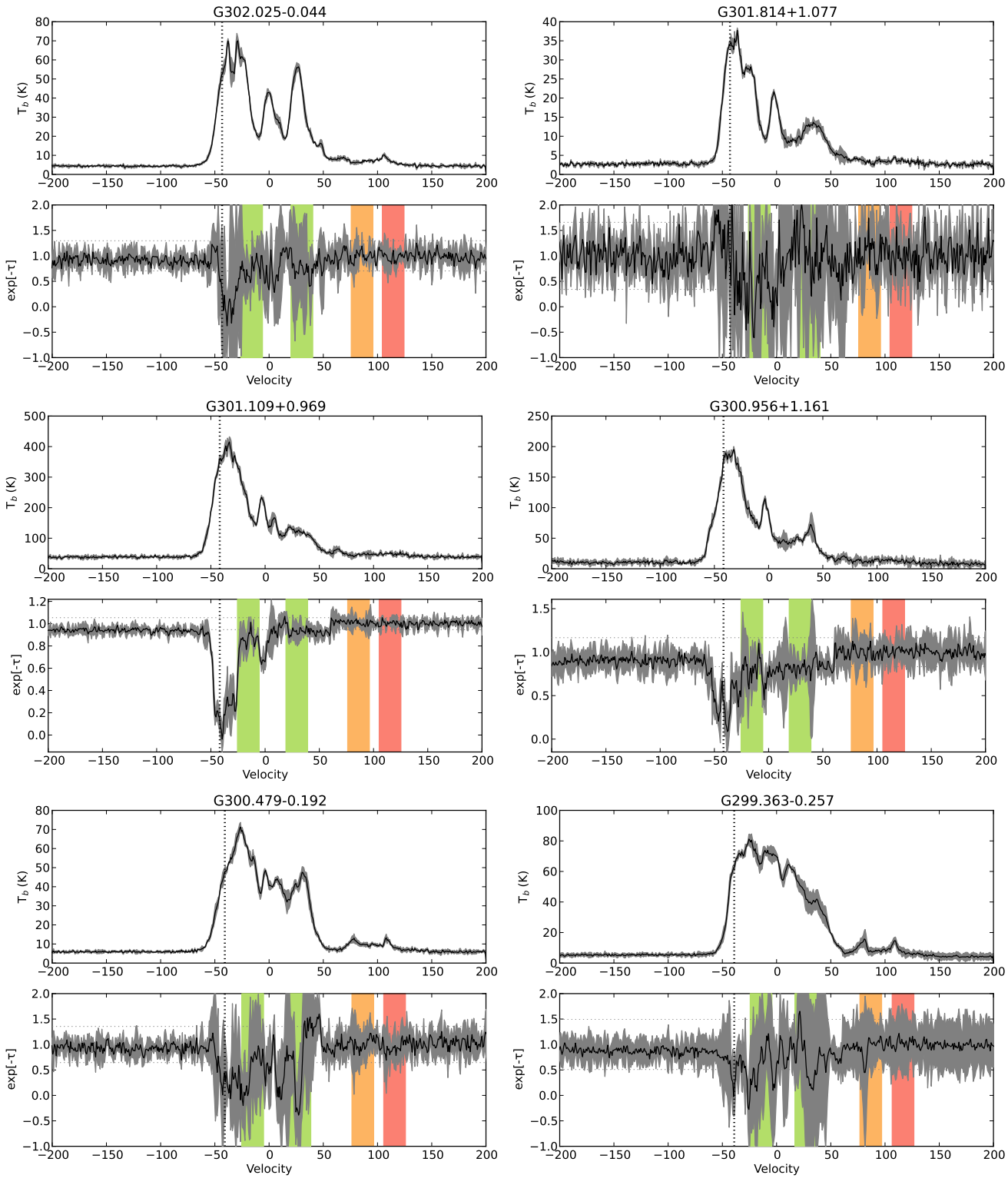
G302.025-0.044
G301.814+1.077
G301.109+0.969
G300.956+1.161
G300.479-0.192
G299.363-0.257
T_b (K)
exp[-τ]
Velocity

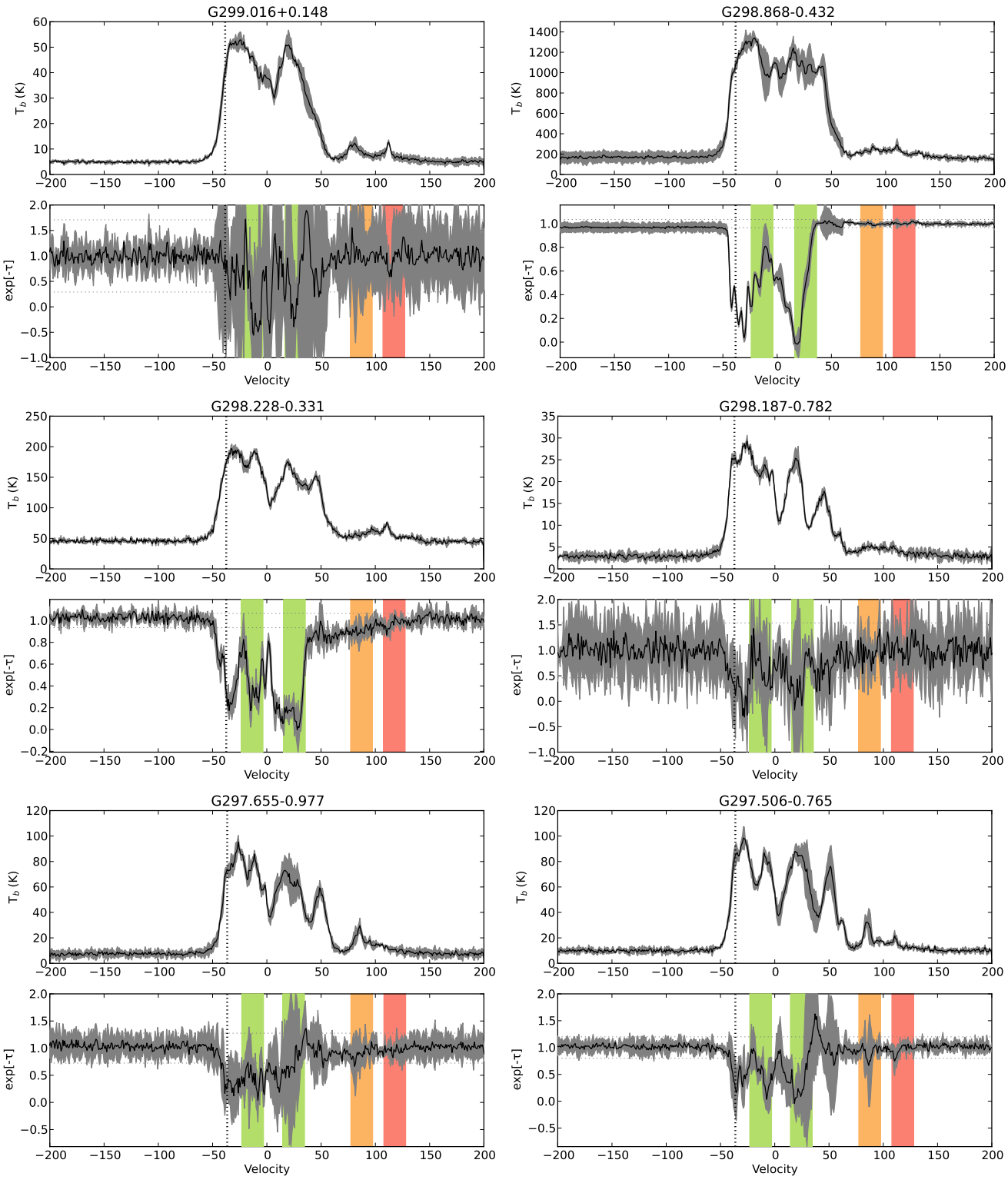
G299.016+0.148
G298.868-0.432
G298.228-0.331
G298.187-0.782
G297.655-0.977
G297.506-0.765
T_b (K)
exp[-τ]
Velocity

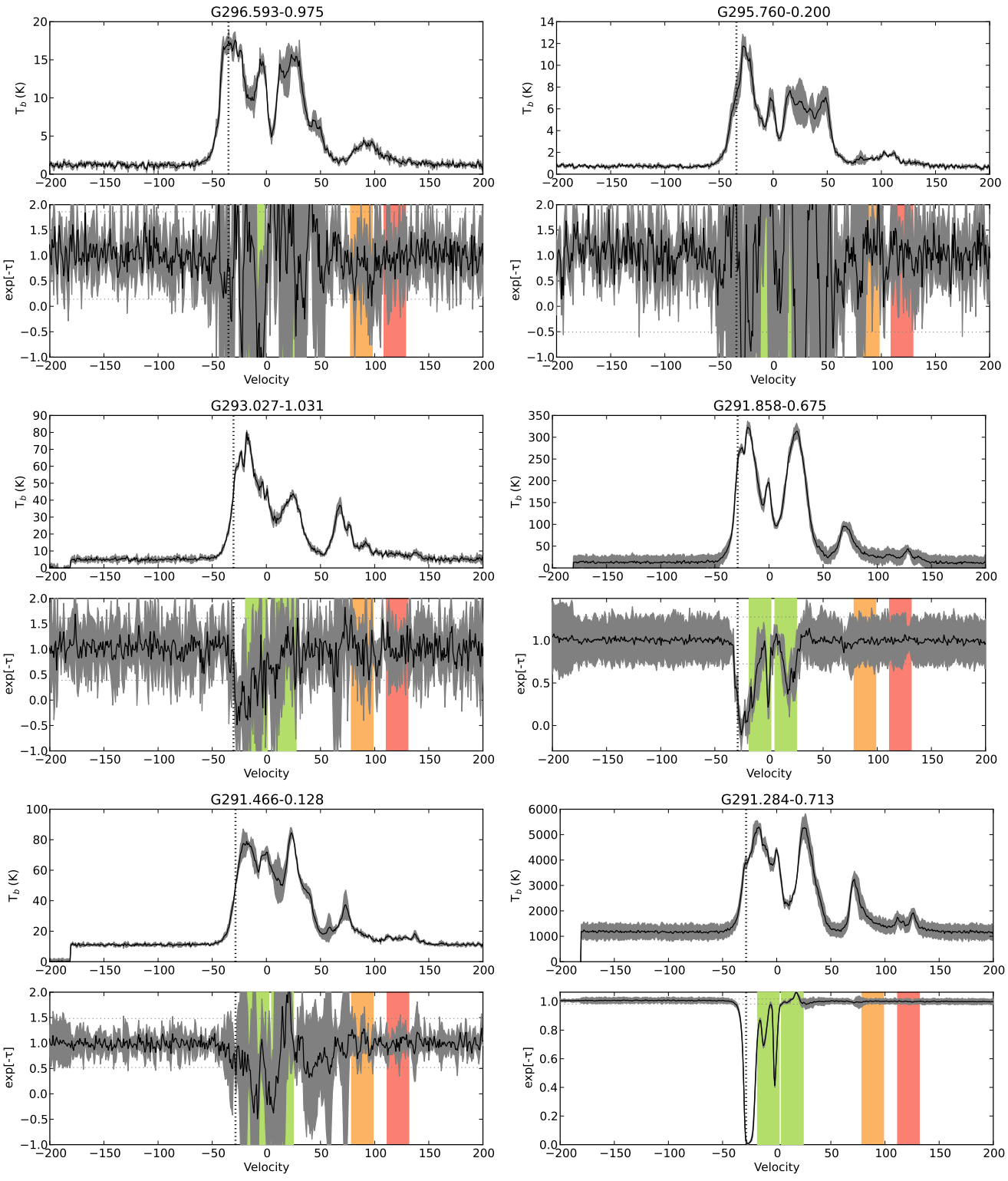
G296.593-0.975
G295.760-0.200
G293.027-1.031
G291.858-0.675
G291.466-0.128
G291.284-0.713
T_b (K)
exp[-τ]
Velocity

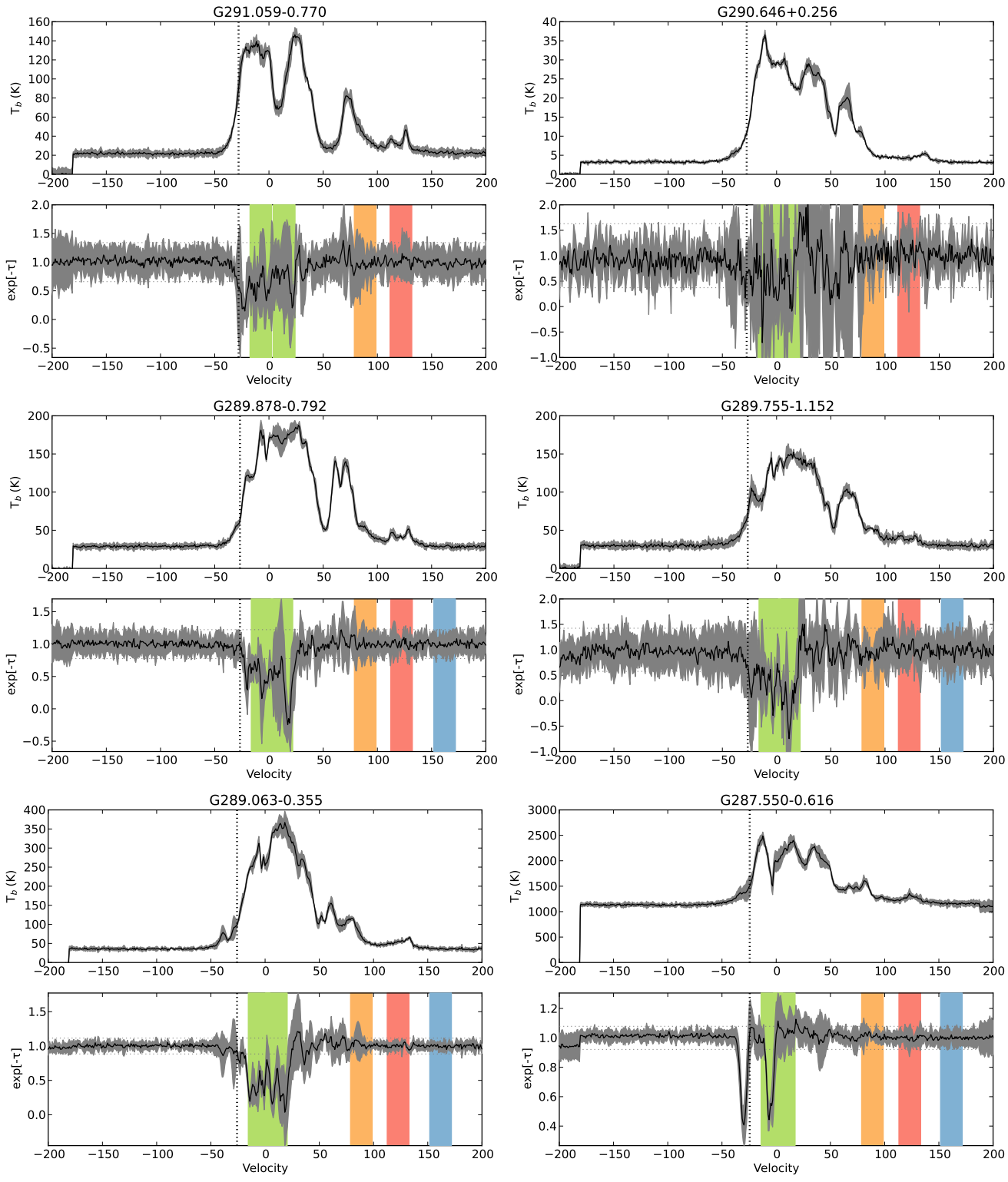
G291.059-0.770
G290.646+0.256
G289.878-0.792
G289.755-1.152
G289.063-0.355
G287.550-0.616
T_b (K)
exp[-τ]
Velocity

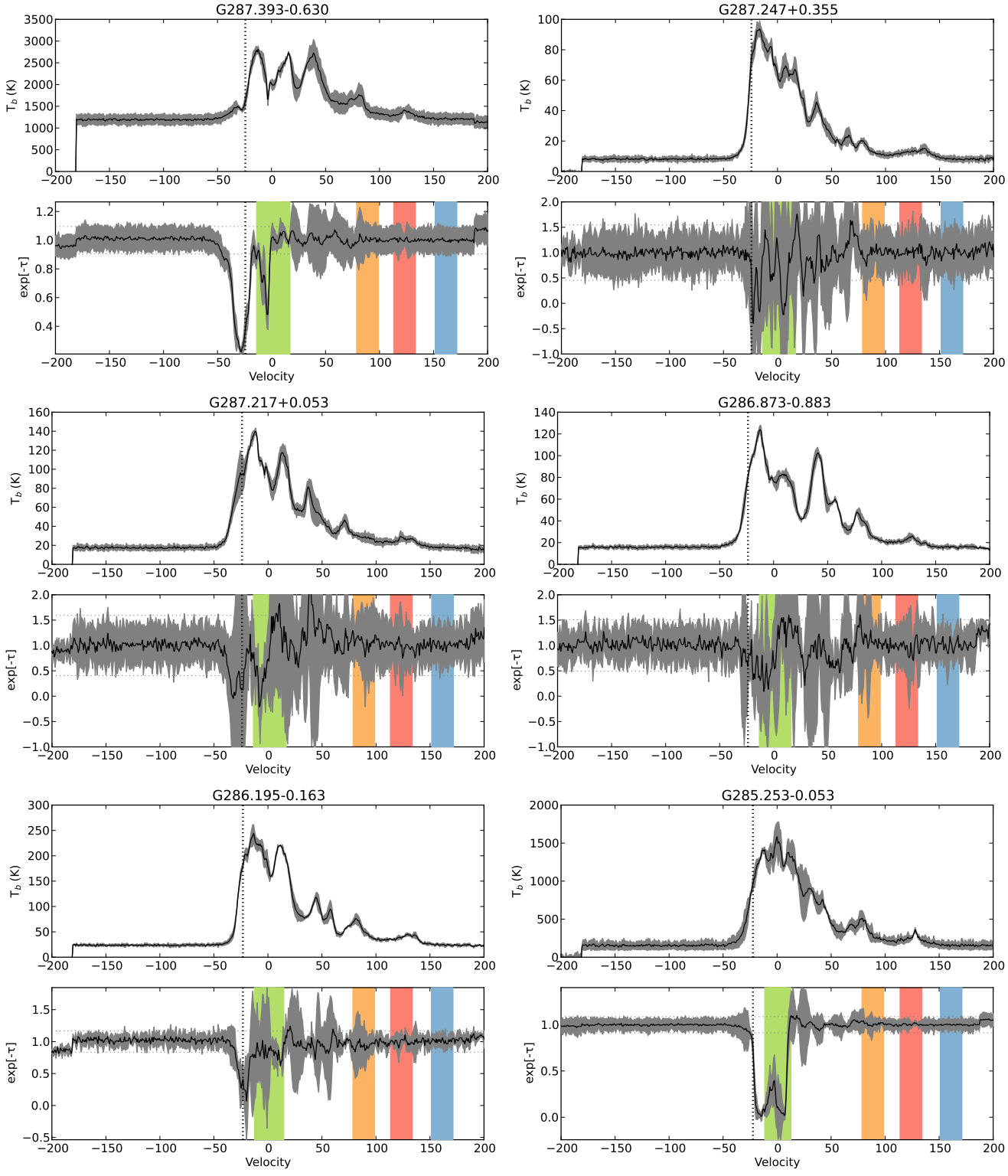
G287.393-0.630
G287.247+0.355
G287.217+0.053
G286.873-0.883
G286.195-0.163
G285.253-0.053
T_b (K)
exp[-τ]
Velocity

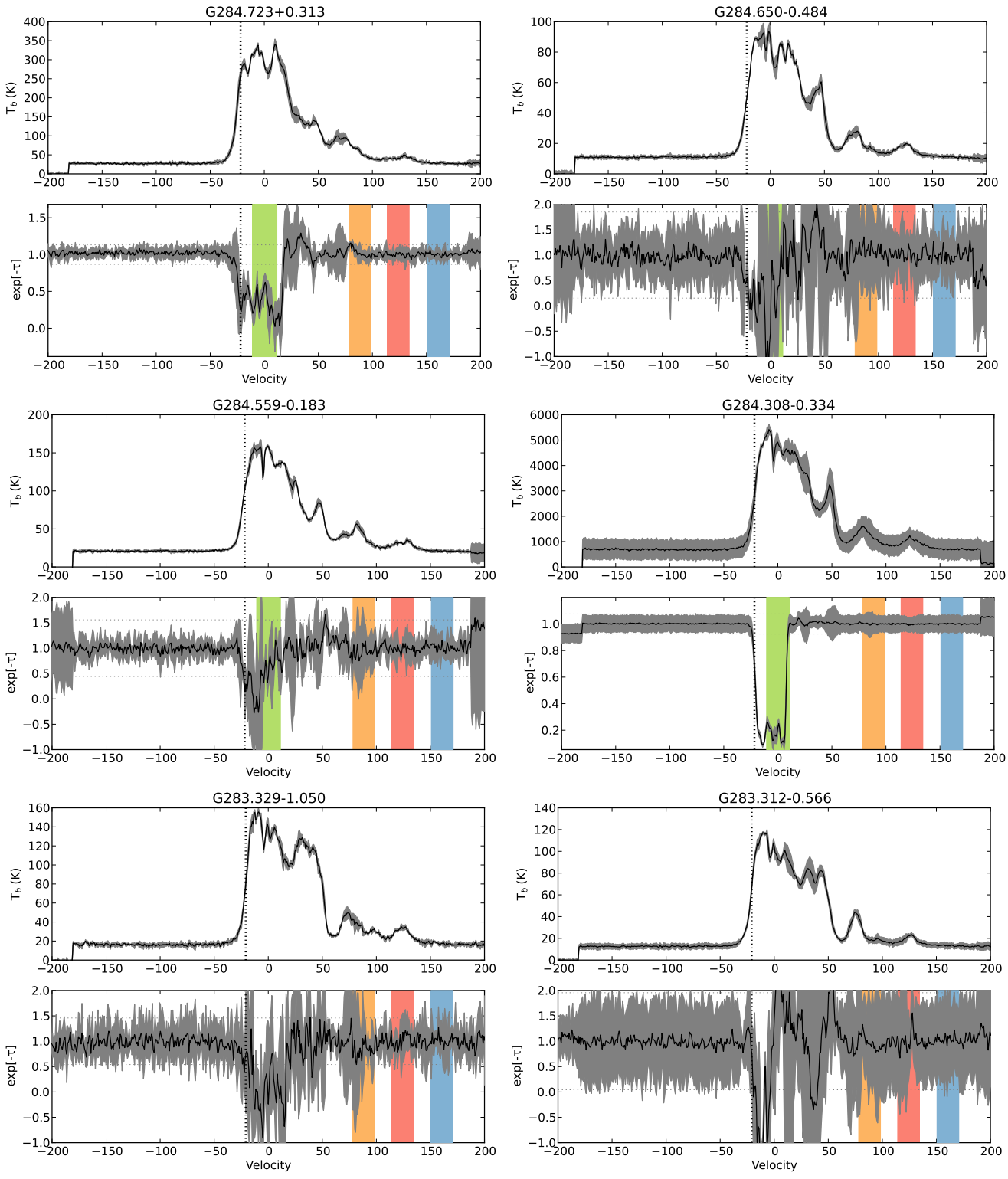
G284.723+0.313
G284.650-0.484
G284.559-0.183
G284.308-0.334
G283.329-1.050
G283.312-0.566
T_b (K)
exp[-τ]
Velocity

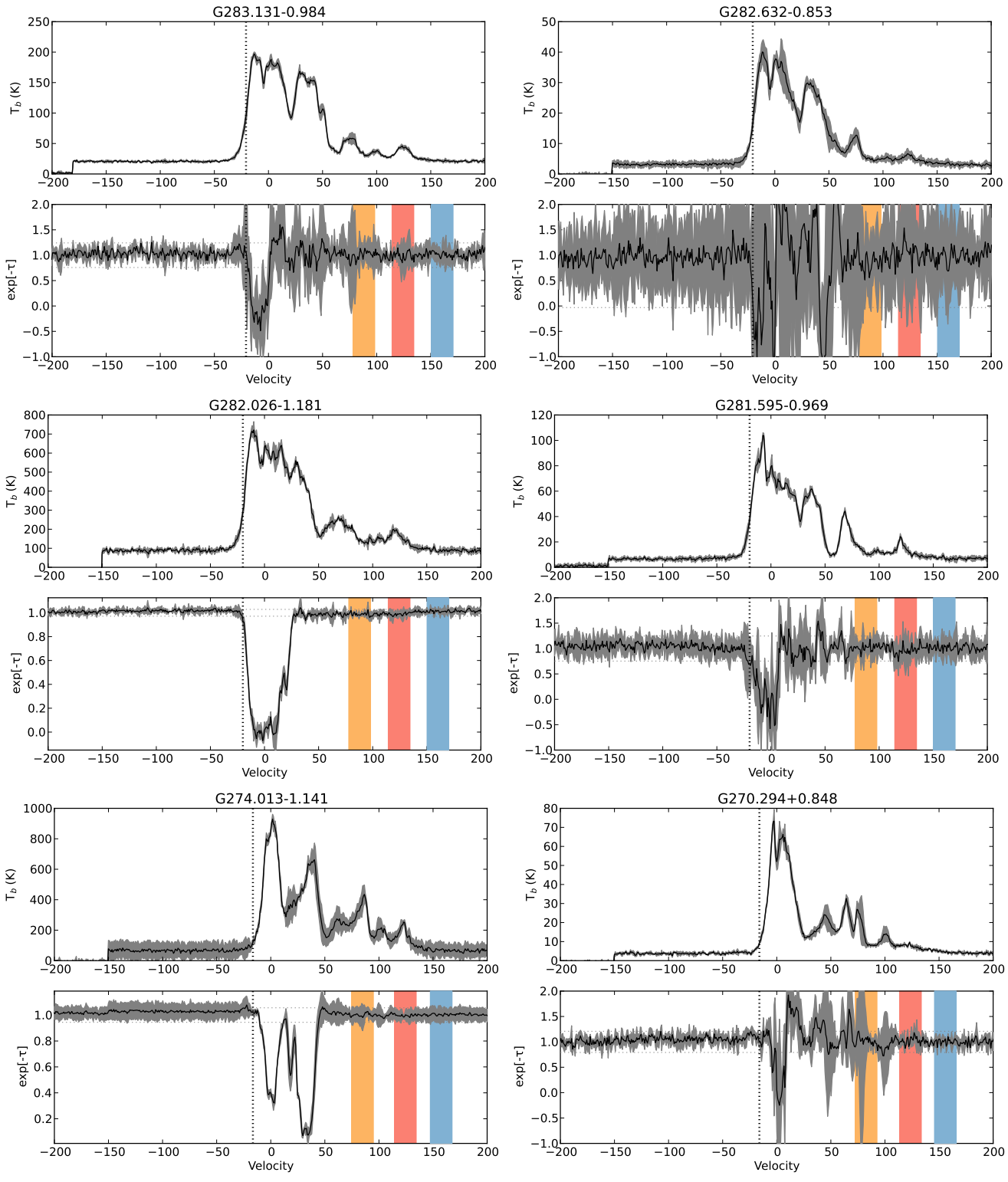
G283.131-0.984
G282.632-0.853
G282.026-1.181
G281.595-0.969
G274.013-1.141
G270.294+0.848
T_b (K)
exp[-τ]
Velocity

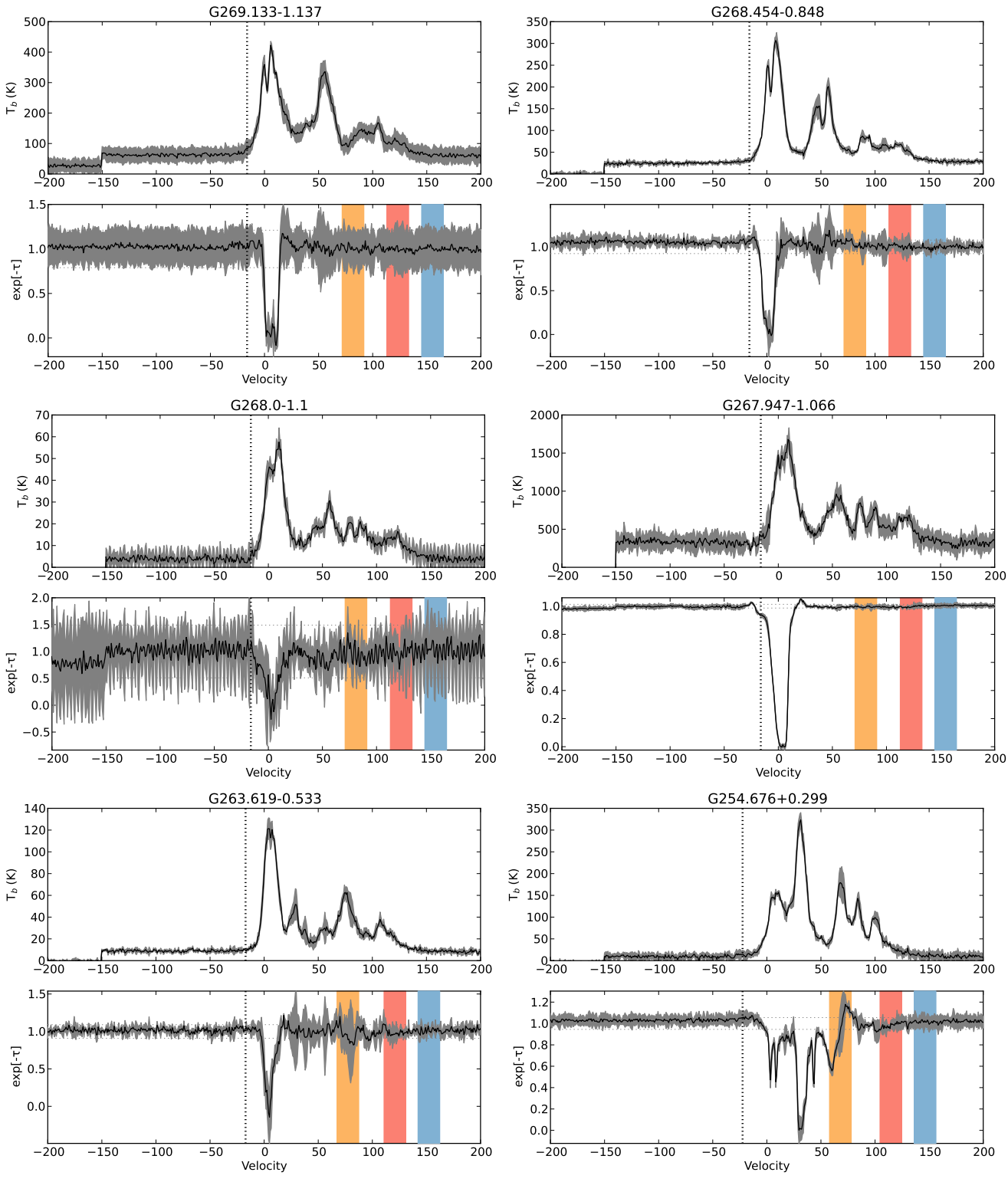
G269.133-1.137
G268.454-0.848
G268.0-1.1
G267.947-1.066
G263.619-0.533
G254.676+0.299
T_b (K)
exp[-τ]
Velocity